



**Flow Boiling and Condensation with Refrigerant
HFE-7100 for Cooling High Heat Flux Devices**

by

Ali Hameed Mumen Al-Zaidi

Supervisor: **Professor Tassos G. Karayiannis**

Department of Mechanical and Aerospace Engineering

College of Engineering, Design and Physical Sciences

Brunel University London

United Kingdom

A thesis submitted for the degree of *Doctor of Philosophy*
(*PhD*) in *Air-Conditioning and Refrigeration*

September 2019

Abstract

A continuous demand on effective miniature cooling systems for high heat flux applications encourages researchers to propose and investigate different cooling techniques. Two-phase flow in small-scale pumped loop systems is considered a promising solution for these applications. However, two-phase characteristics in micro passages are still to be resolved. Accordingly, the objectives of this study can be summarized as follows: (i) clarify the complex fundamental aspects of flow boiling and condensation in multi-microchannels, (ii) investigate the effect of heat flux, mass flux, vapour quality, channel aspect ratio and surface material on the boiling flow patterns, pressure drop and heat transfer coefficient, (iii) examine the influence of refrigerant mass flux, vapour quality and coolant side conditions on the condensation flow patterns and heat transfer coefficient, (iv) evaluate the existing flow pattern maps, pressure drop and heat transfer correlations available in the literature and (v) propose a new design of pumped loop system for cooling electronic components and compare its performance with other cooling techniques.

An experimental investigation was conducted during this study to achieve the research objectives. Three heat sinks made of copper having different channel aspect ratios ($\frac{W_{ch}}{H_{ch}} = 0.5, 1$ and 2) but the same channel hydraulic diameter (0.46 mm), base area (500 mm²) and nearly the same surface roughness (0.3 μ m) were manufactured. Another heat sink made of aluminium having channel aspect ratio of 1 was fabricated. A counter-current condenser having channel hydraulic diameter of 0.57 mm, cooled by water and made of copper, was also manufactured. HFE-7100 was chosen as a working fluid since it is suitable for electronics cooling that require surface temperature below 85 °C, such as microprocessors, IGBTs and fuel cell stacks, and considered a dielectric and eco-friendly refrigerant. Flow boiling experiments were conducted under a system pressure of 1 bar (which corresponds to a saturation temperature of 59.6 °C), inlet sub-cooling of 5 K, mass flux range of 50 – 250 kg/m²s, base heat flux range of 21.7 – 531.2 kW/m² and exit vapour quality up to one. Flow condensation experiments were performed at a system pressure of 1 bar, inlet vapour quality near superheat, refrigerant mass flux range of 48 – 126 kg/m²s, inlet water temperature range of 20 – 40 °C and water flow rate range of 0.5 – 1.1 L/min. All the two-phase flow calculations corresponding to flow visualization were

conducted locally and along the channels. A Phantom digital high-speed camera mounted on a microscope was used to capture the flow patterns inside the test section.

The flow boiling visualization showed that bubbly, slug, churn and annular flow were captured along the channels and with increasing heat flux. Confined bubble was also seen for a short period. The size of bubbles became larger and the slug ends had bullet shapes with decreasing channel aspect ratio, while no clear effect on the annular flow was found. The effect of surface material on the flow patterns was insignificant. The present flow patterns data points were not predicted well by the existing maps.

The flow boiling pressure drop was found to increase with increasing mass flux and heat flux (exit vapour quality). When the channel aspect ratio decreased, the flow boiling pressure drop increased. Aluminium surface provided higher flow boiling pressure drop compared to copper. The two-phase pressure drop correlation proposed for horizontal rectangular microchannel by Keepaiboon et al. (2016) provided a reasonable agreement with the present data with a mean absolute error $\leq 20\%$.

The flow boiling heat transfer results indicated that the local and average heat transfer coefficient increased with heat flux. Higher local heat transfer coefficient was reached at boiling incipience and then decreased with local vapour quality. In contrast, for a given heat flux, insignificant effect of mass flux was found. A noticeable increase in the heat transfer coefficient was found with increasing the aspect ratio. At low heat fluxes, the material effect was insignificant. However, at moderate and high heat fluxes, aluminium surface showed higher heat transfer coefficient than copper. The two-phase flow heat transfer correlation by Shah (2017) showed the best prediction of all present data with a mean absolute error of 15–22%.

The condensation flow visualization indicated that annular, slug and bubbly flow were visualized along the channels. Neck region was also captured as a transition from annular to slug flow. There was no existing flow patterns map that can predict all the data points of the present study.

The local condensation heat transfer coefficient increased with increasing refrigerant mass flux and local vapour quality. The effect of coolant side conditions was negligible. The correlation by Cavallini et al. (2006a), for conventional channels, predicted the data with a mean absolute error of 11%. The mini/microchannels heat transfer correlations by Kim and Mudawar (2013c) and Shah (2016) predicted the experimental data with a mean absolute error of 15–16%.

The proposed pumped loop system was more efficient, *i.e.* higher cooling load and lower pumping power, than other cooling techniques. In this system, lower pumping power was required due to the low mass flow (high latent heat of vaporization). Maximum cooling load was reached up to 265 W using microchannel evaporator having channel aspect ratio of 0.5. The working surface temperature was controlled near 80 °C. Maximum cooling load at the condenser was found to be 520.2 W at outlet sub-cooling of 3.5 K, coolant flow rate of 0.5 L/min and inlet coolant temperature of 30 °C. A microchannel evaporator having large surface enhancement, *i.e.* deeper channels and large number of channels, made of aluminium could be a suitable design for cooling electronic components that require high cooling loads.

Declaration

The present study is the original work of the author except where otherwise specified, or where acknowledgements are made by references. This research was performed at the Department of Mechanical and Aerospace Engineering, Brunel University London, under the supervision of Prof. T.G. Karayiannis and Prof. L.C. Wrobel.

The work has not been submitted for another degree or award to any other institution.

Signed: Date:

by

Ali Hameed Mumun Al-Zaidi

Acknowledgments

First of all, I would like to acknowledge the Iraqi Ministry of Higher Education and Scientific Research (MOHESR), Iraqi Cultural Attaché and University of Misan in Iraq for granting me a fully funded scholarship during my study.

I would like to express my gratitude to my supervisor Professor T.G. Karayiannis for his support, encouragement and guidance throughout this work. Without his fruitful comments and discussions through very regular research meetings, this work would not have been possible. I would also like to thank Dr. M.M. Mahmoud for his useful comments and advice during this work. His valuable knowledge about the experimental facility helped me to complete my study. I am grateful to my second supervisor Professor L.C. Wrobel for his support.

I am grateful to the technicians Mr. Costas Xanthos and Mr. Paul Yates for their help and support in the preparation of the experimental facility and manufacture of the examined test sections.

Finally, I would like to express my sincere gratitude to my parents, family and friends for their support and encouragement during this study.

Contents

Abstract	ii
Declaration	v
Acknowledgments	vi
Contents	vii
List of Figures	xvi
List of Tables	xxxii
Nomenclature	xxxiv
Dimensionless Groups	xl
1. Introduction	1
1.1. Background and Motivation	1
1.2. Research Objectives	12
1.3. Summary of Methodology	13
1.4. Thesis Structure	14
2. Literature Review	16
2.1. Introduction	16
2.2. Definition of Micro and Macro Scale	16
2.3. HFE-7100 for Cooling High Heat Flux Devices	21
2.4. Boiling Incipience in Channels	26
2.4.1. Flow patterns in conventional and microchannels	27
2.4.1.1. Flow patterns in horizontal and vertical channels	27
2.4.1.2. Flow patterns in different channel dimensions	30
2.4.1.3. Flow patterns in a horizontal single channel	33
2.4.1.4. Flow patterns in multi-channels	34
2.4.1.5. Nucleation in the liquid film	39

2.4.1.6. Effect of channel aspect ratio on flow patterns	41
2.4.1.7. Effect of channel surface material on flow patterns	43
2.4.2. Flow Pattern Maps	44
2.4.3. Flow Boiling Pressure Drop	52
2.4.3.1. Effect of heat flux	52
2.4.3.2. Effect of mass flux	54
2.4.3.3. Effect of channel aspect ratio	54
2.4.3.4. Effect of channel surface material	57
2.4.4. Flow Boiling Pressure Drop Correlations	58
2.4.4.1. Conventional channel correlations	58
2.4.4.2. Mini/microchannel correlations	59
2.4.5. Flow Boiling Heat Transfer Characteristics	61
2.4.5.1. Heat transfer mechanism(s)	61
2.4.5.2. Effect of channel aspect ratio	72
2.4.5.3. Effect of channel surface material	76
2.4.6. Flow Boiling Heat Transfer Correlations	85
2.4.6.1. Conventional channel correlations	89
2.4.6.2. Mini/microchannel correlations	90
2.4.7. Flow Boiling Instability	94
2.5. Flow Condensation in channels	97
2.5.1. Flow patterns in conventional and microchannels	98
2.5.2. Flow pattern maps	104
2.5.3. Flow condensation pressure drop	108
2.5.3.1. Effect of mass flux and vapour quality	109
2.5.3.2. Effect of saturation temperature	110

2.5.4. Flow condensation heat transfer	110
2.5.4.1. Effect of refrigerant mass flux and vapour quality	110
2.5.4.2. Effect of saturation temperature	114
2.5.4.3. Effect of channel geometry	115
2.5.4.4. Effect of coolant side	116
2.5.5. Flow condensation heat transfer correlations	118
2.5.5.1. Conventional channel correlations	119
2.5.5.2. Mini/microchannel correlations	119
2.6. Summary and Conclusions	122
3. Experimental Facility and Methodology	129
3.1. Introduction	129
3.2. Experimental Facility	129
3.2.1 An auxiliary cooling loop	132
3.2.2 Main reservoir	133
3.2.3 Sub-cooler	134
3.2.4 Micro-gear pump	135
3.2.5 Coriolis and turbine flow meters	135
3.2.6 Electric pre-heater	136
3.2.7 Pressure transducers	137
3.2.8 Thermocouples	138
3.2.9 Power meter	139
3.2.10 Variable autotransformers	139
3.2.11 Visualization system	139
3.2.12 Data acquisition system (DAQ)	140
3.2.13 Software	141

3.3. Microchannel Test Sections	142
3.3.1. Microchannel evaporator	143
3.3.2. Microchannel condenser	147
3.3.3. Surface analysis	150
3.4. Calibration Process	153
3.4.1. Thermocouple calibration	154
3.4.2. Pressure transducer calibration	155
3.5. Data Reduction	156
3.5.1. Microchannel evaporator	157
3.5.1.1. Single-phase data reduction	157
3.5.1.2. Flow boiling data reduction	160
3.5.1.3. Flow pattern map data reduction	163
3.5.2. Microchannel condenser	164
3.5.2.1. Single-phase data reduction	164
3.5.2.2. Flow condensation data reduction	165
3.6. Propagated Uncertainty Analysis	166
3.7. Experimental Procedure	173
3.7.1. Preparation for experiments	173
3.7.2. Single-phase experiments	174
3.7.3. Flow boiling experiments	176
3.7.4. Flow condensation experiments	177
3.8. Experimental Test Conditions	178
3.9. Overall Validation	179
3.9.1. Temperature and heat flux distribution	180
3.9.2. Single-phase validation	186

3.10. Repeatability of the Data	193
3.11. Summary	195
4. Flow Boiling Patterns: Results and Discussion	196
4.1. Introduction	196
4.2. Experimental Flow Visualization Patterns	196
4.3. Experimental Flow Pattern Maps	204
4.4. Effect of Heat Flux	205
4.5. Effect of Mass Flux	210
4.6. Effect of Channel Aspect Ratio	212
4.7. Effect of Channel Surface Material	216
4.8. Comparison with Existing Flow Pattern Maps	218
4.8.1. Flow patterns map by Akbar et al. (2003)	218
4.8.2. Flow patterns map by Revellin and Thome (2007a)	220
4.8.3. Flow patterns map by Harirchian and Garimella (2010)	221
4.8.4. Flow patterns map by Mahmoud and Karayiannis (2016a)	223
4.8.5. Flow patterns map by Choi et al. (2017)	224
4.8.6. Flow patterns map by Li and Hrnjak (2019)	226
4.9. Summary	229
5. Flow Boiling Pressure Drop: Results and Discussion	231
5.1. Introduction	231
5.2. Effect of Heat Flux	232
5.3. Effect of Mass Flux	233
5.4. Effect of Channel Aspect Ratio	235
5.5. Effect of Channel Surface Material	238
5.6. Comparison with Existing Correlations	241

5.6.1. Conventional scale two-phase pressure drop correlations	242
5.6.1.1. The correlation of Lockhart-Martinelli (1949)	242
5.6.1.2. The Homogenous flow model (1994)	244
5.6.2. Mini/micro-scale two-phase pressure drop correlations	245
5.6.2.1. The correlation of Qu and Mudawar (2003b)	245
5.6.2.2. The correlation of Lee and Garimella (2008)	246
5.6.2.3. The correlation of Keepaiboon et al. (2016)	248
5.6.2.4. The correlation of Huang and Thome (2017)	249
5.6.2.5. The correlation of Markal et al. (2017b)	251
5.6.2.6. The correlation of Gao et al. (2019)	252
5.7. Summary	257
6. Flow Boiling Heat Transfer: Results and Discussion	258
6.1. Introduction	258
6.2. Flow Boiling Incipience	259
6.3. Flow Boiling Instability	266
6.4. Flow Boiling Heat Transfer Results	274
6.4.1. Effect of heat Flux	274
6.4.2. Effect of mass flux	278
6.4.3. Effect of channel aspect ratio	280
6.4.4. Effect of channel surface material	287
6.5. Force analysis	294
6.6. Comparison with Existing Correlations	298
6.5.1. Conventional scale flow boiling heat transfer correlations	299
6.5.1.1. The correlation of Shah (1982)	299
6.5.1.2. The correlation of Kandlikar (1990)	301

6.5.1.3. The correlation of Liu and Winterton (1991)	302
6.5.2. Mini/micro-scale flow boiling heat transfer correlations	303
6.5.2.1. The correlation of Warriier et al. (2002)	303
6.5.2.2. The correlation of Lee and Mudawar (2005)	304
6.5.2.3. The correlation of Mahmoud and Karayiannis (2013)	305
6.5.2.4. The correlation of Li and Jia (2015)	307
6.5.2.5. The correlation of Lim et al. (2015)	308
6.5.2.6. The correlation of Thiangtham et al. (2016)	310
6.5.2.7. The correlation of Markal et al. (2017a)	311
6.5.2.8. The correlation of Shah (2017)	312
6.5.2.9. The correlation of Wen et al. (2019)	314
6.7. Summary	317
7. Condensation Flow Patterns: Results and Discussion	320
7.1. Introduction	320
7.2. Experimental Flow Visualization Patterns	320
7.3. Experimental Flow Pattern Maps	323
7.4. Effect of Refrigerant Mass Flux	325
7.5. Effect of Coolant Conditions	326
7.6. Comparison with Existing Flow Pattern Maps	327
7.6.1. Flow patterns map by Cavallini et al. (2002)	327
7.6.2. Flow patterns map by Kim and Mudawar (2012)	328
7.6.3. Flow patterns map by Nema et al. (2014)	329
7.6.4. Flow patterns map by Zhuang et al. (2017)	330
7.7. Summary	331

8. Flow Condensation Heat Transfer: Results and Discussion	333
8.1. Introduction	333
8.2. Effect of Refrigerant Mass Flux	333
8.3. Effect of Coolant Conditions	335
8.4. Comparison with Existing Correlations	337
8.4.1. Conventional scale flow condensation heat transfer correlations	338
8.4.1.1. The correlation of Shah (1979)	338
8.4.1.2. The correlation of Dobson and Chato (1998)	339
8.4.1.3. The correlation of Cavallini et al. (2006a)	340
8.4.2. Mini/micro-scale flow condensation heat transfer correlations	341
8.4.2.1. The correlation of Wang et al. (2002)	341
8.4.2.2. The correlation of Koyama et al. (2003b)	342
8.4.2.3. The correlation of Bohdal et al. (2011)	342
8.4.2.4. The correlation of Park et al. (2011)	343
8.4.2.5. The correlation of Kim and Mudawar (2013c)	344
8.4.2.6. The correlation of Shah (2016)	345
8.4.2.7. The correlation of Rahman et al. (2018)	346
8.5. Summary	348
9. Small-scale Thermal Management System	350
9.1. Introduction	350
9.2. Pumping Power	350
9.3. Comparison with other Cooling Techniques	353
9.4. Upper Cooling Performance	359
9.5. Summary	359

10. Conclusions and Recommendations	360
10.1. Conclusions	360
10.1.1. Flow boiling pattern characteristics	361
10.1.2. Flow boiling pressure drop characteristics	362
10.1.3. Flow boiling heat transfer characteristics	363
10.1.4. Condensation flow pattern characteristics	365
10.1.5. Flow condensation heat transfer characteristics	366
10.1.6. Small-scale thermal management system	367
10.2. Summary of Novel Contributions	369
10.3. Recommendations	370
References	371
Appendix A	391
Appendix B	394
Appendix C	398
Appendix D	401
Appendix E	407
Publications	409

List of Figures

Fig.		Page
1.1	Heat flux for various applications.	2
1.2	Photograph of CPUs liquid cooling system: (a) Loop parts of Liquid Freezer 360, adapted from ARCTIC (2016) (b) Different cold plates, adapted from Mr3D (2011).	3
1.3	Computer data centre: (a) Photograph of Summit, Gottschalk (2018) (b) Photograph of power AC922 server and (c) Schematic diagram of cooling loop for one server, Vetter et al. (2019).	4
1.4	Schematic diagram of: (a) Miniature vapour compression refrigeration and (b) Microchannel evaporator, adapted from Poachaiyapoom et al. (2019).	5
1.5	Lithium-ion battery pack: (a) Tesla Model (S) battery module, Tesla (2017) (b) Coolant loop in one module, Nilsson (2017).	6
1.6	Schematic description of: (a) Mirai car, Toyota UK (2018) (b) Cooling channels in single fuel cell, Choi et al. (2018).	7
1.7	Rocket engine: (a) Photograph of Vulcain 2 European rocket engine and (b) Fluid/Cooling loop, Safran (2011) (c) Cut of the Vulcain chamber wall (cooling channels), Pizzarelli (2017).	7
1.8	Fusion reactor: (a) International Thermonuclear Experimental Reactor (ITER), Kaita (2018) (b) Helium cooled first wall, Abdou et al. (2001).	8
1.9	Two-phase flow in small-scale pumped loop cooling system for electronics: (a) System loop (b) Exploded drawing of multi-microchannel evaporator.	9
2.1	Threshold diameter from macro to micro scale based on a number of criteria compared to the present hydraulic diameter in [mm].	20
2.2	Different channel geometries using flow boiling of HFE-7100: (a) Saw-teeth channels, Fu et al. (2017) (b) Integrated channels, Li et al. (2018) (c) Straight channels, Hsu et al. (2015) (d) Diverging channels, Fu et al. (2013).	23

2.3	Flow boiling of HFE-7100 using hybrid cooling module, Sung and Mudawar (2009b).	24
2.4	Maximum heat flux reported in the literature using flow boiling of HFE-refrigerants in multi-channels.	24
2.5	Flow patterns in large vertical upwards flow and horizontal channels, Collier and Thome (1994). B: bubbly, S: slug, C: churn, WA: wispy-annular, A: annular, P: plug, St: stratified, W: wavy.	28
2.6	Two-phase flow patterns in horizontal channels, Kawaji and Chung (2004): (a) Minichannel (b) Microchannel.	30
2.7	Flow patterns of R134a in vertical small tubes at system pressure of 10 bar with inner diameter of (a) 1.1 mm, (b) 4.26 mm, Chen et al. (2006). D.B: dispersed bubble, B: bubbly, C.B: confined bubble, S: slug, C: churn, A: annular, M: mist.	31
2.8	Flow patterns of HFE-7000 in a vertical tube at mass flux of 100 kg/m ² s and heat flux of: (a) 8.8 (b) 20.3 (c) 35.7 (d) 51.4 (e) 61.7 kW/m ² , Eraghubi et al. (2019).	32
2.9	Flow patterns of water in a horizontal microchannel at different heat fluxes and mass flow rate of 0.2 ml/min, Singh et al. (2009).	33
2.10	Flow patterns of R245fa in horizontal tube of 0.5 mm diameter at G=500 kg/m ² s and saturation temperature of 35 C, Revellin and Thome (2007b).	34
2.11	Flow patterns of FC-77 in horizontal multi-microchannels, Harirchian and Garimella (2009a). Labels introduced by present author based on their description.	35
2.12	Flow patterns of de-ionized water in horizontal multi-microchannels at different mass and heat fluxes, Balasubramanian et al. (2013).	36
2.13	Flow patterns of R134a in horizontal multi-microchannels at saturation temperature of 13 °C, mass flux of 150 kg/m ² s and different heat fluxes, Thiangtham et al. (2016).	37
2.14	Flow patterns of R134a in horizontal multi-microchannels at mass flux of 50 kg/m ² s and different heat fluxes, Fayyadh et al.	38

	(2017). Labels introduced by present author.	
2.15	Flow patterns of HFE-7100 in vertical multi-channels at mass flux of 200 kg/m ² s and heat flux of: (a) 13.2 (b) 24.8 (c) 40.6 (d) 59.7 (e) 71.9 kW/m ² , Choi et al. (2019). Labels introduced by present author.	39
2.16	Nucleating bubbles during plug flow in vertical down-flow, Kandlikar and Balasubramanian (2005). Label introduced by present author.	40
2.17	Nucleating bubbles in the liquid film of wispy-annular flow, Harirchian and Garimella (2009a).	40
2.18	Nucleating bubble in the liquid film of annular flow, Borhani and Thome (2014).	40
2.19	Nucleating bubble in the liquid film of annular flow, Fayyadh et al. (2017).	41
2.20	Flow patterns map in circular and near-circular channels ($D_h \leq 1$ mm), Akbar et al. (2003).	45
2.21	Flow patterns map for R134a in horizontal single tube (D=0.509 mm) and inlet sub-cooling of 3 °C, Revellin and Thome (2007a).	46
2.22	Flow patterns map for FC-77 in horizontal multi-microchannels, Harirchian and Garimella (2010).	47
2.23	Flow patterns map for R134a in horizontal channels with different diameters, Ong and Thome (2011a).	48
2.24	Flow patterns map for R245fa in vertical tube, proposed by Chen (2006) and modified by Mahmoud and Karayiannis (2016a).	50
2.25	Flow patterns map for FC-72 in horizontal multi-microchannels, Choi et al. (2017).	51
2.26	Flow patterns map of R32 at saturation temperature of 30 °C, Li and Hrnjak (2019).	51
2.27	Schematic diagram of different heat transfer mechanisms in flow boiling using small and micro channels, Karayiannis and Mahmoud (2017). This figure is re-drawn by the present author.	62
2.28	Surface roughness parameters.	76

2.29	Different surface structures having the same average roughness, Kandlikar and Spiesman (1997) [taken from Pike-Wilson and Karayiannis (2014)].	77
2.30	SEM images of different surface microstructures reported in the literature.	79
2.31	Different forces acting on a liquid–vapour interface of growing bubble in microchannels. Similar figure was presented by Alam et al. (2016).	87
2.32	Photograph of serrated fins multi-channels with 1.28 mm hydraulic diameter, Wen et al. (2019).	93
2.33	Several techniques were adopted by the past studies to overcome flow boiling instabilities. (T) Top view (S) Side view.	97
2.34	Condensation flow patterns classification by Coleman and Garimella (2003).	98
2.35	Flow patterns of FC-72 predicted by simulation study at mass flux of $68 \text{ kg/m}^2\text{s}$, Chen et al. (2014).	100
2.36	Flow Patterns of steam: (a) Annular, $G=188.13 \text{ kg/m}^2\text{s}$ (b) Droplet, $G=179.62 \text{ kg/m}^2\text{s}$ (c) Injection, $G=179.62 \text{ kg/m}^2\text{s}$ (d) Bubble, $G=143.04 \text{ kg/m}^2\text{s}$, Ma et al. (2011).	102
2.37	Flow patterns of FC-72 at mass flux of $68 \text{ kg/m}^2\text{s}$ and coolant mass flow rate of 6 g/s , Kim et al. (2012).	103
2.38	Flow patterns of ethanol–water at ethanol concentration of 20%, Jiang et al. (2015).	103
2.39	Flow patterns map proposed by Cavallini et al. (2002).	104
2.40	Two-phase flow patterns map of FC-72 and 639 data points from different sources proposed by Kim and Mudawar (2012).	105
2.41	Two-phase flow patterns map at different inlet ethanol concentrations proposed by Jiang et al. (2017), W_{in} is the inlet ethanol concentrations.	107
2.42	Condensation flow patterns of R50, Zhuang et al. (2017): (a) Smooth-annular (b) Wavy-annular (c) Transition (d) Slug (e) Plug.	107
2.43	Condensation flow patterns map of R50 proposed by Zhuang et	108

	al. (2017).	
2.44	Different channel geometries, Agarwal et al. (2010).	112
2.45	Photograph of the rectangular multi-channels with and without fins, Rahman et al. (2018).	113
3.1	Schematic diagram of the experimental facility for flow boiling experiments.	130
3.2	Schematic diagram of the experimental facility for flow condensation experiments.	131
3.3	Photograph of the test rig: (a) Flow boiling experiments (b) Flow condensation experiments.	132
3.4	Photograph of the chiller system.	133
3.5	Photograph of the liquid reservoir and the reflux condenser.	134
3.6	Photograph of the Sub-cooler.	134
3.7	Photograph of Cole-Parmer gear pump.	135
3.8	Photograph of (a) Coriolis flow meters, model KROHNE Optimass 3300C S01 (b) Omega turbine flow meter, model FLR1000 ST-I.	136
3.9	Photograph of the pre-heater.	137
3.10	Photograph of (a) Pressure transducer (Omega PX209-100A5V) (b) Differential pressure transducer (Omega PX409-005DWUI).	138
3.11	Photograph of a thermocouple: (a) T-type (source: www.omega.co.uk) (b) K-type (source: www.labfacility.com).	138
3.12	Photograph of power meter.	139
3.13	Photograph of visualization system.	140
3.14	Photograph of DAQ system.	141
3.15	Test section construction, microchannel evaporator: (a) Photograph (b) Overall assembly (c) Exploded drawing.	144
3.16	Heat sink block: (a) Dimensions in mm (b) Block parts (c) Photograph of TS.2 (copper) and TS.4 (aluminium).	145
3.17	Schematic diagram of the measuring instruments (top view).	147

3.18	Test section construction, microchannel condenser: (a) Photograph (b) Exploded drawing.	148
3.19	Photograph of the condenser block.	149
3.20	Condenser block details; dimensions in mm.	149
3.21	Roughness values and surface characteristics for TS.1.	151
3.22	Topography images from SEM at a magnification of 400 for: (a) Copper (TS.2) (b) Aluminium (TS.4).	152
3.23	Topography images from SEM for copper (TS.2) at a magnification of: (a) 2000 and (b) 5000.	153
3.24	Topography images from SEM for aluminium (TS.4) at a magnification of: (a) 2000 and (b) 5000.	153
3.25	Photograph of the thermocouple calibration bath equipment.	155
3.26	Photograph of the dead-weight tester.	156
3.27	Pressure losses in the test section.	158
3.28	Flow boiling regions along the channel.	160
3.29	Thermal element of the condenser.	165
3.30	Flow boiling along the test section.	181
3.31	Contours of temperature and heat flux distribution for TS.1: (a) Temperature in the heat sink block (b) Temperature in the heat sink (c) Heat flux in the heat sink. The scale of (b and c) is changed to clarify the contour distribution.	182
3.32	Heat losses at the inlet and outlet plena for TS.1.	184
3.33	Temperature distribution in the axial direction during single-phase flow for TS.3.	184
3.34	Temperature distribution during two-phase flow for TS.3 at mass flux of (a) 200 kg/m ² s (b) 250 kg/m ² s.	185
3.35	Single-phase Fanning friction factor versus Reynolds number for: (a) TS.1 (b) TS.2 (c) TS.3 (d) TS.4 (e) TS.5.	187
3.36	Single-phase average Nusselt number versus Reynolds number for: (a) TS.1 (b) TS.2 (c) TS.3 (d) TS.4 (e) TS.5.	191

3.37	Repeatability of the experimental flow boiling heat transfer data for: (a) TS.1 (b) TS.2 (c) TS.3 (d) TS.4.	194
3.38	Repeatability of the experimental flow condensation heat transfer data at mass flux of 126 kg/m ² s, inlet coolant temperature of 40 °C and coolant flow rate of 1.1 L/min for the test section (5).	195
4.1	Camera location along the heat sink during flow boiling experiments.	197
4.2	Experimental flow visualization patterns along TS.3 corresponding to the local vapour quality at mass flux of 50 kg/m ² s and wall heat flux of: (a) 29.2 kW/m ² (b) 36 kW/m ² .	198
4.3	Nucleating bubble over a surface cavity, obtained from Kandlikar (2006).	199
4.4	Flow boiling structure observed in this study.	200
4.5	Sequence of pictures of flow reversal cycle for TS.3 at wall heat flux of 114.8 kW/m ² and mass flux of 250 kg/m ² s (between channel inlet and middle), yellow arrow indicates forward motion and blue backward motion.	201
4.6	Sequence of pictures of bubble growth for TS.3 at wall heat flux of 29.2 kW/m ² and mass flux of 50 kg/m ² s.	203
4.7	Experimental flow pattern maps at system pressure of 1 bar, inlet sub-cooling of 5 K, wall heat flux of 9.6–191.6 kW/m ² and mass flux of 50–250 kg/m ² s for: (a) TS.1 (b) TS.2 (c) TS.3 (d) TS.4.	205
4.8	Effect of heat flux on the bubble flow for TS.3 at mass flux of 50 kg/m ² s, corresponding to the local vapour quality, near the channel inlet and two wall heat fluxes of: (a) 29.2 kW/m ² (b) 58.2 kW/m ² .	206
4.9	Effect of heat flux on the flow patterns for TS.3 at mass flux of 150 kg/m ² s, corresponding to the local vapour quality, near the channel middle and three wall heat fluxes of: (a) 30.4 kW/m ² (b) 58.3 kW/m ² (c) 113.1 kW/m ² .	207
4.10	Effect of heat flux on the histogram of flow patterns for TS.1 at mass flux of 100 kg/m ² s and three different locations along the channels.	208

4.11	Flow patterns for TS.3 at mass flux of 100 kg/m ² s and three wall heat fluxes of: (a) 23.7 kW/m ² (b) 46.5 kW/m ² (c) 57.8 kW/m ² .	209
4.12	Nucleating bubbles in the liquid film of: (a) Annular flow for TS.1 at mass flux of 200 kg/m ² s and wall heat flux of 51 kW/m ² (near the channel middle) (b) Slug flow for TS.4 at mass flux of 100 kg/m ² s and wall heat flux of 55.24 kW/m ² (between the channel inlet and middle).	209
4.13	Hysteresis effect at mass flux of 150 kg/m ² s and wall heat flux near 40 kW/m ² for TS.2 (near the channel inlet): (a) Increasing heat flux (b) Decreasing heat flux.	210
4.14	Effect of mass flux on the flow patterns for TS.3 at wall heat flux of 20 kW/m ² near the channel middle and two mass fluxes of: (a) 50 kg/m ² s (b) 250 kg/m ² s.	211
4.15	Effect of mass flux on the histogram of flow patterns for TS.3 at wall heat flux near 46 kW/m ² and three different locations along the channels.	211
4.16	Effect of aspect ratio on the bubbly flow at wall heat flux near 45 kW/m ² and mass flux of 100 kg/m ² s (near the channel inlet).	213
4.17	Confinement effect on bubble coalescence at different aspect ratios.	214
4.18	Effect of aspect ratio on the slug flow at wall heat flux near 23 kW/m ² and mass flux of 50 kg/m ² s (near the channel middle).	215
4.19	Effect of aspect ratio on the annular flow at wall heat flux near 79 kW/m ² and mass flux of 250 kg/m ² s (at the channel outlet).	215
4.20	Effect of channel surface material on the bubbly flow at wall heat flux near 70 kw/m ² and mass flux of 100 kg/m ² s (near the channel inlet).	216
4.21	Effect of channel surface material on the slug flow at wall heat flux near 39 kw/m ² and mass flux of 150 kg/m ² s (near the channel middle).	217
4.22	Effect of channel surface material on the annular flow at wall heat flux near 127 kw/m ² and mass flux of 200 kg/m ² s (at the channel outlet).	218

4.23	Comparison of experimental data with Akbar et al. (2003) flow map for: (a) TS.1 (b) TS.2 (c) TS.3 (d) TS.4.	219
4.24	Comparison of experimental data with Revellin and Thome (2007a) flow map for: (a) TS.1 (b) TS.2 (c) TS.3 (d) TS.4.	221
4.25	Comparison of experimental data with Harirchian and Garimella (2010) flow map for: (a) TS.1 (b) TS.2 (c) TS.3 (d) TS.4.	222
4.26	Comparison of experimental data with Mahmoud and Karayiannis (2016a) flow map for: (a) TS.1 (b) TS.2 (c) TS.3 (d) TS.4.	224
4.27	Comparison of experimental data with Choi et al. (2017) flow map for: (a) TS.1 (b) TS.2 (c) TS.3 (d) TS.4.	225
4.28	Comparison of experimental data with Li and Hrnjak (2019) flow map for: (a) TS.1 (b) TS.2 (c) TS.3 (d) TS.4.	227
5.1	Effect of wall heat flux on the flow boiling pressure drop for: (a) TS.1 (b) TS.2 (c) TS.3 (d) TS.4.	233
5.2	Effect of mass flux on the flow boiling pressure drop for: (a) TS.1 (b) TS.2 (c) TS.3 (d) TS.4.	234
5.3	Effect of channel aspect ratio on flow boiling pressure drop for TS.1, TS.2 and TS.3 at mass flux of: (a) 200 kg/m ² s (b) 250 kg/m ² s.	235
5.4	Effect of aspect ratio for TS.1, TS.2 and TS.3 at mass flux of 200 kg/m ² s: (a) Acceleration pressure drop component (b) Frictional pressure drop component.	236
5.5	Effect of surface material on the flow boiling pressure drop for TS.2 and TS.4 at mass flux of: (a) 100 kg/m ² s (b) 250 kg/m ² s.	239
5.6	Flow boiling pressure drop versus exit vapour quality for TS.2 and TS.4 at a mass flux of 200 kg/m ² s.	239
5.7	Effect of surface material for TS.2 and TS.4 at mass flux of 200 kg/m ² s: (a) Acceleration pressure drop component (b) Frictional pressure drop component.	240
5.8	Comparison of the two-phase pressure drop data with the correlation by Lockhart and Martinelli (1949) for: (a) TS.1 (b) TS.2 (c) TS.3 (d) TS.4.	243

5.9	Comparison of the two-phase pressure drop data with the homogenous model, Collier and Thome (1994) for: (a) TS.1 (b) TS.2 (c) TS.3 (d) TS.4.	244
5.10	Comparison of the two-phase pressure drop data with the correlation by Qu and Mudawar (2003b) for: (a) TS.1 (b) TS.2 (c) TS.3 (d) TS.4.	245
5.11	Comparison of the two-phase pressure drop data with the correlation by Lee and Garimella (2008) for: (a) TS.1 (b) TS.2 (c) TS.3 (d) TS.4.	247
5.12	Comparison of the two-phase pressure drop data with the correlation by Keepaiboon et al. (2016) for: (a) TS.1 (b) TS.2 (c) TS.3 (d) TS.4.	249
5.13	Comparison of the two-phase pressure drop data with the correlation by Huang and Thome (2017) for: (a) TS.1 (b) TS.2 (c) TS.3 (d) TS.4.	250
5.14	Comparison of the two-phase pressure drop data with the correlation by Markal et al. (2017b) for: (a) TS.1 (b) TS.2 (c) TS.3 (d) TS.4.	251
5.15	Comparison of the two-phase pressure drop data with the correlation by Gao et al. (2019) for: (a) TS.1 (b) TS.2 (c) TS.3 (d) TS.4.	253
6.1	Boiling curve of HFE-7100 at z/L of 0.5 and at system pressure near 1 bar, wall heat flux up to 191.6 kW/m^2 , mass flux of $50\text{--}250 \text{ kg/m}^2\text{s}$ and inlet sub-cooling of 5 K for (a) TS.1 (b) TS.2 (c) TS.3 (d) TS.4.	260
6.2	Effect of channel aspect ratio on the boiling curve at mass flux of $250 \text{ kg/m}^2\text{s}$ and z/L of 0.5 for TS.1, TS.2 and TS.3: (a) Wall heat flux (b) Base heat flux.	261
6.3	Effect of channel surface material on the boiling curve at mass flux of $250 \text{ kg/m}^2\text{s}$ and z/L of 0.5 for TS.2 and TS.4.	264
6.4	Hysteresis effect on the boiling curve at mass flux of $150 \text{ kg/m}^2\text{s}$ for: (a) TS.1 (b) TS.2 (c) TS.3 (d) TS.4.	265
6.5	Measured pressure drop fluctuation at different wall heat fluxes	267

	and mass flux of 250 kg/m ² s for TS.3.	
6.6	Frequency analysis of the measured pressure drop at different wall heat fluxes and mass flux of 250 kg/m ² s for TS.3.	268
6.7	Signal fluctuations in pressure and temperature at wall heat flux of 191.6 kW/m ² and mass flux of 250 kg/m ² s for TS.3.	269
6.8	Effect of channel aspect ratio on the measured pressure drop fluctuation at mass flux of 150 kg/m ² s and two different wall heat fluxes for TS.1, TS.2 and TS.3.	270
6.9	Frequency analysis of the measured pressure drop at wall heat flux of 70 kW/m ² and mass flux of 150 kg/m ² s for TS.1, TS.2 and TS.3.	271
6.10	Effect of channel surface material on the measured pressure drop fluctuation at mass flux of 250 kg/m ² s and two different wall heat fluxes for TS.2 and TS.4.	272
6.11	Frequency analysis of the measured pressure drop at wall heat flux of 143 kW/m ² and mass flux of 250 kg/m ² s for TS.2 and TS.4.	273
6.12	Effect of wall heat flux on the local heat transfer coefficient at mass flux of 250 kg/m ² s for: (a) TS.1 (b) TS.2 (c) TS.3 (d) TS.4. (B) Bubbly (S) Slug (C) Churn (A) Annular.	274
6.13	Effect of wall heat flux on the local heat transfer coefficient as a function of axial distance at mass flux of 250 kg/m ² s for: (a) TS.1 (b) TS.2 (c) TS.3 (d) TS.4.	276
6.14	Local saturation temperature and wall temperature at different wall heat fluxes at mass flux of 250 kg/m ² s for TS.3.	278
6.15	Effect of mass flux on the local heat transfer coefficient at constant wall heat flux for: (a) TS.1 (b) TS.2 (c) TS.3 (d) TS.4.	278
6.16	Effect of wall heat flux and mass flux on the average heat transfer coefficient for: (a) TS.1 (b) TS.2 (c) TS.3 (d) TS.4.	279
6.17	Effect of channel aspect ratio on the local heat transfer coefficient at mass flux of 250 kg/m ² s and different wall heat fluxes for TS.1, TS.2 and TS.3: (a) Low heat flux (b) High heat flux.	280

6.18	Different channel aspect ratios at mass flux of 250 kg/m ² s for TS.1 and TS.3: (a) Nucleation site density (b) Liquid film thickness.	284
6.19	Schematic diagram of the flow patterns at different channel aspect ratios for (a) Nucleating bubbles (b) Liquid film thickness around the channel circumference.	285
6.20	Effect of channel aspect ratio on the local heat transfer coefficient as a function of axial distance at mass flux of 250 kg/m ² s for TS.1, TS.2 and TS.3. (a) Low heat flux (b) High heat flux.	286
6.21	Effect of channel aspect ratio on the average heat transfer coefficient at a mass flux of 250 kg/m ² s for TS.1, TS.2 and TS.3.	287
6.22	Effect of surface material on the local heat transfer coefficient at mass flux of 250 kg/m ² s for TS.2 and TS.4: (a) Low wall heat flux (b) High wall heat flux.	288
6.23	Effect of surface material on the local heat transfer coefficient as a function of axial distance at mass flux of 250 kg/m ² s for TS.2 and TS.4: (a) Low heat flux (b) High heat flux.	288
6.24	Effect of surface material on the average heat transfer coefficient for TS.2 and TS.4 at mass flux of 250 kg/m ² s.	289
6.25	The size range of effective nucleation cavities using the model by Hsu (1962).	290
6.26	Different channel surface materials at mass flux of 250 kg/m ² s for TS.2 and TS.4: (a) Nucleation site density (b) Liquid film thickness.	291
6.27	Schematic diagram of surface microstructures: (a) Surface valley (b) Surface peak.	293
6.28	Magnitude of different forces at different wall heat fluxes for TS.1 and mass flux of: (a) 50 kg/m ² s (b) 250 kg/m ² s.	295
6.29	Average heat transfer coefficient versus wall heat flux at mass flux of 250 kg/m ² s for TS.1.	295
6.30	Magnitude of different forces at different mass fluxes and wall heat flux of 28 kW/m ² for TS.1.	296

6.31	Magnitude of surface tension and inertia forces using all the flow boiling data points for TS.1, TS.2, TS.3 and TS.4 at mass flux of: (I) 50, (II) 100, (III) 150, (IV) 200 and (V) 250 kg/m ² s.	297
6.32	Comparison of the two-phase heat transfer data with the correlation by Shah (1982) for: (a) TS.1 (b) TS.2 (c) TS.3 (d) TS.4.	300
6.33	Comparison of the two-phase heat transfer data with the correlation by Kandlikar (1990) for: (a) TS.1 (b) TS.2 (c) TS.3 (d) TS.4.	301
6.34	Comparison of the two-phase heat transfer data with the correlation by Liu and Winterton (1991) for: (a) TS.1 (b) TS.2 (c) TS.3 (d) TS.4.	302
6.35	Comparison of the two-phase heat transfer data with the correlation by Warriar et al. (2002) for: (a) TS.1 (b) TS.2 (c) TS.3 (d) TS.4.	303
6.36	Comparison of the two-phase heat transfer data with the correlation by Lee and Mudawar (2005) for: (a) TS.1 (b) TS.2 (c) TS.3 (d) TS.4.	305
6.37	Comparison of the two-phase heat transfer data with the correlation by Mahmoud and Karayiannis (2013) for: (a) TS.1 (b) TS.2 (c) TS.3 (d) TS.4.	306
6.38	Comparison of the two-phase heat transfer data with the correlation by Li and Jia (2015) for: (a) TS.1 (b) TS.2 (c) TS.3 (d) TS.4.	308
6.39	Comparison of the two-phase heat transfer data with the correlation by Lim et al. (2015) for: (a) TS.1 (b) TS.2 (c) TS.3 (d) TS.4.	309
6.40	Comparison of the two-phase heat transfer data with the correlation by Thiangtham et al. (2016) for: (a) TS.1 (b) TS.2 (c) TS.3 (d) TS.4.	310
6.41	Comparison of the two-phase heat transfer data with the correlation by Markal et al. (2017a) for: (a) TS.1 (b) TS.2 (c) TS.3 (d) TS.4.	311

6.42	Comparison of the two-phase heat transfer data with the correlation by Shah (2017) for: (a) TS.1 (b) TS.2 (c) TS.3 (d) TS.4.	313
6.43	Comparison of the two-phase heat transfer data with the correlation by Wen et al. (2019) for: (a) TS.1 (b) TS.2 (c) TS.3 (d) TS.4.	314
7.1	Experimental flow visualization patterns along the condenser at mass flux of $108 \text{ kg/m}^2\text{s}$, coolant flow rate of 0.8 L/min and inlet coolant temperature of $25 \text{ }^\circ\text{C}$ with corresponding local vapour quality.	321
7.2	Sequence of pictures of the neck region at local vapour quality of 0.35 and $Z: 9 \text{ cm}$: (a) Slug formation (b) Slug length.	322
7.3	Schematic diagram of a vapour slug after the neck region (Top view), blue arrows indicate surface tension effect and red condensation of vapour.	323
7.4	Condensation flow structure during the present study.	323
7.5	Experimental flow patterns map at five mass fluxes ranging from 48 to $126 \text{ kg/m}^2\text{s}$, coolant flow rate of 0.5 L/min and two different inlet coolant temperatures: (a) $40 \text{ }^\circ\text{C}$ (b) $20 \text{ }^\circ\text{C}$.	324
7.6	Effect of refrigerant mass flux on the experimental flow patterns at coolant flow rate of 0.5 L/min and inlet coolant temperature of $40 \text{ }^\circ\text{C}$ with corresponding local quality: (A) Annular (S) Slug (B) Bubbly (L) Liquid.	325
7.7	Effect of coolant flow rate on the bubble size at mass flux of $108 \text{ kg/m}^2\text{s}$, inlet coolant temperature of $20 \text{ }^\circ\text{C}$ and coolant flow rate of 0.5 and 1.1 L/min .	326
7.8	Sequence of pictures of the condensing bubble at mass flux of $108 \text{ kg/m}^2\text{s}$, inlet coolant temperature of $20 \text{ }^\circ\text{C}$ and coolant flow rate: (a) 0.5 (b) 1.1 L/min .	327
7.9	Comparison of the present results with the proposed map of Cavallini et al. (2002) at coolant flow rate of 0.5 L/min and inlet coolant temperature of $40 \text{ }^\circ\text{C}$.	328
7.10	Comparison of the present results with the proposed map of Kim	329

	and Mudawar (2012) at coolant flow rate of 0.5 L/min and inlet coolant temperature of 40 °C.	
7.11	Comparison of the present results with the map of Nema et al. (2014) at coolant flow rate of 0.5 L/min and inlet coolant temperature of 40 °C: AF: Annular flow, I-AF: Intermittent-annular flow, IF: Intermittent flow.	330
7.12	Comparison of the present results with the proposed map of Zhuang et al. (2017) at coolant flow rate of 0.5 L/min and inlet coolant temperature of 40 °C.	331
8.1	Effect of refrigerant mass flux on the condensation heat transfer coefficient at water flow rate of 0.5 L/min and inlet water temperature of 40 °C.	334
8.2	Local heat transfer coefficient versus local vapour quality corresponding to the flow patterns at mass flux of 108 kg/m ² s, water flow rate of 1.1 L/min, and inlet water temperature of 20 °C.	335
8.3	Effect of inlet water temperature on the local condensation heat transfer coefficient at mass flux of 86 kg/m ² s and water flow rate of 0.5 L/min.	336
8.4	Effect of water flow rate on the local condensation heat transfer coefficient at mass flux of 126 kg/m ² s and inlet water temperature of 30 °C.	336
8.5	Comparison between the experimental condensation heat transfer coefficient and the correlation by Shah (1979).	339
8.6	Comparison between the experimental condensation heat transfer coefficient and the correlation by Dobson and Chato (1998).	339
8.7	Comparison between the experimental condensation heat transfer coefficient and the correlation by Cavallini et al. (2006a).	340
8.8	Comparison between the experimental condensation heat transfer coefficient and the correlation by Wang et al. (2002).	341
8.9	Comparison between the experimental condensation heat transfer coefficient and the correlation by Koyama et al. (2003b).	342
8.10	Comparison between the experimental condensation heat transfer	343

	coefficient and the correlation by Bohdal et al. (2011).	
8.11	Comparison between the experimental condensation heat transfer coefficient and the correlation by Park et al. (2011).	344
8.12	Comparison between the experimental condensation heat transfer coefficient and the correlations by Kim and Mudawar (2013c): Annular data (b) Slug and bubbly data.	345
8.13	Comparison between the experimental condensation heat transfer coefficient and the correlation by Shah (2016).	346
8.14	Comparison between the experimental condensation heat transfer coefficient and the correlation by Rahman et al. (2018).	347
9.1	Pumping power versus cooling load for TS.1.	351
9.2	Effect of channel aspect ratio on pumping power at mass flux of 250 kg/m ² s.	352
9.3	Effect of surface material on pumping power at mass flux of 200 kg/m ² s.	352
9.4	Small-scale pumped loop thermal management system (in scale); * Pump dimensions are mentioned in (www.micropumps.co.uk).	353
9.5	Comparison between the present thermal management system and other cooling techniques. CL: cooling load at evaporator, PC: power consumption.	355
9.6	Comparison between the present system and other pumped loop systems for electronics cooling using HFE-refrigerants in different channel geometries.	356
9.7	Pumping power for various fluids at a mass flux of 400 kg/m ² s, obtained from Olivier and Thome (2010). HFE-7100 result at a mass flux of 250 kg/m ² s from the present study. This figure was plotted for a cooling load of 265 W.	357
9.8	Small-scale pumped loop thermal management system with multiple cooling points.	358
C.1	Surface characteristics of: (a) TS.2, (b) TS.3 (c) TS.4 (d) TS.5.	407

List of Tables

Table		Page
2.1	Transition criteria of different channel sizes reported in the literature.	19
2.2	Flow boiling of HFE-refrigerants in previous studies.	22
2.3	Flow boiling studies using aluminium channels reported in the literature.	26
2.4	Effect of channel aspect ratio on the two-phase pressure drop as reported in the literature.	56
2.5	Heat transfer mechanism(s) as reported in the literature.	70
2.6	Effect of channel aspect ratio on the heat transfer coefficient as reported in the literature.	75
2.7	Summary of the numerical and experimental conditions covered in the past flow condensation studies.	117
3.1	Details of the microchannel evaporator.	145
3.2	Microchannel condenser details (TS.5).	149
3.3	Surface roughness values at different locations.	150
3.4	The values of K_{∞} and C for the test sections.	161
3.5	Uncertainty values of the measured variables.	168
3.6	The uncertainty ranges for single-phase experiments.	172
3.7	The uncertainty ranges for flow boiling experiments.	172
3.8	The uncertainty ranges for flow condensation experiments.	173
3.9	Thermophysical properties of HFE-7100 at 1 bar, based on EES software.	179
3.10	Flow boiling test conditions.	179
3.11	Flow condensation test conditions (TS.5).	179
5.1	Statistical comparison between the experimental data and existing two-phase pressure drop correlations.	256

6.1	Maximum percentage of fluctuation for all measured parameters.	269
6.2	Statistical comparison between the experimental data and existing two-phase heat transfer correlations.	316
8.1	Statistical comparison between the experimental condensation heat transfer data and existing correlations.	348

Nomenclature

Latin

Symbol	Parameter	SI unit
A	Area	m^2
Bd	Bond number, $Bd = \Delta\rho g D_h^2 / \sigma$	-
Bd_{cr}	Critical Bond number, $Bo_{cr} = 1 / [\rho_l (\rho_l - \rho_g)^{-1} - \pi / 4]$	-
Bo	Boiling number, $Bo = q''_w / G i_{lg}$	-
Bx	Systematic uncertainty in a measured parameter X	
b	Length of channel side, the vertical distance between the thermocouple and the channel bottom	m
e	Entrained liquid fraction	-
C	Chisholm parameter, dimensionless correction factor	-
C_o	Confinement number, $C_o = [\sigma / g \Delta\rho]^{0.5} / D_h$	-
c_p	Specific heat capacity	J/kgK
D_h	Hydraulic diameter, $D_h = 2H_{ch}W_{ch} / (H_{ch} + W_{ch})$	m
$Eö$	Eötvös number, $Eö = D_h^2 g (\rho_l - \rho_g) / \sigma$	-
F	Dimensionless number	-
f	Fanning friction factor	-
Fr	Froude number, $Fr = v_l^2 G^2 / g D_h$	-
F''	Force per unit area	N/m ²
G	Mass flux, $G = \dot{m} / A_{sec} N$	kg/m ² s
g	Gravitational acceleration	m/s ²
h	Heat transfer coefficient	W/m ² K
h_{LT}	Heat transfer coefficient with total mass flowing as liquid	W/m ² K
h_{NU}	Heat transfer coefficient, the Nusselt equation	W/m ² K
\bar{h}	Average heat transfer coefficient	W/m ² K
H	Height	m
i	Specific enthalpy	J/kg
i_{lg}	Latent heat of vaporization	J/kg
J_g	Gas superficial velocity	m/s
J_l	Liquid superficial velocity	m/s

J_G	Dimensionless vapour velocity, $J_G = \frac{Gx}{\sqrt{gD\rho_g\Delta\rho}}$	-
k	Thermal conductivity	W/mK
K_{90}	Loss coefficient for the 90° turns	-
K_{∞}	Dimensionless incremental pressure drop number	-
L	Length	m
L_a	Laplace constant, $L_a = [\sigma/g(\rho_l - \rho_g)]^{0.5}$	-
L_e	Dimensionless entrance length	-
L^*	Dimensionless length	-
m	Fin parameter, $\sqrt{2h/k_{cu} W_{fin}}$	1/m
M	Molecular mass	kg/kmol
\dot{m}	Mass flow rate	kg/s
N	Number of channels, number of data points	-
N_{co}	Convection number, $N_{co} = (1 - x/x)^{0.8}(v_l/v_g)^{0.5}$	-
\overline{Nu}	Average Nusselt number, $\overline{Nu} = \bar{h}D_h/k_l$	-
$N\mu$	Viscosity number	-
P	Pressure	Pa
P_{er}	Perimeter	m
P_R	Reduced pressure, $P_R = P_i/P_{cr}$	-
Pr	Prandtl number, $Pr = cp\mu_l/k_l$	-
Q	Heat rate	W
q''	Heat flux	W/m ²
$\overline{q''}$	Average heat flux	W/m ²
r	Radius	m
Ra	Average surface roughness	μm
Re	Reynolds number, $Re = GD_h/\mu$	-
Re_{ls}	Superficial liquid Reynolds number, $Re_{ls} = G(1 - x)D_h/\mu_l$	-
Re_{gs}	Superficial vapour Reynolds number, $Re_{gs} = GxD_h/\mu_g$	-
Rp	Maximum profile peak height	μm
S_x	Standard deviation	-
S_{Bx}	Standard deviation of the systematic uncertainty	-
Su_{go}	Vapour only Suratman number, $Su_{go} = \rho_g\sigma D_h/\mu_g^2$	-
T	Temperature	°C

$t_{95\%}$	95 % confidence limit	-
U	Velocity	m/s
u_c	Combined uncertainty	-
U_r	Absolute uncertainty	-
v	Specific volume	m ³ /kg
W	Width	m
W	Work	W
W_c	Centre to centre distance of microchannel widths	m
We	Weber number, $We = D_h G^2 / \rho \sigma$	-
We_{ls}	Weber number based on the liquid superficial velocity, $We_{ls} = D_h \rho_l J_l^2 / \sigma$	-
We_{gs}	Weber number based on the gas superficial velocity, $We_{gs} = D_h \rho_g J_g^2 / \sigma$	-
We^*	Modified Weber number, $We^* = 2.45(Re_{gs}^{0.64} / Su_{go}^{0.3} (1 + 1.09X_{tt}^{0.039})^{0.4})$	-
X	Martinelli parameter, $X = [(dP/dz)_l / (dP/dz)_g]^{0.5}$	-
x	Vapour quality	-
$y, y1$	Vertical distance between thermocouple and channel bottom	m
$y2$	Vertical distance between thermocouples	m
Z	Shah's correlating parameter, $Z = (1/x - 1)^{0.8} P_R^{0.4}$	-
z	Distance measured from inlet to end of channel	m

Greek

Symbol	Parameter	SI unit
α	Void fraction, area ratio	-
β	Aspect ratio	-
β	Surface area density	m ² /m ³
γ	Surface-liquid interaction parameter	-
δ	Average liquid film thickness	m
δ_t	Thermal boundary layer thickness	m
δ^+	Dimensionless average liquid film thickness	-
ΔP	Pressure drop	Pa

ΔT	Temperature difference	K
ΔT_{LM}	Log mean temperature difference	K
Δz	Axial distance between thermocouples	m
η	Fin efficiency	-
θ	Contact angle, channel orientation	degree
θ	Percentage of predictions within $\pm 30\%$ of data	%
θ	Dimensionless surface roughness parameter	-
λ	Channel geometry constant	-
μ	Viscosity	Pa s
ρ	Density	kg/m ³
σ	Surface tension	N/m
\emptyset	Two phase pressure drop multiplier	-

Subscripts

Symbol	Meaning
3	Based on three-sided heat transfer in rectangular channel
4	Based on four-sided heat transfer in rectangular channel
<i>acc</i>	Acceleration
<i>app</i>	Apparent
<i>b</i>	Base, buoyancy, bubble
<i>B</i>	Bottom
<i>c</i>	Core flow
<i>cav</i>	Cavity
<i>cb</i>	Convective boiling
<i>ch</i>	Channel
<i>cond</i>	Condenser
<i>cr</i>	Critical
<i>cu</i>	Copper
<i>eq</i>	Equivalent
<i>EV</i>	Evaporative
<i>evap</i>	Evaporator
<i>exp</i>	Experimental
<i>f</i>	Fluid

<i>fin</i>	Channel fin
<i>fi</i>	Fluid in
<i>fo</i>	Fluid out
<i>fr</i>	Friction
<i>g</i>	Gas or vapour
<i>h</i>	Heated
<i>ht</i>	Heat transfer
<i>hy</i>	Hydrodynamic
<i>i</i>	Inlet, inertia
<i>ip</i>	Inlet plenum
<i>l</i>	Liquid
<i>lf</i>	Liquid film
<i>ll</i>	Laminar liquid- laminar vapour
<i>lt</i>	Laminar liquid-turbulent vapour
<i>M</i>	Evaporation momentum
<i>meas</i>	Measured
<i>nb</i>	Nucleate boiling
<i>non-cir</i>	Non-circular channel
<i>o</i>	Outlet, exit
<i>op</i>	Outlet plenum
<i>or</i>	Orifice
<i>oth</i>	Other parts
<i>p</i>	Plenum, pump
<i>pred</i>	Predicted
<i>s</i>	Surface tension
<i>sat</i>	Saturation
<i>sc</i>	Sudden contraction
<i>se</i>	Sudden expansion
<i>sec</i>	Section
<i>sp</i>	Single phase
<i>sub</i>	Sub-cooled
<i>sup</i>	Superheat
<i>sys</i>	System

<i>T</i>	Top
<i>th</i>	Thermocouple
<i>tp</i>	Two phase
<i>tt</i>	Turbulent liquid-turbulent vapour
<i>w</i>	Wall, wetted
<i>wi</i>	Internal wall surface
<i>wti</i>	Water in
<i>wto</i>	Water out
<i>z</i>	Axial local

Abbreviations

Symbol	Meaning	SI unit
<i>DAQ</i>	Data Acquisition System	-
<i>FD</i>	Fully Developed	-
<i>HTC</i>	Heat Transfer Coefficient	W/m ² K
<i>MAE</i>	Mean Absolute Error	-
<i>NSD</i>	Nucleation Site Density	n/m ²

Dimensionless Groups

Group	Definition	Expression
Bond number, Bd	$\frac{\text{Gravitational force}}{\text{Surface tension force}}$	$\Delta\rho g D_h^2 / \sigma$
Boiling number, Bo	$\frac{\text{Heat flux}}{\text{Latent heat and mass flux}}$	$q'' / G i_{lg}$
Capillary number, Ca	$\frac{\text{Inertia and viscous force}}{\text{Surface tension force}}$	$U\mu / \sigma$
Confinement number, Co	$\frac{\text{Surface tension force}}{\text{Gravitational force}}$	$[\sigma / g\Delta\rho]^{0.5} / D_h$
Convection number, N_{co}	Vapour quality and density ratio	$\left(\frac{1-x}{x}\right)^{0.8} \left(\frac{\rho_g}{\rho_l}\right)^{0.5}$
Dimensionless vapour velocity, J_G	$\frac{\text{Inertia force}}{\text{Gravitational force}}$	$\frac{Gx}{\sqrt{gD\rho_g\Delta\rho}}$
Eötvös number, $Eö$	$\frac{\text{Gravitational force}}{\text{Surface tension force}}$	$D_h^2 g \Delta\rho / \sigma$
Froude number, Fr	$\frac{\text{Inertia force}}{\text{Gravitational force}}$	$v^2 G^2 / g D_h$
Laplace constant, L_a	$\frac{\text{Surface tension force}}{\text{Gravitational force}}$	$[\sigma / g\Delta\rho]^{0.5}$
Martinelli parameter, X	$\frac{\text{Frictional pressure gradient of liquid}}{\text{Frictional pressure drop of gas}}$	$\left[\frac{(dP/dz)_l}{(dP/dz)_g}\right]^{0.5}$
Nusselt number, Nu	$\frac{\text{Convection resistance}}{\text{Conduction resistance}}$	hD_h / k
Prandtl number, Pr	$\frac{\text{Momentum diffusivity}}{\text{Thermal diffusivity}}$	$cp\mu / k$
Reynolds number, Re	$\frac{\text{Inertia force}}{\text{Viscous force}}$	$G_{ch} D_h / \mu$
Suratman number, Su	$\frac{\text{Surface tension force}}{\text{Viscous force}}$	$\rho\sigma D_h / \mu^2$
Weber number, We	$\frac{\text{Inertia force}}{\text{Surface tension force}}$	$D_h G^2 v / \sigma$

Chapter 1

Introduction

1.1 Background and Motivation

Effective cooling solution for high heat flux applications has attracted significant attention by the industrial and scientific communities to meet market demand for next generation high performance electronic systems. The performance of these systems is pushed to high level of processing speeds, power densities and current ranges, which results in high operating temperatures and high heat fluxes. Failure in thermal control may lead to deterioration in both operational life time and system performance. High heat flux applications are found in different aspects as presented below. Some of these applications are discussed by Kim and Mudawar (2014).

1. Aerospace: Satellite electronics and rocket nozzles.
2. Energy: Wind power, photovoltaic power, power transmission and fusion reactors.
3. High-energy physics: Accelerators.
4. IT and industry: Computer data centres, motor drives, material processing and arc welding systems.
5. Medical: Robotics and x-ray machines.
6. Military: Radars, avionics and laser weapons.
7. Transportation: Electric trains, hybrid electric vehicles (HEVs) and electric vehicles (EVs).

Most of the previous applications include different electronic components, such as insulated-gate bipolar transistor modules (IGBTs), metal oxide semiconductor field-effect transistors (MOSFETs), integrated circuits (ICs), microprocessors and laser

diode bars. High thermal power from a small surface area can be generated by these parts. Fig. 1.1 shows the heat flux ranges for various applications. Thome and Cioncolini (2017) mentioned that the current CPUs can generate heat flux of 0.5 MW/m^2 . Another study by Karayiannis and Mahmoud (2017) showed that computer chips could generate average heat flux of $2\text{--}4.5 \text{ MW/m}^2$ by 2026. Accordingly, several cooling techniques are adopted for maintaining thermal performance within safety limits, such as heat sinks, heat pipes, vapour chambers, thermoelectric modules (TECs), liquid cooling loop, vapour compression cycle, liquid jet impingement, spray cooling, hybrid cooling (microchannel heat sink and micro jets) and direct liquid cooling (immersion in dielectric refrigerant).

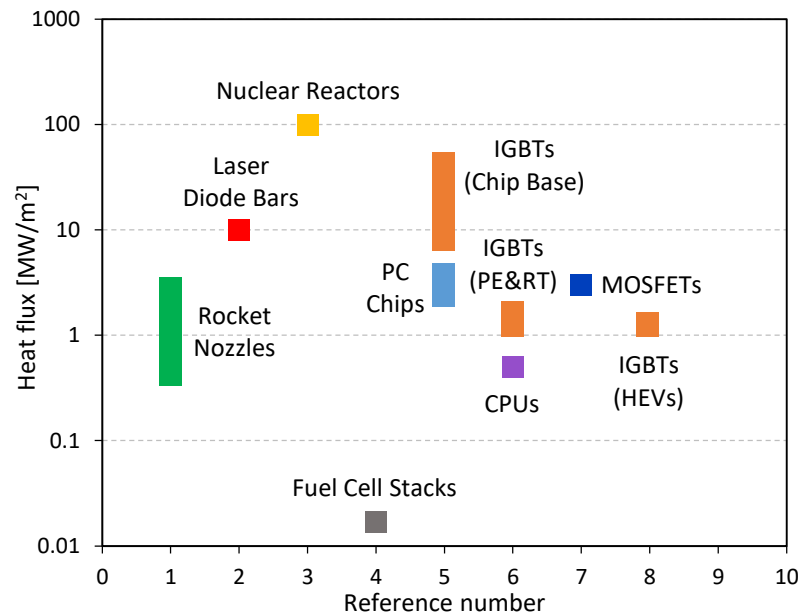


Figure 1.1 Heat flux for various applications*.

CPUs: central processing units. HEVs: hybrid electric vehicles. IGBTs: insulated-gate bipolar transistors. MOSFET: metal oxide semiconductor field-effect transistors.

PE&RT: power electronics and radar transmitters.

Liquid cooling loops are widely used for semiconductor applications. This cooling technique depends on the fluid's sensible heat. Coolant is circulated by a pump through system loop, *i.e.* cold plate and radiator, as shown in Fig. 1.2(a). Generally, water-glycol is used as a working fluid. The cold plate, *i.e.* cooling block, consists of

* Reference number: [1] Ohadi and Qi (2005), [2] Junghans (2011), [3] Kadam and Kumar (2014), [4] Fly (2015), [5] Karayiannis and Mahmoud (2017), [6] Thome and Cioncolini (2017), [7] Jörg et al. (2018) and [8] Qian et al. (2018).

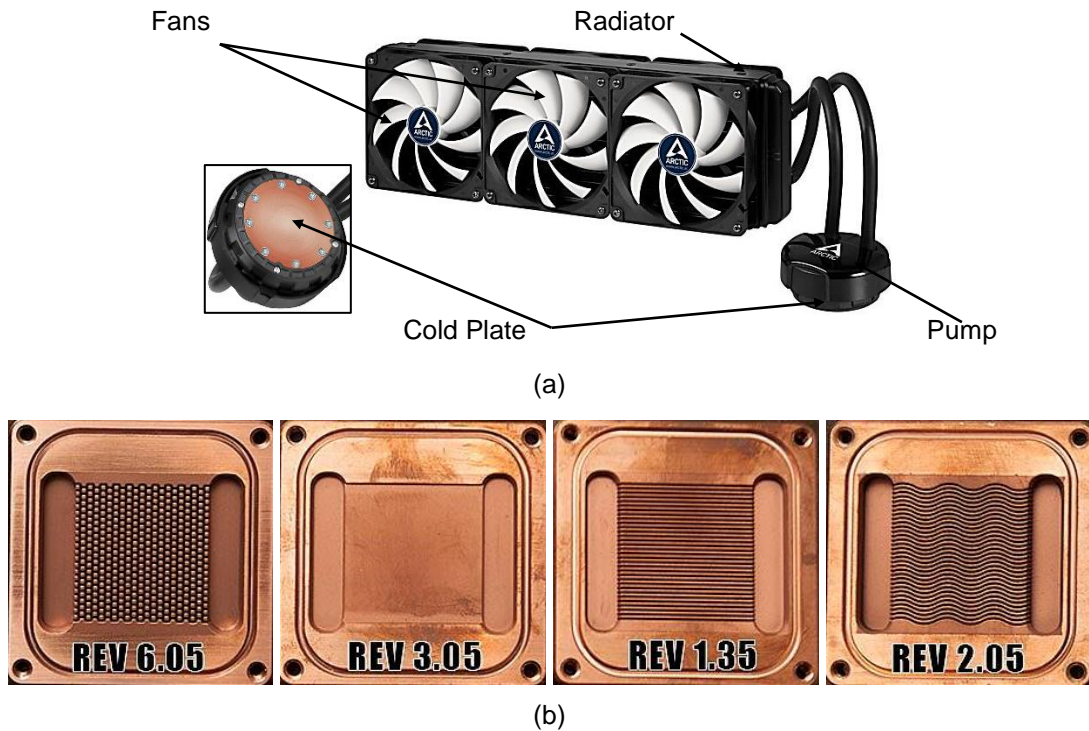


Figure 1.2 Photograph of CPUs liquid cooling system:

- (a) Loop parts of Liquid Freezer 360, adapted from ARCTIC (2016) (b) Different cold plates, adapted from Mr3D (2011).

mini/microchannels attached to the chipset. This plate is usually made from copper using different channel configurations, such as fin-pins, gap, straight and wavy channels, see Fig. 1.2(b). CPUs liquid cooling system, such as Liquid Freezer 360 (ARCTIC), can dissipate cooling loads up to 300 W. Although this cooling solution can dissipate high heat rates, a short circuit could happen during leakage.

Liquid cooling loops are also used in computer data centres. For example, this cooling technique is currently installed in the Summit data centre. In November 2018, Summit (OLCF-4) was classified as the fastest supercomputer in the world as reported by TOP500 (2018). This supercomputer was developed by IBM and located at Oak Ridge National Laboratory for scientific research. Summit occupies 5600 ft² of space and provides a storage capacity of 250 PB, transferring data at 2.5 TB/s and maximum power consumption of 13 MW, Gottschalk (2018). It consists of 256 racks and 4608 nodes, *i.e.* 18 nodes per each rack, see Fig. 1.3(a). Each node (power AC922 server) consists of two 22-core IBM POWER9 processors (up to 2.8 GHz), six NVIDIA Tesla V100 GPUs (3 per POWER9 CPU), 2 TB of DDR4 memory, four

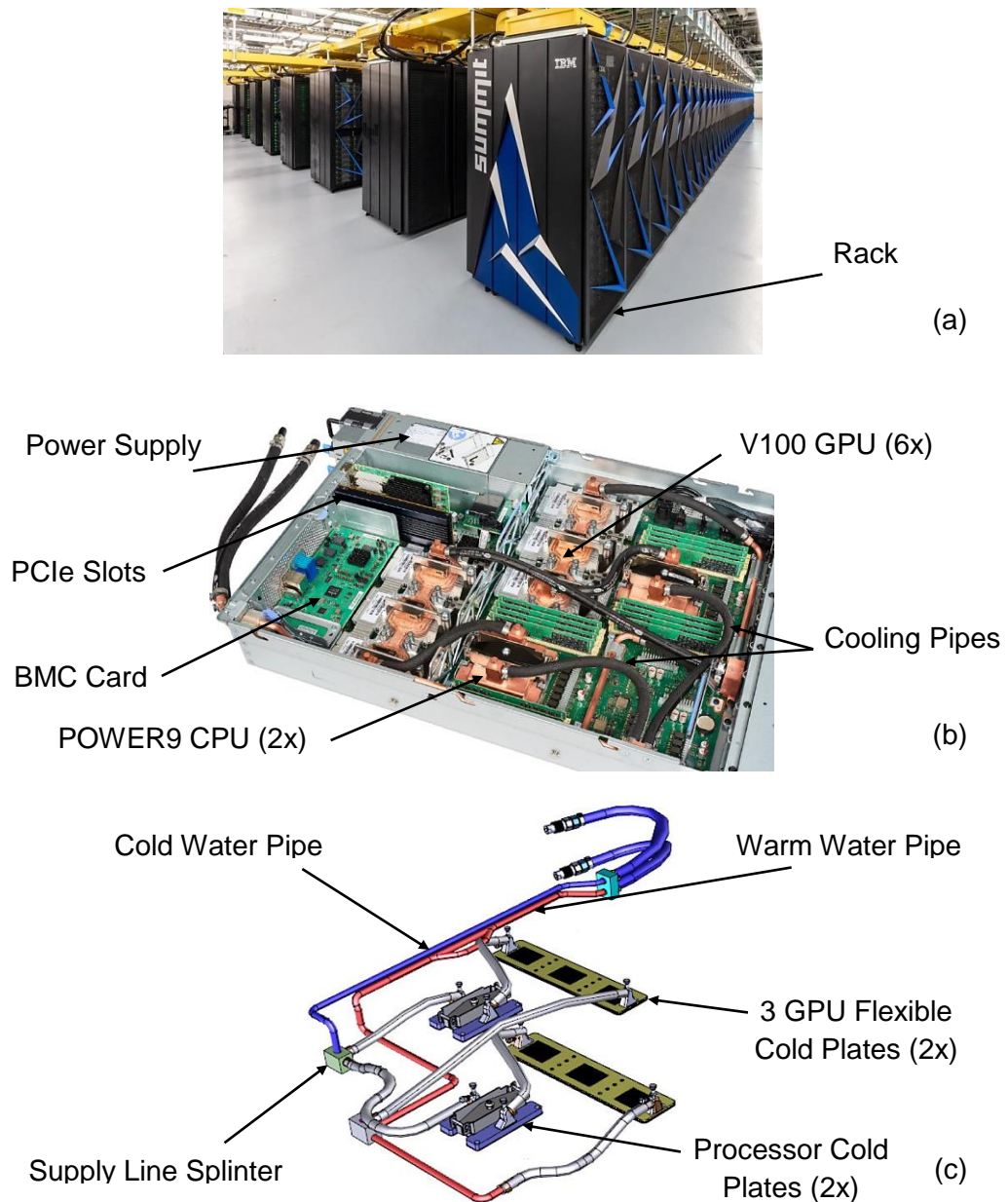


Figure 1.3 Computer data centre: (a) Photograph of Summit, Gottschalk (2018) (b) Photograph of power AC922 server and (c) Schematic diagram of cooling loop for one server, Vetter et al. (2019).

PCIe Gen4 slots, BMC card and two power supplies with 2200 W as shown in Fig. 1.3(b), Vetter et al. (2019). Maximum thermal output by power AC922 server is 8872 BTU/hr, *i.e.* 2600 W, as reported by Vetter et al. (2019). This means that the total thermal power by Summit is approximately 12 MW. This very high thermal power is dissipated using water cooling loop. Water is supplied to each node through cold plates. These plates are attached to two CPUs and six GPUs as shown in Fig. 1.3(b). Therefore, 36,864 chipsets (9,216 CPUs and 27,648 GPUs) are cooled in the

whole system. The internal cooling components for each node are illustrated in Fig. 1.3(c). The outlet warm water flows to the main heat exchangers for cooling using another cooling system (cooling towers).

A miniature vapour compression refrigeration system (VCR) is another cooling technique for electronics. In this system, a miniature compressor is used to drive refrigerant through a closed loop. This loop consists of microchannel evaporator, microchannel condenser, compressor and capillary tube as illustrated in Fig. 1.4. Higher heat flux can be dissipated by this system compared to the liquid cooling system due to the flow boiling process. For example, the miniature vapour compression refrigeration system by Liang et al. (2019) dissipated cooling load of 400 W, *i.e.* heat flux of 2 MW/m², using R134a as refrigerant. However, this system had low coefficient of performance (3.2) and high consumption of power (125 W).

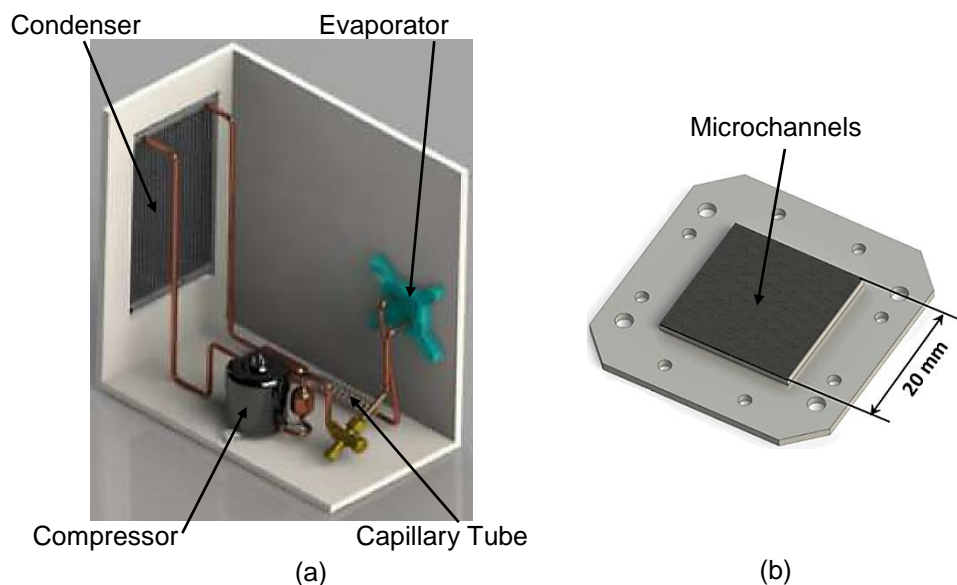


Figure 1.4 Schematic diagram of: (a) Miniature vapour compression refrigeration and (b) Microchannel evaporator, adapted from Poachaiyapoom et al. (2019).

For transportation applications, such as hybrid electric vehicles (HEVs) and electric vehicles (EVs), high heat is generated during operation, *i.e.* from inverters, electric machines, batteries and fuel cell stacks. Lithium-ion battery packs are used in some electric vehicles, while fuel cell stacks are located in others. This pack consists of several individual modules and each module includes a number of cells. For example, the Tesla Model (S) battery system includes 16 modules and 444 battery

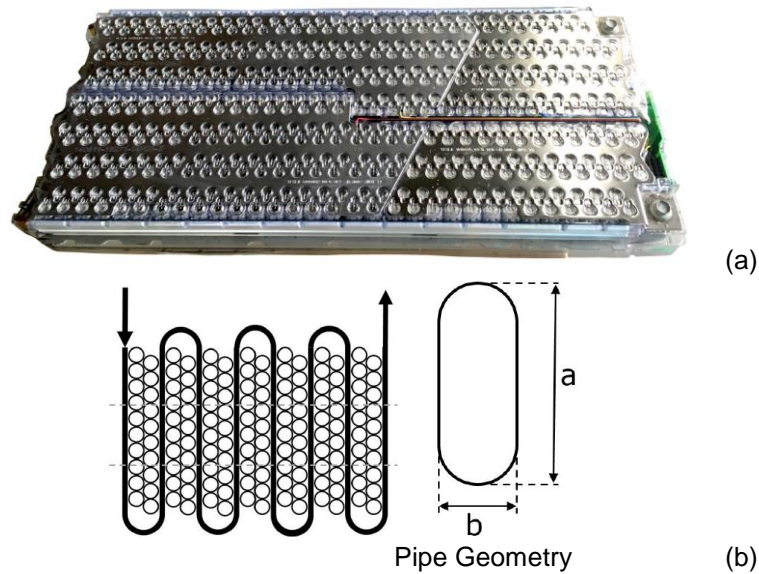


Figure 1.5 Lithium-ion battery pack: (a) Tesla Model (S) battery module, Tesla (2017) (b) Coolant loop in one module, Nilsson (2017).

cells in each module, see Fig. 1.5(a). Therefore, this system consists of 7104 battery cells with a capacity of 3.6 Vdc and 3200 mAh for each cell, Tesla (2017). Water-glycol is usually used as a coolant to reject the generated heat from these modules. The coolant flows through small channels inside each module and around the cells as mentioned by Nilsson (2017). The pipe geometry and coolant loop is illustrated in Fig. 1.5(b).

Other electric vehicles have both battery packs and fuel cell stacks as electric sources, see Fig. 1.6(a). This cell consists of cathode and anode plates separated by an electrolyte. Both fuel (hydrogen) and oxygen (ambient air) are supplied to this cell through bipolar plates and thus an electrical power is generated due to the electrochemical reaction, which leads to high temperature and heat generation rates. The operating temperature of the fuel cell is usually between 60 to 80 °C, Choi et al. (2019). Therefore, an effective cooling system is required to maintain the cell temperature within design limits. Fluid is circulated through small channels located inside the stack between the bipolar plates as shown schematically in Fig. 1.6(b). Liquid cooling loop using water-glycol is usually used for this purpose. Flow boiling of HFE-7100 is another technique that could be used for cooling fuel cells as suggested by Choi et al. (2018).

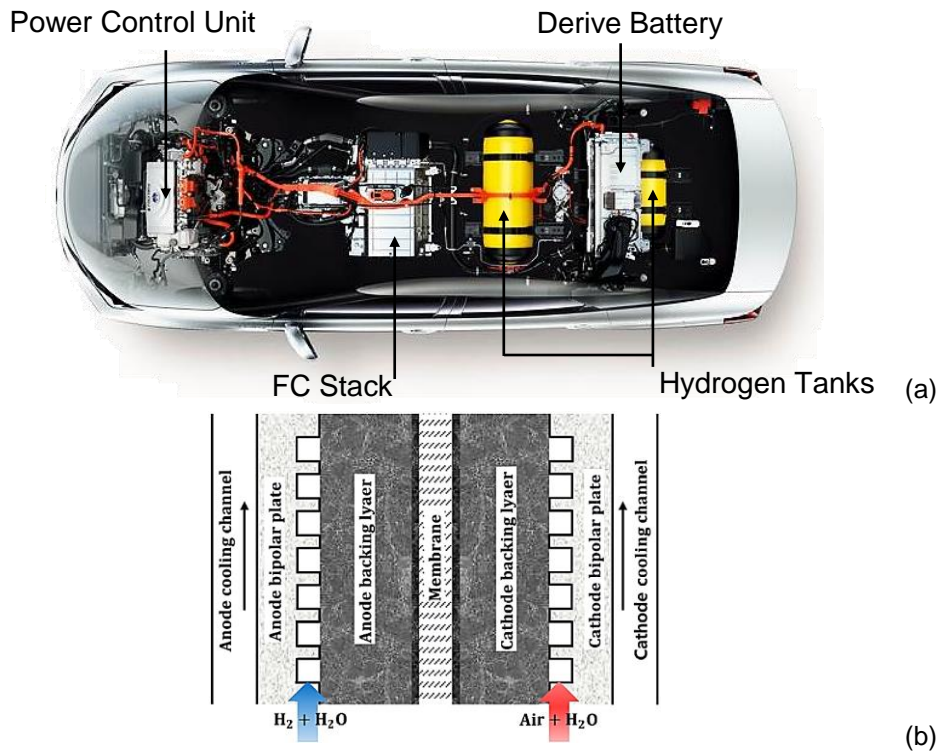


Figure 1.6 Schematic description of: (a) Mirai car, Toyota UK (2018)
 (b) Cooling channels in a single fuel cell, Choi et al. (2018).

For aerospace applications, such as liquid rocket engines, liquid fuel (hydrogen) and liquid oxidizer (oxygen) are pumped to the thrust chamber to supply thrust force. Since this combustion generates high pressure and temperature, liquid fuel is used for cooling the chamber wall, see Fig. 1.7(b). Accordingly, small cooling channels are located around the chamber wall as shown in Fig. 1.7(c).

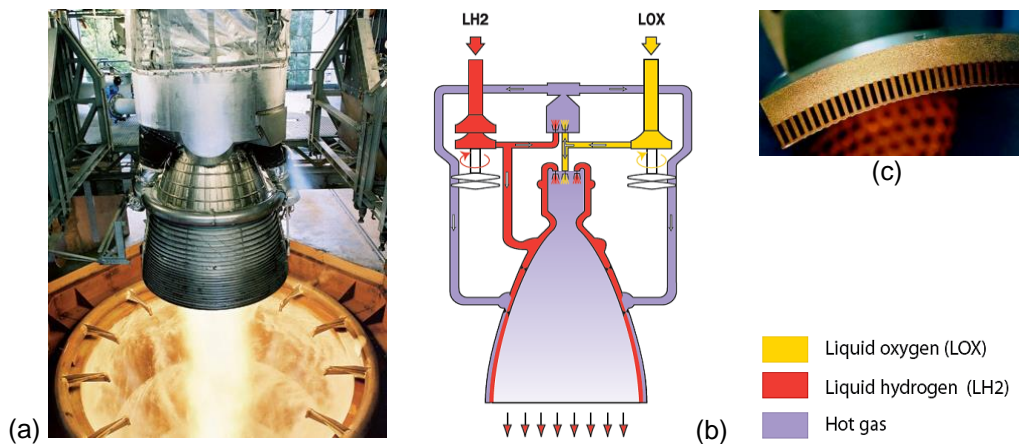


Figure 1.7 Rocket engine: (a) Photograph of Vulcain 2 European rocket engine and
 (b) Fluid/Cooling loop, Safran (2011) (c) Cut of the Vulcain chamber wall (cooling channels), Pizzarelli (2017).

For energy applications, such as fusion reactors, very high heat is produced for generating electricity through nuclear fusion reactions. Deuterium and tritium as hydrogen isotopes are used to create confined plasma at high temperature and density. This plasma is in direct contact with first wall of the reactor. The contact side of this wall consists of thin panels made of high conductivity metals for protection. A coolant flow, such as helium, is driven through small channels that are located behind these panels as illustrated in Fig. 1.8(b).

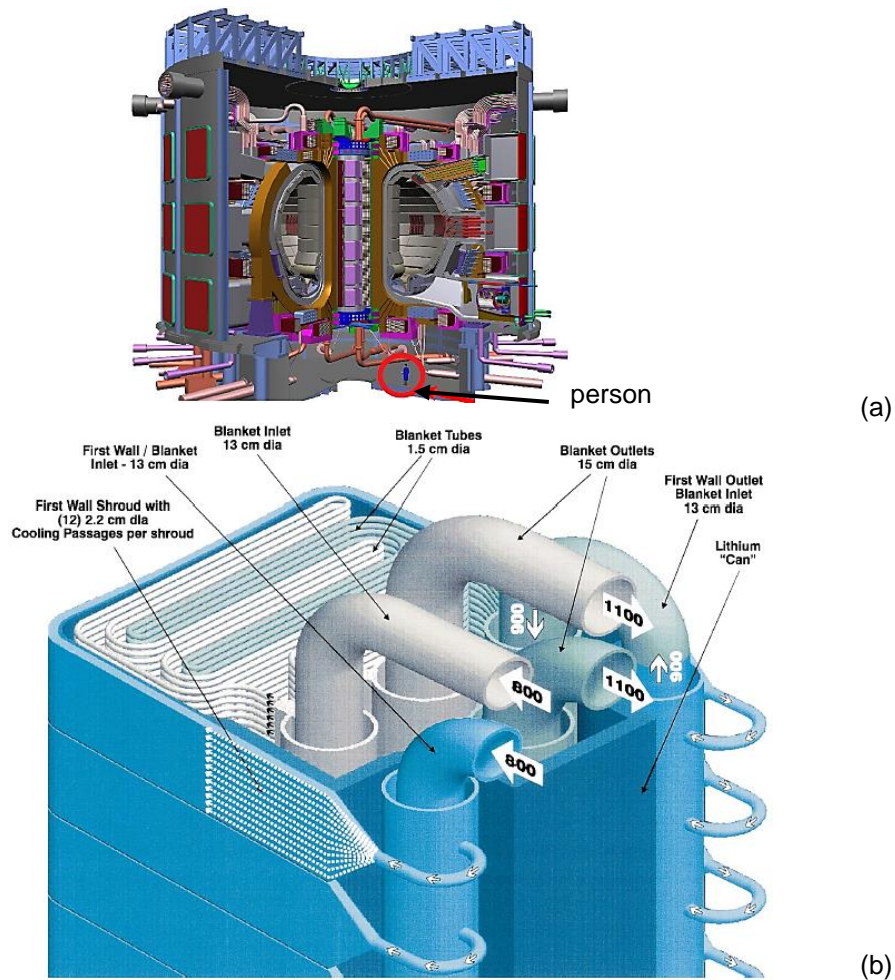
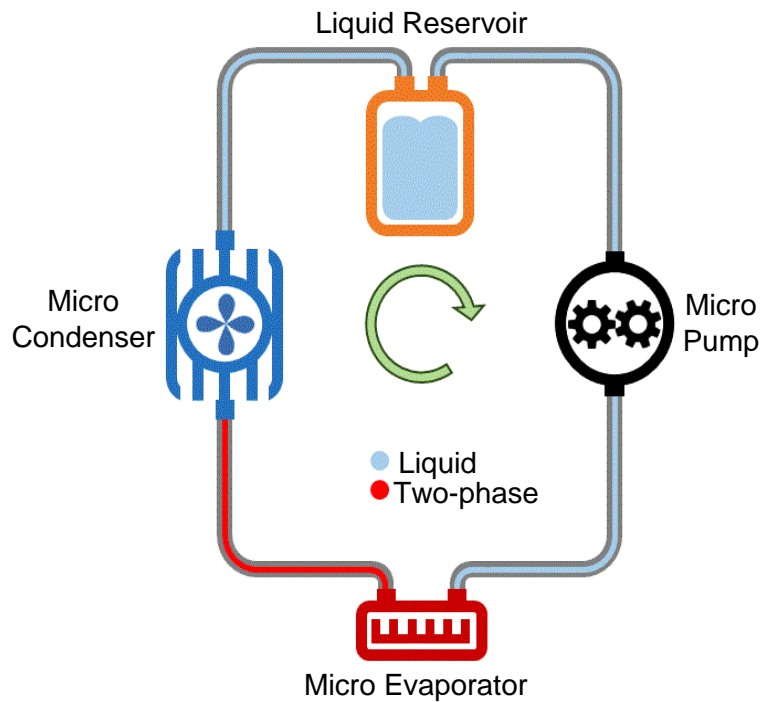
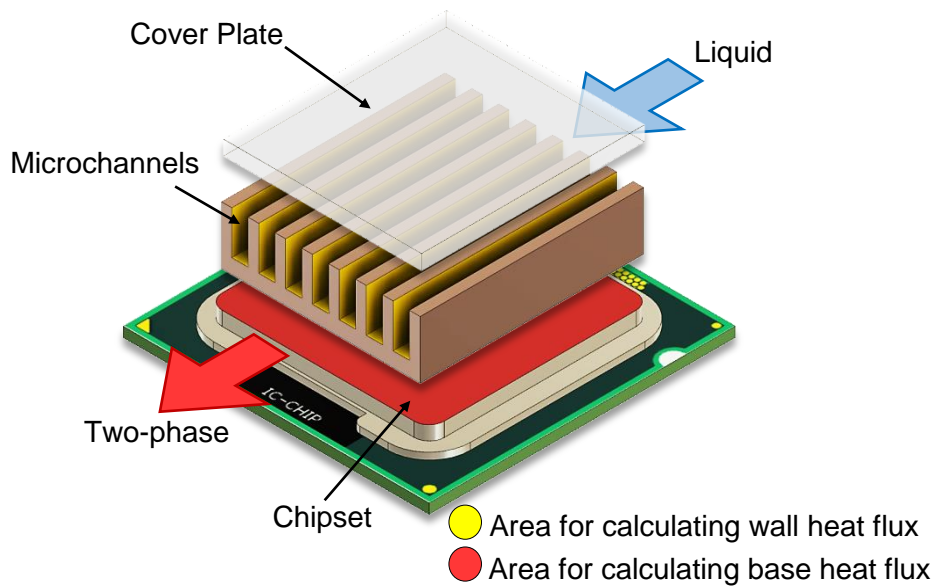


Figure 1.8 Fusion reactor: (a) International Thermonuclear Experimental Reactor (ITER), Kaita (2018) (b) Helium cooled first wall, Abdou et al. (2001).

In addition to the abovementioned cooling techniques, two-phase flow in micro passages, as a part of small-scale pumped loop cooling system, is also considered a promising technique for high heat flux applications. Fig. 1.9(a) shows this system loop that consists of air-cooled microchannel condenser, liquid reservoir, micro-pump and microchannel evaporator.



(a)



(b)

Figure 1.9 Two-phase flow in small-scale pumped loop cooling system for electronics: (a) System loop (b) Exploded drawing of multi-microchannel evaporator.

In order to use this system for cooling electronic components, the microchannel evaporator can be attached to the chipset as shown in Fig. 1.9(b). The coolant enters the heat sink at a sub-cooled state and leaves either as saturated vapour or as a mixture of liquid and vapour. High thermal power can be dissipated from this chipset through the heat sink base area due to the refrigerant phase change, *i.e.* fluid's latent and sensible heat.

The possibility use of two-phase flow in micro scale system is due to the number of advantages that overcome other cooling techniques. Madhour et al. (2011) reported that low mass flow rate is required for flow boiling, *i.e.* low pumping power, due to the latent heat. Thome and Cioncolini (2017) mentioned that the very high heat transfer coefficient of flow boiling is the main advantage of this technique compared to single-phase flow. The flow boiling heat transfer coefficient can be “1-2 orders of magnitude” larger than that in single-phase flow as they stated. Moreover, they reported that the operating temperature can be kept nearly isothermal during flow boiling.

Despite the abovementioned advantages, Karayiannis and Mahmoud (2017) mentioned some of the necessary steps on competing missing knowledge in order to facilitate the use of microchannel in industry as follows: (i) there is no general definition of different channel sizes, (ii) boiling incipience requires very high wall superheat, (iii) the lack of general prediction correlations or methods for two-phase flow patterns, heat transfer coefficient and pressure drop, (iv) system instabilities and flow reversal and (v) disagreement about the dominant heat transfer mechanism(s).

The motivation behind the present study can be summarized as follows:

1. There is no common agreement among researchers on the several fundamental aspects, such as the threshold diameter between conventional and microchannels, the dominant heat transfer mechanism(s), the complex effect of parameters (operating conditions, fluid properties, surface characteristics, and others), general flow patterns map and two-phase pressure drop or heat transfer coefficient prediction correlations. Therefore, more numerical and experimental investigations are still needed.
2. HFE-7100 was chosen as the working refrigerant in this study since it is a dielectric and eco-friendly coolant. Very few flow boiling visualization investigations were conducted using this refrigerant and thus there is lack of flow pattern results with this refrigerant. To the best of the author’s knowledge, there are no data available in the literature for HFE-7100 under flow condensation in single or multi-microchannels at low operating conditions.

3. In the present study, the effects of two major parameters on the flow boiling heat transfer were investigated, namely channel aspect ratio and material effect. From a design point of view, channel dimensions and material should be selected carefully in order to achieve the required cooling load for electronics. Channel aspect ratio is considered an important factor that may affect the thermal performance. Channel material with light weight, low cost, high corrosion resistance and best thermal performance is a required choice for electronics cooling.
4. Few experimental investigations were conducted to study the effect of channel aspect ratio. To the best of the author's knowledge there are just nine studies available in the literature, see Chapter 2. These studies showed that the effect of channel aspect ratio on the flow patterns, two-phase pressure drop and heat transfer coefficient was still unclear, *i.e.* there was no general agreement among the researchers about this effect. Accordingly, more investigations are required in this topic.
5. In some previous studies, the aspect ratio effect was examined at different channel hydraulic diameters. The surface roughness of the test sections was different in some studies and or not mentioned at all in others. Therefore, the effects of these two parameters, *i.e.* hydraulic diameter and surface roughness, were not isolated from the channel aspect ratio, and thus it is difficult to propose a conclusion on the aspect ratio effect.
6. Different surface material could result in different surface finish, surface roughness and thermal conductivity. Although several experimental investigations were carried out on these topics, the effect of these parameters on the flow boiling heat transfer is still not concluded.
7. In order to study the material effect, copper and aluminium were chosen in the present study. Copper was selected due to its high thermal conductivity and widely used in thermal design. Aluminium was chosen due to its different thermal conductivity, light weight, low cost and high corrosion resistance compared with copper. To the best of the author's knowledge, there is only a small number of flow boiling experimental studies using aluminium heat sink, see Chapter 2, Section 2.3. The flow boiling behaviour of HFE-7100 was not examined in a horizontal aluminium multi-microchannel heat sink.

1.2 Research Objectives

The objectives of the present study are summarized as follows:

1. Help clarify the complex fundamental issues of flow boiling and condensation in multi-microchannel configurations by conducting local heat transfer calculations corresponding to flow observations.
2. Investigate the influence of heat flux, mass flux and vapour quality, on the flow boiling characteristics, *i.e.* flow patterns, heat transfer coefficient and pressure drop.
3. Examine the effect of refrigerant mass flux, local vapour quality and saturation-to-wall temperature difference, *i.e.* coolant side conditions, on the condensation flow patterns and heat transfer coefficient.
4. Design channels of the same hydraulic diameter, base area and similar surface roughness in order to isolate and examine the effect of channel aspect ratio (width-to-height) on the flow boiling characteristics, such as flow patterns, pressure drop and heat transfer coefficient.
5. Identify the effect of channel surface material on the boiling flow patterns, heat transfer coefficient and pressure drop.
6. Evaluate the existing flow pattern maps, heat transfer coefficient and pressure drop correlations by comparing the experimental results with these maps and correlations.
7. Add new experimental results to the database in order to modify or propose new correlations in the future.
8. Identify the best existing correlations that give reasonable predictions. This could help in the design a small-scale thermal management system.
9. Propose a new design of small-scale pumped loop thermal management system for electronics cooling using dielectric and eco-friendly refrigerant. In order to reduce the pumping power and the overall system size and weight, the operating conditions are kept at system pressure near atmospheric, low flow rates and low inlet sub-cooling. Moreover, the present investigation aims to study and compare the thermal performance of this system with other cooling techniques.

1.3 Summary of Methodology

In order to achieve the research objectives, an experimental investigation was adopted in this study. The experimental rig was located in Room 304, Tower A building at Brunel University London. This rig includes an auxiliary cooling loop and test loop. Stainless steel construction was used to build this rig, *i.e.* the connecting pipes with ¼" in size, liquid reservoir and pre-heater. This was adopted to (i) minimize the space taken up by the rig, (ii) decrease the fluid losses by leakage, (iii) achieve high corrosion resistance and (iv) reduce the time taken to reach system stability, *i.e.* steady state condition. Digital speed driver connected to the micro-gear pump was used to control specific flow rate during the experiments. Moreover, a high-speed data logger (National Instruments Data Acquisition System) was mounted in this rig to connect all the measuring instruments, such as pressure transducers, thermocouples and flow meters. The data logger frequency was 1 kHz that means 1000 data can be recorded per second. This led to improvement in the accuracy and range of the measured data and helped in conducting frequency analysis. A computer and LabVIEW software were used to record and save all the measured data after overall stability was reached. This data was saved for 2 min, *i.e.* 120,000 data was recorded, and then averaged. A Phantom digital high-speed camera with an image resolution of 512×512 pixel at 1000 fps was mounted on a microscope with LED lighting ring in order to capture the flow patterns inside the test section. High precision micro-milling machine (Kern HSPC-2216) was used to fabricate all the test sections at specific machining conditions. HFE-7100 as the working fluid was tested using single-phase and two-phase flow experiments, *i.e.* flow boiling and condensation. Local heat transfer calculations corresponding to the flow visualization were conducted to explain the complex effects of flow behaviour.

1.4 Thesis Structure

The present thesis is arranged as follows:

Chapter 1 – Introduction: This chapter presents a brief introduction of different issues, such as high heat flux applications, existing cooling techniques and two-phase flow in a small-scale pumped loop cooling system. Moreover, the research motivation and objectives are summarized in this chapter. Finally, a summary of the methodology is discussed.

Chapter 2 – Literature Review: Previous studies are reviewed in this chapter. This includes flow boiling and condensation in horizontal and vertical channels, single and multi-channels and circular and non-circular channels. The effects of several parameters on the two-phase flow patterns, heat transfer coefficient and pressure drop are discussed in detail during this chapter. A summary of key findings of these studies is also concluded.

Chapter 3 – Experimental Facility and Methodology: This chapter provides the details of the experimental facility and the microchannel test sections. The calibration process of the measuring instruments is also described. Both the data reduction process and propagated uncertainty analysis are given in this chapter. The experimental procedure during single-phase and two-phase flow is also presented. This chapter also presents the overall validation. Finally, the repeatability of the experimental two-phase data is discussed.

Chapter 4 – Flow Boiling Patterns: Results and Discussion: This chapter shows the experimental flow visualization patterns and the flow pattern maps. The effect of heat flux, mass flux, channel aspect ratio and material is also presented. A comparison with some existing flow pattern maps is discussed in this chapter.

Chapter 5 – Flow Boiling Pressure Drop: Results and Discussion: The effect of heat flux, mass flux, exit vapour quality, channel aspect ratio and channel metal (copper and aluminium) is presented in this chapter. Moreover, the two-phase pressure drop results are compared with some existing correlations and discussed in this chapter.

Chapter 6 – Flow Boiling Heat Transfer: Results and Discussion: This chapter provides a brief detail of flow boiling incipience and flow boiling instability. The effect of several parameters on the flow boiling heat transfer coefficient is also

discussed. A comparison with some existing flow boiling heat transfer correlations is discussed in this chapter.

Chapter 7 – Condensation Flow Patterns: Results and Discussion: The experimental flow visualization patterns and flow pattern maps are presented in this chapter. This chapter also shows the effect of refrigerant mass flux and coolant side conditions on the experimental flow patterns. The results are compared with some existing flow pattern maps and presented in this chapter.

Chapter 8 – Flow Condensation Heat Transfer: Results and Discussion: This chapter includes the effect of refrigerant mass flux and coolant side conditions on the condensation heat transfer coefficient. A comparison with some existing condensation heat transfer correlations is also discussed.

Chapter 9 – Small-scale Thermal Management System: The effect of different parameters on the required pumping power is discussed in this chapter. A comparison between the present small-scale thermal management system and other cooling techniques is also presented. Finally, this chapter summarizes the upper cooling performance during flow boiling and condensation experiments.

Chapter 10 – Conclusions and Recommendations: The key findings drawn from the present study are given in this chapter. Moreover, some recommendations for future research in the flow boiling and condensation are proposed in this chapter.

Chapter 2

Literature Review

2.1 Introduction

This chapter presents several aspects of flow boiling and condensation in conventional and microchannels. Section 2.2 presents the definition of micro and macro scale, while flow boiling of HFE-refrigerants for cooling high heat flux systems is discussed in Section 2.3. Section 2.4 includes boiling incipience in channels. The latter section includes several topics, such as flow patterns in conventional and microchannels, flow pattern maps, heat transfer mechanism(s), flow boiling heat transfer and pressure drop correlations, flow boiling instabilities and effect of control parameters on the heat transfer coefficient and pressure drop. Section 2.5 presents flow condensation in microchannels. Condensation flow patterns and maps, effect of important parameters on the condensation heat transfer and pressure drop and flow condensation heat transfer correlations are discussed in this section. Finally, a concluding summary is given in Section 2.6.

2.2 Definition of Micro and Macro Scale

Several researchers have proposed a transition criterion from macro-to-micro scale using geometrical approach or bubble confinement approach. The classification criteria using geometrical approach, *i.e.* physical channel size, include surface area density and channel hydraulic diameter. For example, Shah and Sekulić (2003) classified the heat transfer surfaces through using the surface area density. The term surface area density β was related to the ratio of the heat transfer area to the unit volume. They used this term to distinguish between many channel sizes such as micro, meso, compact and conventional heat exchangers. Precisely, their classification was that at $\beta \geq 15000 \text{ m}^2/\text{m}^3$, $1 \mu\text{m} \leq D_h \leq 100 \mu\text{m}$, the heat

exchangers were considered as at micro scale. The meso (macro or mini) scale was classified as $\beta \geq 3000 \text{ m}^2/\text{m}^3$, $100 \text{ }\mu\text{m} \leq D_h \leq 1 \text{ mm}$. Compact heat exchangers had the values $\beta \geq 700 \text{ m}^2/\text{m}^3$, $D_h \leq 6\text{mm}$, for gas side operation, or $\beta \geq 400 \text{ m}^2/\text{m}^3$ for liquid side operation. Mehendale et al. (2000) also classified the ranges of heat exchangers, which are similar to those given by Shah and Sekulić (2003). Other classifications based on the applications were proposed by Kandlikar and Grande (2003). In their study, the ranges of heat exchangers were classified into three groups in term of hydraulic diameter. The first group is conventional heat exchangers where D_h is more than 3 mm. The second group is mini heat exchangers where $200 \text{ }\mu\text{m} < D_h \leq 3 \text{ mm}$. The third group is micro heat exchangers where $10 \text{ }\mu\text{m} < D_h \leq 200 \text{ }\mu\text{m}$.

It is worth mentioning that the abovementioned classifications have some limitations, *i.e.* they do not include the effect of fluid properties. Accordingly other criteria were used by researchers including the bubble confinement approach. This approach is based on the confined bubble in small channels and dominant gravitational and surface tension forces. Dimensionless numbers were proposed to represent the effect of these forces such as Eötvös number, Confinement number, Laplace constant and Bond number. Brauner and Maron (1992) established the first criterion for the microchannel heat sink. They suggested the Eötvös number ($E\ddot{o} = \frac{D_h^2 * g(\rho_l - \rho_g)}{\sigma}$) as a non-dimensional criterion distinguishing macro and micro scale phenomena in channels as follows:

$$E\ddot{o} = 4\pi^2 \quad (2.1)$$

In the Eötvös number, D_h is the hydraulic diameter, g is the gravity, σ is surface tension, and ρ_l and ρ_g are the liquid and vapour densities, respectively. Brauner and Maron (1992) concluded that the transition from macro to micro scale occurred when $4\pi^2/E\ddot{o} > 1$. Another formula was proposed by Kew and Cornwell (1997), who derived a confinement number C_o to recognize the difference between micro and macro scale.

$$C_o = \frac{1}{D_h} \left\{ \frac{\sigma}{g(\rho_l - \rho_g)} \right\}^{0.5} \quad (2.2)$$

The authors recommended the threshold at $C_o = 0.5$, where $C_o < 0.5$ relates to macrochannels and $C_o > 0.5$ to microchannels. Generally, the value of the Eötvös

and Confinement numbers are based on the term of the Laplace constant, which can be calculated from the equation below.

$$L_a = \left\{ \frac{\sigma}{g(\rho_l - \rho_g)} \right\}^{0.5} \quad (2.3)$$

Accordingly, the hydraulic diameter for transition to micro scale which depends on $E\ddot{o}$ and C_o can be defined in terms of L_a , as $D_h < 2\pi L_a$ based on the Eötvös number and $D_h < 2L_a$ for the Confinement number. Triplett et al. (1999) considered that the values of both the hydraulic diameter and the Laplace constant are important to define channel size. Hence, they defined micro scale as a channel with a hydraulic diameter approximately the same as or smaller than the Laplace constant, *i.e.* the transition $\leq L_a$. Ullmann and Brauner (2007) studied the effect of the channel diameter on the flow regime transition mechanism, and adopted the Eötvös number based on flow pattern maps, and the following criterion was found:

$$E\ddot{o} = 1.6 \quad (2.4)$$

They suggested that the channel was micro scale when $E\ddot{o} \leq 1.6$. Harirchian and Garimella (2010) concluded that the transition was affected by the velocity of the fluid, so they proposed the criterion based on the convective Confinement number $Bd^{0.5}Re$ defined as follows:

$$Bd^{0.5}Re = 160 \quad (2.5)$$

For $Bd^{0.5}Re < 160$, the channel was considered micro. Ong and Thome (2011a) conducted an experimental analysis of flow regimes and liquid film thickness. Based on this, they developed a formula using the Confinement number, *i.e.* $C_o = 0.34$, to define the transition diameter between macro and micro scale. They reported that the gravity force dominated when $C_o < 0.34$ (denoting macro-scale) and became weak when $C_o > 1$ (denoting micro-scale). Other researchers such as Tibiriçá and Ribatski (2015) adopted new criteria to identify the differences between micro and macro scale by analyzing flow patterns. They presented their criteria based on two characteristics that occur in flow boiling in a circular horizontal channel, namely non-occurrence of stratified flow and uniform thickness of the liquid film along the tube in annular flow. They reported that in small diameter channels, the stratified flow is absent. Also, the liquid film thickness becomes more uniform than in larger diameter channels. Accordingly, they proposed two criteria; for plug flow (when the

stratified flow absented), see Eq. (2.6), and for annular flow (uniform liquid film thickness) as shown in Eq. (2.7).

$$D = L_a \sqrt{8 \cos \theta} \quad (2.6)$$

$$D = \sqrt{\frac{1}{20}} L_a \quad (2.7)$$

The transition to micro scale occurred when the above criteria were the same as or more than one. All abovementioned transition criteria of different channel scales are summarized in Table 2.1.

Table 2.1 Transition criteria of different channel sizes reported in the literature.

Author(s)	Criterion	Channel classification
Geometrical approach		
Mehendale et al. (2000)	$D_h > 6 \text{ mm}$	Conventional
	$1 \leq D_h < 6 \text{ mm}$	Compact
	$0.1 \leq D_h < 1 \text{ mm}$	Macro/Mini
	$0.001 \leq D_h < 0.1 \text{ mm}$	Micro
Kandlikar and Grande (2003)	$D_h > 3 \text{ mm}$	Conventional
	$0.2 < D_h \leq 3 \text{ mm}$	Macro/Mini
	$0.01 < D_h \leq 0.2 \text{ mm}$	Micro
Bubble confinement approach		
Brauner and Maron (1992)	$4\pi^2/E\ddot{o} > 1$	Micro
Kew and Cornwell (1997)	$C_o < 0.5$	Macro
	$C_o > 0.5$	Micro
Triplett et al. (1999)	$D_h \leq L_a$	Micro
Ullmann and Brauner (2007)	$E\ddot{o} \leq 1.6$	Micro
Ong and Thome (2011a)	$C_o < 0.34$	Macro
	$C_o > 1$	Micro
Harirchian and Garimella (2010)	$Bd^{0.5}Re < 160$	Micro
Tibirićá and Ribatski (2015)	$L_a \sqrt{8 \cos \theta} / D_h \geq 1$ (for plug flow)	Micro
	$\sqrt{1/20} L_a / D_h \geq 1$ (for annular flow)	Micro

In order to make the above criteria clearer, and to recognize the difference between these scales, flow boiling of HFE-7100 at a system pressure of 101 kPa and mass flux of $100 \text{ kg/m}^2\text{s}$ was assumed. The transition diameter was calculated from the above formulae and compared with the current hydraulic diameter as shown in Fig. 2.1. This figure indicates that the threshold diameter from macro to micro scale differed from one formula to another. For example, this threshold diameter was near 3 mm using the formula by Ong and Thome (2011a), while it decreased to around 1 mm using the criteria by Harirchian and Garimella (2010). Moreover, different threshold diameters were found based on different flow patterns as proposed by Tibiriçá and Ribatski (2015). The present hydraulic diameter of 0.46 mm is considered of micro scale size based on a number of criteria, *i.e.* Brauner and Maron (1992), Kew and Cornwell (1997), Triplett et al. (1999), Ullmann and Brauner (2007), Harirchian and Garimella (2010), Ong and Thome (2011a) and Tibiriçá and Ribatski (2015) (using a criterion of plug flow, *i.e.* c1). In contrast, this diameter is classified as a macro or mini scale if it is compared with some criteria that were published by Mehendale et al. (2000), Kandlikar and Grande (2003) and Tibiriçá and Ribatski (2015) (using a criterion of annular flow, *i.e.* c2).

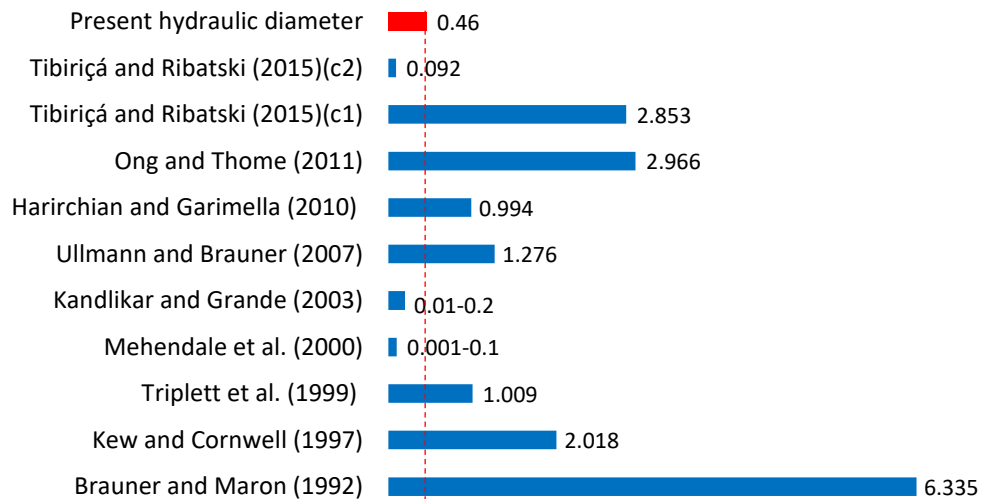


Figure 2.1 Threshold diameter from macro to micro scale based on a number of criteria compared to the present hydraulic diameter in [mm].

The previous comparison showed that the definition of micro scale or the threshold size is still unclear due to the different criteria used to define this term. It seems that large experimental data, including different channel geometries, fluids and operating conditions, is required in order to propose general transition criteria.

2.3 HFE-7100 for Cooling High Heat Flux Devices

Since the flow boiling of dielectric coolants is considered a good choice for cooling electronics, several cooling techniques were proposed using different refrigerants. HFE-7100 as a dielectric and eco-friendly coolant received a considerable attention by the scientific community. This refrigerant is from 3M Novec fluids. The full name is methoxy-nonafluorobutane with a chemical formula $C_4F_9OCH_3$, and it has the following characteristics, 3M (2002):

1. Non-flammability.
2. Low toxicity and minimally skin irritation.
3. Low ozone depletion potential-ODP: 0.00.
4. Low Global Warming potential-GWP: 320 (over 100-year).
5. Low atmospheric lifetime: 4.1 years.
6. Compatible with hard polymers and most metals.

In addition to the previous features, this fluid has high dielectric strength (28 kV, 0.1" gap, see 3M (2002)) and thus it is suitable for cooling electronics as mentioned by Lee and Mudawar (2009). Moreover, its saturation temperature at 101 kPa is approximately 60 °C. Therefore, it is considered a suitable choice for cooling electronic devices that require working surface temperature below 85 °C, such as microprocessors and fuel cells.

Several experimental investigations were carried out using HFE-refrigerants in rectangular multi-channels for electronics cooling as summarized in Table 2.2. HFE-7100 was tested in all these studies, while Yang et al. (2016) tested HFE-7000. Different channel geometries were designed and examined to reach high heat fluxes, such as straight channels, diverging channels, nanowire-coated channels, saw-teeth channels and integrated channels with multiple micro nozzles and re-entry micro cavities, as shown in Fig. 2.2.

Table 2.2 Flow boiling of HFE-7100 in previous studies (Yang et al. (2016) tested HFE-7000).

Author(s)	D_h [mm]	Operating conditions	Channel configuration
Lee and Mudawar (2008a) and Lee and Mudawar (2008b)	0.175–0.416	670–6730 kg/m ² s Inlet fluid: -30–0 °C	Straight channels
Sung and Mudawar (2008)	1.5	Inlet jet velocity: 0.39–7.37 m/s Inlet fluid: -40–20 °C	Hybrid cooling module: microchannels/slot-jet
Lee and Mudawar (2009)	0.175–0.416	670–2345 kg/m ² s Inlet fluid: -30–20 °C	Straight channels
Sung and Mudawar (2009a) and Sung and Mudawar (2009b)	1.5	Inlet jet velocity: 1.05–6.5 m/s Inlet fluid: -40–20 °C	Hybrid cooling module: microchannels/micro-jet (single slot and circular jet)
Yang et al. (2011)	0.48–0.79	100–400 kg/m ² s	Straight channels
Wang et al. (2012)	0.825	100–300 kg/m ² s	Straight channels
Fu et al. (2013)	0.4–1.13	39–180 kg/m ² s	Diverging channels
Hsu et al. (2015)	0.44	100 and 200 kg/m ² s	Straight channels
Yang et al. (2016)	0.23	1018–2206 kg/m ² s	Straight channels with nanowire-coated
Fu et al. (2017)	0.8	127–285 kg/m ² s	Straight channels with saw- teeth
Drummond et al. (2018)	0.0196–0.0317	1300–2900 kg/m ² s	Straight channels
Li et al. (2018)	0.22	231–2772 kg/m ² s	Straight channels integrated with multiple micro nozzles and re-entry micro cavities
Choi et al. (2019)	0.89	200–500 kg/m ² s	Straight channels

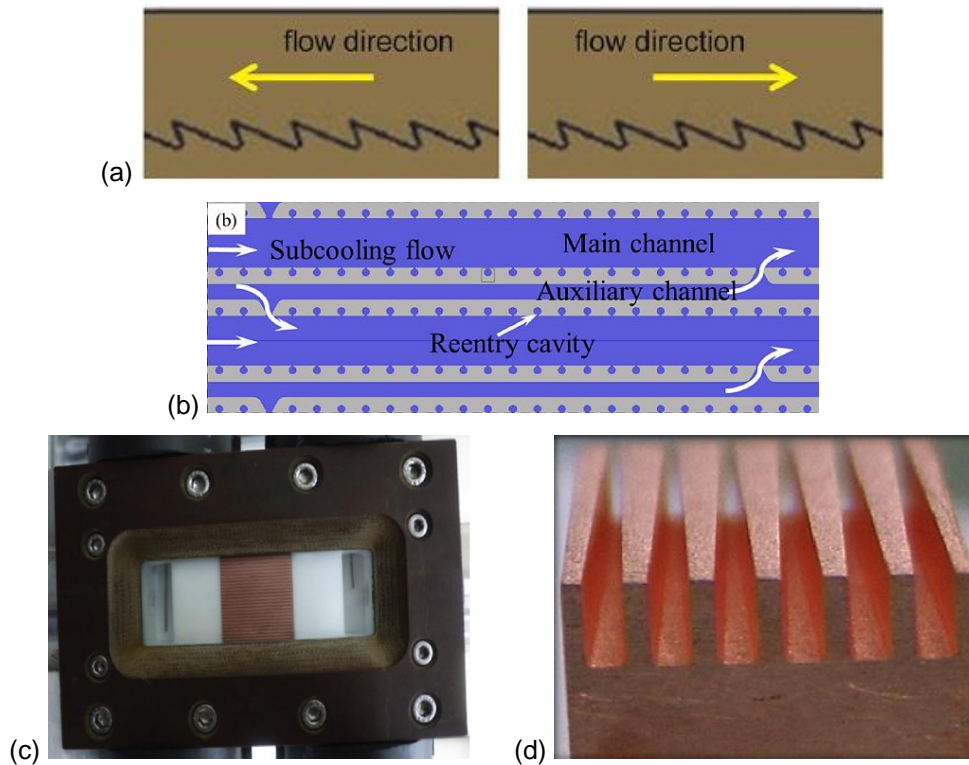


Figure 2.2 Different channel geometries using flow boiling of HFE-7100:
 (a) Saw-teeth channels, Fu et al. (2017) (b) Integrated channels, Li et al. (2018)
 (c) Straight channels, Hsu et al. (2015) (d) Diverging channels, Fu et al. (2013).

HFE-7100 in hybrid cooling module is another technique adopted by researchers to enhance heat flux. This module included microchannels and slot-jet as proposed by Sung and Mudawar (2008) or microchannels and single slot or circular jet as mentioned by Sung and Mudawar (2009b), see Fig. 2.3. This figure shows that the test section has one inlet fluid port, at the topside, and two outlet fluid ports at both sides. Therefore, the coolant enters the test section from the topside through the micro-jets, then flows in both directions through the microchannels. High fluid sub-cooling was set using primary and secondary cooling loops, see Lee and Mudawar (2008a), Sung and Mudawar (2008), Lee and Mudawar (2009) and Sung and Mudawar (2009b). The primary cooling loop included the test section and the coolant HFE-7100, while the secondary cooling loop included a low temperature refrigeration compression system. This system supplied low inlet coolant temperature at the test section ranging from -40 to 20 °C as presented in Table 2.2.

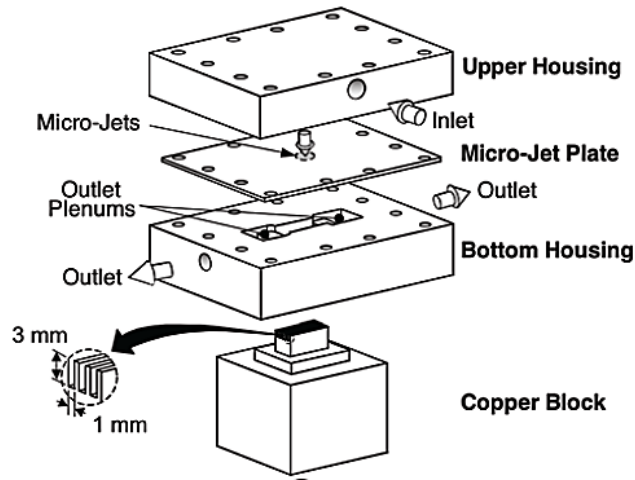


Figure 2.3 Flow boiling of HFE-7100 using hybrid cooling module, Sung and Mudawar (2009b).

Fig. 2.4 illustrates the maximum base heat flux that was reached by the abovementioned studies. A base heat flux as high as 11.27 MW/m^2 was reported by Sung and Mudawar (2009a) using hybrid cooling technique, while Drummond et al. (2018) reached a heat flux of 9.1 MW/m^2 , which is the highest value using straight channels.

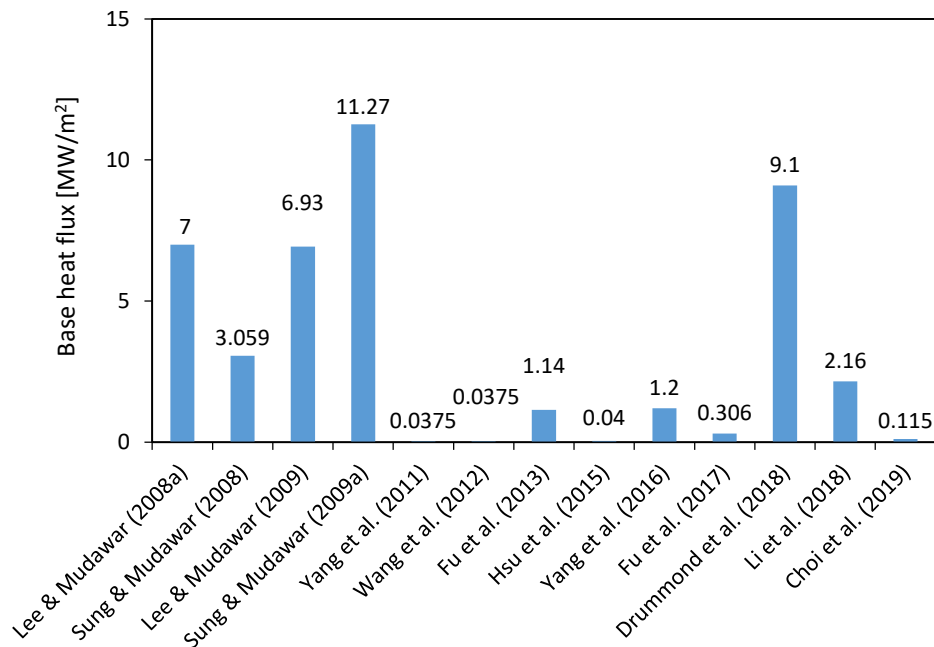


Figure 2.4 Maximum heat flux reported in the literature using flow boiling of HFE-refrigerants in multi-channels.

In addition to flow boiling of HFE-refrigerants in multi-microchannel configurations, other studies were performed using different configurations, such as falling jet by Mahmoudi et al. (2014), pool boiling by Souza et al. (2014), micro-jets by Muszynski and Mikielewicz (2016) and vertical single tube by Eraghubi et al. (2019).

Although several studies in flow boiling of HFE-7100 were conducted, some unresolved issues can be summarized here. Few flow visualization studies were carried out and thus there is lack of flow pattern results for this refrigerant. The average heat transfer coefficient was calculated and presented in some studies, see Lee and Mudawar (2008a), Yang et al. (2011), Wang et al. (2012), Hsu et al. (2015), Yang et al. (2016), Drummond et al. (2018) and Li et al. (2018). It is known that the local heat transfer calculations with flow visualization play a major role in flow boiling results and help to explain the complex influence of flow behaviour. Very high mass fluxes and/or high inlet sub-cooling coolant were used to achieve high heat fluxes. This means that very high pumping power is required and a large condenser or an extra cooling system should be used. In some previous techniques, such as in hybrid cooling modules using circular micro-jets, high pressure drop was measured, *i.e.* around 170 kPa, see Sung and Mudawar (2009a), although high heat flux was dissipated.

As discussed in Chapter 1, the present study aims to examine the effect of channel surface material using copper and aluminium. To the best of the author's knowledge, there are few flow boiling experimental investigations carried out using aluminium heat sinks, as presented in Table 2.3. This table shows that different channel geometries tested such as horizontal/vertical flow and single/multi-channels. Minimum channel hydraulic diameter of 0.63 mm was examined, see Wen et al. (2018). Moreover, flow boiling characteristics were investigated using different fluids; water, R22, R32, R1234yf, R1234ze, R134a and FC-84. It can be concluded that HFE-7100 in aluminium horizontal multi-microchannels was not studied in the literature. The present channel hydraulic diameter of 0.46 mm was also not tested before.

Table 2.3 Flow boiling studies using aluminium channels reported in the literature.

Author(s)	Channel geometry*	D_h [mm] / N [-]	Fluid(s)
Kandlikar and Spiesman (1998)	H, S, R	5.58 / 1	Water
Agostini et al. (2002)	V, M, R	2.01 / 11	R134a
Warrier et al. (2002)	H, M, R	0.75 / 5	FC-84
Kim et al. (2004)	H, M, R	1.41 / 7	R22
Agostini and Bontemps (2005)	V, M, R	2.01 / 11	R134a
Mastrullo et al. (2016)	H, M, R	1.33 / 7	R134a, R1234yf and R1234ze
Mastrullo et al. (2017)	H, M, R	0.8 and 1.3 / 7	R134a, R1234yf, R1234ze and R32
Wen et al. (2018)	H, M, R	0.63 and 0.72 / 23 and 14	R134a
Wen et al. (2019)	H, M, R	1.28 and 1.59 / 11 and 9	R134a
* V: vertical, H: horizontal, S: single channel, M: multi-channels, R: rectangular.			

2.4 Boiling Incipience in Channels

Boiling is defined as a process that changes the phase of fluid from liquid to vapour. It can be divided into pool and flow boiling based on the fluid motion. Generally, flow boiling consists of sub-cooled and saturated boiling. Sub-cooled boiling happens at early stages of boiling, when the fluid inlet temperature is lower than the saturation temperature, while the wall surface temperature exceeds both of them. In this type of boiling, small number of bubbles occurs near the channel surface and suddenly disappears. Saturated boiling occurs when the fluid temperature is equal to the saturation temperature, while the wall surface temperature is higher. In conventional channels, two main mechanisms can be identified in saturated boiling, namely nucleate and convective boiling. In nucleate boiling, bubbles form at the nucleation sites, whose location and number may depend on a number of parameters,

such as fluid properties, channel surface structure, and operating conditions. In convective boiling, a thin liquid film appears around the vapour core, *i.e.* annular flow. Further details about the boiling mechanisms are presented in Section 2.4.5.1.

2.4.1 Flow patterns in conventional and microchannels

It is known that local heat transfer calculations with flow visualization play a major role in understanding the complexity of two-phase flow behaviour. Therefore, the features of two-phase flow patterns are investigated in detail by the scientific community. A high-speed, high-resolution digital camera is widely used to identify the flow patterns. In order to capture the flow regimes in the test section, a transparent part made of glass or polycarbonate is sometimes located at the end, if a metallic tube is used as the test section. This part is located directly after the test section, if a metal tube is tested. On the other hand, the top cover plate of the test section is made as a transparent part for non-circular channels. In this section, the features of flow patterns in different channel sizes and orientations are described. This discussion includes (i) horizontal and vertical channels, (ii) different channel dimensions and (iii) single and multi-channels. Moreover, nucleating bubbles in the liquid film is also discussed and presented.

2.4.1.1 Flow patterns in horizontal and vertical channels

The features of flow patterns in horizontal and vertical channels are expected to be different. Collier and Thome (1994) discussed these features that occur in large horizontal and vertical tubes. These flow patterns are shown schematically in Fig. 2.5, and more details were given by Hewitt and Hall-Taylor (1970) and Collier and Thome (1994).

In vertical upwards flow, five flow patterns were classified as follows:

1. Bubbly flow (B): A number of vapour bubbles appear separately in a liquid phase. These bubbles may form as small or large spherical shapes or as a cap with a tail. Also, the diameter of these bubbles is less than the channel diameter.

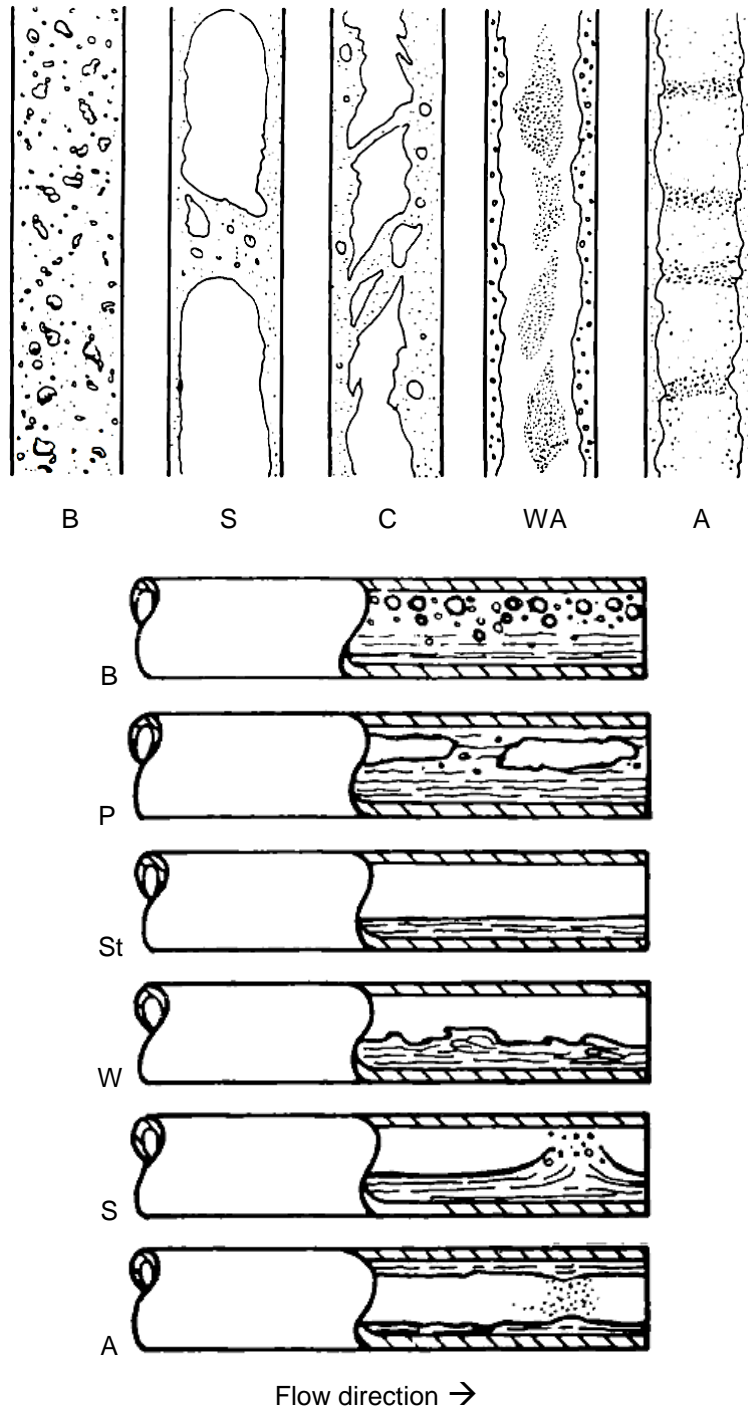


Figure 2.5 Flow patterns in large vertical upwards flow and horizontal channels, Collier and Thome (1994). B: bubbly, S: slug, C: churn, WA: wispy-annular, A: annular, P: plug, St: stratified, W: wavy.

2. Slug flow (S): The bubbles coalesce, then become bigger, and form into a cylindrical shape, their sizes are approximately equal to the channel diameter.

These slugs are surrounded by a liquid film and some small bubbles may be observed in the liquid slugs between them.

3. Churn flow (C): When the vapour velocity becomes higher, the big bubbles in slug flow break and separate, which leads to the appearance of churn flow. This regime is sometimes called slug-annular or semi-annular flow.
4. Wispy-annular flow (WA): At high mass fluxes, a vapour core with small liquid droplets occurs in the middle of the channel. This core is surrounded by a thick liquid film layer, and small vapour bubbles may occur in this layer.
5. Annular flow (A): A liquid film layer becomes more wavy or smooth on the internal channel wall. The vapour core still exists in this regime with or without liquid droplets.

In horizontal flow, six major flow patterns were identified, Collier and Thome (1994):

1. Bubbly flow (B): The flow in this regime is similar to that in vertical channels. Nevertheless, there is a simple difference between them, which is that the bubbles in horizontal channels move towards the upper side of the channel.
2. Plug flow (P): This regime is similar to the slug flow in vertical channels. However, the liquid layer becomes thicker at the bottom side than at the upper side. This regime is also called elongated bubble flow.
3. Stratified flow (St): At very low fluid velocities, the flow separates into two regions; liquid phase at the bottom side of the channel and vapour phase at the upper side. A smooth interface between these phases can be identified.
4. Wavy flow (W): When the vapour velocity increases, stratified flow develops into wavy flow and a number of waves occur on the liquid interface.
5. Slug flow (S): When the vapour velocity becomes higher, the previous flow develops into slug flow. The summits of these waves may reach the upper surface of the channel.
6. Annular flow (A): With further increasing vapour velocity, a liquid film layer occurs around the vapour core, and some liquid droplets may occur in this core. This layer becomes thicker at the bottom surface of the channel compared with the top surface.

2.4.1.2 Flow patterns in different channel dimensions

In the literature, several flow patterns were found at different channel dimensions. A comparative review conducted by Kawaji and Chung (2004) showed that a significant difference in the visualized two-phase flow patterns was between horizontal mini and micro scale channels. This was concluded based on the past adiabatic two-phase flow studies and their experiments. They presented different experimental investigations using a mixture of gas and water in their review. They stated that, for horizontal minichannel, *i.e.* diameter ≈ 1 mm, five flow patterns were found, namely bubbly, slug, churn, slug-annular, and annular flow. The name of slug flow was also reported in other studies using different names, such as capillary slug, plug and bubble-train flow as they mentioned. For horizontal microchannel, dispersed bubbly, gas slug, liquid-ring, liquid lump, and liquid droplet flow were identified. The schematic diagram of these regimes is presented in Fig. 2.6.

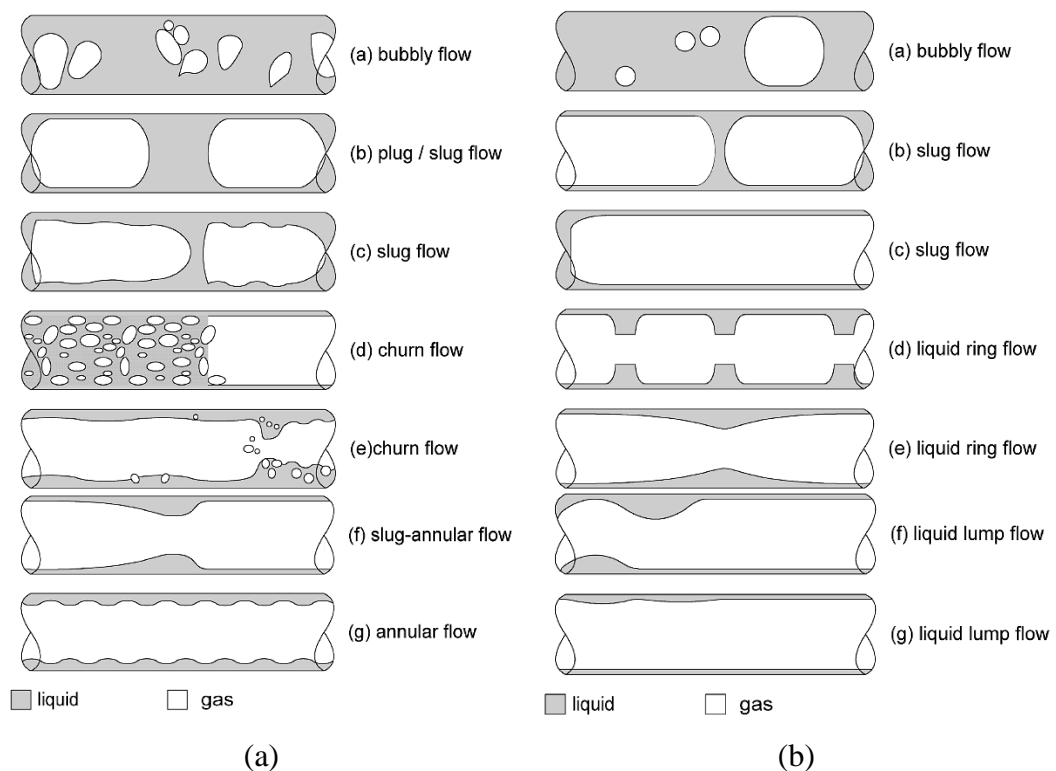


Figure 2.6 Two-phase flow patterns in horizontal channels, Kawaji and Chung (2004): (a) Minichannel (b) Microchannel.

Very clear images of different flow patterns were captured by Chen et al. (2006) using R134a in different small diameter tubes. They tested four vertical stainless steel tubes with inner diameter of 1.1, 2.01, 2.88 and 4.26 mm at system pressure of 6–14 bar. A Phantom high-speed, high-resolution camera was used for flow visualization. Dispersed bubble, bubbly, confined bubble, slug, churn, annular and mist flow were found as shown in Fig. 2.7.

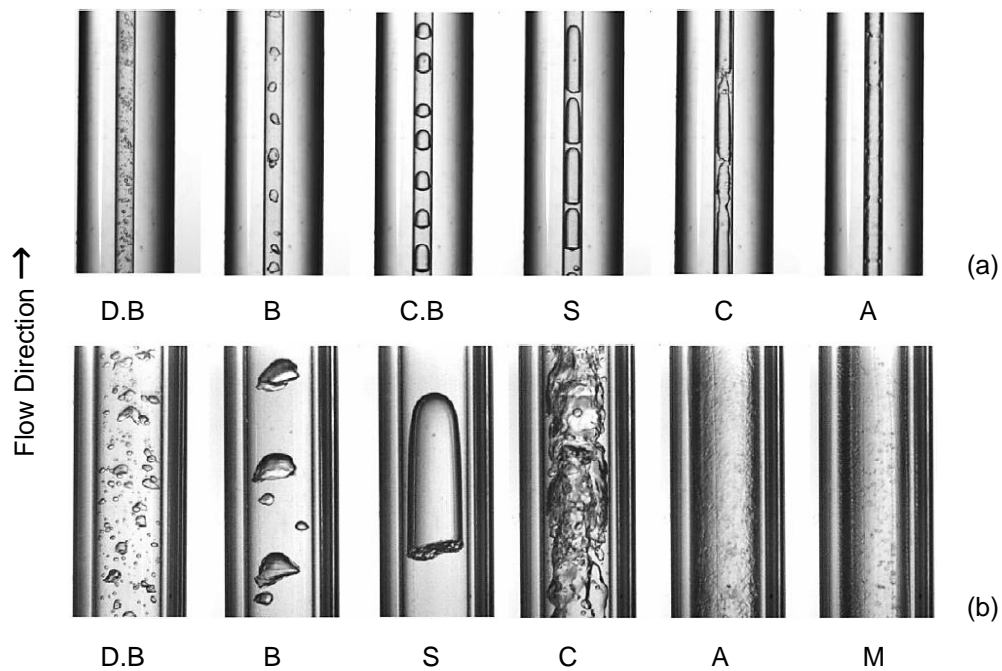


Figure 2.7 Flow patterns of R134a in vertical small tubes at system pressure of 10 bar with inner diameter of (a) 1.1 mm, (b) 4.26 mm, Chen et al. (2006).

D.B: dispersed bubble, B: bubbly, C.B: confined bubble, S: slug, C: churn, A: annular, M: mist.

They reported that the flow patterns in the tubes of 2.88 and 4.26 mm were similar to those visualized in conventional tubes. The last regime, *i.e.* mist flow, was only captured in the diameter of 4.26 mm. They defined the dispersed bubble flow as a number of small bubbles floating in a liquid phase. At bubbly flow, bubble size became larger than in dispersed bubble flow, but remained smaller than the tube diameter. When bubble size reached the tube diameter, confined bubble was observed, which had “spherical cap and bottom”. This regime was found in the tube of 2.01 mm at system pressure of 6 bar. It also occurred in 1.1 mm at all ranges of 6–14 bar. Their result showed that the transition boundaries of churn/annular and

slug/churn occurred at higher vapour velocities, when the tube diameter decreased. Therefore, they concluded that these transition boundaries depend strongly on the tube diameter. In contrast, the transition boundaries of bubbly/slug and dispersed bubble/churn were not significantly affected by diameter.

Recently, Eraghubi et al. (2019) performed flow boiling experiments using HFE-7000 in a vertical tube. A transparent tube coated with Indium Tin Oxide with 8 mm inner diameter and 120 mm length was fabricated. They conducted their experiments at a system pressure of 1.2 bar, inlet sub-cooling of 2 K and mass flux of 50–150 kg/m²s. A high-speed camera was used to capture flow patterns. They reported presence of bubbly, bubbly-slug and churn flow, as shown in Fig. 2.8. Moreover, they mentioned that the nucleation site density, bubble size and frequency increased with increasing heat flux. Fig. 2.8(a) and (b) show bubbly flow at different heat fluxes. Fig. 2.8(c) illustrates that both bubbly and slug flow occurred, while churn flow was observed near exit. Slug flow was seen near the inlet and churn flow became the dominant regime at the upper side as shown in Fig. 2.8(d). Fig. 2.8(e) shows churn flow along the tube.

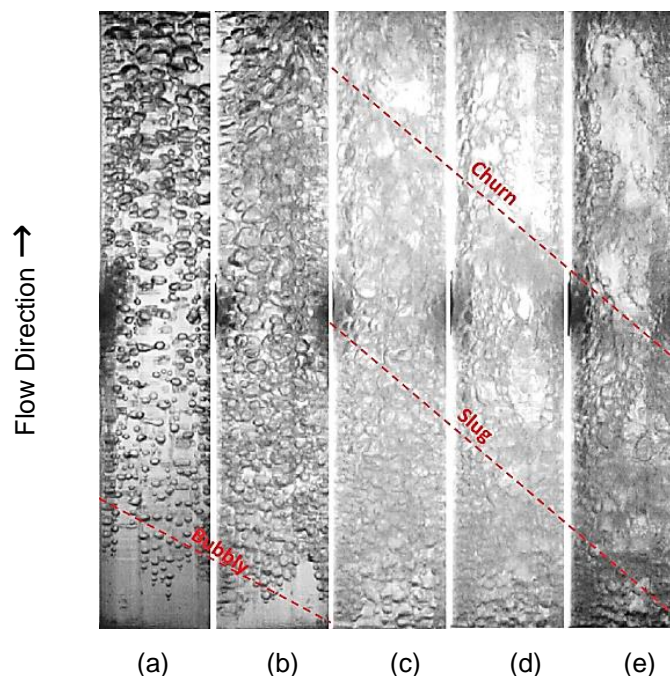


Figure 2.8 Flow patterns of HFE-7000 in a vertical tube at mass flux of 100 kg/m²s and heat flux of: (a) 8.8 (b) 20.3 (c) 35.7 (d) 51.4 (e) 61.7 kW/m², Eraghubi et al. (2019).

2.4.1.3 Flow patterns in a horizontal single channel

Some experimental studies were carried out using a horizontal single microchannel. For example, Singh et al. (2009) captured three flow patterns, namely bubbly, slug and annular flow as shown in Fig. 2.9. These patterns were visualized in a horizontal trapezoidal microchannel with hydraulic diameter of 0.14 mm using water as a working fluid. They stated that, at low flow rates and heat fluxes, bubbly flow occurred along the channel. Slug flow was visualized, when the heat flux increased, while annular flow occurred at high heat fluxes.

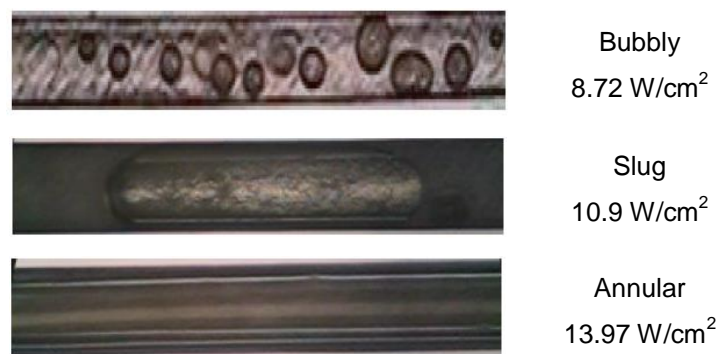


Figure 2.9 Flow patterns of water in a horizontal microchannel at different heat fluxes and mass flow rate of 0.2 ml/min, Singh et al. (2009).

Revellin and Thome (2007b) conducted an experimental investigation of two-phase flow in two horizontal stainless steel tubes with hydraulic diameter of 0.5 and 0.8 mm. R134a and R245fa were tested at a heat flux of 3.2–422.1 kW/m², mass flux of 200–2000 kg/m²s and sub-cooling of 2, 3 and 5 K. Four flow patterns were reported, namely bubbly, slug, semi-annular and annular flow as presented in Fig. 2.10. Moreover, two transition patterns; bubbly/slug and slug/semi-annular were identified. At very low vapour qualities, bubbly flow occurred and was more or less absent when mass flux became high. Vapour bubbles with variable lengths and hemispherical cap were observed during the slug flow, while in the semi-annular flow, liquid slugs was found to disappear. Liquid film occurred at the tube wall with the appearance of vapour core and churning liquid phase.

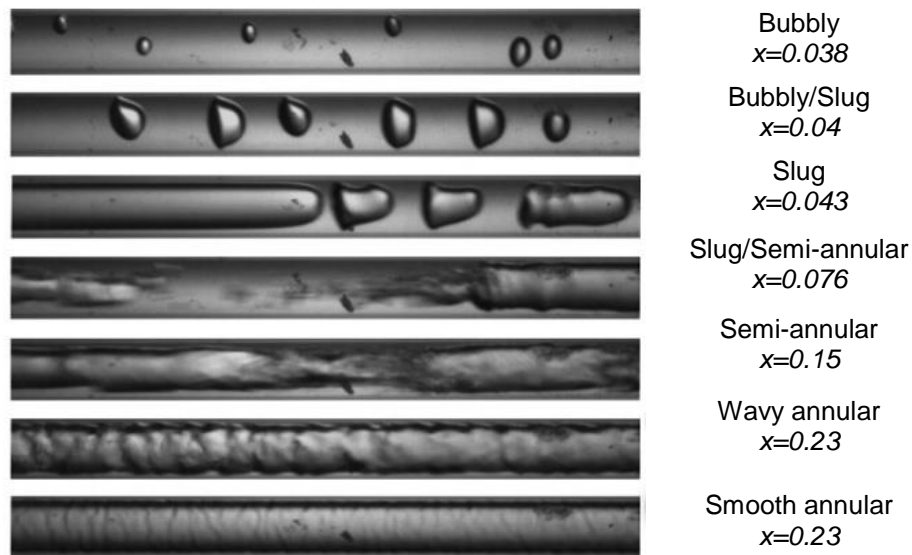


Figure 2.10 Flow patterns of R245fa in horizontal tube of 0.5 mm diameter at $G=500$ $\text{kg/m}^2\text{s}$ and saturation temperature of 35 $^\circ\text{C}$, Revellin and Thome (2007b).

2.4.1.4 Flow patterns in multi-channels

Two-phase flow patterns in horizontal multi-microchannels were also reported by the scientific community. Flow patterns in multi-channels could differ from those in a single channel. Flow reversal and maldistribution are commonly reported in multi-channels leading to different flow rates among the channels. This may result in different features of flow patterns inside these channels. Harirchian and Garimella (2009a) carried out an experimental study of flow boiling heat transfer of FC-77 in horizontal multi-microchannels. They fabricated seven silicon heat sinks with different channel widths and constant channel height. In their study, the channel height was 0.4 mm, while the channel width ranged from 0.1 to 5.85 mm. A high-speed camera was used to capture the flow patterns, while the mass flux was set at 225 – 1420 $\text{kg/m}^2\text{s}$. Generally, six flow patterns were visualized in their study; bubbly, slug, churn, wispy-annular, annular and inverted annular flow as shown in Fig. 2.11. Small bubbles, smaller than channel cross-sectional area, were found at the channel walls. Slug flow occurred when the heat flux increased gradually. Wispy-annular flow was characterized by a vapour core, with large droplets, surrounded by unstable and thick liquid film. In annular flow, this liquid film became thinner than that in the previous regime. Moreover, the interface between the liquid film and vapour core became wavy. Small liquid droplets were also found in this core. When the heat flux increased further, *i.e.* critical heat flux, the inverted annular flow was established.

This regime was characterized by a liquid core surrounded by a “thick vapour blanket”, Harirchian and Garimella (2009a). They mentioned that this regime should be avoided during the flow boiling heat transfer since it caused a sudden increase in the wall temperature and reduction in the heat transfer coefficient. They reported that different flow patterns were visualized when the channel width was changed. For example, in the channel of width 0.1 mm, bubbly flow was not captured, while slug, intermittent churn/annular flow occurred. When the width was 0.4 mm, bubbly, intermittent bubbly/slug, intermittent churn/annular, intermittent churn/wispy-annular flow were found. In the larger channel width, *i.e.* 5.85 mm, bubbly, intermittent churn/wispy-annular and intermittent churn/annular flow were captured. They stated that the flow patterns in the channel width of 1 and 2.2 mm were similar to those in 5.85 mm. However, slug flow was found in these two widths and was not seen in the larger one as they reported.

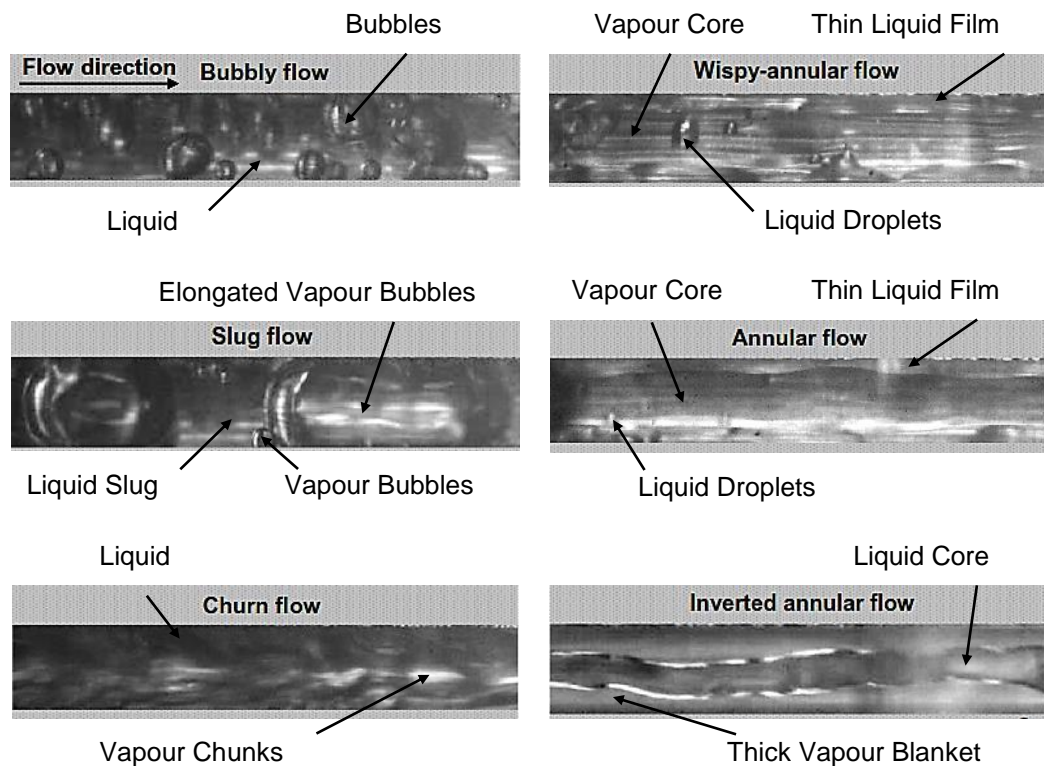


Figure 2.11 Flow patterns of FC-77 in horizontal multi-microchannels, Harirchian and Garimella (2009a). Labels introduced by present author based on their description.

Balasubramanian et al. (2013) conducted an experimental study of flow boiling heat transfer of de-ionized water in horizontal copper multi-microchannels. They fabricated two heat sinks; the first one consisted of 16 channels, while the second heat sink consisted of 40 channels. These channels had hydraulic diameter of 0.488 and 0.504 mm. Their experiments were carried out at heat flux up to 4200 kW/m² and mass flux of 88–751 kg/m²s. Dispersed bubble, intermittent and annular flow were found as shown in Fig. 2.12. They stated that dispersed bubble flow was found for a hydraulic diameter of 0.488 mm at higher mass fluxes and lower heat fluxes. The intermittent flow consisted of elongated bubble and slug flow that occurred alternately during different periods. At given mass flux, the intermittent flow changed to annular flow with increasing heat flux.

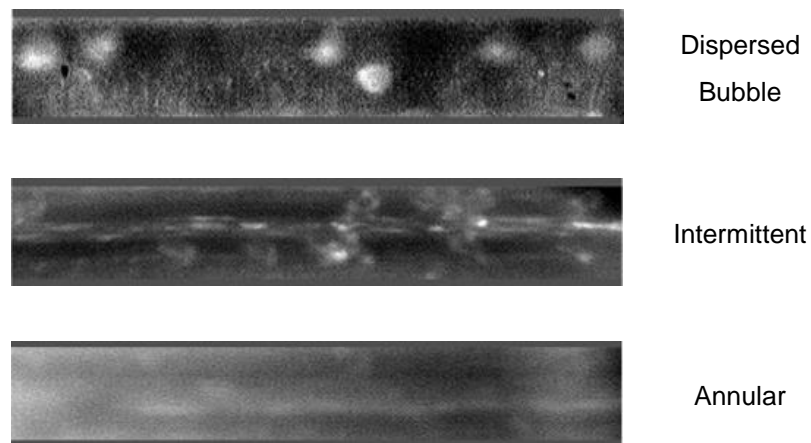


Figure 2.12 Flow patterns of de-ionized water in horizontal multi-microchannels at different mass and heat fluxes, Balasubramanian et al. (2013).

Thiangtham et al. (2016) tested R134a in horizontal rectangular microchannels with hydraulic diameter of 0.421 mm. Twenty seven parallel channels made of copper were fabricated with height, width and length of 0.47, 0.382 and 40 mm, respectively. Their experiments were set at saturation temperature of 13, 18 and 23 °C, heat flux of 3–127 kW/m², mass flux of 150–600 kg/m²s and inlet vapour quality of 0.05–0.92. They conducted their experiments by varying the inlet vapour quality at the test section using an electrical pre-heater. They reported that bubble, bubble and slug, slug, churn, wavy-annular and annular flow were visualized as shown in Fig. 2.13. They also stated that these regimes changed from one to another with increasing heat flux.

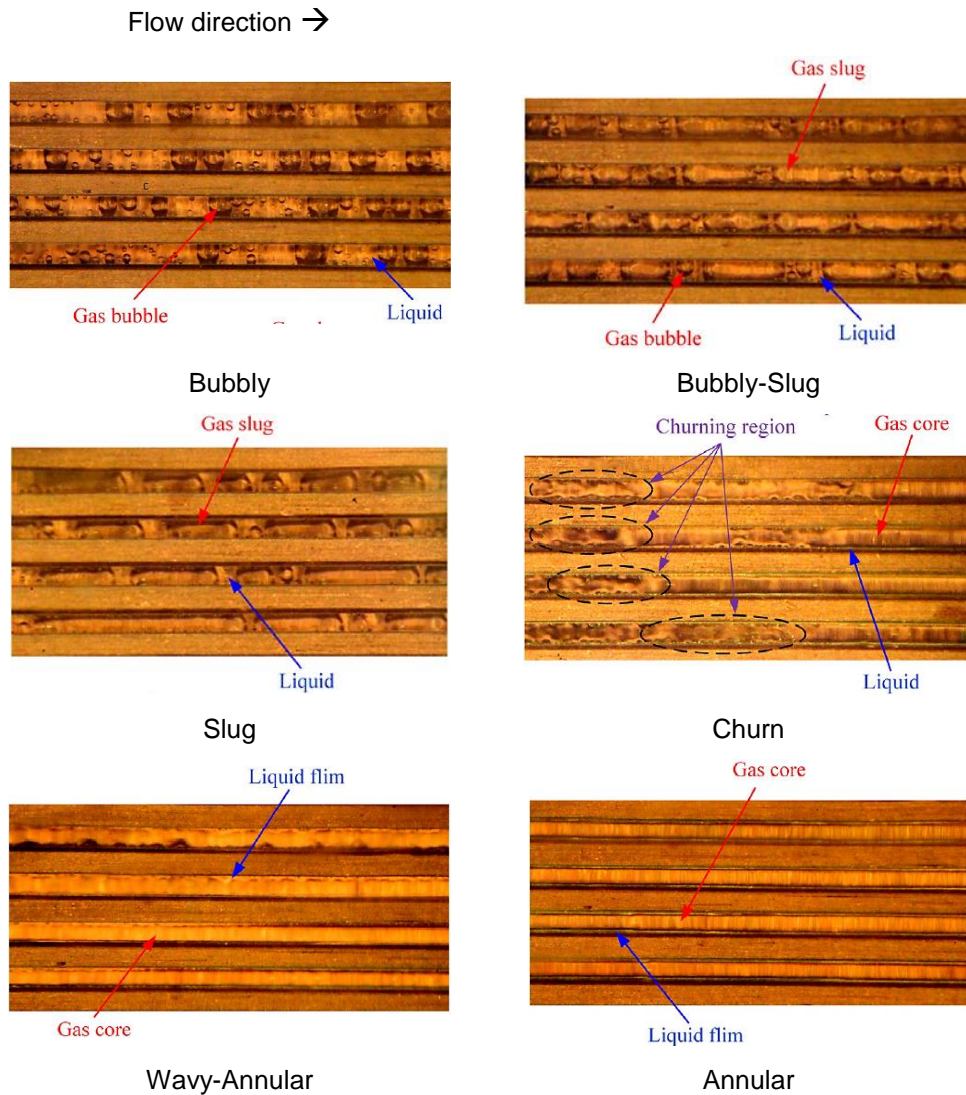


Figure 2.13 Flow patterns of R134a in horizontal multi-microchannels at saturation temperature of 13 °C, mass flux of 150 kg/m²s and different heat fluxes, Thiangtham et al. (2016).

Fayyadh et al. (2017) carried out flow boiling heat transfer of R134a in a horizontal multi-microchannel configuration. The heat sinks was made of oxygen-free copper and consisted of twenty five rectangular microchannels with hydraulic diameter of 0.42 mm. Their flow boiling experiments were set at heat flux of 11.46–403.1 kW/m², mass flux of 50–300 kg/m²s and system pressure of 6.5 bar. Three flow patterns were visualized, using high-speed camera, when the heat flux increased gradually. These regimes were bubbly, slug and wavy-annular flow as they reported and shown in Fig. 2.14.

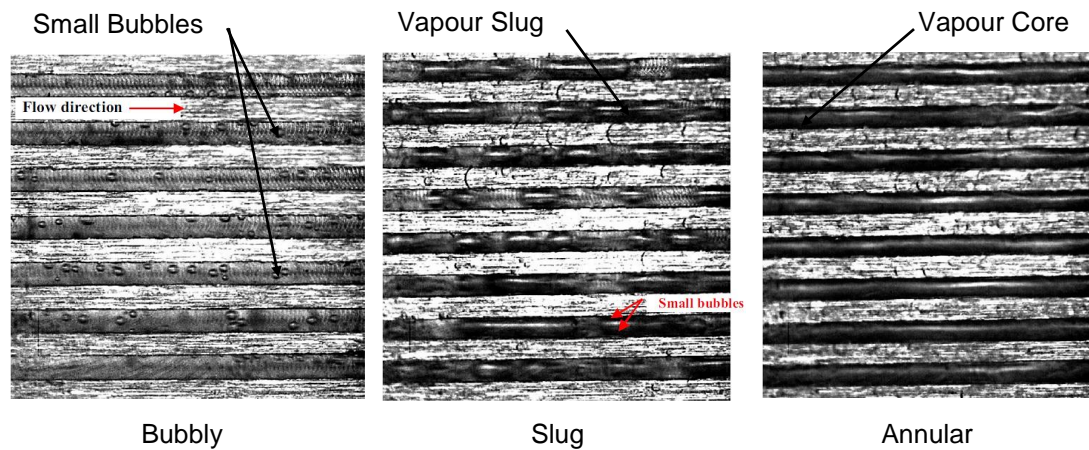


Figure 2.14 Flow patterns of R134a in horizontal multi-microchannels at mass flux of $50 \text{ kg/m}^2\text{s}$ and different heat fluxes, Fayyadh et al. (2017). Labels introduced by present author.

Recently, Choi et al. (2019) carried out an experimental investigation using HFE-7100 in vertical multi-channels. Five rectangular channels with the 0.89 mm hydraulic diameter and 90 mm length were manufactured. A Lexan cover was placed above these channels to allow the capture of flow patterns using a high-speed camera. They conducted their experiments at fluid inlet temperature of $55 \text{ }^\circ\text{C}$, system pressure of 1.02 bar , heat flux of $6.2\text{--}114 \text{ kW/m}^2$ and mass flux of $200\text{--}500 \text{ kg/m}^2\text{s}$. They reported that when the heat flux increased, flow patterns changed during the experiments as shown in Fig. 2.15. For example, at low heat flux, single-phase flow was observed, see Fig. 2.15(a), while small bubbles occurred near the exit. With increasing heat flux, elongated bubbles and a mixture of bubbly and slug flow were visualized as they mentioned, see Fig. 2.15(b). Fig. 2.15(c) show the bubbly flow became smaller, while slug flow moved towards the inlet with increasing heat flux. Fig. 2.15(d) illustrates that slug flow became disruption, while churn flow occurred. At high heat flux, churn flow was the dominant regime along the channel and partial dryout occurred as shown in Fig. 2.15(e). They concluded that there was partial dryout since most channel length was bright (see Fig. 2.15(e)) except the inlet.

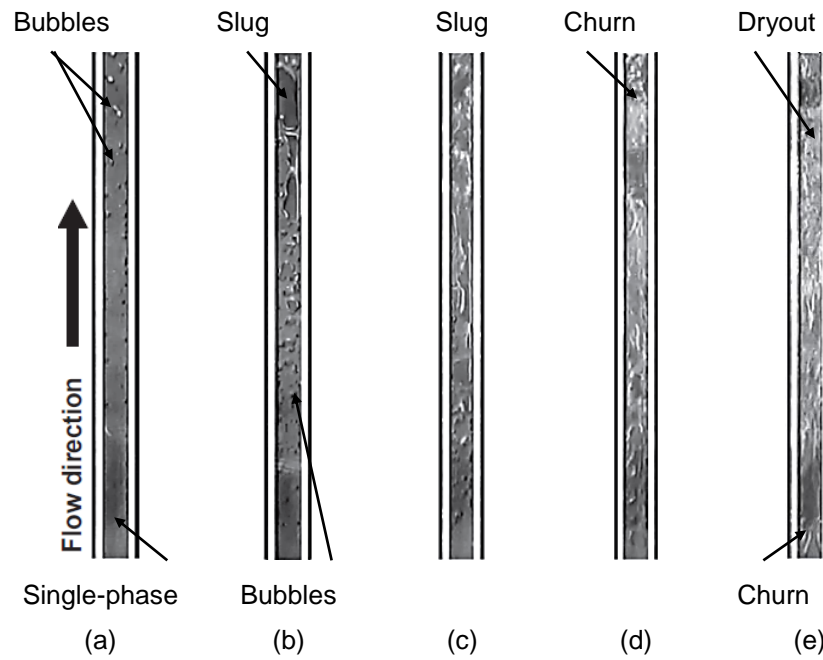


Figure 2.15 Flow patterns of HFE-7100 in vertical multi-channels at mass flux of $200 \text{ kg/m}^2\text{s}$ and heat flux of: (a) 13.2 (b) 24.8 (c) 40.6 (d) 59.7 (e) 71.9 kW/m^2 , Choi et al. (2019). Labels introduced by present author.

2.4.1.5 Nucleation in the liquid film

Some interesting features were captured during flow boiling experiments using different fluids in multi-microchannels. Small nucleating bubbles in the thin liquid film were reported by researchers. For instance, Kandlikar and Balasubramanian (2005) studied the effect of channel orientation on the flow boiling heat transfer of water in multi-channels. Six rectangular channels made of copper were fabricated with channel height, width and length of 0.197 , 1.054 and 63.5 mm , respectively. They conducted their experiments at three different channel orientations; horizontal, vertical up-flow and vertical down-flow, heat flux of 317 kW/m^2 and mass flux of $120 \text{ kg/m}^2\text{s}$. They reported that nucleating bubbles occurred in the thin film around the vapour plug as shown in Fig. 2.16. These bubbles were also found in the liquid film of annular flow.

Nucleating Bubbles in the Thin Film

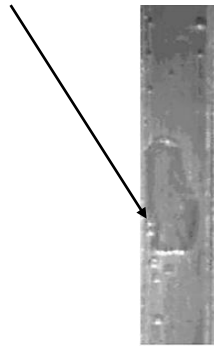


Figure 2.16 Nucleating bubbles during plug flow in vertical down-flow, Kandlikar and Balasubramanian (2005). Label introduced by present author.

Harirchian and Garimella (2009a) stated that few small nucleating bubbles were captured in the liquid film of the wispy-annular flow as illustrated in Fig. 2.17. They tested FC-77 in horizontal rectangular multi-microchannels.

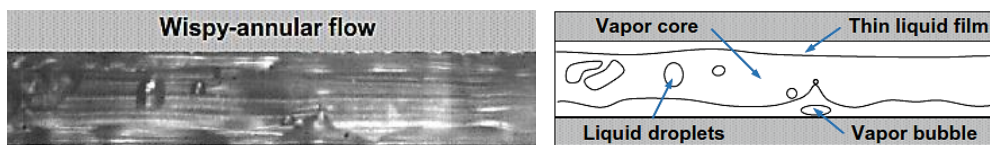


Figure 2.17 Nucleating bubbles in the liquid film of wispy-annular flow, Harirchian and Garimella (2009a).

Borhani and Thome (2014) studied flow boiling of R245fa in horizontal rectangular multi-microchannels. The test section was made of silicon and consisted of sixty seven channels with channel height, width and length of 0.68, 0.223 and 20 mm, respectively. A high-speed (Photron Fastcam) camera was used, and a transparent plate made of LEXAN covered the test section. They captured nucleate boiling in the liquid film of annular flow. Fig. 2.18 shows this visualization at heat flux of 140 kW/m² and mass flux of 150 kg/m²s.



Figure 2.18 Nucleating bubble in the liquid film of annular flow, Borhani and Thome (2014).

Fayyadh et al. (2017) carried out flow boiling heat transfer of R134a in horizontal rectangular multi-microchannels. Bubble nucleation was visualized in the liquid film of slug flow, near the channel sidewalls, as they mentioned. They also captured nucleation in the liquid film of annular flow, when the heat flux became 152.1 kW/m² and mass flux of 100 kg/m²s as shown in Fig. 2.19.

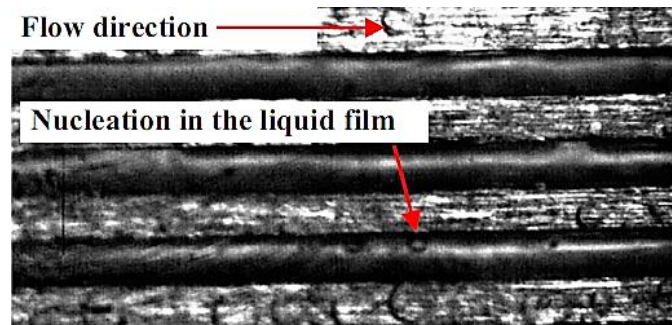


Figure 2.19 Nucleating bubble in the liquid film of annular flow, Fayyadh et al. (2017).

Despite a large amount of research published to date in two-phase flow, there is no general agreement about the most prevailing flow patterns. This is due to the different features and names of flow patterns were reported in the literature.

2.4.1.6 Effect of channel aspect ratio on flow patterns

Choi et al. (2010) and (2011) carried out an experimental study of adiabatic two-phase flow of water and nitrogen gas in a horizontal rectangular glass microchannel. Four channels with different aspect ratio (W_{ch}/H_{ch}) of 1.09, 1.48, 2.11 and 5.92 were tested. The liquid superficial velocity was set at 0.06–1 m/s, while the gas superficial velocity was 0.06–71 m/s. A high-speed camera with long distance microscope was used to capture the flow patterns. Bubbly, slug bubble, elongated bubble, liquid ring flows were captured when the gas superficial velocity increased. The liquid ring flow was characterized by liquid bumps that occurred at the collapsed positions of the long bubbles. They reported that the aspect ratio had a significant effect on the flow patterns. For example, when the channel aspect ratio increased, the area of the bubbles in the channel corners also increased, while the liquid film thickness in these corners reduced due to the confinement effect (side walls).

Soupremanien et al. (2011) investigated the flow boiling heat transfer of Forane-365HX in a horizontal single minichannel with hydraulic diameter of 1.4 mm. Two different rectangular channels with aspect ratio of 2.3 and 7 were fabricated. They conducted their experiments at heat flux of 2.3–160 kW/m² at mass flux of 200–400 kg/m²s. Bubbly, plug, plug/slug, churn, churn/annular and annular flow were visualized in their investigation. They reported that, at lower mass flux, *i.e.* 200 kg/m²s, two flow patterns dominated in both channels, namely churn and churn/annular flow. When the mass flux increased, the annular flow became the dominant flow in the smaller aspect ratio, while churn flow dominated in the larger aspect ratio. Özdemir et al. (2019) carried out an experimental investigation of water in a horizontal rectangular single microchannel with hydraulic diameter of 0.56 mm. Three different channel aspect ratios, *i.e.* 0.5, 2.56 and 4.94, were tested at mass flux of 200–800 kg/m²s. A high-speed, high-resolution camera mounted on a microscope was used to capture the experimental flow patterns. They observed the main flow patterns, namely bubbly, slug, churn and annular flow. They reported that aspect ratio had influence on the bubbly flow. For example, bubbly flow did not occur in the smallest aspect ratio at the outlet. For the largest aspect ratio, dispersed and small bubbles were observed. For the aspect ratio of 2.56, these bubbles were elongated due to the confinement effect (side walls). The effect of aspect ratio on the other flow patterns was insignificant in this study.

The effect of this parameter was also reported in horizontal multi-microchannels studies. Harirchian and Garimella (2009a) conducted visualization study of flow boiling heat transfer of FC-77 in horizontal multi-microchannels. Their experiments were conducted at mass flux ranging from 225 to 1420 kg/m²s using different channel widths of 0.1–5.85 mm at the same channel depth of 0.4 mm. The hydraulic diameter ranged from 0.16 to 0.75 mm. They mentioned the existent of bubbly, slug, churn, wispy-annular, and annular flows. For channel width of 0.1 and 0.25 mm, the flow patterns were similar but differ from those in channel width ≥ 0.4 mm. These flow patterns were slug and intermittent churn/annular flow. For width of 0.25 mm and at moderate mass fluxes, intermittent bubbly/slug flow occurred, while bubbly flow was observed at higher mass fluxes. When the channel width was 0.4 mm and larger, similar flow patterns were found. For example, for width of 1 and 2.2 mm, intermittent churn/wispy-annular and intermittent churn/annular flow occurred.

These flow patterns were also captured for the channel width of 5.85 mm. At low mass fluxes, intermittent bubbly/slug flow was found for the width of 1 and 2.2 mm, while slug flow was not captured for the larger channel width at all mass fluxes. However, bubbly flow occurred in the larger channel width. They reported that when the channel width increased, bubbly flow replaced slug flow, and intermittent churn/wispy-annular flow replaced intermittent churn/annular flow. Moreover, bubbly flow was not visualized in the channel width of 0.1 mm due to the small hydraulic diameter and confinement effect as they mentioned.

The previous investigations showed that the effect of channel aspect ratio on flow patterns is not clear. Moreover, the features and names of these regimes are still not agreed among these studies.

2.4.1.7 Effect of channel surface material on flow patterns

Different material used in test sections could result in different surface roughness, surface finish and of course has different thermal conductivity. More information about these parameters can be found in Section 2.4.5.3.

Different flow patterns were reported at different surface roughness and finish. Karayiannis et al. (2012) carried out a flow boiling experimental study of R134a in two vertical stainless steel tubes with inner diameter of 1.1 mm. Two different manufacturing processes were adopted, namely seamless cold drawn and welded processes. These tubes had surface roughness of 0.52 and 1.27 μm for the welded and cold drawn tubes, respectively. Their experiments were conducted at exit quality up to 0.95, system pressure from 6 to 10 bar and mass flux of 200–500 $\text{kg/m}^2\text{s}$. The inner surface characteristic of these tubes was analyzed using scanning electron microscopy (SEM), and different surface microstructures were found. For the welded tube, a very smooth surface and presence of some debris and fragments was reported. For the cold drawn tube, several “uniform and longitudinal scratches” were reported. A high-speed, high-resolution camera was obtained in their experiments for flow visualization. Different flow patterns were captured with increasing heat flux. Bubbly, slug, churn and annular flow were visualized in the cold drawn tube. In the welded tube, the flow patterns were slug, churn and annular flow. They stated that

the surface characteristics had influence on the flow patterns at very low heat fluxes, when the flow pattern was bubbly flow. Alam et al. (2013) conducted an experimental investigation of flow boiling of de-ionized water in horizontal micro-gap channel. A single silicon channel with width of 12.7 mm and height of 0.2, 0.3 and 0.5 mm was manufactured. The effect of surface roughness was studied at surface average roughness of 0.6, 1, and 1.6 μm , heat flux of 0–850 kW/m^2 and mass flux of 390 and 650 $\text{kg/m}^2\text{s}$. Their flow visualization showed that, for the smoother surface, few bubbles nucleated and moved on the surface, while more bubbles occurred for the other surfaces. This was attributed by the authors to the large number of nucleation sites activated on the rougher surfaces.

Pike-Wilson and Karayiannis (2014) investigated flow boiling of R245fa in a vertical tube with inner diameter of 1.1 mm. Three different metals were tested, *i.e.* copper, stainless steel and brass, using cold drawn process. These tubes had an average roughness of 0.524, 0.716 and 1.249 μm for copper, stainless steel and brass, respectively. They conducted flow boiling experiments at vapour quality of 0–0.95, system pressure of 1.8 and 2.4 bar, heat flux of 10–60 kW/m^2 and mass flux of 100–400 $\text{kg/m}^2\text{s}$. Different surface microstructures were found by analyzing these tubes using scanning electron microscopy. The surface of the copper tube had a smooth structure with some scratches. For the stainless steel tube, some deposits on the surface were found. “Flaky structure” and cracks were noticed for the brass tube. Annular flow was found to be the dominant regime for all tubes. However, at low heat fluxes, slug flow occurred in both of copper and brass tubes, while annular flow was still found in the stainless steel tube. At the lowest heat fluxes, bubbly flow occurred for all tubes.

Different boiling flow patterns are reported using different surface materials or surface roughness values. However, the features of these regimes are still disagreement among the researchers.

2.4.2 Flow Pattern Maps

Generally, flow visualization using a high-speed, high-resolution camera is adopted to study the flow patterns map. Vapour and liquid superficial velocities are used as

coordinates to plot this map. However, other coordinates are commonly used for this purpose, such as mass flux, vapour quality and Weber number. Transition boundary lines are proposed in order to identify the flow regimes on the map. In this section, some existing flow maps are discussed. These maps were proposed for horizontal/vertical flow, single/multi-channels and circular/non-circular channels.

Akbar et al. (2003) proposed a flow patterns map based on the experimental data for horizontal and vertical flow and circular and semi-triangular channels. Air-water was tested as the working fluid in diameter ranging from 0.866 to 1.6 mm. The authors presented their map using the Weber number coordinates as shown in Fig. 2.20 and included four regions as follows:

Surface tension dominated region: Bubbly, slug and plug flow.

$$We_{gs} \leq 0.11We_l^{0.315}, \quad \text{for } We_{ls} \leq 3 \quad (2.8)$$

$$We_{gs} \leq 1, \quad \text{for } We_{ls} > 3 \quad (2.9)$$

Inertia dominated region I: Annular and wavy annular flow.

$$We_{gs} \geq 11We_l^{0.14}, \quad \text{for } We_{ls} \leq 3 \quad (2.10)$$

Inertia dominated region II: Dispersed flow.

$$We_{gs} > 1, \quad \text{for } We_{ls} > 3 \quad (2.11)$$

Transition region, *i.e.* from bubbly, plug and slug to annular flow.

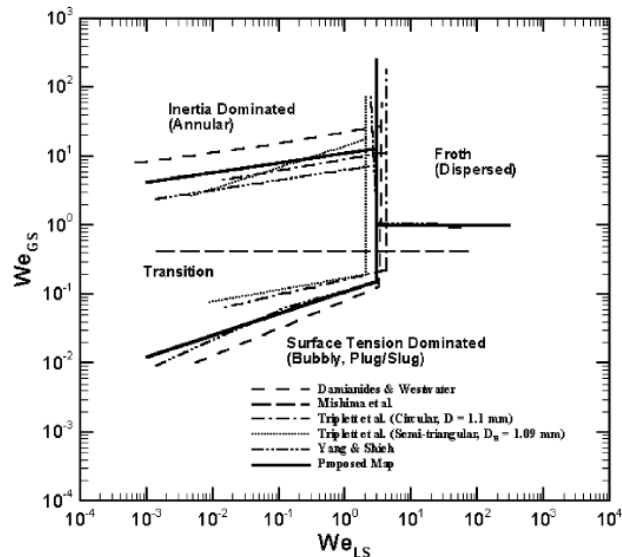


Figure 2.20 Flow patterns map in circular and near-circular channels ($D_h \leq 1$ mm), Akbar et al. (2003).

Revellin and Thome (2007a) developed a map for horizontal single tubes. Two stainless steel tubes with inner diameter of 0.509 and 0.79 mm were fabricated. R134a and R 245fa were tested at heat flux of 3.1–597 kW/m², mass flux of 210–2094 kg/m²s and inlet sub-cooling of 2–15 K. A glass tube was located after the tested tube for flow visualization and optical measurements, such as bubble generation frequency. They used two laser beams, located at different locations, and two photodiodes, located on the opposite side, as an optical instrument. These laser beams were focused to the middle of the glass tube using two lenses. The light intensity can be captured by these photodiodes, and then the voltage signals can be analyzed. They considered the effect of heat flux, mass flux, fluid properties and channel size on the flow patterns. They classified their flow patterns into three categories; isolated bubble regime (IB), coalescing bubble regime (CB) and annular regime (A). The transition criteria between these regimes were proposed as follows:

$$x_{IB/CB} = 0.763 \left(\frac{ReBo}{We_g} \right)^{0.41} \quad (2.12)$$

$$x_{CB/A} = 0.00014 Re^{1.47} We_l^{-1.23} \quad (2.13)$$

Isolated bubble regime included bubbly or/and slug flow, while the coalescing bubble regime included slug/semi-annular flow. Fig. 2.21 illustrates their map using mass flux and vapour quality as coordinates. This figure shows the transition lines between different flow regimes. For example, the transition from semi-annular to annular flow occurred at vapour quality near 0.21 for higher mass flux. This value increased with decreasing mass flux.

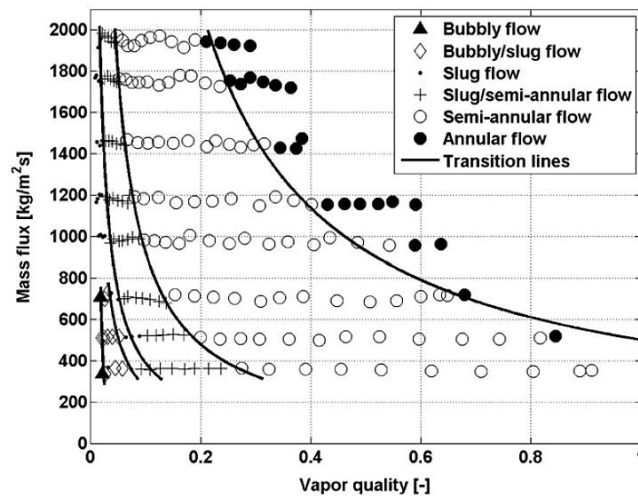


Figure 2.21 Flow patterns map for R134a in horizontal single tube (D=0.509 mm) and inlet sub-cooling of 3 °C, Revellin and Thome (2007a).

Harirchian and Garimella (2010) conducted several flow boiling experiments using FC-77 at heat flux ranging from 25 to 380 kW/m² and mass flux of 225–1420 kg/m²s. Twelve heat sinks with hydraulic diameter ranging from 0.096 to 0.707 mm were manufactured. Each heat sink was made of silicon and consisted of horizontal multi-microchannels. The authors proposed a new dimensionless number, convective-confinement number based on the Bond number and Reynolds number ($Bd^{0.5}Re$), to present their map. Moreover, they classified their map into two groups; confined and unconfined. The confinement effect dominates when the channel cross-sectional area is occupied by the vapour phase with uniform liquid film. Their map was plotted using two coordinates, namely the convective-confinement number and the dimensionless heat flux ($BoRe$) as shown in Fig. 2.22. The following equations were proposed to define the transition lines in their map.

$$Bd^{0.5}Re = 160 \quad (2.14)$$

$$Bo = 0.017(Bd^{0.4}Re^{-0.3}) \quad (2.15)$$

This figure illustrates different flow regimes, namely bubbly, confined slug, churn/confined annular, churn/wispy-annular and churn/annular flow. The transition to confined flow was presented by Eq. (2.14). The transition from bubbly and confined slug to churn, wispy-annular and annular flow was defined using Eq. (2.15). This transition line included the heat flux effect as mentioned by Harirchian and Garimella (2010).

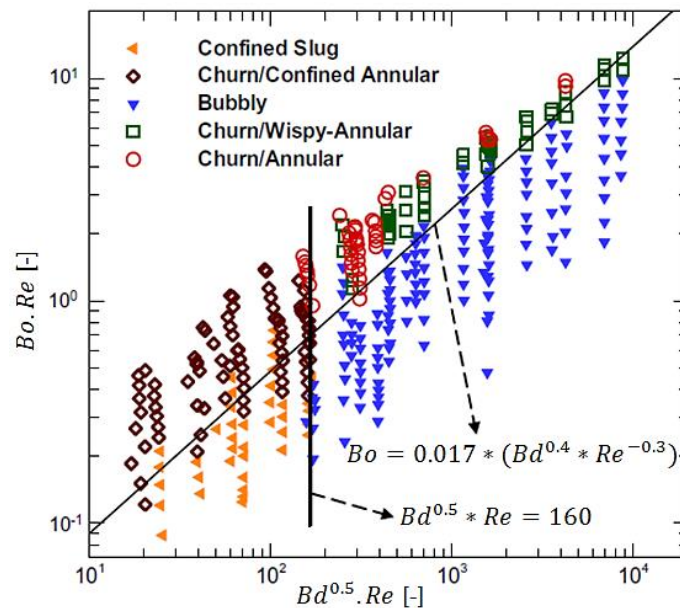


Figure 2.22 Flow patterns map for FC-77 in horizontal multi-microchannels, Harirchian and Garimella (2010).

Costa-Patry and Thome (2013) proposed a map for horizontal single tubes and rectangular multi-microchannels with hydraulic diameter ranging from 0.146 to 3.04 mm. Three different collected data sets were used including four fluids, namely R134a, R236fa, R245fa and R1234ze(E) at wall heat flux of 8–260 kW/m² and mass flux of 100–1100 kg/m²s. The authors found that, for each heat flux, the local heat transfer coefficient decreased to a minimum value then increased again, *i.e.* the trend of the local heat transfer coefficient versus quality was like a V-shape. This minimum value was corresponding to the transition from the coalescing bubble regime to the annular regime. Accordingly, they proposed a transition criterion from the coalescing bubble regime (CB) to the annular regime (A), based on the boiling number and the confinement number, see Eq. (2.16). They also recommended the flow patterns map by Ong and Thome (2011a) for other transition criteria. The transition line from isolated bubble regime (IB) to coalescing bubble regime (CB) can be defined using Eq. (2.17) of Ong and Thome (2011a).

$$x_{CB/A} = 425 \left(\frac{\rho_g}{\rho_l} \right)^{0.1} \left(\frac{Bo^{1.1}}{Co^{0.5}} \right) \quad (2.16)$$

$$x_{IB/CB} = 0.36 Co^{0.2} \left(\frac{\mu_g}{\mu_l} \right)^{0.65} \left(\frac{\rho_g}{\rho_l} \right)^{0.9} \left(\frac{GD_h}{\mu_g} \right)^{0.75} Bo^{0.25} We_l^{-0.91} \quad (2.17)$$

According to Ong and Thome (2011a), the isolated bubble regime included bubbly and slug-plug flow, while the coalescing bubble regime represented slug, churn and slug-annular flow. Both wavy-annular and smooth-annular were classified within the annular regime. Fig. 2.23 presents this flow patterns map using mass flux and vapour quality as coordinates.

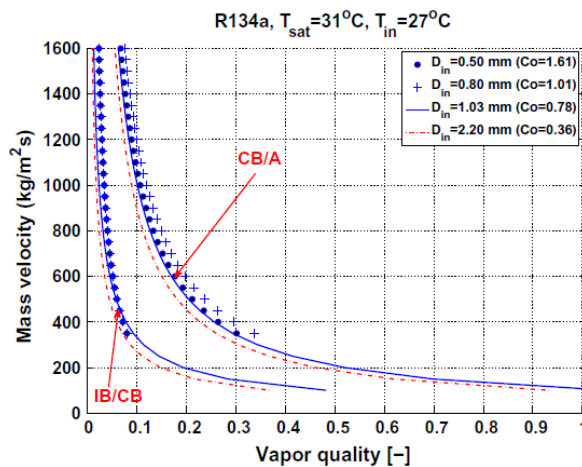


Figure 2.23 Flow patterns map for R134a in horizontal channels with different diameters, Ong and Thome (2011a).

Mahmoud and Karayiannis (2016a) presented a comprehensive evaluation of several correlations and models predicting flow patterns in mini and micro scale tubes. R245fa in a vertical copper tube with inner diameter of 1.1 mm was tested. The experimental conditions were set at heat flux of 3–25 kW/m², mass flux of 100–400 kg/m²s, inlet pressure of 1.85 bar and inlet sub-cooling of 5 K. They evaluated more than ten correlations and models for several flow pattern maps. They stated that only annular flow was captured when the heat flux increased, while bubbly, slug, churn and annular flow were visualized with decreasing heat flux. Therefore, they evaluated the existing maps using the experimental data of decreasing heat flux. Their evaluation showed that there was no existing model that predicted accurately all the transition boundaries. They reported that only the model of Chen (2006) predicted some of the transition boundaries. This model did not predict the transition boundary from bubbly to slug flow. Therefore, they proposed a new modification criterion for this boundary. The effect of channel size, fluid properties and flow inertia were taken into account in their modification. They mentioned that the transition between these regimes occurred when the Weber number equaled a fix value as follows:

$$We_r = \frac{\rho_l U_r^2 D_b}{\sigma} = 4 \quad (2.18)$$

where U_r and D_b are the relative velocity and bubble diameter, respectively. The above dimensionless form was obtained by conducting a force balance on the spherical bubble. The effect of viscous, buoyancy and gravity forces were ignored in their modification. The flow map by Chen (2006) and their modification model is shown in Fig. 2.24. This map was recommended by the authors for mini to micro scale channels.

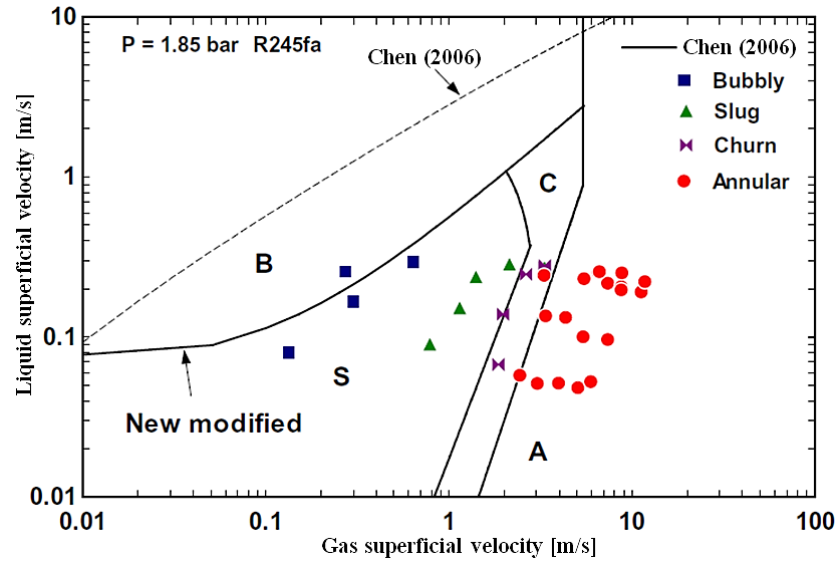


Figure 2.24 Flow patterns map for R245fa in vertical tube, proposed by Chen (2006) and modified by Mahmoud and Karayiannis (2016a).

Choi et al. (2017) carried out an experimental flow boiling study of FC-72 in horizontal multi-microchannels. Fifteen rectangular microchannels made of copper were manufactured with hydraulic diameter of 0.277 mm. Their experiments were conducted at heat flux of 3.2–49 kW/m², mass flux of 100.3–458 kg/m²s, exit quality from 0 to 0.96 and system pressure of 1.05–1.1 bar. They reported that the transition from bubbly/slug flow to annular flow occurred at higher vapour quality when the mass flux decreased. They proposed a new transition criterion based on the Weber number and vapour quality as follows:

$$We_l = \frac{G_{ch}^2 D_h}{\rho_l \sigma} \quad (2.19)$$

$$We_{B/S-A} = 0.021x^{-2.458} \quad (2.20)$$

The Weber number and vapour quality were used as coordinates to present their flow patterns map as shown in Fig. 2.25.

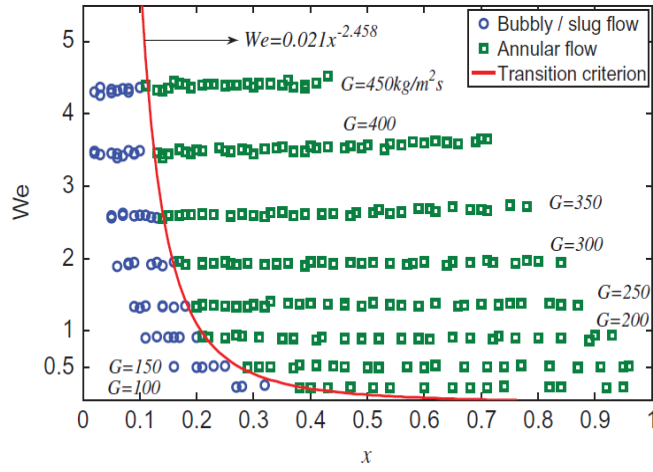


Figure 2.25 Flow patterns map for FC-72 in horizontal multi-microchannels, Choi et al. (2017).

Recently, Li and Hrnjak (2019) carried out an experimental study of two-phase flow of R32 in parallel microchannels with 0.643 mm hydraulic diameter at a mass flux ranging from 50 to 300 kg/m²s. A polycarbonate plate at the top allowed the capture of the flow patterns using a high-speed camera. They visualized plug/slug, transitional and annular flow. Plug/slug flow was characterized by a vapour plug and liquid slug. The interface between plug and slug was clear. In transitional flow, this interface was broken and liquid rings and waves occurred. In annular flow, a liquid film was captured in the channels with vapour core. They also reported that, at mass flux of 50 kg/m²s, plug/slug flow occurred, while annular flow was observed at 100 kg/m²s. At mass flux of 150 kg/m²s, transitional flow, *i.e.* from plug/slug to annular flow, was visualized. They presented their flow patterns map using liquid and vapour superficial velocities as coordinates as shown in Fig. 2.26.

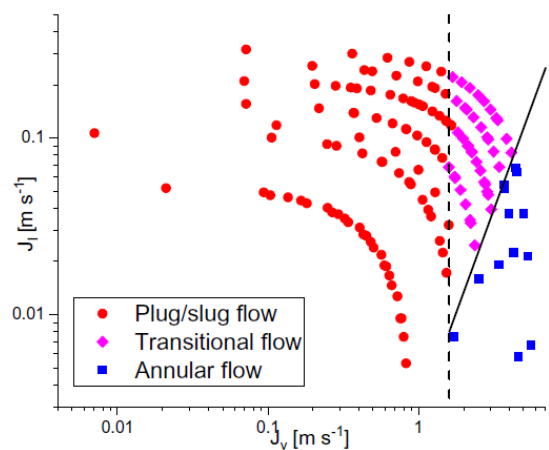


Figure 2.26 Flow patterns map of R32 at saturation temperature of 30 °C, Li and Hrnjak (2019).

Although a large amount of research has been published on flow boiling patterns, so far no general flow pattern maps have been proposed to predict all the transition boundaries for all fluids, operating conditions and channel geometries.

2.4.3 Flow Boiling Pressure Drop

Flow boiling pressure drop is another important parameter in thermal design since it determines the pumping requirements. This section presents the effect of heat flux, mass flux, aspect ratio and surface material on pressure drop in conventional and micro passages.

2.4.3.1 Effect of heat flux

Several experimental investigations were carried out using single channel at different dimensions and showed that the flow boiling pressure drop increased with heat flux. Tong et al. (1997) studied the effect of several parameters, such as inlet temperature, mass flux, exit pressure, inner diameter and length-to-diameter ratio, on the pressure drop during flow boiling of water in four stainless steel tubes. They performed their experiments at mass flux ranging from 25000 to 45000 kg/m²s and inlet temperature from 22 to 66 °C. The inner diameter of these tubes was 1.05, 1.38, 1.8 and 2.44 mm. They found that the pressure drop was strongly affected by heat flux, *i.e.* it increased with increasing heat flux. Kureta et al. (1998) carried out an experimental study of flow boiling heat transfer of water in small tubes ranging from 2 to 6 mm diameter and length from 4 to 680 mm. They conducted their experiments at mass flux ranging from 100 to 10170 kg/m²s, inlet sub-cooling from 70 to 90 K and heat flux up to 33000 kW/m². They found that the pressure drop increased with increasing heat flux. A similar conclusion was also found by Huh and Kim (2007). Karayiannis et al. (2008) carried out an experimental study of flow boiling pressure drop in small vertical stainless steel tubes. They used five tubes with inner diameter of 4.26, 2.88, 2.01, 1.1 and 0.52 mm. R134a was used as a working fluid at the system pressure ranging from 6 to 14 bar. They reported that the pressure drop increased as the heat flux increased, except at high heat fluxes where dryout could occur. Mahmoud et al. (2014) conducted an experimental study of flow boiling pressure drop using R134a as a working fluid in four vertical stainless steel tubes. One tube diameter of 0.52 mm and length of 100 mm was used, while three tubes with inner diameter of 1.1

mm and length of 150, 300 and 450 mm were tested. They conducted their experiments at mass flux ranging from 200 to 500 kg/m²s, heat flux from 1 to 140 kW/m² and system pressure from 6 to 10 bar. They stated that the pressure drop increased with increasing heat flux. This was attributed by them to the increase in the acceleration pressure drop with increasing vapour quality (heat flux).

The effect of heat flux was also reported in multi-microchannels studies as shown by Lee and Garimella (2008). They studied the flow boiling of de-ionized water in horizontal multi-microchannels. Different channel widths ranging from 0.102 to 0.997 mm at constant channel height of 0.4 mm were fabricated. They reported that the pressure drop across the tested microchannels increased rapidly with increasing heat flux. Another experimental study was performed by Markal et al. (2016a) showed the same trend. They carried out flow boiling experiments of de-ionized water in horizontal multi-microchannels with a hydraulic diameter of 0.15 mm. Twenty nine square microchannels made of silicon were fabricated. Their experiments were conducted at heat flux ranging from 59.3 to 84.1 kW/m² and mass flux of 51, 64.5, 78 and 92.6 kg/m²s. They stated that the total pressure drop, *i.e.* between the inlet and outlet plena, increased with increasing heat flux. This was attributed to the increase in the flow resistance when the heat flux increased due to the bubble generation at the inlet.

Although the two-phase pressure drop increased with heat flux as discussed in the previous studies, two experimental studies showed a different trend. Tibiriçá and Ribatski (2011) tested R245fa in vertical stainless steel tube of 2.32 mm diameter. Heat flux ranging from 0 to 55 kW/m², mass flux of 100–700 kg/m²s, and vapour quality from 0.1 to 0.99 were tested. They stated that the two-phase pressure drop was not affected by the heat flux. Xu et al. (2016) carried out an experimental investigation of R134a in horizontal copper tubes with inner diameter of 1.002, 2.168 and 4.065 mm. They conducted their experiments at heat flux of 18–35.5 kW/m², mass flux of 185–935 kg/m²s and vapour quality of 0.03–1. The frictional pressure drop was almost constant with heat flux and there was no explanation for this trend.

2.4.3.2 Effect of mass flux

The effect of mass flux on the two-phase pressure drop was also reported in the previous studies, see Tong et al. (1997), Karayiannis et al. (2008), Lee and Garimella (2008), Mahmoud et al. (2014) and Xu et al. (2016). The authors found that the experimental pressure drop increased with increasing mass flux. For example, Tong et al. (1997) attributed this increasing to the high wall shear stress, when the mass flux increased. Similar trend was also reported by Peng et al. (1998) and Sobierska et al. (2006).

In contrast, Markal et al. (2016a) mentioned that, at a constant heat flux, the total pressure drop from the inlet to the outlet plena generally decreased with increasing mass flux. There was no clear explanation for this decreasing. In their study, de-ionized water in horizontal square multi-microchannels with 0.15 mm hydraulic diameter was tested.

The previous discussion showed that there is a general agreement about the effect of heat flux on the two-phase pressure drop, *i.e.* the pressure drop increases with heat flux. However, just two studies contrast with the previous conclusion. Moreover, the two-phase pressure drop is found to increase with increasing mass flux in all previous studies except one.

2.4.3.3 Effect of channel aspect ratio

Few experimental investigations were carried out to study the effect of this parameter on two-phase pressure drop. In this section, eight available studies are discussed and presented.

It was reported that flow boiling pressure drop varied inversely proportional to the channel aspect ratio or channel width. For example, Singh et al. (2008) performed an experimental study of flow boiling of water in a horizontal single rectangular microchannel. Seven heat sinks were made of silicon at hydraulic diameter of 0.142 mm and different channel aspect ratios of 1.23, 1.44, 1.56, 1.73, 2.56, 3.60, and 3.75. They conducted their experiments at input power of 0, 3 and 3.5 W and mass flow rate of 0.15–0.2 mL/min. The surface roughness was measured for all microchannels

and it was less than 0.1 μm . Their results were presented based on input power and mass flow rate. It is worth mentioning that the mass flux and heat flux values varied with channel aspect ratio due to the different channel cross-sectional areas and heating areas. They mentioned that, at given mass flow rate and input power, the two-phase pressure drop decreased with increasing channel aspect ratio then increased with further increasing aspect ratio. It seems from their results that, at aspect ratio less than 1.56, the pressure drop decreased with increasing aspect ratio. This decrease was attributed to the reduction in the mass flux, when the aspect ratio increased due to an increase in the channel cross-sectional area. At aspect ratio more than 1.56, the pressure drop increased with increasing aspect ratio. Minimum pressure drop was found at channel aspect ratio of 1.56. This could be due to the opposing trends of acceleration and frictional pressure drops with respect to the channel aspect ratio as they mentioned. They stated that the acceleration pressure drop decreased due to the small mass flux, while the frictional pressure drop increased due to the reduction in the liquid film thickness. Harirchian and Garimella (2008) reported that, at given wall heat flux, the flow boiling pressure drop was found to increase with decreasing channel width. Similarly, Holcomb et al. (2009) mentioned that the pressure drop increased with decreasing channel width. Soupremanien et al. (2011) found lower two-phase pressure drop in the larger channel aspect ratio due to the higher cross-sectional area. The experimental results by Özdemir (2016) demonstrated that the flow boiling pressure drop increased with decreasing channel aspect ratio. This could be due to the smallest aspect ratio had higher vapour quality at the similar mass and heat fluxes as he mentioned. Drummond et al. (2018) also reported that the deeper channel (smaller aspect ratio) provided highest pressure drop.

Harirchian and Garimella (2009b) later showed that the channel cross-sectional area was more significant than the channel aspect ratio. For example, the pressure drop was found to increase with decreasing channel cross-sectional area at given mass and heat flux. For test sections with similar channel cross-sectional areas, *i.e.* 0.25 mm \times 0.4 mm and 0.4 mm \times 0.22 mm, the pressure drop was similar although the channel aspect ratio was different.

Contrary to the previous studies, Markal et al. (2016b) reported that there was no easily identifiable relationship between the total pressure drop and channel aspect ratio due to the complex flow boiling phenomenon. This complex effect was also found by Candan et al. (2018) using water in a horizontal single minichannel. They reported that aspect ratio of 0.25 and 4 had lowest total pressure drop.

The previous studies are summarized in Table 2.4. It is obvious that the effect of channel aspect ratio on the flow boiling pressure drop is still unclear and more investigations are needed.

Table 2.4 Effect of channel aspect ratio on the two-phase pressure drop as reported in the literature.

Author(s)	Channel geometry*	Channel material	D_h [mm] / β [-]	Fluid(s)	Aspect ratio effect
Harirchian and Garimella (2008)	H, M, R	Silicon	0.16–0.75/0.25–14.6	FC-77	$DP \uparrow$ with $\beta \downarrow$
Singh et al. (2008)	H, S, R	Silicon	0.142/1.23–3.75	Water	At $\beta < 1.56$: $DP \downarrow$ with $\beta \uparrow$ At $\beta > 1.56$: $DP \uparrow$ with $\beta \uparrow$ At $\beta = 1.56$: DP is minimum
Holcomb et al. (2009)	H, M, R	Silicon	0.299–0.64/0.61–5.88	Water	$DP \uparrow$ with $\beta \downarrow$
Soupremanien et al. (2011)	H, S, R	Stainless steel	1.4/2.3 and 7	Forane-365HX	$DP \downarrow$ with $\beta \uparrow$
Markal et al. (2016b)	H, M, R	Silicon	0.1/0.37–5	Water	$DP \neq \beta$
Özdemir (2016)	H, S, R	Copper	0.56/0.5–4.94	Water	$DP \uparrow$ with $\beta \downarrow$
Candan et al. (2018)	H, S, R	Copper	1.2/0.25–4	Water	At $\beta = 0.25$ and 4: DP is minimum

Drummond et al. (2018)	H, M, R	Silicon	0.0196– 0.0317/0.37– 0.052	HFE-7100	$DP \uparrow$ with $\beta \downarrow$
* H: horizontal, S: single channel, M: multi-channels, R: rectangular.					

2.4.3.4 Effect of channel surface material

Different channel surface materials could result in different surface roughness values, structures and conductivities. The effect of surface roughness on the flow boiling pressure drop was reported in several studies. Jones and Garimella (2009) carried out an experimental investigation of de-ionized water in horizontal multi-channels with hydraulic diameter of 0.5 mm. Three different surfaces, *i.e.* 1.4, 3.9 and 6.7 μm , were examined. The two-phase pressure drop results showed that higher pressure drop was measured for the roughest surface. Jafari et al. (2016) studied the effect of surface roughness at average roughness of 0.21, 0.96 and 2.38 μm . R134a in horizontal multi-microchannels with hydraulic diameter of 0.368 mm was tested. The total pressure drop was found to increase with increasing surface roughness.

In contrast, the experimental study by Alam et al. (2013) showed a different trend. They examined the influence of surface roughness on the flow boiling heat transfer of de-ionized water in horizontal silicon micro-gap channel at gap height of 0.2, 0.3 and 0.5 mm. Three different surface average roughness values, *i.e.* 0.6, 1, and 1.6 μm , were studied. They stated that the experimental pressure drop was independent of the channel surface roughness.

Pike-Wilson and Karayiannis (2014) examined three different metals, namely copper, stainless steel and brass. R245fa in a vertical tube with inner diameter of 1.1 mm and length of 300 mm was tested. The average roughness for these surfaces was 0.524, 0.716 and 1.249 μm for copper, stainless steel and brass, respectively. Their pressure drop results indicated that the brass tube (rougher surface: 1.249 μm) gave the highest measured pressure drop. However, there was no a clear trend between the surface roughness and the two-phase pressure drop as they reported. For example, copper tube (smoother surface: 0.524 μm) did not provided lowest pressure drop. In contrast, stainless steel tube had the lowest pressure drop compared with others. The

average surface roughness of this tube was 0.716 μm , which is in the middle value compared to brass and copper.

It can be concluded from the previous studies that different surface roughness or material show different trends of flow boiling pressure drop.

2.4.4 Flow Boiling Pressure Drop Correlations

The reasonable accuracy of two-phase pressure drop correlations helps to design and select the required pump in the system. It is known that, in horizontal channels, two-phase pressure drop has two components, *i.e.* acceleration and frictional pressure drop. The void fraction should be used in order to calculate the acceleration pressure drop. It can be seen from Appendix A that the Martinelli void fraction correlation was used by Lockhart and Martinelli (1949) to calculate this pressure drop, while other researchers such as Qu and Mudawar (2003b), Lee and Garimella (2008), Kim and Mudawar (2013b), Keepaiboon et al. (2016), Huang and Thome (2017), Li and Hibiki (2017) and Markal et al. (2017b) used the void fraction correlation by Zivi (1964). It is worth mentioning that the void fraction correlation by Zivi (1964) was developed for macro scale channels. However, it is preferred in mini or micro scale since there is lack of generally proposed and accepted models for these scales as mentioned by Lee and Garimella (2008). In this section, further details of these correlations are discussed, while Appendix A presents the equations of each correlation.

2.4.4.1 Conventional channel correlations

Four different sources were used by Lockhart and Martinelli (1949) to develop and propose a two-phase multiplier. These sources included air/water, air/benzene, air/kerosene and air/oils in circular tubes with inner diameter ranging from 1.5 to 25.8 mm. Their two-phase multiplier was computed according to the flow condition, *i.e.* laminar or turbulent flow. The Homogenous flow model was developed based on the assumption that both liquid and vapour phases were modelled as one phase and the slip velocity between them was assumed to be negligible, see Collier and Thome (1994). The two-phase friction factor was assumed to be 0.003 as recommended by Qu and Mudawar (2003b).

2.4.4.2 Mini/microchannel correlations

Mishima and Hibiki (1996) conducted an experimental investigation using different fluids in horizontal and vertical channels with diameter ranging from 1.05 to 4.08 mm. In their study, the Chisholm constant (C) was modified as a function of inner diameter to calculate the frictional pressure drop. This constant was verified based on the five collected data sources, including vertical and horizontal flow and circular and rectangular channels. They found that this constant decreased with decreasing inner diameter. Qu and Mudawar (2003b) studied the hydrodynamic instability and flow boiling pressure drop of water in horizontal rectangular multi-microchannels with a hydraulic diameter of 0.35 mm at mass flux of 134.9–400.1 kg/m²s. Their heat sink was made of copper and had twenty one channels. A two-phase pressure drop correlation was proposed by incorporating the effect of mass flux and channel size. They modified the Chisholm constant based on the experimental data. Lee and Garimella (2008) used water as the working fluid in horizontal rectangular multi-microchannels. The heat sink was made of silicon with hydraulic diameter ranging from 0.162 to 0.571 mm. They also modified the Chisholm constant as a function of mass flux and hydraulic diameter. Kim and Mudawar (2013b) proposed a correlation based on 2378 collected data points. This data set included nine different fluids, R12, R22, R134a, R245fa, R410a, FC-72, CO₂, ammonia and water, for horizontal and vertical flows. Different channel geometries were included in their data, *i.e.* circular and rectangular channels, with a hydraulic diameter ranging from 0.349 to 5.35 mm at mass flux ranging from 33 to 2738 kg/m²s and quality of 0–1. Keepaiboon et al. (2016) conducted an experimental study of flow boiling pressure drop of R134a in a horizontal single rectangular microchannel with a hydraulic diameter of 0.68 mm. Their experiments were set at heat flux of 7.63–49.46 kW/m² and mass flux of 600–1400 kg/m²s. A (C) coefficient was proposed based on their experimental data. This constant included the effect of liquid only Reynolds number, the confinement number and the Martinelli parameter. Huang and Thome (2017) conducted an experimental investigation of flow boiling pressure drop using three different fluids; R1233zd(E), R245fa and R236fa in horizontal square multi-microchannels. Silicon was used to fabricate 67 parallel channels with hydraulic diameter of 0.1 mm. Their experiments were performed at heat flux ranging from 200 to 640 kW/m² and mass flux of 1250–2750 kg/m²s. In their study, the Chisholm constant was modified

including the liquid only Reynolds number and the superficial vapour Reynolds number. Li and Hibiki (2017) proposed a new correlation to compute the two-phase frictional pressure drop based on 1029 collected data. Eleven sources were used including mini and microchannels, eight fluids, R134a, R22, R404a, R236fa, R245fa, FC-72, CO₂, water, with channel diameter ranging from 0.109 to 2.13 mm. All experiments were conducted at heat flux of 0–1400 kW/m² and mass flux of 44–1114 kg/m²s. They divided the database into three groups; laminar liquid-laminar vapour, laminar liquid-turbulent vapour and turbulent liquid-turbulent vapour. The Chisholm constant was modified as a function of the vapour quality, the two-phase viscosity number and the two-phase Reynolds number. In recent study, Markal et al. (2017b) proposed two correlations for low mass fluxes based on an experimental investigation. They tested de-ionized water in horizontal rectangular multi-microchannels at a wall heat flux of 36–121.8 kW/m² and mass flux of 51–324 kg/m²s. Nine heat sinks made of silicon with different aspect ratios ranging from 0.37 to 5 at hydraulic diameter of 0.1–0.25 mm were used. They modified the Chisholm constant in the frictional pressure drop as a function of liquid only Reynolds number, aspect ratio, Boiling number, Weber number, hydraulic diameter and the two-phase length. For bubble confinement flows, a second dimensionless correlation was proposed to predict the total pressure drop. Recently, Gao et al. (2019) carried out experimental study of two-phase flow using ammonia in horizontal stainless steel tubes with inner diameter of 8 mm. They conducted their experiments at mass flux of 20–100 kg/m²s and saturation temperature of -15.8–4.6 °C. The data of their previous work for diameter of 4 mm was also adopted in their study. Several existing correlations were compared with all data and better prediction was found with the correlation by Muller-Steinhagen and Heck (1986). They reported that the correlation by Muller-Steinhagen and Heck (1986) predicted 80% of the data within 30% error bands. Therefore, a new correlation was proposed to calculate the frictional pressure drop by modifying the correlation by Muller-Steinhagen and Heck (1986). Both Reynolds number and Bond number were introduced. They also evaluated their correlation with 951 collected data points from eleven sources including different fluids, horizontal and vertical tubes with inner diameter of 0.81–14 mm, mass flux of 50–800 kg/m²s and vapour quality of 0–1.

2.4.5 Flow Boiling Heat Transfer Characteristics

In this section, different heat transfer mechanism(s) are presented. Moreover, the effects of heat flux, mass flux, vapour quality, channel aspect ratio and surface characteristics on the heat transfer coefficient are discussed.

2.4.5.1 Heat transfer mechanism(s)

In conventional channels, the dominant heat transfer mechanism can be identified as nucleate and convective boiling. When the heat transfer coefficient depends only on heat flux and independent of vapour quality and mass flux, the dominant heat transfer mechanism is considered to be nucleate boiling. Bubbly flow is the prevalent regime during this mechanism. The increase in the heat transfer rate is due to (i) the evaporation process in the thin liquid film underneath the bubbles during bubbles growth and (ii) a strong mixing in bulk fluid when bubbles leave nucleation sites, see Karayiannis and Mahmoud (2017). On other hand, the heat transfer mechanism is considered convective boiling when the heat transfer coefficient depends on vapour quality and mass flux without a heat flux effect. Annular flow is the dominant regime during convective boiling. This enhancement in the heat transfer coefficient is due to the thinner liquid film thickness (between channel wall and vapour core) when mass flux or quality increases. This leads to lower thermal resistance and higher evaporation. Both nucleate and convective boiling could prevail, when the heat transfer coefficient depends on the heat flux, mass flux and vapour quality. This depends on the heat flux and vapour quality ranges. In micro scale channels, these conventional criteria were also applied in most investigations. Moreover, another heat transfer mechanism, *i.e.* thin liquid film evaporation during elongated bubble (vapour slug), was also reported, see In and Jeong (2009). This takes place from the liquid film trapped between channel wall and vapour phase. In this mechanism, the heat flux depends on conduction across this film and bubble frequency as mentioned by Ong and Thome (2011b). Different heat transfer mechanisms in flow boiling using small and micro channels are shown schematically in Fig. 2.27 as presented by Karayiannis and Mahmoud (2017). More details about these mechanisms, *i.e.* the effect of heat flux, mass flux and vapour quality, are presented in this section.

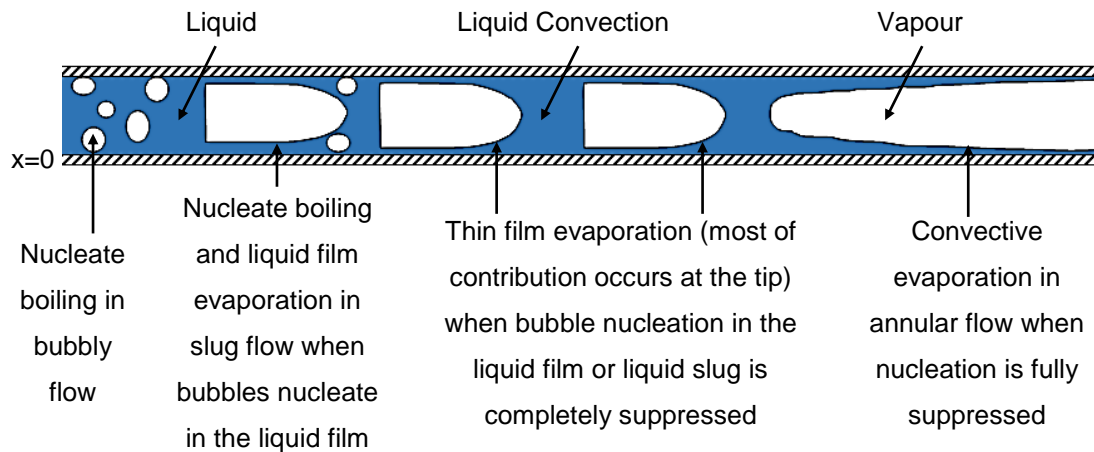


Figure 2.27 Schematic diagram of different heat transfer mechanisms in flow boiling using small and micro channels, Karayiannis and Mahmoud (2017). This figure is re-drawn by the present author.

2.4.5.1.1 Nucleate boiling mechanism

Several researchers reported that the nucleate boiling mechanism dominated in their studies using vertical single channels. Martin-Callizo et al. (2007) studied two-phase flow heat transfer of R134a in a vertical tube with inner diameter of 0.64 mm and heated length of 213 mm. They conducted their experiments at heat flux of 5–70 kW/m², mass flux of 250, 400 and 600 kg/m²s, saturation temperature of 30 and 35 °C and vapour quality up to 0.89. They reported that, at vapour quality less than 0.45–0.5, the heat transfer coefficient increased with increasing heat flux, and was independent of the mass flux and vapour quality. For higher qualities, the heat transfer coefficient was independent of heat flux and decreased with vapour quality. The explanation for this reduction was due to the occurrence of dryout. Shiferaw et al. (2009) investigated flow boiling heat transfer of R134a in a vertical stainless steel tube with inner diameter of 1.1 mm and length of 150 mm. The experimental parameters were: mass flux ranging from 100 to 600 kg/m²s, heat flux from 16 to 150 kW/m² and pressure of 6–12 bar. They reported that, at vapour quality less than 0.5, the heat transfer coefficient increased with heat flux and thus nucleate boiling dominated. Otherwise, at high heat flux and quality more than 0.5, the heat transfer coefficient was independent of heat flux and decreased with quality. They reported that the decrease in the heat transfer coefficient was due to the partial dryout. Karayiannis et al. (2012) studied the effect of surface characteristics and heated length on the heat transfer rate by using seamless cold drawn and welded tubes. The

working fluid was R134a flowing in a vertical stainless steel tube of 1.1 mm diameter. Their experiments were carried out at mass flux ranging from 200 to 500 kg/m²s, system pressure from 6 to 10 bar and quality up to 0.95. They reported that in the seamless cold drawn tube, the dominant heat transfer mechanism was nucleate boiling due to the fact that the heat transfer coefficient increased with increasing heat flux and was independent of mass flux and quality. The heat transfer mechanism in the welded tube was not clear. Maqbool et al. (2012) investigated flow boiling heat transfer of ammonia in vertical stainless steel tubes with two inner diameter of 1.7 and 1.224 mm and heated length of 245 mm. Their operating ranges were set at mass flux ranging from 100 to 500 kg/m²s, heat flux from 15 to 355 kW/m² and saturation temperature of 23, 33 and 43 °C. Based on their results, the heat transfer mechanism was different from one tube to another. In the 1.7 mm diameter tube, the heat transfer coefficient increased as the heat flux increased and was independent of mass flux and quality. They mentioned that the heat transfer mechanism was similar to nucleate boiling. In the 1.224 mm diameter tube and at low vapor qualities, the heat transfer depended on the heat flux, but was independent of mass flux and quality, while at high vapour qualities, it increased with increasing quality without any effect of heat flux. Al-Gaheeshi et al. (2016) carried out flow boiling experiments of R134a and R245fa in vertical stainless steel tube with inner diameter of 4.26 mm. They conducted their experiments at heat flux of 1–189 kW/m², mass flux of 200–500 kg/m²s and inlet sub-cooling of 5 K. They stated that, for both fluids, the local heat transfer coefficient increased with heat flux and independent of local quality and mass flux. The nucleate boiling was the dominant heat transfer mechanism for these fluids as they concluded. A recent experimental investigation by Choi et al. (2019) showed that nucleate boiling was the dominant heat transfer mechanism. They tested HFE-7100 in vertical multi-channels with hydraulic diameter of 0.89 mm. Their experiments were carried out at a system pressure of 1.02 bar, inlet temperature of 55 °C, heat flux of 6.2–114 kW/m² and mass flux ranging from 200 to 500 kg/m²s. They reported that the local heat transfer coefficient increased with heat flux, while insignificant effect of mass flux was found. Moreover, their results showed that the local heat transfer coefficient decreased with increasing local vapour quality due to the partial dryout.

Other researchers reported the same heat transfer mechanism using horizontal single channel. For example, Bao et al. (2000) investigated flow boiling heat transfer of R11 and R123 in a horizontal copper tube with inner diameter of 1.95 mm and heated length of 270 mm. Their operating ranges were set at heat flux of 5–200 kW/m², mass flux of 50–1800 kg/m²s, vapour quality of 0–0.9 and system pressure of 200–500 kPa. According to their results, the heat transfer coefficient was strongly dependent on the heat flux for both coolants and was independent of mass flux and quality. Therefore, the heat transfer mechanism was nucleate boiling as they suggested. Huh and Kim (2007) studied two-phase flow of de-ionized water in a horizontal single channel made of Polydimethylsiloxane (PDMS). The tested channel had hydraulic diameter of 0.1 mm and length of 40 mm. The heat flux ranged from 200 to 500 kW/m², quality from 0 to 0.4 and mass flux of 90, 169 and 267 kg/m²s. They reported that the heat transfer mechanism was nucleate boiling, although annular flow was observed in their study. This was due to the fact that the heat transfer coefficient was independent of mass flux and quality. Yin et al. (2017) carried out an experimental investigation of water in a horizontal microchannel with hydraulic diameter of 0.571 mm. A rectangular channel made of copper was fabricated with height, width and length of 0.3, 6 and 40 mm, respectively. They conducted their experiments at heat flux of 631–987 kW/m² and mass flux of 261–961 kg/m²s. They stated that the heat transfer coefficient mainly depended on the heat flux and the mechanism was nucleate boiling. Flow boiling of water in a horizontal rectangular minichannel was tested by Candan et al. (2018). A copper single channel with 1.2 mm hydraulic diameter and different aspect ratios ranging from 0.25 to 4 was manufactured. Their results showed that the local heat transfer coefficient increased with increasing heat flux, mass flux and vapour quality. Bubble nucleation was visualized in a large part of channel and the bubbly/slug flow was the dominant regime. Therefore, nucleate boiling was the dominant mechanism as they concluded.

2.4.5.1.2 Convective boiling mechanism

Lee and Lee (2001) conducted an experimental study of flow boiling of R113 in a horizontal rectangular channel. They used two plates and could change the gap between them. This method was used to get different channel height from 0.4 to 2

mm with a width of 20 mm. The mass flux ranged from 50 to 200 kg/m²s, quality ranging from 0.15 to 0.75 and heat flux up to 15 kW/m². They reported that the effect of heat flux was insignificant and the heat transfer coefficient increased with increasing mass flux and vapour quality. Convective boiling mechanism was also found by Wang and Sefiane (2012), who studied the effect of hydraulic diameter, heat flux and vapour quality on the heat transfer coefficient using FC-72 as a working fluid. They used a horizontal rectangular channel made of borosilicate glass with hydraulic diameter of 0.571, 0.762 and 1.454 mm. The heat flux ranged from 0 to 18.6 kW/m² with mass flux of 11.2, 22.4 and 44.8 kg/m²s. They stated that the average heat transfer coefficient increased with heat flux and then decreased. This reduction was attributed by the authors to partial dryout. Moreover, the average heat transfer coefficient increased with mass flux. They reported that the heat transfer mechanism was convective boiling and the flow visualization confirmed that, *i.e.* two main regimes were observed, namely slug-annular and annular flow.

Qu and Mudawar (2003a) studied flow boiling heat transfer of de-ionized water in horizontal rectangular multi-microchannels. The test section was made of oxygen-free copper and consisted of 21 channels with hydraulic diameter of 0.348 mm. They conducted their experiments for a mass flux range of 135–402 kg/m²s and inlet fluid temperature of 30 and 60 °C. They reported that convective boiling was dominant due to the fact that the heat transfer coefficient depended on the mass flux and there was a weak effect of heat flux. They also found that the heat transfer coefficient decreased with increasing vapour quality and the explanation for this was due to the liquid droplets inside the vapour core collapsed and deposited within the annular liquid film which lead to an increase of the film thickness and a decrease in the heat transfer coefficient. Markal et al. (2016a) conducted flow boiling of de-ionized water in horizontal square multi-microchannels. Twenty nine microchannels made of silicon with a hydraulic diameter of 0.15 mm were tested. They conducted their experiments at heat flux of 59.3–84.1 kW/m² and four mass fluxes ranging from 51 to 92.6 kg/m²s. Their results showed that the local flow boiling heat transfer coefficient decreased with increasing heat flux and local quality due to the partial dryout as they mentioned. However, it increased significantly with increasing mass flux. They attributed this to an increase in mass flux led to promote the liquid film

and diminished or removed the dryout. Therefore, they concluded that the convective boiling was the dominant heat transfer mechanism.

2.4.5.1.3 Nucleate and convective boiling mechanisms

Both nucleate and convective boiling mechanisms occurred in several experiments using vertical or horizontal single channel. For instance, Lin et al. (2001) studied the flow boiling heat transfer of R141b in vertical square and circular stainless steel tubes. The inner diameter of the circular tubes was 1.1, 1.8, 2.8 and 3.6 mm, while the hydraulic diameter of the square tube was 2 mm. The mass flux ranged from 50 to 3500 kg/m²s, heat flux from 1 to 300 kW/m², and vapour quality from 0 to 1. At low vapour qualities, the heat transfer coefficient was dependent on the heat flux, while at high vapour qualities it was dependent on the quality and independent of heat flux. Díaz et al. (2006) also found the same mechanisms. They carried out an experimental study of flow boiling heat transfer of hydrocarbons and water in vertical narrow channels. Two nickel test sections were used, one was a circular channel with inner diameter of 1.5 mm and another was rectangular channel with hydraulic diameter ranging from 0.583 to 1.31 mm. Heat flux ranging from 20 to 350 kW/m², mass flux of 25–350 kg/m²s and inlet pressure of 300 kPa were tested. Based on their results and at low qualities, the heat transfer coefficient increased with increasing heat flux. In contrast, at high vapour qualities, the heat transfer coefficient was independent of heat flux and increased with quality, so nucleate and convective boiling mechanisms were dominant. Huh and Kim (2006) conducted flow boiling heat transfer of water in a horizontal single microchannel. Rectangular microchannel with hydraulic diameter of 0.103 and 0.133 mm was tested. Their experiments were carried out at heat flux of 180–500 kW/m² and mass flux of 77.5, 154.9, and 309.8 kg/m²s. Flow visualization was conducted to capture the flow patterns. They reported that, at the middle of the test section and near zero vapour quality, the heat transfer coefficient was dependent on the heat flux and independent of mass flux and vapour quality, hence the nucleate boiling dominated as they mentioned. Near the exit of the test section, the heat transfer coefficient depended on the vapour quality. They stated that the convective boiling was the dominant mechanism at this region.

Several studies were performed using horizontal multi-microchannel configurations. Lee and Garimella (2008) investigated flow boiling heat transfer of de-ionized water in horizontal silicon multi-microchannels with width ranging from 0.102 to 0.997 mm and height of 0.4 mm. They found that, at low and medium heat flux ranges, the heat transfer coefficient depended on the heat flux, while at high heat flux ranges, it was independent of heat flux. This may indicate that the nucleate boiling changed to the convective boiling as they concluded. Deng et al. (2015) studied flow boiling of ethanol in horizontal multi-microchannels. Reentrant porous channels with Ω -shaped configurations were made of sintered copper powder with a hydraulic diameter of 0.786 mm. Their experiments were conducted at mass flux of 125, 200 and 300 kg/m²s and sub-cooling temperature of 10 and 40 K. They found that, at low heat flux and quality, nucleate boiling dominated, while convective boiling mechanism was dominant at moderate and high heat flux and quality. Thiangtham et al. (2016) performed flow boiling heat transfer experiments using R134a in horizontal rectangular microchannels. Twenty seven multi-microchannels made of copper were fabricated with hydraulic diameter of 0.421 mm. Their experiments were conducted at saturation temperature of 13, 18 and 23 °C, heat flux of 3–127 kW/m², mass flux of 150–600 kg/m²s and inlet vapour quality of 0.05–0.92. Flow visualization was conducted in their study. They stated that, at low heat fluxes, the heat transfer coefficient increased with increasing heat flux. The flow patterns were bubbly and slug flow, and nucleate boiling was dominant as they mentioned. In contrast, at high heat fluxes, the heat transfer coefficient was found to increase with mass flux, and the flow patterns were wavy-annular and annular. They concluded that convective boiling dominated during these regimes. Complex heat transfer mechanisms were reported using horizontal multi-microchannel configurations as shown by Fayyadh et al. (2017). They conducted an experimental study of flow boiling heat transfer using R134a as the working fluid in horizontal multi-microchannels. Twenty five microchannels made of oxygen-free copper with a hydraulic diameter of 0.42 mm were used in this experiment. The mass flux ranged from 50 to 300 kg/m²s, heat flux from 11.46 to 403.1 kW/m² and system pressure of 6.5 bar. They found that when the heat transfer coefficient plotted versus heat flux, the heat transfer coefficient increased with increasing heat flux with a weak effect of mass flux. This indicated that the heat transfer mechanism was nucleate boiling as they mentioned. However, when the heat transfer coefficient was plotted versus vapour quality, it was

dependent on both of mass flux and quality and thus the convective boiling dominated as they stated. Therefore, they concluded that the conventional criteria are difficult to infer the heat transfer mechanism.

2.4.5.1.4 Thin film evaporation

This mechanism was reported by several authors such as Sumith et al. (2003), In and Jeong (2009), Ali et al. (2012) and Balasubramanian et al. (2013). Jacobi and Thome (2002) stated that their experimental investigations of flow boiling in microchannels showed the local heat transfer coefficient depended strongly on heat flux, was weakly influenced by mass flux, was almost independent of vapour quality and moderately dependent on saturation pressure. Thin film evaporation could be the dominant heat transfer mechanism during the elongated bubble as they suggested. Therefore, they proposed a model to calculate the local heat transfer coefficient in this region. In this model, the heat transfer coefficient increased with increasing heat flux due to thinner liquid film, *i.e.* reduction in the conductive resistance of this film. They validated their model with a series of simulations and experimental data with different fluids. Their result showed that the heat transfer coefficient increased with heat flux and saturation pressure. This increase with heat flux was low at small heat fluxes and high at large values. Moreover, the effect by mass flux was insignificant and no dependence on quality was found. In and Jeong (2009) also reported that the heat transfer coefficient increased with increasing heat flux due to the thinner liquid film thickness around the elongated bubble (slug flow). Balasubramanian et al. (2013) investigated flow boiling heat transfer in horizontal multi-microchannels. They used de-ionized water as the working fluid in two copper heat sinks with hydraulic diameter of 0.488 and 0.504 mm. Mass flux ranging from 88 to 751 kg/m²s and heat flux up to 4200 kW/m² were tested in their experiments. They stated that, in moderate and high heat fluxes, thin film evaporation dominated when the flow pattern was annular flow. An increase in the heat transfer coefficient was found with decreasing liquid film thickness due to the high evaporation as they mentioned.

Table 2.5 summarizes different heat transfer mechanisms that were reported in the literature. It can be concluded that there is no a general agreement on the dominant heat transfer mechanism(s). Different channel geometries, surface structures,

working fluids, heat fluxes, mass fluxes, inlet sub-cooling and system pressure were examined in the literature. System instability and flow reversal were also reported in some studies. All these parameters could result in different flow patterns during experiments and thus different mechanism(s) could dominate.

Table 2.5 Heat transfer mechanism(s) as reported in the literature.

Author(s)	Channel geometry*	Channel material	D_h [mm]	Fluid(s)
Nucleate boiling is the dominant mechanism				
Bao et al. (2000)	H, S, C	Copper	1.95	R11 & R123
Huh and Kim (2007)	H, S, R	Polydimethylsiloxane	0.1	De-ionized water
Martin-Callizo et al. (2007)	V, S, C	----	0.64	R134a
Shiferaw et al. (2009)	V, S, C	Stainless steel	1.1	R134a
Karayiannis et al. (2012)	V, S, C	Stainless steel	1.1	R134a
Maqbool et al. (2012)	V, S, C	Stainless steel	1.7 and 1.224	Ammonia
Al-Gaheeshi et al. (2016)	V, S, C	Stainless steel	4.26	R134a and R245fa
Yin et al. (2017)	H, S, R	Copper	0.571	Water
Candan et al. (2018)	H, S, R	Copper	1.2	Water
Choi et al. (2019)	V, M, R	Carbon graphite	0.89	HFE-7100
Convective boiling is the dominant mechanism				
Lee and Lee (2001)	H, S, R	Stainless steel	0.78–3.6	R133
Qu and Mudawar (2003a)	H, M, R	Copper	0.348	De-ionized water
Wang and Sefiane (2012)	H, S, R	Borosilicate glass	0.571–1.454	FC-72
Markal et al. (2016a)	H, M, Sq	Silicon	0.15	De-ionized water
Nucleate and convective boiling are the dominant mechanisms				
Lin et al. (2001)	V, S, C & Sq	Stainless steel	1.1–2	R141b

Table 2.5 Continued.

Author(s)	Channel geometry*	Channel material	D_h [mm]	Fluid(s)
Díaz et al. (2006)	V, S, C & R	Nickel	0.583–1.5	Hydrocarbons and water
Huh and Kim (2006)	H, S, R	Polydimethylsiloxane	0.103 & 0.133	Water
Lee and Garimella (2008)	H, M, R	Silicon	0.16–0.57	De-ionized water
Deng et al. (2015)	H, M, Ω -shaped	Copper	0.786	Ethanol
Thiangtham et al. (2016)	H, M, R	Copper	0.421	R134a
Thin film evaporation is the dominant mechanism				
Sumith et al. (2003)	V, S, C	Stainless steel	1.45	Water
In and Jeong (2009)	H, S, C	Stainless steel	0.19	R123 & R134a
Ali et al. (2012)	H, S, C	Fused silica	0.781	R134a & R245fa
Balasubramanian et al. (2013)	H, M, R	Copper	0.488 & 0.504	De-ionized water
* V: vertical, H: horizontal, S: single channel, M: multi-channels, Sq: square, R: rectangular, C: circular.				

2.4.5.2 Effect of channel aspect ratio

Only a small number of studies were conducted to study the effect of channel aspect ratio on the heat transfer characteristics. In this section, aspect ratio is defined as a ratio between channel width to channel height. Some researchers studied this parameter using horizontal single channel, such as Soupremanien et al. (2011) and Özdemir (2016). The first authors studied the effect of channel aspect ratio on the flow boiling heat transfer of Forane-365HX in a horizontal single minichannel. Two heat sinks at the same hydraulic diameter of 1.4 mm and different channel aspect ratios of 2.3 and 7 were manufactured. In their study, the heat flux ranged from 2.3 to 160 kW/m² at mass flux of 200–400 kg/m²s. They stated that there was a clear effect of the channel aspect ratio on the heat transfer coefficient depending on the heat flux value. For example, at low heat fluxes, higher heat transfer coefficient was found for the larger aspect ratio. In contrast, at high heat fluxes, the smaller channel aspect ratio given a higher heat transfer coefficient. The reduction in the heat transfer coefficient for the aspect ratio of 7 was attributed to the earlier dryout occurrence. Candan et al. (2018) conducted flow boiling experiments using water in a horizontal rectangular minichannel with hydraulic diameter of 1.2 mm. They tested five heat sinks made of copper with different channel aspect ratios of 0.25, 0.5, 1, 2 and 4. The average surface roughness was 0.086 µm. Different mass fluxes ranging from 70 to 310 kg/m²s were examined. They reported that the aspect ratio of 1 provided better heat transfer coefficient, while the smallest aspect ratio showed lowest performance. Uniform liquid film at the channel corners could be the reason for this enhancement in the aspect ratio of 1 as they explained. They also mentioned that the poorest thermal performance with aspect ratio of 0.25 (deeper channel) was due to the dryout. Özdemir et al. (2019) performed an experimental study of flow boiling heat transfer of water in a horizontal single microchannel. Three rectangular copper channels with hydraulic diameter of 0.56 mm and aspect ratio of 0.5, 2.56 and 4.94 were examined. The bottom surface of these channels had surface average roughness of 0.496, 0.39 and 0.102 µm. Flow boiling experiments were conducted at a heat flux of 4–1350 kW/m² and mass flux ranging from 200 to 800 kg/m²s. A high-speed camera mounted on a microscope was used to capture the experimental flow patterns. The heat transfer results indicated that, at heat flux up to 480–500 kW/m², the heat transfer coefficient

increased with decreasing channel aspect ratio. In contrast, no effect was found when the heat flux increased further. This better heat transfer coefficient in the smallest aspect ratio could be due to the buoyancy effect as they mentioned. For deeper channels, *i.e.* smallest aspect ratio, high buoyancy could lead to the detachment of bubbles from the surface. This allows the bubbles to flow towards the upper cross-section and thus thicker liquid film could occur at the channel bottom and corners. At high heat fluxes, the nucleate boiling was suppressed and thus the results were less sensitive to the aspect ratio.

Horizontal multi-microchannels at different channel aspect ratios were also studied by the scientific community. For instance, Harirchian and Garimella (2008) conducted an experimental investigation of flow boiling heat transfer of FC-77 in horizontal silicon multi-microchannels. Seven heat sinks at the same channel depth, *i.e.* 0.4 mm, and different channel widths ranging from 0.1 to 5.85 mm were manufactured to study the effect of channel width on the heat transfer performance. In their study, the channel hydraulic diameter was not constant for all heat sinks, *i.e.* ranged from 0.16 to 0.75 mm. The surface average roughness of the channel bottom wall also different and ranged from 0.1 to 1.4 μm . The experimental conditions were set at a mass flux of 250 to 1600 $\text{kg}/\text{m}^2\text{s}$. They found that, at the same wall heat flux and width ≥ 0.4 mm, the heat transfer coefficient was independent of channel width. Similar for smaller channels, a weak dependence was found, while the heat transfer coefficient was slightly lower than that in the larger sizes when the channel width was 0.25 mm. However, when they presented their heat transfer results based on the base heat flux, the effect of channel width became clearer. It was found that the heat transfer coefficient increased with increasing channel width. Later, the same authors Harirchian and Garimella (2009b) investigated the effect of channel dimensions using the same previous working fluid in twelve silicon test sections. Each test section consisted of rectangular multi-microchannels with different channel heights, widths and cross-sectional areas. The aspect ratio was varied from 0.27 to 15.55 for cross-sectional area of 0.009–2.201 mm^2 , while the hydraulic diameter ranged from 0.096 to 0.707 mm. The bottom wall of microchannels had an average roughness ranging from 0.1 to 1.4 μm . They stated that

the channel dimensions, *i.e.* channel width, depth, or aspect ratio, were not individually determinative factors on the heat transfer characteristics in micro scale channels. The cross-sectional area played a determining role in the heat transfer results as they mentioned. Their heat transfer results showed that, for small cross-sectional areas, *i.e.* smaller than 0.089 mm^2 , the vapour bubble confined by the channels resulted in higher heat transfer rates. The heat transfer coefficient was found to increase with decreasing channel cross-sectional area before dryout occurred at high heat fluxes. For areas equal or larger than 0.089 mm^2 , the heat transfer coefficient was independent of channel dimensions. They found that the channels with similar aspect ratio but different cross-sectional area had different heat transfer coefficients. For example, the channel of $0.1 \times 0.1 \text{ mm}$ showed higher heat transfer coefficient than the channel of $0.4 \times 0.4 \text{ mm}$. Holcomb et al. (2009) conducted flow boiling heat transfer of de-ionized water in horizontal rectangular multi-microchannels. They tested three heat sinks made of silicon with different channel widths of 0.25, 1 and 2.2 mm and constant channel height of 0.4 mm. The hydraulic diameter was varied for all these tested channels, *i.e.* 0.299, 0.531 and 0.64 mm. They reported that when the wall heat flux was used to present the boiling curve and heat transfer results, there was a weak effect of channel width. Fu et al. (2013) studied the effect of channel aspect ratio on the flow boiling heat transfer of HFE-7100 in horizontal multi-microchannels. Six diverging microchannels with a hydraulic diameter of 1.12 mm and aspect ratio ranging from 0.16 to 1.2 were fabricated and tested at mass flux of 39–180 $\text{kg/m}^2\text{s}$. They reported that higher wall heat flux was found at the channel aspect ratio of 0.99 due to the liquid film thickness. They stated that, in channels of aspect ratio other than 0.99, part of the walls was not wetted, which resulted in lower heat transfer rates. This included the channels of aspect ratio 1.2. Markal et al. (2016b) carried out an experimental investigation of flow boiling heat transfer of de-ionized water in horizontal rectangular multi-microchannels. Six heat sinks made of silicon with 29 microchannels were manufactured. These channels have different aspect ratios of 0.37, 0.82, 1.22, 2.71, 3.54 and 5 and the same hydraulic diameter 0.1 mm. The experimental operating conditions were set at wall heat flux of 71–131 kW/m^2 and mass flux ranging from 151 to 324 $\text{kg/m}^2\text{s}$. The heat transfer coefficient was found to increase with increasing channel aspect ratio up to 3.54, while it decreased with further increase

in the aspect ratio. This could be due to the corner effect, *i.e.* the amount of liquid in the channel corners (corner effect) increased up to 3.54, while it was less in the aspect ratio of 5. Recently, Drummond et al. (2018) conducted flow boiling heat transfer experiments using HFE-7100 in horizontal rectangular multi-microchannels. Three silicon heat sinks were manufactured with different channel aspect ratios of 0.37, 0.096 and 0.052. These channels had different hydraulic diameters of 0.0196, 0.0288 and 0.0317 mm. The average surface roughness of these channels was not mentioned. High mass fluxes were examined in their study, *i.e.* at ranges of 1300, 2100 and 2900 kg/m²s. They presented heat transfer coefficient, based on the average wall temperature, versus exit vapour quality. Their results showed that the effect of channel aspect ratio on the heat transfer coefficient was not clear. However, they stated that smaller channel height (larger aspect ratio) had highest heat transfer coefficient compared with others.

Table 2.6 presents a summary of the previous studies. It can be concluded from the above experimental studies that the effect of channel aspect ratio on the heat transfer characteristics is still unclear and more investigations are required. The hydraulic diameters of the channels with different aspect ratios are not the same in some studies. Moreover, the average surface roughness of the tested channels differs from channel to another, or it was not mentioned. Therefore, it is difficult to propose a final conclusion on the effect of channel aspect ratio.

Table 2.6 Effect of channel aspect ratio on the heat transfer coefficient as reported in the literature.

Author(s)	Channel geometry*	Channel material	D_h [mm] / β [-]	Fluid	Aspect ratio effect
Harirchian and Garimella (2008)	H, M, R	Silicon	0.16–0.75/0.25–14.6	FC-77	At wall heat flux: $h \neq \beta$ At base heat flux: $h \uparrow$ with $\beta \uparrow$
Holcomb et al. (2009)	H, M, R	Silicon	0.299–0.64/0.61–5.88	Water	$h \neq \beta$
Soupremanien et al. (2011)	H, S, R	Stainless steel	1.4/2.3 and 7	Forane-365HX	At low q : $h \uparrow$ with $\beta \uparrow$ At high q : $h \uparrow$ with $\beta \downarrow$

Fu et al. (2013)	H, M, R(D)	Copper	1.12/0.16–1.2	HFE-7100	At $\beta = 0.99$: h is maximum
Markal et al. (2016b)	H, M, R	Silicon	0.1/0.37–5	Water	At $\beta \leq 3.54$: $h \uparrow$ with $\beta \uparrow$ At $\beta > 3.54$: $h \downarrow$ with $\beta \uparrow$
Candan et al. (2018)	H, S, R	Copper	1.2/0.25–4	Water	At $\beta = 1$: h is maximum At $\beta = 0.25$: h is minimum
Drummond et al. (2018)	H, M, R	Silicon	0.0196– 0.0317/0.37– 0.052	HFE-7100	$h \neq \beta$ At $\beta = 0.37$: h is maximum
Özdemir et al. (2019)	H, S, R	Copper	0.56/0.5–4.94	Water	At low and moderate q : $h \uparrow$ with $\beta \downarrow$ At high q : $h \neq \beta$
* H: horizontal, S: single channel, M: multi-channels, R: rectangular, D: diverging channel.					

2.4.5.3 Effect of channel surface material

Different surface roughness, surface finish and thermal conductivity could occur due to different materials are used for the test sections. These parameters may affect the flow boiling heat transfer performance especially in micro scale. Different manufacturing processes and materials could result in differences in surface roughness and finish. The average roughness from the mean line (R_a), the maximum peak above the mean line (R_p), the minimum valley below the mean line (R_v) and the distance from the maximum peak to the minimum valley (R_t) are considered the mean surface roughness parameters as shown in Fig. 2.28.

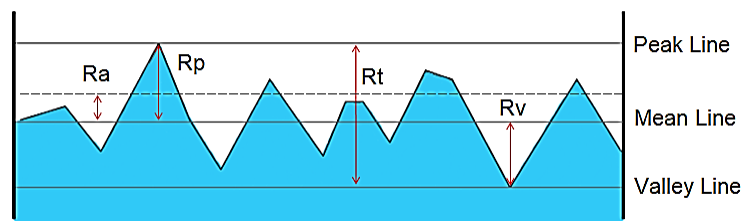


Figure 2.28 Surface roughness parameters.

However, the same average surface roughness could be found for different surface profiles as reported by Rodriguez et al. (2011). Fig. 2.29 shows different surface structures having the same (R_a). Therefore, the influence of surface microstructures should be considered rather than the average surface roughness.

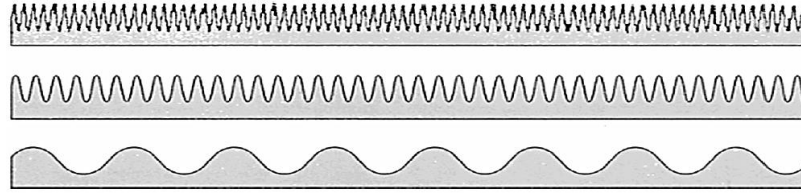
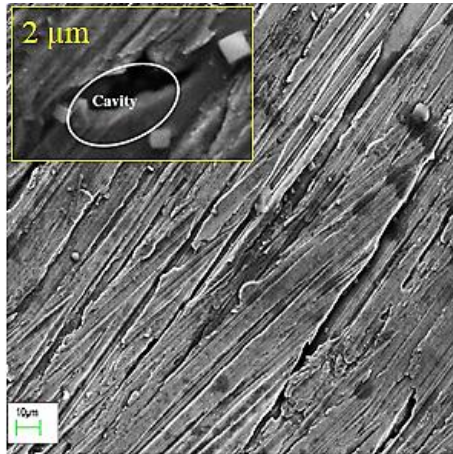


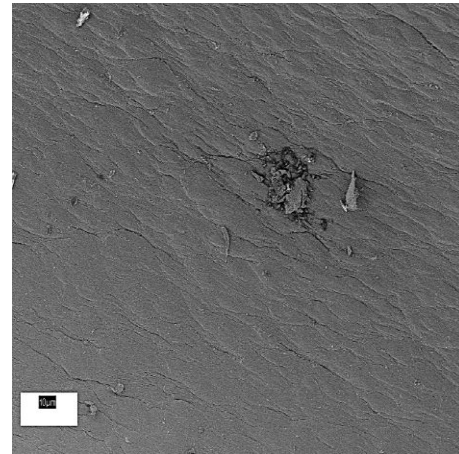
Figure 2.29 Different surface structures having the same average roughness, Kandlikar and Spiesman (1997) [taken from Pike-Wilson and Karayiannis (2014)].

Different surface finish mean different surface microstructures, which could be deposits, flakes, cracks and scratches. Surface microstructures define the number and size of nucleation sites that could influence the flow patterns, pressure drop and heat transfer results especially as the channel diameter reduces as concluded by Pike-Wilson and Karayiannis (2014). Kandlikar and Spiesman (1998) stated that the surface with more active cavities is expected to show better thermal performance. Different surface microstructures were reported in the literature using different materials, manufacturing processes and coated surfaces as shown in Fig. 2.30. This figure indicates that the surface microstructures are affected by surface material, machining conditions and manufacturing process. It also shows that Mahmoud (2011) and Pike-Wilson (2014) tested cold drawn stainless steel tubes with inner diameter of 1.1 mm. Although they used the same tube diameter, metal and manufacturing process, the surface microstructures were completely different. Moreover, the study by Mirmanto (2013) showed that some differences in surface microstructures were found using copper rectangular single channel having different hydraulic diameters. A milling machine was used by the author to manufacture these channels. It can be concluded that these differences in the previous studies may be due to other parameters that affect surface microstructures, such as the type, condition and size of cutting tool and machining vibration.

Seamless Cold Drawn Process

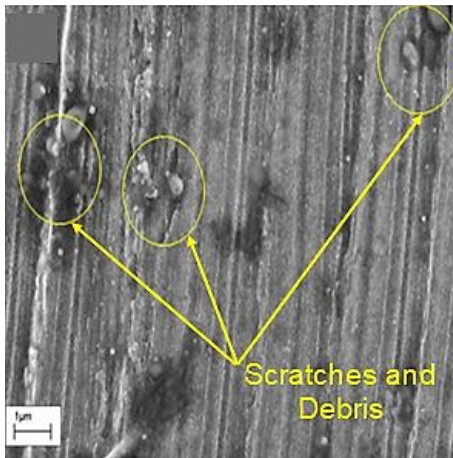


Welded Process

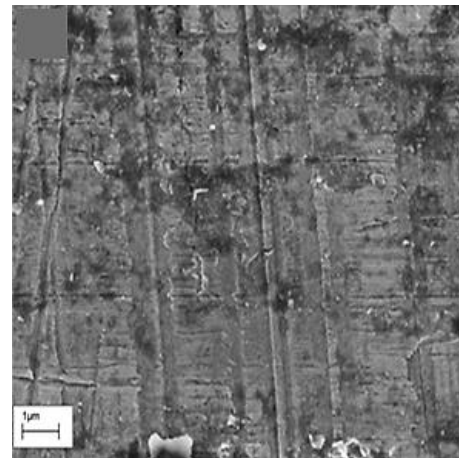


Stainless steel tubes with diameter of 1.1 mm, Karayiannis et al. (2012)

Hydraulic Diameter of 0.635 mm

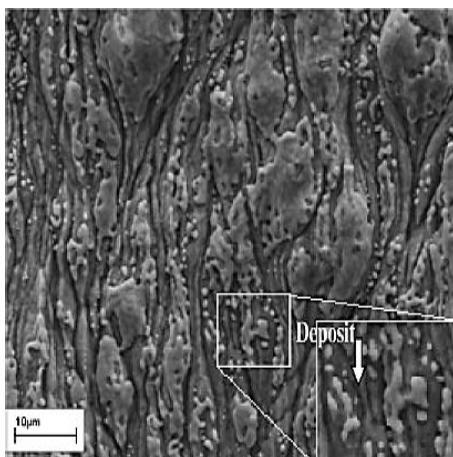


Hydraulic Diameter of 0.561 mm

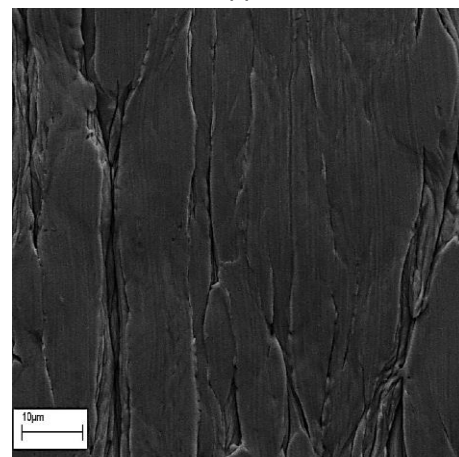


Copper rectangular single channel using milling machine, Mirmanto (2013)

Stainless Steel



Copper



Cold drawn tubes with diameter of 1.1 mm, Pike-Wilson and Karayiannis (2014)

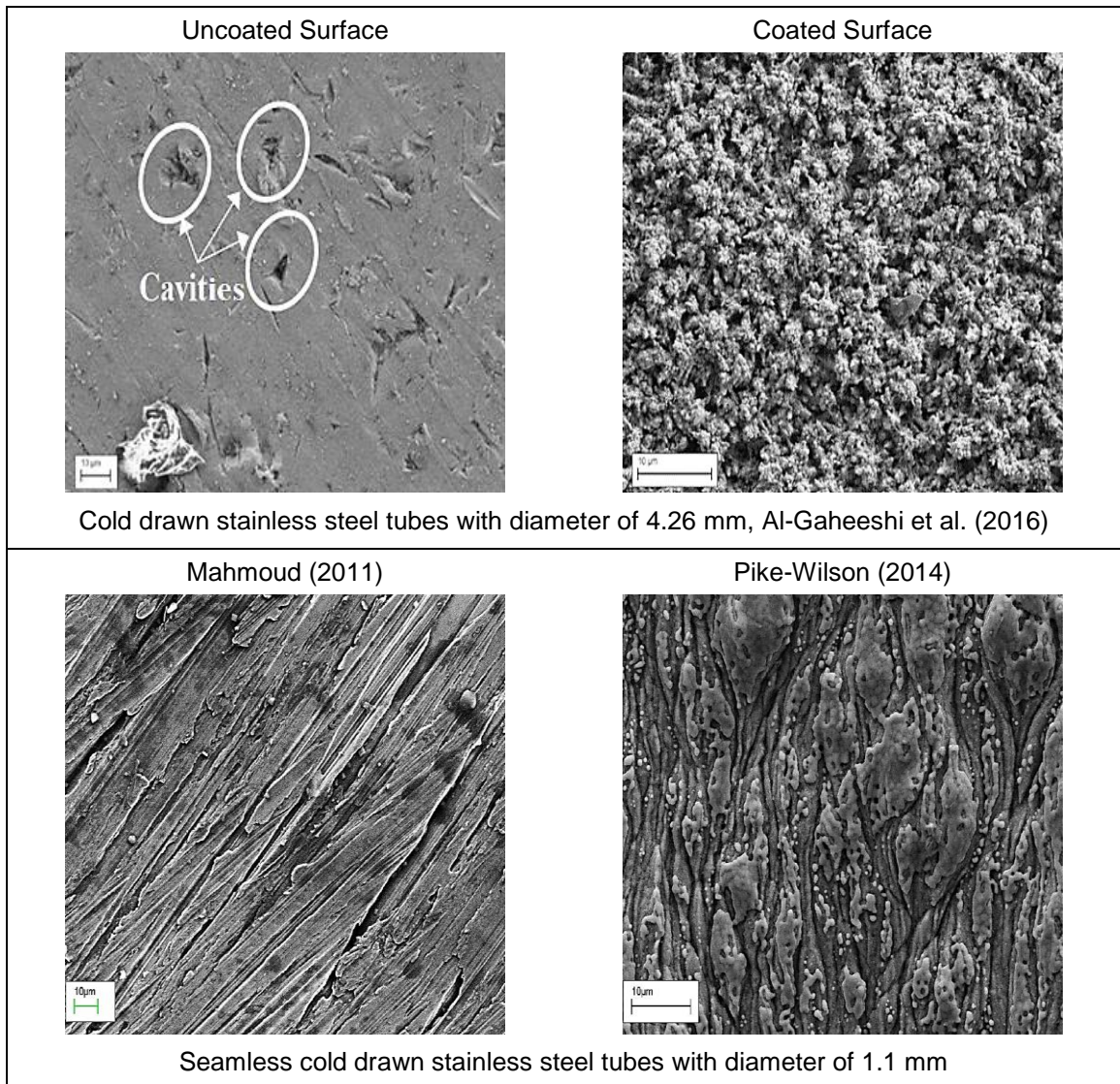


Figure 2.30 SEM images of different surface microstructures reported in the literature.

Thermal conductivity or conjugate effect may also affect the heat transfer characteristics. Karayiannis and Mahmoud (2017) mentioned that high thermal conductivity could lead to flow instabilities. They explained this as follows; a surface with high thermal conductivity causes uniform temperature distribution along the channel surface. This may lead to the activation of more nucleation sites near the channel inlet. Therefore, large fluctuations in the inlet pressure may happen. Kandlikar (2006) attributed flow reversal to the occurrence of bubble nucleation near the channel inlet and the low flow resistance to the back flow. In this section the effect of these

parameters, *i.e.* surface roughness, surface finish and thermal conductivity, on the thermal performance are discussed.

The effect of different surface materials on the pool boiling was examined by researchers. Jabardo et al. (2009) studied the effect of surface roughness and surface material on the nucleate pool boiling of R123 and R134a. Cylindrical test surface with diameter of 19 mm was fabricated using three different metals, namely copper, brass and stainless steel. The heat flux was ranged from 0.6 to 120 kW/m². In order to study the effect of surface material, the surface roughness for these metals was approximately kept at the same value. Three different roughness values were tested; 0.16, near 0.07 and near 2.5 μm. Their results depicted that the heat transfer coefficient of brass surface was slightly better than that of copper. The stainless steel surface showed lowest thermal performance. Suriyawong and Wongwises (2010) conducted pool boiling experiments using TiO₂-water and distilled water with different volume concentrations of 0.00005, 0.0001, 0.0005, 0.005, and 0.01%. They tested horizontal circular plates made of aluminium and copper. Two different surface roughness values of 0.2 and 4 μm were examined. They presented their results using heat transfer coefficient versus heat flux and boiling curve. Their results showed that, for given heat flux and surface roughness, aluminium surface had lower wall superheat than copper. Moreover, aluminium surface showed higher heat transfer coefficient than that in copper surface. The thermal performance of these surfaces became clear at high heat fluxes. This enhancement was found at 30% and 27% when the surface roughness was 0.2 and 4 μm, respectively. Hosseini et al. (2011) carried out an experimental investigation of R113 in horizontal circular plate. Three different metals were tested, namely copper, brass and aluminium at heat flux of 8–200 kW/m². The measured roughness of these surfaces was 0.901, 1.404 and 1.285 μm for copper, brass and aluminium, respectively. Their results showed that highest heat transfer coefficient was reached with copper surface (smoothest surface), while lowest thermal performance was found with aluminium surface (roughest surface). At low heat fluxes, negligible difference was reported by the author. However, at high heat fluxes, the thermal performance of copper increased by 23% and 18% than those in aluminium and brass, respectively as they mentioned. This difference in thermal

performance was attributed by the authors to the copper surface had better wettability than aluminium. When the contact angle between the fluid and surface decreased, the fluid better wetted the surface, and thus higher heat transfer coefficient. This increase in heat transfer coefficient with copper was also contributed to better thermal conductivity that resulted in higher bubble growth.

Several investigations were carried out to study the effect of surface roughness on the flow boiling heat transfer, and showed there was a significant effect of this parameter. For instance, Jones and Garimella (2009) conducted an experimental study of de-ionized water in horizontal multi-channels. Ten square microchannels with hydraulic diameter of 0.5 mm were fabricated using oxygen-free copper. Three different surfaces were tested with average roughness of 1.4, 3.9 and 6.7 μm . Their experiments were conducted at heat flux up to 3,000 kW/m^2 and mass flux ranging from 200 to 1000 $\text{kg/m}^2\text{s}$. Their results showed that, at low heat fluxes, there was a small roughness effect on the wall superheat, boiling incipience, critical heat flux and heat transfer coefficient. However, when the heat flux became higher, the heat transfer coefficient for the rougher surfaces, *i.e.* 3.9 and 6.7 μm , was similar and higher than that for the surface of 1.4 μm . They stated that, at heat fluxes more than 1,500 kW/m^2 , these two surfaces; 3.9 and 6.7 μm , showed an increase in the heat transfer coefficient by 20% and 35% compared with the smoothest surface. Alam et al. (2013) studied the influence of surface roughness of flow boiling heat transfer of de-ionized water in horizontal micro-gap channel. A micro-gap channel made of silicon with width of 12.7 mm was fabricated, while the gap height was kept at 0.2, 0.3 and 0.5 mm. Three different surfaces were examined at average roughness of 0.6, 1, and 1.6 μm . The experimental conditions were set at heat flux of 0–850 kW/m^2 and mass flux of 390 and 650 $\text{kg/m}^2\text{s}$. They reported that the heat transfer coefficient was found to increase with increasing surface roughness. This increase in the heat transfer rate was attributed by them as follows: in the single-phase region, this increase was due to increase wetted surface area. In the two-phase region, it was due to an increase in the “nucleation site density”. Rougher surface showed uniform and lower wall temperature. Jafari et al. (2016) carried out an experimental investigation of flow boiling heat transfer of R134a in horizontal multi-microchannels. Forty rectangular

microchannels were manufactured from copper with hydraulic diameter of 0.368 mm and channel length of 19 mm. They studied the effect of surface roughness using three different surfaces with average roughness of 0.21, 0.96 and 2.38 μm . Their experiments were conducted at base heat flux of 10–480 kW/m^2 and mass flux of 85 and 200 $\text{kg/m}^2\text{s}$. A vapour compression cycle was used in their study. The heat transfer results showed that, at inlet vapour quality of 0.3 and 0.5, the two-phase heat transfer coefficient increased with increasing surface roughness. They stated that, at low and moderate heat fluxes, the heat transfer coefficient increased by 45%, when the surface roughness increased. However, at inlet vapour quality of 0.8, the heat transfer coefficient did not change with the roughness. It is worth mentioning that the authors did not explain the reason for these differences.

Surface roughness effect of flow boiling in vertical tubes was also studied by researchers. Al-Gaheeshi et al. (2016) studied the effect of channel surface roughness using R245fa as a working fluid in vertical stainless steel tube with inner diameter of 4.26 mm and heated length of 500 mm. They conducted flow boiling experiments at mass flux of 200–500 $\text{kg/m}^2\text{s}$ and saturation temperature of 31 $^{\circ}\text{C}$. The tested tube was fabricated using cold drawn process with average roughness of 0.197 μm . In order to increase the surface roughness of this tube, copper coating was adopted with surface roughness of 0.675 μm . They stated that the average heat transfer coefficient was found to increase by 33%, when the surface roughness increased. In contrast, Pike-Wilson and Karayiannis (2014) reported that the roughness effect was complex and not easy to assess. They investigated flow boiling of R245fa in three vertical tubes with inner diameter of 1.1 mm and length of 300 mm. These tubes were made of copper, stainless steel and brass using cold drawn process with surface average roughness of 0.524, 0.716 and 1.249 μm , respectively. Their experiments were carried out at heat flux ranging from 10 to 60 kW/m^2 , mass flux of 100–400 $\text{kg/m}^2\text{s}$, system pressure of 1.8 and 2.4 bar and vapour quality of 0–0.95. SEM analysis was carried out for these surfaces and showed that the surface microstructure was not the same. They stated that some deposits on the surface of the stainless steel tube were found, while a “flaky structure” and cracks were noticed for the brass tube. The surface of the copper tube had a smooth structure

with some scratches. These differences in the surface microstructure could be due to the material as they reported. They stated that, at given heat and mass flux, for quality less than 0.35, the effect of surface roughness was not clear. However, at quality more than 0.35, the brass tube (rougher surface) showed highest heat transfer coefficient, while the copper tube (smoother surface) was the lowest. This trend was not found for all mass fluxes. Accordingly, there was no a clear effect of the surface roughness on the heat transfer coefficient. The material itself did not have a significant influence on the heat transfer coefficient as they concluded.

In the literature, the number of cavities was reported as a major parameter that affects the heat transfer results rather than the surface roughness. Kandlikar and Spiesman (1998) studied the effect of surface characteristics on the flow boiling heat transfer of water. The test section was made of aluminium and consisted of 3 mm × 40 mm channel. Four different surfaces were examined with surface average roughness of 0.188, 0.363, 0.716 and 3.064 μm. A camera integrated with microscope was used. After the surface was captured, the size and number of surface cavities were measured using image processing software (Image-Pro PLUS™). Since the captured images were white and black, the surface cavities showed as dark spots. Therefore, the number and average diameter of each spot was measured via this software. They mentioned that “the cavity size distribution” were quite similar, although these surfaces had different average roughness values. Their results showed that the roughest surface showed slightly better thermal performance than the others. However, the effect of surface roughness on the thermal performance was very complex as they mentioned. These surfaces showed similar performance. They concluded that the thermal performance could depend on the cavity size distributions and the number of cavities. Karayiannis et al. (2012) conducted an experimental investigation of flow boiling heat transfer of R134a in vertical tubes. Two stainless steel tubes with inner diameter of 1.1 mm were fabricated using different manufacturing processes, *i.e.* seamless cold drawn and welded tubes. Their experiments were carried out at mass flux ranging from 200 to 500 kg/m²s, system pressure from 6 to 10 bar and exit quality up to 0.95. A high-speed camera was obtained in their experiments for flow visualization. Scanning electron microscopy was used in order to

analysis the inner surface characteristics. They reported that different surface structures were found for these tubes. For example, very smooth surface was noticed for the welded tube. Moreover, some debris and fragments were also found on this tube surface. In contrast, several “uniform and longitudinal scratches” were found for the cold drawn tube. The surface average roughness was measured and was 0.52 and 1.27 μm for the welded and cold drawn tubes, respectively. Their heat transfer results showed that, for the welded tube, there is no a clear effect of the heat flux on the local heat transfer coefficient. The local heat transfer coefficient was found to vary significantly along the tube. In contrast, for the cold drawn tube, a clear effect was found, *i.e.* the local heat transfer coefficient increased with increasing heat flux, while it was independent of the local quality. There were small variations along the channel, which was attributed by the authors to nucleation sites, *i.e.* surface scratches, may exist along the channel of the cold drawn tube.

Pike-Wilson and Karayiannis (2014) studied the effect of surface metal on the flow boiling heat transfer. Their study showed that the thermal performance in the highest thermal conductivity surface, *i.e.* copper surface, was lower than stainless steel and brass. Zou and Jones (2013) depicted the opposite trend. They carried out an experimental investigation of flow boiling of R134a in a horizontal channel with width of 12.7 mm and height of 12.7 mm. Two different materials, *i.e.* copper and stainless steel, were tested. Same treatment (sand papers) was used on these surfaces in order to avoid the surface roughness effect. There was no further information about the values of surface average roughness. A Photron high-speed camera with speed of 2000 to 4000 fps was used to record the bubbles during their experiments. For each experiment, thousands images were recorded and Visual C++[®] was used to display these images frame by frame. During their experiments, the nucleation sites were visually marked and identified, and then the sites coordinates were recorded automatically. They stated that the bubble departure size, bubble growth rate and nucleation site density showed similar behaviour for these surfaces. However, the thermal performance of copper surface showed better than that of stainless steel. For example, at given wall superheat, higher heat flux was found for copper. Moreover, at given wall heat flux, higher heat transfer

coefficient was reached when the surface metal was copper. This enhancement was attributed to the difference in the thermal conductivities as they mentioned. Better thermal conductivity could affect the heat conduction and heat flux distribution.

The previous literature showed that there is no general agreement on the effect of surface roughness. Some researchers reported that the surface finish is an important parameter during flow boiling heat transfer. A second group reported that higher thermal conductivity does not always show better thermal performance.

2.4.6 Flow Boiling Heat Transfer Correlations

The accuracy of two-phase heat transfer correlations is considered an important feature in the thermal design of heat transfer systems. These correlations can define the heat sink dimensions, *i.e.* the heat transfer area. Therefore, several flow boiling heat transfer correlations and models were proposed and developed for conventional and microchannels. They were proposed for horizontal/vertical flows, macro and mini/microchannels, circular/non-circular channels and single and multi-channels. It is worth mentioning that the conventional correlations are compared with the present experimental data since they were widely used for predicting the heat transfer coefficient in the microchannel studies.

As discussed in the abovementioned sections, nucleate and convective boiling are the main contributions during flow boiling in conventional channels. These contributions are widely used by researchers to propose heat transfer correlations for conventional as well as mini/micro scale channels. These heat transfer correlations can be classified into four groups according to the organizational form as mentioned by Zhang et al. (2019):

The first group, named the superposition models, includes both components of nucleate boiling (h_{nb}) and convective boiling (h_{cb}). The two-phase heat transfer correlation can be expressed as follows:

$$h_{tp} = h_{nb} + h_{cb} \quad (2.21)$$

The correlation by Chen (1966) for conventional vertical tubes included this model.

The second group, the enhancement models, includes single-phase heat transfer coefficient (h_{sp}) multiplied by an enhancement factor (E) as follows:

$$h_{tp} = Eh_{sp} \quad (2.22)$$

Shah (1982) used this model to propose a two-phase heat transfer correlation for conventional channels.

The third group, the asymptotic models, is similar to the superposition models, *i.e.* both nucleate and convective boiling components are included. However, in this model, an asymptotic index (n) is added as follows:

$$h_{tp}^n = h_{nb}^n + h_{cb}^n \quad (2.23)$$

where n is more than one. This model was proposed by several researchers such as Kim and Mudawar (2013a).

The fourth group, the dimensionless methods, includes two-phase heat transfer coefficient as a function of several dimensionless groups as follows:

$$h_{tp} = f(Bo, Re, Bd, We, X \dots \dots) \frac{k_l}{D} \quad (2.24)$$

for example, the correlation by Li and Wu (2010b) for vertical and horizontal channels consisted of different dimensionless parameters. The dimensionless method is commonly used by the scientific community. In this method, the influence of different forces can be presented through the dimensionless parameters. Some of these parameters are adopted extensively, *i.e.* Bond number, Boiling number, Capillary number, Reynolds number, Weber number and Martinelli parameter, see Nomenclature for more details. These parameters represent the ratio between controlling forces during bubble growth. For example, the Capillary number represents the surface tension force with viscous and inertia forces, while the Weber number is the ratio between inertia and surface tension force, see Kandlikar (2010). Further details on the controlling forces during flow boiling heat transfer are presented in the following section.

Kandlikar (2010) provided a discussion on the effect of different forces during flow boiling in microchannels. Inertia, surface tension, shear, buoyancy and evaporation momentum forces can be identified as shown schematically in Fig. 2.31.

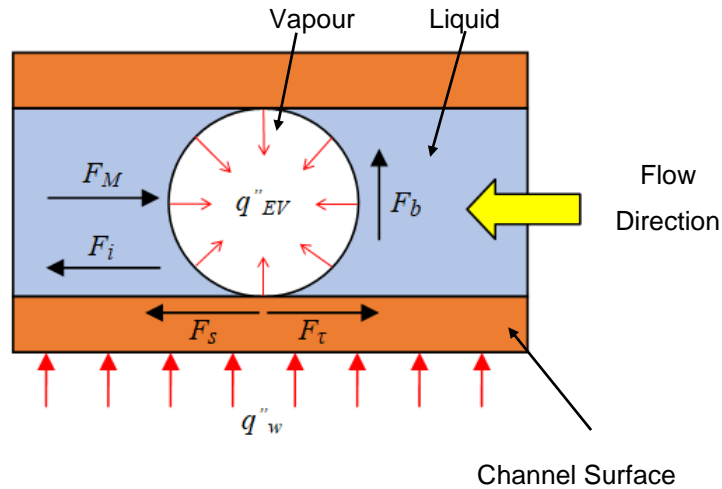


Figure 2.31 Different forces acting on a liquid–vapour interface of growing bubble in microchannels. Similar figure was presented by Alam et al. (2016).

The inertia force (F_i) is due to the flow motion and acts in the flow direction. This force per unit area is expressed as follows:

$$F''_i = \frac{G^2}{\rho} \quad (2.25)$$

where G and ρ are the mass flux and the fluid density, respectively. As shown in the above equation, the inertia force increases with increasing mass flux with the power of two.

The surface tension force (F_s) acts at the liquid-vapour interface, across the channel cross-section. This force helps to rewet the channel walls by pulling the liquid from wetter to dryer channel end, see Alam et al. (2016). The surface tension force per unit area can be expressed as follows:

$$F''_s \sim \frac{\sigma}{D} \quad (2.26)$$

where σ and D are the surface tension and the channel diameter, respectively.

The shear force (F_τ) is due to the contact between channel wall and fluid. It acts against the flow direction at the wall-liquid interface. This force promotes a homogeneous distribution of the liquid and tries to stabilize the liquid film as mentioned by Alam et al. (2016). It can be expressed using Eq. (2.27).

$$F''_\tau = \frac{\mu G}{\rho D} \quad (2.27)$$

where μ is the fluid viscosity (in contact with channel walls).

The buoyancy (gravity) force (F_b) results from the large density difference between the vapour and liquid phase. This force tries to push the bubble upward and is expressed as:

$$F''_b = (\rho_l - \rho_g) D g \cos \theta \quad (2.28)$$

where ρ_l , ρ_g , g and θ are the liquid density, the vapour density, the gravitational acceleration and the channel orientation, respectively.

The evaporation momentum force (F_M) works at the liquid–vapour interface due to the phase change, *i.e.* from liquid to vapour phase, during the evaporation process. The high velocity of vapour phase leads to develop this force. The evaporation momentum force acts against the flow direction and increases with increasing evaporative heat flux at the interface. High heat fluxes result in high evaporation momentum force that promotes flow reversal as stated by Alam et al. (2016). Eq. (2.29) is used to express this force per unit area.

$$F''_M \sim \left(\frac{q''_{EV}}{i_{lg}} \right)^2 \left(\frac{1}{\rho_g} \right) \quad (2.29)$$

where q''_{EV} and i_{lg} are the evaporative heat flux at the liquid–vapour interface and the latent heat of vaporization, respectively.

Several experimental studies in the literature were carried out to examine flow boiling characteristics using different parameters, such as working fluids, channel geometry, channel orientation and operating conditions. Numerous empirical correlations were then proposed, as a form of dimensionless groups, by taking into account the dominant forces. The magnitude of each force may be influenced by these parameters. For

instance, in mini/microchannels at high mass fluxes, the inertia force becomes the dominant force, while surface tension dominates at low mass fluxes as stated by Shah (2017). Moreover, both surface tension and shear forces increase while the gravitational force decreases with decreasing channel diameter as mentioned by Gao et al. (2019). In this section, details of each correlation are discussed, while the applicability and the equations of the existing correlations are presented in Appendix B.

2.4.6.1 Conventional channel correlations

The contribution of nucleate and/or convective boiling components was considered during development of flow boiling heat transfer correlation for conventional channels. For instance, Shah (1982) proposed a new flow boiling heat transfer correlation by selecting the larger value of the heat transfer coefficient in the nucleate and convective boiling. He defined the nucleate boiling component (E) as a function of the Boiling number, while the convective boiling component (S) was described as a function of the Convection number (N_{co}). This correlation was valid over a range of experimental data including different fluids, water, R11, R12, R22 and R113, in vertical and horizontal channels with a diameter ranging from 6 to 25.4 mm. Kandlikar (1990) followed the same approach, for calculating the total heat transfer coefficient, as Shah (1982). Both nucleate boiling and convective boiling were assumed. The Boiling number and the Convection number were proposed in his correlation. Moreover, a fluid dependent parameter (F_{fl}) was proposed to include the influence of the fluid. His correlation was developed based on 5264 data points including seven fluids, water, R11, R12, R22, R113, R134a and R152a, in vertical and horizontal tubes with inner diameter of 4–32 mm. The heat flux ranged from 0.3 to 228 kW/m², while the mass flux was 13–8179 kg/m²s. Liu and Winterton (1991) correlated the nucleate boiling component by using the pool boiling correlation, *i.e.* the Cooper (1984) correlation. Moreover, they combined the nucleate and convective contributions by using the power of 2. They found that the enhancement factor (E) depended on the liquid Prandtl number and the density ratio (liquid to vapour). Their correlation was proposed based on seven different fluids, water, R11, R12, R113, R114, R22 and ethylene glycol, in vertical and horizontal

channels with a diameter ranging from 2.95 to 32 mm. These experiments were conducted at heat flux of 0.35 to 2620 kW/m² and mass flux of 12.4–8179.3 kg/m²s.

2.4.6.2 Mini/microchannel correlations

Several empirical correlations were proposed for mini/micro scale channels. For example, Lazarek and Black (1982) conducted an experimental investigation of flow boiling heat transfer of R113 in vertical stainless steel tubes with inner diameter of 3.1 mm. The operating conditions were set at heat flux of 14–380 kW/m² and mass flux of 125–750 kg/m²s. The nucleate boiling was found to be the dominant mechanism in their data. This was concluded since the heat transfer coefficient depended on the heat flux, *i.e.* increased with increasing heat flux, and was independent of vapour quality. They correlated 728 data points by fitting local heat transfer coefficients with several dimensionless groups, and the form of the liquid Reynolds number and Boiling number was found to be the most successful one as they mentioned. Warriar et al. (2002) carried out an experimental investigation of flow boiling of FC-84 in horizontal rectangular multi-microchannels. The heat sink was made of aluminum including five parallel channels with hydraulic diameter of 0.75 mm. In their study, the operating conditions were set at a heat flux up to 59.9 kW/m² and mass flux of 557–1600 kg/m²s. They included the Boiling number and vapour quality in their new correlation. Furthermore, single-phase heat transfer coefficient for laminar fully developed flow was proposed in this correlation. Their correlation was valid for the range: $0.03 \leq x \leq 0.55$ and $0.00027 \leq Bo \leq 0.00089$. Lee and Mudawar (2005) carried out an experimental study of flow boiling heat transfer using two fluids, namely water and R134a in horizontal parallel rectangular microchannels. These channels were made of oxygen-free copper with a hydraulic diameter of 0.348 mm. Their experiments were performed at heat flux ranging from 159 to 938 kW/m² and mass flux of 127–654 kg/m²s. Three correlations were proposed according to the vapour quality ranges, *i.e.* $x < 0.05$, $0.05 < x < 0.55$ and $x > 0.55$. They found that, at vapour quality less than 0.05, the nucleate boiling was the dominant mechanism, while the convective boiling dominated at moderate and high qualities. They correlated the heat transfer coefficient as a function of liquid Weber number, Boiling number, Martinelli parameter and single-phase heat transfer coefficient.

Sun and Mishima (2009) compared their flow boiling database with 13 existing correlations. This database included 2505 data points for eleven different fluids, vertical and horizontal flows and hydraulic diameter ranging from 0.21 to 6.05 mm. The heat flux of 5–109 kW/m² and mass flux of 44–1500 kg/m²s were covered in their collected data. They reported that the correlation by Lazarek and Black (1982) predicted the data very well. Therefore, they proposed their own correlation by modifying the correlation of Lazarek and Black (1982). They included the liquid Weber number, which represents the convective boiling component. A large number of flow boiling databases were collected by Li and Wu (2010b) including different fluids, vertical and horizontal flows at hydraulic diameter ranging from 0.16 to 3.1 mm. They proposed a new flow boiling heat transfer correlation, based on more than 3700 data points, as a function of the superficial liquid Reynolds number, Boiling number and Bond number. The last dimensionless parameter was used to consider the effect of surface tension. A universal correlation was proposed by Kim and Mudawar (2013a) based on 37 sources including 18 working fluids, vertical and horizontal flows and single and multi-channels with a hydraulic diameter of 0.19–6.5 mm. Their data included heat flux ranging from 5 to 109 kW/m² and mass flux from 19 to 1608 kg/m²s. Both heat transfer coefficients nucleate and convective boiling were proposed to calculate the total heat transfer coefficient. Mahmoud and Karayiannis (2013) proposed an empirical correlation for flow boiling of R134a in vertical stainless steel tubes with diameter ranging from 0.52 to 4.26 mm. Their correlation was developed based on 5152 data points including heat flux of 1.7–158 kW/m² and mass flux ranging from 100 to 700 kg/m²s. They proposed a new experimental enhancement factor (F) according to an approach used by Chen (1966). They also used the pool boiling correlation by Cooper (1984) in their new correlation. Li and Jia (2015) proposed two correlations for saturated boiling in horizontal rectangular multi-microchannels. One correlation was for nucleate boiling dominant regime, while the other was proposed for convective boiling regime. R134a as a test fluid in three-sided heated multi-microchannels with a hydraulic diameter of 0.5 mm was examined. Their experiments were conducted at a heat flux up to 802.12 kW/m² and mass flux ranging from 373.33 to 1244.44 kg/m²s. Lim et al. (2015) conducted an experimental study of flow boiling heat transfer of water in a horizontal square microchannel with

hydraulic diameter of 0.5 mm. Their experiments were performed at heat flux of 100–400 kW/m², vapour quality of 0–0.2 and mass flux of 200, 400 and 600 kg/m²s. They compared their data with some existing correlations and over prediction was found. A new correlation was proposed as a function of Reynolds number, Boiling number and the liquid Froude number. Thiangtham et al. (2016) carried out an experimental investigation of flow boiling heat transfer of R134a in horizontal multi-microchannels. Twenty seven rectangular microchannels were made of oxygen-free copper with a hydraulic diameter of 0.421 mm. They conducted their experiments at a heat flux of 3–127 kW/m², mass flux of 150–600 kg/m²s and quality of 0.05–0.92. They reported that flow patterns had a significant effect on the heat transfer results. At low heat fluxes, the heat transfer coefficient was found to increase with increasing heat flux when the flow patterns were bubbly and slug flow. The nucleate boiling could be the dominant mechanism as they mentioned. At high heat fluxes, the heat transfer coefficient increased with mass flux when both wavy-annular and annular flows were found. They stated that the heat transfer mechanism was convective boiling. At wall heat fluxes more than 80 kW/m², the heat transfer coefficient decreased due to the partial dryout. An empirical flow boiling heat transfer coefficient correlation was proposed by taking into account these mechanisms as a function of dimensionless groups. These groups included Boiling number, liquid Weber number and liquid Reynolds number. Markal et al. (2017a) carried out an experimental study of flow boiling heat transfer of de-ionized water in horizontal rectangular multi-microchannels. Different aspect ratios (W_{ch}/H_{ch}) ranging from 0.37 to 5 at constant hydraulic diameter of 0.1 mm and different hydraulic diameters of 0.1–0.25 mm at constant aspect ratio of 1 were tested. They conducted their experiments at a heat flux of 36–221.7 kW/m² and mass flux of 51–728.7 kg/m²s. They reported that the heat transfer coefficient remained constant with heat flux or decreased with increasing heat flux in some operating conditions. Moreover, they reported that the heat transfer coefficient was found to increase with increasing channel aspect ratio and mass flux. An empirical correlation was proposed by considering that the influence of nucleate boiling was negligible. This correlation covered several parameters such as aspect ratio, superficial liquid Reynolds number, Boiling number, vapour quality, Weber number, Prandtl number, hydraulic diameter and the fluid thermal conductivity. Their

correlation was recommended in the range of $0.37 \leq \beta \leq 5$, $0.01 \leq x \leq 0.69$, $7.72 \leq Re_{ls} \leq 190$, $9.56 \times 10^{-5} \leq Bo \leq 70.4 \times 10^{-5}$, $1.92 \leq Pr_l \leq 2.42$ and $0.006 \leq We \leq 0.86$. Shah (2017) compared an extensive database with his previous correlation, Shah (1982). This database included several channel shapes and partial/fully heated channels with a hydraulic diameter equal or less than 3 mm. His correlation fairly predicted most data, while under prediction was found at low flow rates. He mentioned that this under prediction could be due to the surface tension effect. The inertia force became the dominant force at high flow rates, while surface tension dominated at low ranges as he explained. Since the Weber number represented the ratio between these forces, it was proposed to quantify this behavior. The surface tension force was found to be dominant at We_g less than 100 as stated by Shah (2017). Moreover, the Weber number was noticed to decrease with increasing Boiling number. Accordingly, the author developed a new correlation by taking into account the effect of the Weber number and the Boiling number. A factor (F) was proposed to modify his correlation, Shah (1982) as shown in Appendix B. This new correlation was verified with a database of 4852 data points, including 31 fluids, different channel shapes, vertical and horizontal flows and fully or partly heated channel with a diameter ranging from 0.38 to 27.1 mm at a mass flux ranging from 15 to 2437 kg/m²s, and a good prediction was found with a MAE of 18.6%. Recently, Wen et al. (2019) conducted flow boiling experimental investigation using R134a in two rectangular minichannels with hydraulic diameter of 1.28 and 1.59 mm. Two heat sinks, with a number of channels of eleven and nine, were manufactured using channels serrated fins as shown in Fig. 2.32. These heat sinks were made of aluminium and heated from the bottom. They conducted their experiments at a heat flux of 6–48 kW/m², mass flux of 60–308 kg/m²s, saturation pressure of 2.7–4.5 bar and vapour quality of 0–1.



Figure 2.32 Photograph of serrated fins multi-channels with 1.28mm hydraulic diameter, Wen et al. (2019).

Their results showed that, at low vapour qualities, the local heat transfer coefficient was found to increase with increasing heat flux and saturation pressure, while the mass flux had insignificant effect. At high vapour qualities, the effect of heat flux and saturation pressure was insignificant. In contrast, the local heat transfer coefficient increased with mass flux. Their data was compared with some existing correlations and no reasonable prediction was found. Therefore, they proposed an empirical correlation based on 1429 data points by introducing the dimensionless number (F) to present the Boiling number and Weber number. This correlation predicted the experimental data with a MAE of 15% as they mentioned. It must be noted however, that their geometry is very specific and differs from other studies (simple single or multichannel arrangement, tubes or rectangular channels).

It can be concluded that several two-phase heat transfer correlations were developed and proposed. The accuracy and the capability of each correlation varied from study to another. A comprehensive correlation for predicting two-phase heat transfer coefficient is still required.

2.4.7 Flow Boiling Instability

Flow boiling instabilities and flow reversal may cause system failure by decreasing thermal performance or result in mechanical vibration and heat sink breakdown. A large amplitude of oscillations in temperature, pressure and mass flow rate occurs when the flow is unstable as mentioned by Karayiannis and Mahmoud (2017). They also summarized the possible reasons for these phenomena as follow: (1) Rapid bubble growth. When bubble remains at the same location for a short time period, local dryout occurs due to the evaporation of the liquid layer underneath the bubble. (2) The size of the outlet plenum in a single channel. When the outlet plenum is larger than the channel size, the bubble velocity reduces suddenly. This leads to accumulate bubbles inside this part leading to a temporary blockage and reduction in mass flux. As a result of this, vapour quality and surface temperature increase suddenly. (3) The location of boiling incipience. Flow resistance in the back flow direction decreases when nucleation occurs near the channel inlet. This leads to flow reversal and unstable system. (4) Surface

characteristics may affect the flow instability. When the channel surface is very smooth, high wall superheat is required for boiling incipience. This leads to a rapid bubble growth inside the channel and large fluctuation in temperature and pressure. (5) High contact angle and surface tension cause large bubble departure diameter. When this diameter becomes much larger than channel size, bubble is confined by channel leading to local dryout underneath it. (6) High inlet compressibility. This problem happens when boiling occurs in the pre-heater or due to the incorrect de-gassing procedure resulting in dissolved gases in the system. As a result of this, confined bubbles expand axially in both directions (upward and downward) until it reaches the channel inlet. (7) The conjugate effect, *i.e.* high thermal conductivity surface, leads to boiling incipience near the channel inlet. This causes a large fluctuation in the inlet pressure. (8) The size of the exit tubing and outlet plenum in multi-channels. Very small size of the exit tubing with large outlet plenum may cause bubbles accumulation at the outlet plenum. This leads to increase the outlet pressure and negative pressure drop.

In order to overcome the flow instabilities in micro system, several techniques and modifications have been adopted. For example, inlet restrictors were used by Koşar et al. (2006), who studied the effect of these restrictors on the flow instabilities. They used five inlet orifices with width of 0.02 mm, height of 0.264 mm and length ranging from 0 to 0.4 mm. Five rectangular microchannels with width, height and length of 0.2, 0.264 and 10 mm, respectively were tested. They proposed a dimensionless parameter M to present the ranges of flow instability suppression, which can be found from the equation below.

$$M = (\Delta P_{or} + \Delta P_{ch}) / \Delta P_{ch} \quad (2.30)$$

They reported that, at high values of M , the instabilities were completely eradicated. Another technique such as diverging channel was carried out by Lu and Pan (2008) to reduce flow reversal. They tested ten diverging silicon microchannels with hydraulic diameter of 0.12 mm. The diverging angle of these channels was 0.5 degrees with channel height of 0.076 mm. They concluded that the flow boiling stability in these microchannels was superior to uniform microchannels. This is due to the fact that bubbles produced in these microchannels can pass the channels smoothly.

Balasubramanian et al. (2011) suggested expanding microchannels to improve the performance of the heat sink. They tested two types of microchannel heat sinks: straight and expanding. Copper heat sinks were used with a base area of 25 mm × 25 mm and channel width and height of 0.3 and 1.1 mm, respectively. The channel length of expanding microchannel was 15 and 20 mm. They stated that the expanding microchannel heat sink reduced the pressure drop and wall temperature fluctuation and improved the heat transfer performance. Another modification was invented by Qu W. (2013), who designed cross-connected microchannels. They author used microchannels with width and height of 0.1 and 0.6 mm, respectively. The cross-connected microchannels had the same width with a height cut at 1 mm in the transverse direction. He reported that this modification achieved uniform pressure fluctuation and decreased the flow boiling instability. Miner et al. (2014) studied the flow boiling of R134a in cross-sectional expansion microchannels. Four copper microchannel heat sinks with channel width of 0.1 mm and channel depth of 0.591, 0.528, 0.626 and 0.623 mm were used. The expansion angle of these channels was 0, 0.5, 1 and 2 degrees. They reported that the microchannels cross-sectional expansion reduced the system instabilities and the system became more capable. Another modification such as expanding silicon micro-gap was used by Tamanna and Lee (2015) to mitigate the flow boiling instabilities. They studied the effect of three different micro-gap heat sink configurations, namely straight micro-gap with a depth of 0.2 mm, expanding micro-gap with an inlet depth of 0.2 mm and an exit depth of 0.3 and 0.46 mm. De-ionized water as a working fluid at mass flux of 400–1000 kg/m²s and heat flux ranging from 0 to 800 kW/m² was tested. They reported that the expanding micro-gap heat sink mitigated the flow boiling instabilities and flow reversal due to the reduction of the shear force along the direction of expansion. For example, for expanding micro-gap configuration with an exit depth of 0.3 mm, the inlet pressure fluctuation was approximately 50% lower than that for the straight micro-gap configuration. The previous techniques of overcoming flow boiling instabilities are shown in Fig. 2.33. It can be seen that different channel geometries and flow restrictors were proposed and tested to reduce system instability. A micro-gap between channels and cover plate is another solution.

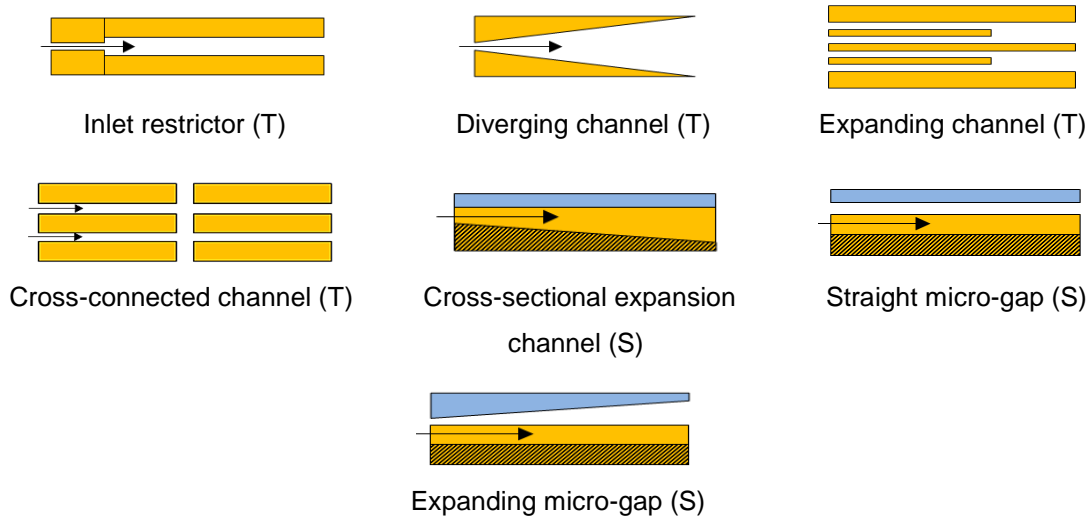


Figure 2.33 Several techniques were adopted by the past studies to overcome flow boiling instabilities. (T) Top view (S) Side view.

2.5 Flow Condensation in channels

Flow condensation characteristics in microchannels may differ compared to conventional channels due to the different dominant forces. Del Col et al. (2016) reported that the condensation mechanism depends on the relative importance of the surface tension, gravity and shear forces, which, in turn, depend on several parameters, such as vapour quality, mass flux, fluid properties and channel geometry. In larger tubes, the gravity and shear forces are more dominant, while in mini/microchannels, the surface tension force can also become important. Del Col et al. (2014) mentioned that, in non-circular mini/microchannels, the surface tension force can pull the liquid phase towards the channel corners leading to a thin liquid film and low thermal resistance at the flat sides. This means that the heat transfer coefficient in non-circular channels is expected to be higher compared to circular channels. Kim and Mudawar (2012) reported that when the mass flux increased, the interfacial shear stress between liquid and vapour phase also increased. This led to a thinner liquid film and higher heat transfer coefficient. As mentioned above, in larger tubes, gravity force can also affect the heat transfer coefficient by draining the liquid condensed to the channel bottom leading to a thicker liquid film. Moreover, Zhang and Li (2016) reported that, in the larger tubes and at low vapour quality, the liquid film became thinner at the upper section of the tube

leading to low thermal resistance and thus high heat transfer coefficient, when gravitational force increased. Further information about their study is presented in Section 2.5.3.1. In the following sections, the flow patterns, heat transfer coefficient, heat transfer correlations and pressure drop are reviewed and discussed.

2.5.1 Flow patterns in conventional and microchannels

Various condensation flow patterns were reported by researchers, when conventional channels were examined. For example, Coleman and Garimella (2003) conducted an experimental investigation of condensation flow using R134a as a working fluid. They tested six horizontal different channels made of glass; circular channel with inner diameter of 4.91 mm, square channel with hydraulic diameter of 4 mm and four rectangular channels, *i.e.* 4×2, 2×4, 6×4 and 4×6 mm, with hydraulic diameter of 2.67 and 4.8 mm. Their experiments were carried out at mass flux between 150 and 750 kg/m²s and inlet vapour quality near one. A counter-current flow, tube-in-tube, condenser was fabricated and cooled by compressed air. This coolant air was supplied at a pressure of 483–827 kPa. A digital video camera was used to capture the flow patterns during the flow condensation. They classified the condensation flow patterns by dividing them into four major groups; annular, wavy, intermittent and dispersed as shown in Fig. 2.34. They also classified these regimes into other classifications depending on the flow structure as illustrated in this figure.

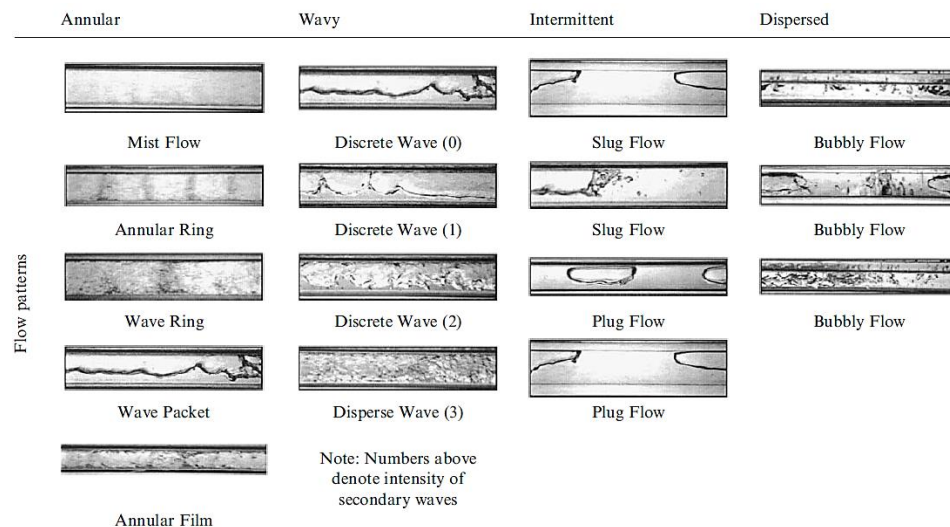


Figure 2.34 Condensation flow patterns classification by Coleman and Garimella (2003).

They defined each regime as follows:

1. Annular flow: This regime can be identified when a vapour core occurred surrounded by a liquid layer. The flow patterns in this region were classified into five categories as follows:
 - Mist flow: This flow occurred at high vapour quality and high mass flux. In this regime, a vapour mist surrounding by a very thin liquid film was observed.
 - Annular ring flow: The flow in this pattern was similar to the previous flow, but liquid rings were observed periodically.
 - Wavy ring flow: This regime was similar to the annular ring flow, but the liquid rings became thicker at the bottom compared to the top.
 - Wave packet flow: Individual waves were observed periodically, which did not reach the top of the channel due to the gravity effect.
 - Annular film flow: a uniform and thick liquid film occurred on the channel circumference.
2. Wavy flow: In this regime, the fluid flow separated into two zones; liquid flow at the bottom and vapour flowing above. This regime was divided into the following patterns:
 - Discrete wave flow: The fluid interface, *i.e.* between liquid and vapour phase, can be clearly distinguished with large amplitudes and wavelengths. This regime was classified into three numbers; 0, 1, and 2 depending on the intensity of the secondary waves.
 - Disperse waves flow: In this regime “disperse waves (3)”, the fluid interface became indistinguishable due to the multiple waves of smaller amplitudes and wavelengths.
3. Intermittent flow: This regime consisted of two patterns, namely plug and slug flow. These vapour plugs or slugs were surrounded by thin liquid, and liquid slugs were observed between them. The plug flow was characterized by individual and solitary vapour plugs without trailing bubbles. In the slug flow, vapour slugs moved through the liquid phase. Discrete waves and trailing bubbles were also captured during this regime. These two patterns were located

at different locations inside the channel depending on the channel diameter. For example, in smaller channels, these patterns were located in the channel centre. In contrast, they were located near the top of the channel, when the diameter became large, due to the buoyancy force effect.

4. Dispersed flow: This regime occurred at high mass flux and low vapour quality. It was characterized by small vapour bubbles that moved through the liquid flow. Two flow patterns were classified during this regime; bubble and dispersed flow. Bubble flow was visualized at the top of the channel due to the buoyancy effect. At higher velocities, dispersed flow occurred that was characterized by small vapour bubbles scattered across the entire cross section.

Although several flow patterns were captured in the large channels, as discussed in the previous study, different flow patterns were also reported in several experimental and numerical studies, when a small single channel was tested. For instance, Chen et al. (2014) conducted a numerical study of the flow condensation of FC-72 in a rectangular microchannel with a hydraulic diameter of 1 mm using the Volume of Fluid method (VOF). In their simulation and at mass flux of 100–150 kg/m²s, five flow patterns were reported, namely; smooth-annular, wavy-annular, transition, slug and bubbly flow. They reported that when the cooling rate decreased or mass flux increased, the vapour column length increased along the channel, and the initial bubble size increased. Fig. 2.35 shows their flow patterns.

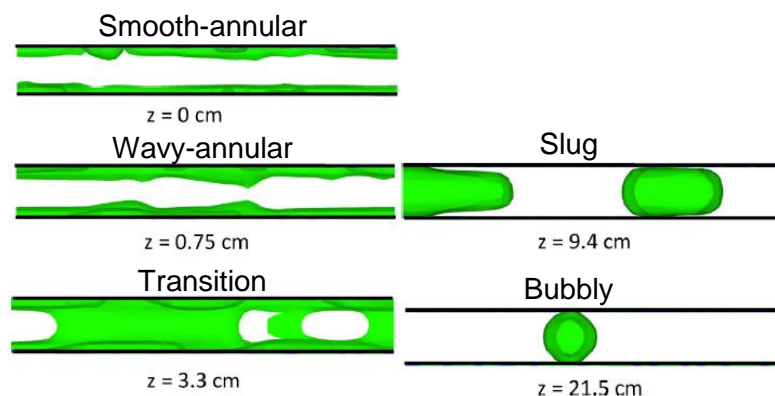


Figure 2.35 Flow patterns of FC-72 predicted by simulation study at mass flux of 68 kg/m²s, Chen et al. (2014).

EL Achkar et al. (2014) carried out an experimental study of flow condensation of n-pentane in a transparent square microchannel with a hydraulic diameter of 0.553 mm. Their experiments were carried out at low mass fluxes ranging from 3.78 to 11.98 kg/m²s. They reported that annular, intermittent and spherical bubble flows were the main regimes. The intermittent flow was identified as a slug flow or elongated bubble flow.

Other researchers studied flow condensation in multi-microchannel configurations. For example, Chen et al. (2009) investigated the condensation of steam in triangular silicon multi-microchannels with a hydraulic diameter of 0.25 and 0.1 mm. Droplet, annular, injection and slug-bubbly flow were observed. Injection flow was a transition between annular and slug-bubbly flow. They reported that when the mass flux or the hydraulic diameter increased at the same Reynolds number, the injection location moved towards the channel outlet. Ma et al. (2011) studied flow condensation of steam in trapezoidal silicon multi-microchannels with a hydraulic diameter of 0.134, 0.138 and 0.165 mm. Their experiments were conducted at mass flux range of 90–290 kg/m²s. They captured four flow patterns namely: annular, droplet, injection and bubble flow and no slug flow was observed, see Fig. 2.36. The annular flow was described as a vapour core surrounded by a liquid film. It was reported that the condensate film thickness on the side walls in annular flow varied with time for the same location and operating conditions. These variations in the liquid film thickness were attributed to two reasons (i) the interfacial instability arising from the velocity difference between liquid and vapour and (ii) the merging of the condensate into the liquid film during the condensation process. The droplet flow was characterized by small droplets growing in size on the bottom wall of the channel, while the condensate liquid film covered the side walls. The growth of the droplets was due to condensation and merging with other small droplets. The injection flow was found as a transition regime between annular flow and bubble flow. In this regime, the condensate film thickness on the side walls increased along the axial direction. When the condensate thickness became large enough, the liquid slug formed and vapour bubbles were released leading to the formation of bubbly flow. The axial location at which the injection flow (formation of bubbly flow) occurred

was found to move towards the channel exit as the mass flux and vapour quality increased, *i.e.* the high flow inertia induced by high mass flux promoted the core of vapour to travel long distance along the channel. They also reported that the annular/droplet flow expanded and spanned along the channels, when the mass flux and vapour quality increased.

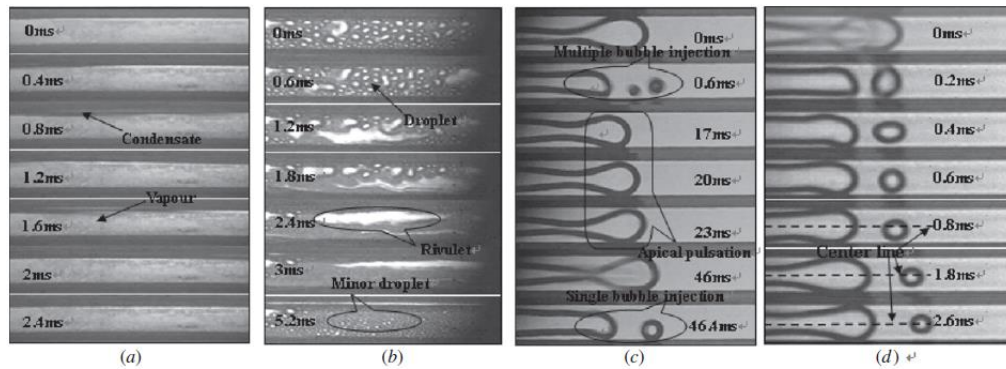


Figure 2.36 Flow Patterns of steam: (a) Annular, $G=188.13 \text{ kg/m}^2\text{s}$ (b) Droplet, $G=179.62 \text{ kg/m}^2\text{s}$ (c) Injection, $G=179.62 \text{ kg/m}^2\text{s}$ (d) Bubble, $G=143.04 \text{ kg/m}^2\text{s}$, Ma et al. (2011).

In contrast, different flow patterns were found by Kim et al. (2012) who investigated the flow condensation of FC-72 in a copper multi-microchannels condenser of square cross sectional area and 1 mm hydraulic diameter and length of 299 mm. Their experiments were conducted at mass flux ranging from 68 to 367 $\text{kg/m}^2\text{s}$, coolant mass flow rate of $3\text{--}6 \times 10^{-3} \text{ kg/s}$ and saturation temperature of 57.2 and 62.3 °C. A high-speed camera was used to capture the flow patterns during the experiments. They reported that smooth-annular, wavy-annular, transition, slug and bubbly flow were observed as shown in Fig. 2.37. The transition regime was identified as bridging of liquid ligaments through the vapour core. They found that when the mass flux increased, the smooth-annular flow extended towards the low quality region, while the slug flow became narrow in this region.
















Annular		Transition	Slug	Bubbly
Smooth	Wavy			
				
				
				
z = 0 cm	z = 0.635 cm	z = 2.86 cm	z = 8.89 cm	z = 20.32 cm

Figure 2.37 Flow patterns of FC-72 at mass flux of $68 \text{ kg/m}^2\text{s}$ and coolant mass flow rate of 6 g/s , Kim et al. (2012).

Jiang et al. (2015) conducted a visualization investigation of ethanol–water in trapezoidal silicon multi-microchannels with a hydraulic diameter of 0.165 mm and channel length of 50 mm . Six inlet ethanol concentrations of 2%, 4%, 6%, 20%, 31% and 60% were tested. A camera system integrated with a set of microscope lenses was used to capture the flow patterns during their experiments. They reported that annular, annular-streak, annular-streak-droplet, churn, injection, droplet-injection and bubble flow were observed, see Fig. 2.38. The annular-streak flow was characterized by a thick streak that generated from the bottom liquid film of the channel, while some droplets were observed in the annular-streak-droplet regime. The injection flow was found in all experiments. They reported that there were two dominant types of this regime, namely droplets-injection and injection flow.

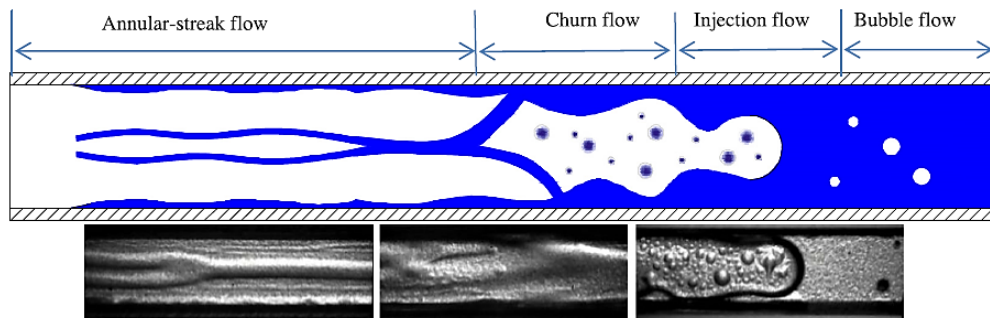


Figure 2.38 Flow patterns of ethanol–water at ethanol concentration of 20%, Jiang et al. (2015).

It can be concluded from the above studies that the names and features of the condensation flow patterns differ from one study to another. This could be due to the fact that different fluids, operating conditions and channel geometries were examined. However, at this stage no final conclusion can be made on the most common or prevailing flow patterns.

2.5.2 Flow pattern maps

Cavallini et al. (2002) proposed a new flow patterns map for conventional channels. Their map was developed based on the experimental database including several fluids; R22, R134a, R125, R32, R236ea, R404A and R410A, in inner diameter tube ranging from 3.1 to 8.8 mm at mass flux of 63–1022 kg/m²s. They presented their map using the Martinelli parameter and dimensionless gas velocity as coordinates, see Fig. 2.39. Their model can be used for different refrigerants in tubes with inner diameter of 3–21 mm, reduced pressure < 0.75 and density ratio, liquid-to-vapour density, more than 4 as they mentioned. The transition criteria were proposed as follows:

For annular flow: $J_G > 2.5$

For transition and wavy stratified flow: $J_G < 2.5$ and $X_{tt} < 1.6$

For slug flow: $J_G < 2.5$ and $X_{tt} > 1.6$

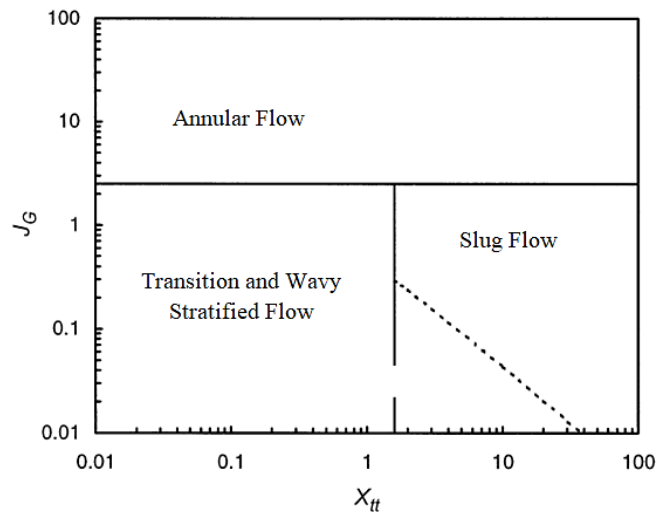


Figure 2.39 Flow patterns map proposed by Cavallini et al. (2002).

Kim and Mudawar (2012) conducted flow condensation of FC-72 in horizontal square microchannels with hydraulic diameter of 1 mm. They also presented 639 data points collected from eight sources including different fluids in mini and microchannels. A flow pattern map was proposed based on the turbulent-turbulent Martinelli parameter and the modified Weber number as shown in Fig. 2.40. They proposed three boundary relations between smooth-annular, wavy-annular, transition and slug flow. Their modified Weber number and the boundaries are presented as follows:

For $Re_{ls} \leq 1250$

$$We^* = 2.45 \frac{Re_{gs}^{0.64}}{Su_{go}^{0.3} (1 + 1.09X_{tt}^{0.039})^{0.4}} \quad (2.31)$$

For $Re_{ls} > 1250$

$$We^* = 0.85 \frac{Re_{gs}^{0.79} * X_{tt}^{0.157}}{Su_{go}^{0.3} (1 + 1.09X_{tt}^{0.039})^{0.4}} \left[\left(\frac{\mu_g}{\mu_l} \right)^2 \left(\frac{v_g}{v_l} \right) \right]^{0.084} \quad (2.32)$$

From smooth-annular to wavy-annular flow:

$$We^* = 90X_{tt}^{0.5} \quad (2.33)$$

From wavy-annular to transition flow:

$$We^* = 24X_{tt}^{0.41} \quad (2.34)$$

From transition to slug flow:

$$We^* = 7X_{tt}^{0.2} \quad (2.35)$$

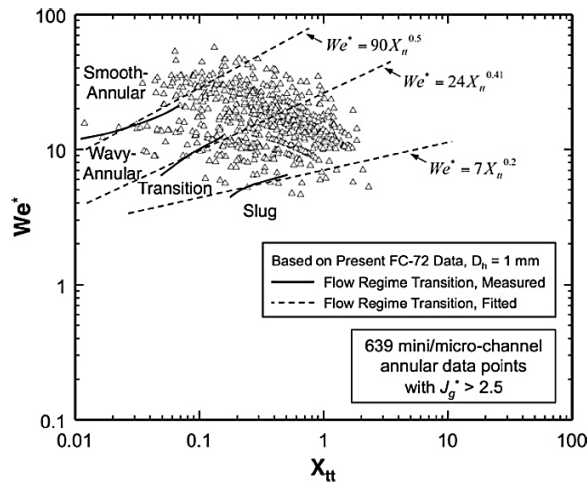


Figure 2.40 Two-phase flow patterns map of FC-72 and 639 data points from different sources proposed by Kim and Mudawar (2012).

Nema et al. (2014) proposed a flow pattern map for R134a in horizontal mini and microchannels. They used the experimental database of Coleman and Garimella (2003) that included different channel geometries, *i.e.* circular and rectangular tubes, with hydraulic diameter ranging from 1 to 4.91 mm at vapour quality ranging from 0 to 1 and mass flux from 150 to 750 kg/m²s. They classified the flow regimes into four categories, namely dispersed, intermittent, wavy and annular flow. They divided their transition boundaries based on the tube diameter effect, *i.e.* for small tubes, when $Bo \leq Bo_{cr}$, and large tubes, when $Bo > Bo_{cr}$. For small tubes, the transition criteria can be identified as follows:

For mist flow (MF): $We_g > 700$ and $X_{tt} < 0.175$

For dispersed flow (DF): $We_g < 35$ and $X_{tt} > 0.3521$

For annular flow (AF), if the previous flows are not presented: $We_g \geq 35$ or $We_g < 35$ and $X_{tt} \leq 0.3521$

For intermittent/annular flow (I-AF), if dispersed flow is not presented: $6 \leq We_g < 35$ and $X_{tt} > 0.3521$

For intermittent flow (IF), if dispersed flow is not presented: $We_g < 6$ and $X_{tt} > 0.3521$

Jiang et al. (2017) conducted an experimental study of ethanol and water in horizontal multi-microchannels. Triangular microchannels made of silicon with hydraulic diameter of 0.155 mm were fabricated. A Pyrex glass cover was clamped on these channels, while a high-speed camera mounted on the microscope was used to capture the flow patterns through this cover. Different inlet ethanol concentrations were tested, *i.e.* at mass concentrations ranging from 1% to 60%. They stated that four flow patterns were visualized during their experiments, namely annular, injection, droplet-injection and bubble. They reported that the frequency of injection flow was found to increase when the vapour Reynolds number and inlet concentration increased. They developed new flow pattern maps for different inlet ethanol concentrations as shown in Fig. 2.41.

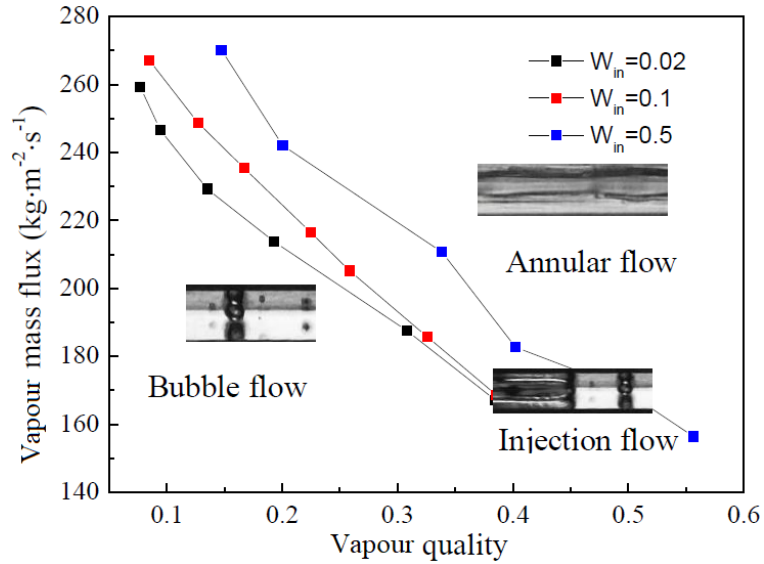


Figure 2.41 Two-phase flow patterns map at different inlet ethanol concentrations proposed by Jiang et al. (2017), W_{in} is the inlet ethanol concentrations.

Zhuang et al. (2017) conducted a condensation and an adiabatic experimental investigation using R50 in horizontal tubes with 4 mm inner diameter. Their experiments were conducted at temperature difference of 4.8–20.2 K and mass flux of 99–255 kg/m²s using high-speed camera. Different flow patterns were observed, namely plug, slug, transition, wavy-annular and smooth-annular flow as shown in Fig. 2.42.

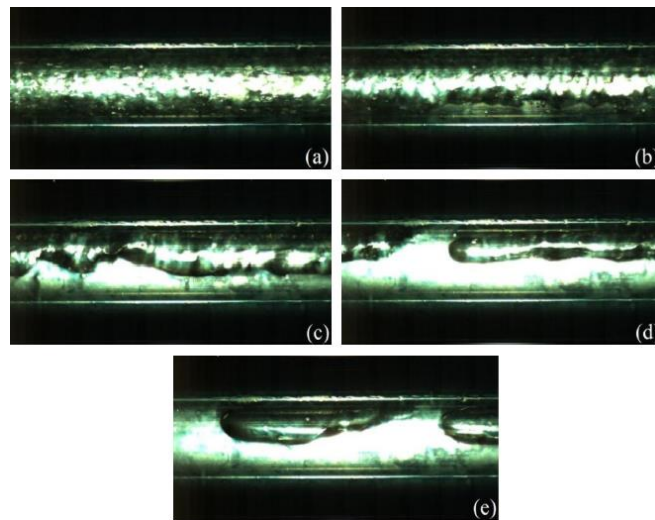


Figure 2.42 Condensation flow patterns of R50, Zhuang et al. (2017): (a) Smooth-annular (b) Wavy-annular (c) Transition (d) Slug (e) Plug.

They reported that when the mass flux increased, the flow regimes changed. Moreover, they reported that there was a little effect of saturation pressure on the transition lines. The effect of temperature difference was also studied by the authors. They indicated that, for slug/plug and transition/slug, the vapour quality decreased with increasing temperature difference. In contrast, the temperature difference had a little effect on the wavy-annular and transition flow. Accordingly, they divided the data into annular and non-annular flow, and a new transition criterion between these regimes was proposed as follows:

$$We^* = 18.91X_{tt}^{0.33} \quad (2.36)$$

They presented their map using the modified Weber number and the Martinelli parameter as coordinates, see Fig. 2.43.

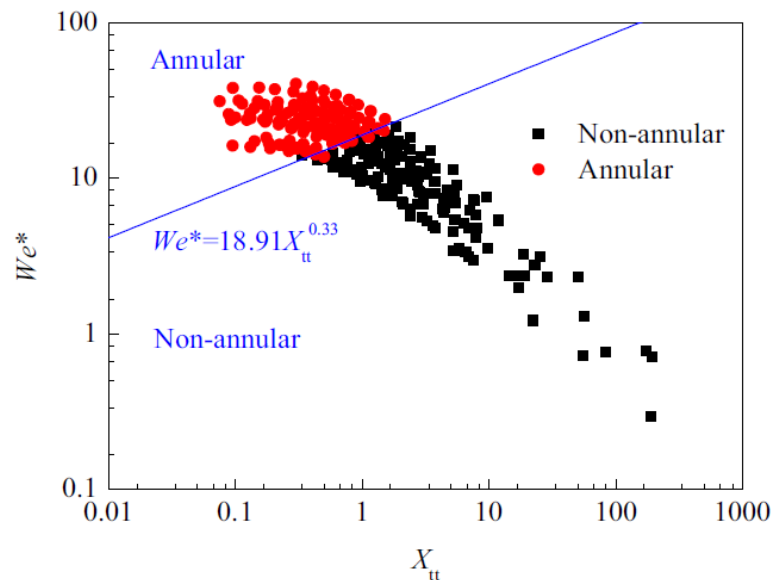


Figure 2.43 Condensation flow patterns map of R50 proposed by Zhuang et al. (2017).

2.5.3 Flow condensation pressure drop

The pressure drop is considered an important factor during flow condensation and several numerical and experimental investigations were carried out to understand the effect of operating conditions on the pressure drop. In this section, the effect of mass flux, vapour quality and saturation temperature are presented.

2.5.3.1 Effect of mass flux and vapour quality

Several condensation studies were performed and showed that the two-phase pressure drop increased with increasing refrigerant mass flux. Fronk and Garimella (2012) investigated pressure drop during condensation of ammonia in a single circular tube of 1.435 mm inner diameter. Their experiments were performed at mass flux of 75 and 150 kg/m²s and different saturation temperatures. Their results showed that the frictional pressure drop depended on mass flux. They mentioned that when the mass flux increased, the average velocity increased which led to high pressure drop. Similar results were reported by Heo et al. (2013), Al-Hajri et al. (2013) and Liu et al. (2013). Sakamatapan and Wongwises (2014) studied the pressure drop during condensation of R134a in rectangular channels with hydraulic diameter of 1.1 and 1.2 mm at mass flux of 345–685 kg/m²s and saturation temperature of 35–45 °C. They stated that the frictional pressure drop increased with increasing mass flux and vapour quality. The same conclusion was found by Goss et al. (2015), who conducted flow condensation of R134a in circular microchannels with inner diameter of 0.77 mm. Their test conditions were conducted at a pressure ranging from 7.3 to 9.7 bar, vapour quality from 0.55 to 1 and mass flux from 230 to 445 kg/m²s. They found that the experimental pressure drop increased with increasing mass flux. Zhang and Li (2016) also reported the same effect.

Other researchers, such as Fronk and Garimella (2012), Liu et al. (2013), Sakamatapan and Wongwises (2014) and Zhang and Li (2016) reported the effect of vapour quality on the two-phase pressure drop during flow condensation. They agreed on the fact that the two-phase pressure drop increased as the vapour quality increased. This was due to an increase in the velocity and vapour shear stress as reported by Fronk and Garimella (2012).

All the previous studies show that the flow condensation pressure drop increases with mass flux and vapour quality due to the high mixture velocity.

2.5.3.2 Effect of saturation temperature

The effect of saturation temperature on the pressure was also investigated by Fronk and Garimella (2012). Their results showed, when the saturation temperature increased, the pressure drop decreased due to the reduction in the interfacial shear stress. Heo et al. (2013) also reported this trend. They stated that the pressure drop increased with decreasing condensation temperature. This was explained by the authors as follows: when the condensation temperature decreased, the liquid viscosity increased and the vapour density decreased. This reduction in the vapour density resulted in an increase in the vapour superficial velocity. This led to increase the interface shear stress between the liquid and vapour and hence the pressure drop increased. This inversely proportional trend was also mentioned by Al-Hajri et al. (2013), Sakamatapan and Wongwises (2014) and Goss et al. (2015).

The abovementioned discussion showed that the pressure drop during flow condensation increases with decreasing saturation temperature due to the high vapour superficial velocity and thus high interfacial shear stress as explained in the previous studies.

2.5.4 Flow condensation heat transfer

Several experimental and theoretical studies in both conventional and microchannel condensers were conducted to understand the effect of control parameters such as refrigerant mass flux, vapour quality, saturation temperature, channel geometry and coolant side conditions on the condensation heat transfer coefficient. In the following sections, the effect of each parameter is presented and discussed.

2.5.4.1 Effect of refrigerant mass flux and vapour quality

Wang and Rose (2011) and Zhang and Li (2016) conducted a numerical study on flow condensation in non-circular and circular microchannels, respectively. Wang and Rose (2011) indicated that, for part of the channel, the local averaged heat transfer coefficient (averaged along the perimeter) was independent of mass flux, gravity and axial distance (local vapour quality). As the vapour mass flux increased, the length of this part of

channel along which the heat transfer coefficient remained almost constant also increased. They reported that the surface tension was the dominant regime for this part. Zhang and Li (2016) presented a numerical study of R410A in horizontal mini/micro tubes with inner diameter ranging from 0.25 to 4 mm at mass flux ranging from 400 to 1000 kg/m²s. The volume of fluid method was adopted in this simulation to track the vapour-liquid interfaces. Their results showed that the local heat transfer coefficient increased with increasing mass flux. They also varied the gravity force from 0 to 19.62 m/s² to study the effect of this parameter on the heat transfer coefficient. They reported that in the 4 mm diameter and at low quality and mass flux, higher gravity force led to heat transfer enhancement by thinning liquid film at the upper wall. Moreover, they mentioned that when gravity increased, the liquid film thickness at the bottom wall became thicker. However, the bottom part had a smaller effect compared to the upper part on the heat transfer rates, according to Da Riva and Del Col (2012).

Contrary to the abovementioned numerical studies, several researchers such as Cavallini et al. (2005), Agarwal et al. (2010), Fronk and Garimella (2012), Al-Hajri et al. (2013), Heo et al. (2013) and Illán-Gómez et al. (2015) investigated experimentally flow condensation in microchannels and agreed on the effect of mass flux on the average heat transfer coefficient. When the average heat transfer coefficient was plotted versus average vapour quality, it was found to increase with increasing mass flux. In these studies, the average heat transfer coefficient was calculated using the average heat flux (from an energy balance on the coolant side and the surface area), the average saturation temperature along the condenser and the averaged surface temperature. The average vapour quality was the average of the inlet and outlet vapour quality. Cavallini et al. (2005) studied experimentally condensation of R134a and R410A in multi-port minichannels with a hydraulic diameter of 1.4 mm. For R134a, the condensation experiments were conducted at mass flux ranging from 200 to 1000 kg/m²s, while for R410A, the mass flux was ranged from 200 to 1400 kg/m²s. They found that the experimental heat transfer coefficient increased with mass flux. Similarly, Agarwal et al. (2010) presented condensation heat transfer coefficient of R134a in six different minichannel shapes: rectangular, square, triangular, barrel, N and W-shaped as shown in

Fig. 2.44 with hydraulic diameters of 0.424, 0.536, 0.732, 0.762, 0.799 and 0.839 mm. Their results showed that the heat transfer coefficient increased, when mass flux increased from 150 to 750 kg/m²s.

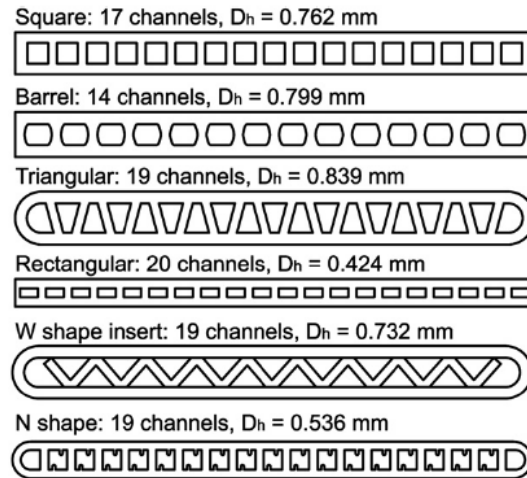


Figure 2.44 Different channel geometries, Agarwal et al. (2010).

Fronk and Garimella (2012) studied the condensation heat transfer of ammonia in a single circular tube with inner diameter of 1.435 mm. They used tube-in-tube condenser made of stainless steel. Two mass fluxes of 75 and 150 kg/m²s at vapour quality ranging from 0 to 1 and saturation temperature from 30 to 60 °C were tested. The heat transfer coefficient was calculated using the Log Mean Temperature Difference approach. Their results showed that the heat transfer coefficient increased with increasing mass flux. They attributed this to the fact that the liquid film became thinner when the mass flux increased. This led to an increase in the heat transfer coefficient. The experimental study by Al-Hajri et al. (2013) also showed a similar conclusion. Two working fluids, namely R134a and R245fa in a single microchannel with hydraulic diameter of 0.7 mm were tested. Their experiments were conducted at saturation temperature of 50 °C and mass flux ranging from 50 to 500 kg/m²s. They stated that the average heat transfer coefficient increased with mass flux. Heo et al. (2013) conducted an experimental investigation of condensation heat transfer of CO₂ in aluminium rectangular microchannels with a hydraulic diameter of 1.5 mm. The operating conditions were set at mass flux ranging from 400 to 1000 kg/m²s and condensation temperature from -5 to 5 °C. They concluded

that the heat transfer coefficient increased with increasing mass flux. Illán-Gómez et al. (2015) conducted an experimental investigation of condensation heat transfer of two working fluids, namely R1234yf and R134a. These fluids were tested in a horizontal minichannel with hydraulic diameter of 1.16 mm at mass flux ranging from 350 to 940 $\text{kg/m}^2\text{s}$ and six different saturation temperatures of 30, 35, 40, 45, 50 and 55 °C. They reported that the heat transfer coefficient increased with increasing mass flux. Recently, Rahman et al. (2018) carried out flow condensation of R134a in an aluminium condenser cooled by water. Twenty horizontal rectangular multi-channels with hydraulic diameter of 0.64 and 0.81 mm were manufactured. These channels were designed with and without fins as shown in Fig. 2.45. They conducted their experiments at saturation temperature of 30–35 °C and mass flux of 50–200 $\text{kg/m}^2\text{s}$. They reported that the average heat transfer coefficient increased with increasing mass flux for all channels.

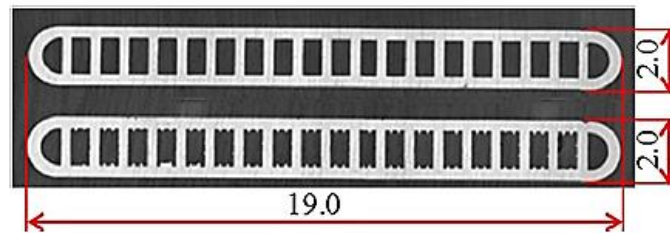


Figure 2.45 Photograph of the rectangular multi-channels with and without fins, Rahman et al. (2018).

The effect of average vapour quality on the average heat transfer coefficient was reported by several researchers, such as Fronk and Garimella (2012) conducted an experimental investigation using ammonia in a single tube with 1.435 mm diameter. Their experiments were conducted at saturation temperature ranging from 30 to 60 °C and mass flux of 75 and 150 $\text{kg/m}^2\text{s}$. They stated that the heat transfer coefficient increased with increasing vapour quality due to the thinning liquid film. This increase in the heat transfer coefficient with quality was also reported by Liu et al. (2013), Illán-Gómez et al. (2015), Zhang and Li (2016) and Rahman et al. (2018).

In contrast, some studies showed some different trends. For instance, Del Col et al. (2015) investigated the condensation heat transfer characteristics of R1234ze(E) in a horizontal rectangular channel having hydraulic diameter of 0.96 mm at the mass flux ranging from 100 to 800 kg/m²s. Their results showed that, at mass flux equal or more than 200 kg/m²s, the heat transfer coefficient increased rapidly with vapour quality and also with mass flux. However, at mass flux below 200 kg/m²s, the heat transfer coefficient was found to increase slightly with vapour quality, while an insignificant effect of mass flux was found. Jige et al. (2016) investigated condensation heat transfer characteristics of four refrigerants; R134a, R32, R1234ze(E) and R410A in a horizontal multi-port tube. Seventeen rectangular channels made of aluminium were fabricated with hydraulic diameter of 0.85 mm. They conducted their experiments at mass flux of 100 to 400 kg/m²s and saturation temperature of 40 and 60 °C. They stated that at mass flux more than 100 kg/m²s, the heat transfer coefficient decreased monotonically as the vapour quality decreased. This was attributed to the reduction in the shear stress and thus increase in the condensate thermal resistance. In contrast, at the lowest mass flux, the heat transfer coefficient exhibited a plateau in the vapour quality range of 0.2–0.6, *i.e.* it did not decrease continuously as was the case for high mass fluxes. This trend was attributed to the dominance of the surface tension force, *i.e.* the condensate film was kept thin between the channel corners.

It can be concluded that, in micro scale channels, shear stress and surface tension forces are considered the main forces that affect the heat transfer coefficient. When the shear stress dominates, the heat transfer coefficient increases with increasing refrigerant mass flux and vapour quality, while in the surface tension dominated regime, it is independent of mass flux and quality.

2.5.4.2 Effect of saturation temperature

Some researchers such as Fronk and Garimella (2012), Al-Hajri et al. (2013), Heo et al. (2013), Liu et al. (2013), Illán-Gómez et al. (2015) and Rahman et al. (2018) investigated the effect of saturation temperature on the condensation heat transfer coefficient. Fronk and Garimella (2012) found that the heat transfer coefficient

decreased with increasing saturation temperature due to the reduction in the density ratio and interfacial shear stress. Al-Hajri et al. (2013) attributed this reduction to an increase in the vapour density that led to a decrease in the vapour velocity. Another explanation was given by Heo et al. (2013), who stated that when the condensation temperature decreased, the thinning of the liquid film due to the difference in the density ratio led to an enhancement of the heat transfer coefficient. Liu et al. (2013) carried out an experimental investigation of flow condensation of R152a in minichannels with a hydraulic diameter of 0.952 and 1.152 mm. In their experiments, the saturation temperature was set at 40 and 50 °C and mass flux of 200–800 kg/m²s. They found that the heat transfer coefficient decreased with increasing saturation temperature. This reduction was attributed to the vapour phase velocity. When the saturation temperature increased the vapour density also increased. This led to a decrease in the vapour phase velocity and the shear stress between the vapour and liquid phase leading to thicker liquid film.

It is obvious that the heat transfer coefficient increases with decreasing saturation temperature. This is due to the effect of density ratio on the liquid film thickness as explained in the previous studies, such as Fronk and Garimella (2012) and Heo et al. (2013).

2.5.4.3 Effect of channel geometry

Matkovic et al. (2009a) investigated experimentally condensation heat transfer of R134a in a single square minichannel with hydraulic diameter of 1.18 mm. Their experiments were conducted at mass flux ranging from 200 to 800 kg/m²s and saturation temperature of 40 °C. They compared their results with the results of a study that used a circular tube of 0.96 mm inner diameter, Matkovic et al. (2009b). They found that at high mass fluxes, the values of the local heat transfer coefficient in the square and circular were very close to each other. At mass flux of 200 kg/m²s, the heat transfer coefficient in the square channel was higher than that in the circular channel by 20–30%. This enhancement was attributed to the surface tension effect that pulled the liquid towards the channel corners leading to a thinner film at the flat channel sides. Liu et al. (2013)

investigated condensation heat transfer of R152a in a square and circular minichannel with a hydraulic diameter of 0.952 and 1.152 mm, respectively. Their experiments were conducted at mass flux ranging from 200 to 800 kg/m²s, vapour quality from 0.1 to 0.9 and saturation temperature of 40 and 50 °C. They reported that, at low mass fluxes, the heat transfer coefficient in a square channel was higher than that in a circular channel due to the influence of surface tension. The results of Del Col et al. (2011) were compared against the study by Bortolin et al. (2014), who conducted steady state numerical simulations of R134a in a square minichannel of 1 mm hydraulic diameter. They also compared their results with simulations conducted by Da Riva et al. (2012), for a circular minichannel. Their experiments were conducted at saturation temperature of 40 °C and mass flux of 400 and 800 kg/m²s. They stated that, at higher mass flux, the heat transfer coefficient was roughly the same in both geometries. However, at lower mass flux, the heat transfer coefficient in the square channel was higher by 15% due to the surface tension effect.

It can be concluded from the previous investigations that, at low mass fluxes, it is expected that the heat transfer rate in a rectangular channel is higher than that in a circular channel due to the surface tension effect. However, a small effect of channel geometry is found at high mass fluxes.

2.5.4.4 Effect of coolant side

Some researchers studied the effect of coolant side, the saturation-to-wall temperature difference, on the condensation heat transfer. Matkovic et al. (2009b) studied the effect of coolant conditions, *i.e.* the inlet coolant temperature and coolant mass flow rate, on the local heat transfer coefficient. R134a was tested in a single circular channel with inner diameter of 0.96 mm at mass flux of 417 kg/m²s and saturation temperature of 40 °C. The inlet coolant temperature and coolant mass flow rate were varied from 15 to 29 °C and from 0.0027 to 0.0056 kg/s, respectively. They stated that the temperature difference had an insignificant effect on the local heat transfer coefficient. The same effect was also found when R32 was tested in the same test section at mass flux of 200 kg/m²s and inlet coolant temperature ranging from 19 to 29 °C. Matkovic et al. (2009a)

also investigated experimentally condensation heat transfer of R134a in a single square minichannel with hydraulic diameter of 1.18 mm. Water as a coolant was used at inlet temperature of 18.9, 22.4, 25.8, 29.9 and 32.5 °C and refrigerant mass flux of 260 kg/m²s. Their results showed that there was insignificant effect of the saturation-to-wall temperature difference on the experimental local heat transfer coefficient. A similar conclusion was found by Del Col et al. (2011).

The coolant conditions seem to have an insignificant effect on the condensation heat transfer coefficient. Table 2.7 presents a summary of the numerical and experimental conditions covered in the past studies. This table shows that different fluids, channel geometries and metals were tested. Aluminium is the common metal that was tested in the previous studies. Low mass fluxes, *i.e.* lower than 50 kg/m²s, were not examined in these studies.

Table 2.7 Summary of the numerical and experimental conditions covered in the past flow condensation studies.

Author(s)	Channel geometry*	Channel material	D_h [mm]	Fluid(s)	T_{sat}/G
Cavallini et al. (2005)	R, M	Aluminium	1.4	R134a & R410A	40 °C 200–1400 kg/m ² s
Agarwal et al. (2010)	D, M	Aluminium	0.424–0.839	R134a	55 °C 150–750 kg/m ² s
Matkovic et al. (2009a)	Sq, S	Copper	1.18	R134a	40 °C 200–800 kg/m ² s
Wang and Rose (2011)	R, T, S	--	0.5–2	R134a, R22, R410A, Ammonia, R152a, Propane, CO ₂	25 and 50 °C 100–1300 kg/m ² s
Fronk and Garimella (2012)	C, S	Stainless steel	1.435	Ammonia	30–60 °C 75 and 150 kg/m ² s
Kim and Mudawar (2012)	Sq, M	Copper	1	FC-72	57.2–62.3 °C 68–367 kg/m ² s
Al-Hajri et al. (2013)	R, S	Copper	0.7	R134a & R245fa	30–70 °C 50–500 kg/m ² s
Heo et al. (2013)	R, M	Aluminium	1.5	CO ₂	-5–5 °C 400–1000 kg/m ² s
Liu et al. (2013)	Sq, C, S	Stainless steel	0.952 and 1.152	R152a	40 and 50 °C 200–800 kg/m ² s

Bortolin et al. (2014)	Sq, C, S	--	1	R134a	40 °C 400 and 800 kg/m ² s
Sakamatapan and Wongwises (2014)	R, M	Aluminium	1.1 and 1.2	R134a	35–45 °C 345–685 kg/m ² s
Goss et al. (2015)	C, M	Copper	0.77	R134a	28–38 °C 230–445 kg/m ² s
Illán-Gómez et al. (2015)	R, M	Aluminium	1.16	R1234yf & R134a	30–55 °C 350–940 kg/m ² s
Zhang and Li (2016)	C	--	0.25–4	R410A	46.85 °C 400–1000 kg/m ² s
Rahman et al. (2018)	R, M	Aluminium	0.64 and 0.81	R134a	30–35 °C 50–200 kg/m ² s
* S: single channel, M: multi-channels, Sq: square, R: rectangular, C: circular, T: triangular, D: different shapes (e.g. rectangular, square, triangular, barrel, N and W-shaped).					

2.5.5 Flow condensation heat transfer correlations

Several correlations were developed and proposed for predicting the condensation heat transfer coefficient in conventional and mini/microchannels. Most of these correlations were proposed for annular flow since this was the main regime during flow condensation. In the present study, these correlations are divided into two groups; conventional and mini/microchannels, based on the classification of Kandlikar and Grande (2003). Their classification, originally referring to boiling was adopted by some researchers in flow condensation studies, such as Matkovic et al. (2009b), Bohdal et al. (2011) and Shah (2016). The authors classified the channels based on the hydraulic diameter as follows:

Conventional Channels: $D_h > 3 \text{ mm}$

Minichannels: $0.2 \text{ mm} < D_h \leq 3 \text{ mm}$

Microchannels: $0.2 \text{ mm} \geq D_h > 0.01 \text{ mm}$

In this section, some of these correlations are described, while the details of each correlation and the dimensionless parameters are presented in Appendix C.

2.5.5.1 Conventional channel correlations

Shah (1979) proposed a correlation for condensation heat transfer coefficient in different pipe diameters based on dimensionless groups. They developed their correlation for vertical, horizontal and inclined pipes with diameter ranging from 7 to 40 mm. Several fluids such as R11, R12, R22, R113, water, ethanol, methanol, toluene, benzene, and trichloroethylene were included. The operating conditions were set at a mass flux ranging from 10.83 to 210.5 kg/m²s, vapour quality of 0–1, Reynolds number from 100 to 63000, saturation temperature from 21 to 310 °C and reduced pressure from 0.002 to 0.44. The correlation was exactly the same as the Dittus-Boelter single-phase equation but multiplied by a two-phase multiplier. The two-phase multiplier was correlated as a function of the vapour quality and the reduced pressure. They reported that the new correlation predicted the data with a MAE of 15.4%. Dobson and Chato (1998) conducted an experimental investigation of condensation heat transfer in horizontal pipes with diameter of 3.14 and 7.04 mm. Different working fluids, namely R12, R22, R134a and R32/R125 were tested at mass flux ranging from 75 to 800 kg/m²s and reduced pressure from 0.21 to 0.57. An annular flow correlation was proposed for the shear dominated regime. They noted that in this regime, the heat transfer coefficient depended on the mass flux and quality. The correlation was similar to the one proposed by Shah (1979) but the two-phase multiplier was given as a function of the turbulent liquid-turbulent vapour Martinelli parameter. Cavallini et al. (2006a) proposed a model to predict the condensation heat transfer coefficient inside horizontal tubes with inner diameter > 3 mm. Their model was developed from 425 data points including different fluids; R134a, R125, R236ea, R32 and R410A. This model took into account the dependency or independency of the heat transfer coefficient on the temperature difference. They compared their model with 5478 data points that were collected from several experiments using different fluids. They reported that their model predicted the results very well with a mean absolute error of 14%.

2.5.5.2 Mini/microchannel correlations

Wang et al. (2002) carried out flow condensation experiments of R134a in horizontal rectangular multi-channels. The test section was fabricated from aluminium with hydraulic diameter of 1.46 mm. An air-cooled condenser was tested at mass flux of

75–750 kg/m²s, inlet pressure of 18–19.3 bar, inlet quality of 0.03–0.94 and air inlet temperature of 20–24 °C. They compared their experimental data with some existing correlations, and over prediction were found. Therefore, they proposed a correlation for calculating the condensation annular heat transfer coefficient. 700 data points for annular flow were compared with their correlation, and better agreement was found with an average deviation of 7.9%. Koyama et al. (2003b) conducted an experimental investigation on condensation of R134a in two multiport extruded tubes with a hydraulic diameter of 0.807 and 1.114 mm. One test section consisted of eight channels, while the other one consisted of nineteen channels. In their study, the local pressure drop and heat transfer coefficient were investigated. The results of the local heat transfer coefficient were compared with the correlations of Moser et al. (1998) and Haraguchi et al. (1994). They found that at high mass flux, the correlation of Moser et al. (1998) agreed with their results, while the trend was different for the data of low mass flux. They also reported that the correlation of Haraguchi et al. (1994) showed a better agreement and a similar trend to the experimental results, when the two-phase pressure drop multiplier for the vapour phase in the previous correlation was replaced using the correlation of Mishima and Hibiki (1995). This is due to the fact that the Mishima–Hibiki correlation was in good agreement with their results. Finally, they proposed their own correlation for condensation heat transfer coefficient based on the modification of the correlation of Haraguchi et al. (1994). Bohdal et al. (2011) investigated experimentally the condensation heat transfer and pressure drop of R134a and R404A in stainless steel mini pipes with inner diameter of 0.31–3.3 mm. Their experiments were conducted at mass flux ranging from 100 to 1300 kg/m²s, vapour quality of 0–1 and saturation temperature of 20–40 °C. They reported that the correlation of Akers et al. (1958) and Shah (1979) could be used within a limited range of inner diameter and mass flux. For example, at mass flux $G < 400\text{--}600$ kg/m²s and diameter less than 1.4 mm, the correlation of Akers et al. (1958) was in a good agreement with their results. At mass flux higher than 600 kg/m²s, better results were found when using the correlation of Shah (1979). They proposed their own correlation to calculate the local condensation heat transfer coefficient. Park et al. (2011) investigated experimentally condensation heat transfer of R1234ze(E), R134a and R236fa in vertical multiport tubes. Their test section consisted of seven rectangular aluminium minichannels with a hydraulic diameter of 1.45 mm. In their experiments, the mass flux ranged from 50 to 260 kg/m²s, and the

heat transfer coefficient was calculated locally and compared with other correlations, such as Koyama et al. (2003a), Cavallini et al. (2006b) and Moser et al. (1998). Their results were higher at high Nusselt number and lower at low Nusselt number than those predicted by the past correlations. However, their results were predicted quite well at the mid-range. Accordingly, they modified the correlation of Koyama et al. (2003a), which was proposed as a combination of gravity controlled and forced convection to include the effect of non-circular channel geometries. The modification included optimising the empirical constant in the original correlation by fitting the experimental data and adjusting this constant. Their modified correlation showed a good agreement with their experimental results for all fluids. Wang and Rose (2011) conducted a numerical study on flow condensation in non-circular microchannels. They reviewed their original theory that was proposed for different fluids, channel geometries and dimensions. They reported that for part of the channel, the local average heat transfer coefficient (averaged along the perimeter) was independent of gravity and shear stress and depended on surface tension. Therefore, they updated their theory and proposed a correlation for the surface tension dominated regime. Kim and Mudawar (2013c) presented a universal approach to calculate the condensation heat transfer coefficient in single and multi-channels. They collected 4045 data points from 28 sources for circular and rectangular channels. The consolidated database consisted of different fluids: R134, R12, R22, R123, R1234ze(E), R1234yf, R245fa, R236fa, R404, R32, R410A, R600a, FC-72, CO₂ and methane, hydraulic diameter ranging from 0.424 to 6.22 mm, mass flux from 53 to 1403 kg/m²s, Reynolds number from 276 to 89798, vapour quality of 0–1 and reduced pressure from 0.04 to 0.91. They proposed two correlations, one for annular flow and another for slug and bubbly flows. They reported that the consolidated database was predicted very good with overall mean absolute error of 16.0%. Shah (2016) proposed a correlation of condensation heat transfer coefficient in horizontal mini/microchannels for a hydraulic diameter equal or less than 3 mm. He collected 67 data sets from 31 sources for 13 different fluids (R134a, R22, R32, R152a, R1234ze(E), R245fa, R410A, R1234fa, FC-72, propane, butane, water and CO₂) with a hydraulic diameter ranging from 0.1 to 2.8 mm. His correlation was verified with data sets in single and multi-channels of various shapes at mass flux ranging from 20 to 1400 kg/m²s, aspect ratio from 0.14 to 13.9 and reduced pressure from 0.0055 to 0.94. He developed his correlation by modifying the correlation of Shah

(2013). In his correlation, the heat transfer coefficient was proposed for three regions, representing the dimensionless vapour velocity, see Appendix C. The boundaries between these regimes can be identified based on the dimensionless vapour velocity. He reported that the new correlation predicted 1017 data points with a MAE of 15.5%. Recently, Rahman et al. (2018) conducted an experimental study using R134a in horizontal condenser cooled by water. Twenty rectangular aluminium multi-channels with hydraulic diameter of 0.64 and 0.81 mm were manufactured. These channels were designed with and without fins. Their experimental investigation was performed at a mass flux of 50–200 kg/m²s and saturation temperature of 30–35 °C. Their results indicated that the heat transfer coefficient depended on saturation temperature, vapour quality, mass flux and channel geometry. They compared their experimental data with some existing correlations. They found that these correlations over predicted their data. They correlated their data and proposed a correlation for annular flow by introducing reduced pressure and vapour quality to consider the variation of fluid properties with saturation temperature. This correlation predicted their experimental results with a MAE of 17.4%.

2.6 Summary and Conclusions

A review on the flow boiling and condensation in conventional and mini/microchannels was presented. This review covers several topics including; (i) the definition of macro and microchannels, (ii) HFE-7100 for cooling high heat flux systems, (iii) flow patterns in different channel dimensions and orientations, (iv) heat transfer mechanisms, (v) effect of different parameters on the flow patterns, pressure drop and heat transfer coefficient, (vi) flow pattern maps, prediction of pressure drop and heat transfer coefficient and (vii) flow boiling instabilities.

It can be concluded that there is no agreed conclusion on the criteria used for defining channel threshold from macro to micro. This is due to the fact that different criteria were adopted by researchers using different operating conditions. For example, fluid properties are affected by operating conditions resulting in different criteria. Two-phase flow of HFE-refrigerants is considered a good choice for cooling high heat flux applications, such as computer data centres, semiconductor devices

and fuel cells. Different channel geometries and techniques were adopted to increase the dissipated heat flux. Maximum base heat flux was reached up to 11.27 MW/m^2 using hybrid cooling module. However, high mass fluxes, inlet sub-cooling and pressure drop are the major limitations of some techniques.

Although several experimental investigations in two-phase flow of HFE-7100 were carried out, few flow visualization studies were conducted and thus there is lack of experimental flow pattern results for this refrigerant. The average heat transfer coefficient was calculated and presented in the literature. It is known that the local heat transfer calculations corresponding to flow visualization play a major role in two-phase results and help to explain the complex effect of flow behaviour. The effect of channel aspect ratio on flow boiling heat transfer at constant channel hydraulic diameter, base area and channel surface roughness was not tested in most studies. Flow boiling of HFE-7100 in aluminium horizontal multi-microchannels was not investigated in the literature. Moreover, flow condensation of this refrigerant in horizontal multi-microchannel condenser at low operating conditions was also not studied. Finally, two-phase flow of HFE-7100 at atmospheric pressure, low mass fluxes and low inlet sub-cooling was not examined before.

In addition to the previous conclusion, other points can be summarized as follows:

A. Flow boiling characteristics

Boiling flow patterns and maps

1. In conventional channels, different flow patterns were reported in vertical channels compared to those in horizontal channels. For example, plug and stratified flows occurred in horizontal channels, and were not observed in vertical channels. Buoyancy force could lead to this difference in flow patterns, which becomes clear in horizontal conventional channels.
2. A significant difference in flow patterns was found with reducing channel diameter. In microchannels, confined bubbles and slug occurred, while plug and stratified flow were not visualized. Surface tension may overcome the buoyancy force leading to these confined flows, especially in micro scales.

3. In multi-microchannels, the experimental flow patterns differed from one study to another. Flow reversal and maldistribution could affect the appearance of these patterns.
4. Few nucleating bubbles in the liquid film of slug or annular flow were visualized in rectangular multi-microchannels. This was attributed to the fact that the channel corners could act as active nucleation sites leading to the generation of these bubbles.
5. Dispersed and small bubbles occurred in the large channel aspect ratio, while these bubbles became elongated with decreasing aspect ratio due to the confinement effect. However, the effect of channel aspect ratio on flow patterns is still unclear.
6. Surface microstructures (number, diameter and depth of surface cavities) could define the number and size of nucleation sites.
7. More bubbles occurred when the channel surface roughness increased. This was attributed to the large number of nucleation sites activated on the rougher surface.
8. There was no general flow patterns map or predictive models that can be used to predict all the transition boundaries. This could be due to the different features and names of flow patterns were reported in the literature.

Flow boiling Pressure drop

1. Most studies agreed on the fact that the pressure drop increased with increasing heat flux (exit vapour quality) and mass flux. This was attributed to an increase in the acceleration and frictional pressure drop components. However, the pressure drop was independent of heat flux in some studies, see Tibirićá and Ribatski (2011) and Xu et al. (2016). Markal et al. (2016a) showed that the total pressure drop decreased with increasing mass flux at given heat flux. The authors did not present a clear explanation for this trend. It is worth mentioning that they presented their result using total pressure drop from the inlet to the outlet, *i.e.* including single-phase pressure drop, versus wall heat flux. Moreover, high inlet sub-cooling of 50 K was tested in their experiments. At a given heat flux, when the mass flux increases, the single-phase length also increases leading to a reduction of the flow boiling region and thus lower total pressure drop.

2. Some studies showed that the pressure drop increased with decreasing channel aspect ratio or channel width. This could be due to the confinement effect, *i.e.* channel sidewalls. In contrast, a complex effect by channel aspect ratio was reported in others, see Markal et al. (2016b) and Candan et al. (2018).
3. Pressure drop was found to increase with increasing average surface roughness. However, insignificant effect or unclear trend between surface roughness and two-phase pressure drop were stated by other researchers, such as Alam et al. (2013) and Pike-Wilson and Karayiannis (2014).
4. Although several two-phase pressure drop correlations were developed and proposed, the accuracy of these correlations varied from study to another. Different fluid properties, channel geometries, surface finish and operating conditions were tested and thus different empirical correlations were proposed.

Flow boiling heat transfer

1. Two main heat transfer mechanisms were reported in conventional channels, namely nucleate and convective boiling. This terminology was also adopted in mini and microchannels. Thin film evaporation was another mechanism that could dominate in microchannels. The dominance of each mechanism depended on the features of flow patterns, which could be affected by fluid properties, channel geometries, operating conditions and channel surface material and structures.
2. The effect of channel aspect ratio on the heat transfer coefficient differed from one study to another. For example, some studies showed that the heat transfer coefficient increased with increasing aspect ratio. On the contrary, other studies indicated that the heat transfer coefficient decreased with aspect ratio, or there was no a clear trend. In some studies, the channel hydraulic diameters with different aspect ratios were not the same. Furthermore, the average surface roughness of the tested channels differed from one channel to another, or in some channels the average surface roughness was not provided. Therefore, different heat transfer trends were found, and thus it is difficult to propose a final conclusion on the aspect ratio effect.
3. In most studies, the heat transfer coefficient was found to increase with increasing channel surface roughness. This was attributed to the higher number

of nucleation sites generated with rougher surfaces. In contrast, the influence of surface roughness was complex and not easy to assess as reported by Pike-Wilson and Karayiannis (2014).

4. Surface characteristics (microstructures) may affect the thermal performance by defining the size (mouth radius and depth) and number of cavities. Surfaces with more active cavities are expected to show better heat transfer coefficient.
5. Different surface microstructures were reported by researchers. These differences may be due to the fact that different surface materials, machining conditions and manufacturing processes were used. Moreover, the type, condition and size of the cutting tool and machining vibration may also affect the surface microstructures.
6. Higher thermal conductivity did not always show better thermal performance as shown in some studies.
7. Four methods (the superposition, the enhancement, the asymptotic and the dimensionless groups) were adopted to propose two-phase heat transfer correlations in the literature. These correlations were developed for conventional and mini/microchannels using different fluid properties, channel geometries and operating conditions. Different tested parameters may lead to different heat transfer data and mechanisms. This may explain the discrepancy in the accuracy of these correlations. Accordingly, a comprehensive correlation for predicting two-phase heat transfer coefficient is still required.
8. Five forces can be identified during flow boiling heat transfer in channels. These forces are inertia, surface tension, shear, buoyancy and evaporation momentum forces. The magnitude of these forces may be influenced by several parameters. The surface tension and shear forces were found to increase while gravity (buoyancy) force decreases with decreasing channel diameter. In mini/microchannels, inertia force dominates at high mass fluxes, while surface tension becomes the dominant force at low mass fluxes. This difference in the dominant forces may result in different heat transfer mechanisms and thus different heat transfer correlations.

Flow boiling instability

1. Flow boiling instabilities and flow reversal may cause system failure. Large amplitude of oscillations in temperature, pressure and mass flow rate was

reported. Flow instabilities may be caused by rapid bubble growth, surface characteristics, high inlet compressibility, conjugate effect and the size of the outlet plenum and the exit tubing.

2. Several modifications were proposed to reduce this problem, such as inlet pressure restrictor, diverging channel, expanding channel, cross-connected microchannels, cross-sectional expansion microchannels, straight micro-gap, expanding micro-gap and large manifolds.

B. Flow condensation characteristics

Condensation flow patterns and maps

1. The names and features of condensation flow patterns differ from one study to another. This could be due to the fact that different fluids, channel geometries and operating conditions were examined.
2. The location of the injection flow (formation of bubbly flow) moved towards the downstream side as the mass flux and vapour quality increased.
3. Annular flow expanded and spanned along the channel when the mass flux and vapour quality increased or cooling heat rate decreased.
4. Different flow maps were proposed for different flow regimes. However, the annular flow was found to be the dominant regime during flow condensation.

Flow condensation pressure drop

1. All experimental investigations agreed on the two-phase pressure drop increased with increasing mass flux and vapour quality due to the high mixture velocity.
2. When the saturation temperature decreased, the condensation pressure drop was found to increase. This was attributed to the high vapour superficial velocity (low vapour density) and thus high interfacial shear stress.

Flow condensation heat transfer

1. Some researchers stated that the heat transfer coefficient increased with increasing mass flux and vapour quality. In contrast, the heat transfer coefficient was independent of mass flux and quality in other studies. In large channels,

gravity and shear forces are more dominant, while in mini/microchannels, surface tension and shear forces can become important.

2. All studies showed that the heat transfer coefficient increased with decreasing saturation temperature. This was attributed to the thinning liquid film due to the difference in the density ratio.
3. At low mass fluxes, it was expected that the heat transfer coefficient in rectangular channels was higher than that in circular channels due to the surface tension effect. In contrast, a small effect of channel geometry was found at high mass fluxes.
4. Coolant side conditions seem to have an insignificant effect on the condensation heat transfer coefficient.
5. Several condensation heat transfer correlations were proposed. However, these correlations predicted the experimental data reported in the literature with different accuracy.

Chapter 3

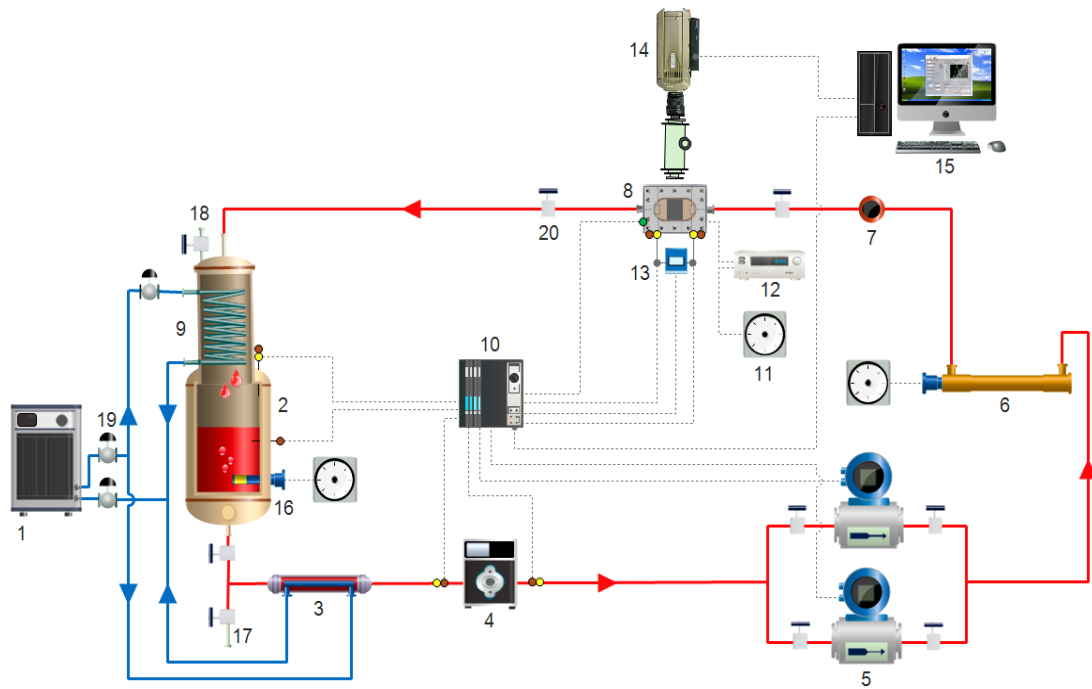
Experimental Facility and Methodology

3.1 Introduction

In this chapter, details of the experimental facility and methodology are described as follows: Section 3.2 presents a description of the main components of the HFE-7100 flow loop and an auxiliary cooling loop, while the detail construction of all test sections are provided in Section 3.3. The calibration process of thermocouples and pressure transducers is described in Section 3.4. All the single and two-phase flow data reduction is presented in Section 3.5, while the propagated uncertainty analysis is set out in Section 3.6. Section 3.7 presents the experimental procedure including single-phase, flow boiling and flow condensation experiments. The experimental operating conditions are presented in Section 3.8, while the overall validation is discussed in Section 3.9. The repeatability of the data is discussed in Section 3.10. Finally, a summary is presented in Section 3.11.

3.2 Experimental Facility

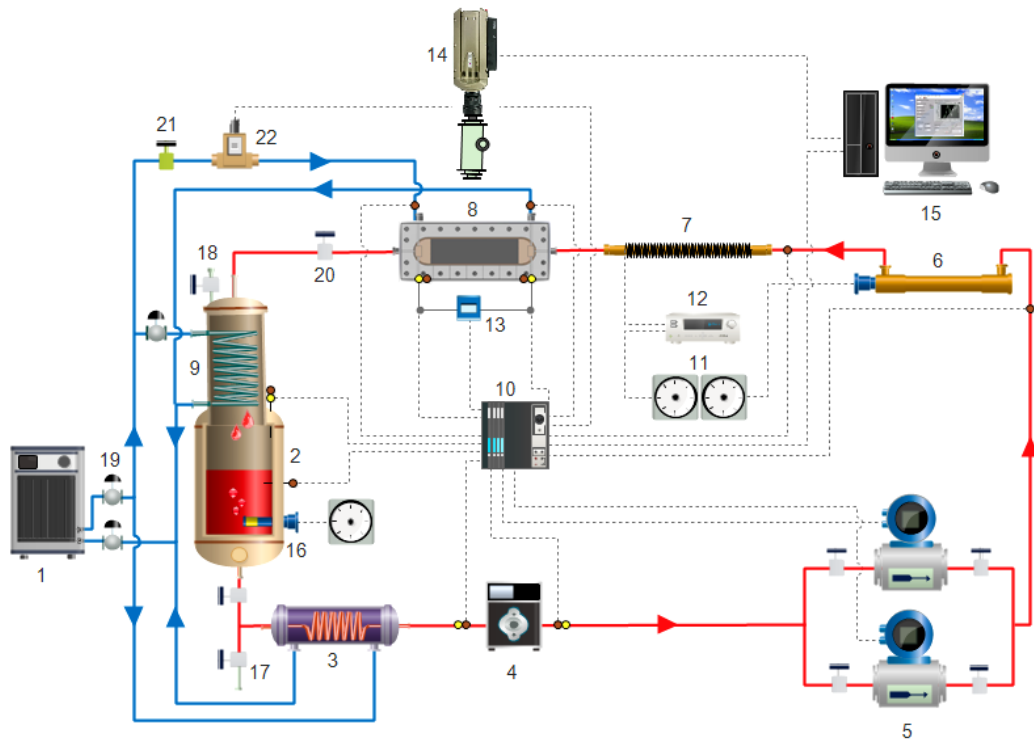
Research in this area started under the Engineering and Physical Sciences Research Council Grant (EPSRC) led by my current supervisor. Dr. M.M. Mahmoud was the Postdoc. Research Fellow working on the project, see for example Mahmoud and Karayiannis (2016b). The experimental rig is located at Brunel University London in room 304, tower (A) building. This rig was used to conduct single-phase, flow boiling and flow condensation experiments during the present study. Fig. 3.1 shows a schematic diagram of the test rig, for flow boiling experiments, which consists of two main closed loops, namely an auxiliary cooling loop and the test loop.



- | | | | |
|----|---|----|---|
| 1 | Recirculating Chiller System | 11 | Variac |
| 2 | Main Reservoir | 12 | Power Meter |
| 3 | Sub-cooler | 13 | Differential Pressure Transducer |
| 4 | Micro-Gear Pump | 14 | Phantom High-Speed Camera
integrated with a microscope |
| 5 | Coriolis Flow Meter | 15 | Computer |
| 6 | Electric Pre-heater | 16 | Immersion Heater |
| 7 | Sight Glass | 17 | Drain Valve |
| 8 | Test Section / Microchannel
Evaporator | 18 | Vent Valve |
| 9 | Reflux Condenser | 19 | Ball Valve |
| 10 | Data Acquisition System | 20 | Needle Valve |
| ● | Pressure Transducer | | |
| ● | Fluid/Wall Thermocouple | | |

Figure 3.1 Schematic diagram of the experimental facility for flow boiling experiments.

This rig was then modified by the present author to conduct the flow condensation experiments as shown in Fig. 3.2. The current rig was built using stainless steel pipes, ¼" (6.35 mm) in size, as shown in Fig. 3.3. This construction achieved a high corrosion resistance, minimized the space taken up by the rig, decreased the flow losses, and minimized the time taken to reach system stability.



- | | | | |
|----|--|----|---|
| 1 | Recirculating Chiller System | 13 | Differential Pressure Transducer |
| 2 | Main Reservoir | 14 | Phantom High-Speed Camera
integrated with microscope |
| 3 | Sub-cooler | 15 | Computer |
| 4 | Micro-Gear Pump | 16 | Immersion Heater |
| 5 | Coriolis Flow Meter | 17 | Drain Valve |
| 6 | Electric Pre-heater | 18 | Vent Valve |
| 7 | Tubular Evaporator | 19 | Ball Valve |
| 8 | Test Section / Microchannel
Condenser | 20 | Needle Valve |
| 9 | Reflux Condenser | 21 | Regulator Valve |
| 10 | Data Acquisition System | 22 | Coolant Flow Meter |
| 11 | Variac | | |
| 12 | Power Meter | | |

Figure 3.2 Schematic diagram of the experimental facility for flow condensation experiments.

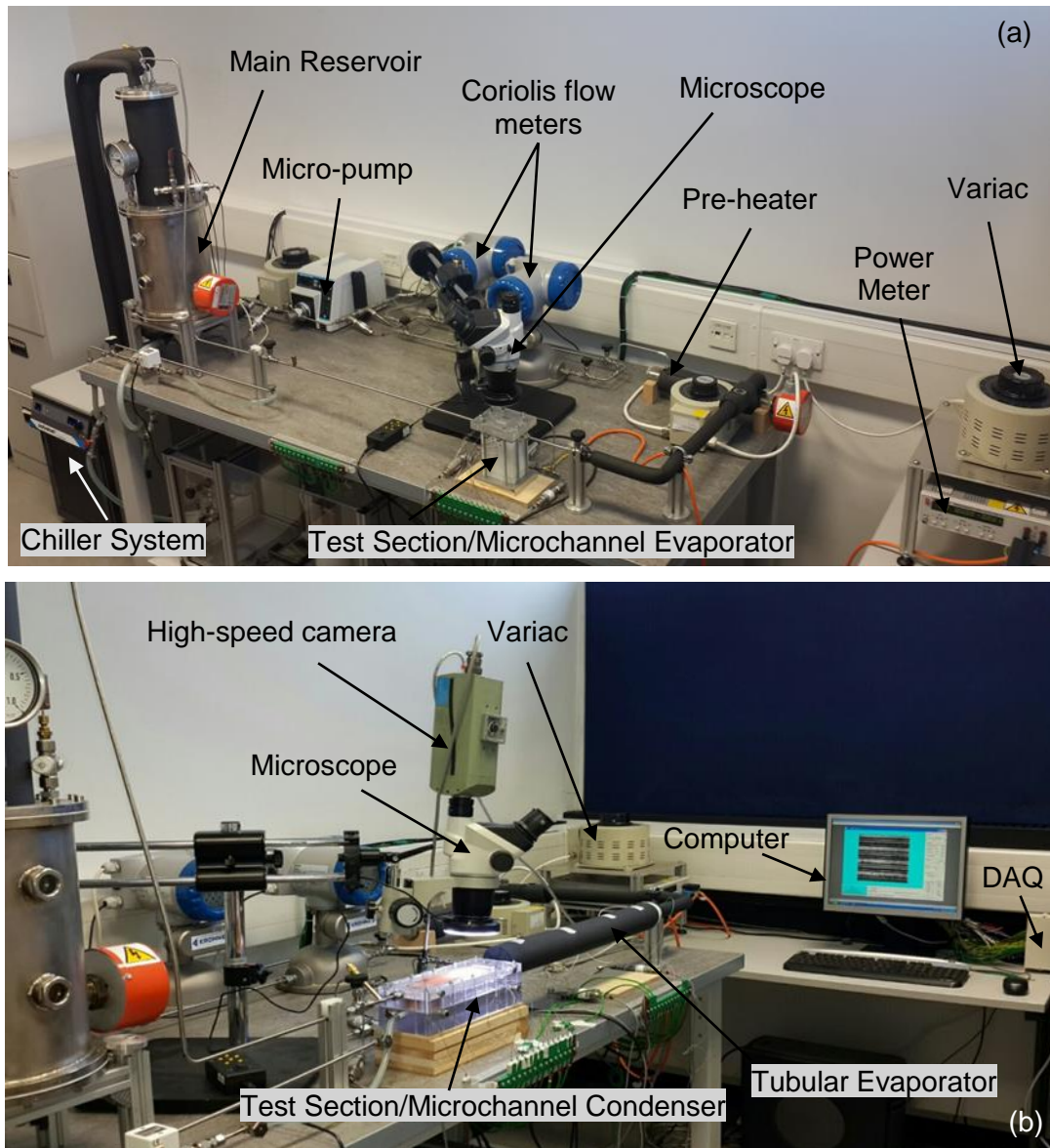


Figure 3.3 Photograph of the test rig: (a) Flow boiling experiments (b) Flow condensation experiments.

3.2.1 The auxiliary cooling loop

A refrigerated recirculating chiller system was connected to the rig to reject the heat from the reservoir, the sub-cooler and the microchannel condenser during the experiments. A re-circulating chiller system (Cole-Parmer Polystat chiller, 6160T21C130D) with a cooling capacity of 2900 W was used. This system supplied water-glycol solution with temperatures ranging from -10 to 40 °C using a vapour compression refrigeration cycle with R134a refrigerant, as shown in Fig. 3.4.

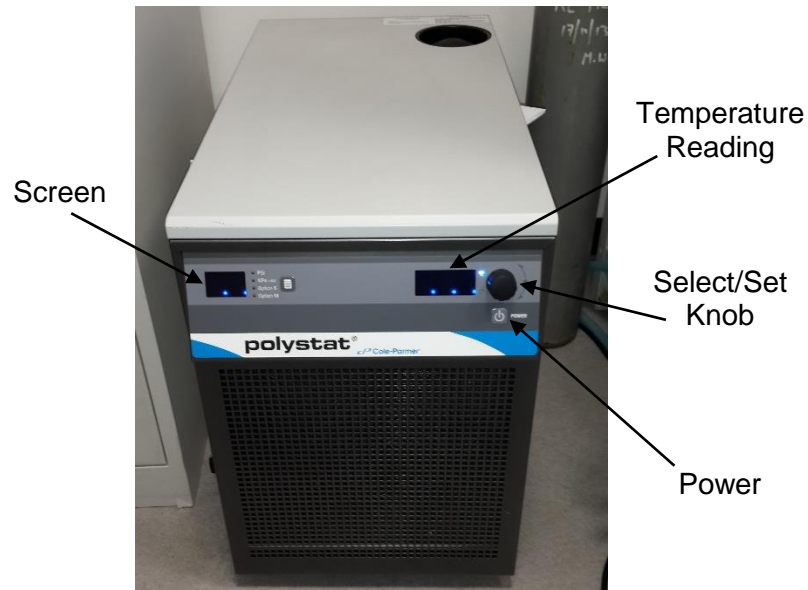


Figure 3.4 Photograph of the chiller system.

The outlet fluid temperature from this chiller can be controlled at a specific value using the select/set knob as shown in this figure.

3.2.2 Main reservoir

A stainless steel cylindrical vessel was used as the main reservoir with a total volume of 9 liters as shown in Fig. 3.5. An electric immersion heater of 1500 W was inserted in the tank to control the fluid saturation temperature and hence the system pressure during the experiments. This heater was controlled by a Variac model CMV15E-1. A safety valve was fitted to protect the reservoir from excessive pressure. Moreover, two sight glasses were mounted in this reservoir for monitoring the liquid level. One pressure gauge and pressure transducer were located in the tank to measure the vapour pressure. Two T-type thermocouples were inserted into the reservoir to detect the liquid and vapour temperature during the experiments. A vent valve was located above the reservoir and used to release any trapped gasses from the system during the degassing process. It was also used to fill the tank with the working fluid. A cooling coil condenser was mounted on the top side of the reservoir. This part was used to (i) control the fluid temperature and (ii) condense the outlet vapour from the test section. This reflux condenser was cooled by the water-glycol solution supplied from the chiller unit.

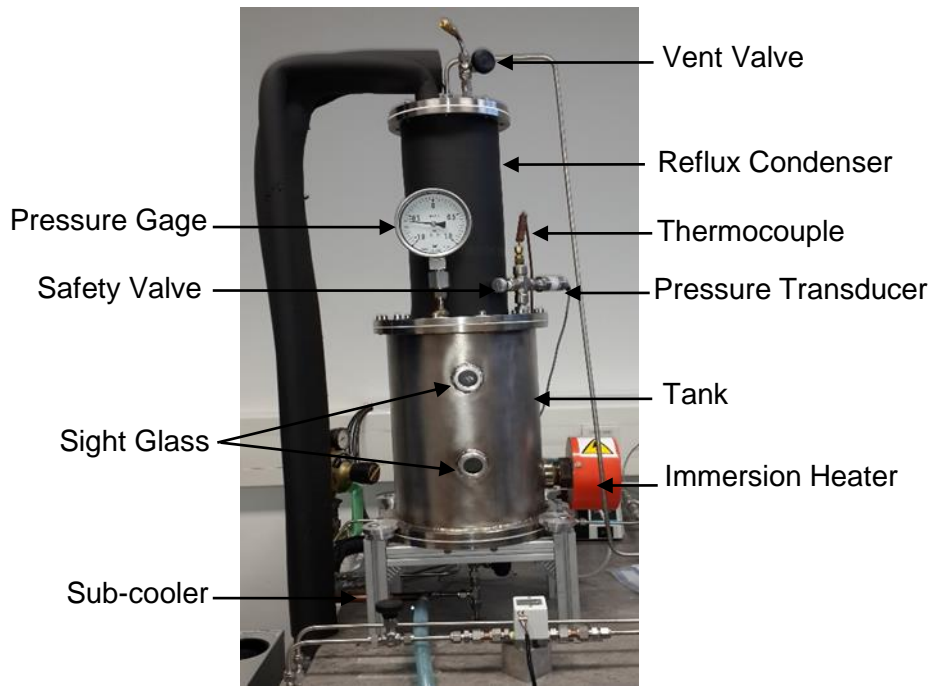


Figure 3.5 Photograph of the liquid reservoir and the reflux condenser.

3.2.3 Sub-cooler

A tube-in-tube heat exchanger was located after the main reservoir to cool the working fluid before entering the micro-gear pump, see Fig. 3.6. It is worth mentioning that the fluid temperature at the pump suction should be kept well under the saturation temperature, corresponding to the inlet pump pressure, to avoid pump cavitation. Water-glycol solution, supplied from the chiller unit, was used to reject the heat from this heat exchanger.

Tube-in-Tube Heat Exchanger

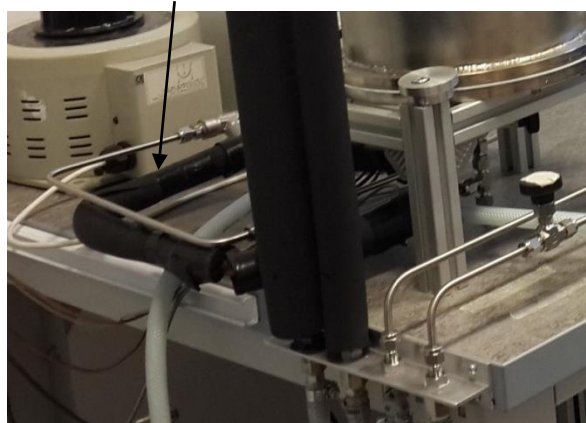


Figure 3.6 Photograph of the Sub-cooler.

3.2.4 Micro-gear pump

A micro-gear pump (Cole-Parmer, model TW-74014-25) was used to control and drive the working fluid around the test rig as shown in Fig. 3.7. This pump consisted of a magnetic gear pump head fitted with a digital speed driver. This digital speed driver was used to control a specific flow rate during the experiments. The maximum differential pressure was 5.17 bar and the working temperature range was from -46 to 121 °C. This pump provided a flow rate up to 2304 ml/minute, 0.64 ml/rev, at a motor rotation speed ranging from 60 to 3600 rpm.

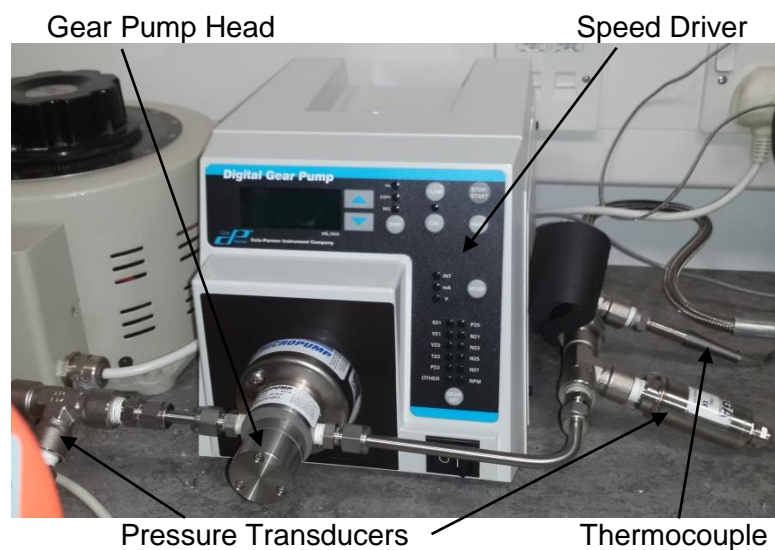


Figure 3.7 Photograph of Cole-Parmer gear pump.

3.2.5 Coriolis and turbine flow meters

Two Coriolis flow meters (model KROHNE Optimass 3300C S01), one for low mass flow rate up to 5 kg/hr and another one for high rate ranging from 5 to 130 kg/hr, were installed in the rig as shown in Fig. 3.8(a). These flow meters were used to measure the fluid flow rate at different ranges with an accuracy of $\pm 0.1\%$. The supply voltage of the model MFC 300C signal converter was 100–230 Vac, and the output signal was 4–20 mA. Therefore, an SCXI-1308 current-input terminal block with a built-in 249 Ω resistor was used to convert this signal to the voltage ranging from 1 to 5 V. An Omega turbine flow meter (model FLR1000 ST-I) with range of 0.3–5 L/min and an accuracy of $\pm 1\%$ was used to measure the coolant flow rate before entering the condenser, see Fig. 3.8(b).

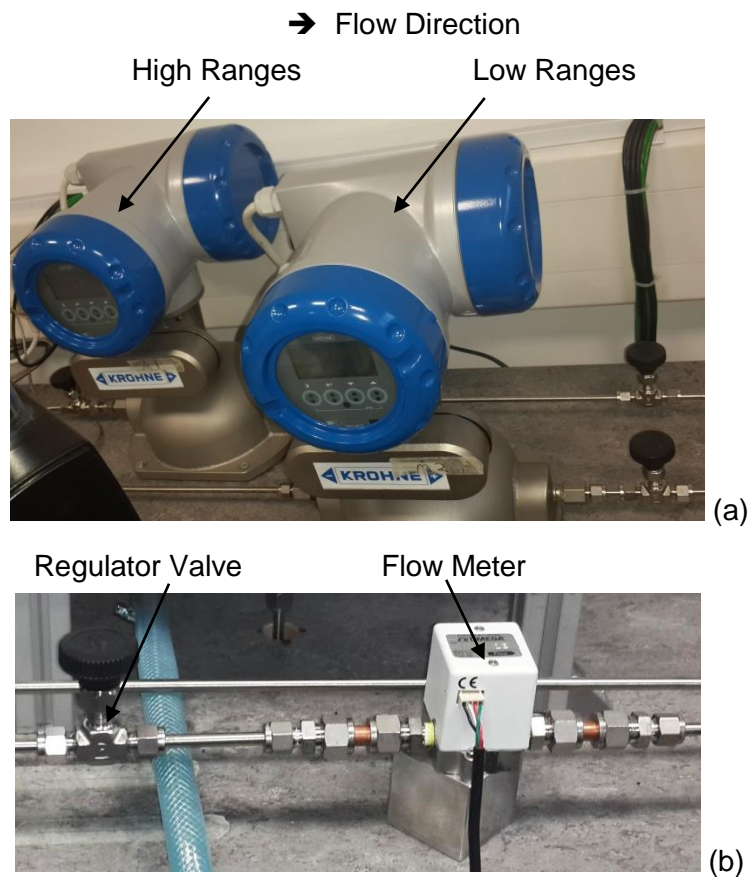


Figure 3.8 Photograph of (a) Coriolis flow meters, model KROHNE Optimass 3300C S01 (b) Omega turbine flow meter, model FLR1000 ST-I.

3.2.6 Electric pre-heater

A screw plug immersion heater, model FIREBAR-BDNF7R10S, with a heating capacity of 1500 W inserted into a stainless-steel block was used as a pre-heater, see Fig. 3.9. This pre-heater was located after the Coriolis flow meters and controlled by a Variac model CMV5E-1. The pre-heater was used to adjust the sub-cooling, *i.e.* inlet fluid temperature, during flow boiling experiments. For flow condensation experiments, this pre-heater and a tubular evaporator were used to create slightly superheated vapour at the inlet of the condenser. A stainless steel tubular evaporator wrapped by a rope heater of 500 W was located after the pre-heater. A Variac model CMV15E-1 was used to control the power of the evaporator and thus the exit vapour condition. Both the pre-heater and evaporator, *i.e.* 6 and 7 reported in Fig. 3.2, were perfectly insulated using thermal insulation strips.

→ Flow Direction



Figure 3.9 Photograph of the pre-heater.

Two thermocouples were located in the pre-heater and evaporator to measure the fluid temperature.

3.2.7 Pressure transducers

Stainless steel body, absolute pressure transducers (Omega, model PX209-100A5V) were fitted in the current rig to measure the inlet and outlet fluid pressure at the test section, see Fig. 3.10(a). Furthermore, two other transducers were mounted before and after the micro-gear pump. One transducer was located at the main reservoir to measure the vapour pressure. These transducers required an excitation voltage of 7 to 35 Vdc for an output voltage of 0 to 5 Vdc, corresponding to the ranges of 0–6.9 bar. Moreover, one Omega (model PX409-005DWUI) differential pressure transducer was inserted at the test section, covering a range from 0 to 0.35 bar with an accuracy of $\pm 0.08\%$, as shown in Fig. 3.10(b). This differential pressure transducer was used to measure the total pressure drop between the inlet and outlet plena.

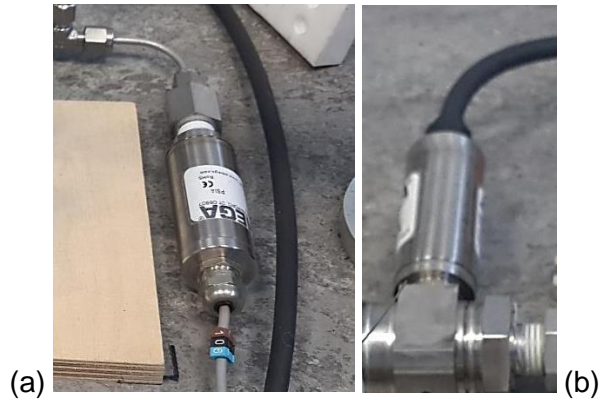


Figure 3.10 Photograph of (a) Pressure transducer (Omega PX209-100A5V) (b) Differential pressure transducer (Omega PX409-005DWUI).

3.2.8 Thermocouples

In this study, two types of thermocouple were used and fitted in different locations, namely K and T-type, see Fig. 3.11. For K-type, the diameter and length of all probes were 0.5 mm and 150 mm, respectively. This type of thermocouple has the ability to measure temperatures ranging from -200 to 1250 °C. They were used to measure the wall temperatures during the experiments. T-type thermocouples, with the probe diameter of 1 mm, were used to measure the fluid temperatures. The measuring ranges for T-type were -200 to 350 °C. Two thermocouples were located after and before the micro-gear pump, and two others were inserted into the main reservoir. A set of thermocouples were located inside the test sections (see Section 3.3), the pre-heater and the tubular evaporator.



Figure 3.11 Photograph of a thermocouple: (a) T-type (source: www.omega.co.uk) (b) K-type (source: www.labfacility.com).

3.2.9 Power meter

A Hameg HM8115-2 power meter was used to measure the power supply with an accuracy of $\pm 0.4\%$, see Fig. 3.12. This meter can measure the voltage and current ranging from 0.1 to 500 V and from 0.001 to 16 A, respectively.



Figure 3.12 Photograph of power meter.

3.2.10 Variable autotransformers

Three variable autotransformers (Variac) were used to control the input power to the cartridge heaters inside the test section (evaporator), the liquid reservoir, the pre-heater and the tubular evaporator (during flow condensation experiments). This allowed control of the supplied heat flux to the test section, system pressure, the test section inlet sub-cooling and inlet vapour quality. Two models were connected to the rig, namely CMV5E-1 and CMV15E-1, manufactured by Carroll & Meynell. The power rating of the first model was 1.2 kVA/5A and was connected to the pre-heater (see Fig. 3.9). Two more variacs (model 3.6 kVA/15A) were connected the cartridge heaters, the liquid reservoir and the tubular evaporator.

3.2.11 Visualization system

This system was used to capture and record all images and videos of the two-phase flow patterns inside the test sections. A Phantom (V6.0) digital high-speed camera fitted on a movable stand was used. This camera had an image resolution of 512×512 pixels with a speed of 1000 frames per second. The Phantom Camera Control software (PCC) was installed on a computer to save and analyze all the images and videos. This camera was mounted on a microscope (Huvitz HSZ-645TR) and adjustable LED lighting system to enhance the clarity of flow visualization. Fig. 3.13

illustrates this system. In the present study, flow visualization was recorded for each run at the test section centre and three different locations; near the channel inlet, near the middle and near the channel outlet. Flow visualization was sometimes carried out at other different locations, *i.e.* between the channel inlet and middle or between the channel middle and outlet, to capture any possible flow features along the channel.

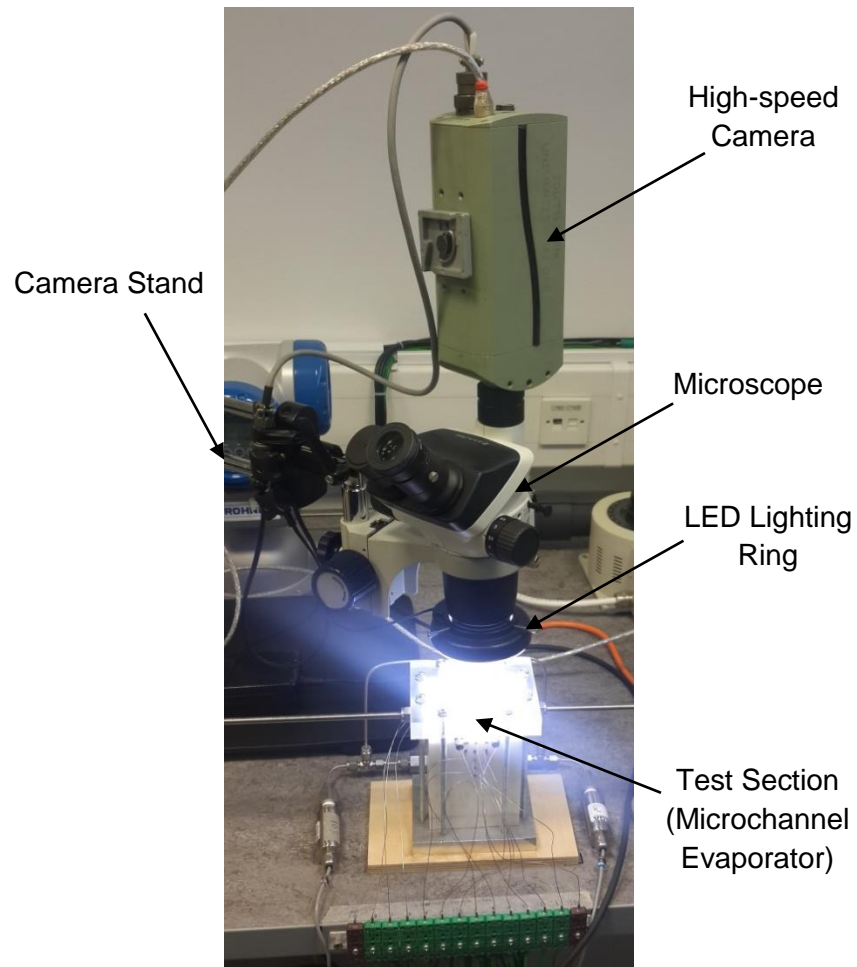


Figure 3.13 Photograph of visualization system.

3.2.12 Data acquisition system (DAQ)

A National Instruments (DAQ) system was used for processing, measuring, and recording all the signals from the measuring instruments as shown in Fig. 3.14. Two terminal blocks, namely SCXI-1303 and SCXI-1308 were connected to the two modules; SCXI-1100 and SCXI-1102B, respectively. Then all the measuring sensors were connected to these two terminal blocks. SCXI-1303 was suitable for high accuracy thermocouples, while SCXI-1308 was a current-input terminal block that

included a resistor of $249\ \Omega$ for each input, so it was suitable to read the input current from 4 to 20 mA. All these components were located in SCXI-1000 chassis, which was connected to a DAQ board inside a computer via a SHC68-68-EPM shielded cable. The logging frequency of this system was 1 kHz that means one thousand data was recorded per second. After the system reached steady state, *i.e.* small variations in pressure, temperature and mass flux, the data were saved for 2 minutes (using LabView software) and then averaged for further calculations in the data reduction process.

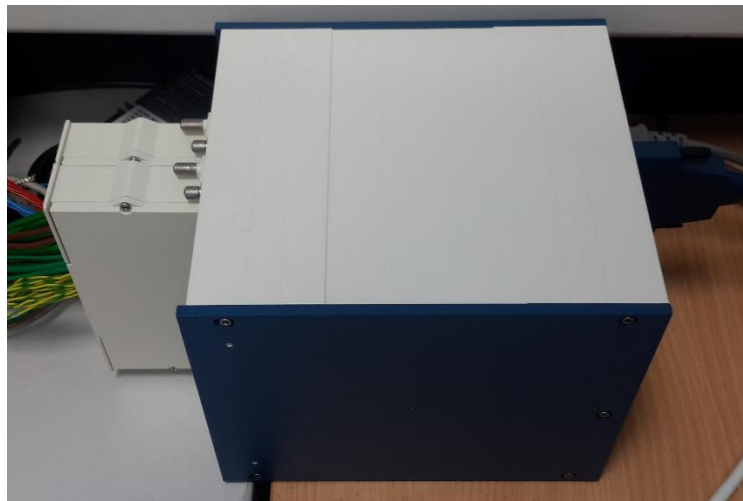


Figure 3.14 Photograph of DAQ system.

3.2.13 Software

In the present study, LabView software version 15 was used to record all the signals from the measuring instruments, such as temperatures, pressures and mass flow rates during the experiments. Moreover, this software was provided by a dual channel frequency analysis for observing the signal fluctuation. Two input signals were used in this channel; pressure or temperature and time, then the output results were presented in frequency (Hz) and related amplitude. All the necessary equations were inserted in this software to check the output parameters during the experiments. Engineering Equation Solver (EES) (www.fchart.com) was used for computing all the calculations and obtaining the thermophysical properties of HFE-7100. It was also suitable for drawing all graphs. The Phantom Camera Control software (PCC) (www.phantomhighspeed.com) was adopted in order to analyze the flow patterns

during the experiments, *i.e.* the features and shapes of flow patterns, bubble size and velocity and slug length. This software was also used to convert the experimental videos to the sequence of pictures.

3.3 Microchannel Test Sections

In this study, five multi-microchannel test sections were used to conduct two-phase flow experiments. Four microchannel evaporators and one microchannel condenser were designed and manufactured. The original design of these test sections was adopted by taking into account the suggestions by Dr. M.M Mahmoud (PDRA that worked on the EPSRC funded project). As mentioned above, this study aims to design test sections that are suitable for cooling electronic components. Therefore, the following criteria were considered for designing the test sections in this study by the present author:

1. The microchannels and the inlet and outlet plena (with semi-circular shape) were fabricated as one part, *i.e.* a real microchannel heat sink. This design is acceptable for commercial applications since all parts, *i.e.* the heat sink and the cover plate, can easily be assembled and attached to any chipset. This design also prevents any leakage that could happen during the experiments by inserting an O-ring seal around the heat sink.
2. The base area of the heat sink had a width and length of 20 and 25 mm, respectively. This base area of 500 mm^2 was chosen based on the chipset die size. It is known that the value of die size differs according to the chipset performance. For example, the die size of Intel Sandy Bridge 4C processor is 216 mm^2 , while it is 503 mm^2 for Intel Xeon E7440 (source: www.intel.com).
3. Very thin bottom thickness of the inlet and outlet plena was fabricated, *i.e.* just 1.8 mm, to ensure minimum heat loss in these parts.
4. Both the inlet and outlet plena were manufactured in the cover plate. These two parts were designed as a semi-circular shape with volume of 1.8 cm^3 . Mahmoud and Karayiannis (2016b) reported that the volume and shape of the inlet/outlet plenum affected the flow instability. They tested two different shapes and sizes of the inlet/outlet plenum. Semi-circular shape with size of 0.8 cm^3 and rectangular shape with 0.48 cm^3 volume were examined. They

found that the semi-circular plenum resulted in better flow instability, *i.e.* lower amplitude of the pressure drop and inlet/outlet pressure signals.

5. According to the ITRS (2011) (International Technology Roadmap of Semiconductors), the power dissipation from a chip will exceed 500 W by 2023. Therefore, maximum base heat flux of 1 MW/m^2 was assumed, which corresponds to the total heat rate of 500 W.
6. In the present study, three criteria were taken into consideration, *i.e.* surface roughness, hydraulic diameter and base area, in order to study the effect of channel aspect ratio. All these parameters should be kept constant for all tested heat sinks. The surface roughness was kept to similar values using the same machining conditions, *i.e.* cutting feed rate and rotation speed, as discussed in Sections 3.3.1 and 3.3.3. The spindle of the machine was set at a cutting feed rate and rotation speed of 550 mm/min and 20,000 rpm, respectively. The average surface roughness for three tested heat sinks was nearly constant ($\approx 0.3 \text{ }\mu\text{m}$), while the hydraulic diameter and the base area were designed at 0.46 mm and $20 \text{ mm} \times 25 \text{ mm}$, respectively.
7. A simple thermal simulation was conducted to find the necessary height of the heat sink block that can provide uniform wall temperature distribution near the microchannel bottom. This simulation showed that a height of 92 mm can achieve this. More details about this simulation are given in Section 3.9.1.

3.3.1 Microchannel evaporator

The test section consisted of four main parts, namely cover plate, housing, bottom plate and the heat sink block as shown in Fig. 3.15. A transparent polycarbonate sheet was used to fabricate the cover plate to allow flow visualization. This plate was clamped on the topside of the housing and the inlet and outlet plena (semi-circular shape) were formed in this part. Six tapping holes were drilled into this plate to connect the inlet and outlet flow tube, T-type thermocouples for inlet and outlet fluid temperature and the inlet, outlet and differential pressure transducers. An O-ring seal was inserted in a slot between the cover plate and the microchannel heat sink to prevent any possible fluid leakage. The housing and bottom plate were made of Polytetrafluoroethylene block, PTFE, to ensure a good insulation of the test section.

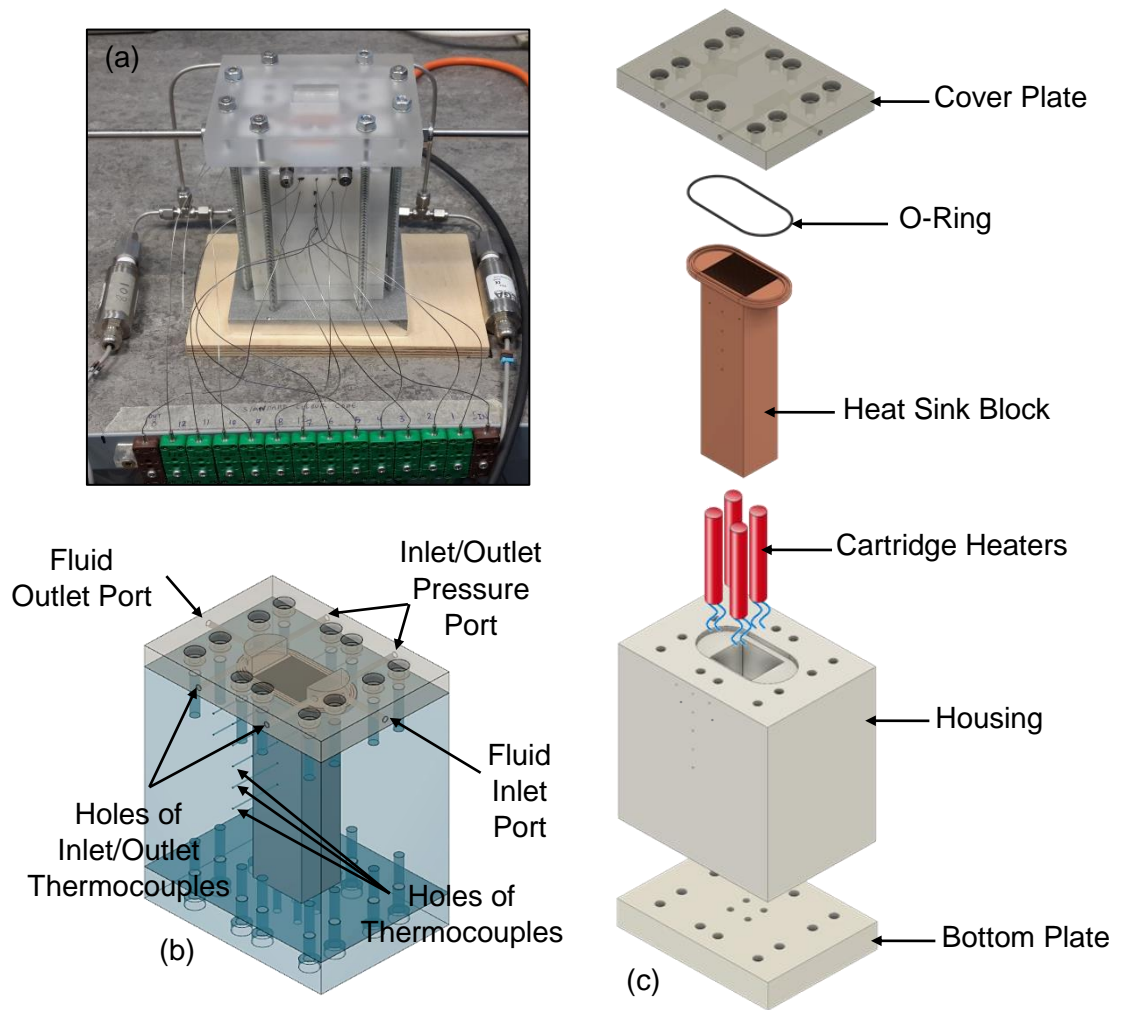


Figure 3.15 Test section construction, microchannel evaporator: (a) Photograph (b) Overall assembly (c) Exploded drawing.

Twelve holes of 0.6 mm diameter were drilled into the housing. These holes were used to pass the thermocouple wires through this part. The overall dimensions of the heat sink block were 26 mm width, 51 mm length and 94.5 mm height, see Fig. 3.16(a). Table 3.1 shows the dimensions of each heat sink, while all the engineering drawings are presented in Appendix D. This block consisted of two main parts as shown in Fig. 3.16(b). These parts included the heat sink, which consisted of the inlet/outlet plenum and the microchannels, and the heating part. The inlet and outlet plena with semi-circular shape were formed into the heat sink part. Two different metals were used for manufacturing the heat sink block, namely oxygen-free copper and aluminium as shown in Fig. 3.16(c).

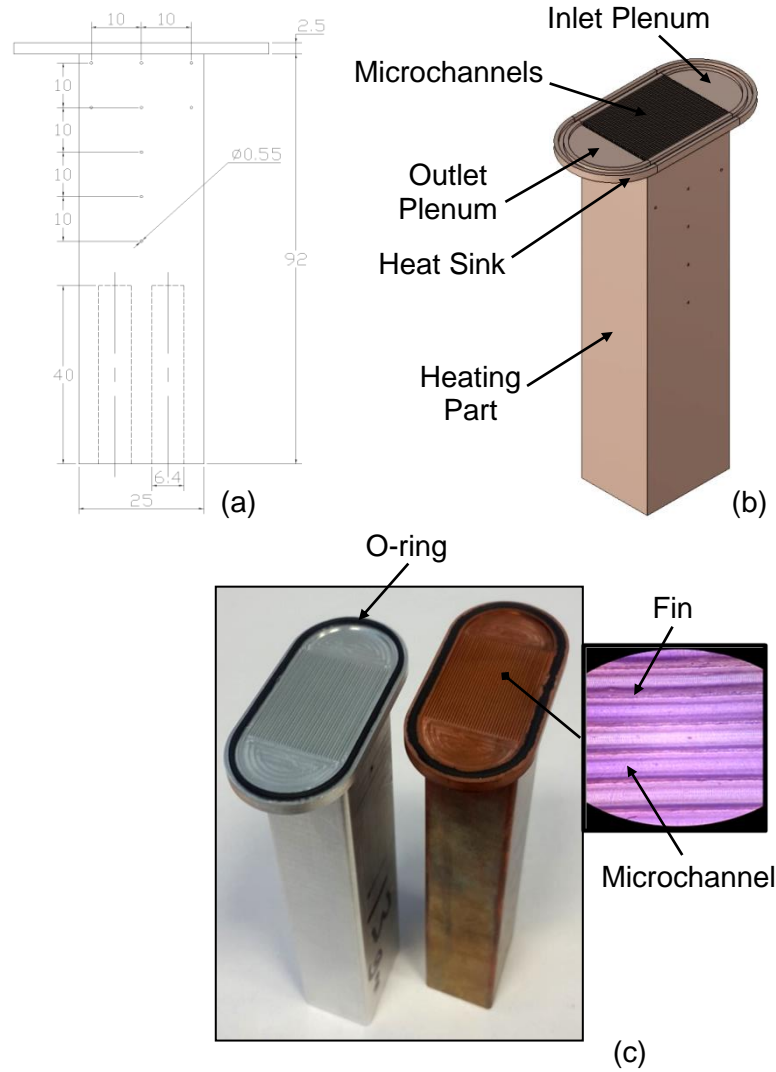


Figure 3.16 Heat sink block: (a) Dimensions in mm (b) Block parts
(c) Photograph of TS.2 (copper) and TS.4 (aluminium).

Table 3.1 Details of the microchannel evaporator.

Test Section	H_{ch} [mm]	W_{ch} [mm]	W_{fin} [mm]	L_{ch} [mm]	D_h [mm]	β [-]	A_{ht} [m ²]	N [-]	Metal
TS.1	0.7	0.35	0.15	25	0.46	0.5	0.00175	40	Copper
TS.2	0.46	0.46	0.1	25	0.46	1	0.00123	36	Copper
TS.3	0.35	0.7	0.1	25	0.46	2	0.000875	25	Copper
TS.4	0.46	0.46	0.1	25	0.46	1	0.00123	36	Aluminium

The microchannels were fabricated at the top surface of the heat sink, as shown in Fig. 3.16(b-c), using a high precision micro-milling machine, model Kern HSPC-2216. The machining process for these microchannels was conducted at a rotation speed of 20,000 rpm and cutting feed rate of 550 mm/min. Four vertical holes were drilled into the bottom side of this block, with an inner diameter of 6.4 mm and length of 40 mm, to insert the cartridge heaters. Four cartridge heaters with total heating power of 700 W were used as a heat source. Moreover, nine horizontal holes of 0.55 mm diameter and 8 mm length were drilled into the heat sink block for inserting thermocouples as shown in Fig. 3.16(a). Three additional holes, with diameter and length of 0.55 mm and 3 mm, respectively were drilled at the opposite side of the block. This is discussed in detail in Appendix D. A set of twelve K-type thermocouples were inserted into the heat sink block to measure the temperature distribution along the channel and in the vertical direction. These thermocouples were distributed as follows, see Fig. 3.16(a): (i) six thermocouples were inserted underneath the channels in the axial direction in two opposite rows with three thermocouples per row. The first row represented the mid plane of the heat sink, while the second row represented the side plane. This could help estimate the uniformity of the heat flux. (ii) Another horizontal row of three thermocouples was inserted below the top row at 10 mm vertical distance to assess if there was no axial heat conduction, *i.e.* our case is 1D heat conduction. (iii) Three additional thermocouples were inserted vertically (normal to the flow direction) in this block for the heat flux estimation. It is worth mentioning that five vertical thermocouples in total were used to estimate the heat flux (two from the top rows and three additional). The total pressure drop was measured directly across the heat sink (from inlet to outlet plenum) using one differential pressure transducer. Moreover, the inlet and outlet pressure at the test section were measured using two pressure transducers. Fig. 3.17 depicts a schematic diagram of the locations of the measuring instruments that were connected to the test section.

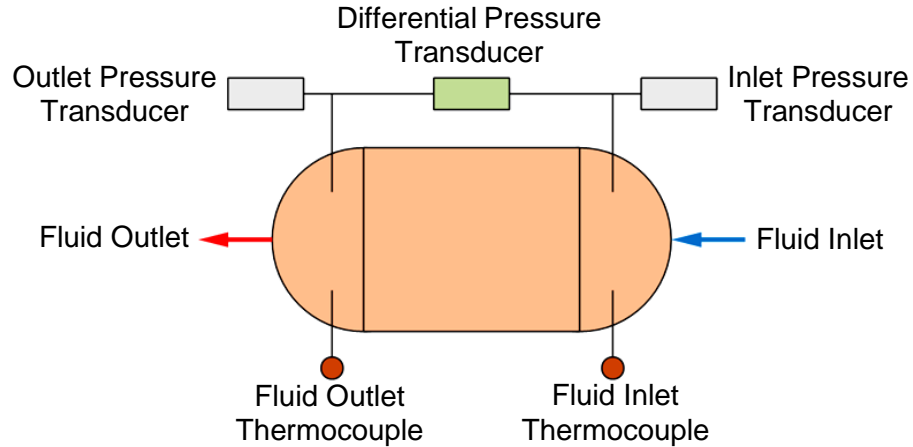


Figure 3.17 Schematic diagram of the measuring instruments (top view).

3.3.2 Microchannel condenser

Fig. 3.18 shows the test section construction of the microchannel condenser. This condenser consisted of three parts, namely cover plate, housing and condenser block. Both the cover plate and housing were made of polycarbonate to minimize the heat loss during the experiments. The cover plate was made of a transparent sheet to allow flow visualization. The inlet and outlet plena with a semi-circular shape were formed in this part, and six tapping holes were drilled into the cover plate to connect the inlet/outlet thermocouple, inlet/outlet pressure transducer and fluid inlet/outlet pipe. An O-ring seal was inserted in a slot between the cover plate and the condenser block to prevent any leakage. This plate clamped on the housing and fitted with a set of screws. Twelve holes of 0.6 mm diameter were drilled into the housing. The purpose of these holes was to pass thermocouple wires through the housing. Four T-type thermocouples were used for measuring the inlet and outlet temperatures of the refrigerant and coolant (water). Two pressure transducers and one differential pressure transducer were connected to the test section at the refrigerant side to measure the inlet/outlet pressure and the total pressure drop along the condenser. The condenser block was made of oxygen-free copper using a high precision micro-milling machine (Kern HSPC-2216) with a rotation speed of 12,000 rpm and cutting feed rate of 300 mm/min.

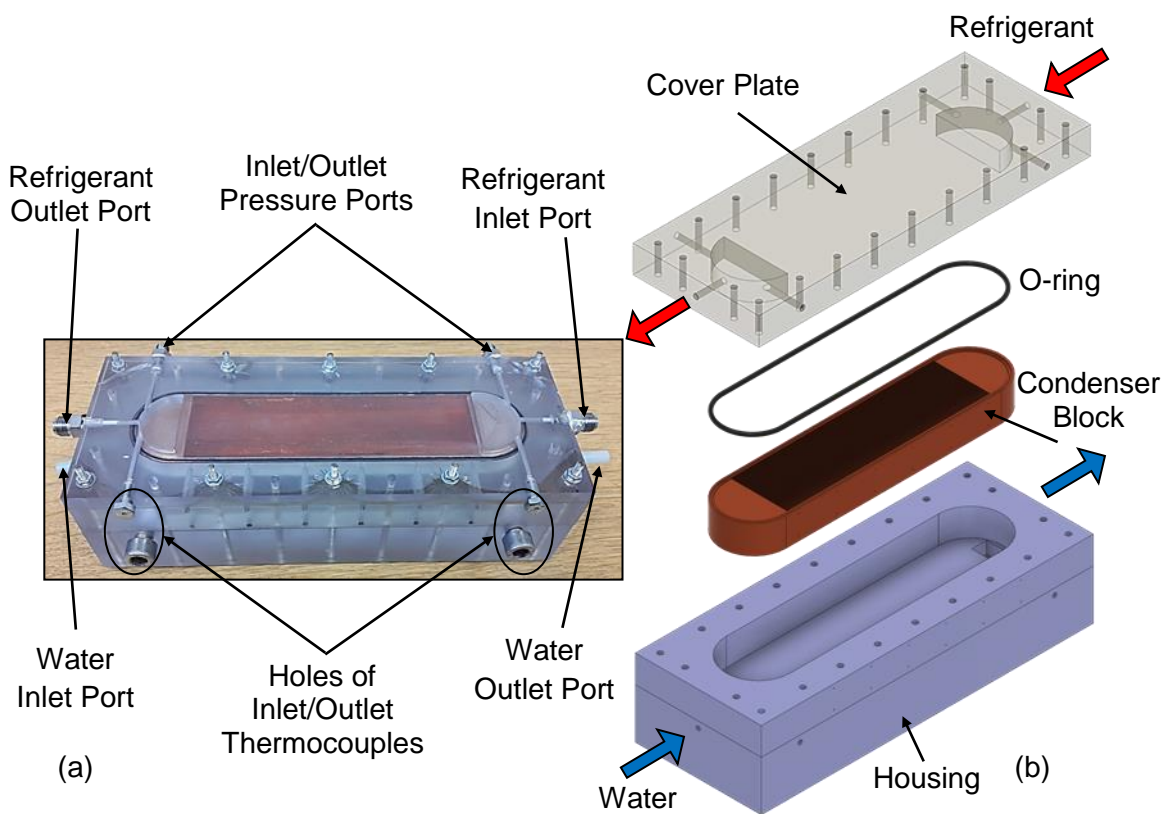


Figure 3.18 Test section construction, microchannel condenser: (a) Photograph
(b) Exploded drawing.

This block consisted of multi-channels and inlet/outlet plenum on both faces as shown in Fig 3.19. In this study, a counter-current flow condenser was tested with overall dimension of 22 mm height, 51 mm width and 221 mm length. At the refrigerant side, ninety microchannels of 1 mm height, 0.4 mm width and 0.1 mm fin thickness were formed, while at the water side, fifteen square minichannels with side length of 2 mm were milled. Twelve holes of 0.6 mm diameter and 20 mm length were drilled into the condenser block for inserting thermocouples. Twelve K-type thermocouples were inserted in two rows, 6 at the top and 6 at the bottom, to measure the temperature gradient during the condensation and consequently the local heat flux. The dimensions of the microchannel condenser are presented in Table 3.2 and Fig. 3.20. More information about the engineering drawings is presented in Appendix D.

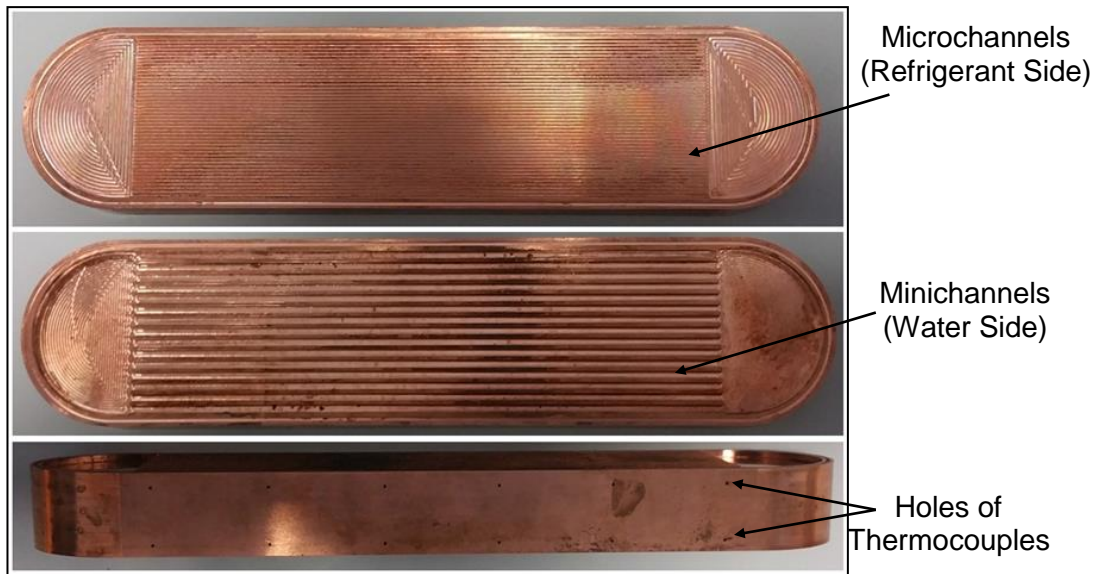


Fig. 3.19 Photograph of the condenser block.

Table 3.2 Microchannel condenser details (TS.5).

Refrigerant side: HFE-7100				
H_{ch} [mm]	W_{ch} [mm]	W_{fin} [mm]	D_h [mm]	β [-]
1	0.4	0.1	0.57	0.4
L_{ch} [mm]	A_{ht} [m ²]	$W_b \times L_b$ [mm]	H_b [mm]	N [-]
160	0.035	45×216	22	90
Coolant side: Water				
H_{ch} [mm]	W_{ch} [mm]	W_{fin} [mm]	L_{ch} [mm]	N [-]
2	2	1	160	15

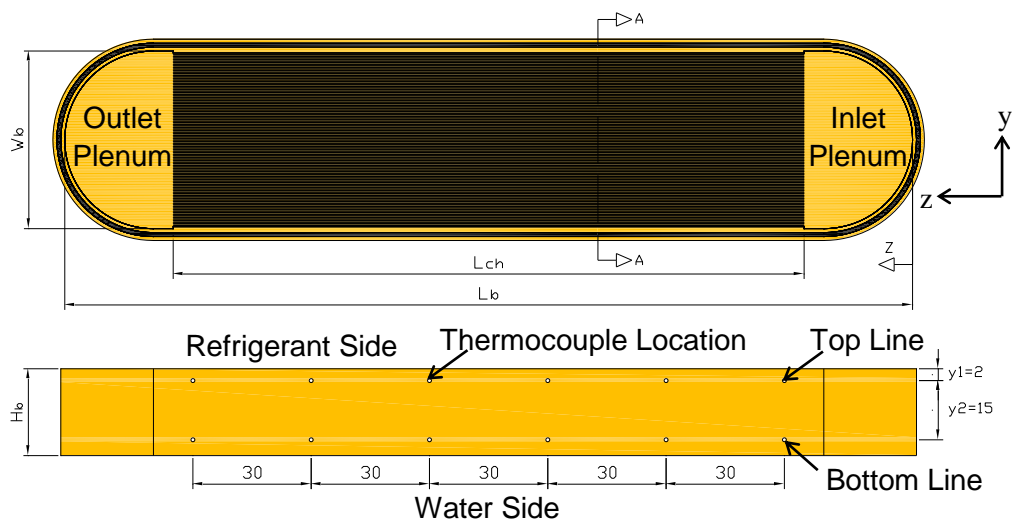


Figure 3.20 Condenser block details; dimensions in mm.

3.3.3 Surface analysis

Before conducting surface analysis, geometrical measurements were carried out for each test section. All channel dimensions were measured using an optical coordinate measuring machine (TESA-VISIO 200GL) with an accuracy of $\pm 2 \mu\text{m}$. The length and width of the test section were measured using a digital vernier calliper with a resolution of $\pm 0.1 \text{ mm}$. In this study, a surface analysis was performed for each test section to measure the surface roughness. Surface roughness is considered an important parameter that could affect the thermal performance. Therefore, this parameter was measured using a Zygo NewView 5000 surface profiler. For each test section, the surface roughness of the channel bottom was measured for different channels and at three locations; near the inlet, near the middle and near the outlet, then the average value was taken. The surface roughness value for each test section is presented in Table 3.3. This table demonstrates that the average surface roughness for three copper test sections, *i.e.* TS.1, TS.2 and TS.3, was nearly at the same value. This is an important point when the effect of channel aspect ratio is studied.

Table 3.3 Surface roughness values at different locations.

Test Section	Near Inlet [μm]	Near Middle [μm]	Near Outlet [μm]	Average Value [μm]
TS.1	0.275	0.270	0.268	0.271
TS.2	0.262	0.273	0.323	0.286
TS.3	0.310	0.326	0.277	0.304
TS.4	0.201	0.182	0.195	0.192
TS.5	0.213	0.254	0.221	0.229

Fig. 3.21 shows the roughness values and the surface characteristics for test section (1), while others are presented in Appendix E. This scan was conducted over a sample test area of $0.132 \text{ mm} \times 0.176 \text{ mm}$. This figure shows the surface map (2D and 3D), the surface profile and the intensity map. The surface map illustrates surface parameters, such as the surface roughness, the maximum peak height, the minimum valley depth and the maximum peak to valley height. It can be seen from this figure that the average surface roughness was $0.27 \mu\text{m}$, while the maximum peak height and the minimum valley depth were 1.86 and $1.57 \mu\text{m}$, respectively. Moreover, the maximum peak to valley height over this area was measured to be $3.43 \mu\text{m}$.

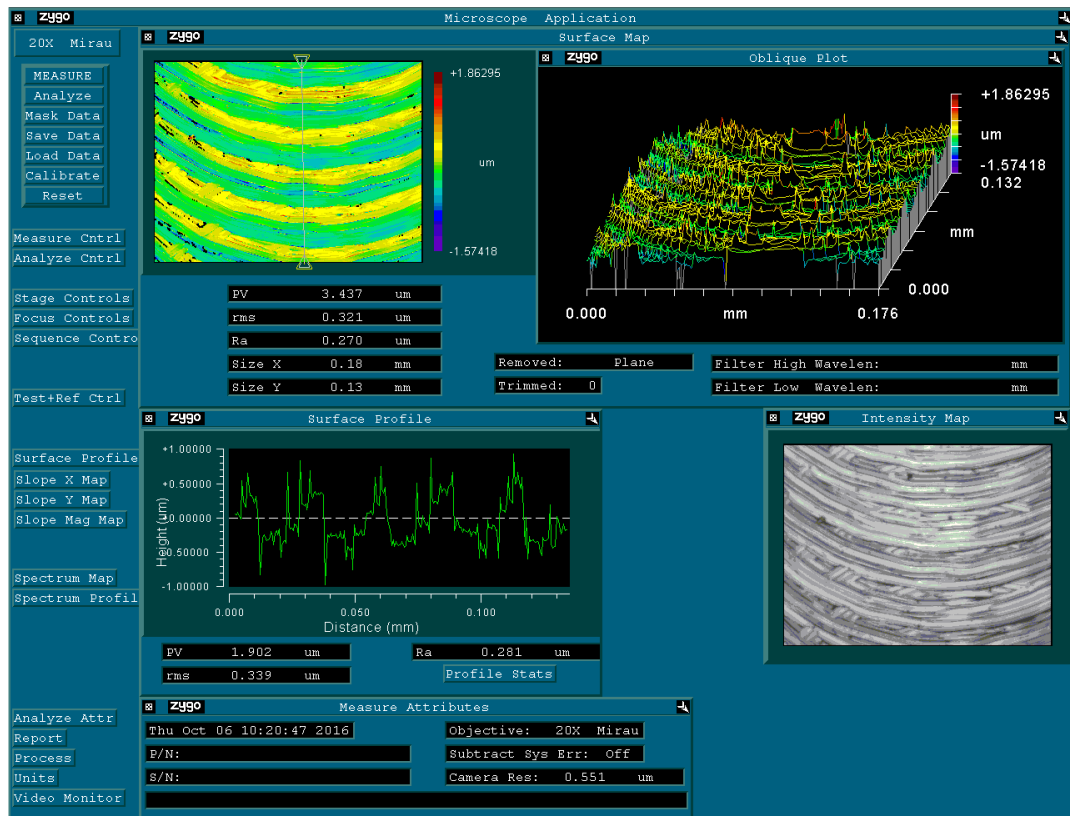


Figure 3.21 Roughness values and surface characteristics for TS.1.

The surface profile shows surface parameters along a specific line (see the vertical line), while the intensity map illustrates the surface topography. Since different surface materials may result in different surface microstructures, a Scanning Electron Microscope (SEM) analysis was conducted for both copper and aluminium surfaces. This was conducted at the Experimental Techniques Centre (ETC), Brunel University London using a LEO 1455VP electron microscope with setting of 30 μm aperture size and different magnification levels. Several images were taken for different channels, surface bottom, of each test section under a vacuum process. The initial SEM images of copper and aluminium surfaces at a magnification of 400X are shown in Fig. 3.22. These images were taken at this scale to show a large scale view of the channel bottom structure. This figure shows that the topography of aluminium surface was completely different from that of copper surface, although the same machining conditions were used. For example, the cutting marks on the aluminium surface were not similar to those on copper. These marks could lead to different surface peaks and valleys. Moreover, several grey spots were seen on the aluminium surface, see Fig. 3.22(b).

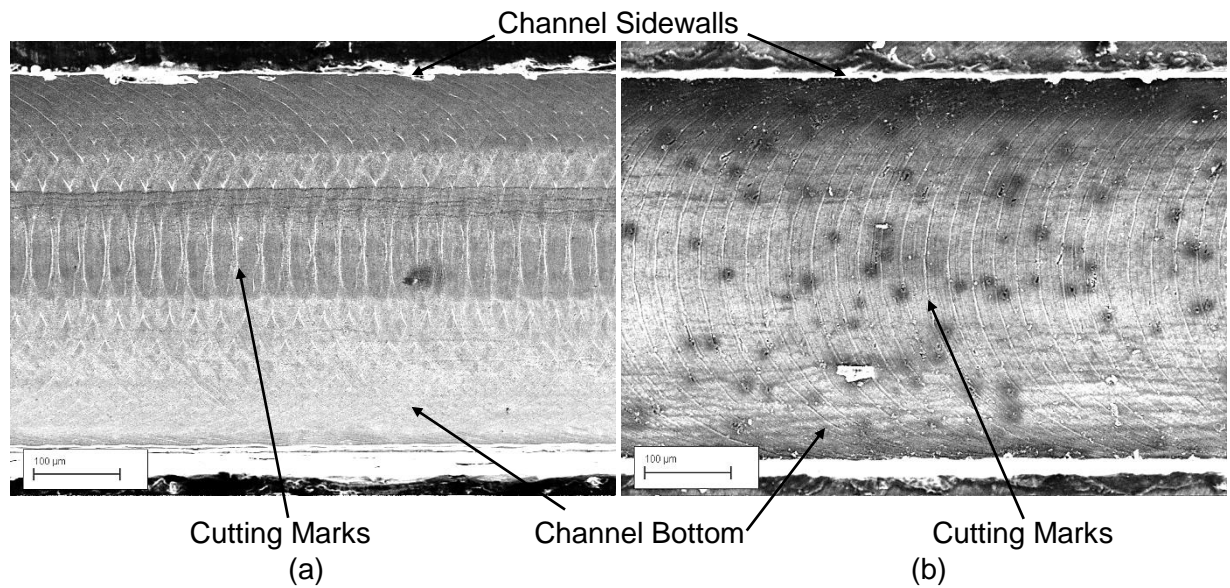


Figure 3.22 Topography images from SEM at a magnification of 400 for:
 (a) Copper (TS.2) (b) Aluminium (TS.4).

In order to capture more details about these surface microstructures, the magnification increased to 2000X and 5000X as shown in Fig. 3.23 and 3.24. It can be seen that the copper surface had a smoother texture than aluminium. The aluminium surface had more debris compared to the copper surface, see red circles. It also showed more surface cavities, see yellow circles. The cavity mouth size of aluminium looks larger than those of copper. These figures also show that, at a magnification of 2000X, more and clear peaks can be seen on the aluminium surface, see the cutting marks. For example, aluminium surface had six peaks, while four peaks can be seen on the copper surface as shown in Fig. 3.23(a) and 3.24(a). These differences in the surface microstructures could be due to the material properties. For example, the surface hardness of aluminium and copper is 27 HB and 35 HB, respectively, see Wong et al. (2012). This means that aluminium surface is softer than copper and thus more scratches and grooves could occur on this surface even at the same machining conditions. These different microstructures may play a significant role in flow boiling characteristics.

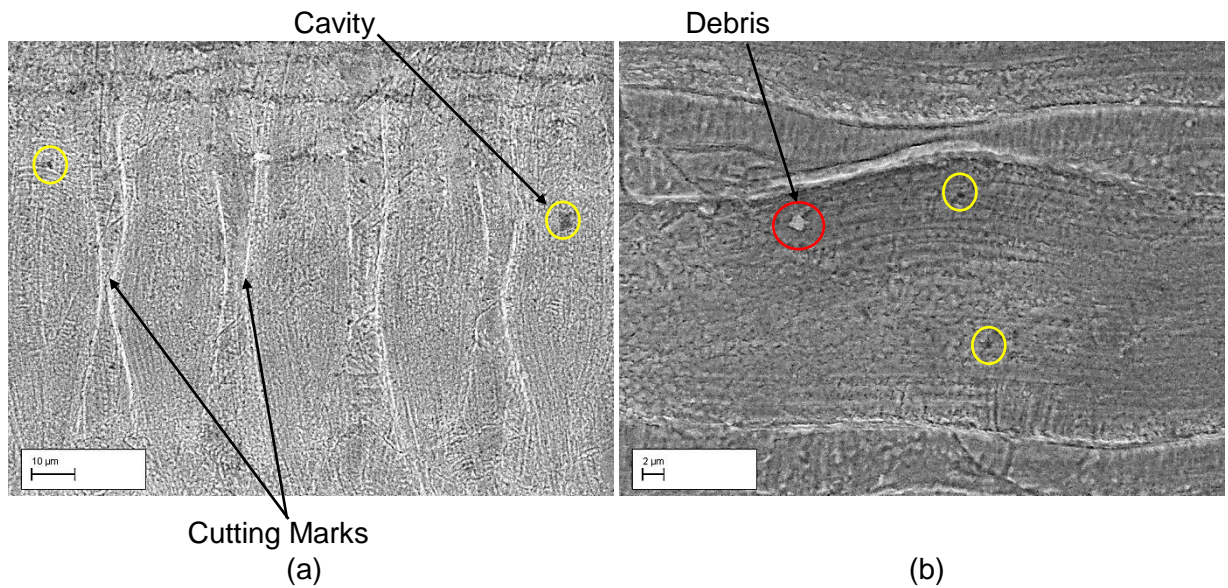


Figure 3.23 Topography images from SEM for copper (TS.2) at a magnification of:
 (a) 2000 and (b) 5000. Red circles: debris, yellow circles: cavities.

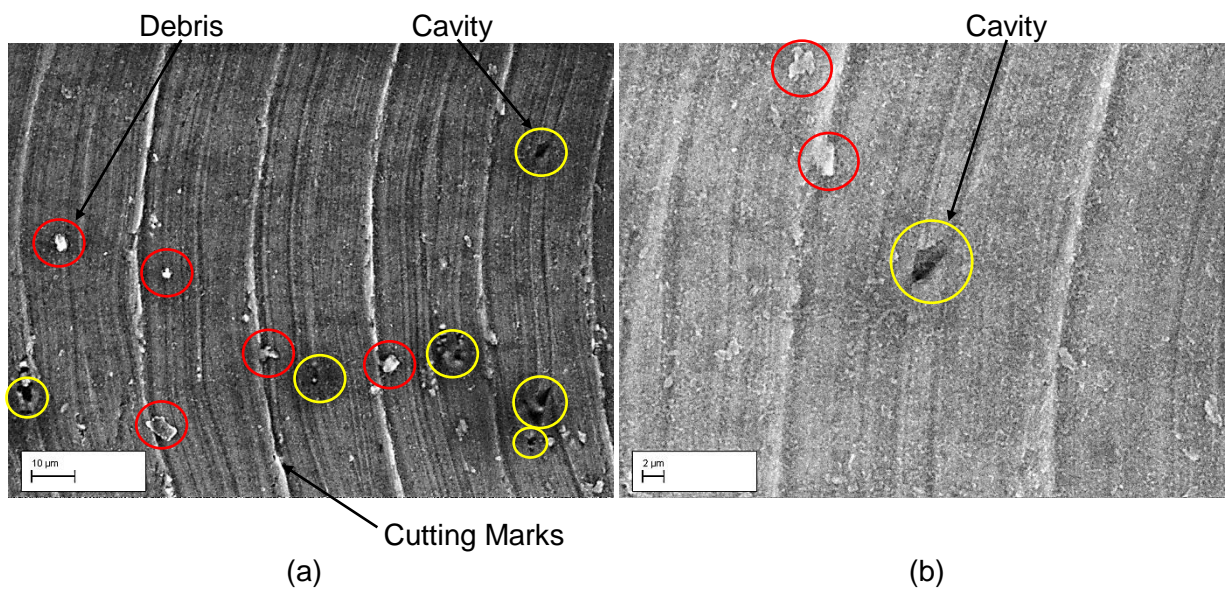


Figure 3.24 Topography images from SEM for aluminium (TS.4) at a magnification of: (a) 2000 and (b) 5000.

3.4 Calibration Process

The calibration process is considered an important initial step before conducting experiments in order to reduce the systematic errors of the measuring instruments. Therefore, this step should be performed to all the measuring sensors such as thermocouples, Coriolis flow meters and pressure transducers. In this section, the calibration procedure for thermocouples and pressure transducers is described. This

procedure was conducted at an ambient temperature and pressure of 14 °C and 101.3 kPa, respectively.

3.4.1 Thermocouple calibration

Two types of thermocouple were used during the present study, namely K and T-type. These thermocouples were used to measure the inlet and outlet fluid temperatures and wall temperatures of the test section. A calibration bath, Omega constant-temperature liquid circulating bath, was used to calibrate these thermocouples that consisted of a number of equipment as follows:

- Data acquisition system (DAQ): This data logger was used to connect all the thermocouple modules to a computer, so all the measuring signals from these modules were recorded by LabVIEW software.
- Reference thermometer system: This system consisted of a precision thermometer model ASL F250 MK II and a platinum resistance thermometer probe. The model of this probe was T100-250 with 250 mm long and 6 mm diameter. The accuracy of this system was ± 0.25 mK for a temperature ranging from -50 to 250 °C (www.isotechna.com). This system was used to compare the reference temperature readings with the thermocouple readings.
- Constant-temperature circulating bath: A stainless steel bath was filled with anti-freeze liquid such as (Water-Glycol) which created a temperature stability of ± 0.005 °C. Two instruments were fitted to this bath; thermo-regulator and dip cooler to control fluid temperature. The model of the thermo-regulator was Omega-HCTB-3030 that consisted of circulation pump, immersion heater and temperature controller for controlling the bath temperature from -40 to 200 °C, whereas the dip cooler had a flexible coil containing a refrigerant which was immersed in the fluid bath, see Fig. 3.25.

The calibration procedure for all thermocouples is described as follows:

- Connect all the thermocouple modules to a computer via data logger.
- Turn computer on and run the LabVIEW software.
Immerse the platinum resistance thermometer probe and all thermocouples (the terminal) inside the bath.
- Run the precision thermometer and the dip cooler.

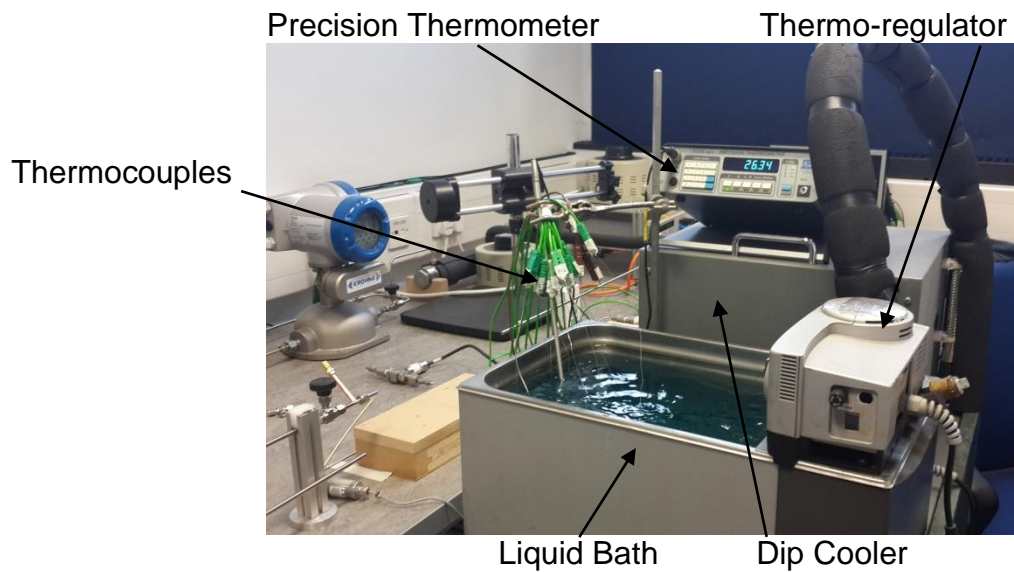


Figure 3.25 Photograph of the thermocouple calibration bath equipment.

- Set the bath temperature through adjusting the thermo-regulator.
- Record the readings from these thermocouples via LabVIEW software when the reading of the platinum resistance thermometer becomes steady, which can be recorded manually from the thermometer screen.
- Plot the results on the calibration curve, using two coordinates, namely a platinum resistance thermometer and thermocouple readings, to obtain a linear calibration equation. After that, implement this equation in the LabVIEW software data for each thermocouple. The uncertainty value of the measured variables can be found as standard deviations.

3.4.2 Pressure transducer calibration

Three pressure transducers were connected to the test section for measuring the inlet and outlet fluid pressure and the total differential pressure between the inlet and outlet plena along the test section. A dead-weight tester, see Fig. 3.26, with an accuracy of $\pm 0.01\%$ was used to calibrate the two pressure transducers as follows:

- Place the dead-weight tester on a flat stable table and check the level of the instrument by looking at the spirit level on the tester.
- Connect the pressure transducer to the test port, and then connect it to a computer via data logger.
- Run the LabVIEW software after turning the computer on.

- Place the calibrated weights on the measuring piston.
- Turn the handle of the oil pump to apply pressure to the transducer and the measuring piston.
- When the weights and the measuring piston are floating freely due to the balance between the mass load and pressure, rotate them by hand clockwise to void friction.
- Wait a few seconds for the system stability, and then record the voltage via the LabVIEW software and the total supplied pressure in PSI.
- Repeat the procedure by using a wide range of calibrated weights.
- A linear calibration equation can be obtained by drawing the readings of both pressure and voltage on the calibration curve. Then the uncertainty value of these readings can be estimated as standard deviations.

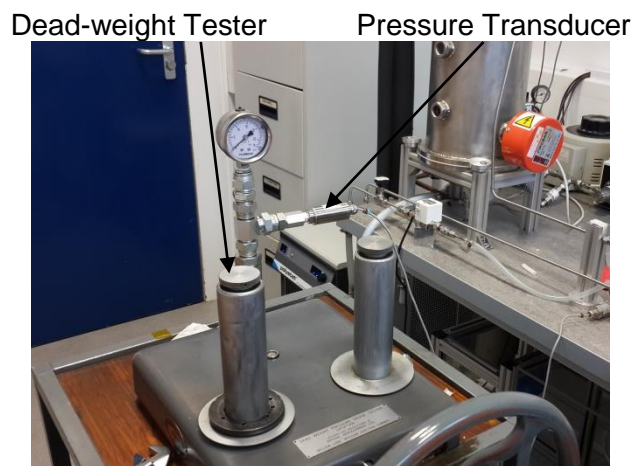


Figure 3.26 Photograph of the dead-weight tester.

It is worth mentioning that the linear calibration equations of the differential pressure transducer and mass flow meters were obtained from the calibration certificate by the manufacturer.

3.5 Data Reduction

This section presents all the equations of heat transfer coefficient, pressure drop, vapour quality and flow pattern maps. Data reduction is described for both microchannel evaporator and condenser. Single-phase data reduction is used to determine the experimental Fanning friction factor and the average Nusselt number.

This is an important initial step to validate the entire rig performance. Two-phase data reduction is adopted to calculate the two-phase heat transfer coefficient, pressure drop and vapour quality.

3.5.1 Microchannel evaporator

3.5.1.1 Single-phase data reduction

The experimental Fanning friction factor is calculated from the following equation.

$$f_{exp} = \frac{\Delta P_{ch} D_h}{2 L_{ch} v_l G_{ch}^2} \quad (3.1)$$

where ΔP_{ch} , D_h , L_{ch} , v_l and G_{ch} are the channel pressure drop, channel hydraulic diameter, channel length, liquid specific volume and channel mass flux (assuming uniform distribution of the flow rate), respectively. The channel pressure drop is calculated as follows:

$$\Delta P_{ch} = \Delta P_{meas} - (\Delta P_{ip} + \Delta P_{sc} + \Delta P_{se} + \Delta P_{op}) \quad (3.2)$$

ΔP_{meas} is the total measured pressure drop along the channel (from the differential pressure transducer). ΔP_{ip} is the pressure drop in the inlet plenum due to the change in flow direction by 90°. ΔP_{sc} is the sudden contraction pressure drop at the channel inlet. ΔP_{se} is the sudden expansion pressure drop at the channel outlet. ΔP_{op} is the pressure drop in the outlet plenum due to the change in flow direction by 90°, see Fig. 3.27 for more details. The values of the components in Eq. (3.2) are calculated from the following equations, described by Remsburg (2001).

$$\Delta P_{ip} = \frac{1}{2} K_{90} G_p^2 v_l \quad (3.3)$$

$$\Delta P_{op} = \frac{1}{2} K_{90} G_p^2 v_l \quad (3.4)$$

$$\Delta P_{sc} = \frac{1}{2} G_{ch}^2 v_l [1 - \alpha^2 + 0.5(1 - \alpha)] \quad (3.5)$$

$$\Delta P_{se} = \frac{1}{2} G_{ch}^2 v_l \left[\frac{1}{\alpha^2} - 1 + (1 - \alpha)^2 \right] \quad (3.6)$$

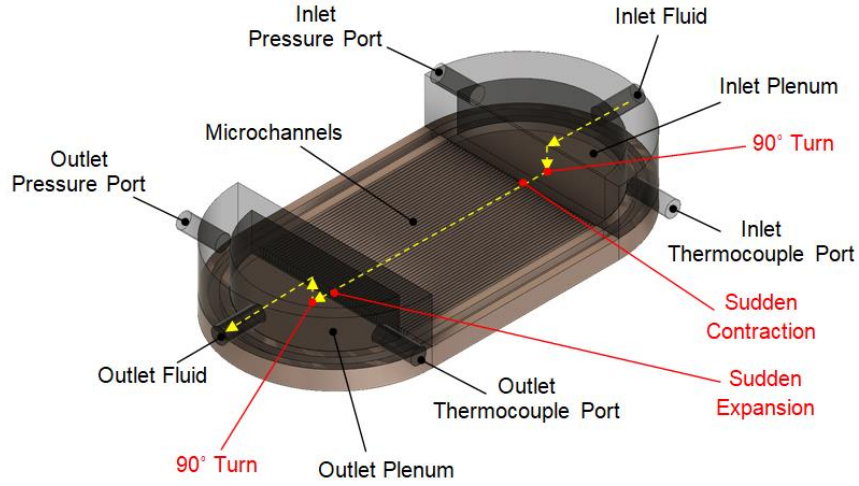


Figure 3.27 Pressure losses in the test section.

where K_{90} is the loss coefficient of the 90 degree turns, which is 1.2 as suggested by Phillips (1988). G_p and G_{ch} are the mass flux in the plenum and channel, respectively. The channel mass flux and the area ratio α are found from Eq. (3.7) and (3.8).

$$G_{ch} = \frac{\dot{m}}{(H_{ch}W_{ch})N} \quad (3.7)$$

$$\alpha = \frac{H_{ch}W_{ch}N}{H_{ch}W_b} \quad (3.8)$$

where \dot{m} , H_{ch} , W_{ch} , N and W_b are the mass flow rate, channel height, channel width, number of channels and base width, respectively. The hydraulic diameter D_h and the channel aspect ratio β are defined as follows:

$$D_h = 2H_{ch}W_{ch}/(H_{ch} + W_{ch}) \quad (3.9)$$

$$\beta = W_{ch}/H_{ch} \quad (3.10)$$

The Reynolds number is given by Eq. (3.11), where ρ_l and μ_l are the liquid density and viscosity, respectively.

$$Re = G_{ch}D_h/\mu_l \quad (3.11)$$

It is worth mentioning that the wall temperature distribution along the channel was indeed uniform, as presented in Section 3.9. This is because high thermal conductivity metals and very short channel length are tested. Therefore, a uniform wall temperature method (UWT) is used to calculate the average heat transfer coefficient as follows:

$$\bar{h} = \frac{q_b'' W_b L_{ch}}{A_{ht} \Delta T_{LM}} \quad (3.12)$$

$$\Delta T_{LM} = (T_{fo} - T_{fi}) / \ln \left\{ \frac{(T_{wi} - T_{fi})}{(T_{wi} - T_{fo})} \right\} \quad (3.13)$$

where q_b'' , A_{ht} , T_{fi} , T_{fo} and T_{wi} are the base heat flux, heat transfer area, inlet and outlet fluid temperature and average internal surface temperature, respectively. The base heat flux is estimated from the calculated vertical temperature gradient at the wall using Eq. (3.14). The wall heat flux is calculated from Eq. (3.15).

$$q_b'' = k \left. \frac{dT}{dy} \right|_{y=0} \quad (3.14)$$

$$q_w'' = \frac{q_b'' A_b}{A_{ht}} \quad (3.15)$$

where k , A_b and A_{ht} are the thermal conductivity of metal, the heat sink base area and the heat transfer area, respectively. The cover plate was assumed to be adiabatic during the experiments. Therefore, the heat transfer area is calculated from Eq. (3.16) by assuming uniform heat flux in the transverse and axial direction with three-sides heated. The same procedure was used by Harms et al. (1999) and Qu and Mudawar (2005).

$$A_{ht} = (2H_{ch} + W_{ch}) L_{ch} N \quad (3.16)$$

The average internal surface temperature in Eq. (3.13) is found as follows:

$$T_{wi} = \frac{\sum T_{wi(z)}}{n} \quad (3.17)$$

where n is the number of thermocouples along the channel, *i.e.* three thermocouples. The local internal surface temperature $T_{wi(z)}$ can be calculated from the following equation.

$$T_{wi(z)} = T_{th(z)} - \frac{q_b'' b}{k_{cu}} \quad (3.18)$$

where $T_{th(z)}$ and b are the local thermocouple temperature and the vertical distance between the thermocouple and the channel bottom, respectively. The average Nusselt number is calculated as follows:

$$\overline{Nu} = \frac{\bar{h} D_h}{k_l} \quad (3.19)$$

where k_l is the liquid thermal conductivity. All the thermophysical properties of HFE-7100 are found at the inlet pressure and the mean fluid temperature using EES software.

3.5.1.2 Flow boiling data reduction

In flow boiling experiments, the parameters that should be determined are two-phase pressure drop, local two-phase heat transfer coefficient and local vapour quality. Generally, the fluid enters the test section at subcooled condition, *i.e.* at sub-cooling nearly 5 K, and leaves it at saturation condition, *i.e.* near 60 °C. In this analysis, the channel was divided into two regions; the single-phase (subcooled region) and the two-phase region as shown in Fig. 3.28.

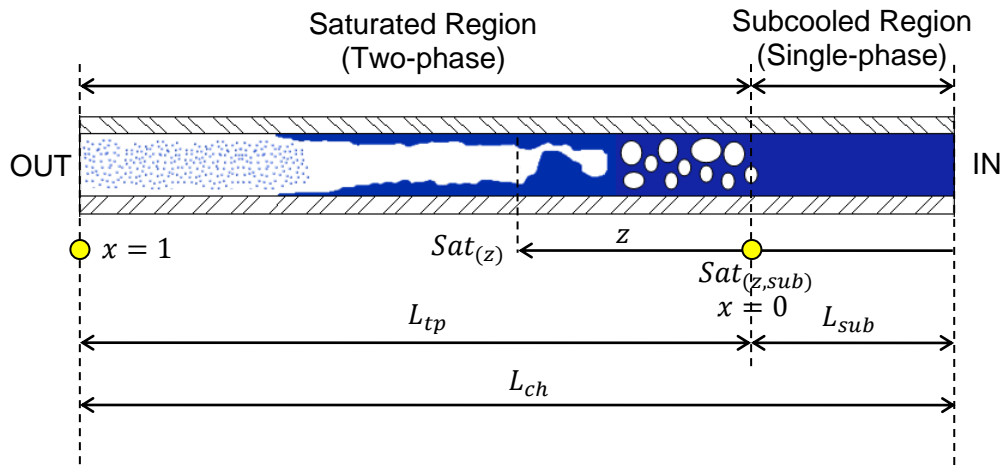


Figure 3.28 Flow boiling region along the channel.

The length of the single-phase region is calculated from Eq. (3.20).

$$L_{sub} = \frac{\dot{m}c_p(T_{sat(z,sub)} - T_{fi})}{q_b''W_b} \quad (3.20)$$

The local saturation temperature of the fluid at the end of the single-phase region $T_{sat(z,sub)}$ is found from the local saturation pressure at the subcooled region $P_{sat(z,sub)}$ which is calculated from Eq. (3.21).

$$P_{sat(z,sub)} = P_i - \frac{2fG_{ch}^2L_{sub}}{\rho_l D_h} \quad (3.21)$$

An iteration process was used to determine the subcooled length using the above two equations, *i.e.* between Eq. (3.20) and (3.21). The friction factor f is calculated from Eq. (3.22) for developing laminar flow and Eq. (3.24) for fully developed flow as proposed by Shah and London (1978).

$$f_{app} = \frac{3.44}{Re\sqrt{L^*}} + \frac{f_{FD}Re + \frac{K_\infty}{4L^*} - 3.44/\sqrt{L^*}}{Re(1 + C(L^*)^{-2})} \quad (3.22)$$

$$L^* = L_{sub}/ReD_h \quad (3.23)$$

$$f_{FD}Re = 24(1 - 1.355\beta + 1.946\beta^2 - 1.7012\beta^3 + 0.9564\beta^4 - 0.2537\beta^5) \quad (3.24)$$

K_∞ , C and L^* are the dimensionless incremental pressure drop number, the dimensionless correction factor and the dimensionless length, respectively. The values of K_∞ and C are found based on the channel aspect ratio β as proposed by Shah and London (1978). Table 3.4 presents these values.

Table 3.4 The values of K_∞ and C for the test sections.

β	0.5	1	2
K_∞	1.28	1.43	1.28
C	0.00021	0.00029	0.00021

The two-phase length L_{tp} can be calculated from Eq. (3.25).

$$L_{tp} = L_{ch} - L_{sub} \quad (3.25)$$

The two-phase pressure drop along the channels can be found from Eq. (3.26). The pressure drop due to the sudden expansion and outlet plenum in Eq. (3.2) should be calculated as two-phase flow, see Collier and Thome (1994).

$$\Delta P_{tp} = \Delta P_{ch} - \Delta P_{sp} \quad (3.26)$$

The pressure drop at single-phase region is determined as follows:

$$\Delta P_{sp} = \frac{2fG_{ch}^2L_{sub}}{\rho_l D_h} \quad (3.27)$$

The local single-phase heat transfer coefficient is calculated from Eq. (3.28).

$$h_{sp(z)} = \frac{q_b''(W_{ch} + W_{fin})}{(T_{wi(z)} - T_{f(z)})(W_{ch} + 2\eta H_{ch})} \quad (3.28)$$

The local fluid temperature $T_{f(z)}$ can be calculated by Eq. (3.29), while the local internal surface temperature $T_{wi(z)}$ can be found from Eq. (3.18).

$$T_{f(z)} = T_{fi} + \frac{q_b'' W_b z}{\dot{m} c p_l} \quad (3.29)$$

where z and $c p_l$ are the axial distance from the channel inlet and the liquid specific heat, respectively. The fin efficiency η and fin parameter m can be found from Eq. (3.30) and (3.31), respectively.

$$\eta = \frac{\tanh(m H_{ch})}{m H_{ch}} \quad (3.30)$$

$$m = \sqrt{\frac{2 h(z)}{k_{cu} W_{fin}}} \quad (3.31)$$

The local two-phase heat transfer coefficient is given as follows:

$$h_{tp(z)} = \frac{q_b'' (W_{ch} + W_{fin})}{(T_{wi(z)} - T_{sat(z)}) (W_{ch} + 2\eta H_{ch})} \quad (3.32)$$

The local specific enthalpy and local vapour quality at the two-phase region can be calculated using Eq. (3.33) and (3.34), respectively.

$$i_{(z)} = i_i + \frac{q_b'' W_b z}{\dot{m}} \quad (3.33)$$

$$x_{(z)} = \frac{i_{(z)} - i_{l(z)}}{i_{lg(z)}} \quad (3.34)$$

where $T_{sat(z)}$, i_i , $i_{l(z)}$ and $i_{lg(z)}$ are the local saturation temperature, the inlet specific enthalpy, the local liquid specific enthalpy of saturated liquid and the local enthalpy of vaporization, respectively. The inlet specific enthalpy is found from the thermophysical properties of HFE-7100 at the inlet pressure and the fluid inlet temperature, while the rest of the values are found from the corresponding local pressure in the saturated region $P_{sat(z)}$ that can be calculated from Eq. (3.35), by assuming a linear pressure drop with axial length. This assumption is necessary since it is difficult to insert pressure sensors inside these tiny channels without disturbing the flow.

$$P_{sat(z)} = P_{sat(z,sub)} - \left(\frac{z - L_{sub}}{L_{ch} - L_{sub}} \right) \Delta P_{tp} \quad (3.35)$$

The average heat transfer coefficient is calculated from Eq. (3.36).

$$\bar{h} = \frac{1}{L} \int_0^L h_{(z)} dz \quad (3.36)$$

The cooling load at the evaporator is calculated from Eq. (3.37).

$$Q_{evap} = q''_b A_b \quad (3.37)$$

where q''_b and A_b are the base heat flux and the base area, respectively. The consumption power by the pump is calculated using Eq. (3.38) by assuming that the efficiency of the pump is 100%.

$$W_p = \dot{m} \Delta P_{sys} / \rho_l \quad (3.38)$$

where \dot{m} , ΔP_{sys} and ρ_l are the mass flow rate, the system pressure drop and the liquid density, respectively. The system pressure drop ΔP_{sys} (in a small-scale system) is calculated from Eq. (3.39).

$$\Delta P_{sys} = \Delta P_{evap} + \Delta P_{cond} + \Delta P_{oth} \quad (3.39)$$

where ΔP_{evap} , ΔP_{cond} and ΔP_{oth} are the total measured pressure drop inside the microchannel evaporator, the total measured pressure drop inside the microchannel condenser and the pressure drop inside other parts, *i.e.* pipes, connecting joints and liquid reservoir, respectively. The last pressure drop was assumed to be 10% of the pressure drop of the evaporator and condenser.

3.5.1.3 Flow pattern map data reduction

Both vapour and liquid superficial velocities are used to present the flow pattern maps. These parameters are calculated as follows:

$$J_{g(z)} = \frac{G_{ch} x_{(z)}}{\rho_{g(z)}} \quad (3.40)$$

$$J_{l(z)} = \frac{G_{ch} (1 - x_{(z)})}{\rho_{l(z)}} \quad (3.41)$$

where $x_{(z)}$, $\rho_{l(z)}$ and $\rho_{g(z)}$ are the local vapour quality, local liquid and vapour densities, respectively. All these values are found at the local saturation pressure from Eq. (3.35). The thermophysical properties of HFE-7100 are given in the EES software.

3.5.2 Microchannel condenser

3.5.2.1 Single-phase data reduction

The experimental Fanning friction factor and the channel pressure drop in the condenser are calculated from Eq. (3.1) and (3.2) after calculating the pressure losses due to the inlet and outlet plena and the sudden contraction and expansion, see Eq. (3.3–6). Since the base heat flux and wall temperature vary along the channels, the single-phase heat transfer coefficient is calculated locally as follows:

$$h_{sp(z)} = \frac{q_{b(z)}''(W_{ch} + W_{fin})}{(T_{f(z)} - T_{wi(z)})(W_{ch} + 2\eta H_{ch})} \quad (3.42)$$

The fin efficiency η is calculated using Eq. (3.30) by assuming adiabatic fin tips. The local base heat flux $q_{b(z)}''$ during the experiments is calculated directly from the vertical temperature gradient at six axial locations by assuming 1D heat conduction as given in Eq. (3.43).

$$q_{b(z)}'' = k_{cu} \frac{(T_{T(z)} - T_{B(z)})}{y_2} \quad (3.43)$$

where $T_{T(z)}$, $T_{B(z)}$ and y_2 are the local thermocouple temperature at the top line, the local thermocouple temperature at the bottom line and the vertical distance between thermocouples, respectively, see Fig. 3.20 for more details. As mentioned before, the inlet and outlet plena were formed in the condenser block. Therefore, the best fit equation (third or fourth order polynomial equation) of the curve resulting from plotting the local base heat flux versus axial distance is used to calculate the base heat flux at these parts, see Eq. (3.44). This approach was adopted by Ma et al. (2011) and Jiang et al. (2015).

$$q_b'' = az^4 + bz^3 + cz^2 + dz + e \quad (3.44)$$

The above coefficients, *i.e.* a , b , c , d and e , of this fourth order polynomial equation change with the experimental operating conditions. The base heat flux at the inlet and outlet plena is found at the axial location (z) of 5 and 205 mm, respectively. The condenser block is divided into thermal elements as shown in Fig. 3.29. Therefore, the local refrigerant temperature during single-phase flow is calculated using an energy balance by Eq. (3.45) below.

$$T_{f(z)n} = T_{f(z)n+1} + \frac{\left[\frac{q_{b(z)n}'' + q_{b(z)n+1}''}{2} \right] W_b \Delta z}{\dot{m} c p_l} \quad (3.45)$$

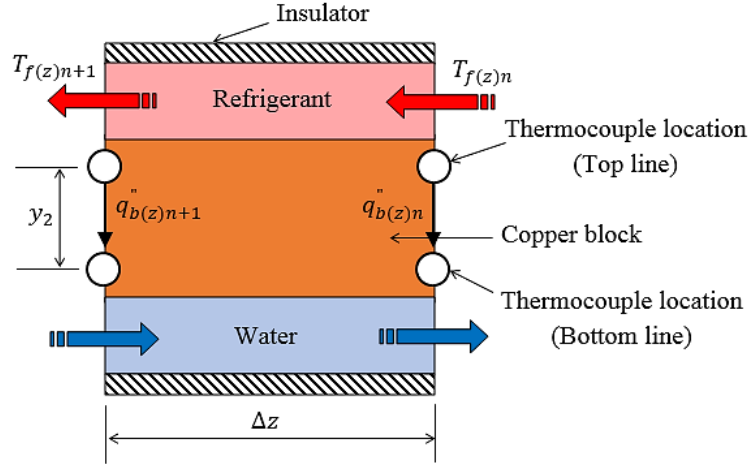


Figure 3.29 Thermal element of the condenser.

where $T_{f(z)n+1}$ and Δz are the local outlet refrigerant temperature at the thermal element and the axial distance between thermocouples, respectively. The local internal surface temperature in the Eq. (3.42) is determined as follows:

$$T_{wi(z)} = T_{T(z)} + \frac{q_{b(z)}'' y_1}{k_{cu}} \quad (3.46)$$

where y_1 is the vertical distance between the thermocouple at the top line and the channel bottom, which is 2 mm. The average single-phase heat transfer coefficient is derived from integrating Equation (3.42) with distance, and then the average Nusselt number is calculated using Eq. (3.19).

3.5.2.2 Flow condensation data reduction

The local two-phase heat transfer coefficient is calculated using Eq. (3.47) as follows:

$$h_{tp(z)} = \frac{q_{b(z)}'' (W_{ch} + W_{fin})}{(T_{sat(z)} - T_{wi(z)}) (W_{ch} + 2\eta H_{ch})} \quad (3.47)$$

The local saturation temperature $T_{sat(z)}$ is determined using the local saturation pressure. Eq. (3.48) is used to determine this pressure as follows:

$$P_{sat(z)} = P_i - (P_i - P_{sat(z,sp)}) \left(\frac{z}{L_{ch} - L_{sp}} \right) \quad (3.48)$$

where P_i and L_{sp} are the inlet pressure and the length of the condenser in the single-phase region, respectively. The local saturation pressure at the onset of the single-phase region $P_{sat(z,sp)}$ is found from Eq. (3.49).

$$P_{sat(z,sp)} = P_o + \frac{2fG_{ch}^2 L_{sp}}{\rho_l D_h} \quad (3.49)$$

where P_o , f and ρ_l are the outlet pressure, the Fanning friction factor and the liquid density, respectively. The single-phase length can be calculated from Eq. (3.50) as follows.

$$L_{sp} = \frac{\dot{m} c p_l (T_{sat(z,sp)} - T_{fo})}{\overline{q''}_b W_b} \quad (3.50)$$

The local saturation temperature at the onset of the single-phase region $T_{sat(z,sp)}$ is found from the local saturation pressure at the onset of the single-phase region $P_{sat(z,sp)}$. Therefore, an iteration process should be used between Eq. (3.49) and (3.50) to find this length. Eq. (3.43) is integrated with distance to find the average base heat flux $\overline{q''}_b$. The local vapour quality along the channels is calculated from the equation below.

$$x_{(z)n+1} = x_{(z)n} - \frac{\left[\frac{q_{b(z)n}'' + q_{b(z)n+1}''}{2} \right] W_b \Delta z}{\dot{m} i_{lg(z)}} \quad (3.51)$$

The inlet vapour quality at the condenser is calculated from an energy balance in the pre-heater and the tubular evaporator as follows:

$$x_i = \frac{Q_i}{\dot{m} i_{lg}} + \frac{c p_l (T_{fi} - T_{sat})}{i_{lg}} \quad (3.52)$$

where Q_i , T_{fi} , T_{sat} and i_{lg} are the input electric power to the pre-heater and the tubular evaporator (see 6 and 7 in Fig. 3.2), the refrigerant temperature at the inlet of the pre-heater, the saturation temperature and the latent heat of vaporization estimated at the inlet pressure of the pre-heater, respectively. The EES software was used to obtain the thermophysical properties of HFE-7100.

3.6 Propagated Uncertainty Analysis

The first objective of any experiment is to obtain and record accurate experimental measurements. The difference between the real and measured values can be defined as error, while the quantification of doubt about the measured value is referred to the uncertainty, Bell (1999). The total error is the sum of bias and random errors. The bias or systematic error is due to the errors in the measuring devices and this type of error can be reduced through instrument calibration. The precision (random) error is

due to a number of influences beyond the control of the experimentalist when an experiment is conducted such as surrounding temperature, humidity, pressure, etc. This error can be estimated via statistical analysis and can be reduced by conducting a large number of readings (measurements) over time. According to Coleman and Steele (2009), the bias and precision uncertainties, combined uncertainty, can be calculated as follows:

$$u_c = \sqrt{B_x^2 + S_x^2} \quad (3.53)$$

where B_x and S_x are the systematic uncertainty of a measured variable X and the standard deviation of a sample of N , respectively. Their values can be calculated using Eq. (3.54) and (3.55).

$$B_x = \sqrt{\sum_{k=1}^M (B_x)_k^2} \quad (3.54)$$

$$S_x = \sqrt{\frac{1}{N-1} \sum_{i=1}^N (X_i - \bar{X})^2} \quad (3.55)$$

where $(B_x)_k$, N , X_i and \bar{X} are the bias uncertainties from the element k which can be evaluated from the technical details of instrument or calibration curve, the sample population, the sample value and the mean value, respectively. The overall uncertainty value of a measured variable with a 95% confidence level can be determined from Eq. (3.56) as described by Coleman and Steele (2009).

$$U = t_{95\%} u_c \quad (3.56)$$

where $t_{95\%}$ is the value from the t distribution that reaches 95% confidence level. Assume r is a function of j measured variables as follows:

$$r = r(X_1, X_2, \dots, X_j) \quad (3.57)$$

Then the absolute uncertainty value can be calculated by Eq. (3.58). Moreover, Eq. (3.59) can be used to calculate the relative uncertainty.

$$U_r = \sqrt{\left\{ \frac{\partial r}{\partial X_1} U_{X1} \right\}^2 + \left\{ \frac{\partial r}{\partial X_2} U_{X2} \right\}^2 + \dots + \left\{ \frac{\partial r}{\partial X_j} U_{Xj} \right\}^2} \quad (3.58)$$

$$\frac{U_r}{r} = \sqrt{\left\{ \frac{X_1}{r} \frac{\partial r}{\partial X_1} \right\}^2 \left\{ \frac{U_{X1}}{X_1} \right\}^2 + \left\{ \frac{X_2}{r} \frac{\partial r}{\partial X_2} \right\}^2 \left\{ \frac{U_{X2}}{X_2} \right\}^2 + \dots + \left\{ \frac{X_j}{r} \frac{\partial r}{\partial X_j} \right\}^2 \left\{ \frac{U_{Xj}}{X_j} \right\}^2} \quad (3.59)$$

Table 3.5 Uncertainty values of the measured variables.

Variable	Measuring instrument	Uncertainty value	Source
Channel Dimensions	TESA-VISIO 200GL	±0.002mm	Manufacturer (TESA Technology)
Base Width and Length	Digital vernier calliper	±0.01mm	Manufacturer
DC Voltage	Power Meter: HM8115-2	±0.4%	Manufacturer (HAMEG)
DC Current			
Mass Flow Rate	Coriolis flow meter: Optimass 3300C	±0.1%	Manufacturer (KROHNE)
Water Flow Rate	OMEGA	±1%	Manufacturer (OMEGA)
Differential Pressure Transducer	OMEGA: PX409-005DWUI	±0.08%	Manufacturer (OMEGA)
Inlet Pressure Transducer	OMEGA: PX209-100A5V	±0.46kPa	Calibration
Outlet Pressure Transducer	OMEGA: PX209-100A5V	±0.37kPa	Calibration
Fluid Temperature	T-type thermocouple	±0.024K	Calibration
Wall Temperature	K-type thermocouple	±0.038–0.12K	Calibration

The uncertainty analysis for the experimental variables was performed based on approach described above. Table 3.5 summarizes the uncertainty values of the measured variables. Eq. (3.59) is used to calculate the uncertainty analysis for the experimental variables, *i.e.* the derived variables. The channel hydraulic diameter is defined in Eq. (3.9). Therefore, the relative uncertainty in this parameter is expressed as follows:

$$\frac{U_{Dh}}{D_h} = \sqrt{\left\{ \frac{H_{ch}}{(H_{ch} + W_{ch})} \frac{U_{W_{ch}}}{W_{ch}} \right\}^2 + \left\{ \frac{W_{ch}}{(H_{ch} + W_{ch})} \frac{U_{H_{ch}}}{H_{ch}} \right\}^2} \quad (3.60)$$

where $U_{H_{ch}}$ and $U_{W_{ch}}$ are the absolute uncertainty in the channel height and width, respectively. The relative uncertainties in the mass flux, the channel cross-sectional area and aspect ratio are calculated from Eq. (3.61), (3.62) and (3.63), respectively.

$$\frac{U_G}{G} = \sqrt{\left\{\frac{U_{\dot{m}}}{\dot{m}}\right\}^2 + \left\{\frac{U_{A_{sec}}}{A_{sec}}\right\}^2} \quad (3.61)$$

$$\frac{U_{A_{sec}}}{A_{sec}} = \sqrt{\left\{\frac{U_{W_{ch}}}{W_{ch}}\right\}^2 + \left\{\frac{U_{H_{ch}}}{H_{ch}}\right\}^2} \quad (3.62)$$

$$\frac{U_{\beta}}{\beta} = \sqrt{\left\{\frac{U_{W_{ch}}}{W_{ch}}\right\}^2 + \left\{\frac{U_{H_{ch}}}{H_{ch}}\right\}^2} \quad (3.63)$$

Eq. (3.64) is used to express the relative uncertainty in the logarithmic mean temperature difference.

$$\frac{U_{\Delta T_{LM}}}{\Delta T_{LM}} = \sqrt{\left\{\frac{U_{\Delta T_f}}{\Delta T_f}\right\}^2 + \left\{\frac{U_{\Delta T_i}}{\Delta T_i \ln\left\{\frac{\Delta T_i}{\Delta T_o}\right\}}\right\}^2 + \left\{\frac{U_{\Delta T_o}}{\Delta T_o \ln\left\{\frac{\Delta T_i}{\Delta T_o}\right\}}\right\}^2} \quad (3.64)$$

$$U_{\Delta T_f} = \sqrt{(U_{T_{fo}})^2 + (U_{T_{fi}})^2} \quad (3.65)$$

$$U_{\Delta T_i} = \sqrt{(U_{T_{wi}})^2 + (U_{T_{fi}})^2} \quad (3.66)$$

$$U_{\Delta T_o} = \sqrt{(U_{T_{wi}})^2 + (U_{T_{fo}})^2} \quad (3.67)$$

The relative uncertainty in the base heat flux and wall heat flux can be expressed in Eq. (3.68) and (3.69), respectively. The uncertainty in the heat transfer area is defined in Eq. (3.70).

$$\frac{U_{q_b''}}{q_b''} = \sqrt{\left\{\frac{U_{\Delta T_{th}}}{\Delta T_{th}}\right\}^2 + \left\{\frac{U_{\Delta y}}{\Delta y}\right\}^2} \quad (3.68)$$

$$\frac{U_{q_w''}}{q_w''} = \sqrt{\left\{\frac{U_{q_b''}}{q_b''}\right\}^2 + \left\{\frac{U_{A_{ht}}}{A_{ht}}\right\}^2 + \left\{\frac{U_{W_b}}{W_b}\right\}^2 + \left\{\frac{U_{L_{ch}}}{L_{ch}}\right\}^2} \quad (3.69)$$

$$\frac{U_{A_{ht}}}{A_{ht}} = \sqrt{\left\{\frac{2U_{H_{ch}}}{2H_{ch} + W_{ch}}\right\}^2 + \left\{\frac{U_{W_{ch}}}{2H_{ch} + W_{ch}}\right\}^2 + \left\{\frac{U_{L_{ch}}}{L_{ch}}\right\}^2} \quad (3.70)$$

where ΔT_{th} and Δy are the temperature difference of thermocouples and the distance between thermocouples, respectively. $U_{\Delta T_{th}}$ is the absolute uncertainty of the thermocouples, while $U_{\Delta y}$ is the absolute uncertainty of the vertical distance (± 0.01 mm). The uncertainty in the average heat transfer coefficient is expressed in Eq. (3.71) as follows:

$$\frac{U_{\bar{h}}}{\bar{h}} = \sqrt{\left\{\frac{U_{q_b''}}{q_b''}\right\}^2 + \left\{\frac{U_{W_b}}{W_b}\right\}^2 + \left\{\frac{U_{L_{ch}}}{L_{ch}}\right\}^2 + \left\{\frac{U_{A_{ht}}}{A_{ht}}\right\}^2 + \left\{\frac{U_{\Delta T_{LM}}}{\Delta T_{LM}}\right\}^2} \quad (3.71)$$

Eq. (3.72) is used to express the relative uncertainty in the average Nusselt number.

$$\frac{U_{\overline{Nu}}}{\overline{Nu}} = \sqrt{\left\{\frac{U_{\bar{h}}}{\bar{h}}\right\}^2 + \left\{\frac{U_{D_h}}{D_h}\right\}^2} \quad (3.72)$$

The absolute uncertainty in the channel pressure drop is found from Eq. (3.73).

$$U_{\Delta P_{ch}} = \sqrt{(U_{\Delta P_{meas}})^2 + (U_{\Delta P_{ip}})^2 + (U_{\Delta P_{sc}})^2 + (U_{\Delta P_{se}})^2 + (U_{\Delta P_{op}})^2} \quad (3.73)$$

$U_{\Delta P_{ip}}$, $U_{\Delta P_{sc}}$, $U_{\Delta P_{se}}$ and $U_{\Delta P_{op}}$ are calculated using the error propagation method for Eq. (3.3), (3.4), (3.5) and (3.6), respectively. The relative uncertainty in the Fanning friction factor is expressed in Eq. (3.74), while the uncertainty in the subcooled length is defined in Eq. (3.75).

$$\frac{U_f}{f} = \sqrt{\left\{\frac{U_{\Delta P_{ch}}}{\Delta P_{ch}}\right\}^2 + \left\{\frac{U_{D_h}}{D_h}\right\}^2 + \left\{\frac{U_{L_{ch}}}{L_{ch}}\right\}^2 + \left\{\frac{2U_G}{G}\right\}^2} \quad (3.74)$$

$$\frac{U_{L_{sub}}}{L_{sub}} = \sqrt{\left\{\frac{U_{\dot{m}}}{\dot{m}}\right\}^2 + \left\{\frac{U_{T_{fi}}}{\Delta T}\right\}^2 + \left\{\frac{U_{q_b''}}{q_b''}\right\}^2 + \left\{\frac{U_{W_b}}{W_b}\right\}^2} \quad (3.75)$$

The absolute uncertainty in the two-phase length is found from Eq. (3.76).

$$U_{L_{tp}} = \sqrt{(U_{L_{ch}})^2 + (U_{L_{sub}})^2} \quad (3.76)$$

Eq. (3.77) is used to find the uncertainty in the single-phase pressure drop. The uncertainty in the two-phase pressure drop is expressed in Eq. (3.78).

$$\frac{U_{\Delta P_{sp}}}{\Delta P_{sp}} = \sqrt{\left\{\frac{U_{D_h}}{D_h}\right\}^2 + \left\{\frac{2U_G}{G}\right\}^2 + \left\{\frac{U_{L_{sub}}}{L_{sub}}\right\}^2} \quad (3.77)$$

$$\frac{U_{\Delta P_{tp}}}{\Delta P_{tp}} = \sqrt{\left\{\frac{U_{\Delta P_{ch}}}{\Delta P_{ch}}\right\}^2 + \left\{\frac{U_{\Delta P_{sp}}}{\Delta P_{sp}}\right\}^2} \quad (3.78)$$

The relative uncertainty in the local single-phase and two-phase heat transfer coefficient is found from Eq. (3.79) and (3.80), respectively.

$$\frac{U_{h_{sp}(z)}}{h_{sp}(z)} = \sqrt{\left\{ \frac{U_{q_b''}}{q_b''} \right\}^2 + \left\{ \frac{U_{W_b}}{W_b} \right\}^2 + \left\{ \frac{2U_{H_{ch}}}{2H_{ch} + W_{ch}} \right\}^2 + \left\{ \frac{U_{W_{ch}}}{2H_{ch} + W_{ch}} \right\}^2 + \left\{ \frac{U_{T_{wi}(z)}}{\Delta T} \right\}^2 + \left\{ \frac{U_{T_{f}(z)}}{\Delta T} \right\}^2} \quad (3.79)$$

$$\frac{U_{h_{tp}(z)}}{h_{tp}(z)} = \sqrt{\left\{ \frac{U_{q_b''}}{q_b''} \right\}^2 + \left\{ \frac{U_{W_b}}{W_b} \right\}^2 + \left\{ \frac{2U_{H_{ch}}}{2H_{ch} + W_{ch}} \right\}^2 + \left\{ \frac{U_{W_{ch}}}{2H_{ch} + W_{ch}} \right\}^2 + \left\{ \frac{U_{T_{wi}(z)}}{\Delta T} \right\}^2 + \left\{ \frac{U_{sat}(z)}{\Delta T} \right\}^2} \quad (3.80)$$

where ΔT is the temperature difference between the wall temperature and the fluid temperature (for single-phase region) or saturation temperature (for two-phase region). The uncertainty of the local fluid temperature $U_{T_{f}(z)}$ can be calculated as follows:

$$U_{T_{f}(z)} = \sqrt{\left(U_{T_{fi}} \right)^2 + \left\{ \frac{W_b z U_{q_b''}}{\dot{m} c_{p_l}} \right\}^2 + \left\{ \frac{q_b'' z U_{W_b}}{\dot{m} c_{p_l}} \right\}^2 + \left\{ \frac{q_b'' W_b U_z}{\dot{m} c_{p_l}} \right\}^2 + \left\{ \frac{q_b'' W_b z U_{\dot{m}}}{\dot{m}^2 c_{p_l}} \right\}^2} \quad (3.81)$$

The absolute uncertainty of the local internal wall temperature $U_{T_{wi}(z)}$ can be found by Eq. (3.82).

$$U_{T_{wi}(z)} = \sqrt{\left(U_{Th(z)} \right)^2 + \left\{ \frac{y U_{q_b''}}{k_w} \right\}^2 + \left\{ \frac{q_b'' U_y}{k_w} \right\}^2} \quad (3.82)$$

where k_w and y are the wall thermal conductivity and the distance between the channel bottom and the thermocouple, respectively. The uncertainty in the local vapour quality is obtained from Eq. (3.83) by assuming the uncertainty in the fluid properties being negligible. Eq. (3.84) is used to find the uncertainty in the local enthalpy.

$$U_{x(z)} = \frac{U_{i(z)}}{i_{lg(z)}} \quad (3.83)$$

$$U_{i(z)} = \sqrt{\left\{ \frac{W_b z U_{q_b''}}{\dot{m}} \right\}^2 + \left\{ \frac{q_b'' z U_{W_b}}{\dot{m}} \right\}^2 + \left\{ \frac{q_b'' W_b U_z}{\dot{m}} \right\}^2 + \left\{ \frac{q_b'' W_b z U_{\dot{m}}}{\dot{m}^2} \right\}^2} \quad (3.84)$$

The relative uncertainty in both liquid and vapour superficial velocities are found from Eq. (3.85) and (3.86), respectively.

$$\frac{U_{J_l(z)}}{J_l(z)} = \sqrt{\left\{\frac{U_G}{G}\right\}^2 + \left\{\frac{U_{x(z)}}{(1-x(z))}\right\}^2} \quad (3.85)$$

$$\frac{U_{J_g(z)}}{J_g(z)} = \sqrt{\left\{\frac{U_G}{G}\right\}^2 + \left\{\frac{U_{x(z)}}{x(z)}\right\}^2} \quad (3.86)$$

All the above absolute and relative uncertainties of the measured variables can be found in Table 3.5. For example, the absolute uncertainty of the channel width $U_{W_{ch}}$ is ± 0.002 mm, while the uncertainty of the base width U_{W_b} is ± 0.01 mm. Moreover, the relative uncertainty of the mass flow rate ($\frac{U_{\dot{m}}}{\dot{m}}$) is $\pm 0.1\%$. The uncertainties of the calculated (derived) variables are summarized in Table 3.6, Table 3.7 and Table 3.8.

Table 3.6 The uncertainty ranges for single-phase experiments.

Parameter	Unit	Uncertainty
Hydraulic diameter	mm	± 0.3 – 0.39 %
Aspect ratio	-	± 0.54 – 0.64 %
Heat transfer area	m ²	± 0.18 – 0.32 %
Mass flux	kg/m ² s	± 0.547 – 0.646 %
Heat flux	kW/m ²	± 1.17 – 5.8 %
Channel friction factor	-	± 1.46 – 2.99 %
Average Nusselt number	-	± 1.3 – 11.9 %

Table 3.7 The uncertainty ranges for flow boiling experiments.

Parameter	Unit	Uncertainty
Mass flux	kg/m ² s	± 0.32 – 0.64 %
Heat flux	kW/m ²	± 0.078 – 6.88 %
Local heat transfer coefficient	kW/m ² K	± 0.66 – 13.48 %
Local vapour quality	-	± 0.302 – 24.7 %

Table 3.8 The uncertainty ranges for flow condensation experiments.

Parameter	Unit	Uncertainty
Mass flux	kg/m ² s	± 0.26–0.7 kg/m ² s
Heat flux	kW/m ²	± 3.8–16 %
Local heat transfer coefficient	kW/m ² K	± 3.6–21 %
Local vapour quality	-	± 0.012–0.07

3.7 Experimental Procedure

This section describes the experimental procedures during single and two-phase flow experiments. The steps of preparation for experiments are first presented in section 3.7.1, while the single-phase flow experiments procedures are described in section 3.7.2. The flow boiling and condensation experiments procedures are then described in section 3.7.3 and 3.7.4, respectively.

3.7.1 Preparation for experiments

A preparation stage is considered an important initial procedure before conducting the experiments to ensure the overall stability of the rig. In a microchannel system, the trapped gases could cause several problems during the experiments, such as delaying the steady state condition, flow instability and inaccurate measurements. It is known that under ambient conditions, this HFE-7100 contains 53% of air by volume, *i.e.* a concentration of about 366 ppm, Hsu et al. (2015). This dissolved air can affect the thermal performance in micro scale heat sinks. Chen and Garimella (2006a) showed that degassing the dielectric refrigerant has a strong impact on the pressure drop and heat transfer coefficient. Therefore, a degassing process was conducted before starting the experiments to ensure that pure refrigerant is circulated in the rig. The steps of this process are summarized as follows:

1. Switch on the data logger, and then run the LabView software after turning the computer on.
2. All valves at the fluid loop, except the drain and vent valves, should be opened.
3. Turn the micro-gear pump on, at high flow rate (e.g. 500 ml/min) for fifteen minutes to flash any trapped gases in the loop to the reservoir.

4. Turn the pump off and close all valves to isolate the liquid reservoir from the rig.
5. Switch on the heater inside the reservoir by running the Variac. This leads to increase the pressure inside the reservoir.
6. Switch on the chiller unit while the liquid is boiling in the reservoir. Thus, the vapour condenses back to the reservoir while the gases remain trapped in the top of the condenser. Note that, at this stage, the saturation pressure, corresponding to the measured fluid temperature in the reservoir, does not equal the measured pressure in the reservoir. This is due to the trapped gases inside the reservoir.
7. When the pressure inside the reservoir reaches 1.3 bar, *i.e.* more than the ambient pressure, open the vent valve periodically to release any gases to the ambient. The vent valve should be opened carefully and closed rapidly to prevent any waste fluid. The previous steps should be repeated for about one hour until the saturation pressure (corresponding to the measured temperature in the reservoir) equals the measured pressure in the reservoir.
8. Open all valves of the rig and turn the pump on to drive the fluid into the flow loop. Note that, the chiller unit supplies chilled water-glycol solution to the sub-cooler. Therefore, the fluid temperature before the pump should be kept lower than the saturation temperature at the pump suction. This is an important point to ensure that cavitation does not occur in the pump.
9. The rig is now ready for conducting experiments.

3.7.2 Single-phase experiments

Single-phase experiments were carried out before two-phase experiments to validate the experimental rig. The Fanning friction factor and average Nusselt number are the major parameters that should be calculated during these experiments. Therefore, two types of experiments were conducted in the present study, namely adiabatic and diabatic experiments. Adiabatic experiments were used to obtain the friction factor data as follows:

1. Switch on the data logger and the computer on. Then run the LabView software.

2. Switch on the heater inside the liquid reservoir to increase the pressure to the required system pressure, e.g. 1 bar.
3. Switch on the chiller unit to supply chilled solution to the reflux condenser, inside the reservoir, and the sub-cooler.
4. Turn the micro-gear pump on and adjust the first mass flow rate using the digital driver. The value of mass flux can be checked from the LabView software.
5. Switch on the pre-heater and set the inlet liquid temperature, at the test section, to the required level. This temperature can be controlled using the Variac.
6. After the steady state condition is reached, *i.e.* temperatures, pressures and mass flow rates become stable, record all the measuring data via the LabView software for about two minutes.
7. Adjust to different mass flow rates and record the data.
8. After finishing the experiments, turn all the equipment off, such as the pre-heater, the micro-gear pump, the heater inside the reservoir, the chiller unit, the data logger and the computer.

Diabatic experiments were carried out to obtain the heat transfer data as follows:

1. Follow the steps from 1 to 5 for the previous experiments.
2. Switch on the cartridge heaters inside the test section. Use the Variac to regulate the input voltage. Note that, the input power should not cause boiling inside the test section.
3. Record all the measuring data using the LabView software, after steady state condition is reached. Steady state is confirmed when there are small oscillations in temperatures, pressures and mass flow rates. The recording time should be saved for two minutes.
4. Increase the mass flow rate to a new value by adjusting the micro-gear pump speed and repeat step 3.
5. Repeat step 4 by choosing different mass flow rates.
6. After finishing the experiments, turn all the equipment off.

Single-phase experiments using the microchannel condenser were also conducted in this study as follows:

1. Follow step 1–4 for the adiabatic experiments.
2. Switch on the tubular evaporator to select the inlet refrigerant temperature at the condenser.
3. Adjust the inlet water temperature and the water flow rate to the required value. The inlet temperature can be selected from the chiller unit (see Fig. 3.4), while the flow rate can be adjusted from the regulator valve (see Fig. 3.8(b)).
4. Record all data after steady state condition is reached.
5. Choose different mass flow rates and record the data.
6. Turn all the equipment off, after finishing the experiments.

3.7.3 Flow boiling experiments

Flow boiling experiments were performed to calculate the flow boiling heat transfer coefficient, flow boiling pressure drop, instability data and flow patterns for a range of heat and mass fluxes. The procedure for these experiments is described as follows:

1. Turn the computer on, switch on the data logger and then run the LabView software.
2. Switch on the heater inside the liquid reservoir to adjust the system pressure at 1 bar.
3. Switch on the chiller unit to supply chilled water to the reflux condenser and the sub-cooler.
4. Turn the micro-gear pump on and adjust the first mass flow rate.
5. Switch on the pre-heater and set the inlet sub-cooling to the required level, e.g. 5 K.
6. Switch on the cartridge heaters inside the test section using the Variac to regulate the power supply.
7. After steady state condition is reached, record all the measuring data for about two minutes.
8. Flow visualization is recorded at three locations (above each thermocouple location) when the measuring data is saved. These locations are at the centre of the test section near the channel inlet, near middle and near outlet.
9. Repeat step 6 and adjust a new power supply. Save all the data when the steady state condition is achieved. Increase the power supply until the exit

vapour quality, at the test section, reaches nearly one. Note that, when the dryout condition happens inside the test section, the thermocouple readings at the first row, *i.e.* near the channel bottom, increase suddenly. It is worth mentioning that the increase in power supply leads to increase the heat flux in the test section and thus high flow resistance occurs during the flow boiling experiments. This leads to an increase in the inlet pressure and a decrease of the mass flow rate. Therefore, the pressure inside the liquid reservoir should be decreased to the required level by decreasing the temperature. Moreover, the micro-gear pump speed should be increased to achieve the required value of the mass flow rate.

10. Choose different mass flow rates, based on the experiment ranges, and repeat the steps from 7 to 9.
11. After finishing the experiments, switch off the cartridge heaters and the pre-heater, and then wait until all the wall temperatures of the test section decrease to prevent burnout of the test section. Then turn all the equipment off.

3.7.4 Flow condensation experiments

The parameters that are calculated during these experiments are local two-phase heat transfer coefficient, local vapour quality and flow pattern maps. The procedure of flow condensation experiments is described step by step as follows:

1. Follow the steps from 1 to 4 for the flow boiling experiments.
2. Adjust the inlet water temperature, at the condenser, to the required level. Note that, the required temperature can be set from the chiller unit.
3. Select the required water flow rate using the regulator valve, see Fig. 3.8(b). Check the LabView software to set the exact value.
4. Switch on the pre-heater and the tubular evaporator. Use the Variac to adjust the power supply to the required level. Note that, the power supply should be increased step by step until the inlet vapour quality at the condenser reaches nearly one. The value of the vapour quality can be monitored from the LabView software.

5. After steady condition is achieved, record all the data for two minutes. A high-speed camera is used to record the flow patterns inside the condenser at three locations, *i.e.* near the channel inlet, middle and outlet.
6. Repeat step 2 to set a new inlet water temperature and wait until the system becomes steady, then save all data.
7. When all the ranges of the inlet water temperature are tested, repeat step 3 to select new water flow rate. Record all the data after steady condition is achieved.
8. Repeat step 7 to test all ranges of the water flow rate.
9. Adjust a new refrigerant mass flux by changing the micro-gear pump speed and repeat steps 2–8.
10. After finishing all experiments, turn the pre-heater and the evaporator off and wait until the flow inside the condenser becomes at single-phase condition. After that, switch off all the equipment.

3.8 Experimental Test Conditions

In the present study, HFE-7100 was examined in four microchannel evaporators and one microchannel condenser at a system pressure near atmospheric. The thermophysical properties of this fluid at 1 bar are presented in Table 3.9. The flow boiling experiments were carried out at inlet sub-cooling of 5 K and five mass fluxes of 50, 100, 150, 200 and 250 kg/m²s. The heat flux was increased gradually until the exit vapour quality became nearly one. The base heat flux reached up to 531.2 kW/m² at a mass flux of 250 kg/m²s during this study. The flow condensation experiments were conducted at saturation temperature of 59.6 °C (inlet pressure of 1 bar) and refrigerant mass flux of 48, 64, 86, 108 and 126 kg/m²s, while the inlet vapour quality was set near superheat. The inlet water temperature ranged from 20 to 40 °C (20, 25, 30, 35 and 40 °C), while three water flow rates were examined, *i.e.* 0.5, 0.8 and 1.1 L/min. The experimental conditions of flow boiling and condensation are presented in Table 3.10 and 3.11, respectively.

Table 3.9 Thermophysical properties of HFE-7100 at 1 bar, based on EES software.

T_{sat} [°C]	i_{lg} [J/kg]	ρ_l [kg/m ³]	ρ_g [kg/m ³]	k_f [W/mK]	C_p [J/kgK]	σ [N/m]
59.6	111661	1373	9.575	0.06206	1157	0.0136

Table 3.10 Flow boiling test conditions.

Condition	TS.1	TS.2	TS.3	TS.4
System pressure [bar]	1	1	1	1
Saturation temperature [°C]	59.6	59.6	59.6	59.6
Inlet sub-cooling [K]	5	5	5	5
Mass flux [kg/m ² s]	50–250	50–250	50–250	50–250
Base heat flux [kW/m ²]	33.5–531.2	25.3–414.8	21.7–335.3	30.05–433.5
Exit vapour quality [-]	0–1	0–1	0–1	0–1

Table 3.11 Flow condensation test conditions (TS.5).

Refrigerant side	HFE-7100
System pressure [bar]	1
Saturation temperature [°C]	59.6
Mass flux [kg/m ² s]	48–126
Inlet vapour quality [-]	0.95–1
Coolant side	Water
Inlet temperature [°C]	20–40
Flow rate [L/min]	0.5–1.1

3.9 Overall Validation

Before conducting flow boiling and condensation experiments, several steps were performed to check the overall validation of the experimental facility. In this section, the temperature and heat flux distribution is presented in Section 3.9.1, while the single-phase validation is described in Section 3.9.2.

3.9.1 Temperature and heat flux distribution

Both the temperature and heat flux distribution along the test section, *i.e.* microchannel evaporator, should be checked to ensure the uniform heat flux and temperature distribution and the validity of the 1D heat conduction assumption. Firstly, a simple thermal simulation was carried out using Fusion 360 software (www.autodesk.com) to check the following issues:

1. Analyse the uniformity of the heat flux and temperature distribution under the channels bottom.
2. Analyse the heat losses at both inlet and outlet plena.
3. Check the height of the heating part (see Fig. 3.16(b)) that provides uniform wall temperature distribution near the channels bottom.

The test section (1) was simulated in this study, with an overall size of 94.5 mm height, 26 mm width and 51 mm long, see Fig. 3.16(a), assuming the following boundary conditions:

1. Three zones were assumed in the heat sink; liquid single-phase at the inlet plenum, two-phase flow at the channels and vapour single-phase at the outlet plenum as shown in Fig. 3.30.
2. A convective heat transfer coefficient was calculated for these zones using Shah and London (1978) (for single-phase laminar flow in three walls heat transfer), Shah (2017) (for flow boiling in multi-microchannels) and Dittus-Boelter equation (for single-phase turbulent flow). These correlations are presented in Appendix B.
3. Inlet fluid temperature of 55 °C, system pressure of 1 bar, mass flux of 250 kg/m² s and vapour quality at the channels exit of 1 were assumed in order to calculate the above correlations.
4. The fluid temperature contacting the superficial area of the inlet plenum, the microchannels and the outlet plenum was assumed to be 55, 60 and 60 °C, respectively.
5. Different heat sources ranging from 50 to 500 W were defined at the cartridge heaters. This corresponds to the base heat flux of 0.1–1 MW/m².
6. An adiabatic condition was assumed for all surfaces of the heat sink block.
7. Steady state condition and constant properties were assumed.

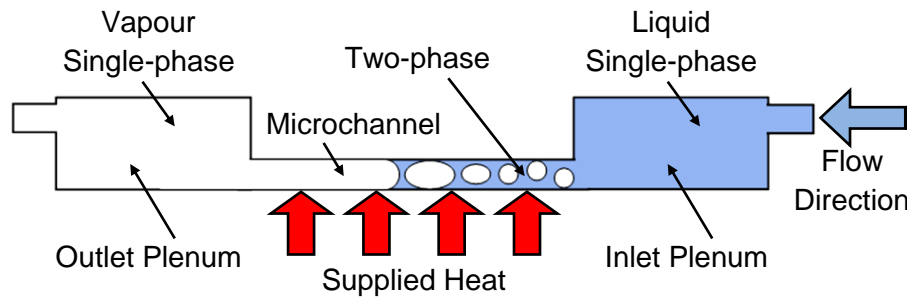
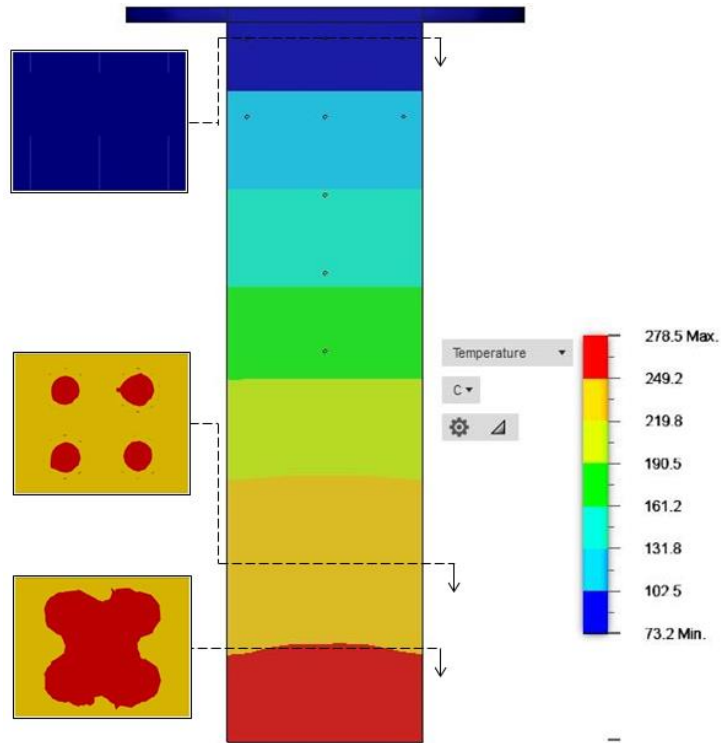
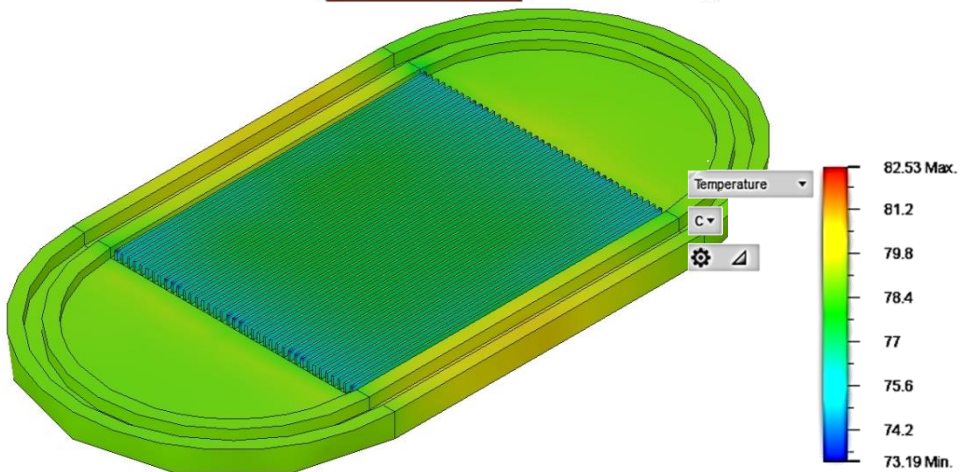


Figure 3.30 Flow boiling along the test section.

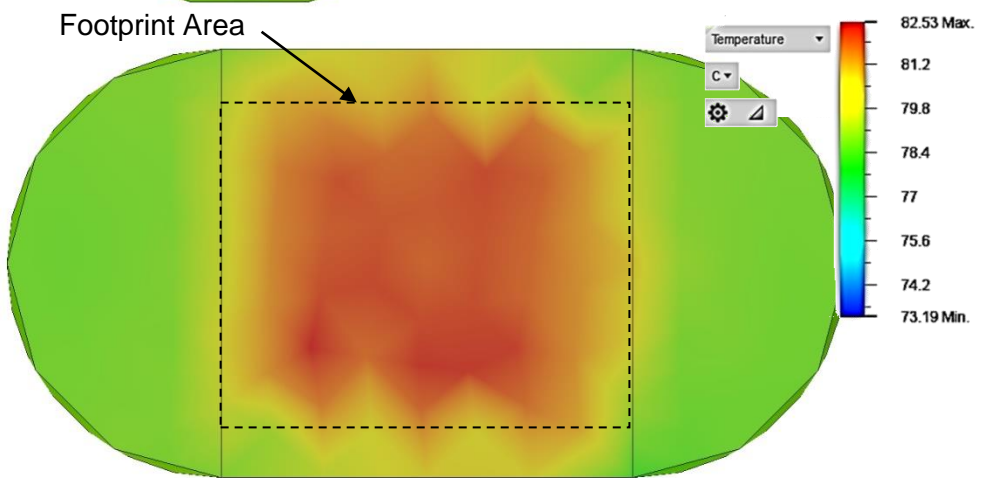
A set of simulation results are presented in Fig. 3.31 that show the contour of temperature and heat flux distribution in the heat sink block. The red and blue areas represent the hottest and coldest parts, respectively. The results indicate that the isothermal lines are not uniform at the heat source, *i.e.* cartridge heaters, as shown in Fig. 3.31(a). However, these lines become uniform near the channels bottom, *i.e.* footprint area. It seems that the heating part with height of 92 mm provides uniform wall temperature distribution near the channels. The uniform temperature distribution along the heat sink is also clear as depicted in Fig. 3.31(b). This figure just presents the heat sink, *i.e.* the heating part is hidden, to clarify the contour of temperature distribution on this part.



(a)



(b)



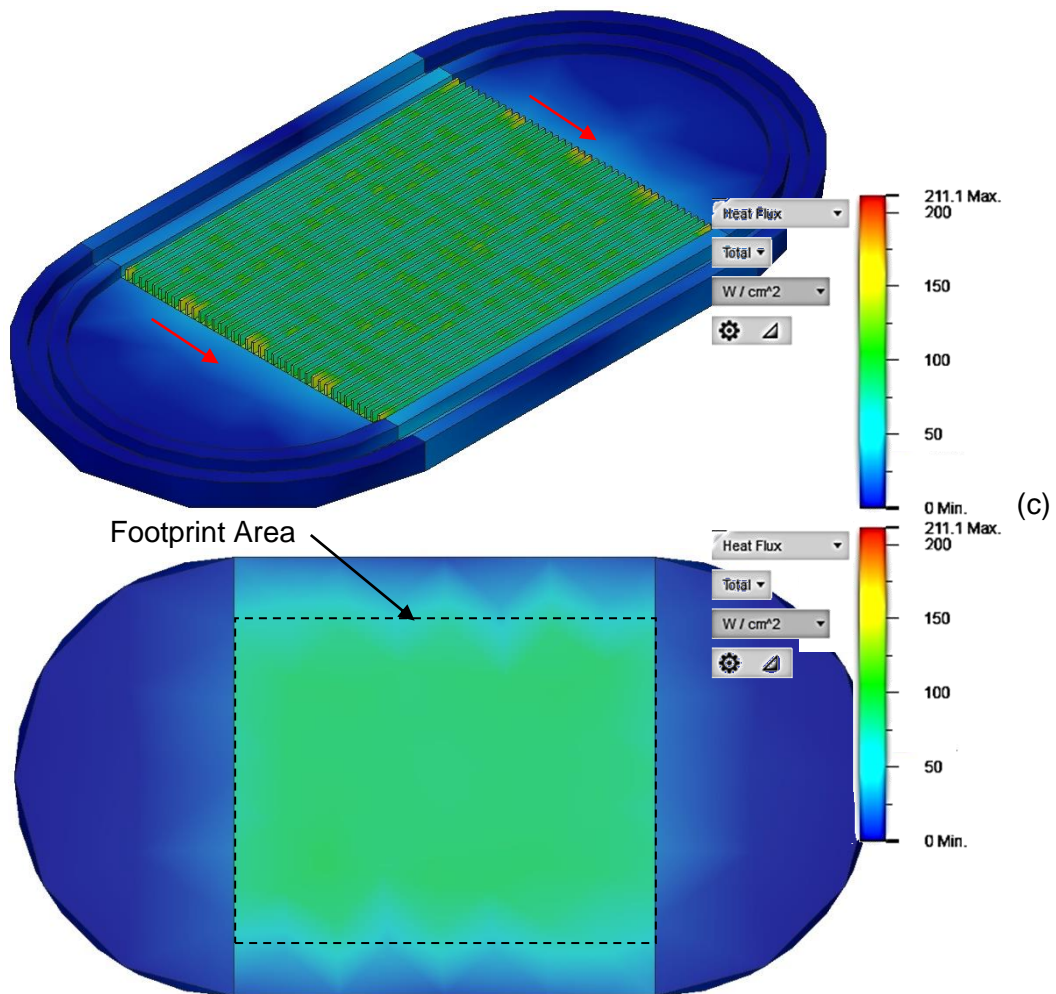


Figure 3.31 Contours of temperature and heat flux distribution for TS.1:

- (a) Temperature in the heat sink block
- (b) Temperature in the heat sink
- (c) Heat flux in the heat sink. The scale of (b and c) is changed to clarify the contour distribution.

This figure demonstrates that uniform heat flux distribution along the channels is found. It also shows that there is a small amount of heat loss in both the inlet and outlet plena, see the red arrows. The percentage of this heat loss is presented in Fig. 3.32. It can be seen that the heat loss varies from 2.5 to 7.5% depending on the supplied heat. The percentage heat loss decreases with increasing input power. It is worth mentioning that most experimental flow boiling ranges were within a heat rate more than 100 W. Accordingly, the heat losses in these two parts is very small, *i.e.* less than 6%.

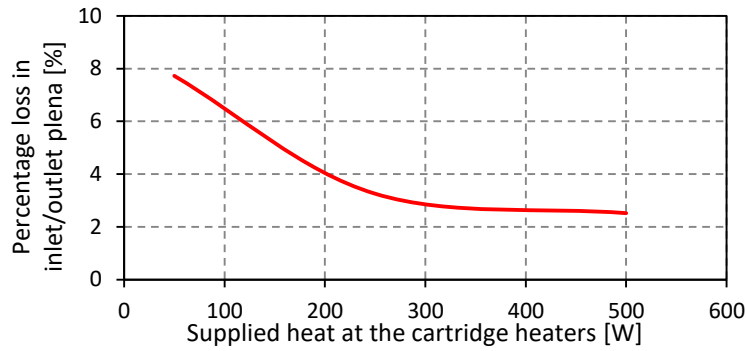


Figure 3.32 Heat losses at the inlet and outlet plena for TS.1.

In addition to the above simulation study, both single and two-phase flow experiments were also conducted. As mentioned above, twelve thermocouples were inserted in the heat sink block to measure and check the temperature distribution during the experiments. Moreover, a set of these thermocouples were used to check the temperature distribution in the vertical direction to validate the 1D heat conduction assumption. In single-phase experiments, the uniform wall temperature method (UWT) was used to determine the average heat transfer coefficient during the evaporator as described in the data reduction section. This was experimentally confirmed by presenting Fig. 3.33, which illustrates the temperature distribution for TS.3 at three locations, *i.e.* the first row of thermocouples, at inlet fluid temperature of 30 °C, two different mass fluxes and wall heat flux of 23 kW/m². As seen in this figure, the temperature variations in the axial direction was very small with the temperature difference being only 0.82 K for 300 kg/m²s and 0.5 K for 700 kg/m²s in this example.

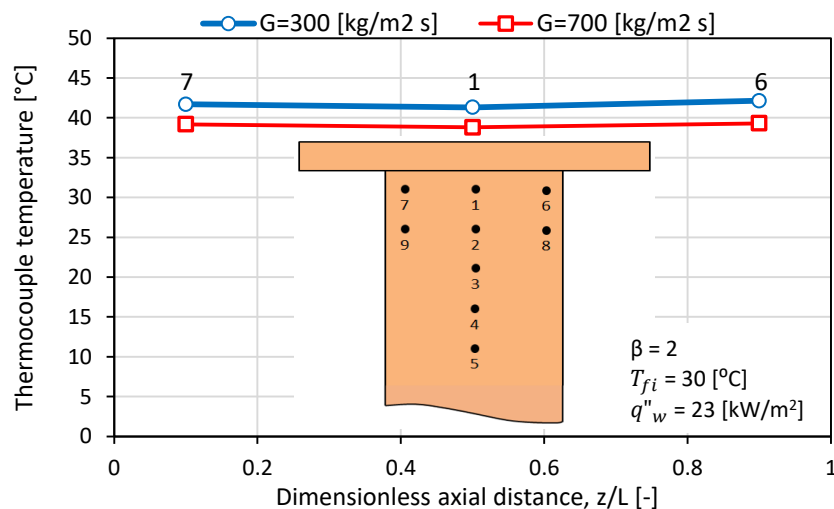
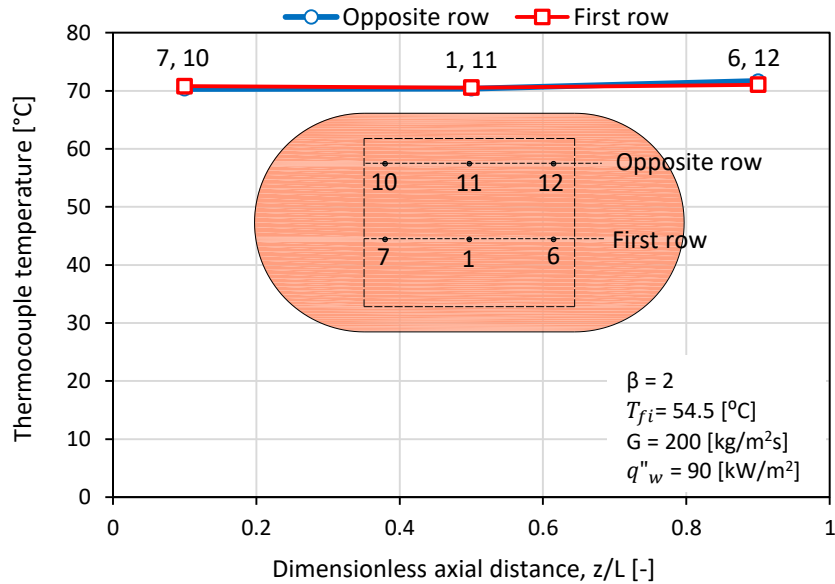
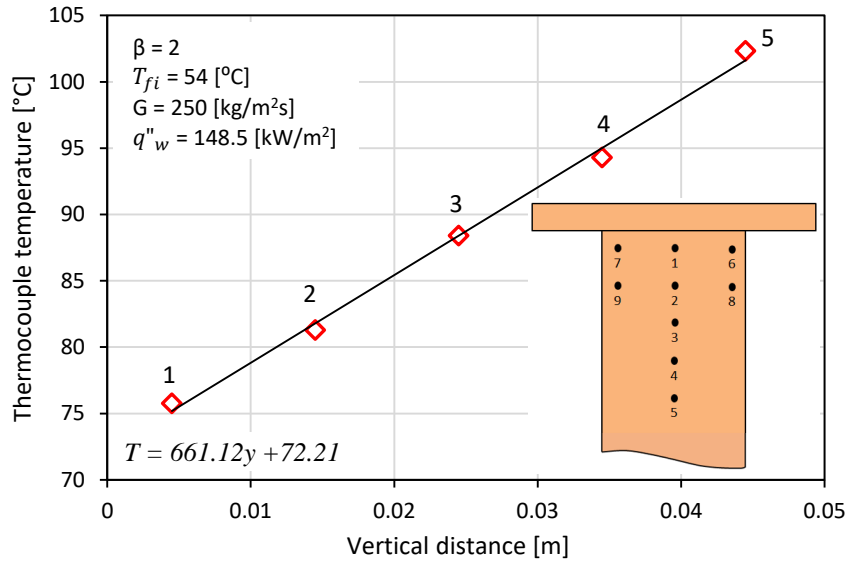


Figure 3.33 Temperature distribution in the axial direction during single-phase flow for TS.3.

Fig. 3.34(a) presents the temperature distribution at six locations underneath the channels at a distance of 4.15 mm, *i.e.* three thermocouples at the mid plane and other three thermocouples at the side plane. This figure was plotted for two-phase flow at wall heat flux of 90 kW/m^2 , inlet fluid temperature of $54.5 \text{ }^\circ\text{C}$ and mass flux of $200 \text{ kg/m}^2\text{s}$.



(a)



(b)

Figure 3.34 Temperature distribution during two-phase flow for TS.3 at mass flux of
(a) $200 \text{ kg/m}^2\text{s}$ (b) $250 \text{ kg/m}^2\text{s}$.

The results clearly demonstrate that the temperature distribution was uniform in the transverse direction, *i.e.* the heat transfer coefficient in the mid channels is nearly similar to that in the side channels. This might also indicate the uniformity of flow

distribution with the present design. In multi-channel configurations, heat flux can be defined using the total channel surface area A_{ht} (wall heat flux) or the heat sink base area A_b (base heat flux), see Fig. 1.9(b). The single/two-phase heat transfer coefficients calculations and the assessment of existing correlations were based on the wall heat flux. The heat flux in the vertical direction was estimated from the vertical temperature gradient at based on the assumption of 1D heat conduction (see Eq. 3.14). Five thermocouples were plotted along the vertical distance from the bottom of the channels and a best-fit linear equation was obtained. As an example, Fig. 3.34(b) presents the two-phase flow results at wall heat flux of 148.5 kW/m^2 (input power by the cartridge heaters of 130.5 W), inlet fluid temperature of $54 \text{ }^\circ\text{C}$ and mass flux of $250 \text{ kg/m}^2\text{s}$. This figure shows that the vertical temperature gradient was almost linear and thus there was negligible heat loss in the transverse directions. In this case, the heat transfer rate was 129.91 W , *i.e.* the present heat loss was 0.45% . This and the above discussion validate the assumption of 1D heat conduction and minimal heat losses in the transverse and axial direction of the channels.

3.9.2 Single-phase validation

Both adiabatic and diabatic experiments were conducted at system pressure near 1 bar and different mass fluxes to ensure all the instruments work properly and within reasonable accuracy. These experiments were performed using four evaporators, *i.e.* test section (1), (2), (3) and (4), at inlet fluid temperature of $30\text{--}32 \text{ }^\circ\text{C}$ and mass flux of $100\text{--}1000 \text{ kg/m}^2\text{s}$. For diabatic experiments, low input powers ranging from 15 to 20 W were set since the boiling incipience of HFE-7100 occurred at low values. Moreover, single-phase experiments were conducted for the counter-current flow condenser at a system pressure of 1 bar, inlet refrigerant temperature ranging from 41 to $44 \text{ }^\circ\text{C}$, mass flux from 48 to $340 \text{ kg/m}^2\text{s}$, inlet water temperature of $17.5 \text{ }^\circ\text{C}$ and water flow rate of 0.3 L/min . The experimental results were compared with existing correlations for calculating the friction factor and Nusselt number. These correlations, see below, were proposed for conventional and microchannels. The mean absolute error was used to evaluate these correlations as follows:

$$MAE = \frac{1}{N} \sum \left| \frac{\Delta P_{pred} - \Delta P_{exp}}{\Delta P_{exp}} \right| 100\% \quad (3.87)$$

where N is the total number of data points.

Fanning friction factor correlations

Shah and London (1978) proposed two correlations for developing and fully developed flow in the laminar region for conventional channels as presented in Eq. (3.88) and (3.90), respectively. These correlations were compared with the experimental Fanning friction factor. The values of K_∞ and C are given in Table 3.4.

$$f_{app} = \frac{3.44}{Re\sqrt{L^*}} + \frac{f_{FD}Re + \frac{K_\infty}{4L^*} - 3.44/\sqrt{L^*}}{Re(1 + C(L^*)^{-2})} \quad (3.88)$$

$$L^* = L/ReD_h \quad (3.89)$$

$$f_{FD} = \frac{24}{Re} (1 - 1.355\beta + 1.946\beta^2 - 1.7012\beta^3 + 0.9564\beta^4 - 0.2537\beta^5) \quad (3.90)$$

The experimental Fanning friction factor versus Reynolds number is shown in Fig. 3.35. It is clear that the experimental results were in a good agreement with the correlation by Shah and London (1978) for fully developed flow. Their correlation predicted the data point of test section (1) with a mean absolute error of 11.1%.

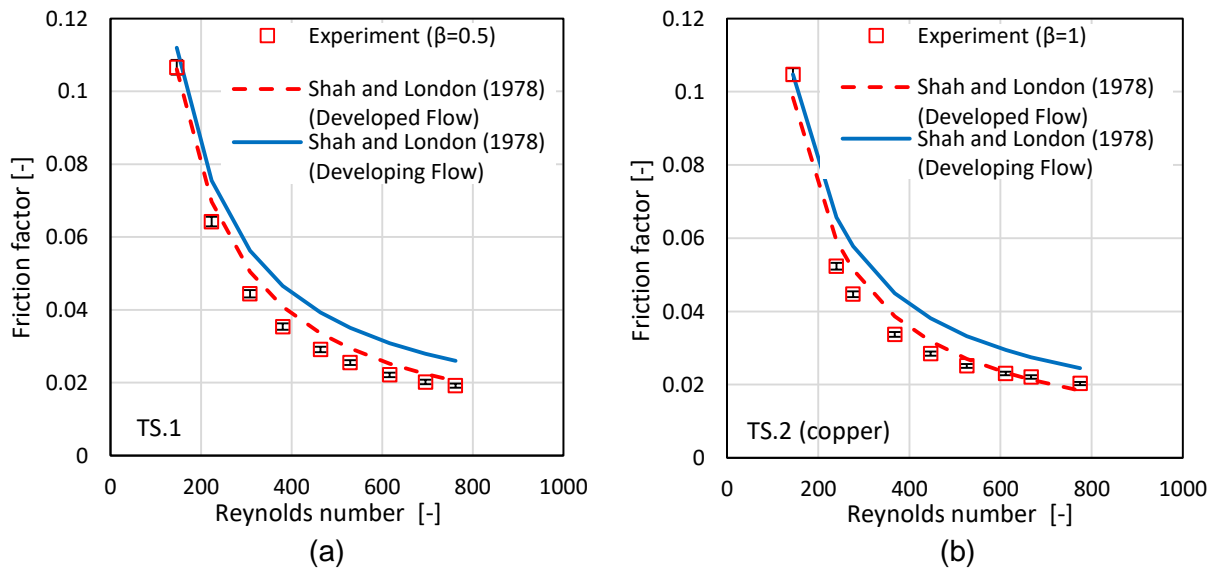


Figure 3.35 Single-phase Fanning friction factor versus Reynolds number for:

(a) TS.1 (b) TS.2 (c) TS.3 (d) TS.4 (e) TS.5.

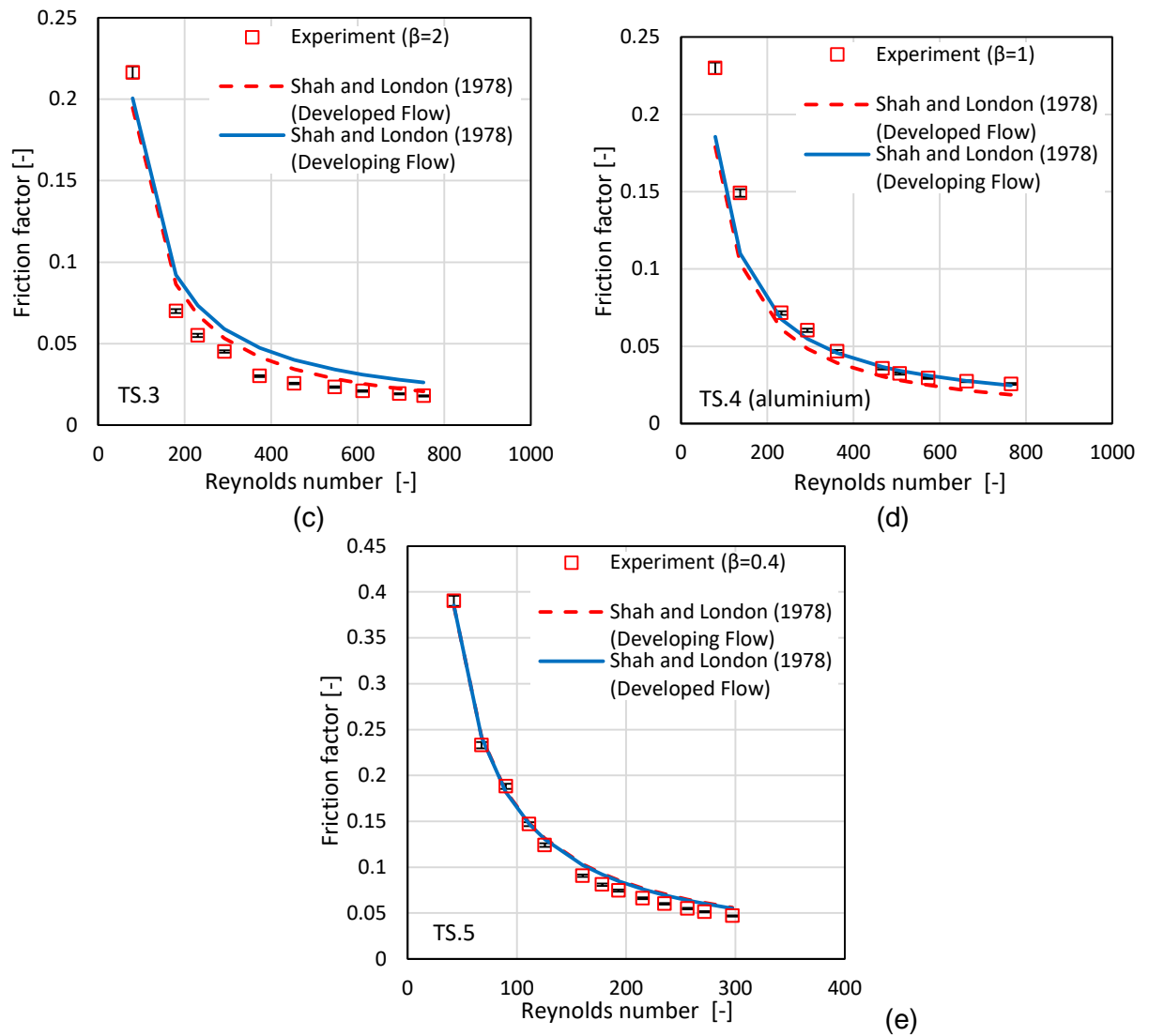


Figure 3.35 Continued.

All the experimental data of test section (2) were predicted well by this correlation with a mean absolute error of 9.2%. A good agreement with the data of test section (3) was found with a mean absolute error of 22.1%. Their correlation also predicted well the data points of test section (4) with a mean absolute error of 19.6%. The comparison with the data of test section (5) showed that there was a reasonable agreement with their correlation, *i.e.* with a mean absolute error of 10.4%.

Single-phase Nusselt number correlations

Existing correlations for calculating the average Nusselt number were compared with the experimental results. These correlations were proposed for horizontal non-circular conventional and microchannels as follows:

Laminar flow correlation by Stephan and Preuber (1979) as mentioned by Liu and Yu (2011):

$$Nu = 4.364 + \frac{0.086(RePrD_h/L)^{1.33}}{1 + 0.1Pr(ReD_h/L)^{0.83}} \quad (3.91)$$

Laminar flow correlation by Peng and Peterson (1996):

$$Nu = 0.1165 \left(\frac{D_h}{W_c}\right)^{0.81} \left(\frac{H_{ch}}{W_{ch}}\right)^{-0.79} Re^{0.62} Pr^{1/3} \quad (3.92)$$

$$W_c = W_{ch} + W_{fin} \quad (3.93)$$

Laminar flow correlation by Jiang et al. (2001):

$$Nu = 0.52L^{*-0.62}, \text{ for } L^* < 0.05 \quad (3.94)$$

$$Nu = 2.02L^{*-0.31}, \text{ for } L^* > 0.05 \quad (3.95)$$

$$L^* = L/RePrD_h \quad (3.96)$$

Developing laminar flow correlation by Lee and Garimella (2006) as mentioned by Lee and Garimella (2008):

$$Nu = 1.766L^{*-0.378}\beta^{0.1224} \quad (3.97)$$

Developing laminar flow correlation by Mirmanto (2013):

$$Nu = Re^{0.283} Pr^{-0.513} L^{*-0.309} \quad (3.98)$$

Fig. 3.36 depicts the experimental average Nusselt number versus Reynolds number for all test sections. The comparison with the results of test section (1) shows that the correlations by Stephan and Preuber (1979), Jiang et al. (2001) and Lee and Garimella (2006) showed poor prediction with a MAE of 48.1%, 53.8% and 60.8%, respectively. In contrast, a reasonable agreement was found with the correlations by Peng and Peterson (1996) and Mirmanto (2013) with a MAE of 11.1% and 14.1%, respectively. The experimental results of test section (2) indicates that the Nusselt number correlations by Stephan and Preuber (1979), Peng and Peterson (1996), Jiang et al. (2001) and Lee and Garimella (2006) predicted the present results with a MAE of 36.5%, 43.7%, 38.2% and 58.1%, respectively. However, the correlation by Mirmanto (2013) predicted well the results with a mean absolute error of 12.8%. The results of test section (3) show that the correlations by Peng and Peterson (1996) and Lee and Garimella (2006) predicted the experimental results with a MAE of 70.6% and 36.5%, respectively. The correlation by Jiang et al. (2001) showed poor prediction with a MAE of 30.2%. In contrast, the correlation by Stephan and Preuber (1979) predicted the results well with a MAE of 22.7%, while The correlation by

Mirmanto (2013) showed better prediction with a MAE of 9.8%. The comparison with the test section (4) depicts higher mean absolute error. The correlations by Stephan and Preuber (1979), Peng and Peterson (1996), Jiang et al. (2001) and Lee and Garimella (2006) showed poor prediction with a MAE of 79.41%, 73.2%, 72.88% and 101.83%, respectively. In contrast, a reasonable agreement was found with the correlation by Mirmanto (2013) with a MAE of 25.12%. It is clear that the existing correlations showed better agreement with the experimental results of test section (2) compared to that of test section (4). This could be due to the low thermal conductivity surfaces, such the aluminium surface of the test section, were not examined in these correlations. The Nusselt number comparison of test section (5) indicates that the correlation by Stephan and Preuber (1979) predicted the results with a MAE of 65.1%, while the correlation by Mirmanto (2013) showed a MAE of 46.4%. However, the experimental results were predicted very well by the correlations of Peng and Peterson (1996), Jiang et al. (2001) and Lee and Garimella (2006) and with a MAE of 21.7%, 19.6%, and 17.5%, respectively. It is worth mentioning that the correlation by Mirmanto (2013) showed a reasonable prediction of all data points of heat sinks, *i.e.* test sections (1), (2), (3) and (4). This could be due to these heat sinks had an adiabatic cover plate and heated from the bottom side, *i.e.* partly heated channels, which were similar to the those of Mirmanto (2013). In contrast, the correlations by Jiang et al. (2001) and Lee and Garimella (2006) predicted very well the single-phase data points of the condenser, *i.e.* test section (5). The reason could be Jiang et al. (2001) examined microchannel heat exchangers cooled by water. The present condenser was also cooled by water. This good agreement with Lee and Garimella (2006) could be due to the long channel length of 120 mm was investigated by them using laminar convective heat transfer in rectangular microchannels.

The single-phase results demonstrate that the calibration and measurement system can provide accurate results for the two-phase flow experiments.

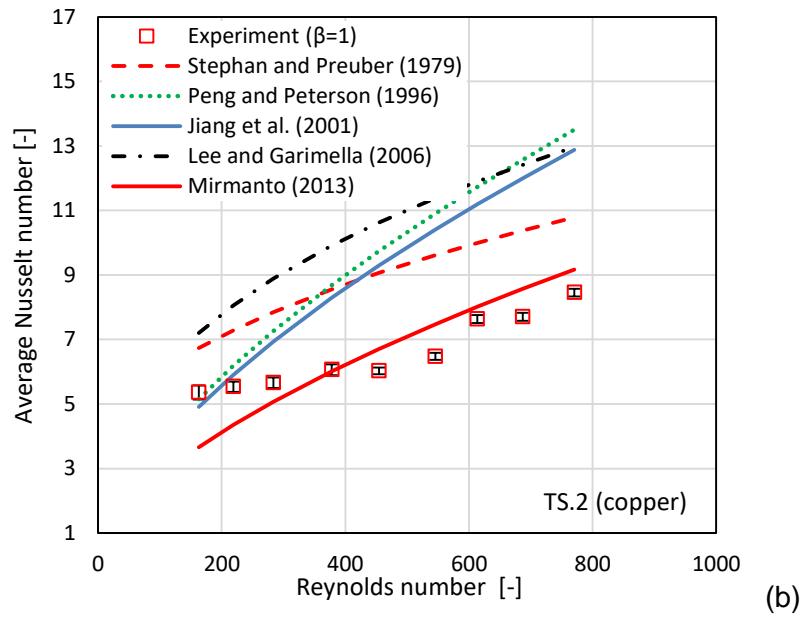
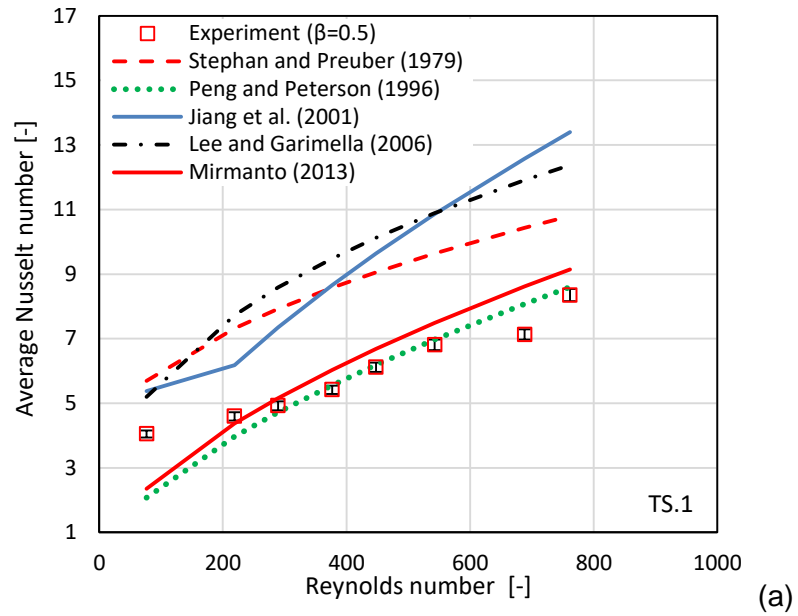
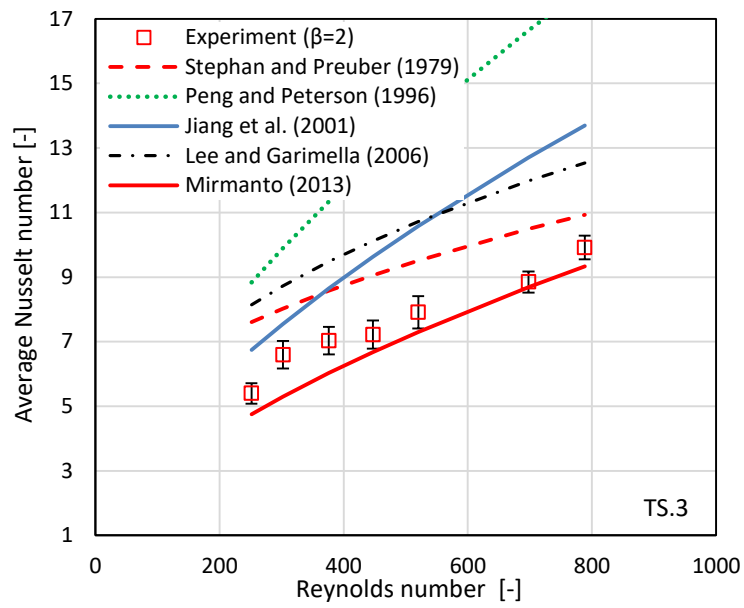
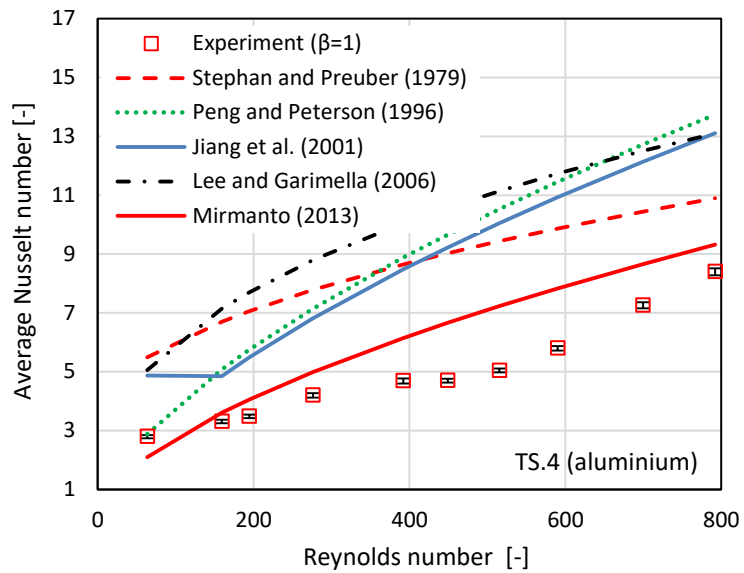


Figure 3.36 Single-phase average Nusselt number versus Reynolds number for:
 (a) TS.1 (b) TS.2 (c) TS.3 (d) TS.4 (e) TS.5.



(c)



(d)

Figure 3.36 Continued.

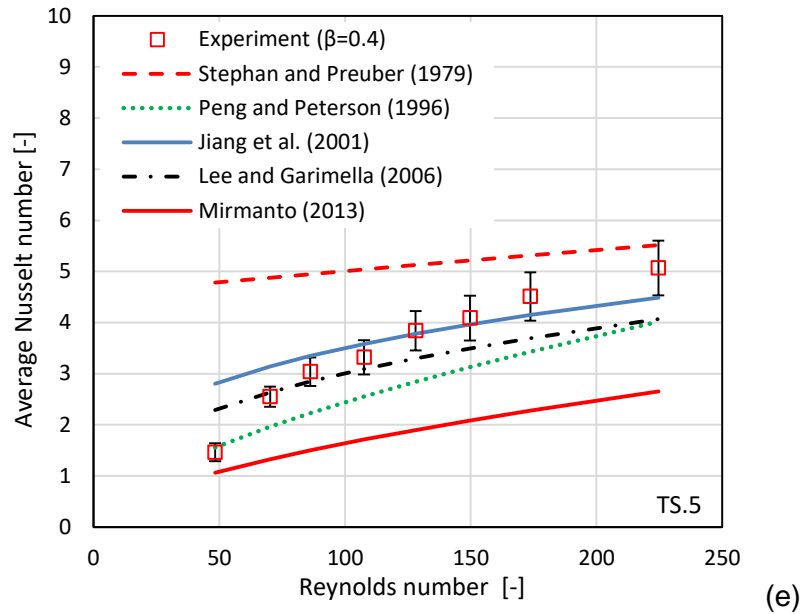


Figure 3.36 Continued.

3.10 Repeatability of the Data

The reliability of the present experimental data was checked by conducting the experiments at the same operating conditions after a period of time. After twenty days of the first flow boiling experiments, one set of experiment was chosen and repeated for each test section. Fig. 3.37 presents the repeatability of the present flow boiling heat transfer data at different wall heat and mass fluxes. It is obvious that the experimental data was repeatable with minor deviations. These minor deviations could be due to the variation in the nucleation density that could be affected by the surface conditions, *i.e.* aging effects. It is known that, for microchannels, the repeatability of the experimental data is not easy to attain since the thermal performance is significantly affected by the channel surface conditions. However, most of these deviations were within the experimental uncertainty values. The corresponding mean absolute error values between the data of day (1) and (2) were 8.8%, 4.85%, 2.37% and 4.65% for TS.1, TS.2, TS.3 and TS.4, respectively.

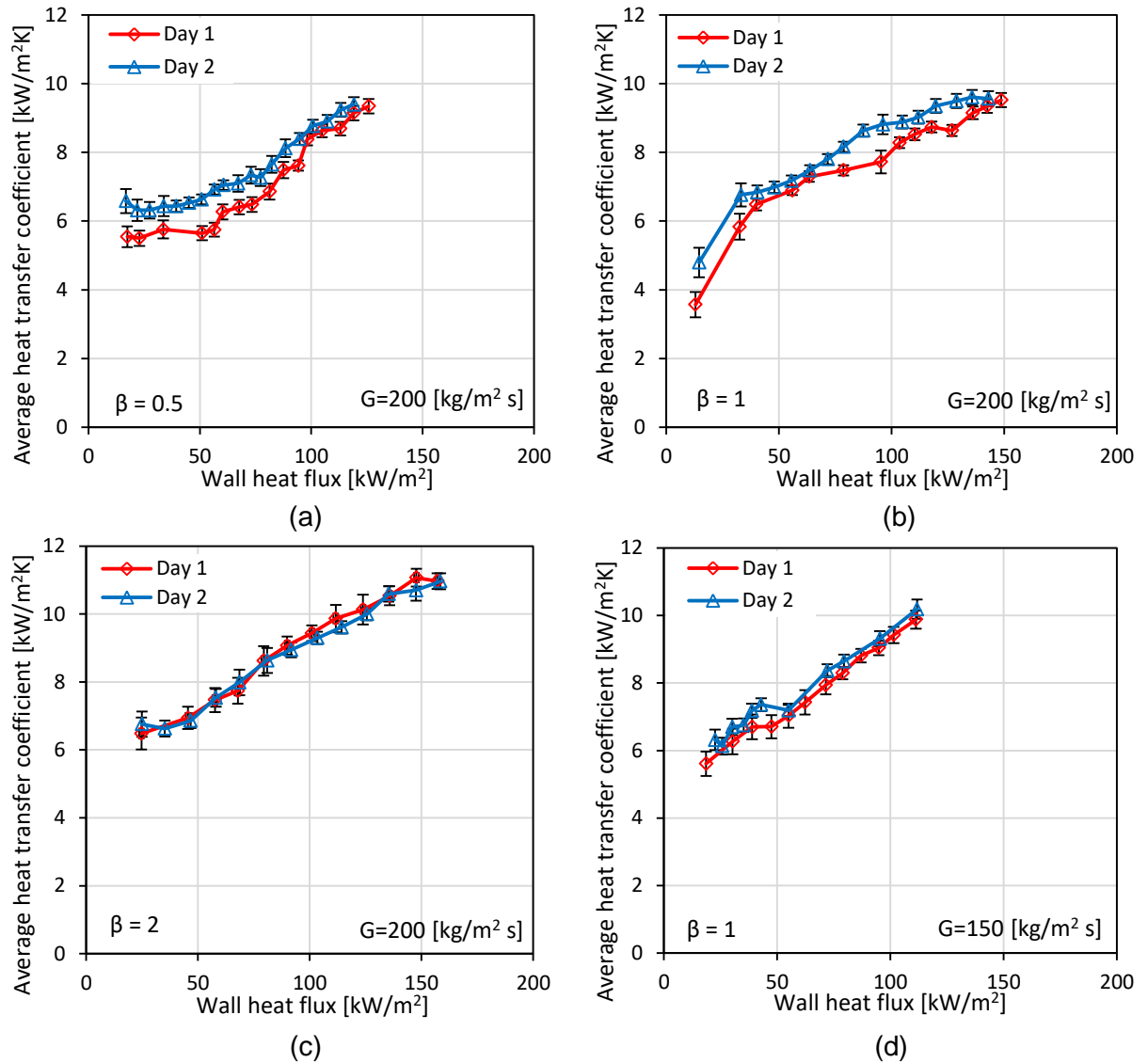


Figure 3.37 Repeatability of the experimental flow boiling heat transfer data for:
 (a) TS.1 (b) TS.2 (c) TS.3 (d) TS.4.

The present flow condensation experiments were also repeated after one month of the first experiment to check the reliability of the present data. Fig. 3.38 shows the repeatability of present heat transfer data at mass flux of $126 \text{ kg/m}^2 \text{ s}$, inlet water temperature of $40 \text{ }^\circ\text{C}$ and water flow rate of 1.1 L/min . This figure indicates that the trend of the local heat transfer coefficient versus local vapour quality for day (1) was similar to that for day (2). Moreover, the experimental data was repeatable with minor deviations, which were within the experimental uncertainty values. The corresponding mean absolute error value between these two sets of data was 9%. The two previous figures demonstrate that the repeatability of the experimental flow boiling and condensation data was reasonable and within the expectable ranges.

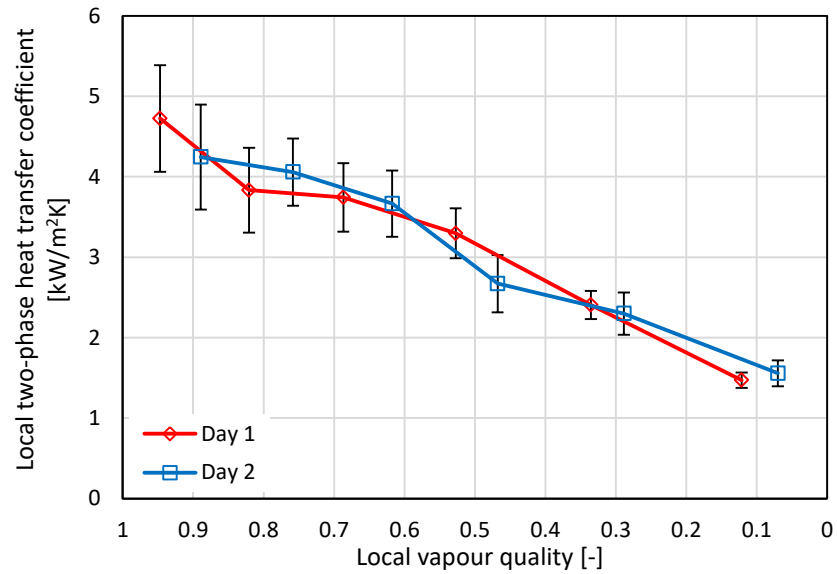


Figure 3.38 Repeatability of the experimental flow condensation heat transfer data at mass flux of $126 \text{ kg/m}^2\text{s}$, inlet water temperature of $40 \text{ }^\circ\text{C}$ and water flow rate of 1.1 L/min for the test section (5).

3.11 Summary

Flow boiling and condensation experiments were carried out at specific ranges during the present study. The test rig was well validated and all the measuring instruments, *i.e.* thermocouples and pressure transducers, were carefully calibrated to ensure high precision results. Three microchannel evaporators made of oxygen-free copper were designed and manufactured. These test sections had the same channel hydraulic diameter and base area and nearly constant surface roughness but different channel aspect ratios. Another microchannel evaporator made of aluminium at aspect ratio of 1 was also manufactured and tested. In order to design and study the thermal performance of a micro-scale cooling system, microchannel condenser was also manufactured and examined during this study. Flow visualization was conducted during flow boiling and condensation experiments using Phantom high-resolution high-speed camera. The experimental flow boiling and condensation data was repeated after a period of time to validate the repeatability of the data. This repeatability was reasonable and within the expected ranges. The experimental facility was then considered well validated and ready to carry out the necessary experiments to achieve the research objectives.

Chapter 4

Flow Boiling Patterns: Results and Discussion

4.1 Introduction

Flow boiling experiments were carried out at system pressure of 1 bar, different mass fluxes and inlet sub-cooling of 5 K. The heating power was supplied gradually until the exit vapour quality reached one. The experimental flow visualization patterns are presented in Section 4.2, while the experimental flow pattern maps are given in Section 4.3. The effect of heat flux, mass flux, aspect ratio and surface material are discussed in Sections 4.4-7. Section 4.8 presents a comparison between the present flow patterns and some existing flow pattern maps. A final summary is given in Section 4.9.

4.2 Experimental Flow Visualization Patterns

In the present study, flow visualization was conducted along the mid plane of the heat sink at three locations; near the channel inlet, middle and outlet, using a Phantom high-speed camera and a microscope. This camera was located above each thermocouple along the channels, see Fig. 4.1. Flow observation was sometimes carried out at other locations, *i.e.* between the previous locations, to capture more details. The visualization study showed that, for all test sections, four main flow patterns namely bubbly, slug, churn and annular flow were captured.

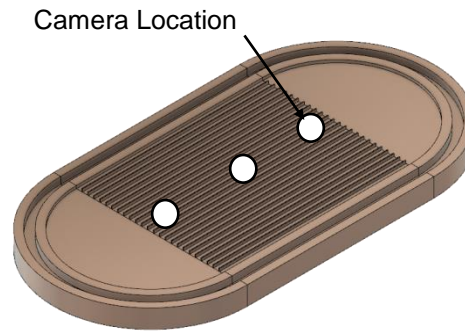


Figure 4.1 Camera location along the heat sink during flow boiling experiments.

Figure 4.2 depicts the observed flow patterns for TS.3 at wall heat flux of 29.2 kW/m² and 36 kW/m² and mass flux of 50 kg/m²s. These photographs were taken within minutes of each other. The features of the present flow patterns are described as follows:

1. Bubbly flow: This regime was seen near the channel inlet as shown in Fig. 4.2(a)(i). The onset of nucleate boiling occurred at the channel corners. Numerous small nucleating bubbles were observed at these locations and the size of these bubbles was smaller than the channel cross-sectional area. As seen in this figure, the channel bottom surface was still not active, while it became active with further heat flux, as discussed later in Section 4.4.
2. Slug flow: This was observed near the channel middle as depicted in Fig. 4.2(a)(ii). This flow pattern was characterized by a long cylindrical vapour slug followed by small bubbles that filled the channel cross-sectional area.
3. Churn flow: This flow regime was found near the channel middle as presented in Fig. 4.2(b). This photograph was captured at wall heat flux of 36 kW/m² and mass flux of 50 kg/m²s. During this regime, the slug shape was distorted and changed into non-uniform and chaotic flow.
4. Annular flow: A vapour core surrounded by a liquid film was observed near the channel outlet as shown in Fig. 4.2(a)(iii). This liquid film was visualized as a black thin layer around the corners. Its thickness decreased with increasing vapour quality or increasing heat flux. Annular flow occurred at high vapour quality ranges.

In addition to the previous regimes, confined bubble was also captured as presented later. This flow was identified by bubbles of round ends that filled the channel cross-sectional area, which was seen for a short period of time.

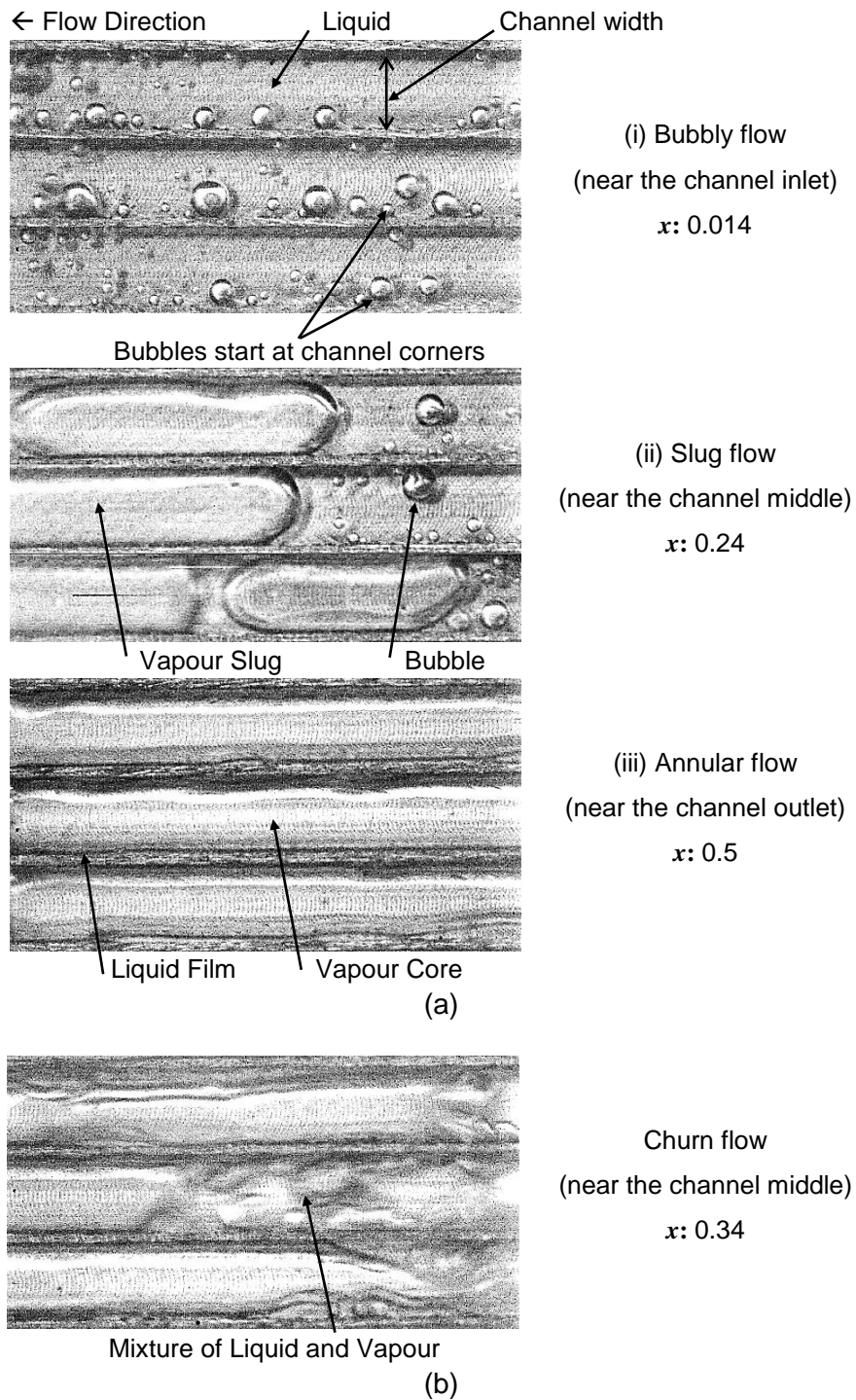


Figure 4.2 Experimental flow visualization patterns along TS.3 corresponding to the local vapour quality at mass flux of $50 \text{ kg/m}^2\text{s}$ and wall heat flux of:
 (a) 29.2 kW/m^2 (b) 36 kW/m^2 .

Flow visualization showed that flow patterns change along the channels for a given heat flux and mass flux. Moreover, flow observation at only one location is not enough when the features of flow patterns are studied. This change in flow patterns

along the entire heat sink can be explained as follows: a small nucleating bubble forms over a surface cavity (nucleation site). This bubble grows at the nucleation site and its growth depends on the surrounding liquid pressure P_l , the bubble pressure P_v and the surface tension σ , see Fig. 4.3. Eq. (4.1) includes these parameters with respect to the bubble radius r_b as given by Kandlikar (2006).

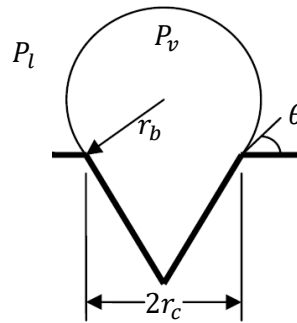


Figure 4.3 Nucleating bubble over a surface cavity, obtained from Kandlikar (2006).

$$r_b = \frac{2\sigma}{(P_v - P_l)} \quad (4.1)$$

This nucleating bubble then departs from the surface cavity with a size smaller than the channel cross-sectional area. This departed bubble with spherical shape becomes larger due to the high evaporation rate from the surrounding liquid and the coalescence with other bubbles while moving along the channels. With increasing bubble volume, the size of the bubble becomes equal to the cross-sectional area of channel and thus a confined bubble occurs. Once this confined bubble touches the channel sidewalls, a high transfer of heat between these walls and bubble occurs. This leads to increase the bubble volume suddenly resulting in long vapour slug. Further details are discussed later in Fig. 4.6. This slug is followed by small bubbles that have size smaller than the channel size. In microchannels, surface tension has a significant effect on flow patterns, see Ong and Thome (2011a). This force dominates during bubbly and slug flow as mentioned by Akbar et al. (2003). It tries to maintain the shape and rigidity of vapour bubble and slug. With further heat transfer and coalescence rate, the volume of the vapour slug increases further leading to high vapour superficial velocity, *i.e.* high vapour quality and low vapour density. This reduces the effect of surface tension force by increasing the dominance of the inertia force. Therefore, the rigidity of vapour slugs becomes weakened leading to break up the liquid film around these slugs. The deformation in the liquid film

resulting in the disappearance of the liquid-vapour interface and thus the flow becomes non-uniform and chaotic, *i.e.* churn flow. With higher vapour superficial velocity, a continuous vapour flow fills the centre of the channel, while a thin liquid film occurs between the vapour core and the channel walls. This flow pattern is annular flow. The increase in vapour superficial velocity along the channels leads a reduction in the thickness of this liquid film. The progress of flow boiling regimes structure observed in this study is shown schematically in Fig. 4.4.

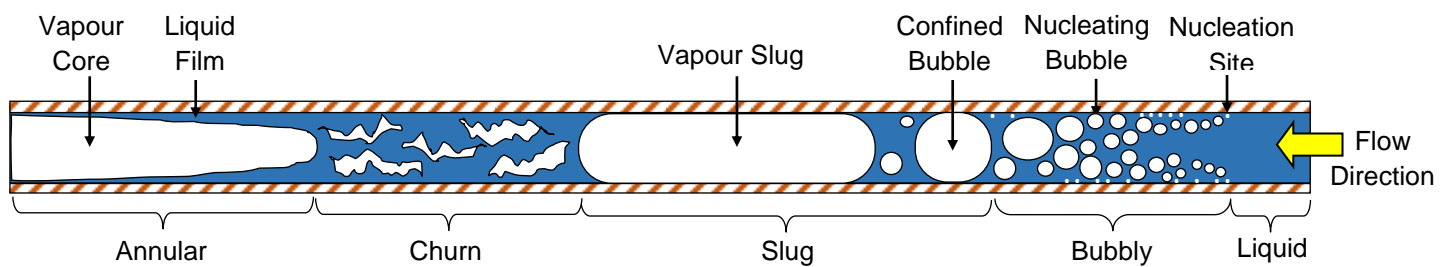


Figure 4.4 Flow boiling structure observed in this study.

In this study, flow reversal was also visualized during the flow boiling experiments as illustrated in Fig. 4.5. This phenomenon occurred after boiling incipience for all test sections and operating conditions. This figure illustrates a sequence of pictures of flow reversal for aspect ratio of 2 at mass flux of $250 \text{ kg/m}^2\text{s}$ and wall heat flux of 114.8 kW/m^2 . These photographs were taken at a location between the channel inlet and middle to detect the cycle of flow reversal. This cycle was found to be forward motion, stagnation period and backward motion, while the captured flow regimes were fluctuating between bubbly, confined bubble and slug flow. At time of 0 ms, small bubbles moved towards the channel outlet. These bubbles were smaller in size than the channel width. The size of these bubbles increased due to the evaporation rate and coalescence with others. After 21 ms, the bubbles stayed at their locations for about 1 ms. During this stagnation period, the bubbles size became larger due to more evaporation and coalescence rate. After that, a back motion was captured and some bubbles became confined as shown at 27 ms. After 37 ms, all the channels were filled with vapour slugs that moved to the upstream direction. This backward motion took about 21 ms. At 43 ms, the flow reversal cycle was complete, and small “new” bubbles occurred inside these channels and moved to the downstream direction.

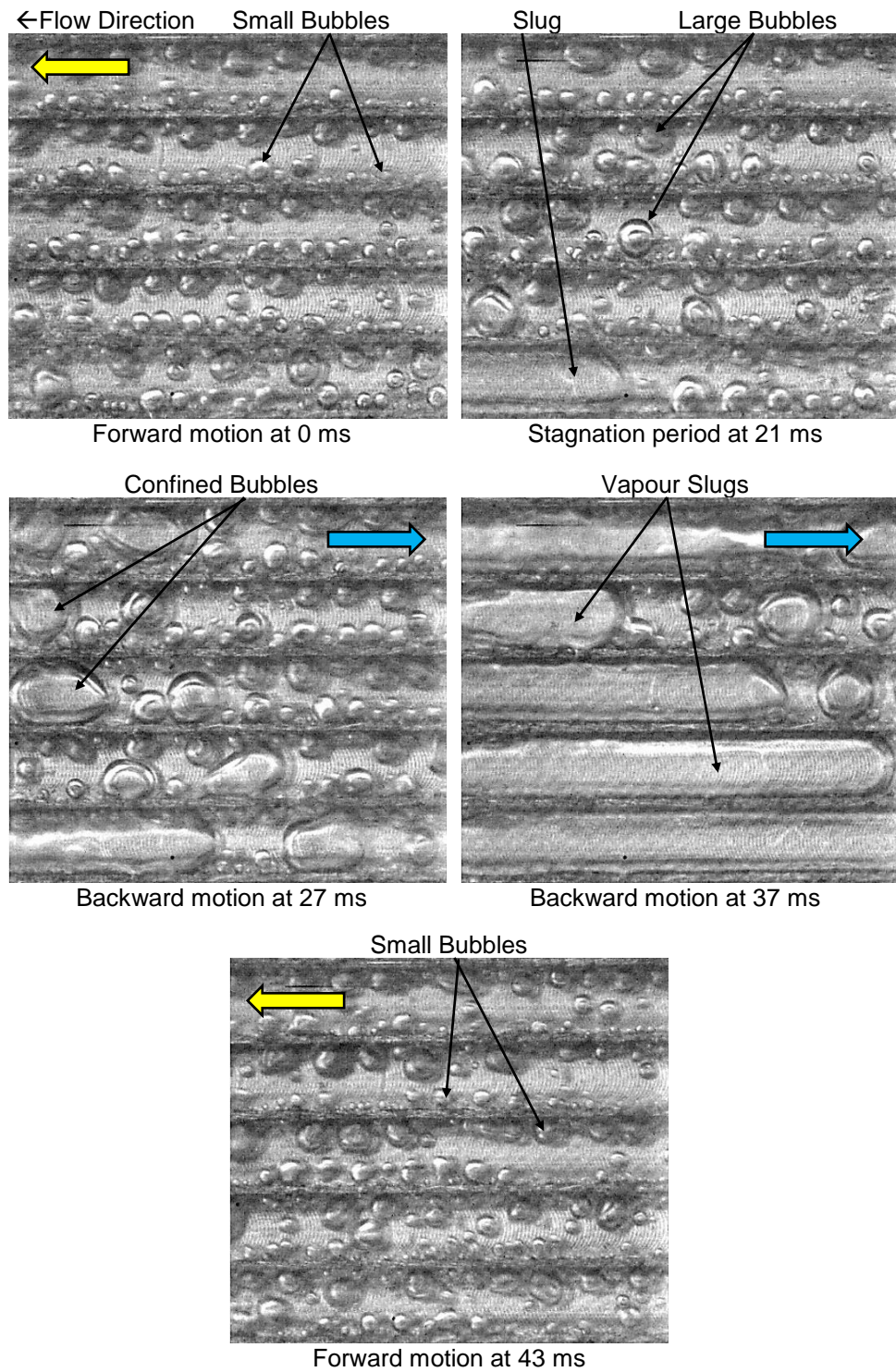


Figure 4.5 Sequence of pictures of flow reversal cycle for TS.3 at wall heat flux of 114.8 kW/m^2 and mass flux of $250 \text{ kg/m}^2\text{s}$ (between channel inlet and middle), yellow arrow indicates forward motion and blue backward motion.

Flow reversal during the present experiments could be due to the bubble generation near the channel inlet and slug formation. Fig. 4.6 shows a sequence of pictures for bubble nucleation during 70 ms period to clarify the bubble growth and coalescence to form confined bubble, elongated bubble and slug flow. At an arbitrary time of 0 ms, a new nucleation site can be identified at the channel corner, see red circle. After 2 ms, the nucleating bubble can be clearly seen at this location. Bubble generation at the channel corners was also observed by other researchers, such as Liu et al. (2005), Soupremanien et al. (2011) and Fayyadh et al. (2017), with the corners behaving as nucleation sites, Qu and Mudawar (2002) and Li and Cheng (2004). This bubble departed the nucleation site, slid along the channel wall and continued to grow due to evaporation rate and coalescence with other small bubbles in the time interval 2–50 ms. After 60 ms, the bubble grew and filled the cross-sectional area of channel resulting in the formation of confined bubble. Confined bubble flow did not sustain for long period as shown in this figure. Once the bubble touched the channel sidewalls, a bidirectional sudden expansion in bubble size, in the downstream and upstream directions, was observed as shown at time of 65 ms. This sudden expansion in size is probably due to the additional high heat transfer rates through the sidewalls. This is also responsible for the flow reversal and instability. At time of 70 ms, a vapour slug occurred followed by small bubbles.

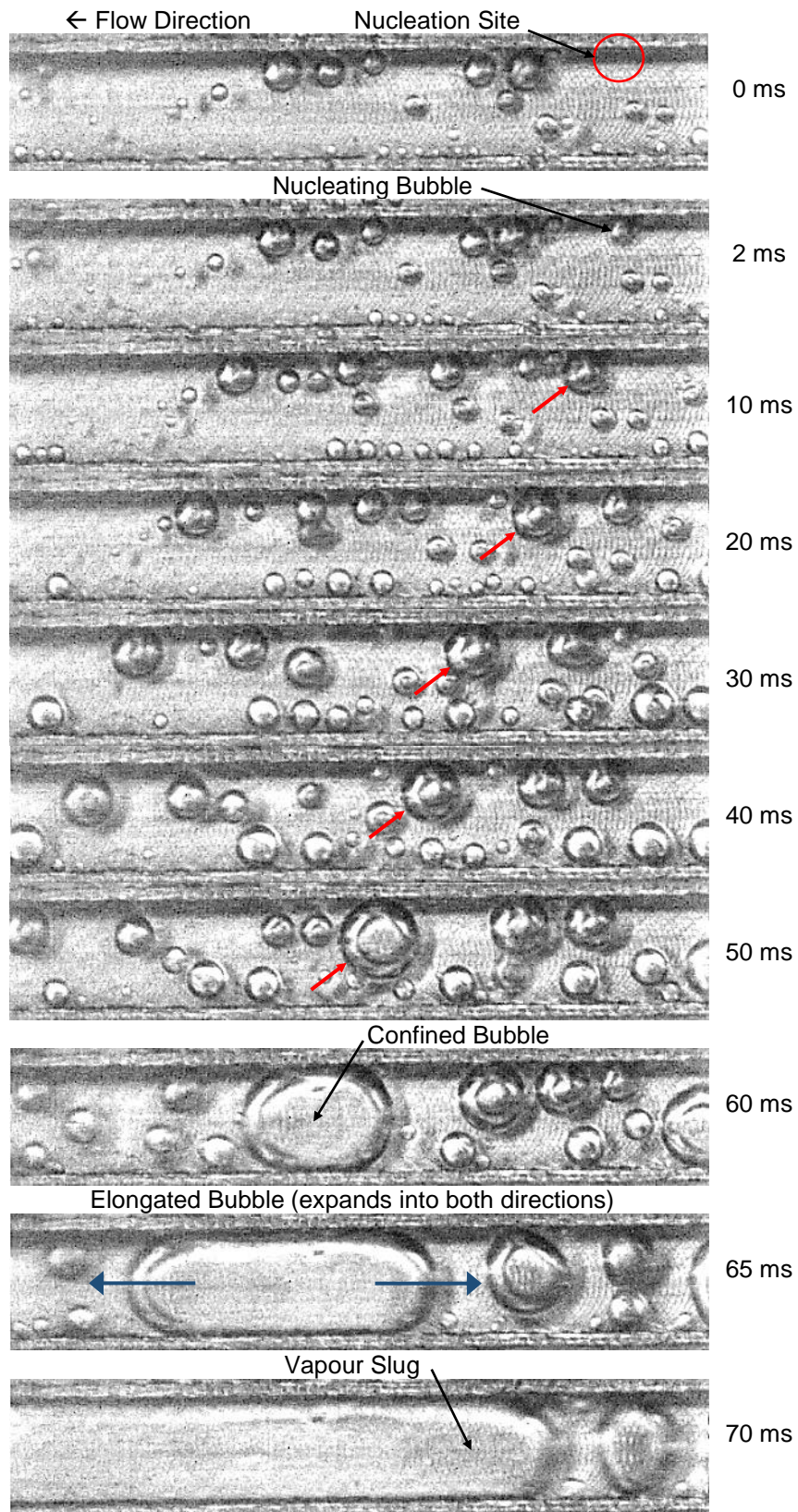


Figure 4.6 Sequence of pictures of bubble growth for TS.3 at wall heat flux of 29.2 kW/m² and mass flux of 50 kg/m²s.

4.3 Experimental Flow Pattern Maps

In the literature, flow patterns maps using superficial liquid and gas velocities are commonly used. This map includes the effect of vapour quality, mass flux and density. However, the effects of surface tension and channel diameter are not included. Other researchers presented their map using only mass flux versus vapour quality, while others used liquid and gas Weber numbers as coordinates. In order to include the effect of surface tension, channel diameter, vapour quality, density and velocity (effect of surface tension and inertia forces), Weber numbers based on liquid and vapour superficial velocities are adopted. The experimental flow patterns map is presented in Fig. 4.7. The symbols represent the experimental flow pattern data, while the dashed lines are the transition boundaries between these regimes. This map was plotted at a system pressure of 1 bar, inlet sub-cooling of 5 K, wall heat flux of 9.6–191.6 kW/m² and five mass fluxes ranging from 50 to 250 kg/m²s. The dimensionless groups during the present flow boiling experiments are summarized as follows:

Bond number: 0.2

Reduced pressure: 0.047

Boiling number: $5\text{--}98 \times 10^{-4}$

Prandtl number: 11

Reynolds number (liquid only): 35–204.2

Superficial liquid Reynolds number: 0.411–199.3

Superficial vapour Reynolds number: 0.26–10038

Liquid Weber number: 0.05–1.76

Vapour Weber number: 7.3–250.9

Vapour superficial velocity increased and liquid superficial velocity decreased with increasing evaporation and coalescence rate along the channels, which led to change the Weber numbers. With an increase in the heat flux, the flow pattern changed into the next regime. Fig. 4.7 shows that both bubbly and slug flow occurred at low Weber number based on vapour superficial velocity, *i.e.* $We_{gs} < 10$. When the Weber number was very low ($We_{gs} \leq 1$), the flow regime was bubbly flow. However, when this number increased further, the flow pattern changed into annular flow. Most data points of the last regime occurred at high Weber number ($10 < We_{gs} \leq 160$).

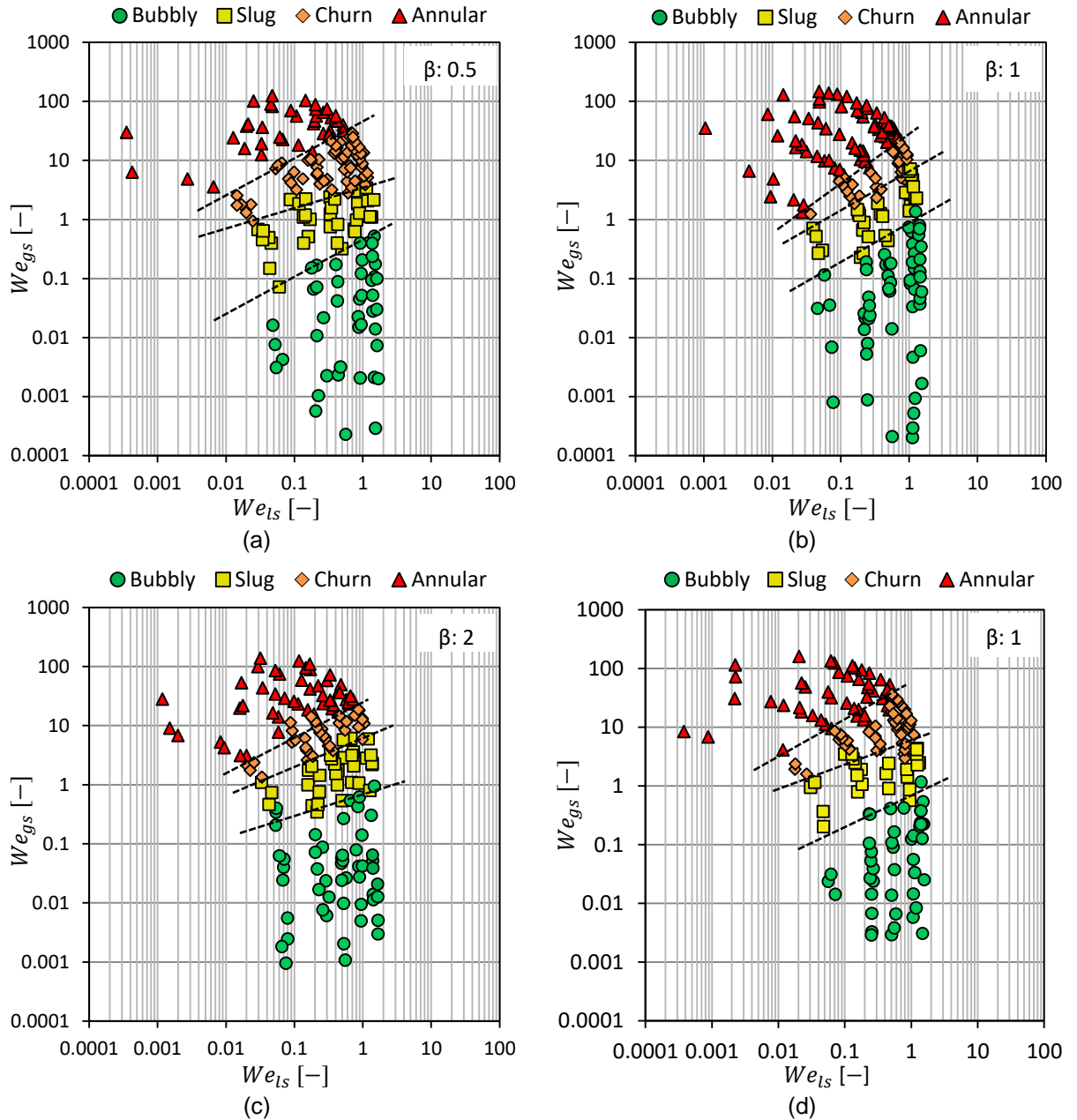


Figure 4.7 Experimental flow patterns map at system pressure of 1 bar, inlet sub-cooling of 5 K, wall heat flux of 9.6–191.6 kW/m² and mass flux of 50–250 kg/m²s for: (a) TS.1 (b) TS.2 (c) TS.3 (d) TS.4.

4.4 Effect of Heat Flux

In this section, different wall heat fluxes for a given mass flux are presented and discussed. Fig. 4.8 shows the bubbly flow for TS.3 at mass flux of 50 kg/m²s and two different heat fluxes. It is obvious that, at low wall heat flux, *i.e.* 29.2 kW/m², few active nucleation sites were observed, most of them were at the channel corners, as shown in Fig. 4.8(a). When the wall heat flux increased from 29.2 to 58.2 kW/m²,

more nucleation sites were activated at the channel corners and bottom surface, see Fig. 4.8(b). Moreover, the bubble size was larger at high heat flux compared to that observed at low heat flux. At low heat fluxes, the wall superheat is also low and thus just large surface cavities are active, more details are described in Chapter 6 using the correlation by Hsu (1962). Therefore, few nucleation sites activate and generate few nucleating bubbles. The size of these bubbles is small due to the low evaporation and coalescence rate. At high heat fluxes, the wall superheat becomes higher leading to more active nucleation sites, *i.e.* small surface cavities are also active. Therefore, the bubble generation increases and the chance of coalescence rate also increases leading to large bubble size.

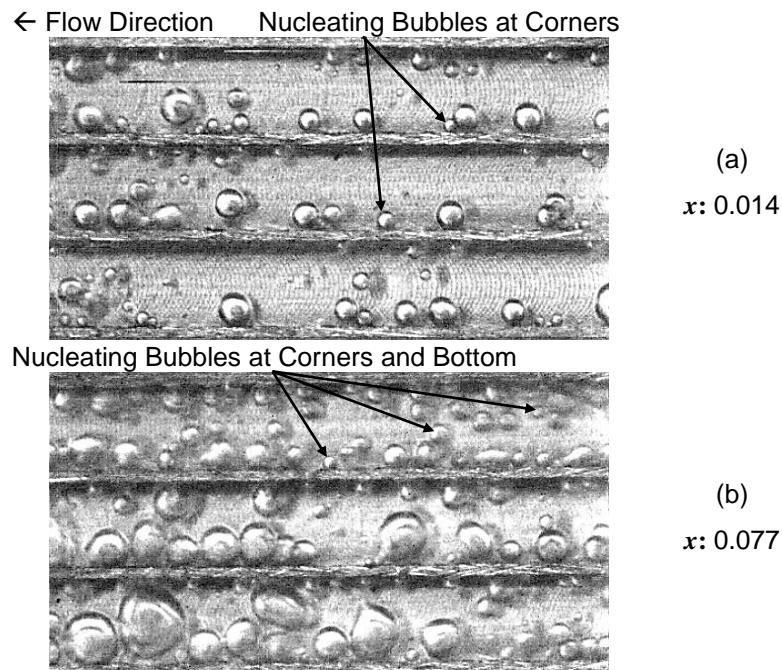


Figure 4.8 Effect of heat flux on the bubbly flow for TS.3 at mass flux of $50 \text{ kg/m}^2\text{s}$, corresponding to the local vapour quality, near the channel inlet and two wall heat fluxes of: (a) 29.2 kW/m^2 (b) 58.2 kW/m^2 .

Fig. 4.9 presents different flow patterns for TS.3 at mass flux of $150 \text{ kg/m}^2\text{s}$ and three wall heat fluxes. The flow patterns in this figure were visualized near the channel middle. This figure demonstrates that, when the wall heat flux was set at 30.4 kW/m^2 , bubbly flow was observed as shown in Fig. 4.9(a). However, slug flow occurred when the heat flux increased to 58.3 kW/m^2 , see Fig. 4.9(b). At wall heat flux of 113.1 kW/m^2 , the flow pattern changed into churn flow, see Fig. 4.9(c).

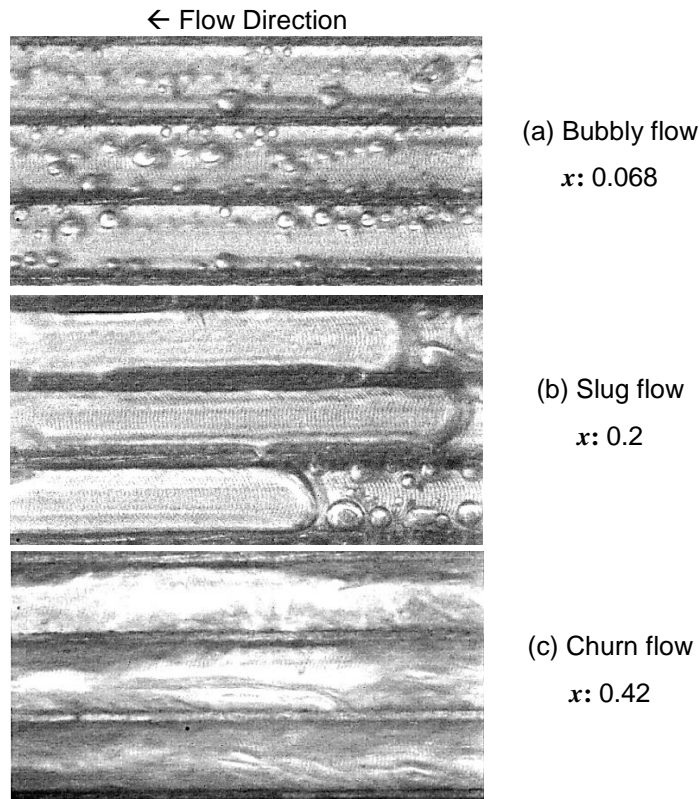


Figure 4.9 Effect of heat flux on flow patterns for TS.3 at mass flux of $150 \text{ kg/m}^2\text{s}$, corresponding to the local vapour quality, near the channel middle and three wall heat fluxes of: (a) 30.4 kW/m^2 (b) 58.3 kW/m^2 (c) 113.1 kW/m^2 .

Fig. 4.10 presents the histogram of flow patterns at three different locations along the channels. This figure is plotted for TS.1 at mass flux of $100 \text{ kg/m}^2\text{s}$ and wall heat flux of 17.15 , 34.64 and 50.65 kW/m^2 . The figure demonstrates that the flow patterns changed along the channels for a given heat flux. It also shows that, at a given location, the flow patterns also changed with increasing wall heat flux. For example, at location near the channel outlet, the flow patterns became slug, churn and annular flow when the heat flux was 17.15 , 34.64 and 50.65 kW/m^2 , respectively. It is known that when the heat flux increases, the evaporation and coalescence rate also increase, *i.e.* high vapour superficial velocity, leading to change the dominant forces and thus the appearance of different flow patterns.

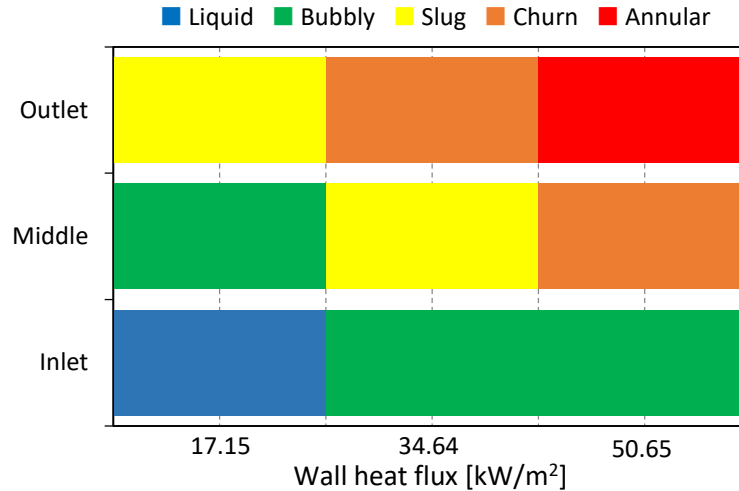


Figure 4.10 Effect of heat flux on the histogram of flow patterns for TS.1 at mass flux of $100 \text{ kg/m}^2\text{s}$ and three different locations along the channel.

In the present study, some interesting features were captured by the camera when the heat flux increased, see Fig. 4.11. This figure shows the flow patterns for TS.3 at mass flux of $100 \text{ kg/m}^2\text{s}$ and different wall heat fluxes. It can be seen that, at low wall heat flux, *i.e.* 23.7 kW/m^2 , slug flow was captured near the channel middle as shown in Fig. 4.11(a). When the heat flux increased to 46.5 kW/m^2 , slug flow was still observed but with small nucleating bubble in the liquid film at the channel sidewalls as depicted in Fig. 4.11(b). Similar features, *i.e.* nucleating bubbles in the liquid film, were visualised in annular flow when the wall heat flux increased to 57.8 kW/m^2 , see Fig. 4.11(c). These bubbles could be suppressed towards the channel outlet, especially when the liquid film became too thin. These changes in the above features with heat flux could be attributed as follows: At low heat flux, the wall superheat is low and consequently nucleation may be suppressed. With increasing heat flux, the wall superheat increases and may become sufficient for activation of these nucleation sites. Small nucleating bubbles in the liquid film of slug or annular flow were also visualised for other test sections, see Fig 4.12 as example for TS.1 and TS.4. The abovementioned features were also reported by other researchers, such as Harirchian and Garimella (2009a) and Borhani and Thome (2014) using dielectric refrigerants, such as FC-77 and R245fa, respectively, in horizontal rectangular multi-microchannels.

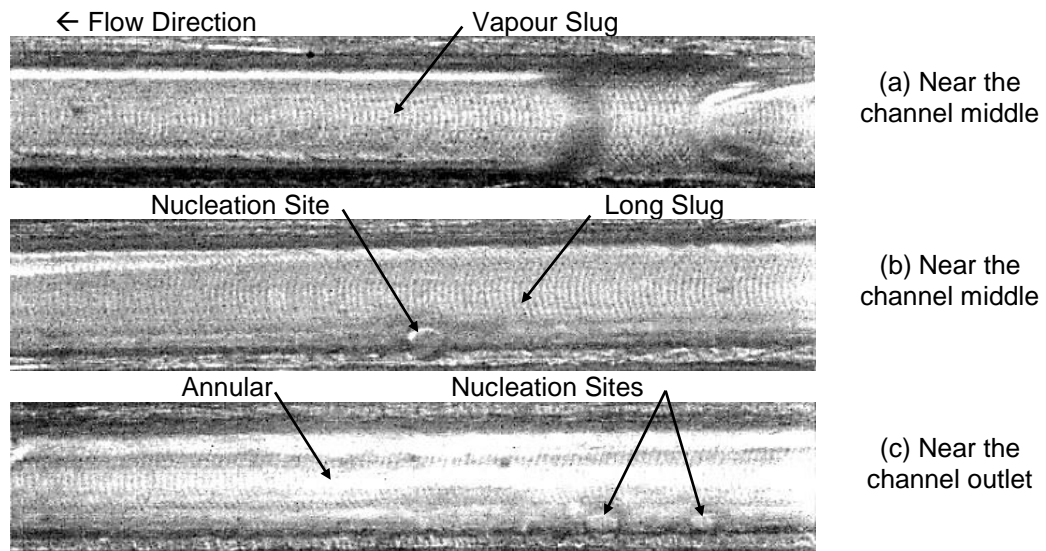


Figure 4.11 Flow patterns for TS.3 at mass flux of $100 \text{ kg/m}^2\text{s}$ and three wall heat fluxes of: (a) 23.7 kW/m^2 (b) 46.5 kW/m^2 (c) 57.8 kW/m^2 .

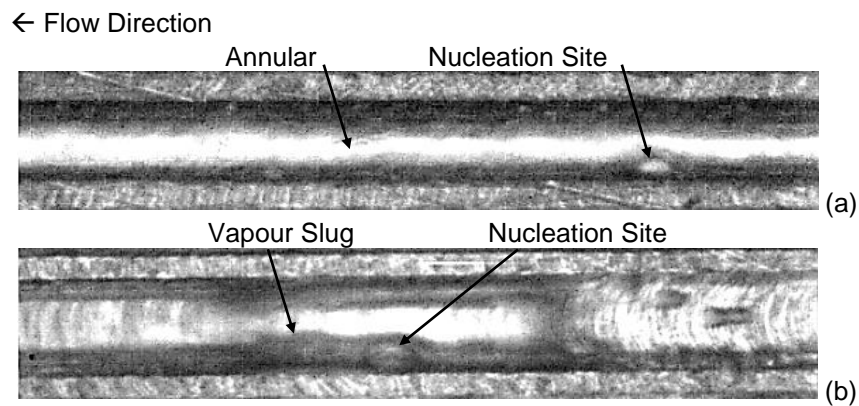


Figure 4.12 Nucleating bubbles in the liquid film of:

- (a) Annular flow for TS.1 at mass flux of $200 \text{ kg/m}^2\text{s}$ and wall heat flux of 51 kW/m^2 (near the channel middle) (b) Slug flow for TS.4 at mass flux of $100 \text{ kg/m}^2\text{s}$ and wall heat flux of 55.24 kW/m^2 (between the channel inlet and middle).

The hysteresis effect on the boiling flow patterns was studied for increasing and decreasing wall heat flux using the same heat sink at the same operating conditions. Fig. 4.13 shows this effect at mass flux of $150 \text{ kg/m}^2\text{s}$ and wall heat flux near 40 kW/m^2 for TS.2. This figure demonstrates that, at 40 kW/m^2 , the flow pattern was simply liquid flow when the wall heat flux increased. In contrast, bubbly flow was visualized with decreasing heat flux at the same condition. This differences in flow patterns were also found by other researchers, see Mahmoud (2011), Karayiannis et

al. (2014) and Al-Gaheeshi (2018). They tested different refrigerants, such as R134a and R245fa, in vertical small to micro tubes at different operating conditions. This was attributed as follows: with increasing heat flux, the nucleation sites are not active at low heat fluxes, while they become activated at high heat fluxes. With decreasing heat flux, these sites remain active even at low heat fluxes and thus lower wall superheat. At low heat fluxes, bubbly flow becomes the dominant regime and thus active nucleation sites affect the hysteresis phenomenon.

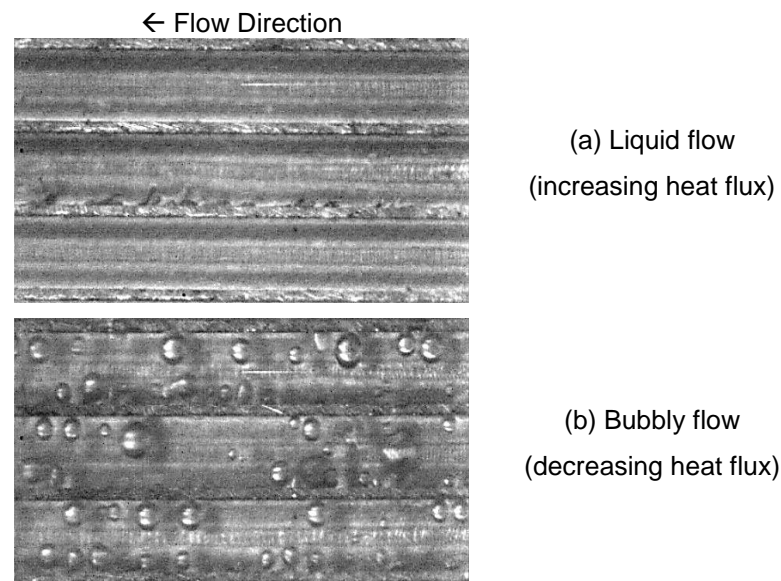


Figure 4.13 Hysteresis effect at mass flux of $150 \text{ kg/m}^2\text{s}$ and wall heat flux near 40 kW/m^2 for TS.2 (near the channel inlet): (a) Increasing heat flux (b) Decreasing heat flux.

4.5 Effect of Mass Flux

The effect of mass flux was studied using different mass fluxes for given wall heat flux at each location of flow visualization. Fig. 4.14 presents two photographs that were taken at wall heat flux of 20 kW/m^2 and mass flux of $50 \text{ kg/m}^2\text{s}$ and $200 \text{ kg/m}^2\text{s}$ at the channel middle. The figure shows that the flow pattern was bubbly flow for both mass fluxes. The size of these bubbles was smaller than the channel size. However, the size of bubbles differed from one mass flux to another. When the mass flux was $50 \text{ kg/m}^2\text{s}$, the bubble size was larger as shown in Fig. 4.14(a). With an increase in mass flux to $200 \text{ kg/m}^2\text{s}$, the bubble size became smaller compared to that for the lower mass flux, see Fig. 4.14(b).

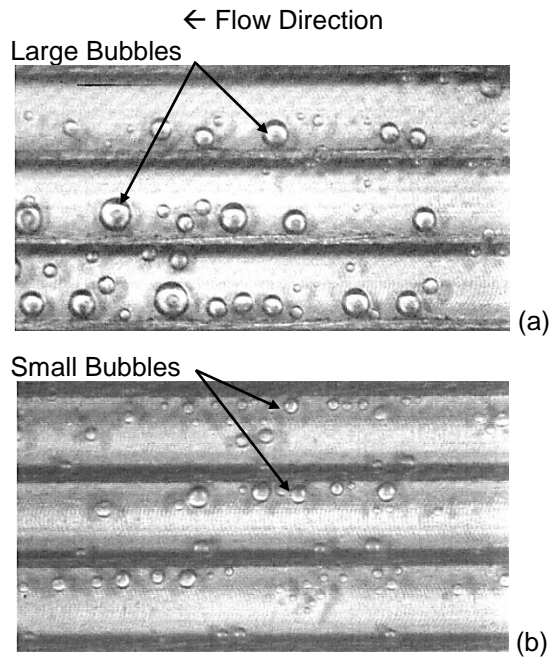


Figure 4.14 Effect of mass flux on the flow patterns for TS.3 at wall heat flux of 20 kW/m^2 near the channel middle and two mass fluxes of:
 (a) $50 \text{ kg/m}^2\text{s}$ (b) $200 \text{ kg/m}^2\text{s}$.

A histogram of flow patterns is shown in Fig. 4.15 to present the effect of mass flux for TS.3 at wall heat flux near 46 kW/m^2 and different locations of flow observation. This figure shows that the flow patterns changed to the lower regime, *i.e.* inverse transition, with increasing mass flux. For example, near the channel middle, the flow pattern became churn, slug and bubbly flow when the mass flux was 50, 150 and $250 \text{ kg/m}^2\text{s}$, respectively. This figure also shows that the flow pattern near the channel outlet changed from annular to slug flow when the mass flux increased from 50 to $250 \text{ kg/m}^2\text{s}$.

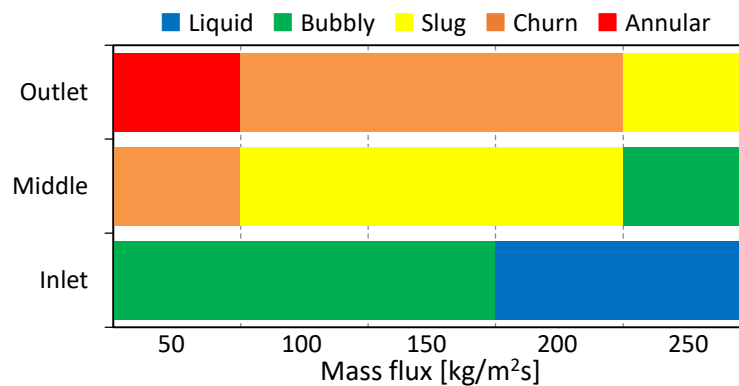


Figure 4.15 Effect of mass flux on the histogram of flow patterns for TS.3 at wall heat flux near 46 kW/m^2 and three different locations along the channels.

The above findings were also reported by other researchers. This inverse transition with increasing mass flux was found by Harirchian and Garimella (2009a), Mirmanto (2013) and Özdemir (2016). The bubble size was also found to be smaller with the increase of mass flux as reported by Harirchian and Garimella (2009a) and Özdemir (2016). Yin et al. (2014) carried out an experimental flow visualization study using de-ionized water in a rectangular microchannel having hydraulic diameter of 0.667 mm. They reported that the bubble growth rate decreased with increasing mass flux in both unconfined and confined growth period. In microchannel flow boiling, they reported that an increase in mass flux leads to delay the occurrence of confined bubbles. They explained this as follows (i) in unconfined growth period, the fluid inertia force increases with increasing mass flux results in a reduction in the bubble growth rate and (ii) in confined growth period, an increase in mass flux (fluid inertia force) leads to decrease the evaporation rate in the liquid film around the elongated bubbles due to the high velocity of these bubbles.

4.6 Effect of Channel Aspect Ratio

Although bubbly, slug, churn and annular flow were visualized for three channel aspect ratios, slight differences in their features were found. For instance, Fig. 4.16 illustrates the features of bubbly flow observed near the channel inlet at wall heat flux near 45 kW/m^2 , mass flux of $100 \text{ kg/m}^2\text{s}$ and different aspect ratios. It can be seen that numerous bubbles were captured by the camera in all test sections. For the larger aspect ratio, the bubble size was smaller than the channel size as shown Fig. 4.16(a). Furthermore, most bubbles were smaller than those observed in the channels with smaller aspect ratio. For the channels with aspect ratio of 1, the bubble size was still smaller than the channel size, see 4.16(b), but the bubble size was larger than that observed in the channels with aspect ratio of 2. For the channels with aspect ratio 0.5, the size of bubbles was still smaller than the channel size, see Fig. 4.16(c). However, some of these bubbles became confined and elongated once they touched the channel sidewalls. Some of the bubbles became larger due to the bubble coalescence and the size of the bubble approached the cross-sectional area of the channels.

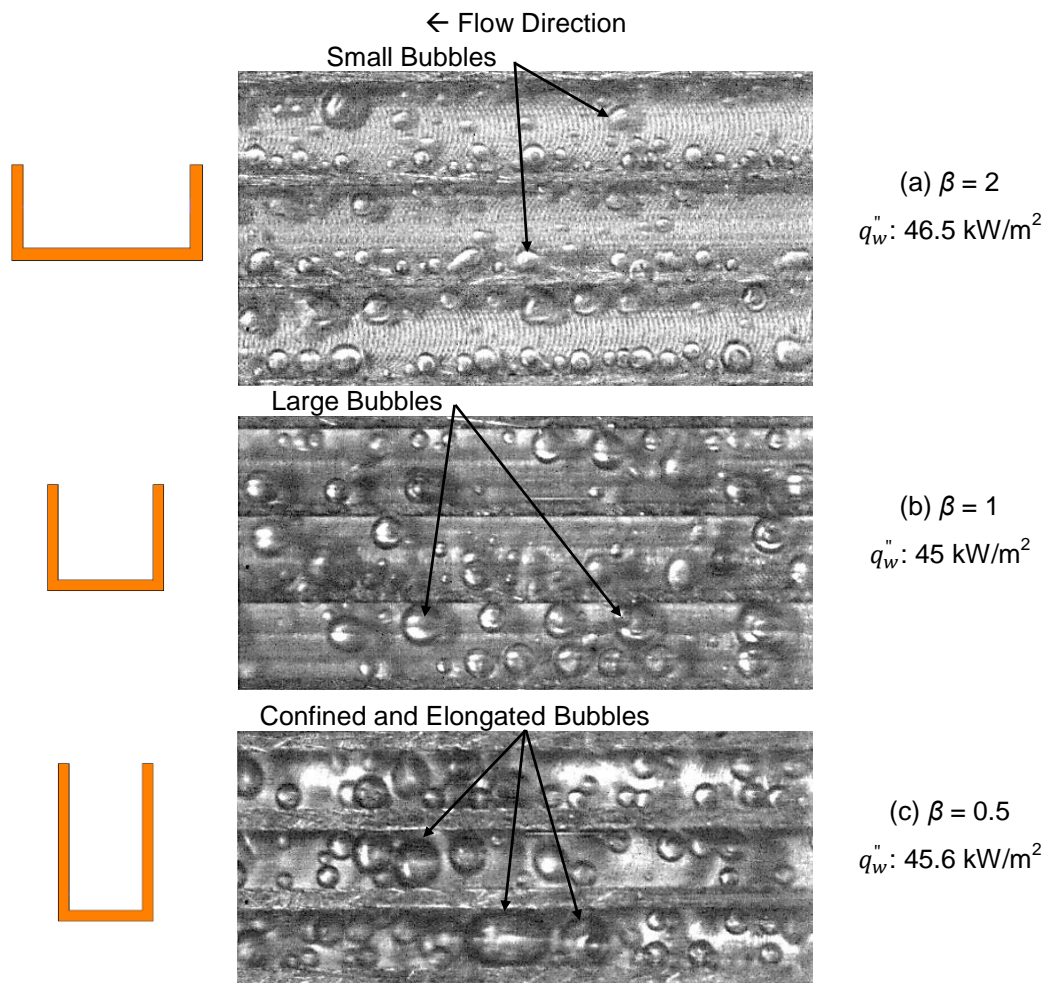


Figure 4.16 Effect of aspect ratio on the bubbly flow at wall heat flux near 45 kW/m² and mass flux of 100 kg/m²s (near the channel inlet).

It can be concluded from Fig. 4.16 that the bubble size increases as the aspect ratio decreases (reduction in the channel width). These differences in the bubble shape are likely due to: (1) The strong confinement effect induced by the channel sidewalls when the channel width decreases. The reduction in channel width leads to an increase in the bubble collisions resulting in high bubble coalescence rate and thus large bubble size. Fig. 4.17 shows a schematic diagram of channel confinement effect at the larger and the smaller aspect ratio. Assume that there are two nucleating bubbles are activated at the channel corners having the same size. Since the smaller aspect ratio provides narrow width, these bubbles can easily coalesce together compared to those in the shallow channel (large aspect ratio). (2) High flow reversal and pressure drop fluctuation with decreasing channel width. In the present study, flow reversal and frequency and amplitude of pressure drop signal were found to

increase with decreasing channel aspect ratio as discussed in Chapter 6. With flow reversal, flow maldistribution may occur among the channels leading to different flow rates among the channels. This may increase the bubble collisions and bubble size.

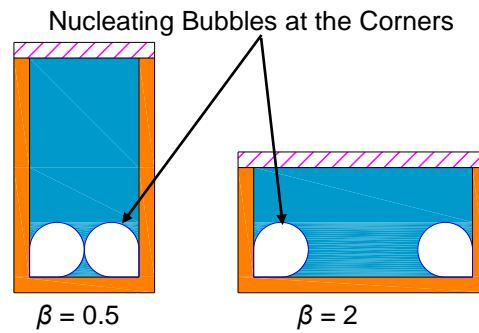


Figure 4.17 Confinement effect on bubble coalescence at different aspect ratios.

Figure 4.18 shows the effect of aspect ratio on the features of slug flow observed near the channel middle at mass flux of $50 \text{ kg/m}^2\text{s}$ and wall heat flux near 23 kW/m^2 . This figure illustrates that the vapour slugs filled the channel cross-sectional area and followed by small bubbles. However, the shape of slugs and the size of bubbles showed some differences when the channel aspect ratio changed. For larger aspect ratio, the slug had round ends, while the bubble size was smaller than the channels size. Small numerous bubbles can be seen for this aspect ratio as shown in Fig. 4.18(a). When the channel aspect ratio decreased to 1, the slug ends became more round and few bubbles were captured, see Fig. 4.18(b). For the channel aspect ratio of 0.5, these ends had a bullet shape. Moreover, a confined bubble can also be seen in Fig. 4.18(c). With decreasing channel aspect ratio, the channel width also decreases and thus the vapour slug is squeezed by channel sidewalls resulting in more curved ends.

Fig. 4.19 depicts the effect of aspect ratio on the features of annular flow at wall heat flux near 79 kW/m^2 and mass flux of $250 \text{ kg/m}^2\text{s}$. A continuous vapour flow was captured at the channel outlet in the centre of the channels. This vapour flow was surrounded by thin liquid film. This figure also demonstrates that there was no clear effect of aspect ratio on annular flow. It is worth mentioning that it was difficult with the camera to measure the distribution and thickness of the liquid film in this regime.

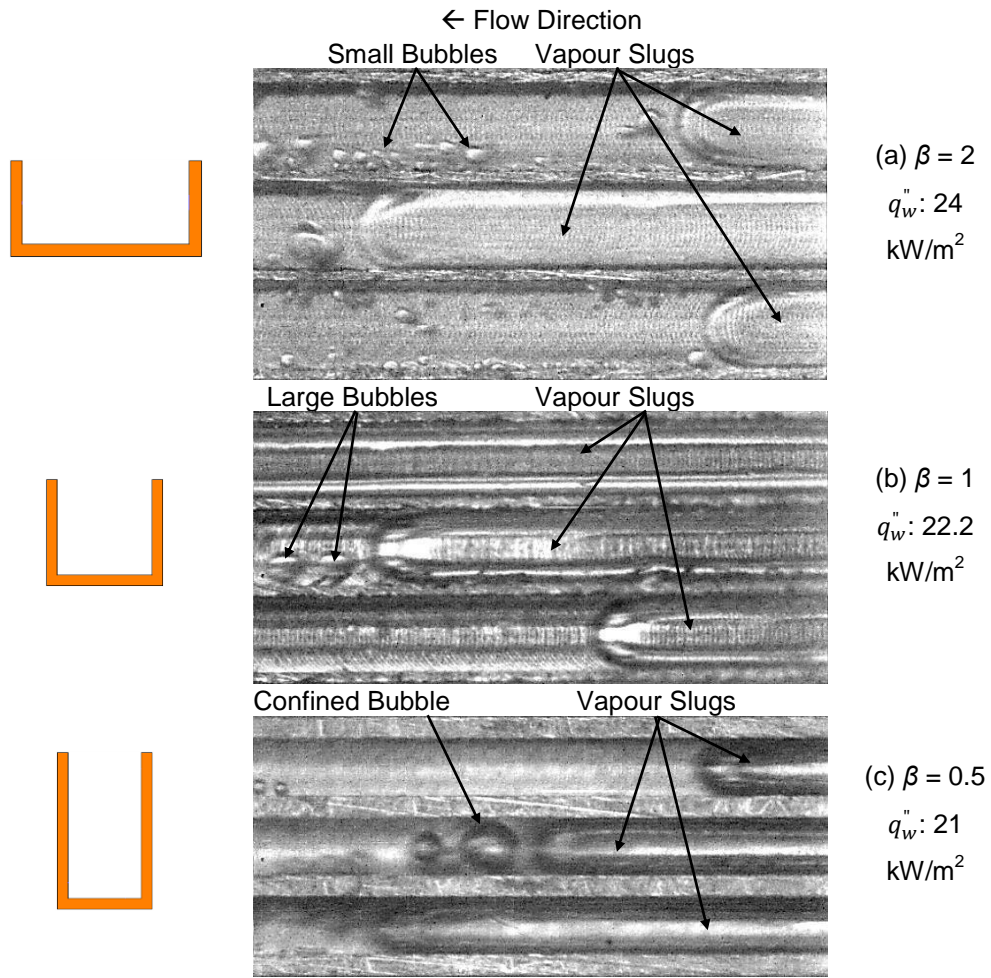


Figure 4.18 Effect of aspect ratio on the slug flow at wall heat flux near 23 kW/m² and mass flux of 50 kg/m²s (near the channel middle).

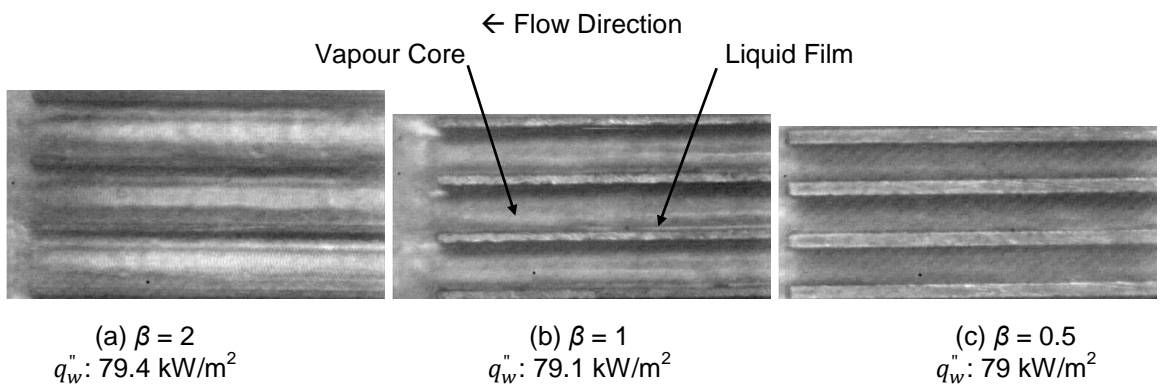


Figure 4.19 Effect of aspect ratio on the annular flow at wall heat flux near 79 kW/m² and mass flux of 250 kg/m²s (at the channel outlet).

4.7 Effect of Channel Surface Material

The material effect on the experimental flow patterns was studied using two heat sinks made of different metals, namely copper and aluminium. These heat sinks had the same channel dimensions (0.46 mm hydraulic diameter and 1 aspect ratio), same base area (500 mm²) and approximately the same surface average roughness (0.28 µm for copper and 0.19 µm for aluminium). Five mass fluxes ranging from 50 to 250 kg/m²s at inlet sub-cooling of 5 K and system pressure of 1 bar were examined. The heat flux was increased gradually until the exit vapour quality reached near one. Flow observation was conducted at different locations along the channels after reaching steady state condition. Fig. 4.20 shows the bubbly flow for TS.2 and TS.4 at wall heat flux near 70 kW/m² and mass flux of 100 kg/m²s near the channel inlet. This figure demonstrates that numerous bubbles were generated and moved along the channels. Most of these bubbles had size smaller than the cross-sectional area of the channels. Some large and confined bubbles were captured due to the evaporation and the coalescence rate. The distribution and the size of these bubbles were similar for both metals.

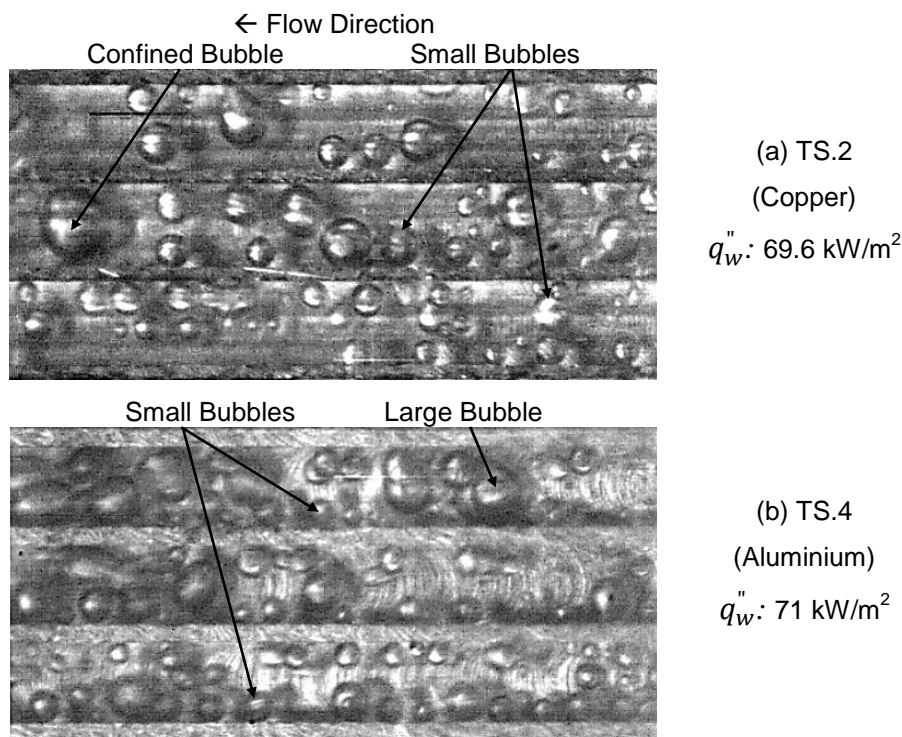


Figure 4.20 Effect of channel surface material on the bubbly flow at wall heat flux near 70 kW/m² and mass flux of 100 kg/m²s (near the channel inlet).

Fig. 4.21 shows the features of slug flow at wall heat flux near 39 kW/m^2 and mass flux of $150 \text{ kg/m}^2\text{s}$ near the channel middle. It is obvious that vapour slugs filled the cross-section of the channels followed by number of bubbles. These slugs had round ends, while the size of bubbles was smaller than the channel size. Some large bubbles can be seen in this figure due to both evaporation and coalescence. The abovementioned features of flow pattern were captured for both surfaces.

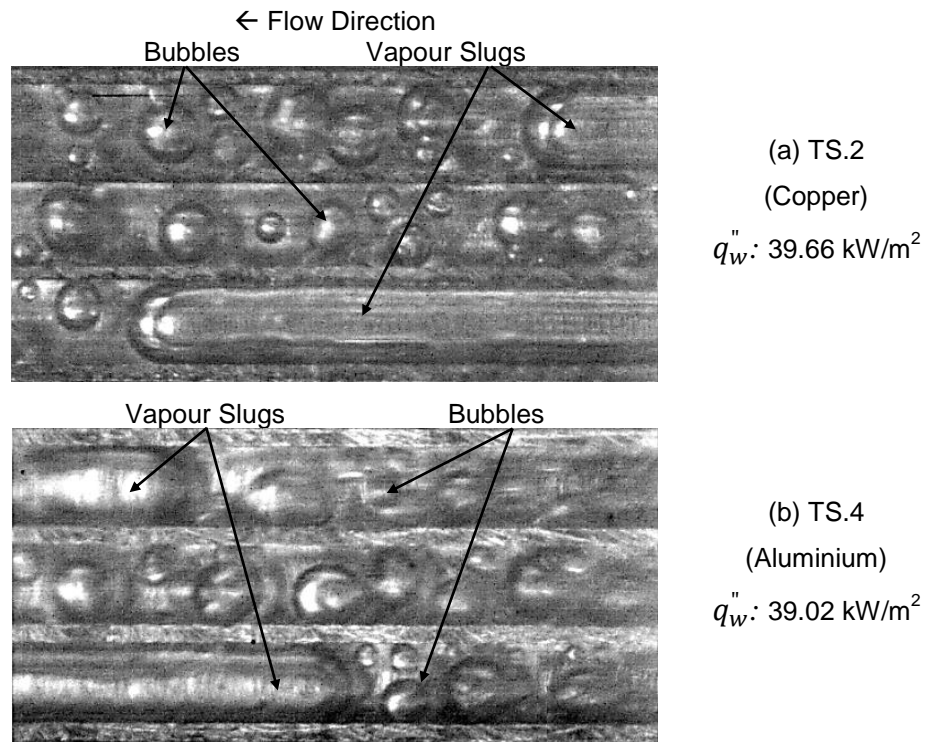


Figure 4.21 Effect of channel surface material on the slug flow at wall heat flux near 39 kW/m^2 and mass flux of $150 \text{ kg/m}^2\text{s}$ (near the channel middle).

Fig. 4.22 illustrates the features of annular flow at wall heat flux near 127 kW/m^2 and mass flux of $200 \text{ kg/m}^2\text{s}$ for two different surface metals. These photographs were taken at the channel outlet. This figure demonstrates that the cross-sectional area of the channels was filled by continuous vapour flow surrounded by liquid film. It also shows that insignificant differences of this regime were found for both test sections. The distribution of liquid film around the channel circumference and the liquid film thickness were difficult to measure using the present camera.

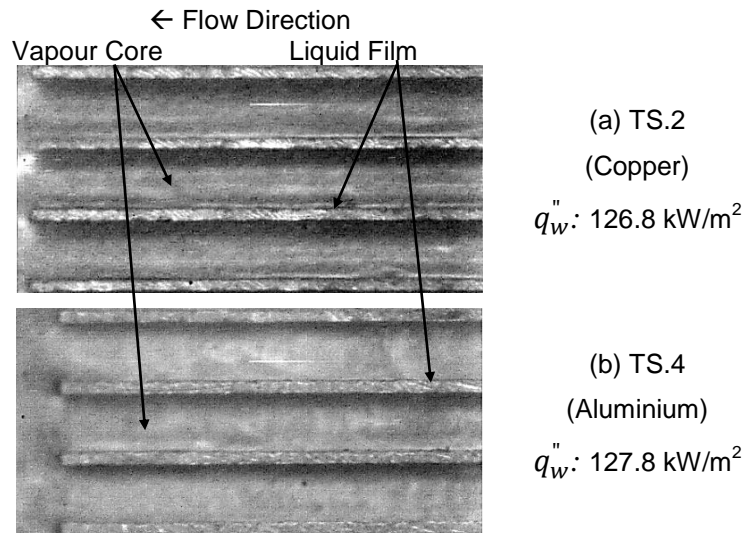


Figure 4.22 Effect of channel surface material on the annular flow at wall heat flux near 127 kW/m^2 and mass flux of $200 \text{ kg/m}^2\text{s}$ (at the channel outlet).

4.8 Comparison with Existing Flow Pattern Maps

The experimental flow patterns data were compared with some existing flow pattern maps, such as Akbar et al. (2003), Revellin and Thome (2007a), Harirchian and Garimella (2010), Mahmoud and Karayiannis (2016a), Choi et al. (2017) and Li and Hrnjak (2019). These maps were chosen since they are widely used in two-phase flow and proposed for horizontal and vertical mini and microchannels. Chapter 2 presents more details of each map and their transition boundaries.

4.8.1 Flow patterns map by Akbar et al. (2003)

This map was developed based on the experimental data using air-water in channels with diameter ranging from 0.866 to 1.6 mm. Weber numbers based on liquid and vapour superficial velocities were used as coordinates in their map. They classified their map into four regions, namely surface tension dominated region, transition region and inertia dominated region (I and II). The surface tension region included bubbly, slug and plug flow, while inertia region included annular, wavy annular and dispersed flow. Fig. 4.23 depicts the comparison with this map for four test sections. It shows that, most data points of bubbly flow were well predicted by this map, while the rest were located inside the transition region for all test sections. In other words, as the vapour Weber number increased, their map showed poor prediction to this

flow pattern. Slug flow was poorly predicted by this map, *i.e.* all the data were within the transition region. Most data points of churn flow were within the transition region. However, at the vapour Weber number more than ten, these points were inside the annular region. Most data points of annular flow were predicted well by this map for all test sections. In contrast, when the vapour Weber number was less than 5, the annular flow data points were located within the transition region.

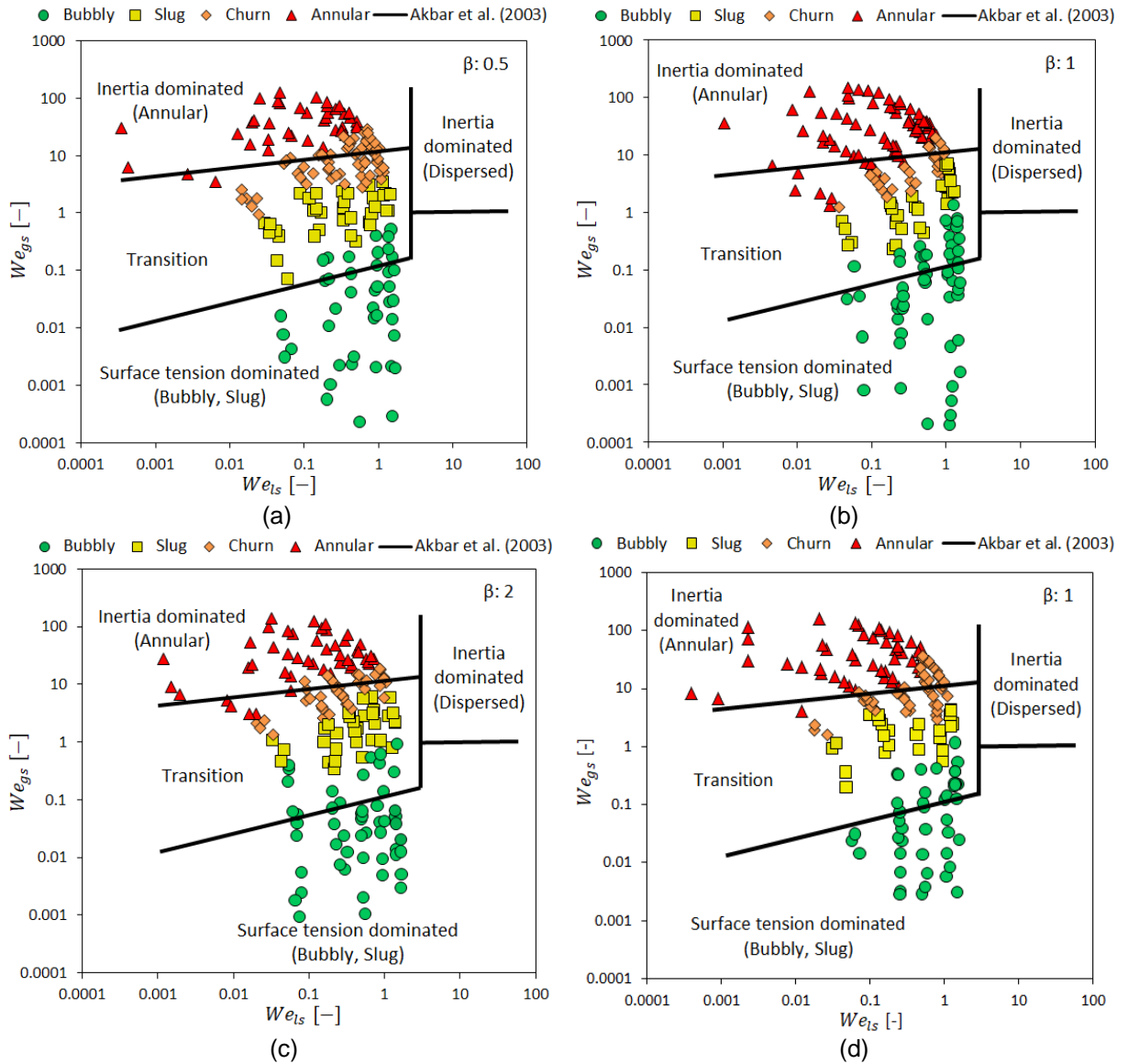


Figure 4.23 Comparison of experimental data with Akbar et al. (2003) flow map for:
 (a) TS.1 (b) TS.2 (c) TS.3 (d) TS.4.

It can be concluded that their map does not predict well all the present data points. This could be due to the fact that their map was proposed based on adiabatic

experiments using air-water flow, *i.e.* there is no heat effect. Another possible reason could be the range of the present liquid and vapour superficial velocities. Their map covers the ranges: $J_g = 0.04\text{--}100$ m/s and $J_l = 0.003\text{--}20$ m/s, while the present ranges are $J_g = 0.001\text{--}21.5$ m/s and $J_l = 0.001\text{--}0.19$ m/s. The present low velocities, *i.e.* $0.001 \leq J_g < 0.04$ m/s and $0.001 \leq J_l < 0.003$ m/s, are not covered by this map resulting in low prediction. Further details about the effect of different operating conditions are discussed later.

4.8.2 Flow patterns map by Revellin and Thome (2007a)

This map was developed based on the experimental data including R134a and R245fa using two micro tubes with inner diameter of 0.509 and 0.79 mm. The effects of heat flux, mass flux, fluid properties and channel size on the flow patterns were considered by the author. Their map included two transition boundaries from isolated bubble regime (IB) (bubbly and slug flow) to coalescing bubble regime (CB) (slug/semi-annular) and from coalescing bubble regime (CB) to annular regime (A). Fig. 4.24 shows the comparison between the present flow patterns and their map using mass flux and vapour quality as coordinates. It illustrates that most present data of bubbly flow was within the isolated bubble regime, while all data of slug flow was within the coalescing bubble regime. In other words, the transition from (IB) to (CB) predicted fairly by their map. However, this map did not predict all the data of churn flow. Although churn flow was located within the coalescing bubble regime, most of these points were within the annular region. It can be seen that most data of annular flow was predicted well by their map. However, at low mass flux, the data points of this flow were located within the coalescing bubble regime. It can be concluded that there is some agreement and some disagreement between the experimental data and their map. This could be due to the heat flux in their transition from isolated bubble regime (IB) to coalescing bubble regime (CB). The sensitivity of their map to this parameter may make the comparison more complicated. For example, the transition boundary shifts to the higher vapour qualities when the heat flux increases. Different heat fluxes mean different Boiling numbers. This can be seen by comparing their range of Boiling number with the present study. Their range is $3 \times 10^{-5}\text{--}632 \times 10^{-5}$, while the present study covers $50 \times 10^{-5}\text{--}980 \times 10^{-5}$. It is obvious that the experimental data are within their ranges except $632 \times 10^{-5} < Bo \leq 980 \times 10^{-5}$.

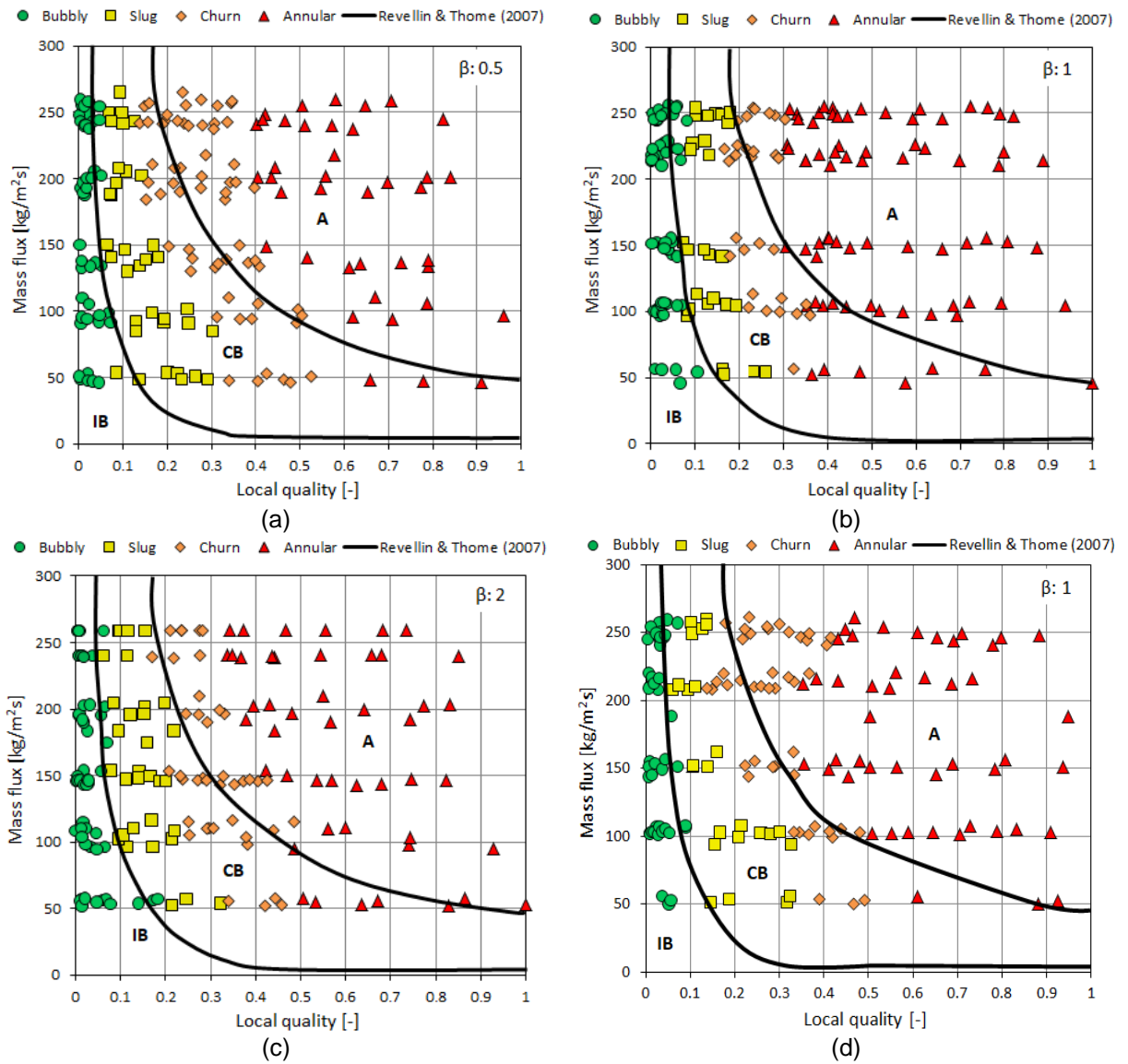


Figure 4.24 Comparison of experimental data with Revellin and Thome (2007a) flow map for: (a) TS.1 (b) TS.2 (c) TS.3 (d) TS.4.

4.8.3 Flow patterns map by Harirchian and Garimella (2010)

Flow boiling of FC-77 using twelve heat sinks at heat flux of 25–380 kW/m² and mass flux of 225–1420 kg/m²s was experimentally examined by the authors. They tested horizontal rectangular multi-microchannels with hydraulic diameter ranging from 0.096 to 0.707 mm. A flow patterns map was developed from this experimental data including two groups, *i.e.* confined (confined slug and confined annular) and unconfined (bubbly, churn, annular and wispy-annular). They presented their map using the convective-confinement number ($Bd^{0.5}Re$) and the dimensionless heat flux

($BoRe$). Their map was compared with the present data as illustrated in Fig. 4.25. It is obvious that their model predicted poorly the experimental data of bubbly flow for all test sections. Few points of slug flow were located inside the confined slug region, while the rest were within churn/confined annular region. In contrast, all the experimental data points of both churn and annular flow were predicted well for all test sections. This low prediction for bubbly and most data points of slug could be due to the low mass fluxes. Their map was proposed based on high mass fluxes, *i.e.* 225–1420 kg/m²s, while the present study covers low ranges (50–250 kg/m²s).

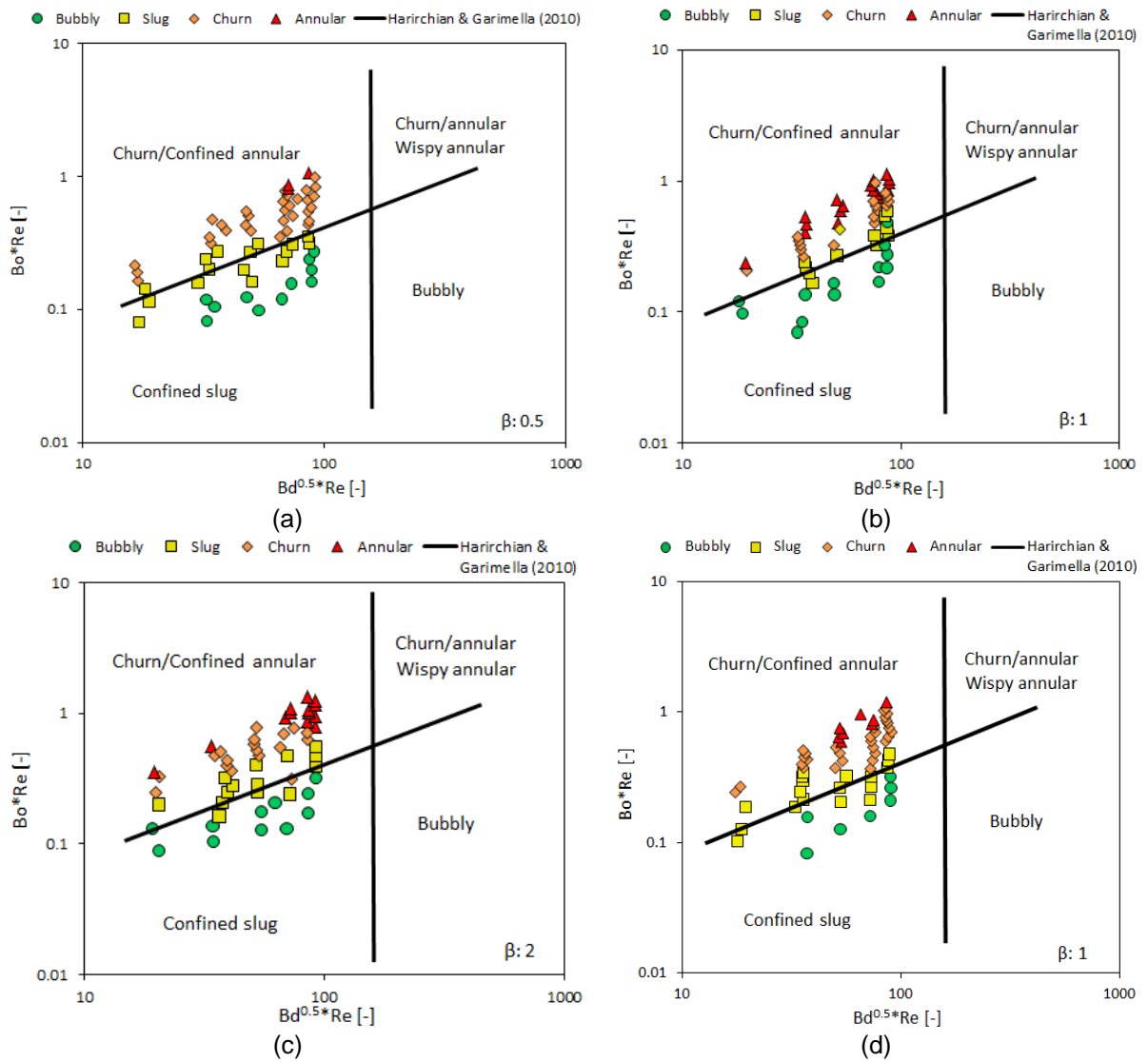


Figure 4.25 Comparison of experimental data with Harirchian and Garimella (2010) flow map for: (a) TS.1 (b) TS.2 (c) TS.3 (d) TS.4.

4.8.4 Flow patterns map by Mahmoud and Karayiannis (2016a)

The authors evaluated many existing maps by comparing them with experimental database using R245fa in vertical tube having 1.1 mm inner diameter. Their data included heat flux ranging from 3 to 25 kW/m², mass flux from 100 to 400 kg/m²s, inlet sub-cooling of 5 K and inlet pressure of 1.85 bar. They found that the experimental transition boundaries were not predicted well by the existing maps. Some of their data were predicted well by the map of Chen (2006). However, the transition boundary from bubbly to slug flow was not predicted by this map. Accordingly, they modified this transition by taking into account the effect of inertia, tube size and fluid properties on the bubble confinement. Fig. 4.26 shows the comparison between the present data and the map by Chen (2006) and the modified transition by Mahmoud and Karayiannis (2016a). It is obvious that few points of bubbly flow were predicted by this map, while the rest were within slug region. Some data points of slug flow were predicted well. However, most data points of slug flow were within churn and annular regions. Churn flow was not predicted well by this map. In contrast, this map showed a reasonable prediction to annular flow. This low prediction by this map could be due to the low heat fluxes examined in their study. Maximum heat flux was reached by them up to 25 kW/m², while it became 192 kW/m² during the present experimental investigation. Moreover, the heated length during their experiment was 300 mm, which is much longer than the present length (25 mm). This may result in different transition boundaries and thus the applicability of the proposed map may also differ. Further details are discussed later.

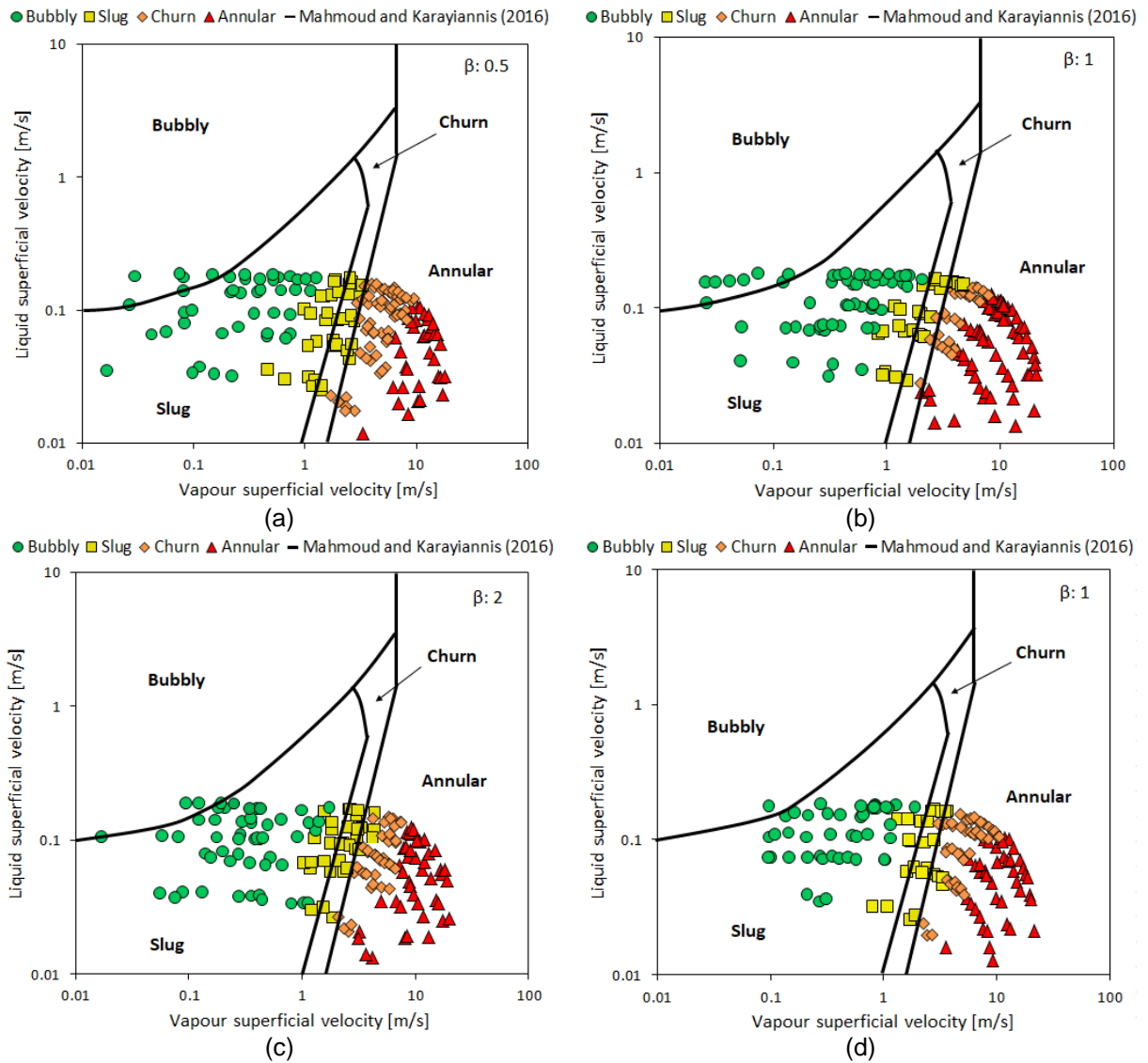


Figure 4.26 Comparison of experimental data with Mahmoud and Karayiannis (2016a) flow map for: (a) TS.1 (b) TS.2 (c) TS.3 (d) TS.4.

4.8.5 Flow patterns map by Choi et al. (2017)

Flow boiling heat transfer experiments were performed by the authors using FC-72 in horizontal multi-microchannels. The heat sink was made of copper and consisted of fifteen parallel rectangular channels with hydraulic diameter of 0.277 mm and channel length of 60 mm. These microchannels were heated from the bottom side and covered by a Polycarbonate cover plate. In their study, the inlet pressure was controlled at 1.05–1.1 bar, while the exit vapour quality was varied from 0 to 0.96. A transition criterion from bubbly/slug to annular flow was proposed by them using the Weber number and vapour quality, see Chapter 2 for more details. Their flow

patterns map was compared with the present data using the Weber number versus vapour quality as depicted in Fig. 4.27. In their proposed map, just two regions were identified, namely bubbly/slug flow and annular flow. However, in the present study, churn flow was also visualized during the experiments. Therefore, this regime was assumed to be within the annular flow in order to compare the present data with their map.

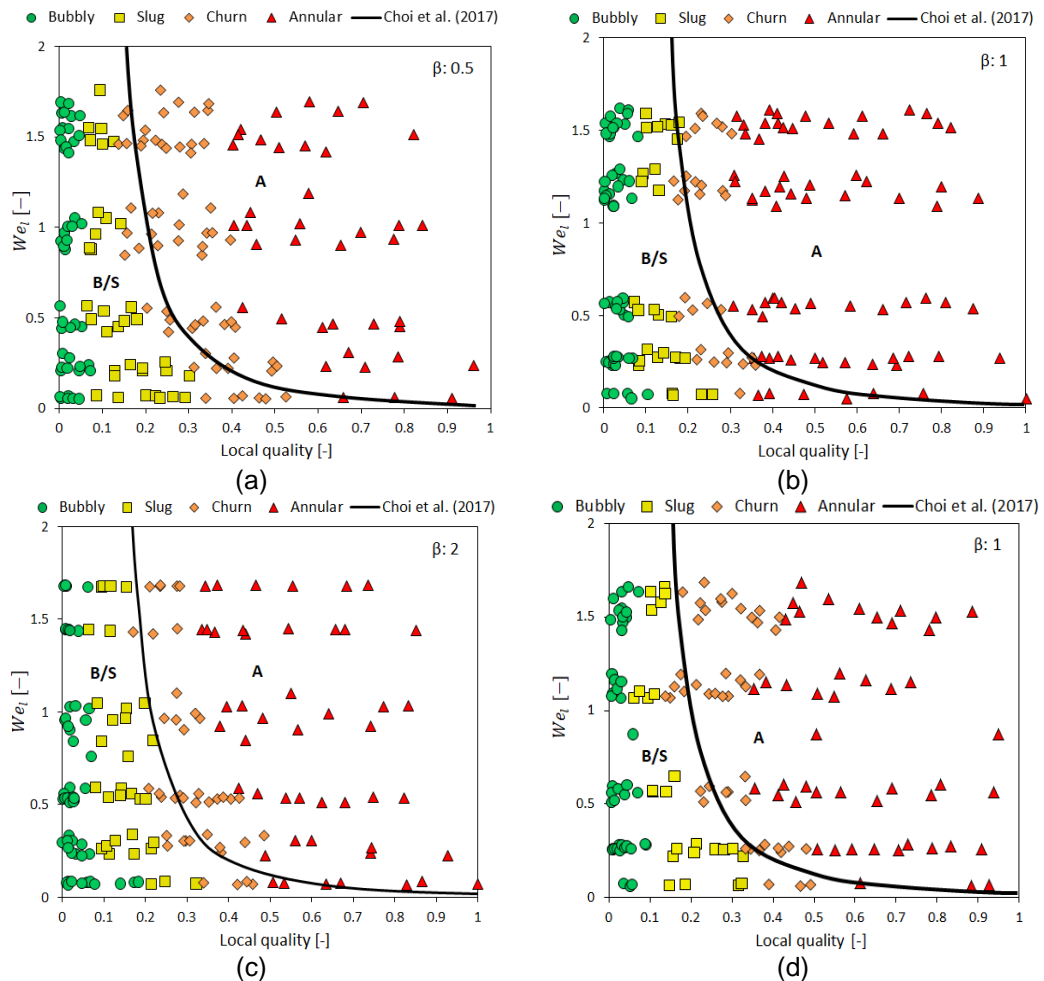


Figure 4.27 Comparison of experimental data with Choi et al. (2017) flow map for: (a) TS.1 (b) TS.2 (c) TS.3 (d) TS.4.

This figure illustrates that all the experimental data of bubbly and slug flow were located inside their prediction region, *i.e.* before their transition line, for all test sections. Although most data points of churn flow were within the annular region, some points can be seen inside the bubbly/slug region for all test sections. Most data points of annular flow were predicted by this map. However, some points were within the bubbly/slug region at lower Weber number and quality less than 0.6, see

Fig. 4.22(b) and (c). This disagreement at lower Weber number could be due to the fact that the lower mass flux range was not examined in their study. Their mass flux range is 100.3–458 kg/m²s and thus the lower present mass flux (50 kg/m²s) is not covered. Moreover, their map just includes one transition line without taking into account the churn flow. The features of this regime completely differ from those in annular flow as discussed in the previous sections.

4.8.6 Flow patterns map by Li and Hrnjak (2019)

Two-phase flow of R32 in parallel microchannel with hydraulic diameter of 0.643 mm was experimentally examined at mass flux of 50–300 kg/m²s. A high-speed camera was used to capture the flow patterns inside the test section. They observed plug/slug (vapour plug and liquid slug), transitional and annular flow, see Chapter 2 for more details. They reported that, at lower mass flux, plug/slug flow was observed, while annular flow occurred at 100 kg/m²s. Transitional flow, from plug/slug to annular flow, was visualized at mass flux of 150 kg/m²s. A flow patterns map was produced by the authors using the liquid and vapour superficial velocities. This map was compared with the present data points as shown in Fig. 4.28. This figure illustrates that most data points of bubbly flow were within the plug/slug regime. It is worth mentioning that they did not capture bubbly flow during their experiments. Some points of slug flow were located in the plug/slug regime. In contrast, most data points of this flow were within the transitional regime. This regime also included some data of churn flow, while the rest of the points were within annular regime. This comparison also shows that the data points of annular flow were predicted fairly by this map. Although the present experimental mass fluxes are within their ranges, most flow patterns are not predicted well by this map. This could be due to the different heating method. They used water for heating and thus the heat flux may vary along the channel leading to different transition boundaries. Moreover, their heated length (152.4 mm) is much longer than that in the present study (25 mm).

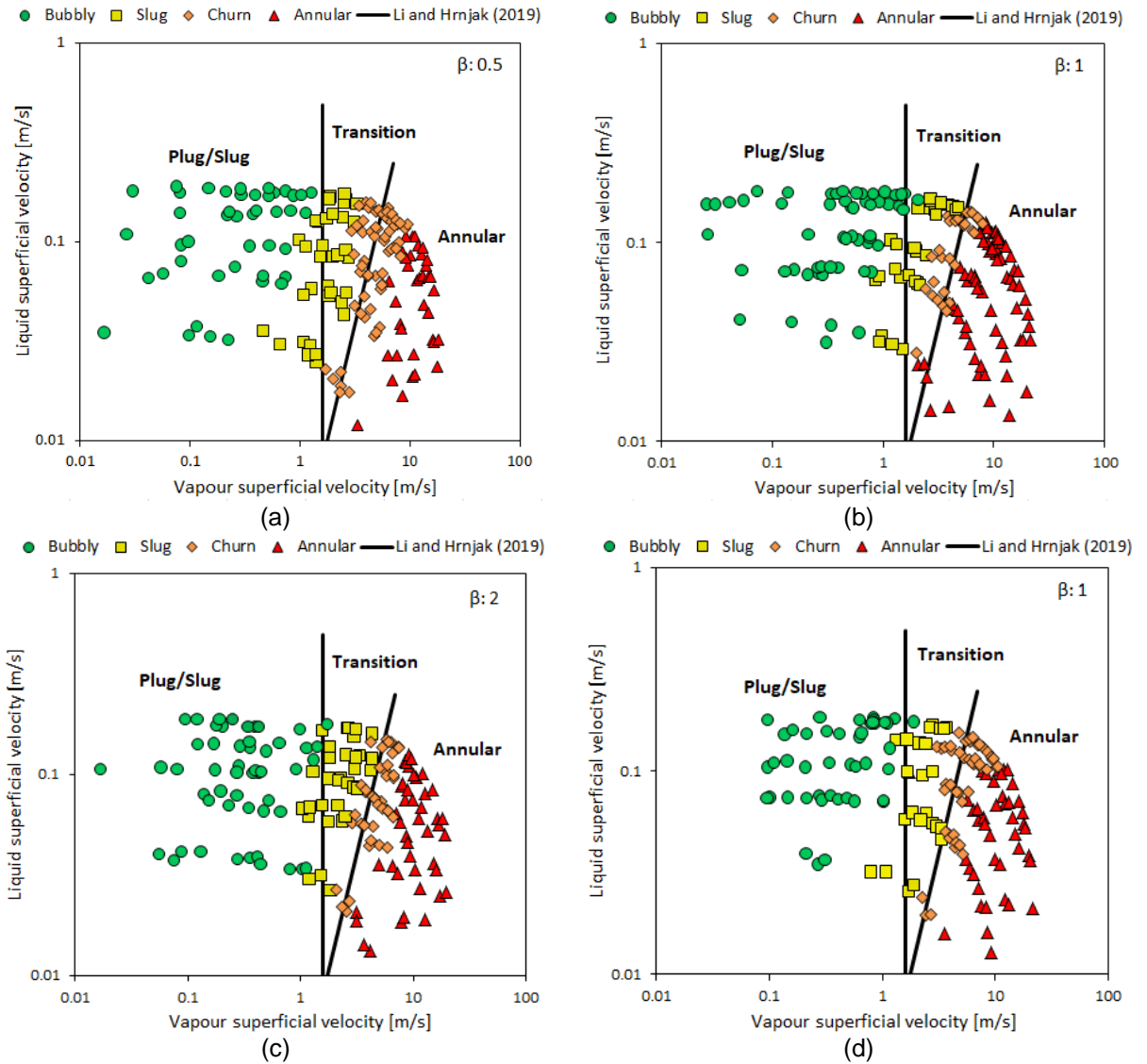


Figure 4.28 Comparison of experimental data with Li and Hrnjak (2019) flow map for: (a) TS.1 (b) TS.2 (c) TS.3 (d) TS.4.

It can be concluded from the abovementioned comparison that there is no proposed map that predict all the experimental transition boundaries although these maps were proposed for micro passages. This large discrepancy is due to different parameters that may affect the applicability of these maps as follows: (1) Different fluids and operating conditions are examined. This can result in different liquid and vapour superficial velocities and thus different dominant forces. The appearance of flow patterns depends strongly on the controlling forces. For example, surface tension dominates during bubbly and slug flow, while inertia becomes the dominant force during annular flow. (2) Different definition of flow patterns is reported. In the literature, the definition of flow patterns differs from one study to another and thus

there is no general method to define these regimes. This makes the proposed map difficult to compare with the experimental data. For example, Li and Hrnjak (2019) used the term (plug/slug) flow to define the observed vapour plug and liquid slug. By examining their images, the shape of this (vapour plug) looks like vapour slug, *i.e.* long vapour slug with round tips fills the channel size. This means that the same feature of flow pattern is observed but with two different terms. (3) Different coordinates of flow maps are used by researchers, such as G - x map, J map, We map. This means that the effect of different parameters is presented among these maps. Flow patterns map having Weber numbers (based on liquid and vapour superficial velocities) as coordinates could be suitable for micro passages since the interaction of surface tension and inertia forces is included. (4) Different surface characteristics and heated length are tested. Karayiannis et al. (2012) reported that surface characteristics resulted in different flow patterns. Two stainless steel tubes using seamless and welded methods were examined by them. They also mentioned that, at a fixed heat flux, the observed flow patterns at the exit of the shorter tube differed from those in the longer one due to the different exit vapour quality. For a given heat flux, slug flow was observed in the shorter tube, while churn flow was visualized in the longer tube. (5) Flow reversal is another important parameter that can cause fluctuation in flow patterns as discussed in Section 4.2. This results in different observed flow patterns among studies. (6) Channel configurations, *i.e.* single or multi-channels, can lead to variances in flow patterns. In multi-channels, fluid flow rate may differ between channels. This maldistribution may lead to change the features of flow patterns inside the channels. (7) The observation location can affect significantly the observed flow patterns. In the literature, most maps were proposed using single channel (tube) having an observation section at the end or multi-channels with one observation location. Flow visualization at one location is not enough to describe different features of flow patterns along the channel. This is confirmed by the present study when flow patterns were found to change along the channels even at a fixed heat and mass flux. A comprehensive flow patterns map is still required. Large database including different fluids, operating conditions and channel configurations and dimensions should be considered to expand the applicability of this map. Local flow observation along the channel helps to understand the flow pattern features and thus the heat transfer phenomenon.

4.9 Summary

The following key findings can be summarized according to the previous experimental flow visualization results:

- Four flow patterns were visualized during the flow boiling experiments. These patterns were bubbly, slug, churn and annular flow. Confined bubbles were also captured. For given heat and mass fluxes, different flow patterns occurred at different locations along the channel due to the evaporation rate and coalescence with other bubbles.
- Flow reversal occurred for all mass fluxes and test sections. This could be due to the rapid bubble generation near the channel inlet and slug formation. This affected the flow patterns for given conditions, *i.e.* the flow patterns were fluctuating between bubbly, confined bubble and slug flow.
- The visualized flow pattern changed into the next regime, *i.e.* from bubbly to slug flow, slug to churn flow and churn to annular flow, with increasing heat flux. More nucleation sites were seen when heat flux increased.
- At high heat fluxes, the observed bubbles had larger size compared to those at low heat fluxes. This was attributed to the high bubble generation and more coalescence bubbles.
- Few nucleating bubbles occurred in the liquid film of slug and annular flow for all test sections especially at high heat fluxes. High wall superheat could lead to the activation of these nucleation sites at high heat fluxes.
- The experimental flow patterns changed to the lower regime (inverse transition) with increasing mass flux for a fixed heat flux. Moreover, bubbles became smaller at high mass fluxes. This was attributed to the reduction in evaporation rate due to the high fluid velocity.
- Hysteresis effect became significant at low wall heat fluxes. The active nucleation sites with decreasing heat flux could be the reason for this effect.
- Bubbles were visualized to be larger with decreasing channel aspect ratio. This difference in the bubble size was likely due to the strong confinement effect inducing by the channel sidewalls and flow reversal. Slug ends became more curved with bullet shape for the smaller aspect ratio. There was no clear difference in the features of annular flow.

- The effect of channel surface material on the experimental flow patterns was not clear.
- The experimental data points were presented as a flow patterns map using Weber numbers based on liquid and vapour superficial velocities. These coordinates are adopted since they represent the effect of surface tension and inertia forces. This map showed that bubbly occurred at $We_{gs} \leq 1$, while slug was found at $We_{gs} < 10$. Annular flow established at $10 < We_{gs} \leq 160$.
- Some existing flow pattern maps were compared with the present data. This comparison showed that most data points of bubbly flow were predicted well by Akbar et al. (2003), Revellin and Thome (2007a) and Choi et al. (2017). This comparison also showed a good prediction to most data of slug flow. Moreover, some data of churn flow were within the prediction region. Finally, most data points of annular flow were predicted well by the existing maps. However, there is no map that can predict all the present data points and thus a universal flow patterns map is still required using large database. Local flow observation along the entire heated length should be considered.
- There is large discrepancy among the proposed maps. Different parameters may affect the applicability of these maps, such as working fluids, operating conditions, definition of flow patterns, surface characteristics, heated length, flow reversal, channel configurations and visualization location.

Chapter 5

Flow Boiling Pressure Drop: Results and Discussion

5.1 Introduction

In the present study, the total pressure drop inside the test section was experimentally measured using differential pressure transducer located at the inlet and outlet plena. This total pressure drop consists of the pressure drop in the inlet plenum due to the change in flow direction by 90° , the sudden contraction pressure drop at the channel inlet, the channel pressure drop, the sudden expansion pressure drop at the channel outlet and the pressure drop in the outlet plenum due to the change in flow direction by 90° . Therefore, the pressure drop inside the channels is calculated by subtracting the total measured pressure drop from the pressure loss components. Since the fluid is delivered to the test section at a sub-cooled condition, the channel pressure drop is due to the single-phase pressure drop and two-phase pressure drop. The pressure drop in a single-phase region can be found by calculating the subcooled length. The two-phase pressure drop is calculated by subtracting the channel pressure drop from the single-phase pressure drop, see Chapter 3, Eq. (3.26). In horizontal channels, two-phase pressure drop includes acceleration and frictional pressure drop components. The first component is a result of acceleration of vapour, *i.e.* the bubble expansion and motion, when the liquid converts to vapour. This component can be calculated using existing void fraction correlations. The void fraction correlation proposed by Zivi (1964) is commonly used, see Appendix A. The second pressure

drop component is due to the shear force between fluid and channel walls and between liquid and vapour interface. This component is calculated by subtracting the two-phase pressure drop from the acceleration pressure drop component. This chapter discusses the characteristics of two-phase pressure drop. The effects of heat flux (exit vapour quality) and mass flux on the two-phase pressure drop are presented in Section 5.2 and 5.3. The effect of channel aspect ratio is given in Section 5.4, while the channel surface material effect is presented in Section 5.5. The present two-phase pressure drop data was compared with some existing correlations and discussed in Section 5.6. Section 5.7 gives final key findings.

5.2 Effect of Heat Flux

The dependence of flow boiling pressure drop on wall heat flux is depicted in Fig. 5.1. This figure is plotted at system pressure of 1 bar, three different mass fluxes (50, 150 and 250 kg/m²s) and all range of wall heat fluxes. As seen in this figure, for a fixed mass flux, the flow boiling pressure drop increased linearly with increasing wall heat flux. Maximum flow boiling pressure drop was found to be 7.8 kPa for TS.4 at maximum mass flux, *i.e.* 250 kg/m²s. With an increase in heat flux, the wall temperature also increases leading to more activate surface cavities, *i.e.* both small and large cavity mouth become active. This results in high bubble generation and thus high coalescence rate between bubbles. Therefore, the flow resistance inside the channels increases resulting in high two-phase pressure drop. The above pressure drop results agree with the results reported by many researchers such as Qu and Mudawar (2004), Harirchian and Garimella (2008), Markal et al. (2016a) and Al-Gaheeshi (2018).

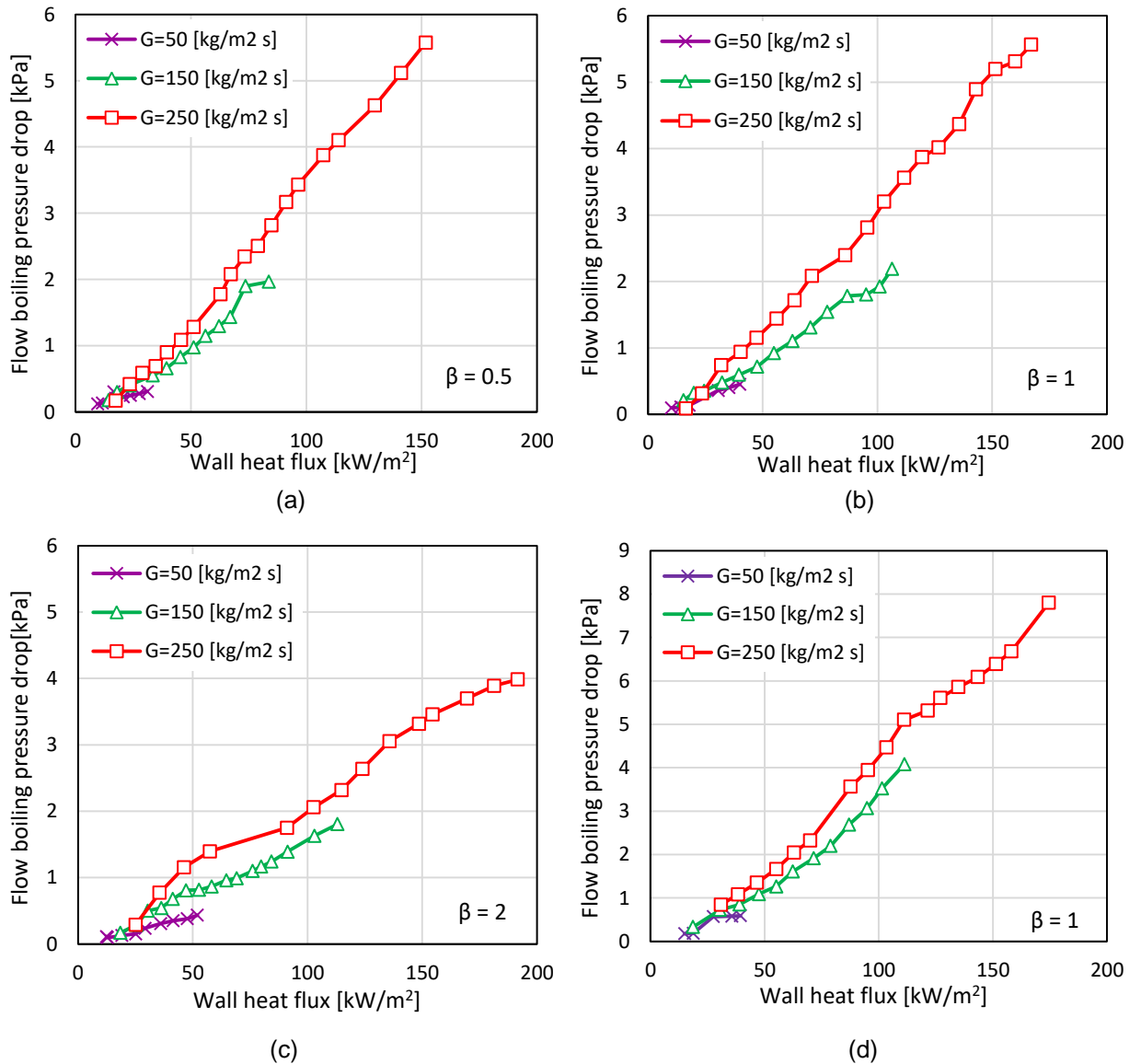


Figure 5.1 Effect of wall heat flux on the flow boiling pressure drop for:
 (a) TS.1 (b) TS.2 (c) TS.3 (d) TS.4.

5.3 Effect of Mass Flux

Five mass fluxes of 50, 100, 150, 200 and 250 kg/m²s were examined to clarify this effect. Fig. 5.2 shows the flow boiling pressure drop versus exit vapour quality at system pressure of 1 bar and for four test sections. This figure is presented at exit vapour quality up to one, *i.e.* increasing heat flux. It is obvious that the flow boiling pressure drop increased with increasing mass flux for a given exit vapour quality. This trend was seen for all test sections. An increase in mass flux leads to increase flow velocity and shear force and thus high two-phase pressure drop. Other

researchers also found that the two-phase pressure drop increased with increasing mass flux, such as Harirchian and Garimella (2008), Huang et al. (2016) and Al-Gaheeshi (2018).

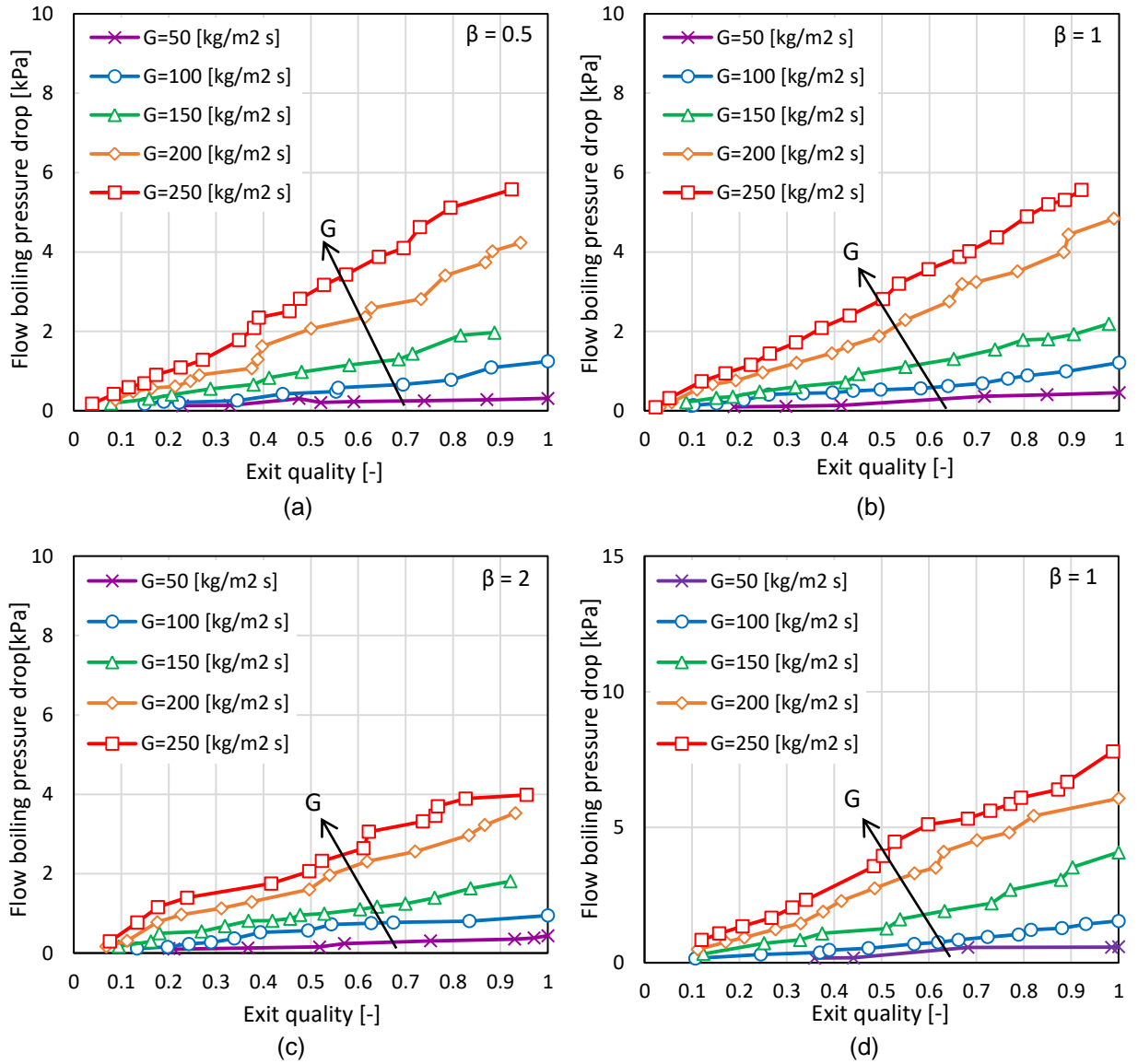


Figure 5.2 Effect of mass on the flow boiling pressure drop for:

(a) TS.1 (b) TS.2 (c) TS.3 (d) TS.4.

5.4 Effect of Channel Aspect Ratio

Three different channel aspect ratios were examined to study the effect of this parameter on the flow boiling pressure drop. Fig. 5.3 shows the flow boiling pressure drop versus wall heat flux at system pressure for 1 bar, inlet sub-cooling of 5 K and mass flux of 200 and 250 kg/m²s. This figure demonstrates that the flow boiling pressure drop increased linearly with increasing wall heat flux as discussed previously. It also shows that no effect of aspect ratio was found at the low wall heat fluxes. The effect of channel aspect ratio on the flow boiling pressure drop became significant at moderate and high wall heat fluxes.

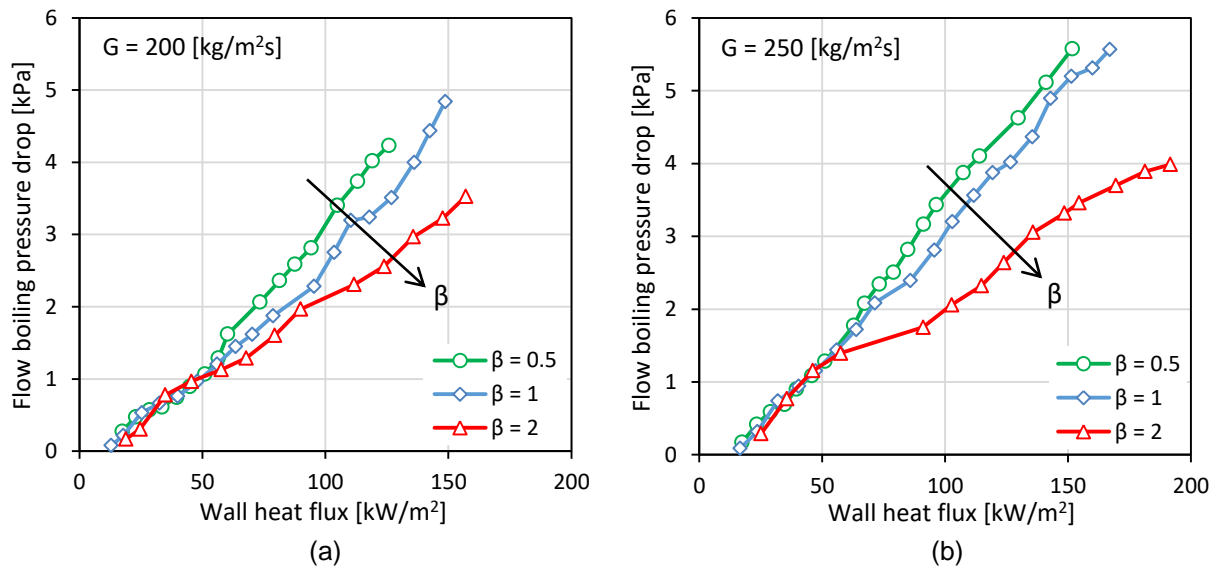


Figure 5.3 Effect of channel aspect ratio on flow boiling pressure drop for TS.1, TS.2 and TS.3 at mass flux of: (a) 200 kg/m²s (b) 250 kg/m²s.

It is known that the type of flow pattern has a significant effect on the flow boiling pressure drop. At low heat fluxes, bubbly and slug flow are the prevailing flow patterns. Since the vapour qualities are small for these regimes, the void fraction is small compared to other regimes, *i.e.* churn and annular flow, resulting in low pressure drop and unnoticeable effect of aspect ratio in low vapour qualities (low heat fluxes). In contrast, at moderate and high wall heat fluxes, the coalescence rate increases and churn and annular flow occur. High void fraction, *i.e.* vapour quality, with increasing heat flux leads to high two-phase pressure drop and thus a noticeable effect occurs. Further details are discussed in Fig. 5.4. For example, at given wall

heat flux, *i.e.* 100 kW/m^2 , and mass flux of $250 \text{ kg/m}^2\text{s}$, the flow boiling pressure drop increased by 55.6%, when the channel aspect ratio decreased from 2 to 1. Further reduction in the channel aspect ratio from 1 to 0.5 resulted in smaller increase, *i.e.* 7.2%. When the channel aspect ratio decreased from 2 to 0.5, the flow boiling pressure drop was found to increase to 66.8% at the same operating condition. Fig. 5.3(b) shows that maximum flow boiling pressure drop was found to be 3.98, 5.5 and 5.6 kPa when the channel aspect ratio was 2, 1 and 0.5, respectively. Moreover, for wall heat fluxes up to 151 kW/m^2 , the flow boiling pressure drop increased by 48.6% when the channel aspect ratio decreased from 2 to 0.5.

It is worth mentioning that the channels with aspect ratio of 2 and 0.5 had exactly the same cross sectional area while the cross sectional area of the square channel (aspect ratio of 1) was smaller by about 14%. Bearing in mind that the three examined test sections had the same hydraulic diameter, and thus the pressure drop was expected to be higher in the square channels that had smaller cross sectional area. However, Fig. 5.3 indicates that the pressure drop was higher in the channels with smaller aspect ratio (deep channels). Both acceleration and frictional pressure drop components were calculated and presented in Fig. 5.4 in order to clarify this effect.

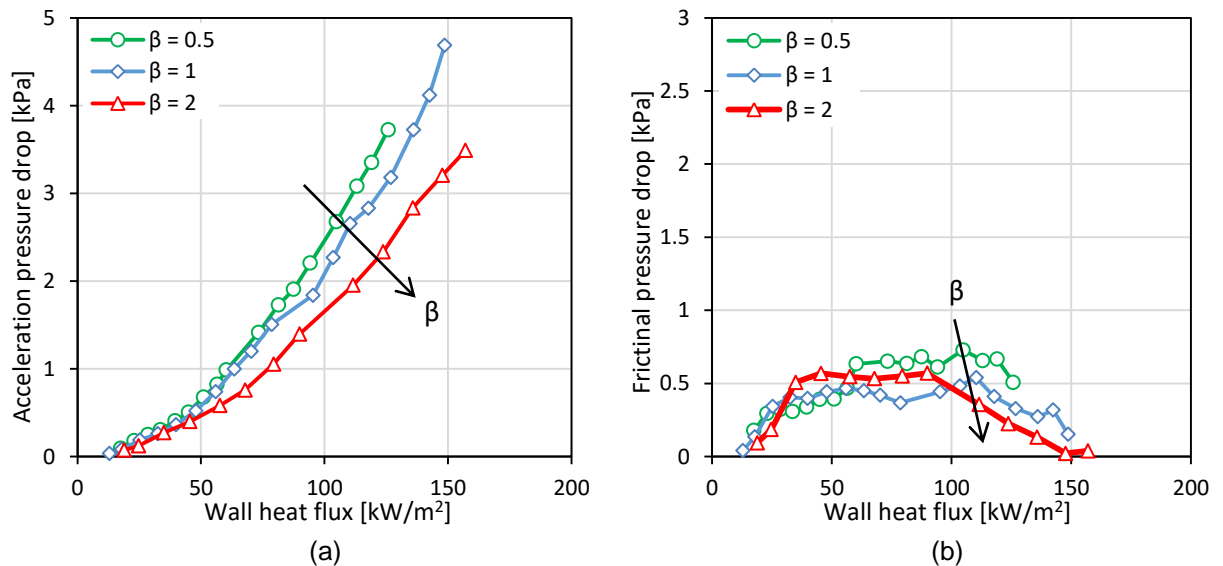


Figure 5.4 Effect of aspect ratio for TS.1, TS.2 and TS.3 at mass flux of $200 \text{ kg/m}^2\text{s}$:
 (a) Acceleration pressure drop component (b) Frictional pressure drop component.

In this figure, the acceleration component was calculated using the void fraction by Zivi (1964). This was also adopted by others, see Lee and Garimella (2008), Kim and Mudawar (2013b), Huang and Thome (2017) and Li and Hibiki (2017). This component was then subtracted from the two-phase pressure drop to calculate the frictional component. Fig. 5.4(a) shows that the acceleration pressure drop component increased with increasing heat flux for all test sections. When the heat flux increases, the wall temperature becomes high leading to increase in bubble generation and the coalescence rate. Therefore, the vapour quality increases with heat flux leading to increase the void fraction and thus the acceleration pressure drop component becomes higher. This figure also illustrates that this component became higher with decreasing channel aspect ratio at moderate and high wall heat fluxes. This could be due to the difference in the exit vapour quality. It is worth mentioning that, for a fixed wall heat flux, the test section with channel aspect ratio of 0.5 has the highest heat transfer rate compared to aspect ratio of 2 due to the largest heat transfer area. This will result in higher exit vapour quality in the test section with aspect ratio of 0.5, *i.e.* about 20% larger. Higher vapour quality means higher void fraction that leads to increase the acceleration pressure drop component.

Fig. 5.4(b) depicts the frictional pressure drop component versus wall heat flux for three heat sinks. It can be seen that the frictional component increased with heat flux and then remained almost constant with heat flux. At high wall heat fluxes, *i.e.* $q''_w \approx 100 \text{ kW/m}^2$, this component was found to decrease with increasing heat flux. When the wall heat flux increases, the coalescence rate also increases leading to high vapour velocity. As a result, the shear stress increases resulting in an increase in the frictional pressure drop component. However, with further increase in heat flux, the liquid viscosity decreases. Moreover, the liquid film thickness of annular flow becomes thinner at high heat fluxes. Therefore, the wall shear stress (between fluid and channel surface) decreases leading to reduction in frictional component. Fig. 5.4(b) also demonstrates that there was no effect of channel aspect ratio on the frictional pressure drop at low heat fluxes. In contrast, with further increase in heat flux, the smaller aspect ratio had higher frictional component compared to others. The effect of channel aspect ratio became clear at higher heat fluxes, *i.e.* the frictional pressure drop component increased with decreasing channel aspect ratio. This may be attributed to the difference in the distribution of flow patterns. At

moderate and high heat fluxes, annular flow occurred in the channels. In the channels with aspect ratio of 2 (shallow channels), most of the liquid could collect at the corners leaving a very thin liquid layer at the channel bottom surface. This results in lower shear stress and consequently low frictional contribution from the bottom surface of the channels. On the contrary, for the channels with aspect ratio 0.5 (deep channels), the liquid film at the bottom surface of the channel is expected to be thicker due to stratification effects. Thus, the shear stress in the liquid film covering the bottom surface in addition to the sidewalls is expected to be larger compared to the channels with large aspect ratio. It is worth mentioning that the results of the current study agree with the results reported by some researchers such as Harirchian and Garimella (2008), Holcomb et al. (2009), Soupremanien et al. (2011), Özdemir (2016) and Drummond et al. (2018) who reported that the pressure drop increased as the aspect ratio decreased, channel width decreased at a fixed height or channel height increased at a fixed width.

5.5 Effect of Channel Surface Material

The effect of different materials on the flow boiling pressure drop is presented in Fig. 5.5 at all ranges of wall heat flux and mass flux of 100 and 250 kg/m²s. It is obvious that the aluminium surface showed higher flow boiling pressure drop than that of copper. This influence became significant at moderate and high wall heat fluxes when the annular flow occurred with increasing heat flux (vapour quality). For example, at a mass flux of 250 kg/m²s, the flow boiling pressure drop of aluminium was slightly higher than copper when the wall heat flux was less than 60 kW/m². However, a clear effect was found with increasing heat flux to more than 60 kW/m². It was found that, at maximum mass flux, the flow boiling pressure drop increased by 28.04% when the channel surface was aluminium. Maximum flow boiling pressure drop reached up to 5.5 and 7.8 kPa when the channel surface was copper and aluminium, respectively.

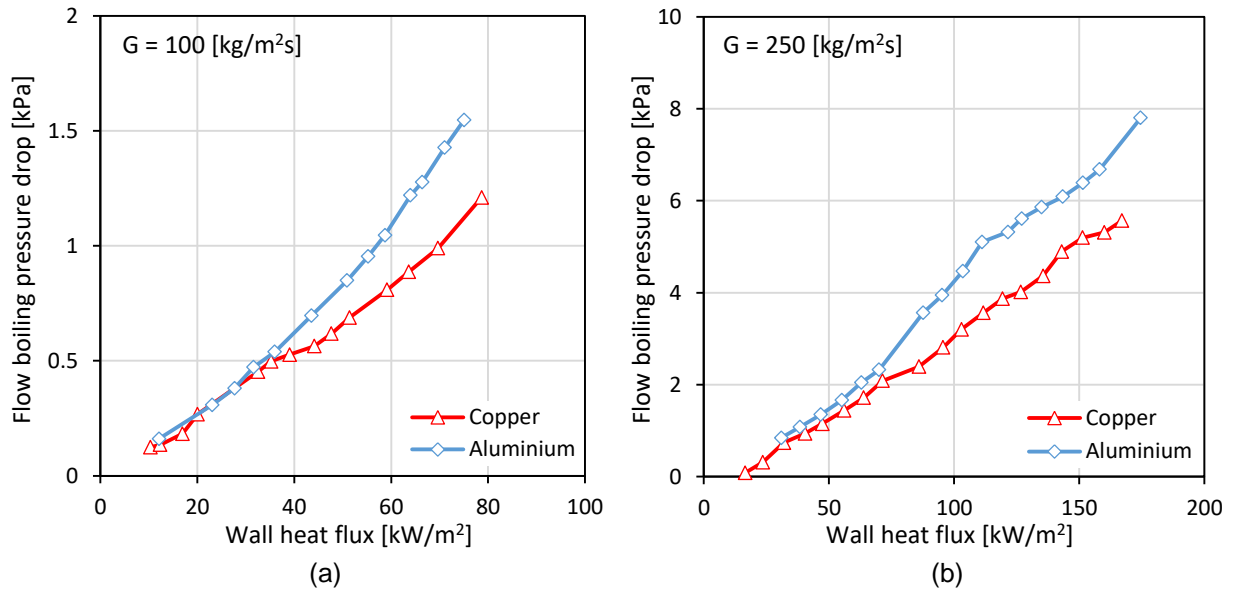


Figure 5.5 Effect of surface material on the flow boiling pressure drop for TS.2 and TS.4 at mass flux of: (a) $100 \text{ kg/m}^2\text{s}$ (b) $250 \text{ kg/m}^2\text{s}$.

Another comparison using flow boiling pressure drop versus exit vapour quality at a mass flux of $200 \text{ kg/m}^2\text{s}$ is plotted in Fig. 5.6. This figure is presented to double check the trend of pressure drop since the flow boiling pressure drop depends on the vapour quality and void fraction. This figure shows that higher flow boiling pressure drop was found for aluminium surface compared to copper. This difference became significant at exit vapour quality more than 0.32, *i.e.* wall heat flux of 55 kW/m^2 .

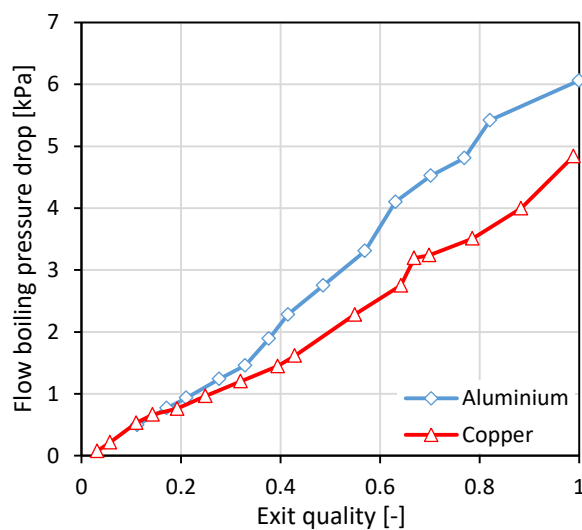


Figure 5.6 Flow boiling pressure drop versus exit vapour quality for TS.2 and TS.4 at a mass flux of $200 \text{ kg/m}^2\text{s}$.

In order to clarify the material effect, both acceleration and frictional pressure drop components are presented in Fig. 5.7 for mass flux of $200 \text{ kg/m}^2\text{s}$. Fig. 5.7(a) shows that, for both metals, the acceleration pressure drop component increased with increasing exit vapour quality (wall heat flux). This trend is explained in Section 5.4. This figure also illustrates that there was no material effect on this pressure drop component. For given heat and mass fluxes, the exit vapour quality is nearly the same for both test sections since they have the same heat transfer area, *i.e.* channel dimension and number of channels. As a result, the void fraction and thus the acceleration pressure drop component show an insignificant difference.

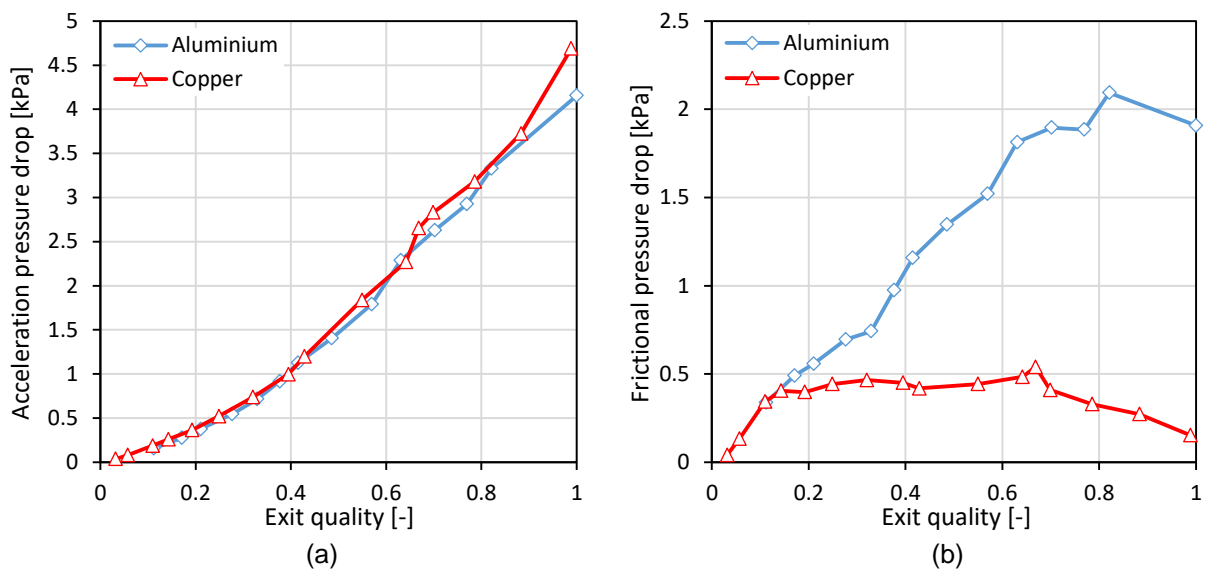


Figure 5.7 Effect of surface material for TS.2 and TS.4 at mass flux of $200 \text{ kg/m}^2\text{s}$:
 (a) Acceleration pressure drop component (b) Frictional pressure drop component.

In contrast, Fig. 5.7(b) depicts another trend when the frictional pressure drop component versus exit vapour quality is presented. For both test sections, the trend of this component increased with increasing vapour quality and then decreased, which is discussed in Section 5.4. This figure also shows that the frictional pressure drop component for aluminium was higher than that of copper. This became significant at moderate and high vapour qualities. It is worth mentioning that aluminium heat sink also showed higher pressure drop during single-phase experiments. This could be due to the surface microstructures. The experimental investigation by Pike-Wilson (2014) showed that different surface microstructures provided different frictional pressure drop. Both number and shape of surface peaks could restrict the flow and

increase the frictional pressure drop as she stated. Flow boiling of R245fa in vertical metallic tubes made of copper, brass and stainless steel were tested by the author. She also reported that the single-phase pressure drop of copper surface was double that of stainless steel, although the average surface roughness of copper (0.524 μm) was lower than that of stainless steel (0.716 μm). In the present study, high flow boiling pressure drop in aluminium heat sink is due to high frictional pressure drop component that could be affected by the surface microstructures. As discussed in Chapter 3, more debris and peaks were seen on the aluminium surface compared to those on copper surface. As a result, the flow could be disturbed by these surface microstructures, which would become apparent in annular flow. In this regime, when the liquid film is thick, more friction between this film and surface microstructures happens leading to high shear stress and frictional component. This is clear for the aluminium surface where the frictional pressure drop component continues to increase, see in Fig. 5.7(b). However, at high heat fluxes, this liquid film becomes thinner resulting in lower shear stress and consequently reduction in the frictional pressure drop component.

5.6 Comparison with Existing Correlations

In this section, a comparison between the present flow boiling pressure drop data and some existing correlations, proposed for conventional and microchannels, is discussed. One model and seven existing two-phase flow pressure drop correlations were chosen in the present study. These correlations are described in Chapter 2, while Appendix A gives full details for each correlation. In order to evaluate these correlations, the mean absolute error (*MAE*) and the percentage of data points predicted within $\pm 30\%$ error bands (Θ) were used as follows:

$$MAE = \frac{1}{N} \sum \left| \frac{\Delta P_{pred} - \Delta P_{exp}}{\Delta P_{exp}} \right| 100\% \quad (5.1)$$

$$\Theta = \frac{N_{pred}}{N} 100\% \quad (5.2)$$

where ΔP_{pred} , ΔP_{exp} , N_{pred} and N are the predicted two-phase pressure drop, experimental two-phase pressure drop, number of predicted data points within $\pm 30\%$ and the total number of data points, respectively. In these correlations, the acceleration pressure drop component was calculated using the Martinelli void

fraction, see Lockhart and Martinelli (1949), or the Zivi void fraction such as Qu and Mudawar (2003b), Lee and Garimella (2008), Keepaiboon et al. (2016), Huang and Thome (2017) and Markal et al. (2017b). The two-phase frictional pressure drop can be calculated by multiplying the two-phase frictional multiplier ϕ_l^2 and the measured single-phase pressure drop as stated by Lockhart and Martinelli (1949), see Eq. (5.3). The two-phase frictional multiplier represents the friction between phases, *i.e.* the interaction between liquid and vapour. Eq. (5.4) is used to calculate this multiplier as proposed by Chisholm (1967).

$$\left(\frac{dP}{dz}\right)_{tp} = \phi_l^2 \left(\frac{dP}{dz}\right)_{sp} \quad (5.3)$$

$$\phi_l^2 = 1 + \frac{C}{X} + \frac{1}{X^2} \quad (5.4)$$

where X is the Martinelli parameter based on the flow conditions, *i.e.* laminar or turbulent, see Appendix A. The present experimental data points included four test sections at wall heat flux ranging from 9.6 to 191.6 kW/m², five mass fluxes of 50–250 kg/m²s, system pressure of 1 bar, inlet sub-cooling of 5 K and exit vapour quality up to 1.

5.6.1 Conventional scale two-phase pressure drop correlations

5.6.1.1 The correlation of Lockhart and Martinelli (1949)

The authors proposed a two-phase multiplier to calculate the frictional pressure drop based on four different sources including different fluids in circular horizontal channels with diameter of 1.5–25.8 mm. They proposed four values of the Chisholm constant (C) according to the flow condition, *i.e.* laminar liquid-laminar vapour, laminar liquid-turbulent vapour, turbulent liquid-laminar vapour and turbulent liquid-turbulent vapour. The Martinelli void fraction correlation was used for calculating the acceleration pressure drop. This correlation was compared with the present data as shown in Fig. 5.8. It is obvious that their correlation over predicted the present data with a MAE of 113.95%, 127.9%, 157.58% and 75.63% for TS.1, TS.2, TS.3 and TS.4, respectively. This over prediction by their correlation could be due to the

difference between the thermophysical properties of HFE-7100 and their fluids (air/water, air/benzene, air/kerosene and air/oils). Further details are discussed later. Moreover, their correlation was proposed for large channels, *i.e.* more than 1.5 mm. Another reason could be the void fraction in this correlation was developed based on annular flow, while other regimes occurred during the present study, such as bubbly, slug and churn flow. This may result in different ranges of pressure drop and consequently the capability of this correlation may vary.

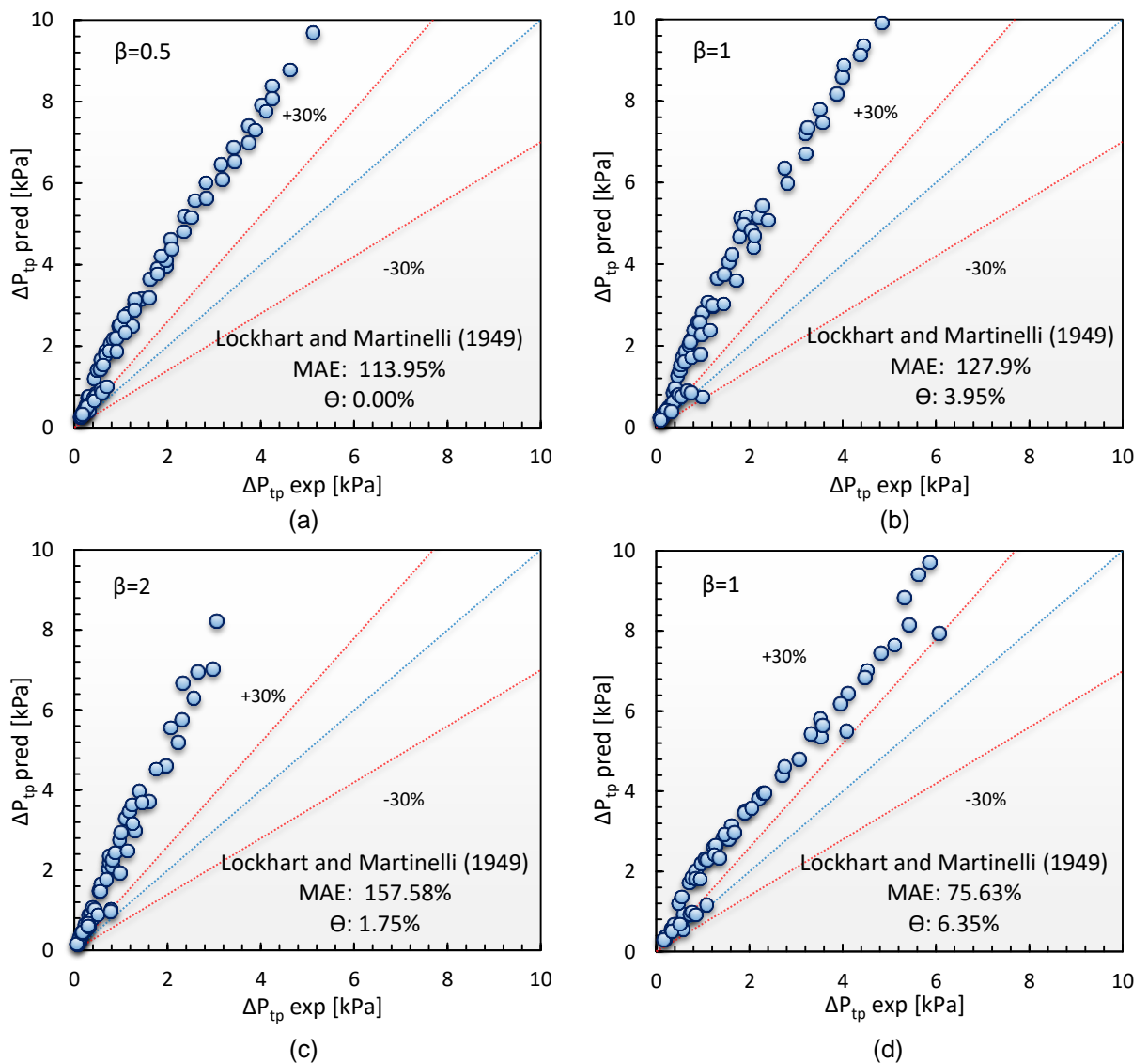


Figure 5.8 Comparison of the two-phase pressure drop data with the correlation by Lockhart and Martinelli (1949) for: (a) TS.1 (b) TS.2 (c) TS.3 (d) TS.4.

5.6.1.2 The Homogenous flow model (1994)

In this model, both phases, *i.e.* liquid and vapour, were modelled as one phase and the slip velocity between them was assumed to be negligible, see Collier and Thome (1994). Further details about this model are given in Appendix A. When this model was compared with the present data, see Fig. 5.9, 38.6% of the present data of the aspect ratio 2 was predicted with a MAE of 37.15%. However, this model showed better prediction when the channel aspect ratio decreased. For example, for aspect ratio of 1, this model predicted 55.26% of the data with a MAE of 30.74%. For aspect ratio of 0.5, 65.33% of the present data was predicted by this model with a MAE of 22.98%. This comparison also shows that the homogenous model predicted well the present data of TS.4 with a MAE of 12.42%.

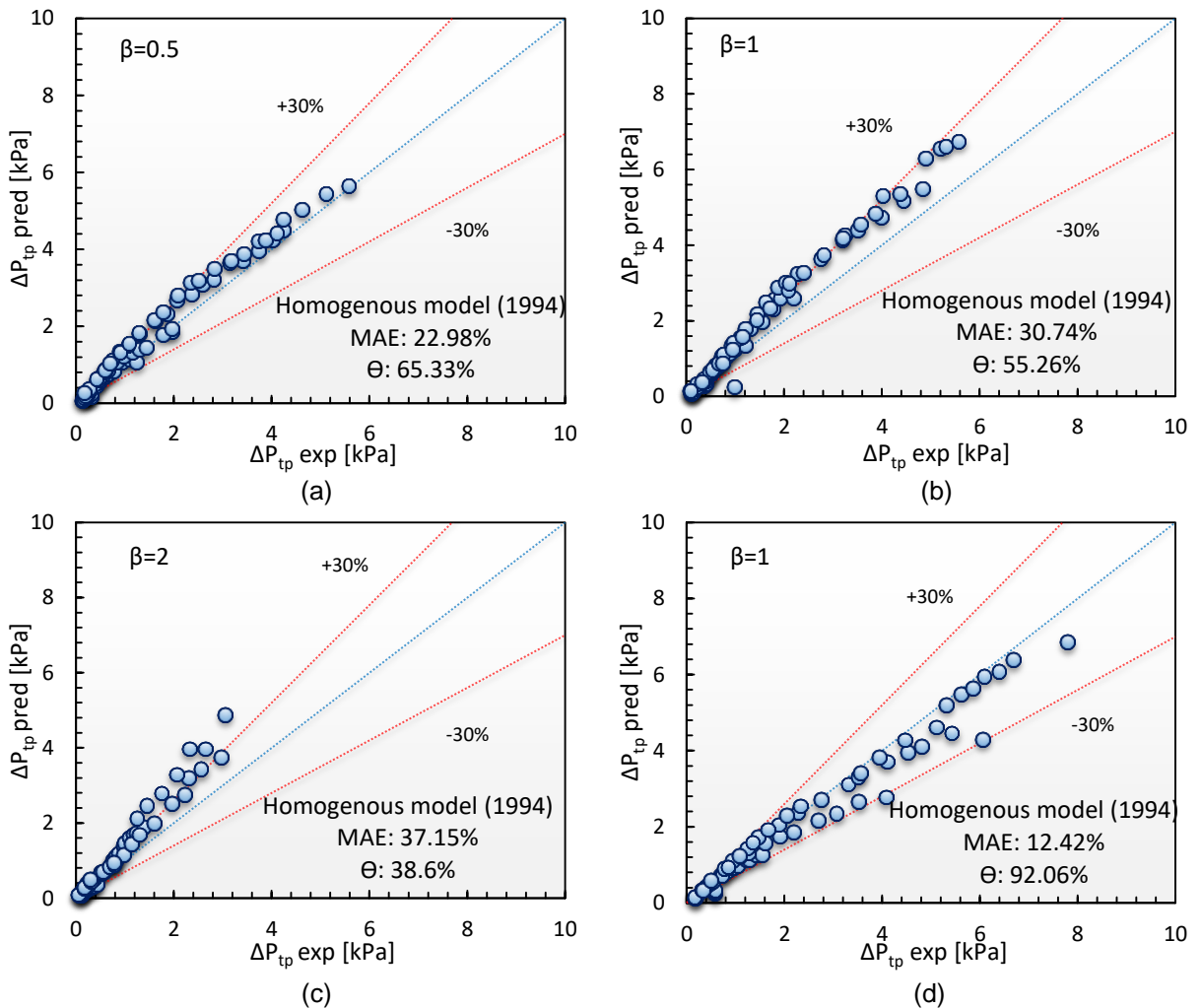


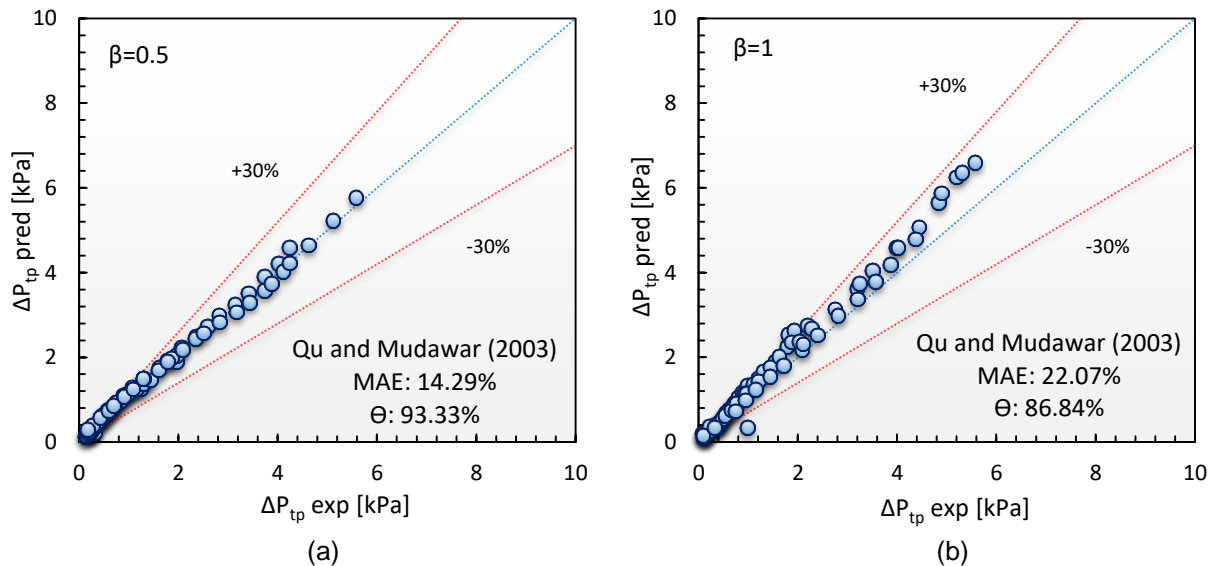
Figure 5.9 Comparison of the two-phase pressure drop data with the homogenous model, Collier and Thome (1994) for: (a) TS.1 (b) TS.2 (c) TS.3 (d) TS.4.

It is worth mentioning that this model is suitable for bubbly and slug flow, which were observed in the present study. This may improve the prediction of this model. Moreover, the best agreement with TS.1 and TS.4 may show that there is good mixing for phases, *i.e.* the slip ratio u_g/u_l between phases is close to unity.

5.6.2 Mini/micro-scale two-phase pressure drop correlations

5.6.2.1 The correlation of Qu and Mudawar (2003b)

An experimental investigation of flow boiling of water in horizontal multi-channels was carried out by the authors. The heat sink consisted of twenty one rectangular microchannels with hydraulic diameter of 0.35 mm. The Chisholm constant was modified in their study to include the effect of mass flux. Fig. 5.10 demonstrates that there was a good agreement between their correlation and the data for TS.1. This correlation was able to predict 93.33% of the data with a MAE of 14.29%. For TS.2, 86.84% of the data was predicted with a MAE of 22.07%. However, this correlation showed less prediction for the larger aspect ratio. It predicted 47.37% of the data with a MAE of 36.51%. This comparison also shows that 96.83% of the experimental data for TS.4 was predicted with a MAE of 12.96%.



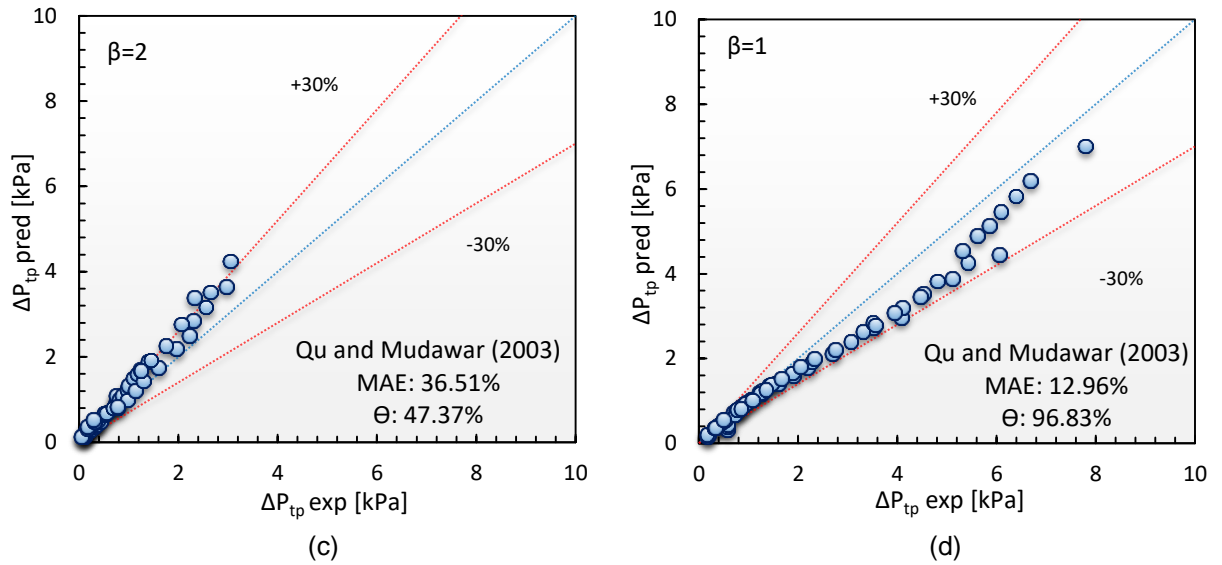


Figure 5.10 Comparison of the two-phase pressure drop data with the correlation by Qu and Mudawar (2003b) for: (a) TS.1 (b) TS.2 (c) TS.3 (d) TS.4.

This reasonable agreement with TS.1 and TS.4 could be due to the effect of mass flux in their Chisholm constant that affects the frictional pressure drop component. Their mass flux ranges were set at 135–400 kg/m²s. High mass fluxes result in high Chisholm constant and two-phase frictional multiplier, see their correlation in Appendix A. This leads to an increase in the ranges of pressure drop, *i.e.* this correlation can predict high ranges. Their data showed that the experimental ranges were around 0.48–20.5 kPa. In the present study, TS.1 showed higher pressure drop compared to TS.2 and TS.3. These high ranges of pressure drop were also found for TS.4. When experimental pressure drop data become higher, the results can be predicted fairly by their correlation, *i.e.* the experimental results become close or within their ranges.

5.6.2.2 The correlation of Lee and Garimella (2008)

Lee and Garimella (2008) conducted an experimental flow boiling study using water in horizontal rectangular multi-microchannels. The hydraulic diameter was varied from 0.162 to 0.571 mm. Similar to Qu and Mudawar (2003b), the Chisholm constant was modified by them as a function of mass flux and hydraulic diameter. The comparison with their correlation is presented in Fig. 5.11.

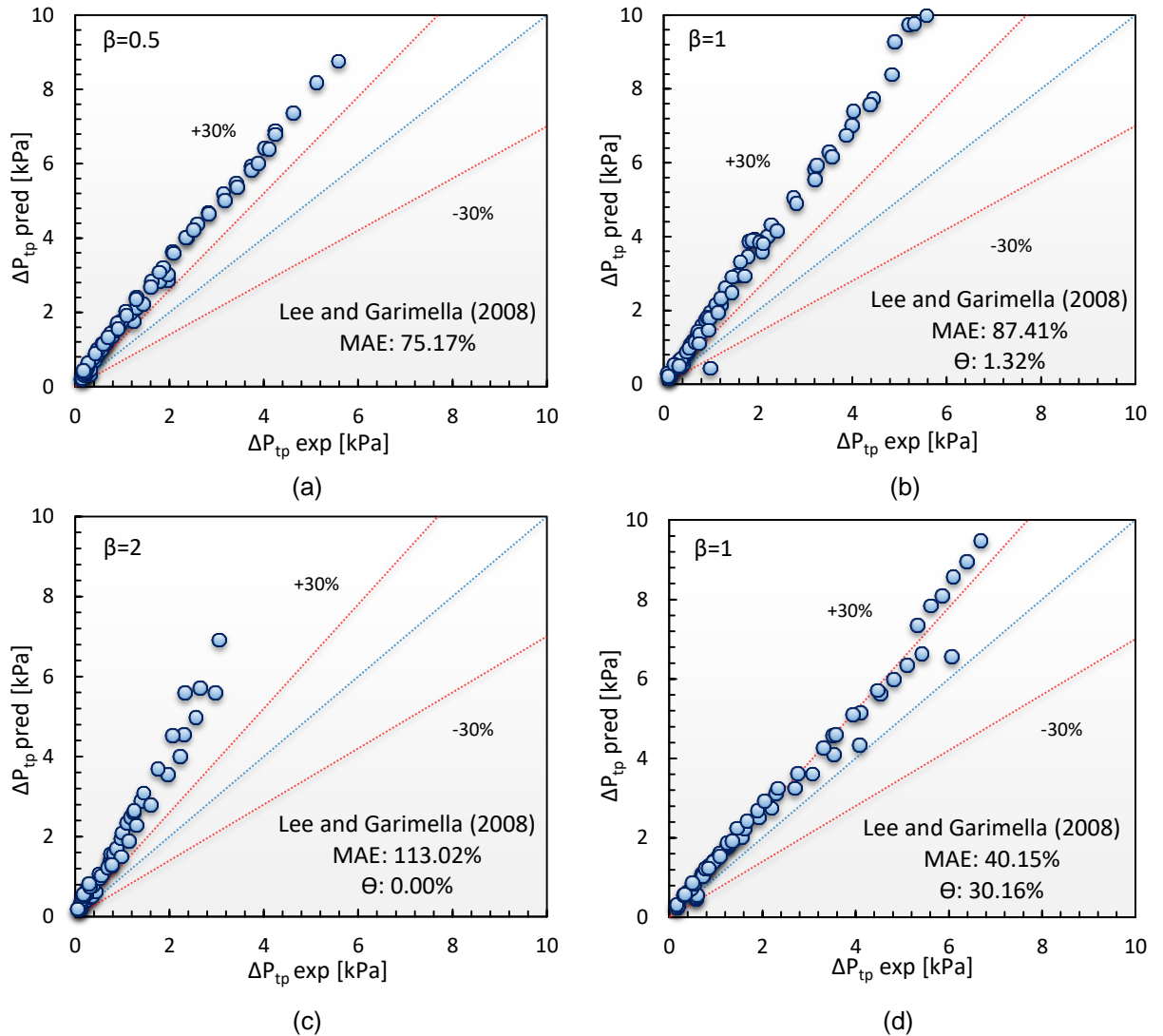


Figure 5.11 Comparison of the two-phase pressure drop data with the correlation by Lee and Garimella (2008) for: (a) TS.1 (b) TS.2 (c) TS.3 (d) TS.4.

This figure demonstrates that their correlation over predicted the present data with a MAE of 75.17%, 87.41% and 113.02% for the aspect ratio of 0.5, 1 and 2, respectively. The comparison with the experimental data of TS.4 showed that 30.16% of data was predicted with a MAE of 40.15%. This poor prediction by their correlation may be attributed to the fact that their Chisholm constant in the two-phase frictional multiplier was proposed for laminar liquid-laminar vapour. The data of the present study include laminar liquid-laminar vapour and laminar liquid-turbulent vapour flow, see Chapter 4, Section 4.3. This may affect the correlation performance, further details are discussed later.

5.6.2.3 The correlation of Keepaiboon et al. (2016)

An experimental investigation of flow boiling pressure drop using R134a was performed by the authors. A horizontal single rectangular microchannel was manufactured with hydraulic diameter of 0.68 mm. They proposed a (*C*) coefficient in the two-phase frictional multiplier, *i.e.* Chisholm constant, based on their experimental data. Dimensionless groups were used in this coefficient including liquid only Reynolds number, confinement number and Martinelli parameter. They did not state the reason for their choice. The present data were compared with their correlation for all test sections as shown in Fig 5.12. This figure demonstrates that there was a reasonable agreement between this correlation and the experimental data points. For example, their correlation predicted 98.67% of the data with a MAE of 9.09% for the aspect ratio of 0.5. When the channel aspect ratio was 1, 86.84% of the present data was predicted with a MAE of 17.89%. With further increase in aspect ratio, *i.e.* 2, their correlation predicted 82.46% of the data with a MAE of 19.19%. Moreover, this correlation predicted well the data points for TS.4 with a percentage of prediction of 84.13% and a mean absolute error of 20.33%. Although their correlation was proposed for a single channel, a reasonable agreement is found with the present data. This may be due to their channel hydraulic diameter (0.68 mm) is close to the present study (0.46 mm). The channel hydraulic diameter has a significant influence on two-phase pressure drop especially in micro passages. Another possible reason could be the Confinement number in their two-phase frictional multiplier. This number takes into account the effect of surface tension, hydraulic diameter and fluid properties. It is known that surface tension plays a significant role in bubbly and slug flow. These two regimes were seen in the present study at all experimental ranges. This may improve the applicability of their correlation for these two regimes.

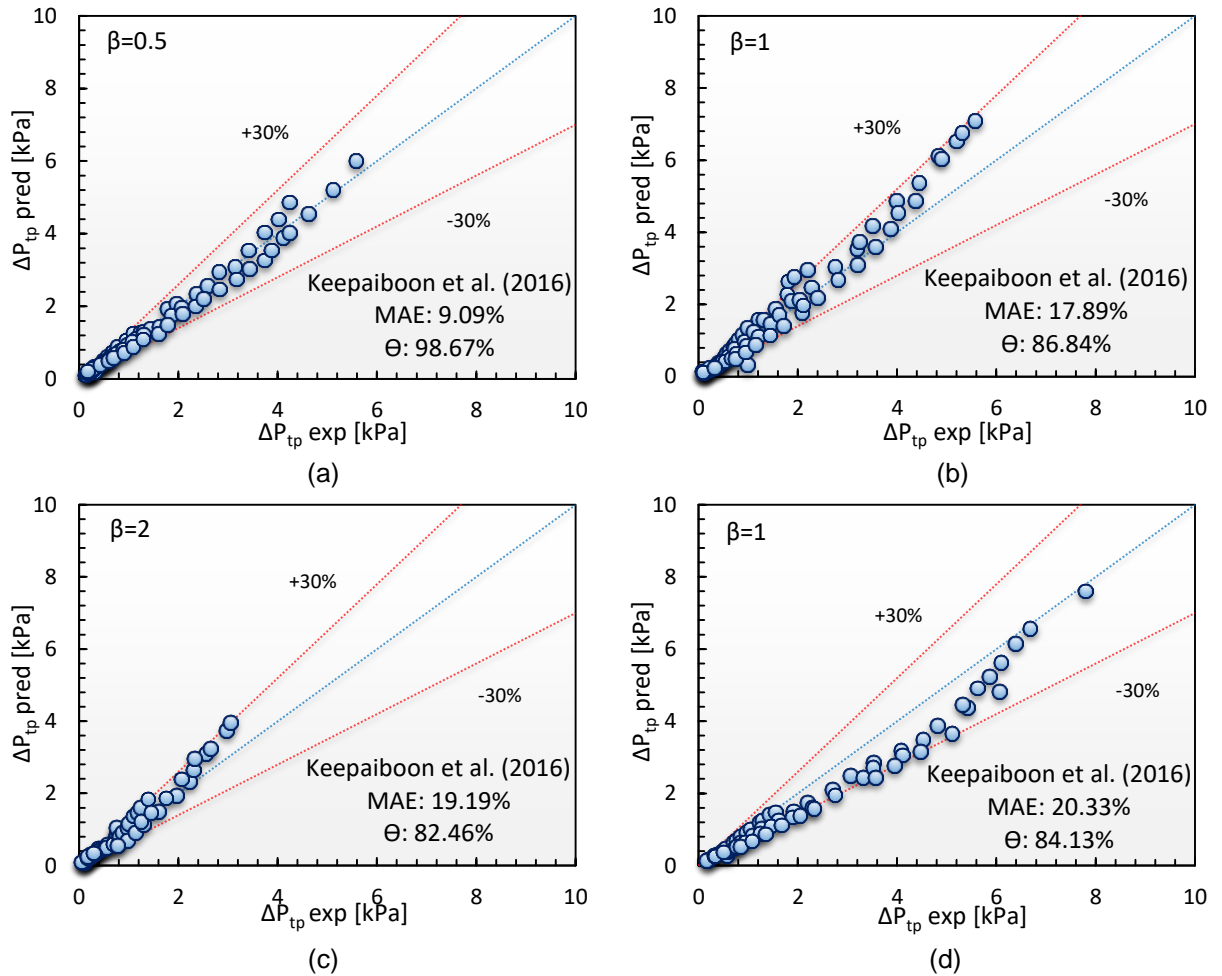


Figure 5.12 Comparison of the two-phase pressure drop data with the correlation by Keepaiboon et al. (2016) for: (a) TS.1 (b) TS.2 (c) TS.3 (d) TS.4.

5.6.2.4 The correlation of Huang and Thome (2017)

An experimental study of flow boiling pressure drop using different fluids was conducted by the authors. R1233zd(E), R245fa and R236fa were tested in horizontal square multi-microchannels. The heat sink consisted of 67 parallel channels with hydraulic diameter of 0.1 mm. They compared their results with some existing correlations and found that the mini/microchannels correlation predicted their results better than those proposed for macrochannels. However, these existing correlations for mini/microchannels under predicted their experimental data when the frictional pressure drop was more than 15 kPa. Therefore, they fitted the Chisholm constant with the experimental data by taking into account the effect of mass flux and vapour quality since high mass fluxes were tested. This constant included the superficial vapour Reynolds number and the liquid only Reynolds number. This correlation was compared with the present data as depicted in Fig. 5.13. It is obvious that this

correlation showed poor prediction, *i.e.* predicted 34.67%, 18.42% and 5.26% of the present data with a MAE of 61.46%, 58.17% and 96.09% for the aspect ratio of 0.5, 1 and 2, respectively. Moreover, the data points of TS.4 were predicted by their correlation with a MAE of 29.4%. This limited prediction could be due the fact that to their correlation was proposed for high mass fluxes. For instance, their mass flux was varied from 1250 to 2750 kg/m²s, which is much higher than the present study (50–250 kg/m²s). Different mass fluxes result in different dominant forces that affect the two-phase pressure drop as discussed later.

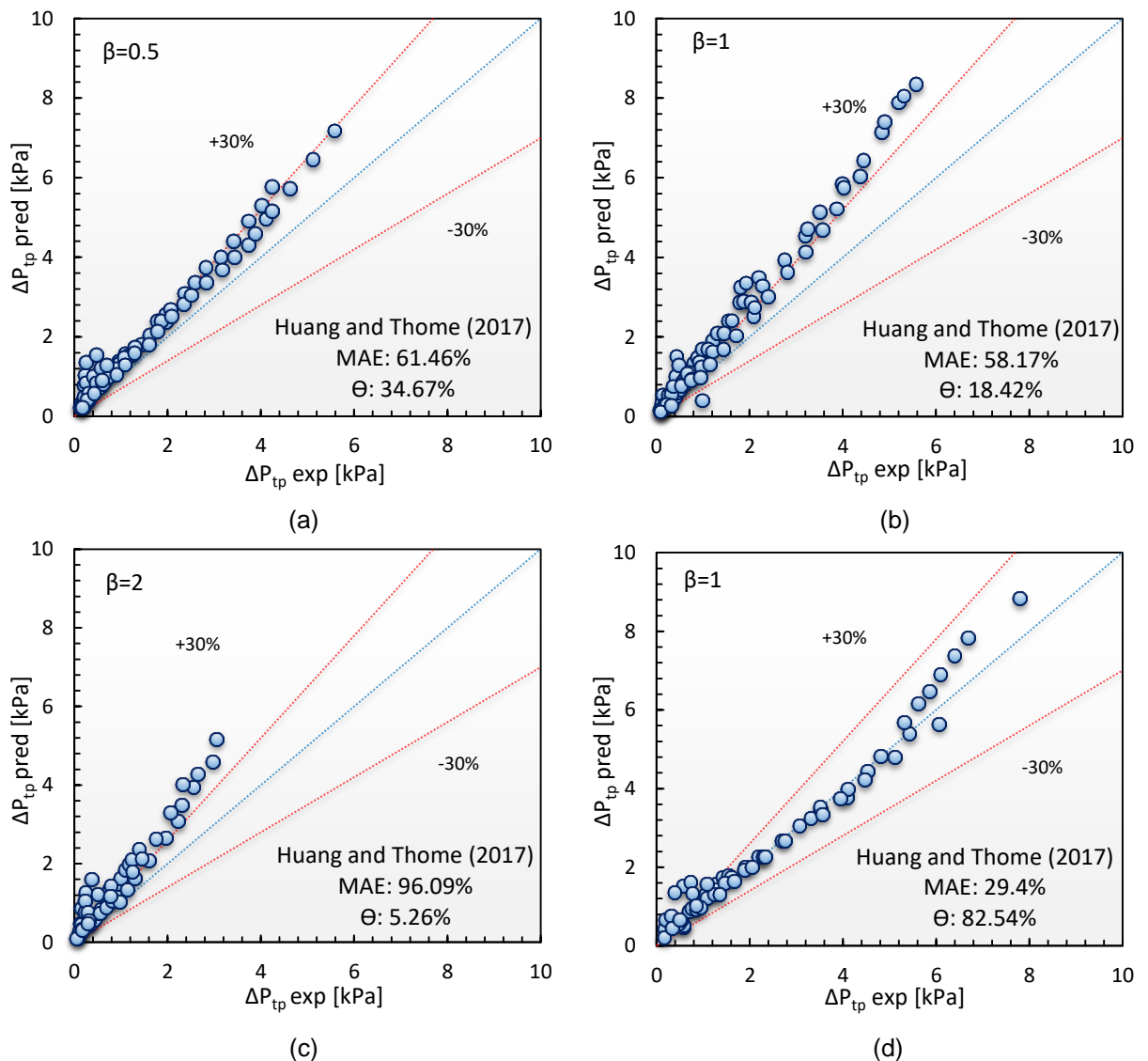
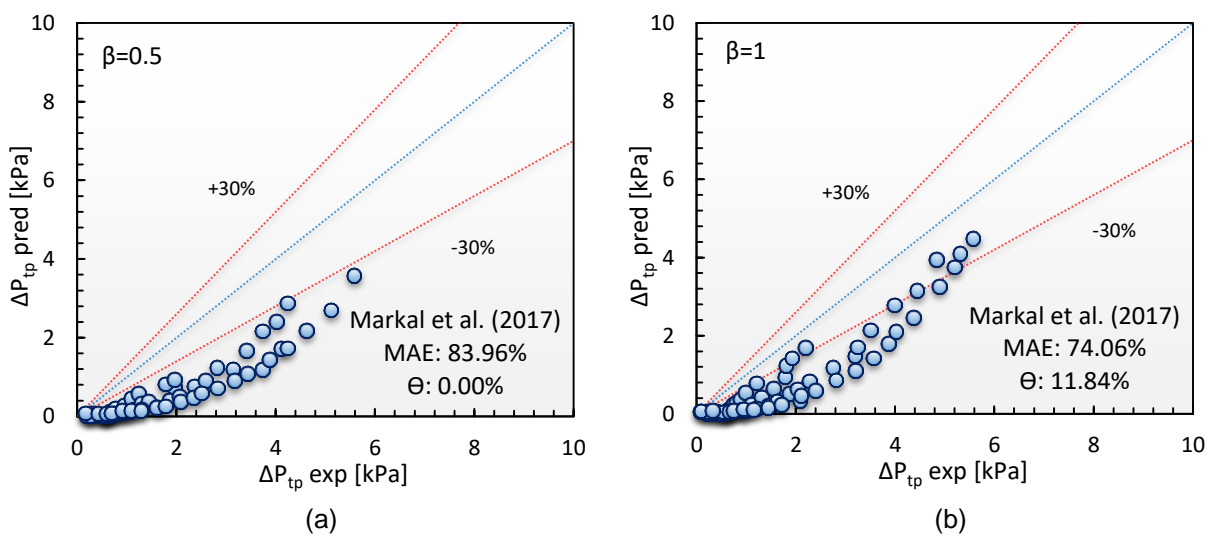


Figure 5.13 Comparison of the two-phase pressure drop data with the correlation by Huang and Thome (2017) for: (a) TS.1 (b) TS.2 (c) TS.3 (d) TS.4.

5.6.2.5 The correlation of Markal et al. (2017b)

Two empirical correlations of flow boiling pressure drop were developed by the authors. De-ionized water was tested in horizontal rectangular multi-microchannels. In their study, different aspect ratios ranging from 0.37–5 at hydraulic diameter of 0.1–0.25 mm were examined. They proposed their first correlation for calculating frictional pressure drop, while the second one for two-phase total pressure drop for bubble confinement flows. They did not explain the conditions of this flow. In their first correlation, the (C) parameter in the two-phase frictional multiplier was proposed as a function of several parameters. This included aspect ratio, liquid only Reynolds number, Webber number, Boiling number, two-phase length, hydraulic diameter, vapour quality and fluid density ratio. Their first correlation was compared with the present data as shown in Fig. 5.14. It is obvious that their correlation under predicted the present data with a MAE of 83.96%, 74.06%, 88.87% and 81.24% for TS.1, TS.2, TS.3 and TS.4, respectively. It can be concluded from this comparison that although the effect of channel aspect ratio was taken into account in their study, their correlation showed poor prediction. This could be attributed to the different thermophysical properties between water and HFE-7100. Another possible reason could be the channel length. Their channels length was 48 mm, which is approximately two times larger than the current channel length (25 mm). Large heated length result in high range of pressure drop as discussed later.



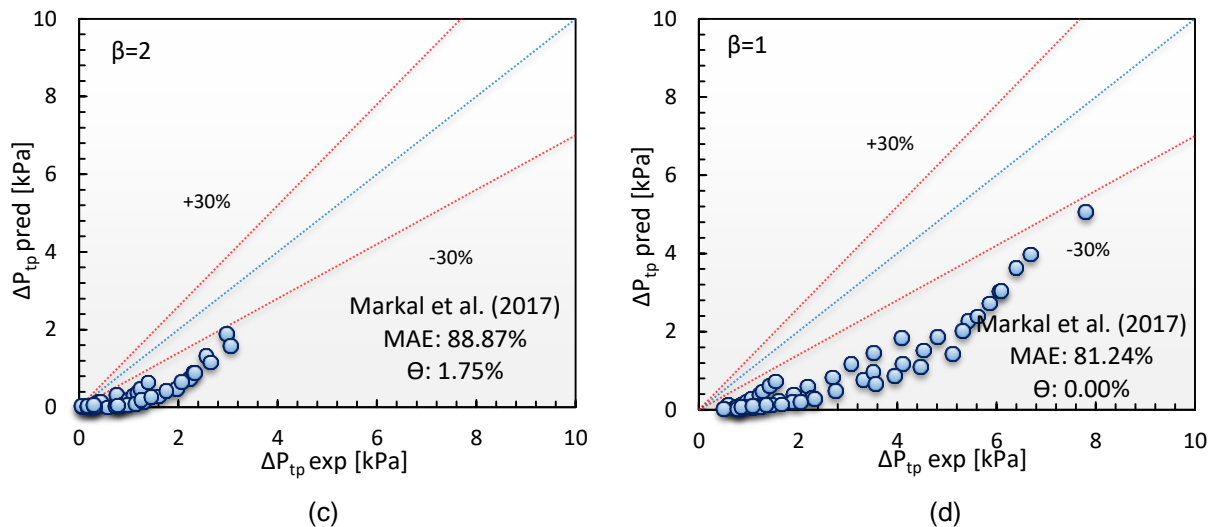


Figure 5.14 Comparison of the two-phase pressure drop data with the correlation by Markal et al. (2017b) for: (a) TS.1 (b) TS.2 (c) TS.3 (d) TS.4.

5.6.2.6 The correlation of Gao et al. (2019)

Two-phase flow experiments of ammonia in horizontal tubes were conducted by the authors. They tested 8 mm inner diameter tube made of stainless steel at saturation temperature of -15.8 – 4.6 °C and mass flux of 20 – 100 $\text{kg/m}^2\text{s}$. They also used the experimental data of their previous work using 4 mm diameter tube. Their data was compared with several existing correlations for computing frictional pressure drop component. They found that the correlation by Muller-Steinhagen and Heck (1986) showed better prediction. This correlation could predict 80% of their data within 30% error bands. Accordingly, they proposed a frictional pressure drop correlation to increase the agreement with predicted data points. They conducted force analysis and reported that surface tension, inertia and gravitational forces were much larger than viscous force. Therefore, they modified the correlation of Muller-Steinhagen and Heck (1986) by introducing Reynolds number (inertia to viscous force) and Bond number (gravity to surface tension force). They evaluated their correlation using collected database from eleven sources including different fluids (R22, R134a, ammonia and CO_2), inner diameter of 0.81 – 14 mm and mass flux of 50 – 800 $\text{kg/m}^2\text{s}$. Fig. 5.15 shows a comparison between the present data and this correlation. It is obvious that their correlation predicted well the data with a MAE of 12.36%, 14.96%, 17.56% and 26.61% for the test sections (1), (2), (3) and (4), respectively.

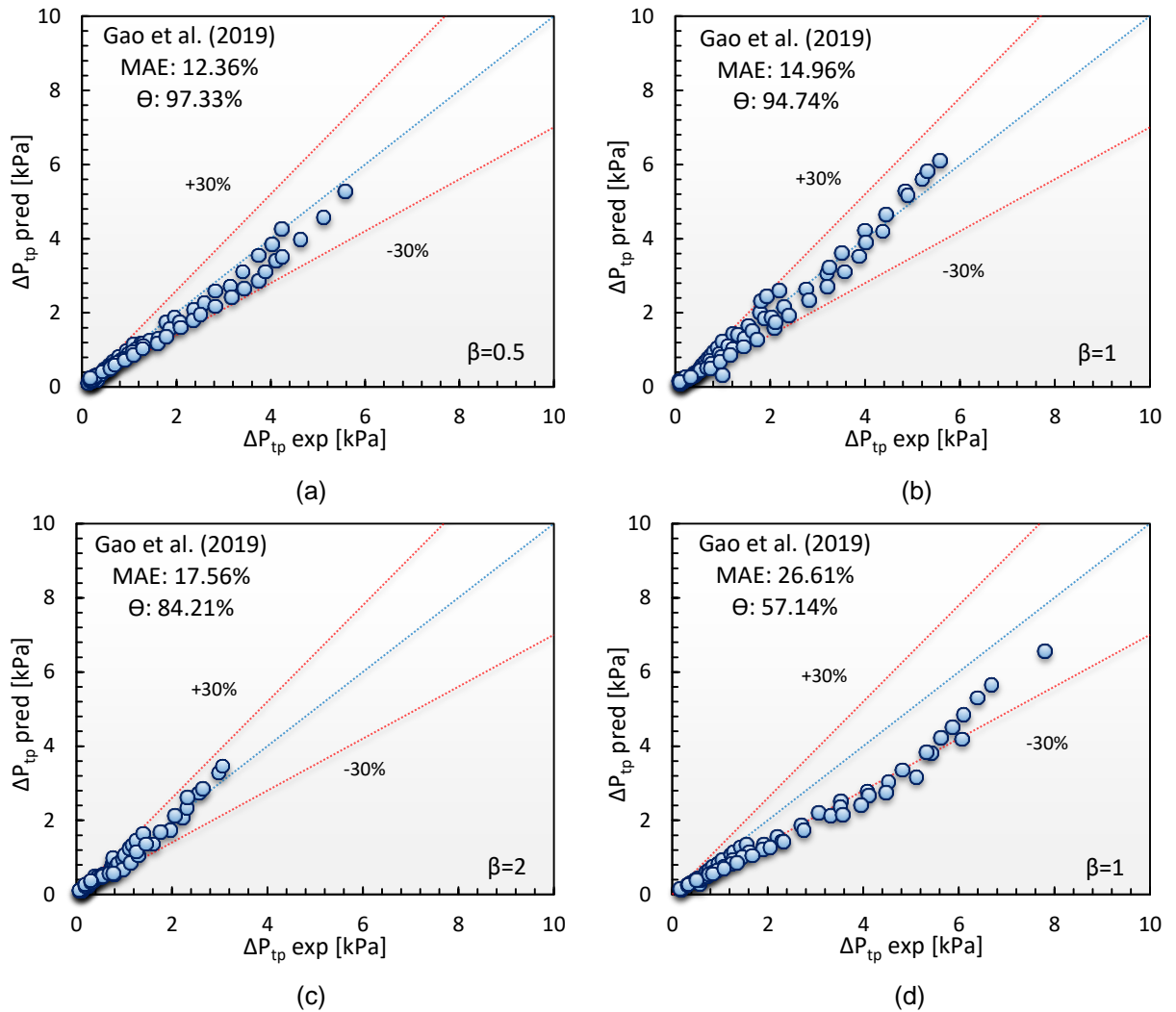


Figure 5.15 Comparison of the two-phase pressure drop data with the correlation by Gao et al. (2019) for: (a) TS.1 (b) TS.2 (c) TS.3 (d) TS.4.

This good agreement could be due to their correlation covered low mass fluxes, *i.e.* $\geq 20 \text{ kg/m}^2\text{s}$, which are within the present ranges. Another possible reason could be due to the Bond number in this correlation. Surface tension is represented by this number and becomes the dominant force during bubbly and slug flow, which were observed during all experimental ranges.

Eight existing two-phase model and pressure drop correlations were compared with 271 experimental data points. A summary of this comparison is presented in Table 5.1. This table demonstrates that most correlations do not predict all the present data for all test sections with a reasonable accuracy. However, the correlation by Keepaiboon et al. (2016) shows a better prediction for all test sections with a mean absolute error equal or less than 20%. Another correlation proposed by Gao et al.

(2019) also predicts the present experimental data well with a MAE of 12–26%. This large discrepancy among the proposed pressure drop correlations could be due to different fluids, channel dimensions, operating conditions and surface structures that were examined and used to propose these correlations.

Different thermophysical properties may result in different pressure drop results. Density ratio (liquid to vapour density) and liquid viscosity are the main parameters that affect the two-phase pressure drop as stated by Pike-Wilson (2014), Huang and Thome (2017) and Al-Gaheeshi (2018). They tested different fluids (R245fa, R134a, R1233zd(E) and R236fa) in vertical tubes and horizontal multi-microchannels. Small density ratio results in low vapour superficial velocity and thus lower wall shear stress (between fluid and channel) and lower interfacial shear stress (between liquid and vapour interface). This leads to reduction in the frictional pressure drop. Low vapour velocity means low void fraction and thus the acceleration pressure drop decreases. The reduction in liquid viscosity also leads to decrease the wall shear stress and the frictional pressure drop component. Different channel dimensions have a significant effect on two-phase pressure drop as reported in the literature. Mahmoud (2011) reported that the reduction in channel diameter leads to an increase in two-phase pressure drop. High vapour velocity with decreasing channel diameter results in high wall shear stress and frictional pressure drop. The Confinement effect also becomes important with decreasing channel diameter resulting in high coalescence rate (high flow resistance) and thus the two-phase pressure drop increases. The channel heated length is another parameter that affects the pressure drop data as stated by Mahmoud (2011). He reported that, at the same exit quality, the shorter length has higher pressure drop per unit length. Shorter channel length requires high heat flux to achieve the same exit vapour quality resulting in appearance of nucleating bubbles (high wall superheat) and thus high frictional pressure drop as he mentioned. Channel aspect ratio also has a significant effect on two-phase pressure drop as discussed in the present study and also by others, see Harirchian and Garimella (2008), Holcomb et al. (2009), Soupremanien et al. (2011), Özdemir (2016) and Drummond et al. (2018). In multi-channels, flow rate may vary between the neighboring channels leading to the appearance of different flow patterns and thus different pressure drop compared to a single channel. Different experimental operating conditions are another possible reason for different pressure

drop results among studies. Huang and Thome (2017) mentioned that the total pressure drop decreases with increasing system pressure or saturation temperature. They attributed to the effect of saturation temperature on both wall and interfacial shear stress. When saturation temperature increases, liquid viscosity decreases leading to lower wall shear stress between liquid and channel wall. Moreover, the density ratio (liquid to vapour density) decreases and thus the slip ratio between liquid and vapour interface decreases leading to lower interfacial shear stress. The present study shows that an increase in heat flux or mass flux leads to an increase in the two-phase pressure drop, which also reported by Qu and Mudawar (2004), Harirchian and Garimella (2008), Markal et al. (2016a) and Al-Gaheeshi (2018). Surface structures (flaws or peaks) can restrict and disturb the liquid film leading to affect the frictional pressure drop component as stated by Pike-Wilson (2014).

All the abovementioned parameters can result in different flow conditions and patterns and thus different dominant forces. In macrochannels, turbulent liquid–turbulent vapour flow is common, while laminar liquid–laminar vapour flow is often seen in microchannels due to low flow rate and small dimensions as stated by Lee and Garimella (2008). Li and Wu (2010a) mentioned that the viscous force dominates in laminar flow at low Reynolds numbers, while inertia becomes the dominant force in turbulent flow at high Reynolds numbers. They also stated that surface tension dominates with decreasing channel hydraulic diameter due to the squeeze bubbles. All these result in different dimensionless parameters that are introduced in the Chisholm constant (in two-phase frictional multiplier) when a new frictional pressure drop correlation is proposed. Moreover, most of the existing correlations are developed by fitting their experimental data. Therefore, the performance of any proposed correlation works properly with specific experimental ranges, *i.e.* for specific dominant forces.

Table 5.1 Statistical comparison between the experimental data and existing two-phase pressure drop correlations.

Author(s)	β [-]	0.5 (TS.1)	1 (TS.2)	2 (TS.3)	1 (TS.4)
	Data points	75	76	57	63
Lockhart and Martinelli (1949)	MAE (%)	113.95	127.90	157.58	75.63
	Θ (%)	0.00	3.95	1.75	6.35
Homogenous model (1994)	MAE (%)	22.98	30.74	37.15	12.42
	Θ (%)	65.33	55.26	38.60	92.06
Qu and Mudawar (2003b)	MAE (%)	14.29	22.07	36.51	12.96
	Θ (%)	93.33	86.84	47.37	96.83
Lee and Garimella (2008)	MAE (%)	75.17	87.41	113.02	40.15
	Θ (%)	1.33	1.32	0.00	30.16
Keepaiboon et al. (2016)	MAE (%)	9.09	17.89	19.19	20.33
	Θ (%)	98.67	86.84	82.46	84.13
Huang and Thome (2017)	MAE (%)	61.46	58.17	96.09	29.4
	Θ (%)	34.67	18.42	5.26	82.54
Markal et al. (2017b)	MAE (%)	83.96	74.06	88.87	81.24
	Θ (%)	0.00	11.84	1.75	0.00
Gao et al. (2019)	MAE (%)	12.36	14.96	17.56	26.61
	Θ (%)	97.33	94.74	84.21	57.15

Table 5.1 indicates that the proposed correlations by Keepaiboon et al. (2016) and Gao et al. (2019) predict all the data well compared to others. This could be due to the fact that the effect of surface tension is included using the Confinement number and Bond number. In this study, force analysis was conducted and discussed in Chapter 6, Section 6.5. This analysis shows that surface tension is the dominant force during the present results, while inertia is the second controlling force. Since these two dimensionless numbers represent the effect of surface tension, a reasonable agreement is expected between these correlations and the experimental data.

5.7 Summary

According to the previous flow boiling pressure drop results, the following key findings can be summarized:

- The flow boiling pressure drop was found to increase with increasing heat flux for a given mass flux. This was attributed to an increase in the coalescence rate and flow resistance.
- The flow boiling pressure drop increased with increasing mass flux for fixed exit vapour quality. This could be due to the high shear stress.
- Decreasing channel aspect ratio led to increase flow boiling pressure drop, *i.e.* by 48.6% from 2 to 0.5. This could be due to the different heat transfer area that resulted in different exit vapour quality and acceleration pressure drop. Moreover, different distribution of liquid film may lead to different shear stress and frictional pressure drop component.
- The aluminium heat sink showed higher flow boiling pressure drop compared to copper by 28%. This was attributed to the high frictional pressure drop component due to different surface microstructures.
- Eight existing two-phase pressure drop correlations developed for conventional and mini/microchannels were compared with the experimental data. The present data of four test sections were not predicted well by most correlations. However, the correlations by Keepaiboon et al. (2016) and Gao et al. (2019) provided a reasonable prediction for all test sections with a MAE of $\leq 20\%$ and 12–26%, respectively.
- Different fluid properties, channel dimensions, operating conditions and surface characteristics result in different dominant forces that affect the Chisholm constant in the two-phase frictional multiplier, *i.e.* frictional pressure drop component. This result in different correlations including different dimensionless parameters for calculating two-phase pressure drop and thus large discrepancy among these correlations can be seen.
- A universal correlation for calculating two-phase pressure drop is still required. Force analysis should be involved using large experimental database. This will help to identify the dominant force(s) and the controlling dimensionless numbers.

Chapter 6

Flow Boiling Heat Transfer: Results and Discussion

6.1 Introduction

This chapter presents the heat transfer results for the four test sections at system pressure near 1 bar, wall heat flux up to 191.6 kW/m^2 , mass flux of $50\text{--}250 \text{ kg/m}^2\text{s}$, inlet sub-cooling of 5 K and exit vapour quality up to one. In the present study, the local heat transfer coefficient corresponding to the flow visualization results were obtained in order to explain the complex effects of the control parameters on heat transfer rates. Flow boiling incipience is presented in Section 6.2, while flow boiling instability is discussed in Section 6.3. Section 6.4 presents the influence of heat flux, mass flux, channel aspect ratio and channel surface material on the heat transfer results. Force analysis using the present experimental data was conducted and presented in Section 6.5. The present heat transfer data were compared with some existing heat transfer coefficient correlations and presented in Section 6.6. A final summary is given in Section 6.7.

6.2 Flow Boiling Incipience

Boiling incipience occurs when the subcooled temperature equals the saturation temperature, while the channel surface temperature exceeds them. Small bubbles grow from some nucleation cavities on the channel surface. This is referred to the onset of nucleate boiling (ONB) and indicates a transition from the single-phase region to flow boiling region. Boiling curve using heat flux versus wall superheat (wall-to-saturation temperature difference) is adopted to present boiling incipience. It can also provide the maximum design limit for flow boiling applications, *i.e.* maximum heat flux, since it is obtained at the exit vapour quality, which nearly one. The onset of nucleate boiling can be identified on the boiling curve using flow visualization and signal fluctuation of temperatures and pressure. At boiling incipience, small bubbles can be captured by the high-speed camera. Moreover, the reading of thermocouples near the channel bottom drops slightly. At the same time, some fluctuations in the pressure drop signal can be detected.

The boiling curve of HFE-7100 at five different mass fluxes and z/L of 0.5 for four test sections is depicted in Fig. 6.1. This figure demonstrates, for all mass fluxes, there was no temperature overshoot and boiling commenced smoothly at wall superheat ranging from 2 to 3.7 K, *i.e.* onset of nucleate boiling (ONB). This range of wall superheat is due to the mass flux. Harirchian and Garimella (2008) and Drummond et al. (2018) found that increasing mass flux led to an increase of the wall superheat (wall temperature) at the boiling incipience. Dielectric fluids (FC-77 and HFE-7100) in horizontal rectangular multi-microchannels were tested in these experimental investigations. When mass flux increases, fluid inlet velocity also increases leading to thinner thermal boundary layer next to the channel wall and thus the linear temperature gradient is not enough to allow bubble formation as explained by Benkheira et al. (2006). This delays nucleation (boiling incipience) to occur at high wall superheat. It is worth mentioning that temperature overshoot was also not found by others, see Fayyadh et al. (2017) and Choi et al. (2019). R134a and HFE-7100 in horizontal rectangular multi-microchannels were examined by the authors. Fayyadh et al. (2017) stated that the temperature overshoot depends on surface microstructures and fluid properties. For high surface tension and smooth surface, boiling starts at high wall superheat (high temperature overshoot). In their study, the

surface average roughness is $0.301 \mu\text{m}$ and the refrigerant R134a used in their study has small surface tension (0.008 N/m at $25 \text{ }^\circ\text{C}$) compared to other fluids such as water (0.072 N/m at $25 \text{ }^\circ\text{C}$). The surface tension was obtained using EES software. In the present study, HFE-7100 has also small surface tension (0.0136 N/m at $25 \text{ }^\circ\text{C}$), and the test sections have surface average roughness of $0.2\text{--}0.3 \mu\text{m}$. Therefore, a small wall superheat, *i.e.* without temperature overshoot, is required to trigger boiling.

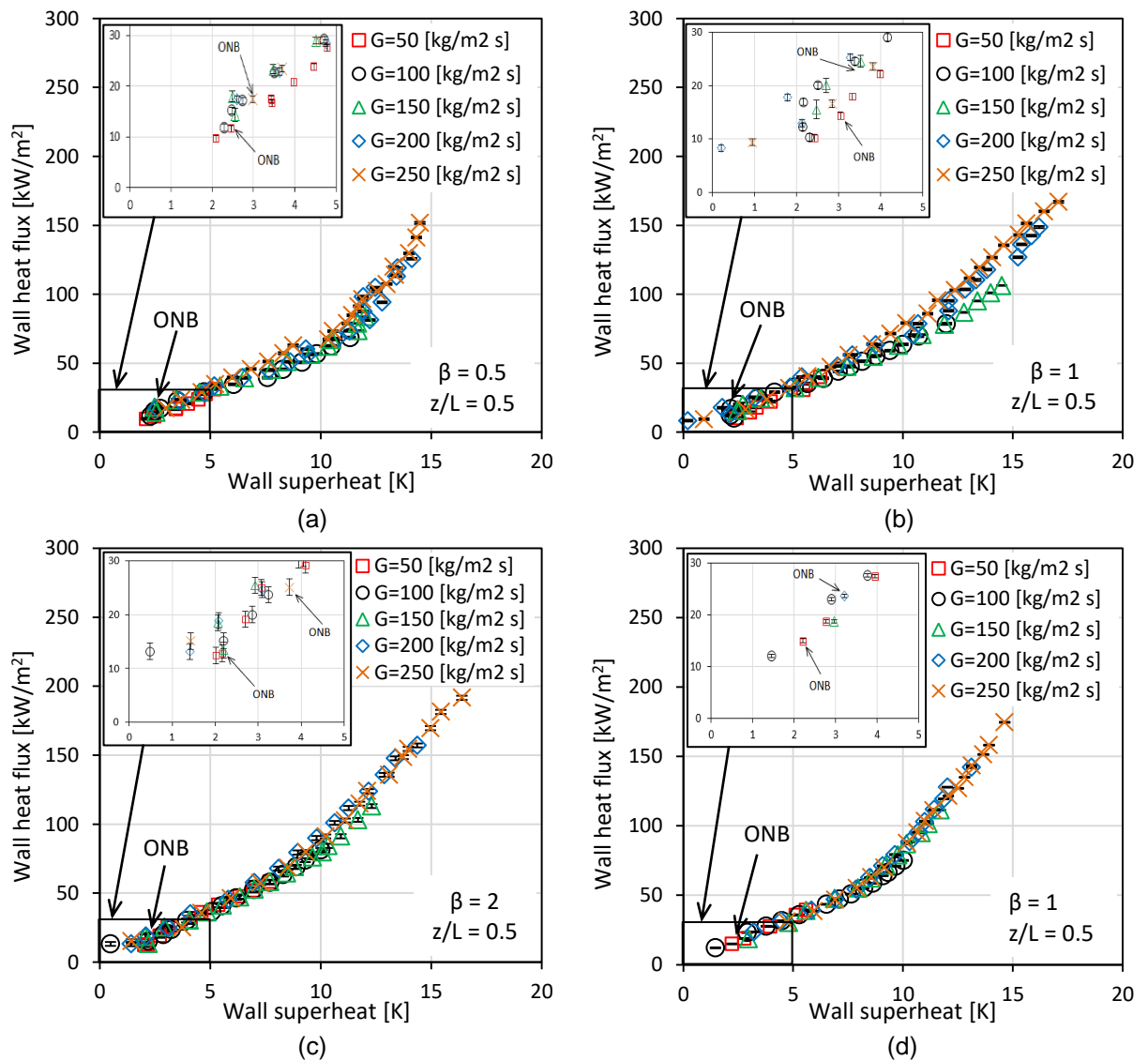


Figure 6.1 Boiling curve of HFE-7100 at z/L of 0.5 and at system pressure near 1 bar, wall heat flux up to 191.6 kW/m^2 , mass flux of $50\text{--}250 \text{ kg/m}^2 \text{ s}$ and inlet sub-cooling of 5 K for (a) TS.1 (b) TS.2 (c) TS.3 (d) TS.4.

Fig. 6.1 also shows that, after boiling incipience, the heat flux was found to increase with wall superheat. When the wall heat flux increased, the wall temperature also increased leading to the activation of more nucleation sites. This figure indicates that the boiling incipience occurred appreciably at low wall heat fluxes for all the test sections, *i.e.* around 15–20 kW/m². It is worth mentioning that the critical heat flux was not reached during these flow boiling experiments for all the test sections. It is obvious that there was no clear influence of mass flux on the boiling curve. This finding was also reported by other researchers, such as Bertsch et al. (2008), Soupremanien et al. (2011), Mirmanto (2013), Fayyadh et al. (2017) and Choi et al. (2019).

Fig. 6.2(a) illustrates the effect of channel aspect ratio on the boiling curve of HFE-7100 at a mass flux of 250 kg/m²s and different wall heat fluxes. This figure demonstrates that, for a fixed wall superheat, there was a noticeable increase in the wall heat flux when the channel aspect ratio increased from 0.5 to 2. This could be due to the nucleation site density and film thickness as discussed in Section 6.4.3. The wall heat flux was found to increase by 22.3%, when the aspect ratio increased from 0.5 to 2. This figure also shows that maximum wall heat flux was reached up to 151.8, 167 and 191.6 kW/m², when the channel aspect ratio was 0.5, 1 and 2, respectively.

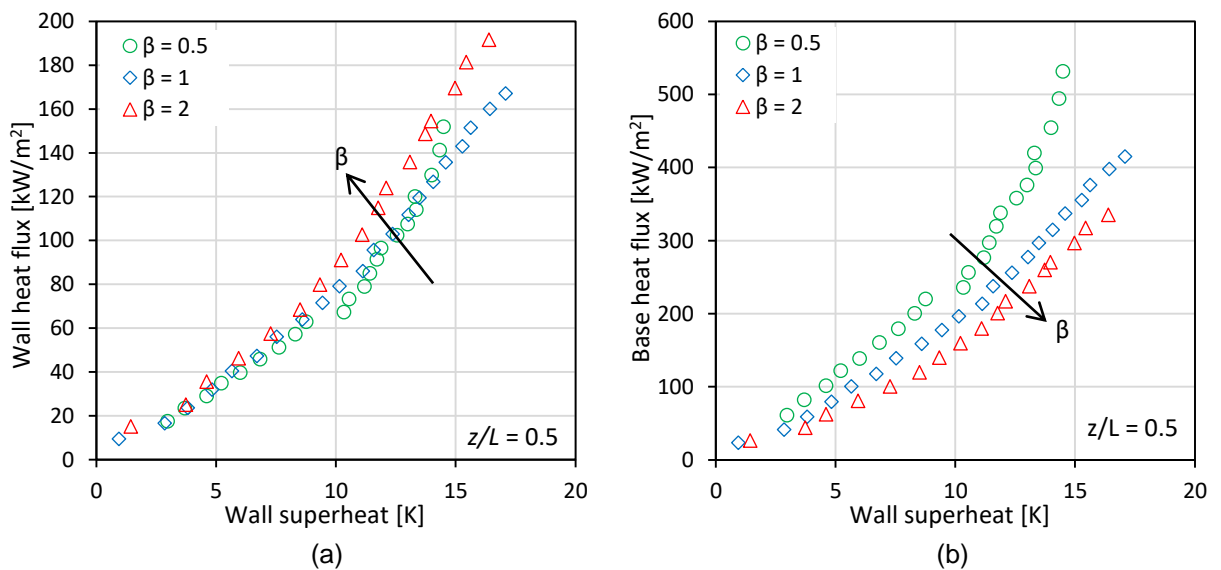


Figure 6.2 Effect of channel aspect ratio on the boiling curve at mass flux of 250 kg/m²s and z/L of 0.5 for TS.1, TS.2 and TS.3: (a) Wall heat flux (b) Base heat flux.

From a design point of view, the dissipated heat from the chipset is considered the most important factor for electronics cooling. Therefore, the base heat flux versus wall superheat is also presented in Fig. 6.2(b) to clarify the effect of channel aspect ratio. It is obvious that the base heat flux was found to decrease with increasing channel aspect ratio. This opposite trend of base heat flux could be attributed to the area ratio effect. Area ratio can be defined using Eq. (6.1) as a ratio between the total heat transfer area and the base area.

$$\alpha = \frac{(2H_{ch} + W_{ch})N}{W_b} \quad (6.1)$$

Since the channel dimensions and number of channels were not the same for these three test sections, the heat transfer area and thus the area ratio differed from heat sink to another. Therefore, for a fixed wall heat flux, the base heat flux increased with increasing area ratio, *i.e.* decreasing channel aspect ratio, due to an increase in the heat transfer area as shown by Eq. (6.2).

$$q''_b = q''_w \alpha \quad (6.2)$$

It is obvious that when the channel aspect ratio varied from 0.5 to 2, the base heat flux decreased up to 46.5%. When the channel aspect ratio increased from 0.5 to 2, the area ratio decreased from 3.5 to 1.75, *i.e.* by 50%. Accordingly, the maximum heat that can be dissipated from the chipset increased with decreasing channel aspect ratio due to the large surface enhancement. This can outweigh the benefits from boiling heat transfer enhancement at larger aspect ratio. Maximum base heat flux was found up to 531.2, 414.8 and 335.3 kW/m², when the channel aspect ratio was 0.5, 1 and 2, respectively. This corresponds to a cooling load of 265.6, 207.4 and 167.6 W, respectively. Moreover, Fig. 6.2(b) illustrates that, at a given base heat flux, the wall superheat was lower for the smaller aspect ratio. For example, at base heat flux of 200 kW/m², the wall temperature decreased by 4 K, when the aspect ratio decreased from 2 to 0.5. For the smaller aspect ratio and at maximum base heat flux (531.2 kW/m²), the wall superheat was found to be 14.5 K, which corresponds to the working surface temperature of 74.5 °C. This range of surface temperature is acceptable for cooling electronic applications. It is worth mentioning that the boiling curve proposed by Harirchian and Garimella (2008) showed that, at a given wall superheat, smaller channel width provided higher base heat flux compared to others. They tested flow boiling of dielectric fluid (FC-77) in horizontal rectangular multi-

microchannels at fixed height and different channel widths. Kim and Mudawar (2017) also stated that, for a fixed channel height, maximum base heat flux was found to increase with decreasing channel width due to the large number of channels. They noted that reduction in channel width led to a decrease in the wall temperature. They also found that, for a fixed channel width, deeper channels provided higher base heat flux. Three different fluids, *i.e.* HFE-7100, R134a and water, were examined by the authors using horizontal rectangular multi-microchannels at different channel dimensions. Drummond et al. (2018) conducted flow boiling of HFE-7100 in horizontal rectangular microchannels. They tested three heat sinks had the same channel width but different channel height, *i.e.* different channel aspect ratios. The boiling curve was presented using base heat flux versus wall superheat. Their results showed that the base heat flux increased with increasing channel height, *i.e.* decreasing channel aspect ratio. Moreover, at given base heat and mass flux, smaller channel aspect ratio provided lower wall temperature. These findings agree with the present results.

Fig. 6.3 depicts the effect of channel surface material on the boiling curve at mass flux of $250 \text{ kg/m}^2\text{s}$. Since the area ratio is the same for both heat sinks TS.2 and TS.4, this figure is plotted using only wall heat flux. It is clear that there was no material effect at low heat fluxes. However, at moderate and high heat fluxes, the wall heat flux became higher for aluminium compared to copper. The flow patterns along the channel may lead to this trend, see Section 6.4.4. The wall heat flux was found to increase by 14% when the surface metal was aluminium. For a given wall superheat, the heat flux for aluminium was higher. For instance, at wall superheat of 13 K, the wall heat flux increased from 111.6 to 143.4 kW/m^2 when the heat sink was made of aluminum compared to copper. Maximum wall heat flux was reached up to 167 and 174 kW/m^2 for copper and aluminium surfaces, respectively. This difference could be attributed to the bubble generation and liquid film thickness as discussed in details in Section 6.4.4.

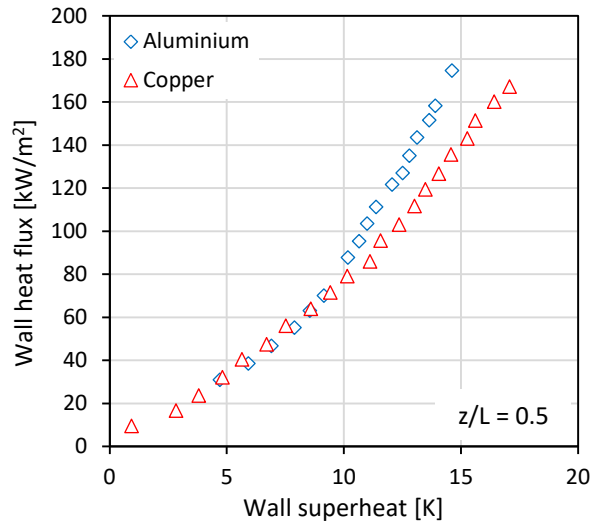


Figure 6.3 Effect of channel surface material on the boiling curve at mass flux of 250 kg/m²s and z/L of 0.5 for TS.2 and TS.4.

It is worth mentioning that low heat flux (or high wall superheat) by high thermal conductivity surfaces was also reported by other researchers. For example, the boiling curve by Pike-Wilson and Karayiannis (2014) showed that the copper surface had lower heat flux than the stainless steel surface. They carried out flow boiling heat transfer of R245fa in vertical tube with inner diameter of 1.1 mm. The pool boiling investigation by Suriyawong and Wongwises (2010) indicated that the copper surface showed higher wall superheat than aluminium. The abovementioned results agree with the present experimental results.

Since the thermal power of the chipset varies during the operation, the effect of hysteresis on the thermal performance should be considered. This can be investigated by increasing and decreasing heat flux at given mass flux. Fig. 6.4 shows the hysteresis effect on the boiling curve at mass flux of 150 kg/m²s for all heat sinks. The heat flux was increased gradually until the exit vapour quality reached one. After that, a reduction in heat flux was carried out step by step until the exit fluid state was single-phase (liquid). It is obvious that, for all test sections, the trends of both increasing and decreasing heat flux were quite similar at moderate and high heat fluxes. However, at low heat fluxes, *i.e.* less than 60 kW/m², the hysteresis effect became clear and lower wall superheat was found with decreasing heat flux.

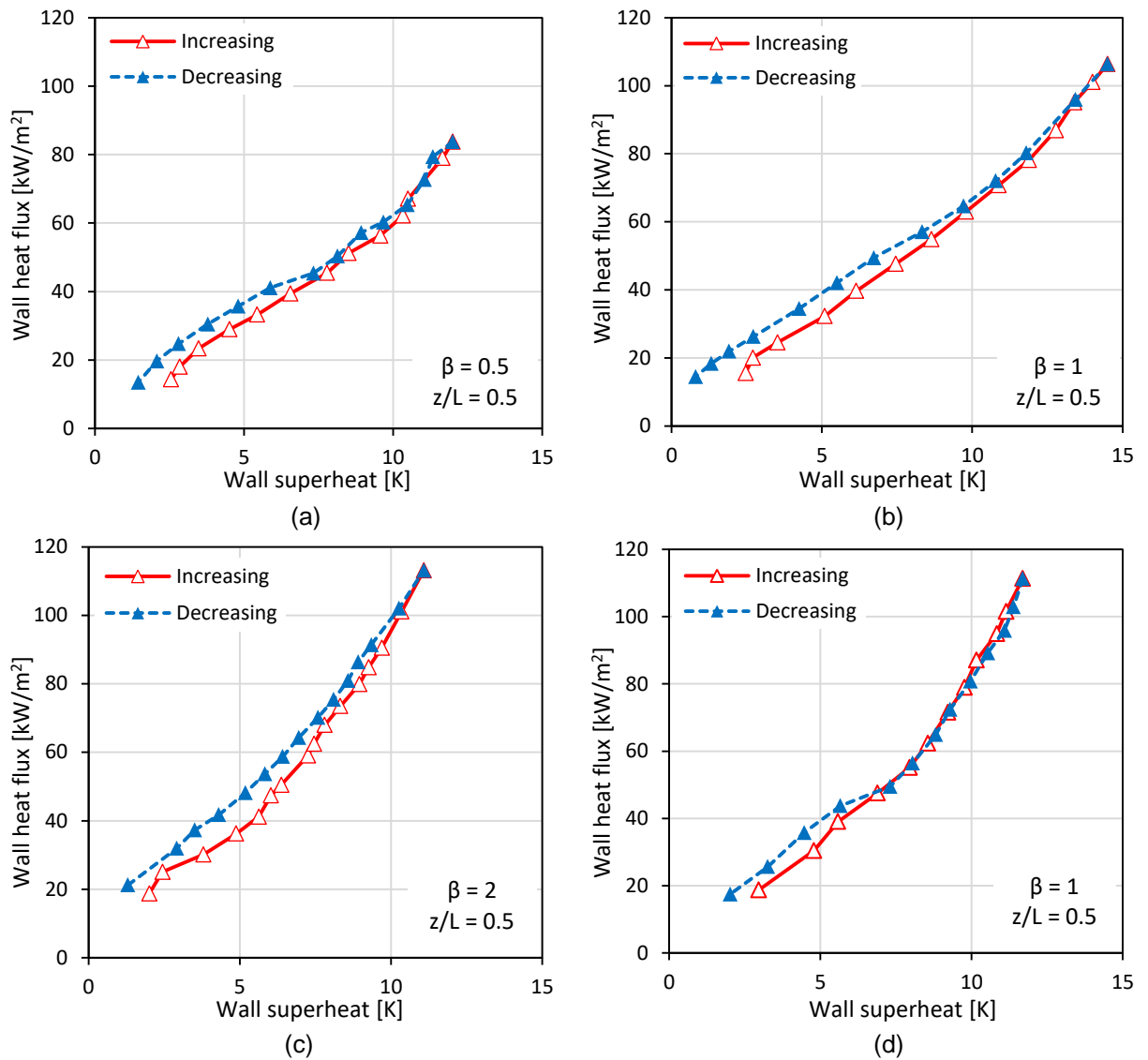


Figure 6.4 Hysteresis effect on the boiling curve at mass flux of $150 \text{ kg/m}^2\text{s}$ for
 (a) TS.1 (b) TS.2 (c) TS.3 (d) TS.4.

Other researchers also reported that the hysteresis phenomenon occurred with decreasing heat flux, such as Mahmoud (2011), Karayiannis et al. (2014) and Al-Gaheeshi (2018). This was attributed to the nucleation sites remained active with decreasing heat flux compared to increasing heat flux. This could lead to lower wall superheat. In the present study, the differences in flow patterns during increasing and decreasing wall heat flux are discussed in Chapter 4. For example, bubbly flow was captured with decreasing heat flux, while liquid flow occurred during increasing heat flux. It is known that the surface conditions of each heat sink may affect the active nucleation sites and thus these sites could vary from one heat sink to another.

6.3 Flow Boiling Instability

Flow reversal and boiling instability are very common in multi-microchannel configurations. Flow reversal in micro scale evaporators can cause high pressure drop and deterioration of flow distribution as mentioned by Tuo and Hrnjak (2013). Flow reversal was also reported by Chen and Garimella (2006b), Yang et al. (2011) and Fayyadh et al. (2017). These experimental studies were conducted using different refrigerants in horizontal multi-microchannel configurations. Consolini and Thome (2009) investigated experimentally the effect of stable and unstable flow on the flow boiling heat transfer data using three different refrigerants; R134a, R236fa and R245fa. In their study, two horizontal stainless steel microchannels with inner diameter of 0.51 and 0.79 mm were manufactured. They conducted their experiments at heat flux up to 200 kW/m^2 and mass flux ranging from 300 to $2000 \text{ kg/m}^2\text{s}$. Their results showed that the trend of local heat transfer coefficient versus vapour quality changed significantly when the flow was stable or unstable. For example, the local heat transfer coefficient for R245fa increased with vapour quality, when the flow was stable. However, this trend became nearly constant, *i.e.* the local heat transfer coefficient did not change with quality, when the flow was unstable, *i.e.* high amplitude instability. Moreover, higher heat transfer coefficient was found for stable flow compared to that for unstable flow. Similar trend was also found for R236fa. In contrast, for refrigerant R134a, the heat transfer coefficient for stable flow was identical to that for unstable flow. The insensitivity of R134a to the flow instabilities makes it as a good refrigerant for cooling electronic components as they mentioned. However, this difference in stable/unstable results between fluids was not commented by the authors. In the present study, flow reversal occurred due to the rapid bubble generation near the channel inlet and slug formation as presented in Chapter 4. It became more pronounced at high heat fluxes. Flow reversal was observed for all examined mass fluxes and for all test sections, since the present experiments were conducted at low flow rates. The recorded signals were analysed to check whether the flow reversal observed in the present study has severe effects on system parameters (pressure, pressure drop, temperature and mass flow rate). The measured pressure drop signal is plotted at mass flux of $250 \text{ kg/m}^2\text{s}$ and different wall heat fluxes and period of oscillation of 30 sec in order to study the effect of heat flux on the oscillations and the amplitude of the fluctuation, as shown in Fig. 6.5.

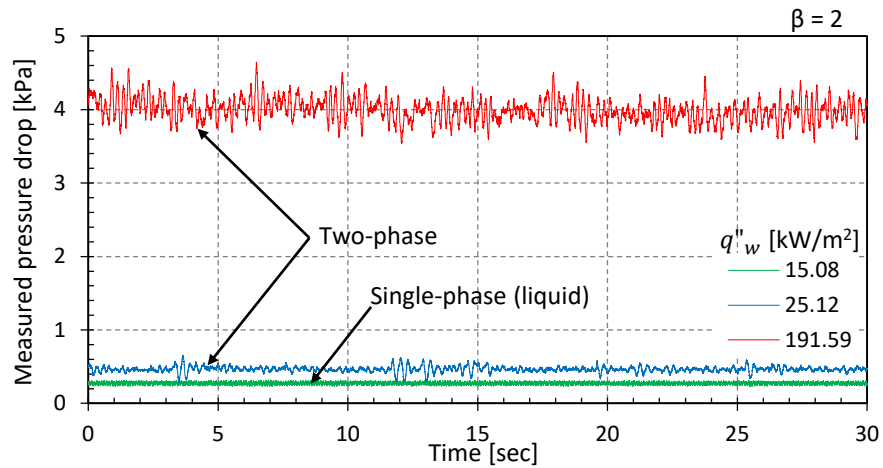


Figure 6.5 Measured pressure drop fluctuation at different wall heat fluxes and mass flux of $250 \text{ kg/m}^2\text{s}$ for TS.3.

It is obvious that the measured pressure drop and amplitude of oscillations increased with increasing heat flux. For example, at lowest wall heat flux, *i.e.* 15.08 kW/m^2 , liquid flow was observed and the measured pressure drop (mean value) was 0.27 kPa . This figure shows that before boiling incipience, the system was very stable with amplitude fluctuation (the difference between the peak and the mean value) of 0.044 kPa . On the onset of boiling, at wall heat flux of 25.12 kW/m^2 , high oscillations in the pressure drop signal were measured with amplitude fluctuation of 0.18 kPa . The pressure drop was measured at 0.46 kPa . With further increase in heat flux, *i.e.* 191.6 kW/m^2 , this fluctuation increased up to 0.65 kPa at measured pressure drop of 4 kPa .

A Fast Fourier Transform analysis was conducted on the measured pressure drop data to clarify the frequency distribution and amplitude for different heat fluxes. The result of this analysis is presented in Fig. 6.6 and shows that the frequency of oscillation and amplitude increased with increasing heat flux at constant mass flux. For instance, at heat flux of 25.12 kW/m^2 , the dominant frequency of the pressure drop reached 3.42 Hz at maximum amplitude of 0.027 . At higher heat flux, *i.e.* 191.6 kW/m^2 , this frequency became higher, *i.e.* 4.15 Hz , at amplitude of 0.103 . In other words, the high frequency of the pressure drop values could mean more intense flow instability.

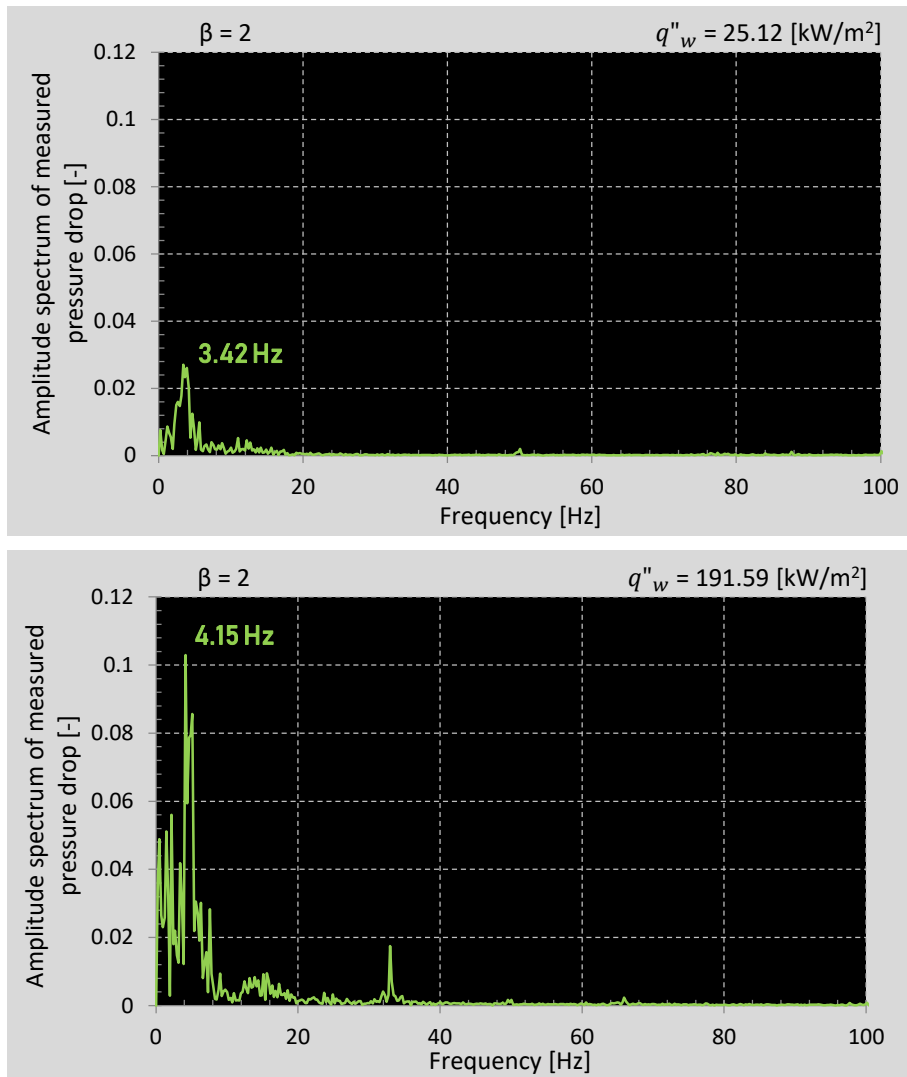


Figure 6.6 Frequency analysis of the measured pressure drop at different wall heat fluxes and mass flux of $250 \text{ kg/m}^2\text{s}$ for TS.3.

Although flow reversal occurred in the present study, the flow boiling heat transfer results were not affected. This is inferred from the measured signals of pressure drop, inlet/outlet pressure, mass flow rate, inlet/outlet fluid temperature and thermocouple temperatures along the channel for all test sections. These signals did not fluctuate significantly during the experiments. Table 6.1 presents the maximum percentage of fluctuation (maximum deviation from the mean value) for all these measured parameters at mass flux of $250 \text{ kg/m}^2\text{s}$ and period of oscillation of 30 sec. Moreover, the measured signals of pressure and temperature for TS.3 are depicted in Fig. 6.7 as an example.

Table 6.1 Maximum percentage of fluctuation for all measured parameters.

Measured parameter	TS.1	TS.2	TS.3	TS.4
Inlet pressure [bar]	2.37%	1.33%	0.81%	0.67%
Outlet pressure [bar]	0.84%	1.11%	0.68%	0.54%
Mass flow rate [kg/hr]	0.27%	0.35%	0.19%	1.28%
Inlet fluid temperature [°C]	0.85%	0.82%	0.37%	0.68%
Outlet fluid temperature [°C]	0.01%	0.03%	0.04%	0.01%
Thermocouple: z/L=0.1 [°C]	0.05%	0.07%	0.11%	0.06%
Thermocouple: z/L=0.5 [°C]	0.14%	0.22%	0.18%	0.05%
Thermocouple: z/L=0.9 [°C]	0.07%	0.46%	0.33%	0.2%

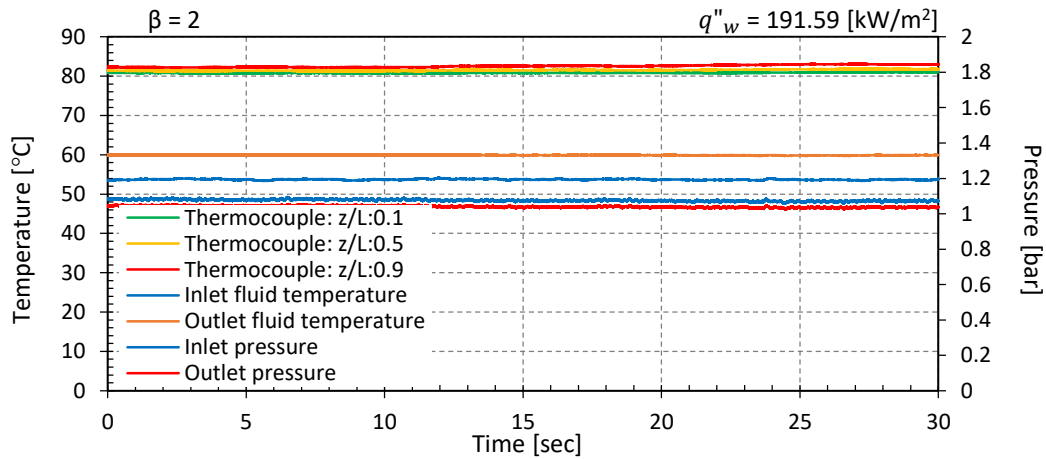


Figure 6.7 Signal fluctuations in pressure and temperature at wall heat flux of 191.6 kW/m² and mass flux of 250 kg/m²s for TS.3.

This figure shows the measured signals from three thermocouples at location (z/L) of 0.1, 0.5 and 0.9. These thermocouples were inserted inside the heat sink block with distance of 4 mm underneath the channel bottom. It is obvious that the maximum percentage of fluctuation was found to be 2.37% for the inlet pressure, 1.11% for the outlet pressure, 1.28% for the mass flow rate, 0.85% for the inlet fluid temperature, 0.04% for the outlet fluid temperature and ranging from 0.05% to 0.46% for the wall temperature. These low fluctuations in the measured parameters indicated that the flow reversal did not significantly affect the present flow boiling heat transfer results for the entire heat sink. It is worth mentioning that Consolini and Thome (2009) also found that the heat transfer results for R134a were not affected by flow instability, although the results of R236fa and R245fa showed significant effect. R134a required

very high heat fluxes for the instability to propagate as they mentioned. However, they did not mention further details. Therefore, further work is needed to clarify the effect of flow instability on the heat transfer results.

The effect of channel aspect ratio on the measured pressure drop fluctuation is depicted in Fig. 6.8. This figure shows the measured pressure drop at mass flux of $150 \text{ kg/m}^2\text{s}$ and low and high wall heat fluxes.

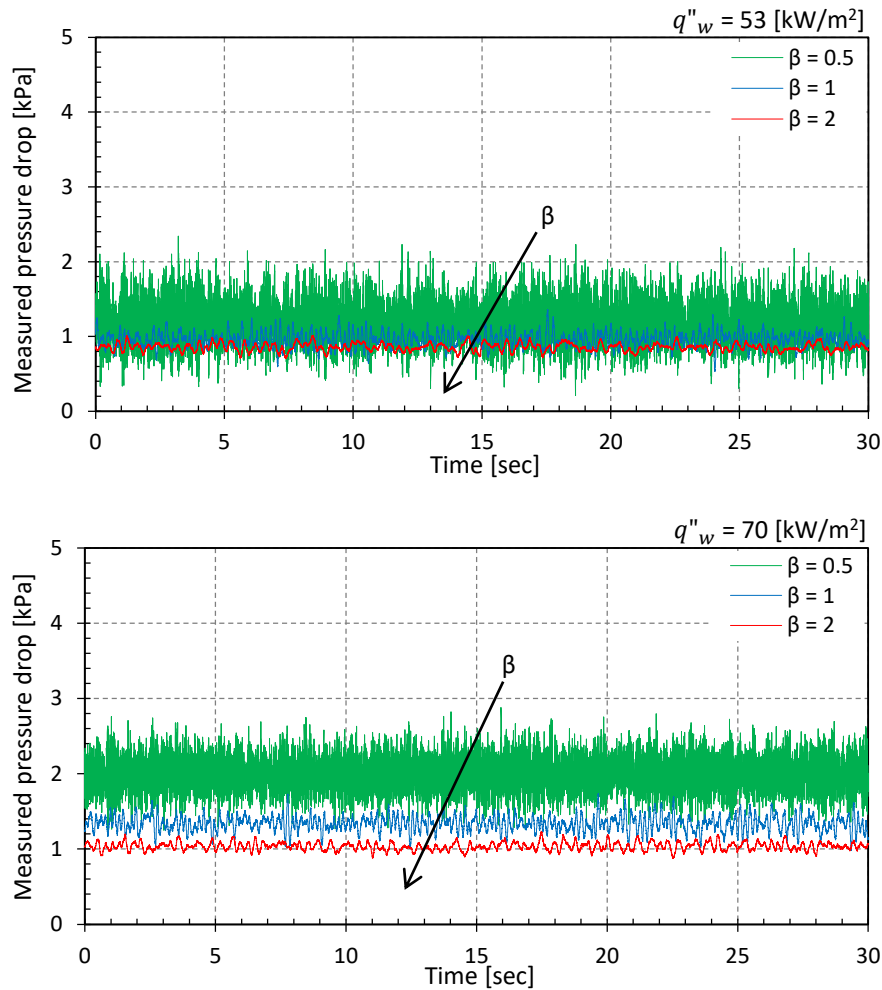


Figure 6.8 Effect of channel aspect ratio on the measured pressure drop fluctuation at mass flux of $150 \text{ kg/m}^2\text{s}$ and two different wall heat fluxes for TS.1, TS.2 and TS.3.

It can be seen that, at given wall heat flux, the pressure drop increased with decreasing channel aspect ratio. This trend became clearer at high heat flux. In addition, the pressure drop fluctuation increased with decreasing channel aspect ratio. For example, at wall heat flux of 53 kW/m^2 , the amplitude of fluctuation increased from 0.16 to 1.15 kPa when the channel aspect ratio decreased from 2 to

0.5. The same effect was also found at high wall heat flux, *i.e.* 70 kW/m^2 . This high pressure drop fluctuation with decreasing channel aspect ratio could be attributed as follows: when the channel aspect ratio decreases, *i.e.* narrow channel width, the bubble coalescence rate increases due to the confinement and thus the bubbles size becomes large. Once these bubbles become confined, a sudden expansion in both directions occurs, as discussed in Chapter 4. This leads to an increase in the pressure drop fluctuation by inducing flow reversal. In other words, the coalescence rate, the confined bubbles and the expansion rate increase with decreasing channel width resulting in high flow reversal and pressure drop fluctuation.

Fig. 6.9 illustrates the effect of channel aspect ratio on the measured pressure drop signal using Fast Fourier Transform analysis. This figure is plotted at wall heat flux of 70 kW/m^2 and mass flux of $150 \text{ kg/m}^2\text{s}$ for TS.1, TS.2 and TS.3. It demonstrates that, for given heat and mass fluxes, both the frequency of oscillation and amplitude increased with decreasing channel aspect ratio. The dominant frequency of the pressure drop signal was 2.93, 5.86 and 23.2 Hz when the aspect ratio was 2, 1 and 0.5, respectively. Moreover, maximum amplitude was reached at 0.036, 0.058 and 0.069 for the aspect ratio of 2, 1 and 0.5, respectively. Significant flow reversal results in high frequency and amplitude of the measured pressure drop signal. In other words, reduction in channel aspect ratio leads to increase both frequency and amplitude.

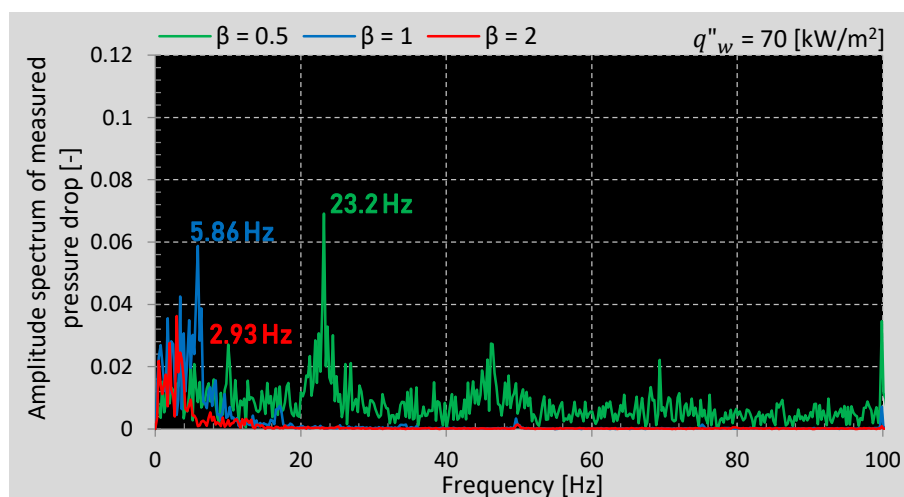


Figure 6.9 Frequency analysis of the measured pressure drop at wall heat flux of 70 kW/m^2 and mass flux of $150 \text{ kg/m}^2\text{s}$ for TS.1, TS.2 and TS.3.

The effect of channel surface material on the measured pressure drop fluctuation was also studied in the present study. Fig 6.10 shows the measured pressure drop at mass flux of $250 \text{ kg/m}^2\text{s}$ and low and high wall heat fluxes for TS.2 and TS.4. This figure demonstrates that high pressure drop was measured for aluminium heat sink compared to copper for given heat and mass fluxes. It also shows that high pressure drop fluctuation was found for the copper surface. For instance, at low wall heat flux, the amplitude fluctuation of pressure drop was 0.16 and 0.44 kPa for aluminium and copper, respectively. For high heat flux, this value increased to 0.56 kPa for aluminium surface and 2.37 kPa for copper.

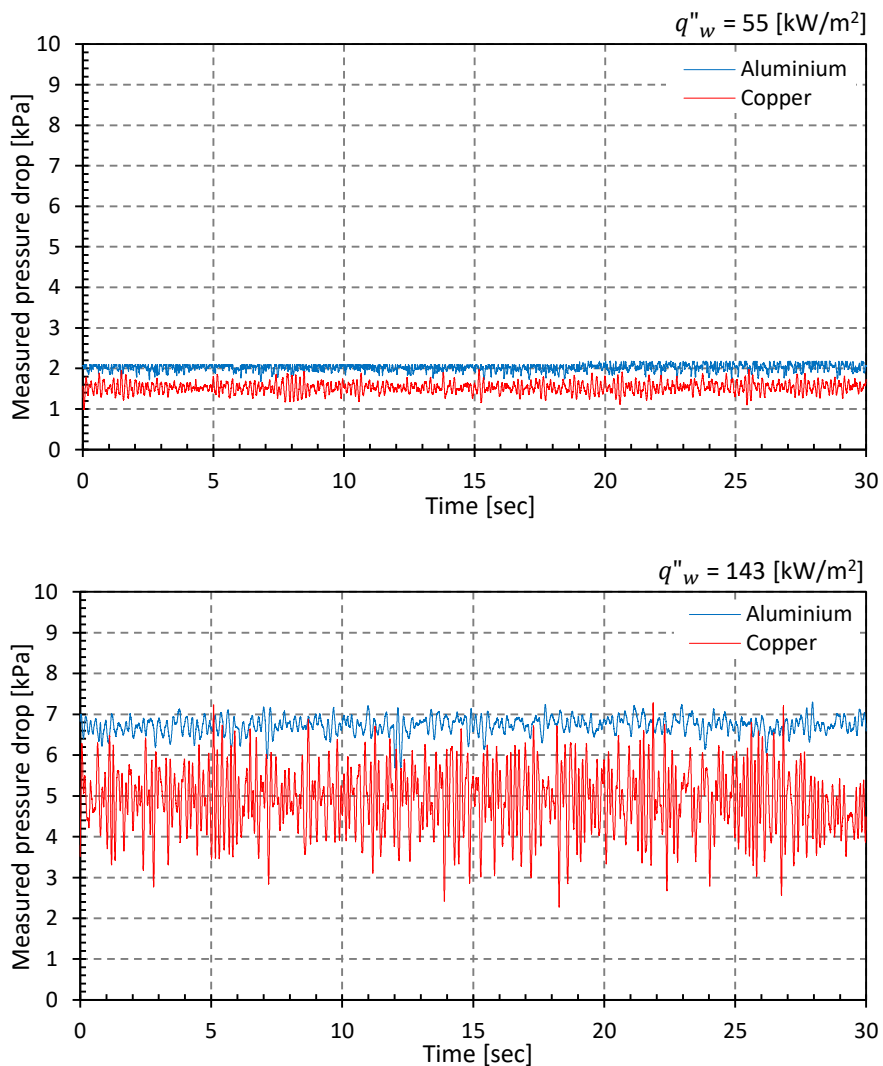


Figure 6.10 Effect of channel surface material on the measured pressure drop fluctuation at mass flux of $250 \text{ kg/m}^2\text{s}$ and two different wall heat fluxes for TS.2 and TS.4.

This high pressure drop fluctuation with copper surface compared to aluminium could be due to the different surface microstructures. The surface topography of these metals is completely different as discussed in Chapter 3. SEM analysis indicates that copper surface has small surface cavities. This means that high wall superheat is required for activation as shown by the correlation of Hsu (1962), see Section 6.4.4. High wall superheat means high wall temperature for a given saturation temperature resulting in high bubble expansion in both directions, *i.e.* high possibility of reversal.

Similar to the abovementioned analysis, the Fast Fourier Transform method was obtained here to analysis the effect of channel surface material on both frequency and amplitude of the measure pressure drop signal. Fig. 6.11 shows this analysis at wall heat flux of 143 kW/m^2 and mass flux of $250 \text{ kg/m}^2\text{s}$. This figure indicates that copper surface provided higher frequency and amplitude than those in aluminium surface. The dominant frequency was found at 7.32 and 3.9 Hz, while the maximum amplitude was 0.28 and 0.099 when the surface metal was copper and aluminium, respectively. In other words, copper surface provides higher frequency and amplitude of the measured pressure drop, *i.e.* high flow reversal.

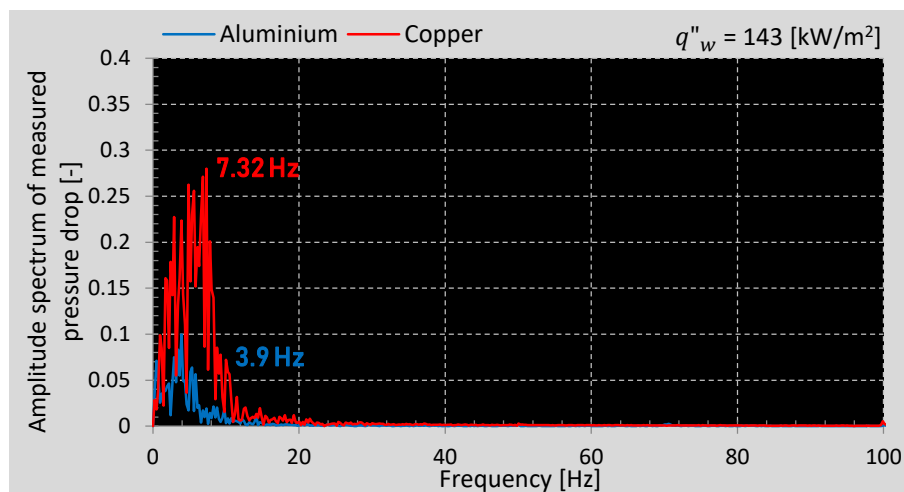


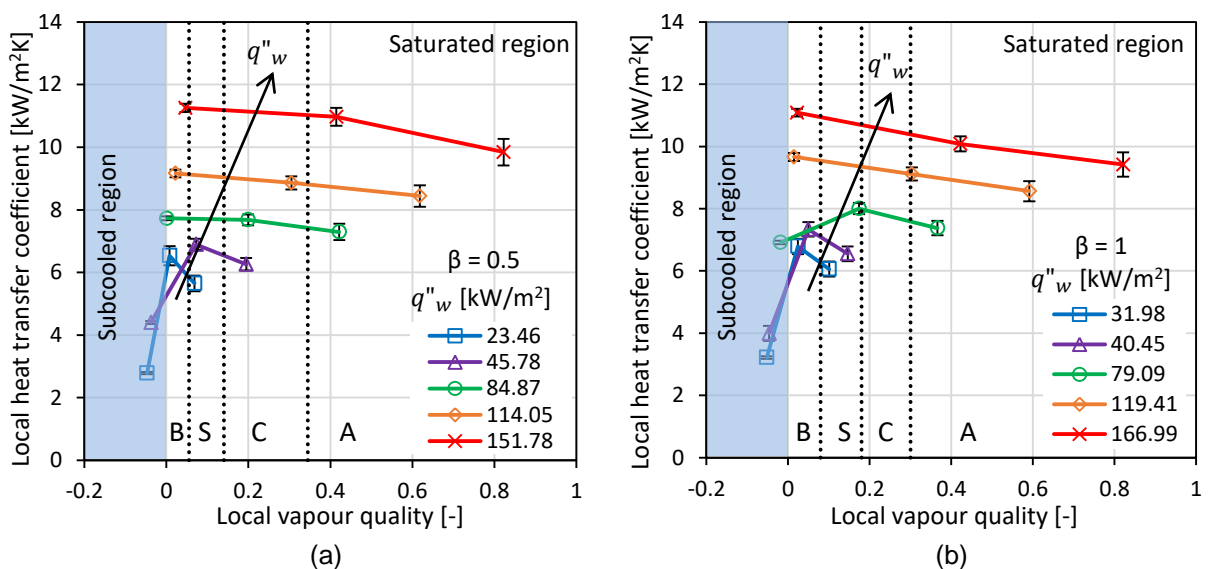
Figure 6.11 Frequency analysis of the measured pressure drop at wall heat flux of 143 kW/m^2 and mass flux of $250 \text{ kg/m}^2\text{s}$ for TS.2 and TS.4.

6.4 Flow Boiling Heat Transfer Results

The heat transfer coefficient was calculated locally along the channel at three different locations, *i.e.* z/L of 0.1, 0.5 and 0.9. Graphs of the local heat transfer coefficient versus local vapour quality were used to present the heat transfer results. The effect of several fundamental parameters on the local and average heat transfer coefficients was studied such as heat flux, mass flux, channel aspect ratio and surface material.

6.4.1 Effect of heat flux

In the present study, the influence of heat flux was studied for a given mass flux and different ranges of wall heat flux. Fig. 6.12 shows the effect of wall heat flux on the local heat transfer coefficient as a function of local vapour quality for a given mass flux of $250 \text{ kg/m}^2\text{s}$. This figure also includes the transition lines of the visualized flow patterns. It is obvious that the local heat transfer coefficient increased with increasing heat flux, which agrees with Lazarek and Black (1982), Bao et al. (2000), Sobierska et al. (2006), Huang and Thome (2016) and Fayyadh et al. (2017). Recently, Choi et al. (2019) examined flow boiling of HFE-7100 in rectangular multi-channels with hydraulic diameter of 0.89 mm, and similar effect of heat flux was found.



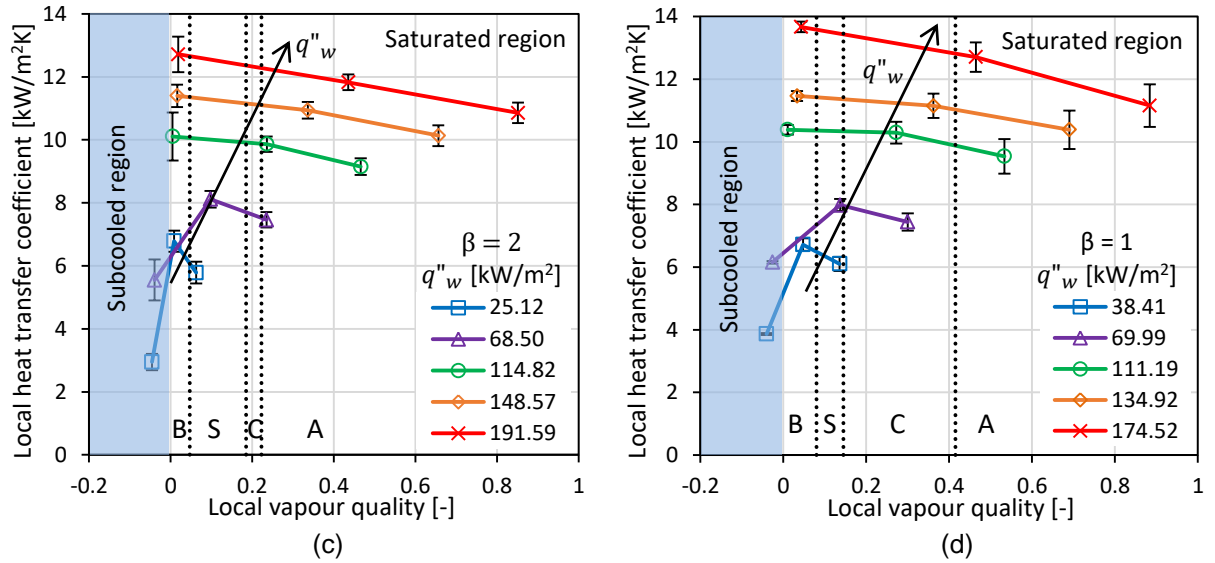


Figure 6.12 Effect of wall heat flux on the local heat transfer coefficient at mass flux of 250 kg/m²s for (a) TS.1 (b) TS.2 (c) TS.3 (d) TS.4.
(B) Bubbly (S) Slug (C) Churn (A) Annular.

The figure was divided into two regions, with respect to the vapour quality, namely low and intermediate/high vapour quality regions, in order to clarify this effect. In low vapour quality region ($x < 0.1$), where the flow pattern was bubbly flow, increase of heat flux led to an increase in the number of active nucleation sites on the channel surface, as shown in Chapter 4. As a consequence, the heat transfer coefficient increased. In the intermediate/high vapour quality region ($x > 0.1$), where the flow pattern was slug or annular flow, the increase in the liquid film evaporation rate could be the reason for increasing the heat transfer coefficient with heat flux, at low heat fluxes. At moderate to high heat fluxes, there was a possibility for the contribution of both liquid film evaporation and nucleation in the liquid film as the heat flux increased. It is worth mentioning that nucleating bubbles in the liquid film of slug or annular flow occurred with increasing heat flux as discussed in Chapter 4.

Fig. 6.13 is also presented here to more clarify the effect of wall heat flux on the local heat transfer coefficient. The local heat transfer coefficient versus the axial distance is plotted in this figure. This figure confirms the abovementioned results, *i.e.* the local heat transfer coefficient increased with increasing wall heat flux for all test sections.

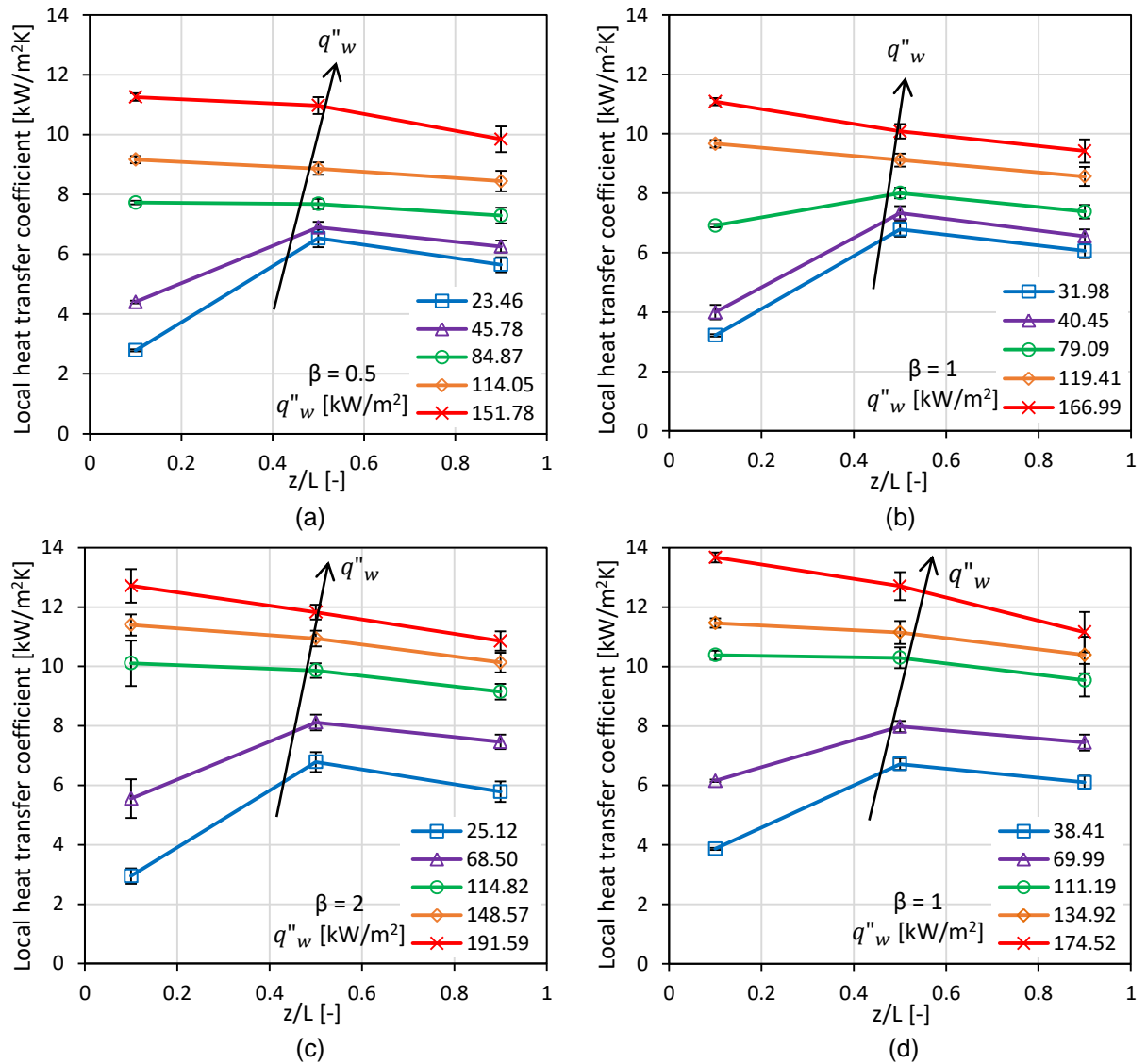


Figure 6.13 Effect of wall heat flux on the local heat transfer coefficient as a function of axial distance at mass flux of $250 \text{ kg/m}^2\text{s}$ for (a) TS.1 (b) TS.2 (c) TS.3 (d) TS.4.

Fig. 6.12 also demonstrates that the peak value of the local flow boiling heat transfer coefficient occurred at vapour qualities slightly above zero, *i.e.* at boiling incipience when the flow regime was bubbly flow. This could be due to the evaporation in the liquid micro-layer underneath the nucleating bubbles. Subsequently, the local heat transfer coefficient decreased with increasing local vapour quality, *i.e.* in the slug, churn and annular flow regimes. This reduction in the heat transfer coefficient with vapour quality could be attributed to the following possible reasons: (i) for low and moderate heat fluxes, the reason could be the reduction in local pressure along the channel and consequently the reduction in saturation temperature. It is known that the local saturation temperature was obtained in the present study based on a linear

pressure drop assumption. Fig. 6.14 illustrates the local saturation temperature obtained from the corresponding local pressure and wall temperature along the channel at different wall heat fluxes. In flow boiling systems, the assumption of linear pressure drop variation is not valid especially in the very low quality region, *i.e.* around boiling incipience, as discussed by Mahmoud and Karayiannis (2013). Huang and Thome (2017) proposed an empirical frictional pressure drop model suitable for high mass fluxes based on the separated flow model assumption and the correlation by Zivi (1964) for void fraction. They used their model to predict the local pressure along the channel and reported that the local pressure decreased according to a parabolic curve rather than a linear curve. At boiling incipience, the local pressure based on the linear assumption was found to be much higher than that based on the model predictions. Accordingly, low local pressure results in low local saturation temperature and thus high wall superheat (low local heat transfer coefficient). In other words, the local heat transfer coefficient at boiling incipience will be higher in the case of a linear pressure drop assumption. It is worth mentioning that the parabolic variation of pressure drop along the channel reported by Huang and Thome (2017) was only based on a model rather than direct measurements, which still is very challenging in microchannels. (ii) At high heat fluxes, the second reason could be the combined effect of the reduction in local pressure and increase in wall temperature along the channel. This figure shows that the local saturation temperature decreased continuously and there was a noticeable increase in the local wall temperature especially at high heat fluxes. This may be due to the local dry patches that can lead to an increase in the local wall temperature towards the channel exit. As a result, the difference between the local wall temperature and saturation temperature (wall superheat) increased towards the channel outlet and thus the calculated local heat transfer coefficient could decrease. It is worth mentioning that the axial wall temperature variation was within ± 1.5 K on the heat sink at maximum wall heat flux, 191.6 kW/m^2 , while this variation became smaller with decreasing heat flux. Both the above points require further investigation. The reduction in heat transfer coefficient with increasing quality was also reported by Qu and Mudawar (2003a), Wang and Sefiane (2012), Mirmanto (2016) and Choi et al. (2019).

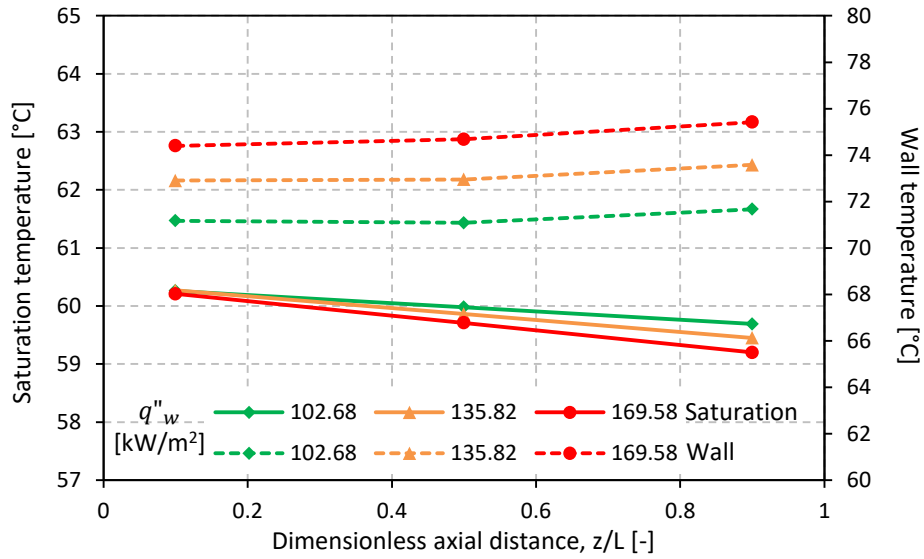
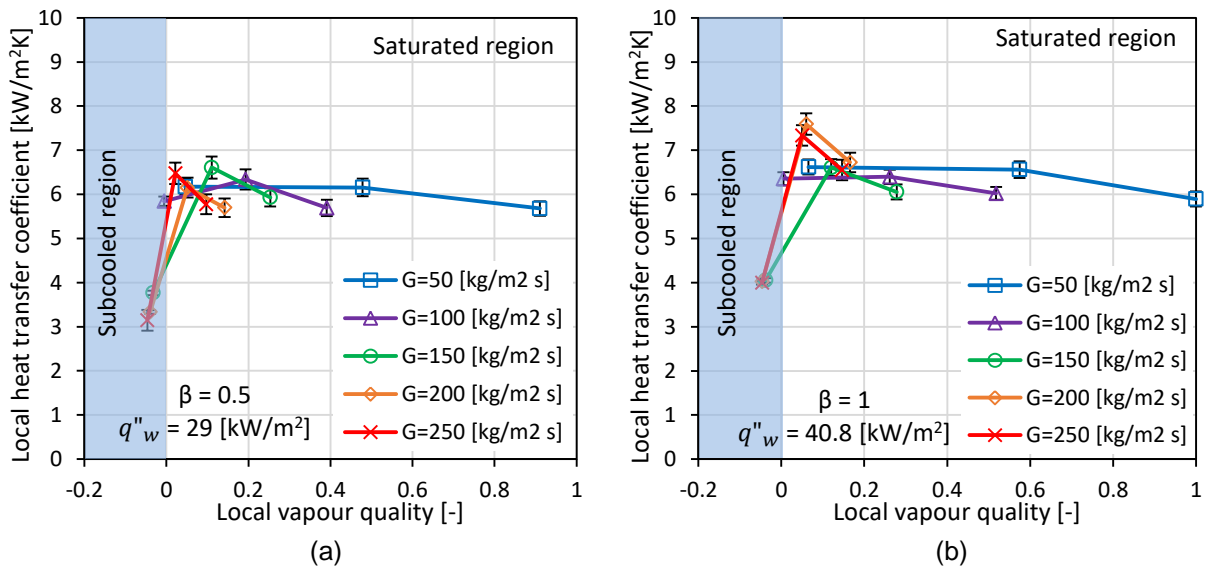


Figure 6.14 Local saturation temperature and wall temperature at different wall heat fluxes at mass flux of 250 kg/m²s for TS.3.

6.4.2 Effect of mass flux

Five mass fluxes ranging from 50 to 250 kg/m²s were conducted to examine the effect of mass flux on the local heat transfer coefficient as depicted in Fig. 6.15. This figure illustrates that, for a given wall heat flux, the influence of mass flux was negligible for all test sections. This insignificant mass flux effect was also reported by other researchers, see Bao et al. (2000), Pettersen (2004), Oh and Son (2011), Lim et al. (2015), Al-Gaheeshi et al. (2016) and Choi et al. (2019).



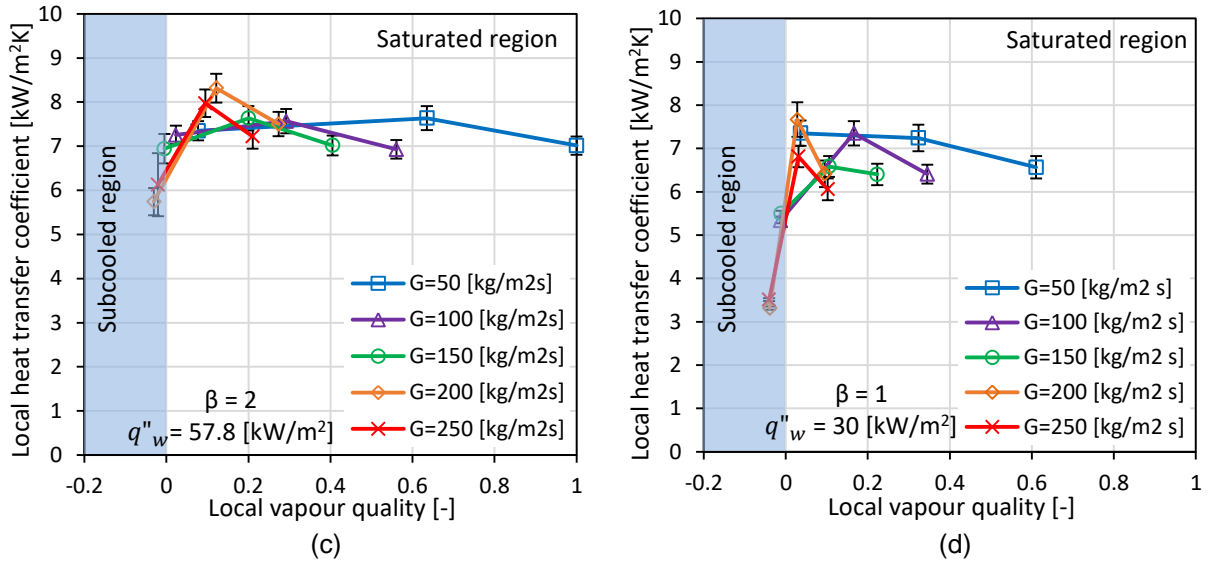
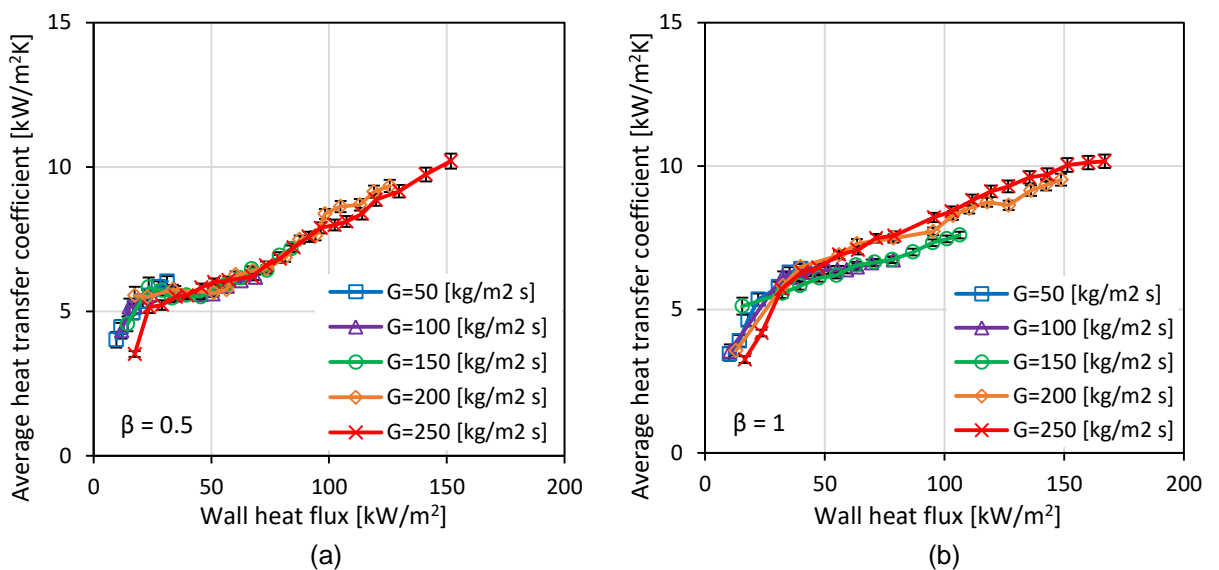


Figure 6.15 Effect of mass flux on the local heat transfer coefficient at constant wall heat flux for (a) TS.1 (b) TS.2 (c) TS.3 (d) TS.4.

Both wall heat flux and mass flux are plotted in Fig. 6.16 to clarify the effect of these two parameters on the average heat transfer coefficient. This figure is plotted using five mass fluxes ranging from 50 to 250 kg/m²s at all ranges of wall heat flux. It can be seen that there was a strong influence of wall heat flux on the average heat transfer coefficient. This figure also indicates that the effect of mass flux was insignificant. These findings were found for all test sections as shown in this figure. The previous results agree with the local heat transfer results.



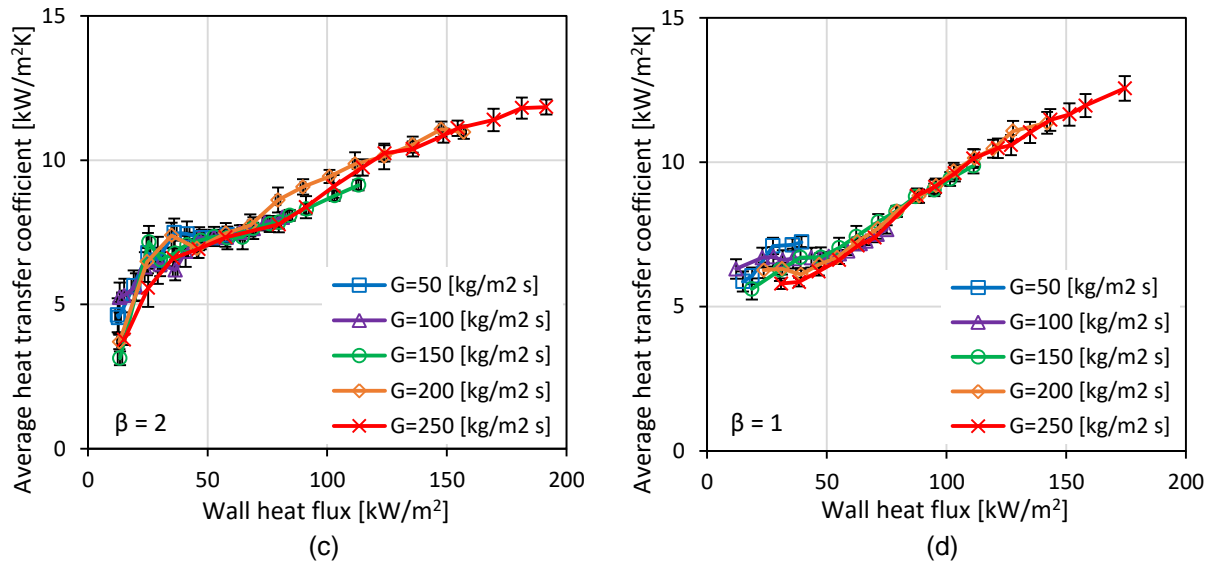


Figure 6.16 Effect of wall heat flux and mass flux on the average heat transfer coefficient for (a) TS.1 (b) TS.2 (c) TS.3 (d) TS.4.

6.4.3 Effect of channel aspect ratio

The effect of channel aspect ratio on the local heat transfer coefficient is shown in Fig. 6.17. This figure is plotted at low and high wall heat fluxes and mass flux of 250 kg/m²s for three test sections; (1), (2) and (3).

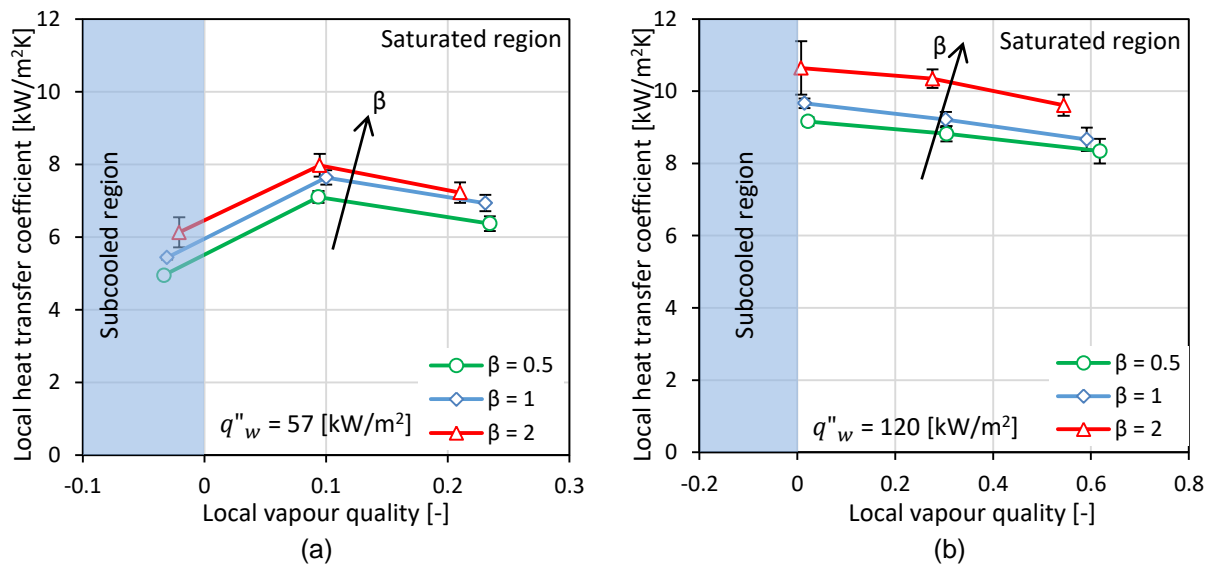


Figure 6.17 Effect of channel aspect ratio on the local heat transfer coefficient at mass flux of 250 kg/m²s and different wall heat fluxes for TS.1, TS.2 and TS.3:

(a) Low heat flux (b) High heat flux.

This figure illustrates that in the subcooled region (vapour quality less than zero), the local heat transfer coefficient increased with increasing channel aspect ratio. This could be due to the fact that the wider channel provided lower wall temperature for a given heat flux and mass flux. In other words, the contribution of the single-phase convective heat transfer coefficient is greater due to the lower wall-to-fluid temperature difference. In this figure, the wall-to-fluid temperature difference was found to be 11.8, 10.5 and 9.4 K for aspect ratio of 0.5, 1 and 2, respectively. In the saturation region (vapour quality greater than zero) and by taking into account the error bars, there was a noticeable increase in the local heat transfer coefficient with increasing channel aspect ratio. This could be due to the flow patterns inside the channels. In the present study, flow visualization showed that channel aspect ratio had an effect on bubble size and slug shape, while it had an insignificant effect on the annular flow. However, it was believed that the channel aspect ratio may affect the nucleating site density and the liquid film thickness around the channel circumference, which caused this increase in the heat transfer coefficient. In the present study, it was difficult to measure these two important features during the experiments due to the capability of the camera and the fact that metallic multi-channels were used. Therefore, the nucleation site density and the liquid film thickness were calculated for the smallest and largest channel aspect ratio using the correlations by Benjamin and Balakrishnan (1997) and Thome and Cioncolini (2016), respectively.

There are many proposed correlations for calculating nucleation site density available in the literature as reviewed by Mohanty and Das (2017). However, most of these correlations were based on one fluid and material, such as water and copper. In contrast, the correlation by Benjamin and Balakrishnan (1997) was proposed using different fluids and materials. It covered several parameters compared to others such as the wall superheat, the thermophysical properties of fluid and heating surface, the heating surface roughness and the surface tension of fluid. Since the properties of HFE-7100 are completely different from water, the correlation by Benjamin and Balakrishnan (1997) was used here. Moreover, both of copper and aluminium surfaces were examined. An empirical correlation was proposed by Benjamin and Balakrishnan (1997) to calculate the nucleation site density in pool boiling. They experimentally examined the pool boiling of different pure fluids, *i.e.* water, CCl₄, n-

hexane and acetone, using stainless steel and aluminium surfaces with different surface roughness values. The nucleation site density was measured using a high-speed camera by taking into account the number of active nucleation sites per heated surface area. They reported that the nucleation site density depended on the surface tension, fluid properties, surface roughness, surface properties and wall superheat. Therefore, they proposed a correlation in terms of Prandtl number, wall superheat, surface-liquid interaction parameter (γ) and dimensionless surface roughness parameter (θ). They also verified their correlation with database from the literature including copper and nickel surfaces.

$$NSD = 218.8Pr_l^{1.63} \left(\frac{1}{\gamma}\right) \theta^{-0.4} (\Delta T_{sup})^3 \quad (6.3)$$

$$\gamma = \left(\frac{k_w \rho_w C p_w}{k_l \rho_l C p_l}\right)^{0.5} \quad (6.4)$$

$$\theta = 14.5 - 4.5 \left(\frac{RaP}{\sigma}\right) + 0.4 \left(\frac{RaP}{\sigma}\right)^2 \quad (6.5)$$

Their correlation covered the following ranges: $13 \times 10^{-3} \text{ N/m} < \sigma < 59 \times 10^{-3} \text{ N/m}$, $5 \text{ K} < \Delta T_{sup} < 25 \text{ K}$, $1.7 < Pr_l < 5$, $0.02 \text{ } \mu\text{m} < Ra < 1.17 \text{ } \mu\text{m}$, $2.2 < \theta < 14$ and $4.7 < \gamma < 93$. It is worth mentioning that the ranges of the present study are: $\sigma = 13.6 \times 10^{-3} \text{ N/m}$, $\Delta T_{sup} \leq 15.27 \text{ K}$, $Pr_l = 11$, $Ra = 0.271 \text{ } \mu\text{m}$ (for $\beta = 0.5$), $Ra = 0.304 \text{ } \mu\text{m}$ (for $\beta = 2$), $\theta = 6.98$ (for $\beta = 0.5$), $\theta = 6.34$ (for $\beta = 2$), $\gamma = 113.6$ (for $\beta = 0.5$) and $\gamma = 113.9$ (for $\beta = 2$). These ranges were calculated based on the inlet pressure and the wall temperature. It can be seen that all the experimental ranges were within their ranges except the Prandtl number and the surface-liquid interaction parameter. These differences could be due to the different fluid properties of HFE-7100, such as thermal conductivity, viscosity and specific heat.

Thome and Cioncolini (2016) developed a heat transfer model for convective boiling and condensation in the annular regime covering both macro and microchannels. A large experimental database with 11498 data points was compared with this model by the authors. This data included water and refrigerants in circular and non-circular multi-microchannels (fully and partial heated). Both local heat transfer coefficient and local average liquid film thicknesses can be predicted using their model as follows:

$$\frac{h\delta}{k_l} = 0.0776\delta^{+0.9}Pr_l^{0.52} \quad (6.6)$$

$$\delta^+ = \max\left(\sqrt{\frac{Re_{lf}}{2}}, 0.0165Re_{lf}\right) \quad (6.7)$$

$$Re_{lf} = (1 - e)(1 - x)\frac{GD}{\mu_l} \quad (6.8)$$

$$e = (1 + 279.6We_c^{-0.8395})^{-2.209} \quad (6.9)$$

$$We_c = \frac{\rho_c J_g^2 D}{\sigma} \quad (6.10)$$

$$\rho_c = \frac{x + e(1 - x)}{\frac{x}{\rho_g} + \frac{e(1 - x)}{\rho_l}} \quad (6.11)$$

$$J_g = \frac{xG}{\rho_g} \quad (6.12)$$

For non-circular channels, the equivalent diameter (d_{eq}) should be used. The average liquid film thickness in non-circular channels is calculated as follows:

$$\delta_{non-cir} = \frac{A_{lf}}{Per_w} \quad (6.13)$$

$$A_{lf} = \frac{\pi}{4}(d_{eq}^2 - (d_{eq} - 2\delta)^2) \quad (6.14)$$

$$d_{eq} = 2\sqrt{\frac{A_{sec}}{\pi}} \quad (6.15)$$

Fig. 6.18 shows the results of these two correlations for a mass flux of 250 kg/m²s. Fig. 6.18(a) depicts the nucleation site density at axial distance (z/L) of 0.1 and moderate and high wall superheat when bubbly flow occurred at this location. The liquid film thickness at axial distance (z/L) of 0.9 is shown in Fig. 6.18(b). This figure is plotted at moderate and high local vapour qualities when slug or annular flow occurred at this location.

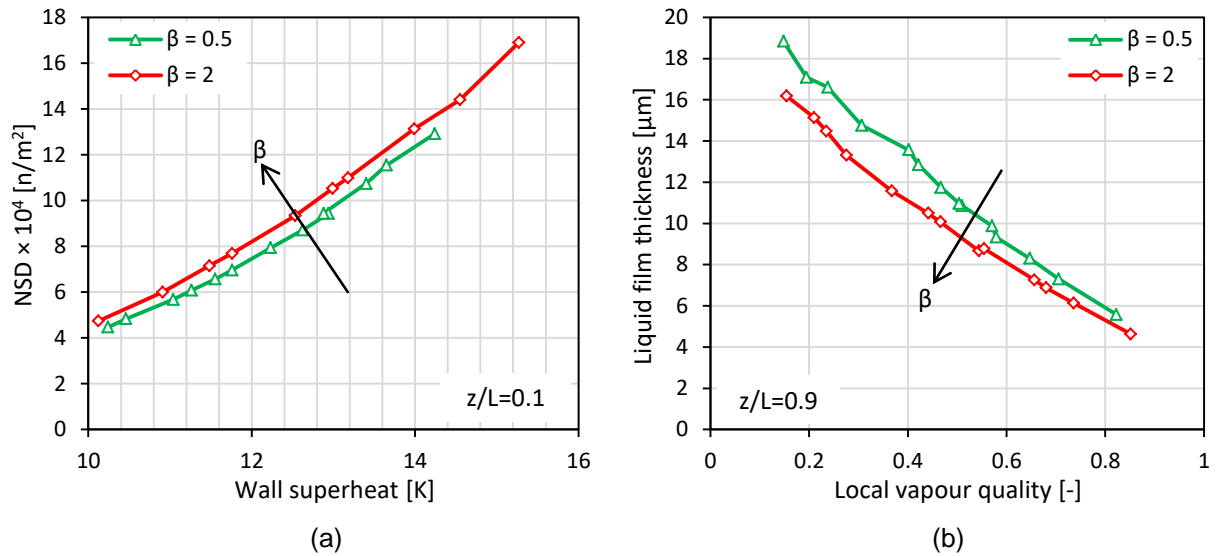


Figure 6.18 Different channel aspect ratios at mass flux of $250 \text{ kg/m}^2\text{s}$ for TS.1 and TS.3: (a) Nucleation site density (b) Liquid film thickness.

It is obvious that the nucleation site density increased with increasing wall superheat as illustrated in Fig. 6.18(a). High wall superheat may lead to the activation of more nucleation sites on the channel surface. Fig. 6.18(a) also shows that, for a given wall superheat, the nucleation site density increased with increasing channel aspect ratio. For example, at wall superheat of 11.7 K , the nucleation site density increased from 6.97×10^4 to $7.7 \times 10^4 \text{ n/m}^2$ when the aspect ratio increased from 0.5 to 2. Fig. 6.18(b) depicts that the liquid film thickness decreased with increasing vapour quality. At low vapour qualities, $x < 0.2$, slug flow occurred at this location, while at $x > 0.2$, annular flow was visualized. It is known that the correlation by Thome and Cioncolini (2016) was proposed for annular regime and thus a good prediction can be found for this regime, *i.e.* $x > 0.2$. This figure demonstrates that, for a given vapour quality, the liquid film thickness decreased with increasing channel aspect ratio. For instance, at vapour quality of 0.65, the liquid film thickness decreased from 8.3 to $7.2 \mu\text{m}$ when the channel aspect ratio increased from 0.5 to 2.

The previous results are shown schematically in Fig. 6.19 to clarify the nucleation site density and the liquid film thickness for different channel aspect ratios. This figure illustrates that the heat is supplied from the channel bottom and then transfers to the fluid through the channel bottom and sidewalls, *i.e.* three-sides heated channel. When the flow pattern is bubbly flow, the enhancement in the heat transfer

coefficient could be due to the activation of more nucleation sites at the channel corners and on the channel bottom surface with increasing channel width, see Fig. 6.19(a). When the channel width decreases (aspect ratio of 0.5 and 1), most bubble nucleation is limited at the channel corners. In other words, the number of nucleation sites per heated surface area (nucleation site density) is larger in the channels with larger bottom surface area. It is known that more nucleation sites result in higher heat transfer coefficient due to the evaporation process in the liquid micro-layer underneath these nucleating bubbles.

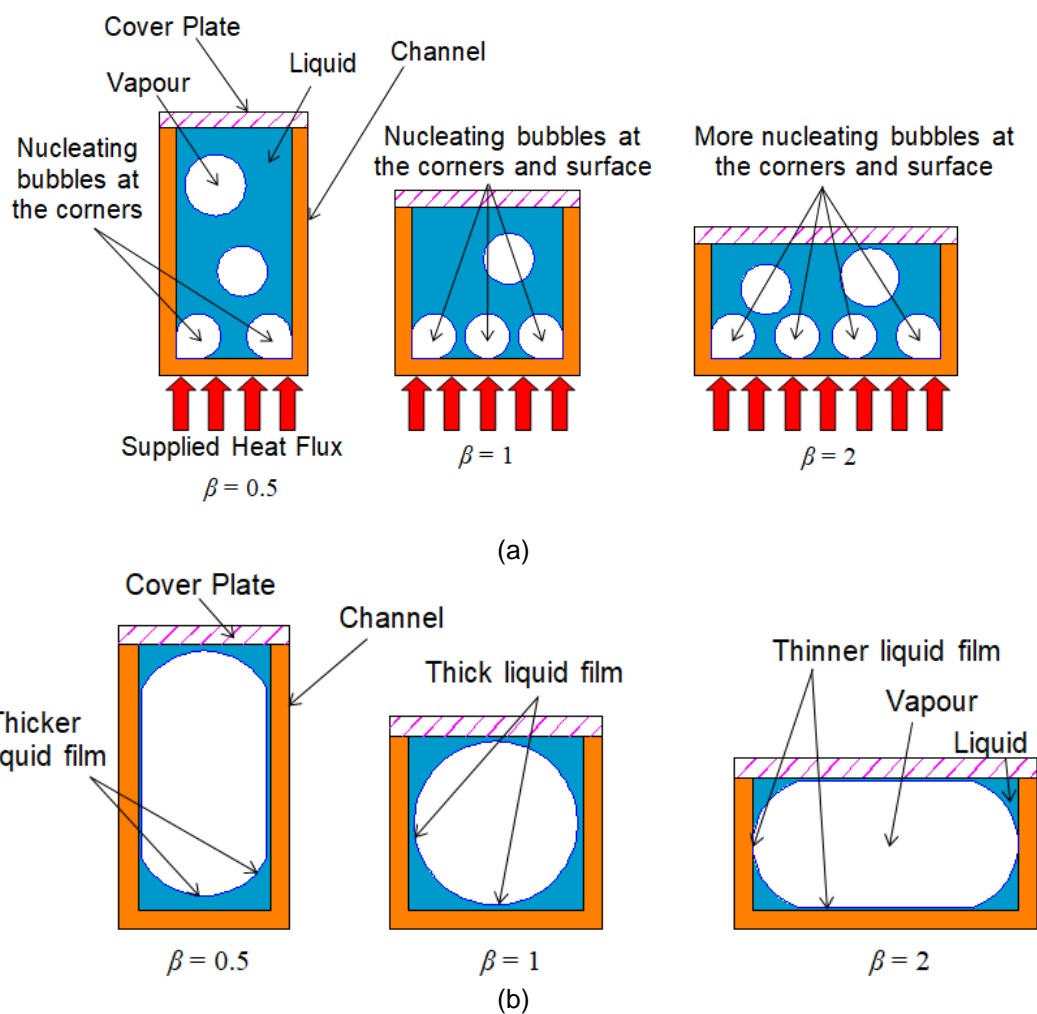


Figure 6.19 Schematic diagram of the flow patterns at different channel aspect ratios for (a) Nucleating bubbles (b) Liquid film thickness around the channel circumference.

When the flow patterns are slug or annular flow, this increase in the heat transfer coefficient with increasing channel aspect ratio could be due to the thinner liquid

film thickness around the channel circumference as explained schematically in Fig. 6.19(b). In the shallow channels (large aspect ratio), the vapour slug or annular flow is confined and squeezed between the top adiabatic surface and the channel bottom surface leaving a thin liquid film. Because most of the heat comes from the bottom surface compared to the sidewalls, the evaporation rate becomes very high at the film interface in contact with the channel bottom surface. Thus, the local wall superheat becomes lower and thus the heat transfer coefficient becomes higher. On the contrary, in deep channels (small aspect ratio), these regimes are confined and squeezed by the channel sidewalls rather than the bottom wall. With some stratification effects, a thicker liquid film may occur on the bottom surface (high thermal resistance) and thus the evaporation rate becomes lower compared to the channels with larger aspect ratio.

The results in Fig. 6.17 are also re-plotted using local heat transfer coefficient versus axial distance as presented in Fig. 6.20. It indicates that the local heat transfer coefficient increased with increasing channel aspect ratio.

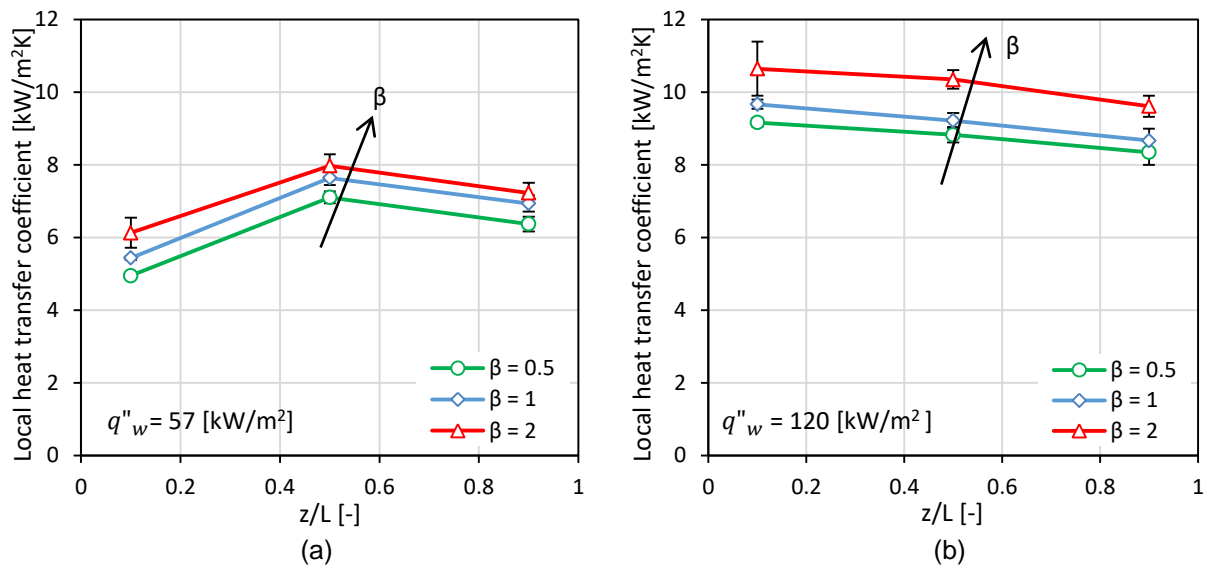


Figure 6.20 Effect of channel aspect ratio on the local heat transfer coefficient as a function of axial distance at mass flux of $250 \text{ kg/m}^2\text{s}$ for TS.1, TS.2 and TS.3.

(a) Low heat flux (b) High heat flux.

Fig. 6.21 presents the effect of channel aspect ratio on the average heat transfer coefficient at mass flux of $250 \text{ kg/m}^2\text{s}$. It is obvious that the average heat transfer

coefficient increased by 14.3% when the channel aspect ratio increased from 0.5 to 2. It is worth mentioning that the increase in the two-phase heat transfer coefficient with increasing aspect ratio was also found by Soupremanien et al. (2011) (at low heat fluxes) and Markal et al. (2016b) (up to aspect ratio of 3.54). Drummond et al. (2018) also mentioned that smaller channel height, *i.e.* larger aspect ratio, provided highest heat transfer coefficient. Flow boiling of HFE-7100 in horizontal rectangular microchannels at fixed channel width and different channel heights was examined in their study.

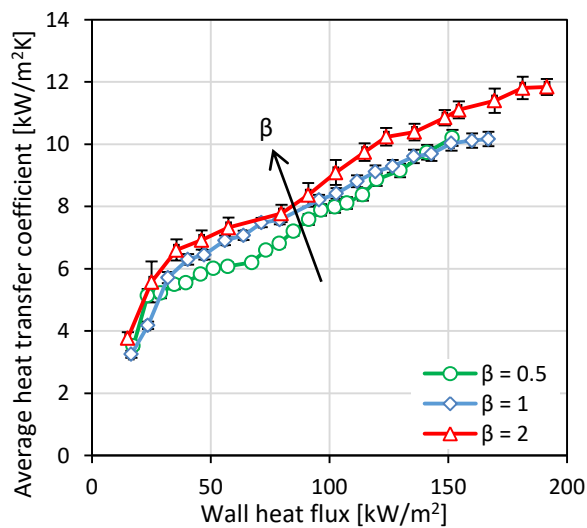


Figure 6.21 Effect of channel aspect ratio on the average heat transfer coefficient at a mass flux of $250 \text{ kg/m}^2\text{s}$ for TS.1, TS.2 and TS.3.

6.4.4 Effect of channel surface material

The material effect on the local heat transfer coefficient is plotted in Fig. 6.22 at mass flux of $250 \text{ kg/m}^2\text{s}$ for low and high wall heat fluxes. Only wall heat flux was used to present this figure since the area ratio is the same for TS.2 and TS.4. It is obvious that, at low heat flux, *i.e.* 31 kW/m^2 , the material effect was insignificant. However, at high wall heat flux, *i.e.* 151 kW/m^2 , aluminium surface showed higher local heat transfer coefficient than copper. These results were also found when the local heat transfer coefficient versus axial distance is presented as shown in Fig. 6.23.

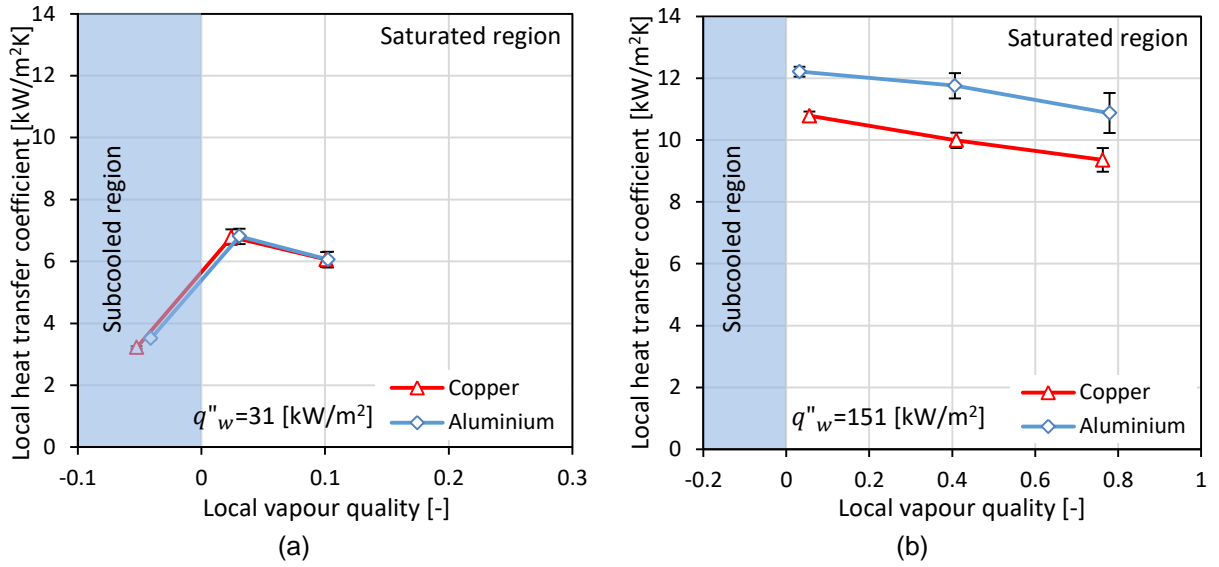


Figure 6.22 Effect of surface material on the local heat transfer coefficient at mass flux of 250 kg/m²s for TS.2 and TS.4: (a) Low wall heat flux (b) High wall heat flux.

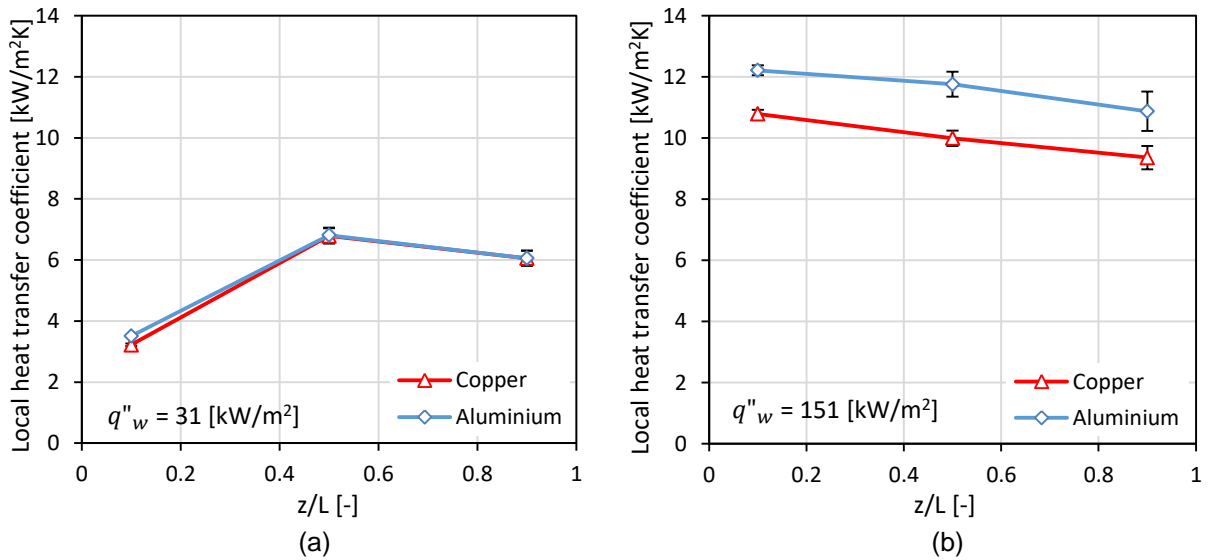


Figure 6.23 Effect of surface material on the local heat transfer coefficient as a function of axial distance at mass flux of 250 kg/m²s for TS.2 and TS.4: (a) Low heat flux (b) High heat flux.

Fig. 6.24 shows the material effect on the average heat transfer coefficient at mass flux of 250 kg/m²s. This figure demonstrates that there was no a clear effect at wall heat flux less than 60 kW/m². At high heat fluxes more than 60 kW/m², significant effect was found. The average heat transfer coefficient increased by 12% when the surface metal was aluminum. It is worth mentioning that, at low wall heat fluxes, few bubbles and some vapour slugs were visualized in the channels. Therefore, the

insignificant effect by these surfaces could be due to the low bubble generation, *i.e.* few active nucleation sites, resulting in low evaporation rates. In other words, at low heat fluxes (low wall superheat), only large surface cavities activate, while the small cavities are still not active yet. More details are discussed in the next section. In contrast, at moderate and high heat fluxes, more nucleation sites activate with increasing heat flux. Moreover, annular flow was also observed at these heat fluxes. Accordingly, the evaporation rates become higher leading to different heat results.

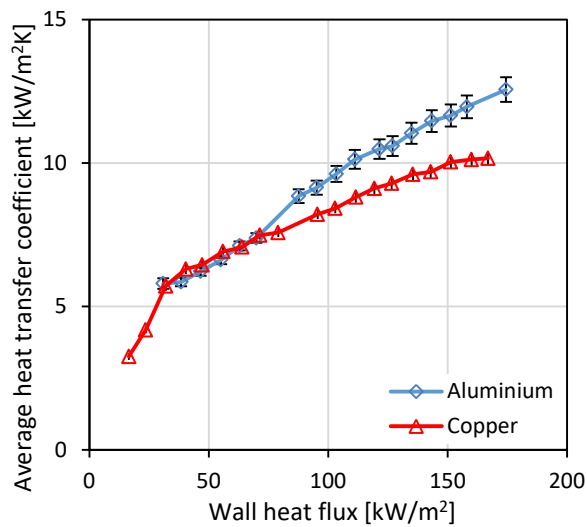


Figure 6.24 Effect of surface material on the average heat transfer coefficient for TS.2 and TS.4 at mass flux of 250 kg/m²s.

In order to evaluate the size of active nucleation sites at different wall heat fluxes (wall superheat), the model by Hsu (1962) was used and presented in Fig. 6.25. The author proposed a model to calculate the size of effective nucleation cavities by assuming the nucleating bubble was a truncated sphere. In this model, the nucleation occurred when the bubble grew until departure. This happened when the liquid temperature, at the height of bubble, was (at least) equal to the bubble temperature. The bubble height was linked to the bubble radius, the static contact angle and the cavity mouth radius. He assumed that the nucleation occurred when the bubble height was $1.6r_b$. This corresponds to the contact angle of 53.1° . Therefore, the cavity radius of the active nucleation site can be calculated using Eq. 6.16. This equation represents the minimum and maximum sizes of effective nucleation cavities.

$$r_{cav(min,max)} = \frac{\delta_t}{4} \frac{\Delta T_{sup}}{(\Delta T_{sup} + \Delta T_{sub})} \left[1 \pm \sqrt{1 - \frac{12.8\sigma T_{sat}(\Delta T_{sup} + \Delta T_{sub})}{\delta_t \rho_g i_{lg} \Delta T_{sup}^2}} \right] \quad (6.16)$$

$$\delta_t = \frac{k_l}{h_{sp}} \quad (6.17)$$

δ_t is the thermal boundary layer thickness. Fig. 6.25 shows the size range of effective nucleation cavities using HFE-7100 at saturation pressure of 1 bar, saturated boiling, *i.e.* $\Delta T_{sub} = 0$ K, and rectangular channel with hydraulic diameter of 0.46 mm. All the fluid properties were found at this pressure. The single-phase heat transfer coefficient was calculated from the laminar flow equation using three-wall heat transfer, see Shah and London (1978). This figure shows that the minimum cavity radius decreased when the wall superheat increased. This means that small size of surface cavities becomes active with increasing wall superheat. For example, at wall superheat less than 10 K, the active cavity radius is more than 0.1 μm , *i.e.* large cavities are active. However, small cavities also activate, *i.e.* less than 0.1 μm , with further increasing wall superheat (increasing heat flux). This figure also indicates that the nucleation sites are possible with HFE-7100 from surfaces with cavity radius between 0.06 to 58 μm . This could be due to the low surface tension (high surface wettability) leading to filling the cavities with fluid even cavities of small size.

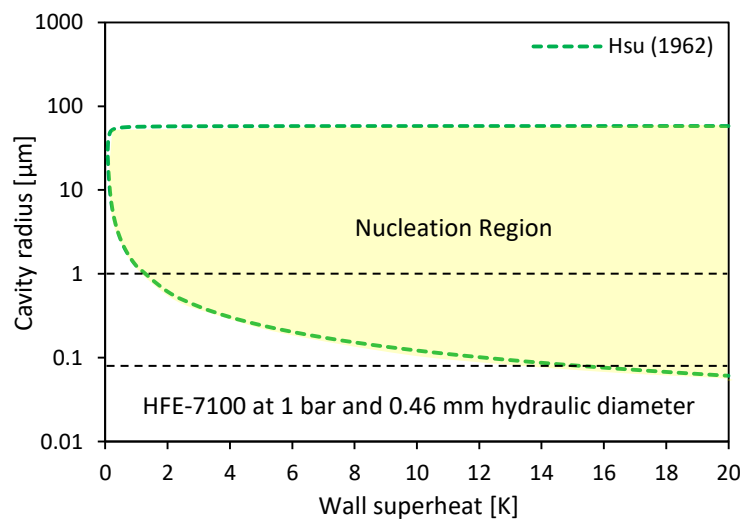


Figure 6.25 The size range of effective nucleation cavities using the model by Hsu (1962).

The correlations by Benjamin and Balakrishnan (1997) and Thome and Cioncolini (2016) were also adopted here to calculate the nucleating site density and the liquid film thickness for different channel surface metals. It was found that the ranges of the present study using aluminium and copper surfaces compared to those reported by Benjamin and Balakrishnan (1997) are: $\sigma = 13.6 \times 10^{-3}$ N/m, $\Delta T_{sup} \leq 15.6$ K, $Pr_l = 11$, $Ra = 0.192$ μm (for aluminium), $Ra = 0.281$ μm (for copper), $\theta = 8.92$ (for aluminium), $\theta = 6.97$ (for copper), $\gamma = 70.24$ (for aluminium) and $\gamma = 113.7$ (for copper). All these experimental ranges were within their ranges except the Prandtl number and the surface-liquid interaction parameter of copper, which could be due to the different fluid properties of HFE-7100. Fig. 6.26 depicts these two parameters at mass flux of $250 \text{ kg/m}^2\text{s}$ for TS.2 and TS.4. This figure is presented at z/L of 0.1 and 0.9 at moderate and high wall superheat and local vapour quality when bubbly, slug or annular flow occurred at these locations.

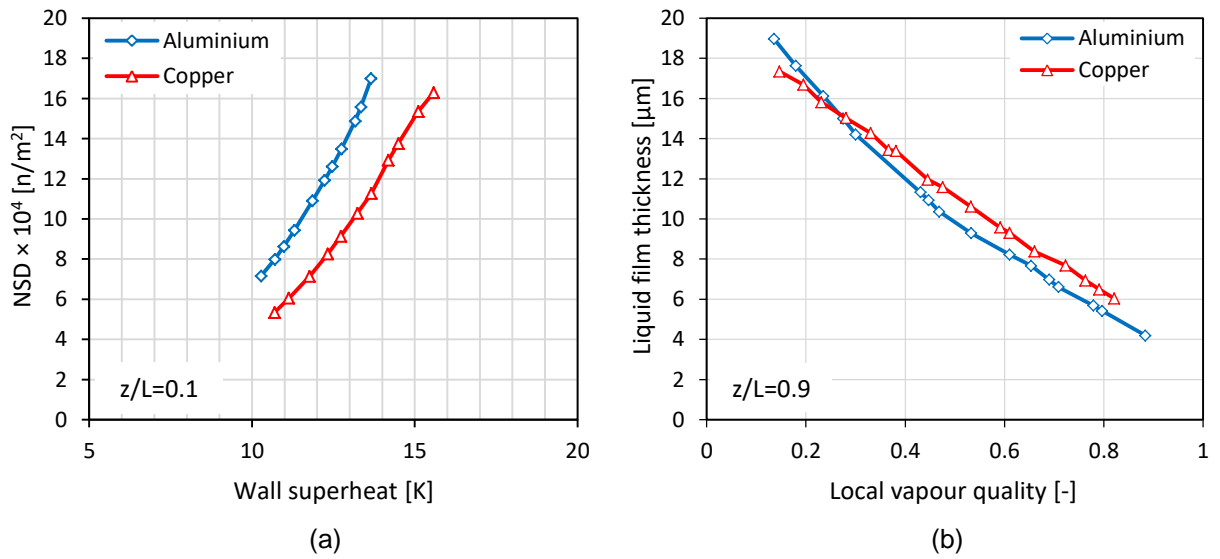


Figure 6.26 Different channel surface materials at mass flux of $250 \text{ kg/m}^2\text{s}$ for TS.2 and TS.4: (a) Nucleation site density (b) Liquid film thickness.

Fig. 6.26 demonstrates that the aluminium surface provided higher nucleation site density than copper for a given wall superheat, see Fig. 6.26(a). For example, at 13.2 K, aluminium had a nucleation site density of $14.8 \times 10^4 \text{ n/m}^2$, while it was less using copper, *i.e.* $10.3 \times 10^4 \text{ n/m}^2$. Fig. 6.26(b) shows that, for given local vapour quality, the liquid film thickness became thinner for the aluminium compared to copper surface. For instance, at vapour quality of 0.6 , the film thickness was $9.6 \mu\text{m}$ for

copper surface. This film decreased to 8.2 μm for aluminium. In other words, the enhancement in the heat transfer coefficient for aluminium surface could be due to the high nucleation site density and thinner liquid film thickness.

In order to highlight the possible reason of these differences in the flow features, the influence of different parameters is presented here. It is known that with changing surface material, four main parameters may also change, *i.e.* surface properties, average surface roughness, surface wettability and surface microstructures. Surface properties include surface thermal conductivity, specific heat and density. Inspecting the surface properties of copper compared to aluminium, one can indicate that the thermal conductivity and the density are higher by 100% and 230%, respectively, while the specific heat is 57% lower. The heat transfer results showed that there was enhancement but only by 12%. This noticeable enhancement in the heat transfer coefficient could not be related to the large differences in the surface properties. However, further studies using different materials are needed to confirm this. The measurement of average surface roughness showed that copper surface was 1.5 times rougher than aluminium. Rougher surface is expected to provide higher heat transfer coefficient, which is in contrast to the present results. HFE-7100 is considered a highly wetting refrigerant due to low surface tension. Its contact angle is nearly zero on all surface types as mentioned by Li et al. (2018). Therefore, it is expected that the surface wettability is the same for both copper and aluminium. Different surface microstructures could result in different number, shape and volume of surface peaks and valleys. In the present study, the aluminium surface has different surface topography, *i.e.* more debris and cavities, compared to copper, see Section 3.3.3. This surface also has larger cavity mouth size than copper. More and clear cutting marks can be seen on the aluminium surface that could result in more peaks and valleys on this surface with different shapes and volumes. Fig. 6.27 illustrates a schematic diagram of one surface peak and valley, where H, D and d are the peak height, the valley depth and the peak or valley diameter (cavity mouth diameter). Surface valleys may act as active cavities leading to the generation of nucleating bubbles. The number, shape and volume of these valleys may define the number of nucleating bubbles, see Fig. 6.27(a). Surface peaks could disturb the liquid film leading to thinner thickness, *i.e.* more contact surface area between channel and fluid interface, as shown in Fig. 6.27(b). More and large peaks may result in thinner film

thickness. Therefore, aluminium surface may provide a higher nucleation site density and thinner liquid film thickness. Accordingly, the differences in the heat transfer results could be due to the variations in the surface microstructures. The number, shape and volume of surface peaks and valleys should be considered in two-phase flow heat transfer. Different parameters could affect these surface microstructures as discussed in Chapter 2.

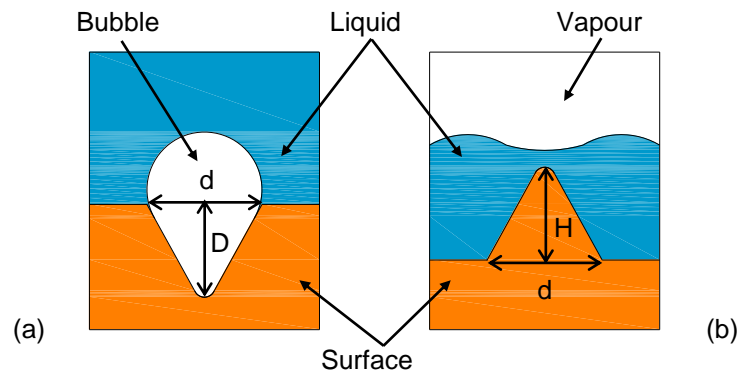


Figure 6.27 Schematic diagram of surface microstructures:

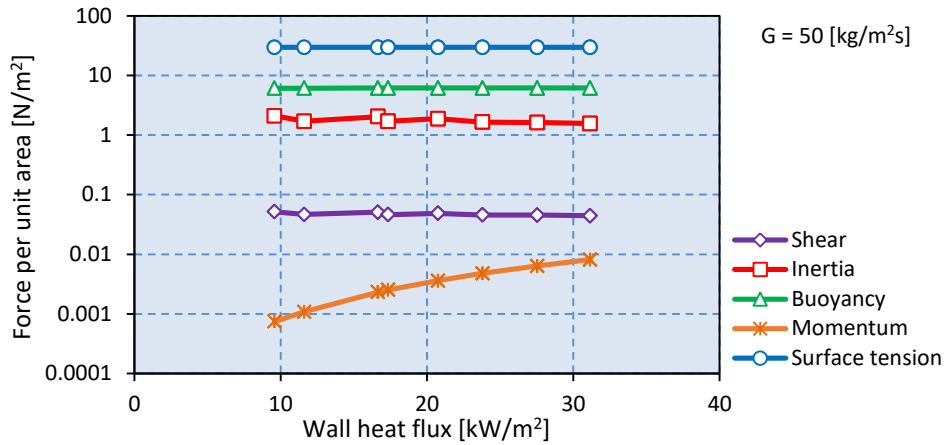
(a) Surface valley (b) Surface peak.

It is worth mentioning that low thermal performance by high thermal conductivity surfaces was also found by other researchers. The flow boiling experimental results by Pike-Wilson and Karayiannis (2014) showed that lower heat transfer coefficient by copper surface was found compared to brass and stainless steel surfaces. Other pool boiling investigations, such as Jabardo et al. (2009) and Suriyawong and Wongwises (2010), indicated that copper surface had lower thermal performance than brass or aluminium surface. Benjamin and Balakrishnan (1997) compared the pool boiling results of copper and aluminium surfaces for given liquid, surface finish and wall superheat. They reported that the nucleation site density of copper surface was lower than that of aluminium surface, which agrees with the present results.

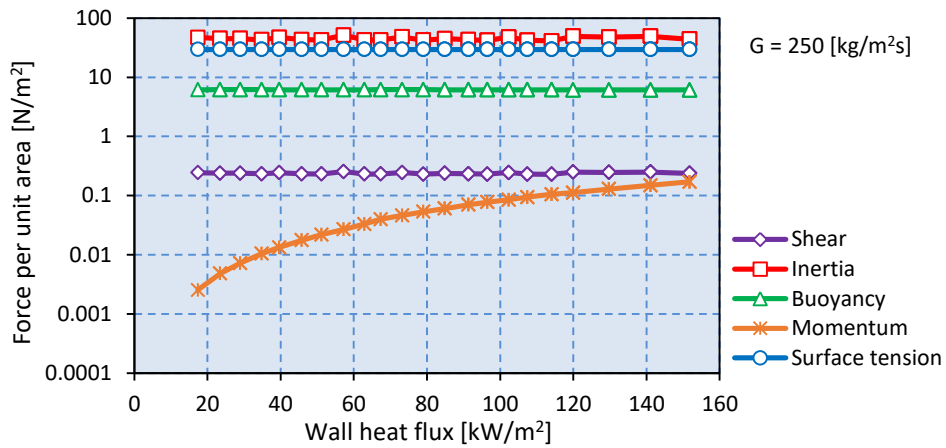
6.5 Force Analysis

The relative importance of different forces in channels plays a significant role in the heat transfer behaviour. This can result in different flow patterns, pressure drop and heat transfer coefficient and thus different flow pattern maps and correlations can be proposed. Five major forces acting on the liquid-vapour interface can be identified during flow boiling as discussed by Kandlikar (2010). These forces are inertia, surface tension, shear, buoyancy and evaporation momentum. The detail and equation of each force were discussed in Chapter 2, Section 2.4.6. In the present study, these forces are calculated and compared at different operating conditions in order to identify the dominant force(s) and the controlling dimensionless groups. The following assumptions are used in order to calculate each force; (i) the diameter of bubble is assumed to be equal to the channel hydraulic diameter, *i.e.* vapour bubble is confined by the channel walls, (ii) the mass flux is calculated per each channel, (iii) the orientation angle is zero since the channels are in horizontal position, (iv) the fluid density and viscosity in the shear and inertia forces are obtained using all liquid flow as suggested by Kandlikar (2010), (v) the evaporative heat flux at the interface is assumed to be equal to the wall heat flux as mentioned by Kandlikar (2010) and (vi) all fluid properties are obtained at a system pressure of 1 bar.

Fig. 6.28 shows the relative effect of five forces at lower and higher mass fluxes and different wall heat fluxes for TS.1. This figure illustrates that the surface tension, inertia, buoyancy and shear forces were independent of heat flux. In contrast, the evaporation momentum force increased gradually with increasing heat flux. These trends were found for both mass fluxes. It can be seen that, at lower mass flux, the surface tension became the dominant force as shown in Fig. 6.28(a), while the inertia force dominated slightly at higher mass flux, see Fig. 6.28(b). Although the inertia force overcame other forces at mass flux of $250 \text{ kg/m}^2\text{s}$, the heat flux still had a strong effect on the heat transfer results. Fig. 6.29 depicts the average heat transfer coefficient versus wall heat flux at mass flux of $250 \text{ kg/m}^2\text{s}$. It illustrates that the average heat transfer coefficient increased with increasing wall heat flux. Therefore, the heat flux effect is an important parameter during the present results even at high mass flux. Further investigations using higher mass fluxes are required to confirm this.



(a)



(b)

Fig. 6.28 Magnitude of different forces at different wall heat fluxes for TS.1 and mass flux of: (a) $50 \text{ kg/m}^2\text{s}$ (b) $250 \text{ kg/m}^2\text{s}$.

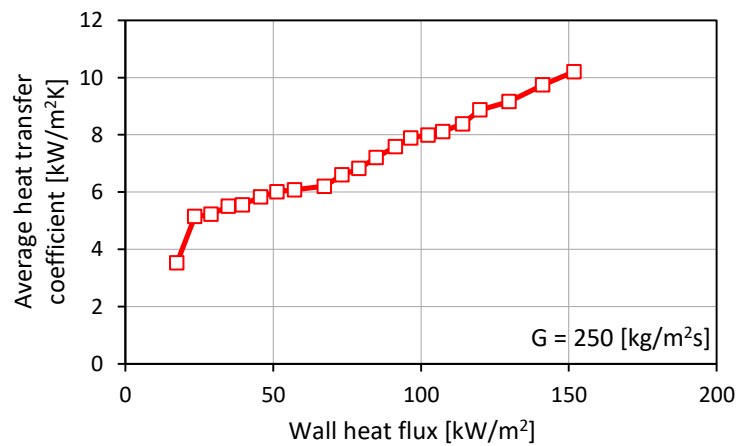


Fig. 6.29 Average heat transfer coefficient versus wall heat flux at mass flux of $250 \text{ kg/m}^2\text{s}$ for TS.1.

Since the wall heat flux affects directly the evaporation momentum force, this force is also important in the microchannels. The shear force tries to stabilize the liquid

film and promotes a homogeneous distribution of the liquid, see Alam et al. (2016). Therefore, both evaporation momentum and shear forces should be studied at low and high mass fluxes and different ranges of heat flux. Fig. 6.28 shows that the evaporation momentum force was always lower than the shear force. When the wall heat flux increased, the evaporation momentum force also increased and became very close to the shear force as shown in Fig. 6.28(b). Alam et al. (2016) reported that the heat transfer coefficient increases with heat flux, when the shear force overcomes the evaporation momentum force due to the homogeneous distribution of the liquid film. However, with further increase in the heat flux, the evaporation momentum force exceeds the shear force leading to reduction in the heat transfer coefficient as they mentioned. They attributed this to the high evaporation momentum force (at high heat fluxes) which causes high flow reversal and channel blockage, *i.e.* lack of channel rewetting, and thus the heat transfer coefficient decreases. The present experimental results agree with their study, *i.e.* the heat transfer coefficient increases with increasing wall heat flux even at high heat fluxes since the shear force exceeds the evaporation momentum force.

Fig. 6.30 depicts the effect of mass flux on the different forces at wall heat flux of 28 kW/m² for TS.1. It is obvious that the surface tension, buoyancy and evaporation momentum forces did not change with increasing mass flux. In contrast, both the inertia and shear forces increased with mass flux.

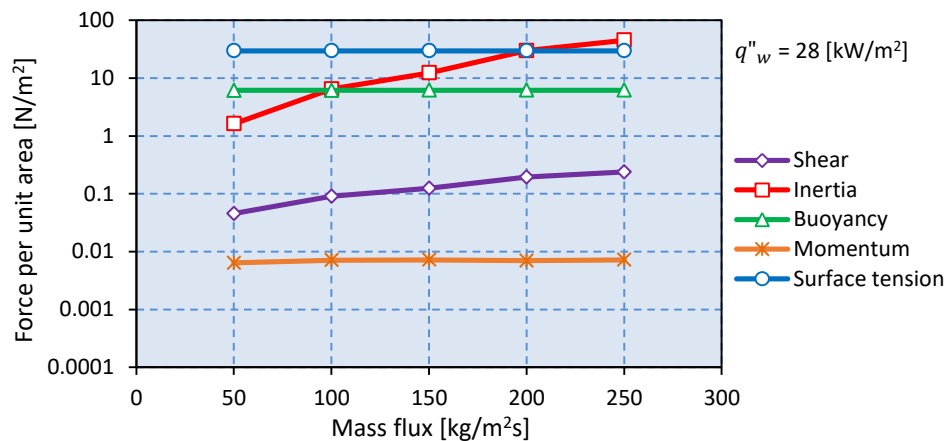


Fig. 6.30 Magnitude of different forces at different mass fluxes and wall heat flux of 28 kW/m² for TS.1.

This figure also shows that the surface tension dominated at mass flux up to 150 kg/m²s. At mass flux of 200 kg/m²s, the surface tension and inertia forces were comparable. When the mass flux increased to 250 kg/m²s, the inertia force became the dominant force.

The above discussion showed that both surface tension and inertia forces are dominant in the present study. The magnitude of each force depends on the mass flux. In order to assess these forces using all the experimental data, these forces versus Weber number are presented in Fig. 6.31. The liquid Weber number is chosen since it represents the ratio between surface tension and inertia. The experimental data in Fig. 6.31 include all test sections and covers the following parameters:

Bond number: 0.2

Reduced pressure: 0.047

Boiling number: $5\text{--}98 \times 10^{-4}$

Prandtl number: 11

Reynolds number (liquid only): 35–204.2

Superficial liquid Reynolds number: 0.411–199.3

Superficial vapour Reynolds number: 0.26–10038

Liquid Weber number: 0.05–1.76

Vapour Weber number: 7.3–250.9

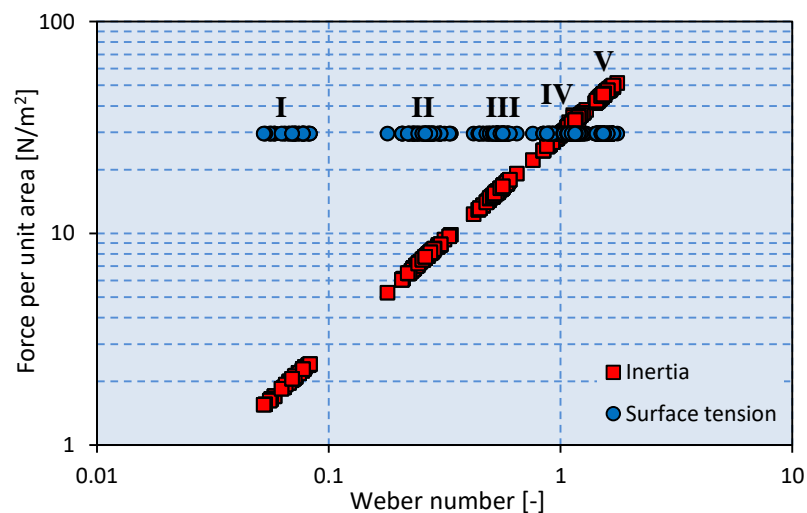


Fig. 6.31 Magnitude of surface tension and inertia forces using all the flow boiling data points for TS.1, TS.2, TS.3 and TS.4 at mass flux of: (I) 50, (II) 100, (III) 150, (IV) 200 and (V) 250 kg/m²s.

Fig. 6.31 illustrates that the surface tension force dominated at three ranges of mass flux, *i.e.* 50, 100 and 150 kg/m²s, see region I, II and III. At mass flux of 200 kg/m²s, both surface tension and inertia forces were comparable, see region IV. At higher mass flux, *i.e.* 250 kg/m²s, the dominant force was found to be the inertia force, see region V. In other words, when $We < 1$, surface tension dominates in 60% of the data, while inertia dominates in 40% of the data when $We > 1$.

It can be concluded that surface tension is the first dominant force, with inertia being the second significant force. Low mass fluxes are covered by the present study and thus surface tension dominates during the experiments. According to the previous force analysis, the dimensionless groups that may control the heat transfer results are Boiling number, Bond number, Confinement number and Weber number. The influence of the wall heat flux is considered in the Boiling number. Bond number takes into account the surface tension and gravitational forces which is similar to the Confinement number. Weber number accounts for the inertia and surface tension forces. Heat flux has a significant influence even when inertia force dominates.

6.6 Comparison with Existing Correlations

Selecting the reasonable heat transfer correlation is an essential step during thermal design. This helps to identify the required channel dimensions in the cooling system. Therefore, twelve existing two-phase heat transfer correlations were selected and compared with the experimental results. These correlations were proposed for horizontal/vertical flows, conventional and mini/microchannels, circular/non-circular channels and single and multi-channels. The full details of each correlation are discussed in Chapter 2 and given in Appendix B. In this section, 703 experimental data points were compared with these correlations. This data base included wall heat flux up to 191.6 kW/m², mass flux ranging from 50 to 250 kg/m²s, system pressure of 1 bar and exit vapour quality up to 1. The mean absolute error (*MAE*) as given in Eq. (6.18) and the percentage of data points predicted within $\pm 30\%$ error bands (Θ), see Eq. (6.19), are used to evaluate the accuracy of these correlations.

$$MAE = \frac{1}{N} \sum \left| \frac{h_{pred} - h_{exp}}{h_{exp}} \right| 100\% \quad (6.18)$$

$$\theta = \frac{N_{pred}}{N} 100\% \quad (6.19)$$

where h_{pred} , h_{exp} , N_{pred} and N are the predicted two-phase heat transfer coefficient, experimental two-phase heat transfer coefficient, number of predicted data points and the total number of data points, respectively. It is worth mentioning that some of the existing correlations were proposed for fully heated channel, *i.e.* all sides heated, while the present heat sinks are heated from the bottom side with an adiabatic cover plate, *i.e.* three-sides heated channel. Therefore, a correction factor should be used to adjust the values of these correlations for a partly heated channel as presented in Eq. (6.20). This was also adopted by other researchers such as Qu and Mudawar (2003a), Kim and Mudawar (2014) and Wang et al. (2016).

$$HTC = \left(\frac{Nu_3}{Nu_4} \right) h_{tp} \quad (6.20)$$

where HTC , h_{tp} , Nu_3 and Nu_4 are the adjusted two-phase heat transfer coefficient, the two-phase heat transfer coefficient calculated from the correlation, Nusselt number for thermally developed laminar flow with three-sides and four-sides heat transfer, respectively. The last two parameters are calculated from Eq. (6.21) and (6.22) based on the channel aspect ratio as proposed by Shah and London (1978).

$$Nu_3 = 8.235(1 - 1.833\beta + 3.767\beta^2 - 5.814\beta^3 + 5.361\beta^4 - 2\beta^5) \quad (6.21)$$

$$Nu_4 = 8.235(1 - 2.042\beta + 3.085\beta^2 - 2.477\beta^3 + 1.058\beta^4 - 0.186\beta^5) \quad (6.22)$$

In the above equations, β is the channel aspect ratio.

6.5.1 Conventional scale flow boiling heat transfer correlations

6.5.1.1 The correlation of Shah (1982)

A flow boiling heat transfer correlation was proposed by the author by selecting the larger value of the heat transfer coefficient in the nucleate and convective boiling. The author defined the nucleate boiling component (E) as a function of boiling number (Bo), while the convective boiling component (S) was a function of convection number (N_{co}). Experimental data points were used to valid this correlation. This data included different fluids, vertical and horizontal channels with

diameter ranging from 6 to 25.4 mm. Fig. 6.32 shows a comparison between the present heat transfer data and his correlation. It is obvious that, this correlation predicted the results well with a MAE of 25.92%, 25.43%, 24.64% and 20.16% for TS.1, TS.2, TS.3 and TS.4, respectively. The percentage of prediction for these test sections was 61.88%, 60.54%, 65.71% and 78.4%, respectively. In this correlation, the larger of the two-phase heat transfer coefficient in the nucleate and convective boiling components is selected. The nucleate boiling component is introduced only as a function of the Boiling number, which represents the effect of wall heat flux. Heat flux has a significant effect on the present results as discussed in Section 6.5.

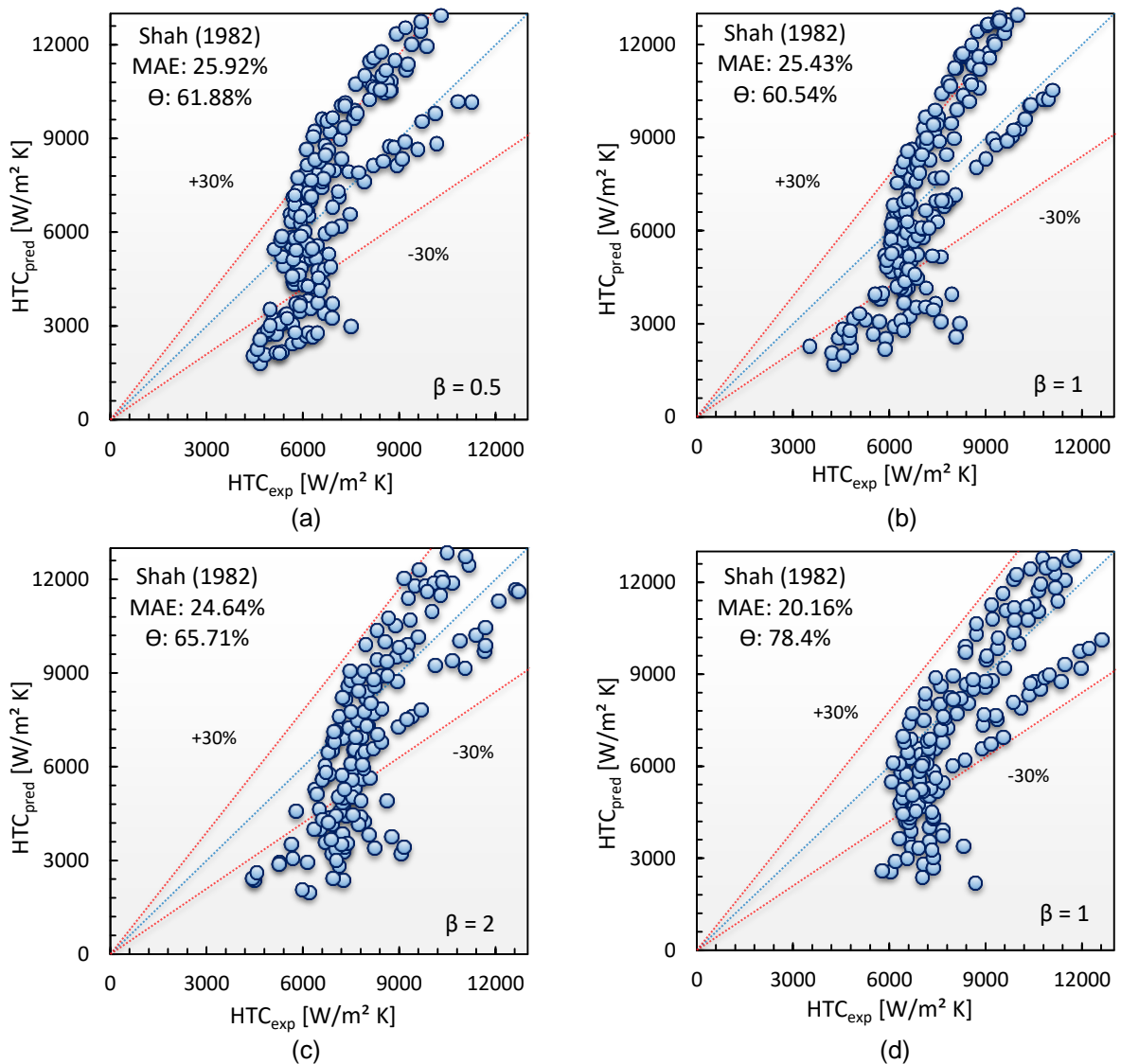


Figure 6.32 Comparison of the two-phase heat transfer data with the correlation by Shah (1982) for: (a) TS.1 (b) TS.2 (c) TS.3 (d) TS.4.

6.5.1.2 The correlation of Kandlikar (1990)

Kandlikar (1990) proposed a correlation for calculating two-phase heat transfer coefficient using the same approach as Shah (1982). His correlation included boiling number (Bo) and convection number (N_{co}). Moreover, the fluid dependent parameter (F_{fl}) was proposed in his correlation to present the fluid properties. 5264 data points including different fluids in vertical and horizontal tubes with inner diameter of 4–32 mm were used to develop this correlation. The comparison in Fig. 6.33 indicates that 61.88%, 61.08%, 62.29% and 67.28% of the data were predicted by his correlation for TS.1, TS.2, TS.3 and TS.4, respectively. This correlation showed a MAE of 25.83%, 25.25%, 26.09% and 23.63% for TS.1, TS.2, TS.3 and TS.4, respectively.

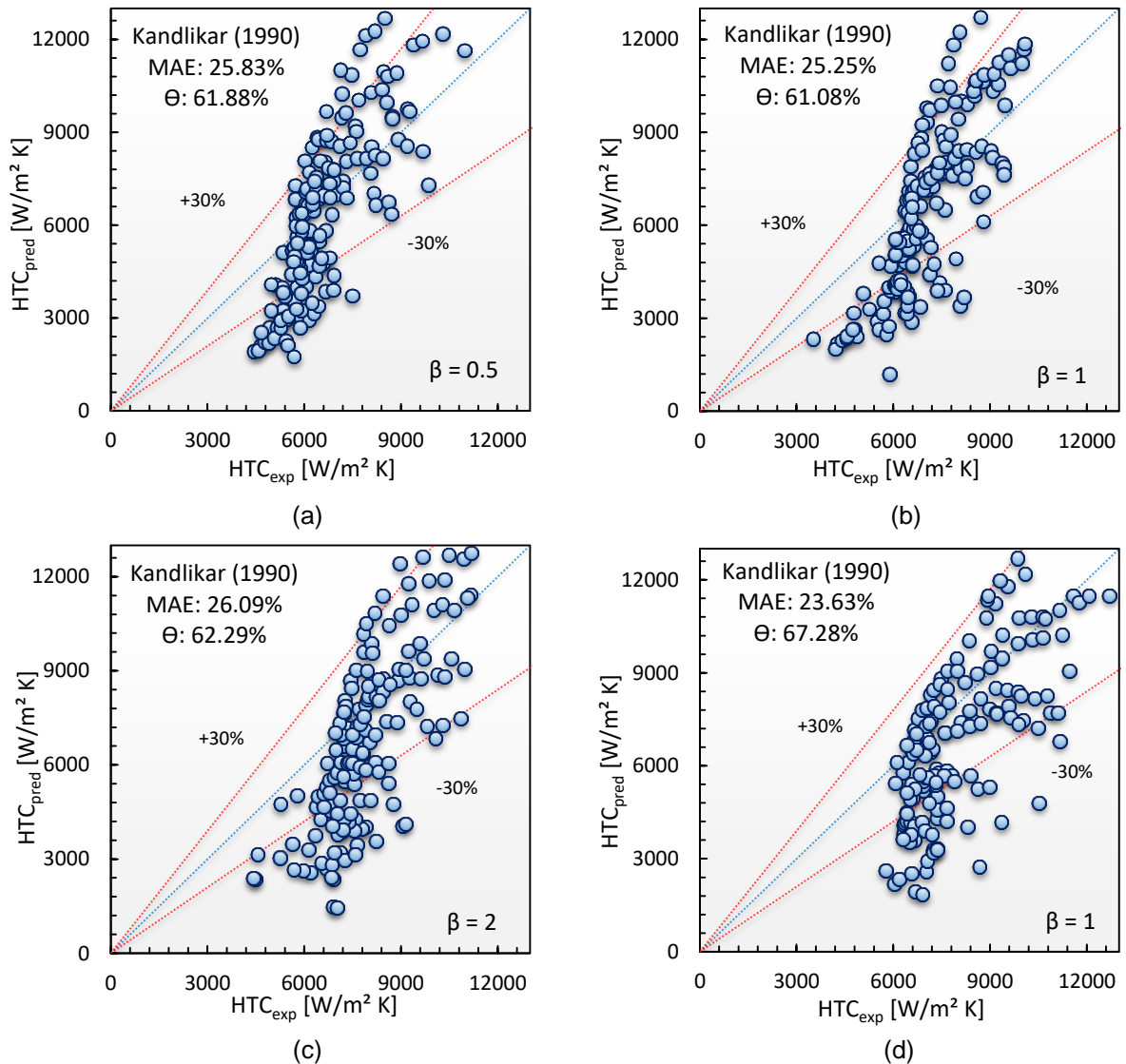
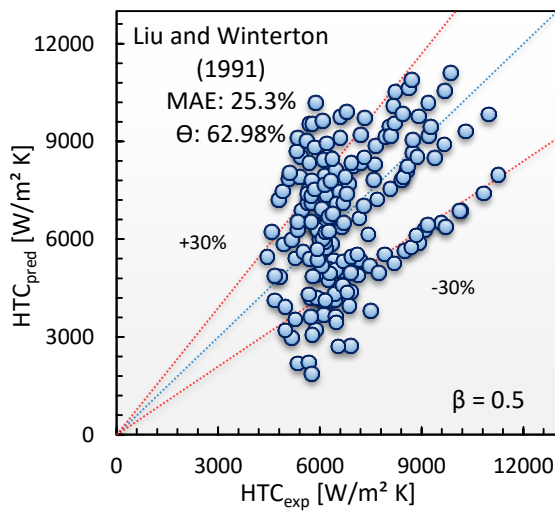


Figure 6.33 Comparison of the two-phase heat transfer data with the correlation by Kandlikar (1990) for: (a) TS.1 (b) TS.2 (c) TS.3 (d) TS.4.

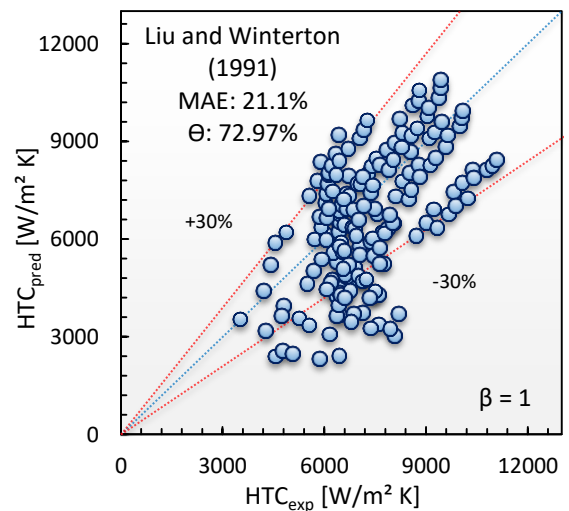
Similar to Shah (1982), the two-phase heat transfer coefficient is calculated by selecting the larger value of the nucleate boiling or the convective boiling component. Therefore, the Boiling number, which represents the wall heat flux effect, in the nucleate boiling component could be the reason for this low MAE.

6.5.1.3 The correlation of Liu and Winterton (1991)

A correlation for calculating two-phase heat transfer coefficient was proposed based on different fluids in vertical and horizontal channels with diameter of 2.95–32 mm. The authors correlated the nucleate boiling component using the pool boiling correlation given by Cooper (1984). They also combined the nucleate and convective contributions by using the power of 2. Fig. 6.34 shows a comparison with their correlation. It can be seen that their correlation predicted 62.98%, 72.97%, 76.57% and 62.35% of the present results with a MAE of 25.3%, 21.1%, 20.57% and 26.14% for TS.1, TS.2, TS.3 and TS.4, respectively. The reason for this good agreement could be due to the correlation by Cooper (1984) that represents the influence of wall heat flux.



(a)



(b)

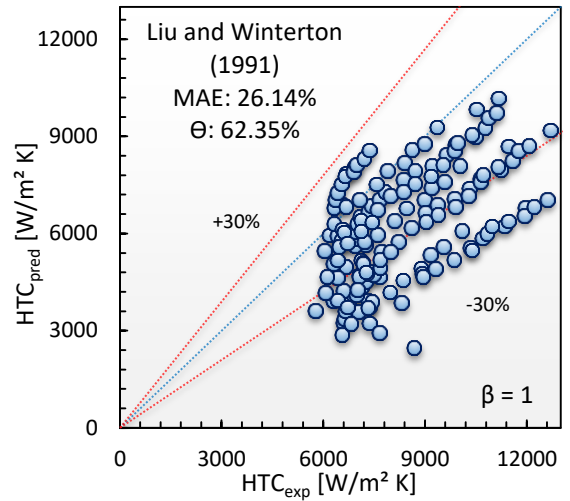
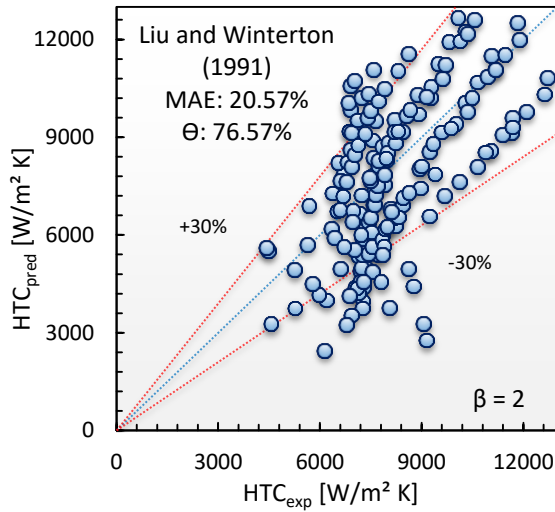
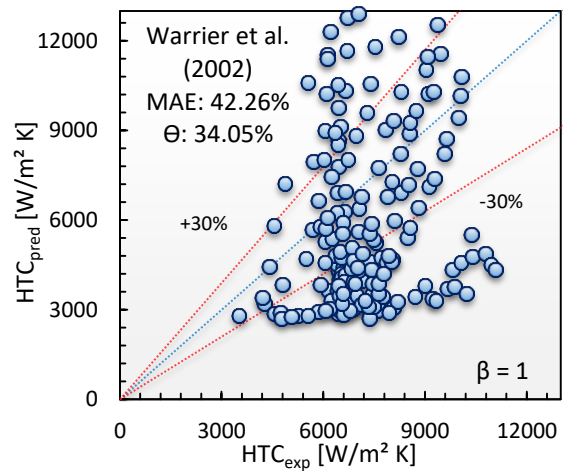
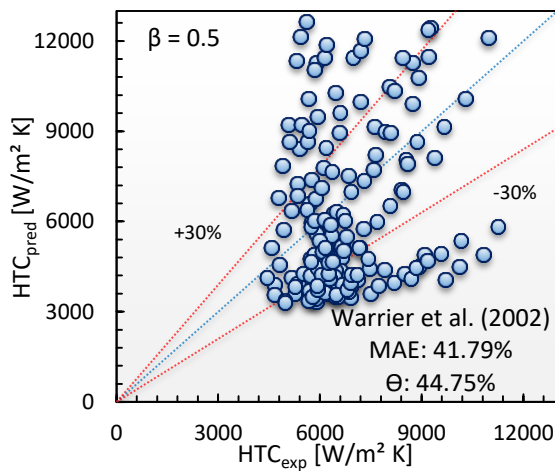


Figure 6.34 Comparison of the two-phase heat transfer data with the correlation by Liu and Winterton (1991) for: (a) TS.1 (b) TS.2 (c) TS.3 (d) TS.4.

6.5.2 Mini/micro-scale flow boiling heat transfer correlations

6.5.2.1 The correlation of Warriier et al. (2002)

An experimental flow boiling investigation was conducted by Warriier et al. (2002) using FC-84 in horizontal rectangular multi-microchannels with hydraulic diameter of 0.75 mm. A correlation was proposed including vapour quality, Boiling number and the single-phase heat transfer coefficient. By comparing with the present data, as shown in Fig. 6.35, their correlation predicted 44.75%, 34.05%, 38.29% and 35.8% of the present experimental data with a MAE of 41.79%, 42.26%, 48.32% and 40.31% for TS.1, TS.2, TS.3 and TS.4, respectively.



(a)

(b)

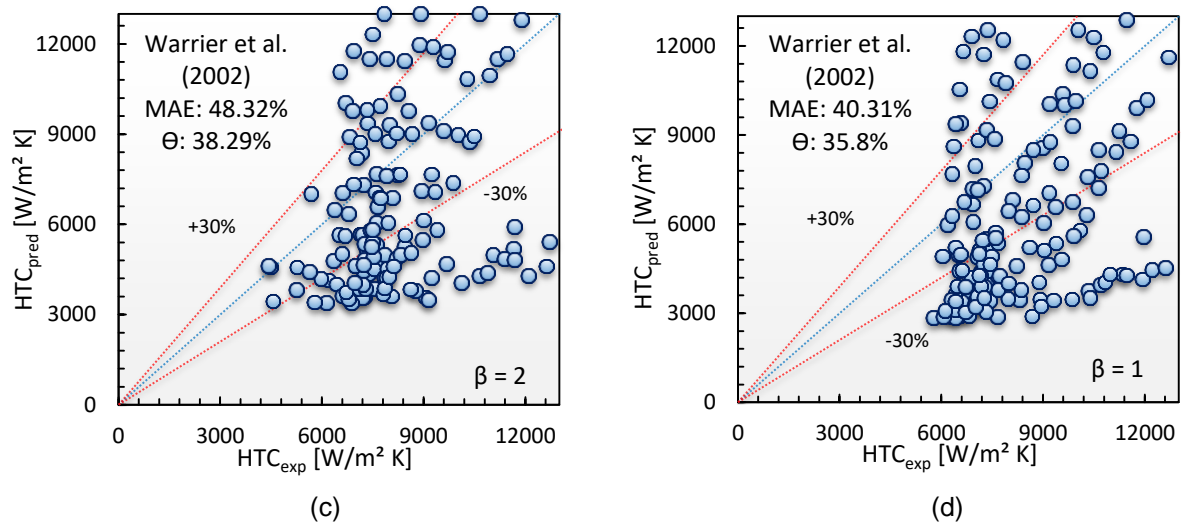


Figure 6.35 Comparison of the two-phase heat transfer data with the correlation by Warrier et al. (2002) for: (a) TS.1 (b) TS.2 (c) TS.3 (d) TS.4.

Although their correlation was proposed for horizontal rectangular multi-microchannels, the present data were not predicted very well. This could be due to the very limited data that was used to propose this correlation. They mentioned that their correlation is only valid for $0.03 \leq x \leq 0.55$ and $2.7 \times 10^{-4} \leq Bo \leq 8.9 \times 10^{-4}$, while the present study covers vapour quality up to one and Boiling number of $5-98 \times 10^{-4}$.

6.5.2.2 The correlation of Lee and Mudawar (2005)

The author proposed three correlations according to the vapour quality ranges, *i.e.* $x < 0.05$, $0.05 < x < 0.55$ and $x > 0.55$. Water and R134a in horizontal parallel rectangular microchannels with channel hydraulic diameter of 0.348 mm were examined. They reported that the nucleate boiling dominated at quality < 0.05 , while the annular film evaporation was the dominant mechanism at moderate and high qualities. Liquid Weber number, Martinelli parameter, Boiling number and single-phase heat transfer coefficient were included in their correlation. Fig. 6.36 depicts a comparison between this correlation and the present data. It can be seen that their correlation resulted in a significant scatter with a MAE of 67.97%, 55.86%, 60.06% and 53.91% for TS.1, TS.2, TS.3 and TS.4, respectively. This correlation showed low percentage of prediction with 18.78%, 27.03%, 21.14% and 37.04% for TS.1, TS.2, TS.3 and TS.4, respectively.

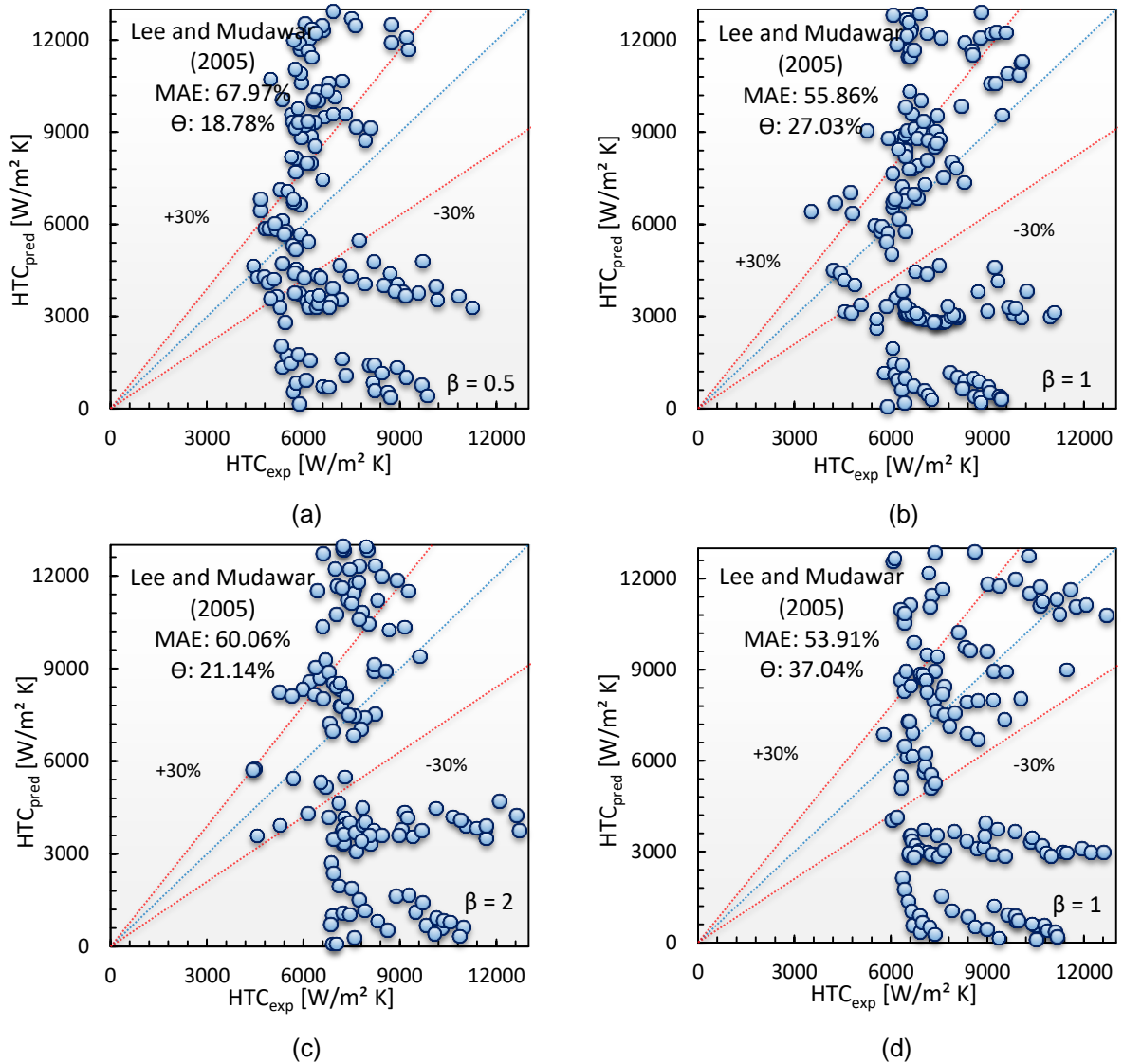


Figure 6.36 Comparison of the two-phase heat transfer data with the correlation by Lee and Mudawar (2005) for: (a) TS.1 (b) TS.2 (c) TS.3 (d) TS.4.

This limited performance of their correlation could be due to the nucleate boiling only dominates at very low heat fluxes and low vapour qualities, *i.e.* less than 0.05. In contrast, the present data show that the heat flux has a significant effect during all ranges.

6.5.2.3 The correlation of Mahmoud and Karayiannis (2013)

An experimental investigation in flow boiling heat transfer of R134a in vertical tubes ranging from 0.52 to 4.26 mm was carried out by the authors. An empirical correlation was proposed by them including enhancement factor (F) according to the approach used by Chen (1966). The pool boiling correlation by Cooper (1984) was

also used in their correlation. Fig. 6.37 illustrates the heat transfer comparison and indicates that their correlation was able to predict 68.51%, 70.27%, 72.57% and 47.53% of the data with a MAE of 22.57%, 22.63%, 21.04% and 30.78% for TS.1, TS.2, TS.3 and TS.4, respectively.

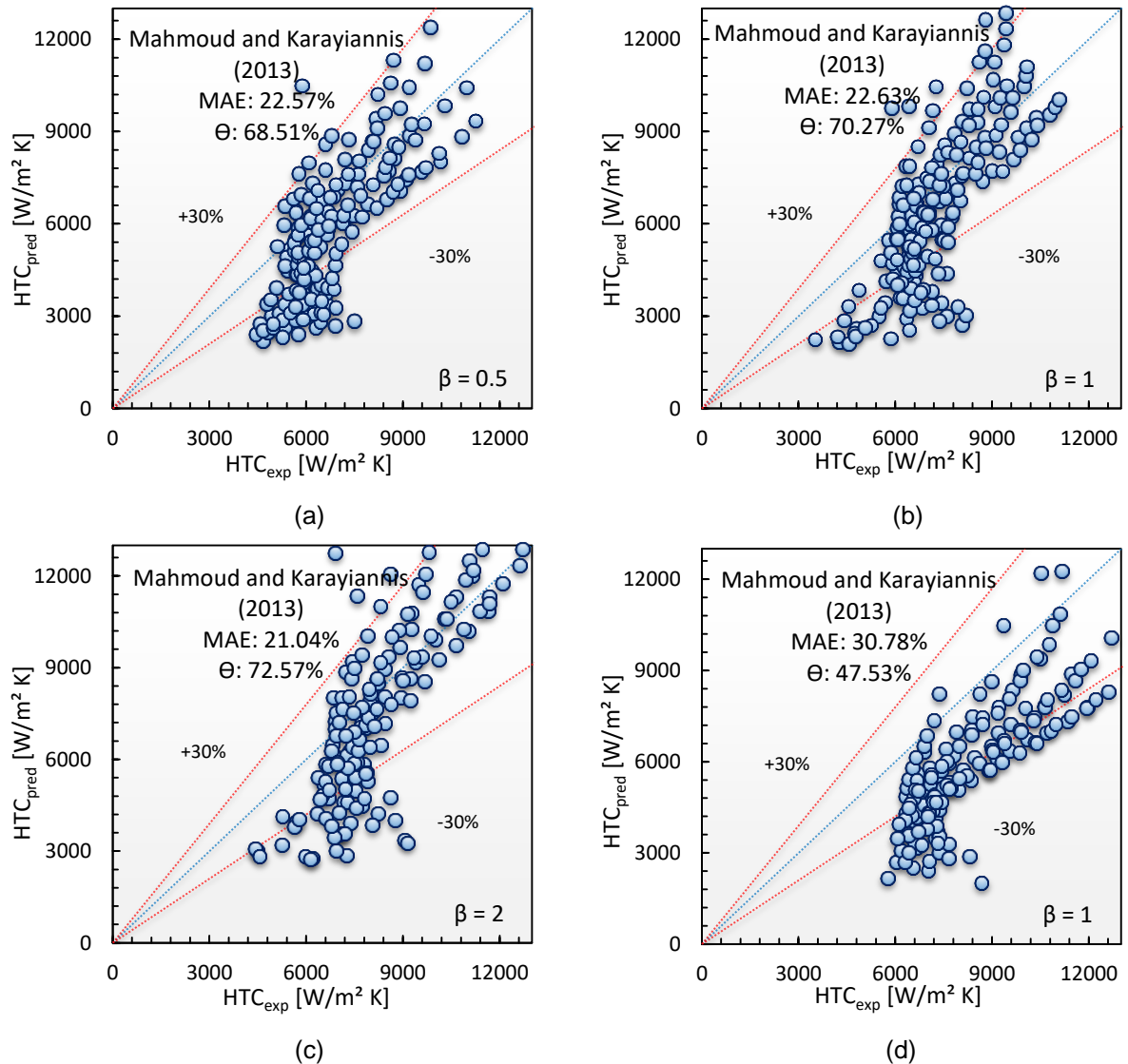


Figure 6.37 Comparison of the two-phase heat transfer data with the correlation by Mahmoud and Karayiannis (2013) for: (a) TS.1 (b) TS.2 (c) TS.3 (d) TS.4.

Although their correlation was proposed for vertical channels, it showed a good agreement with horizontal channels. This was also reported by Sempértegui-Tapia and Ribatski (2017). They compared 3409 flow boiling data points including four fluids; R134a, R1234ze(E), R1234yf and R600a, in a horizontal circular channel with diameter of 1.1 mm. They reported that this correlation predicted their results

with a MAE ranging from 22.3% to 29.2%. The correlation by Mahmoud and Karayiannis (2013) was also in a good agreement when compared with the results of R134a in horizontal multi-microchannels reported by Fayyadh et al. (2017) with a MAE of 19%. This reasonable agreement with the present data could be due to the contribution of nucleate boiling, *i.e.* the effect of heat flux is considered in the correlation by Cooper (1984). Moreover, the Confinement number is also proposed in this correlation which represents the surface tension effect.

6.5.2.4 The correlation of Li and Jia (2015)

An experimental study in flow boiling heat transfer of R134a in three-sides heated horizontal rectangular multi-microchannels with hydraulic diameter of 0.5 mm was investigated by the authors. They divided their results into three regimes, namely I, II and III. Regime I was nucleate boiling when the heat transfer coefficient increased with heat flux for all mass fluxes. A small effect of mass flux was found in this regime. However, a slight reduction in the heat transfer coefficient with heat flux, at high heat fluxes, was reported. Regime II was identified as convective boiling when the mass flux had a significant effect on the heat transfer coefficient. However, heat flux effect was also observed in this regime. The dry out regime, *i.e.* regime III, was characterised when the heat transfer coefficient decreased with heat flux for most mass fluxes. According to their regimes, two correlations were proposed by them for nucleate boiling and convective boiling dominant regime. Their first correlation was compared with the present data. Fig. 6.38 illustrates this comparison and shows that their correlation was able to predict the experimental results with reasonable accuracy. It predicted 49.72%, 68.65% and 96% of the data with a MAE of 27.36%, 21.95% and 13.84% for TS.1, TS.2 and TS.3, respectively. Moreover, their correlation could predict 96.3% of the present data with a MAE of 14.65% for TS.4. This very good agreement between their correlation and the present data could be attributed to the dominance of nucleate boiling. Both Boiling number and Bond number are proposed in their correlation. Moreover, the examined hydraulic diameter in their study (0.5 mm) is approximately similar to the present study (0.46 mm). It is worth mentioning that the comparison with their second correlation was not so good, *i.e.* with a MAE of 51.42% for the test section (3). This could be due to this

correlation was proposed for the convective boiling dominant regime which is not the case here.

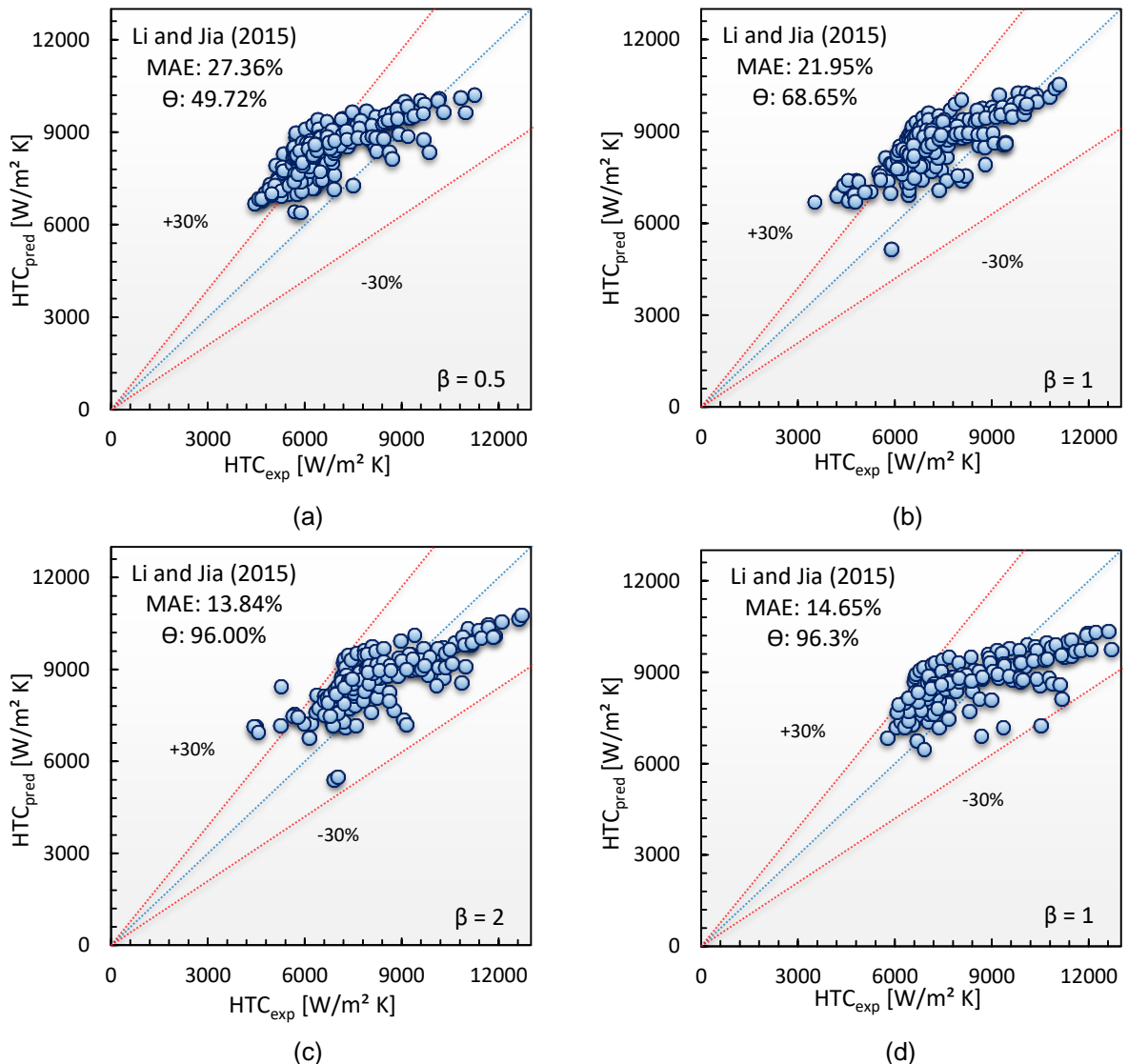


Figure 6.38 Comparison of the two-phase heat transfer data with the correlation by Li and Jia (2015) for: (a) TS.1 (b) TS.2 (c) TS.3 (d) TS.4.

6.5.2.5 The correlation of Lim et al. (2015)

The authors carried out an experimental investigation using water in a horizontal square microchannel with of 0.5 mm hydraulic diameter. Their data was compared with some existing correlations and over prediction was found. Therefore, they proposed a correlation as a function of Boiling number, Reynolds number and liquid Froude number. This correlation was compared with the present experimental data as depicted in Fig. 6.39. Their correlation under predicted the present data, *i.e.* 17.13%,

9.73%, 8% and 3.7% of the present data was predicted with a MAE of 53.74%, 58.03%, 61.42% and 63.56% for TS.1, TS.2, TS.3 and TS.4, respectively. The possible reasons for the under prediction by their correlation could be attributed to the one fluid, *i.e.* water, was examined and their experimental ranges ($G = 200, 400$ and $600 \text{ kg/m}^2\text{s}$). It is known that the thermophysical properties of water completely differ from those of HFE-7100. Moreover, during their experimental study, the vapour quality was set up to 0.2, while it reached up to 0.99 during the present investigation.

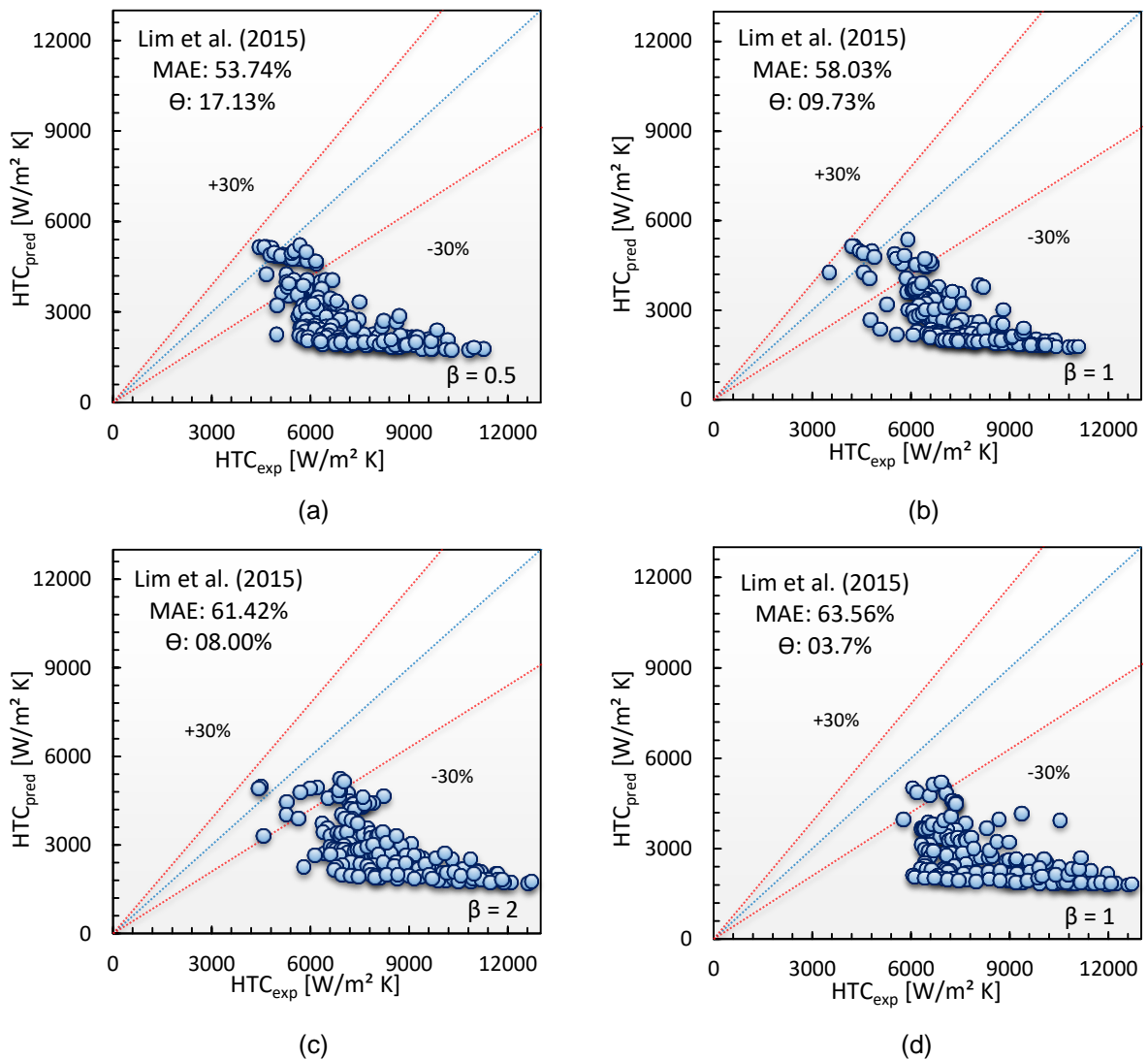


Figure 6.39 Comparison of the two-phase heat transfer data with the correlation by Lim et al. (2015) for: (a) TS.1 (b) TS.2 (c) TS.3 (d) TS.4.

6.5.2.6 The correlation of Thiangtham et al. (2016)

Flow boiling experiments of R134a in horizontal multi-microchannels were conducted by Thiangtham et al. (2016). Rectangular microchannels with hydraulic diameter of 0.421 mm were manufactured. At low heat fluxes, the heat transfer coefficient was found to increase with increasing heat flux, *i.e.* the dominance of nucleate boiling, while, at high heat fluxes, the heat transfer coefficient increased with increasing mass flux, when the convective boiling dominated as they mentioned. They correlated their data and proposed a flow boiling heat transfer correlation as a function of dimensionless groups, see Appendix B. Fig. 6.40 shows a comparison with their correlation.

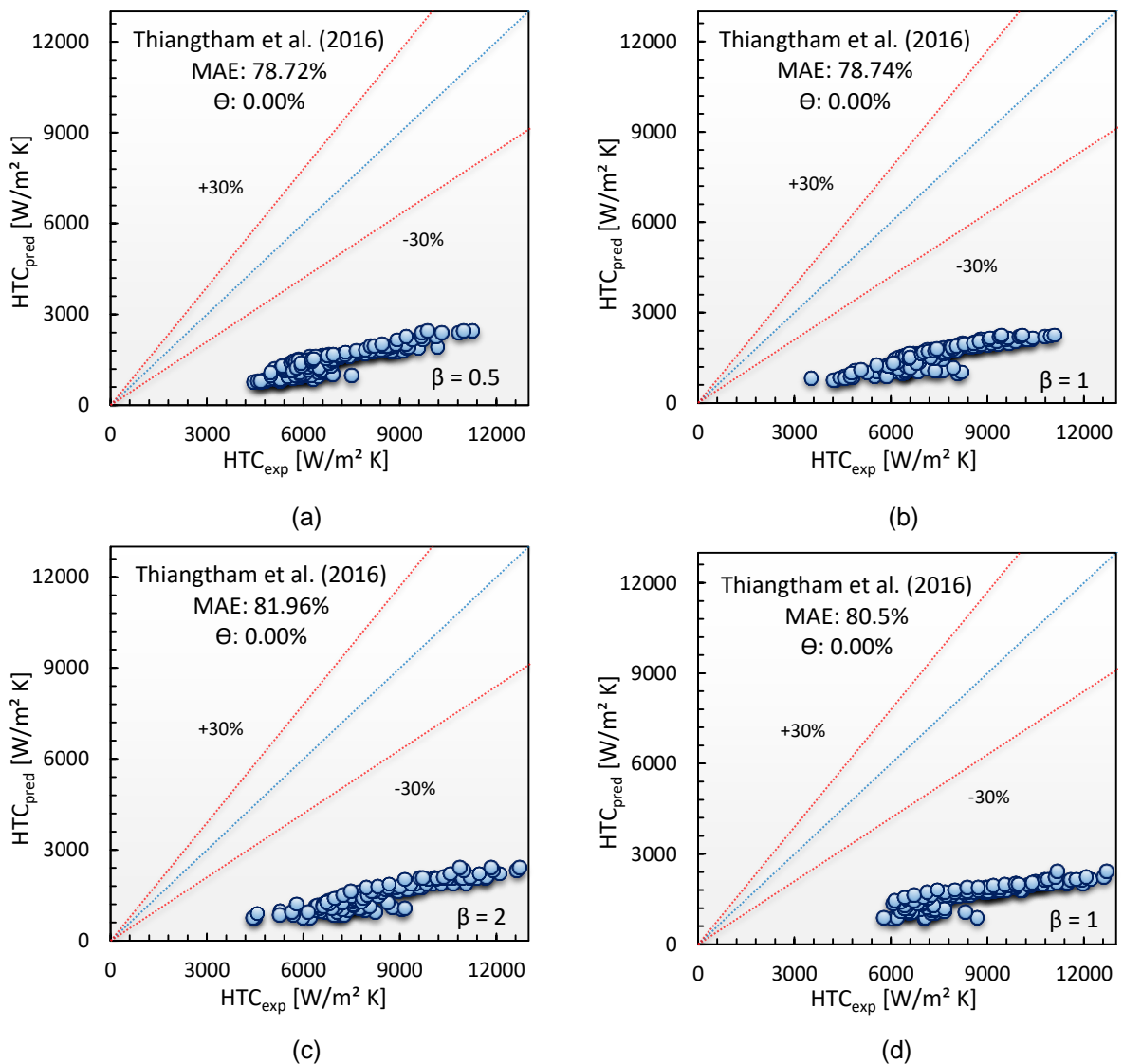
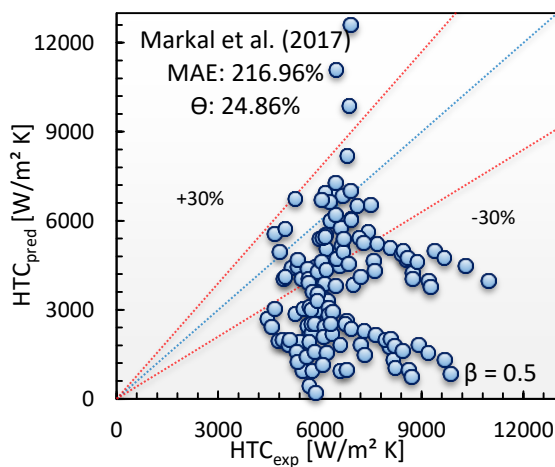


Figure 6.40 Comparison of the two-phase heat transfer data with the correlation by Thiangtham et al. (2016) for: (a) TS.1 (b) TS.2 (c) TS.3 (d) TS.4.

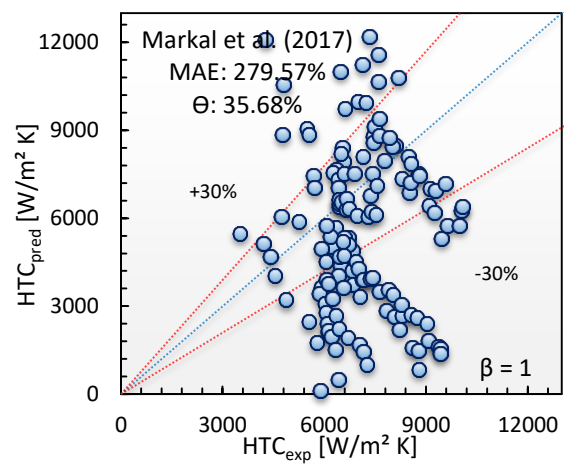
It is obvious that their correlation under predicted the present experimental data with Θ of 0.00%. The mean absolute error for TS.1, TS.2, TS.3 and TS.4 was 78.72%, 78.74%, 81.96% and 80.5%, respectively. This large disagreement by this correlation could be attributed to the convective boiling contribution in their correlation. In other words, the heat transfer coefficient was found by Thiangtham et al. (2016) to increase with increasing mass flux at high heat fluxes. This is in contrast to the present experimental results, *i.e.* insignificant effect of mass flux was found even at high heat fluxes.

6.5.2.7 The correlation of Markal et al. (2017a)

Several flow boiling experiments were conducted by the authors using de-ionized water in horizontal rectangular multi-microchannels. Different hydraulic diameters of 0.1–0.25 mm at constant aspect ratio of 1 and different aspect ratios of 0.37–5 at constant hydraulic diameter of 0.1 mm were examined during their study. They proposed an empirical correlation including superficial liquid Reynolds number, Weber number, Boiling number, Prandtl number, aspect ratio, hydraulic diameter, vapour quality and fluid thermal conductivity. Their correlation was compared with the present data as illustrated in Fig. 6.41. It can be seen that their correlation under predicted the experimental data, *i.e.* the mean absolute error was found to be 216.96%, 279.57%, 397.59% and 199.85% for TS.1, TS.2, TS.3 and TS.4, respectively.



(a)



(b)

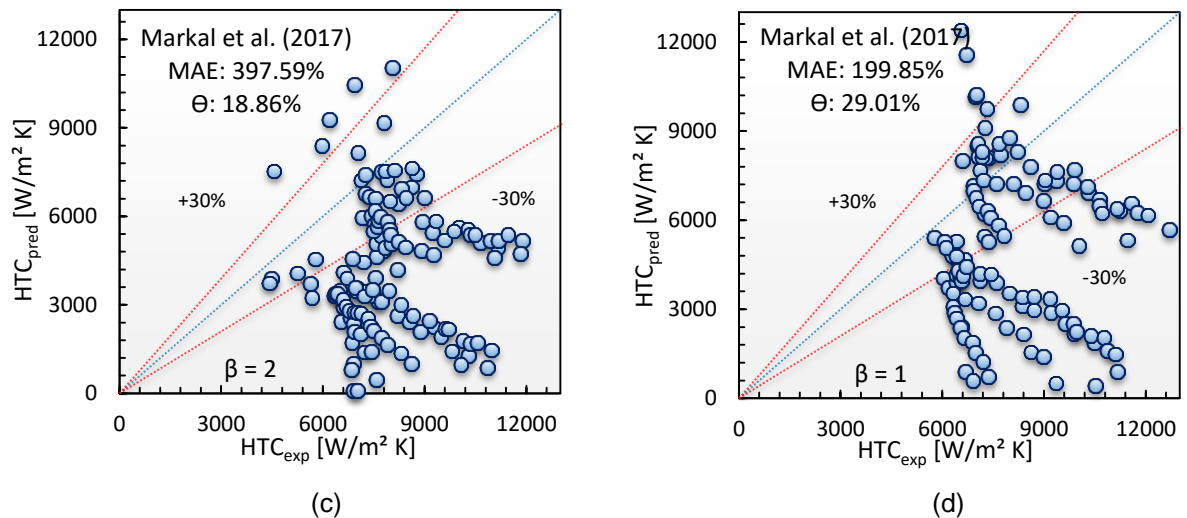


Figure 6.41 Comparison of the two-phase heat transfer data with the correlation by Markal et al. (2017a) for: (a) TS.1 (b) TS.2 (c) TS.3 (d) TS.4.

Although this empirical correlation was proposed for horizontal rectangular multi-microchannels (partly heated channel), it fails to predict the present results well with a large MAE. The reason for this could be due to the limits of their correlation. For example, it is recommended for a vapour quality ranging from 0.01 to 0.69, while the present data includes up to 0.99. Moreover, their correlation covers the following ranges: $9.56 \times 10^{-5} \leq Bo \leq 70.4 \times 10^{-5}$, $0.006 \leq We \leq 0.86$ and $1.92 \leq Pr \leq 2.42$. In contrast, the present experimental data include $50 \times 10^{-5} \leq Bo \leq 980 \times 10^{-5}$, $0.05 \leq We \leq 1.76$ and $Pr = 11$. Another possible reason could be that the influence of nucleate boiling is negligible in their correlation because the heat transfer coefficient is found to be independent of heat flux.

6.5.2.8 The correlation of Shah (2017)

Shah (2017) compared an extensive database with his previous correlation of Shah (1982). He mentioned that most data was fairly predicted by this correlation. However, under prediction of some data was found at low mass fluxes. This could be due to the dominance of surface tension at low mass fluxes as he explained. Therefore, he modified his previous correlation by introducing a new correction factor (F). The effect of Weber number and Boiling number was taken into account in this factor. He verified this new correlation using a large database including thirty one different fluids, vertical and horizontal flows, different channel shapes and fully or partly heated channels with diameter of 0.38–27.1 mm. The new correlation was

compared with the present experimental data points as shown in Fig. 6.42. It is obvious that there was a good agreement between this correlation and the present data. This figure shows that 67.4%, 76.76% and 81.14% of the present data points were predicted with a MAE of 21.99%, 20.81% and 18.74% for TS.1, TS.2 and TS.3, respectively. For TS.4, this correlation also showed good agreement with Θ of 91.36% and MAE of 15.29%. This good agreement could be attributed to the fact that his correlation was modified by taking into account the effect of surface tension at low mass fluxes, which agrees with the present experimental results as discussed in Section 6.5.

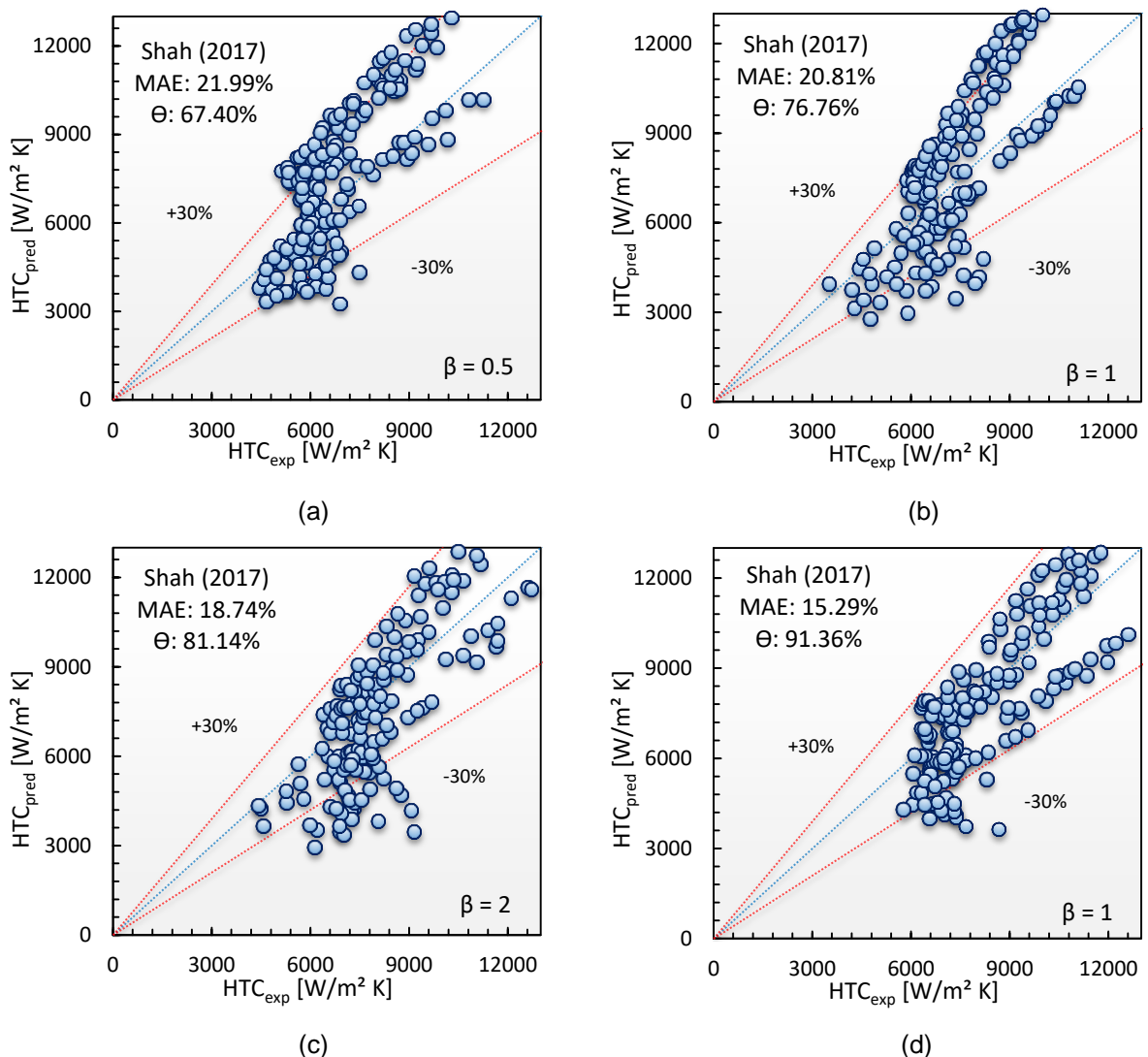
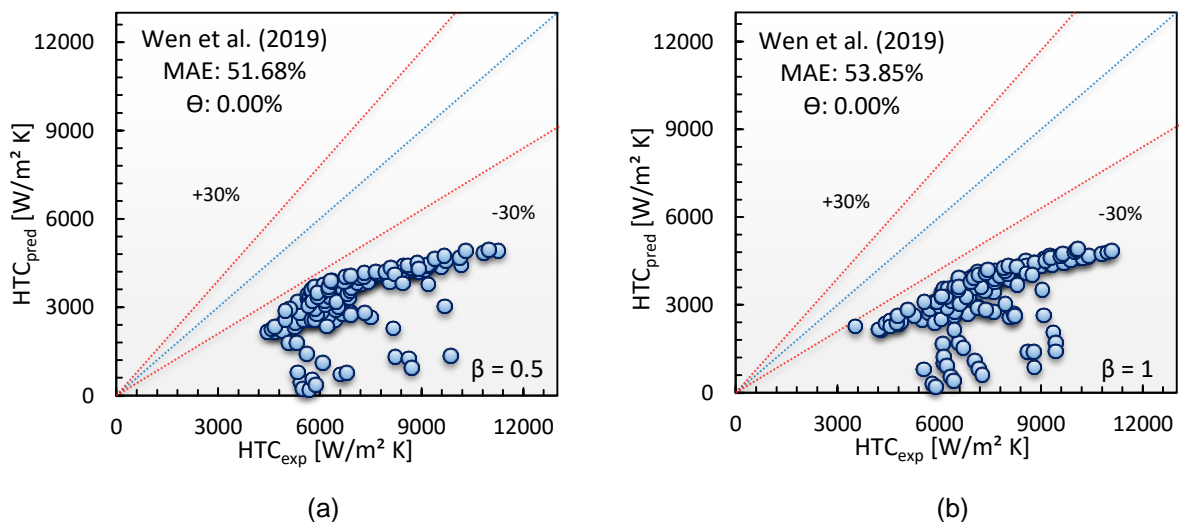


Figure 6.42 Comparison of the two-phase heat transfer data with the correlation by Shah (2017) for: (a) TS.1 (b) TS.2 (c) TS.3 (d) TS.4.

6.5.2.9 The correlation of Wen et al. (2019)

Recently, an experimental investigation of flow boiling heat transfer of R134a was carried out by Wen et al. (2019) using aluminium minichannels. Two rectangular minichannels with hydraulic diameter of 1.28 and 1.59 mm were manufactured. The channel configuration was modified using serrated fins, see Chapter 2 for more details. They reported that, at low qualities, the local heat transfer coefficient increased with increasing heat flux and saturation pressure. Moreover, the mass flux had insignificant effect. In contrast, at high qualities, the effect of heat flux and saturation pressure was insignificant, while the local heat transfer coefficient increased with mass flux. They compared their data with some existing correlations and no reasonable prediction was found. Therefore, an empirical correlation was proposed based on 1429 data points. They proposed an empirical correlation by taking into account the Boiling number, Weber number and Froude number. This correlation also included the correlation by Cooper (1984). Fig. 6.43 shows a comparison between the present data and this correlation. This figure demonstrates that their correlation under predicted the present data with a MAE of 51.68%, 53.85%, 58.9% and 58.64% for TS.1, TS.2, TS.3 and TS.4, respectively. This under prediction could be due to the different prevailing heat transfer mechanism. For example, they reported that the heat transfer coefficient increased with heat flux at low vapour qualities, while insignificant effect of heat flux was found in high qualities. Moreover, mass flux had a significant effect at moderate and high vapour qualities, *i.e.* the heat transfer coefficient increased with mass flux. These results are in contrast with the present study.



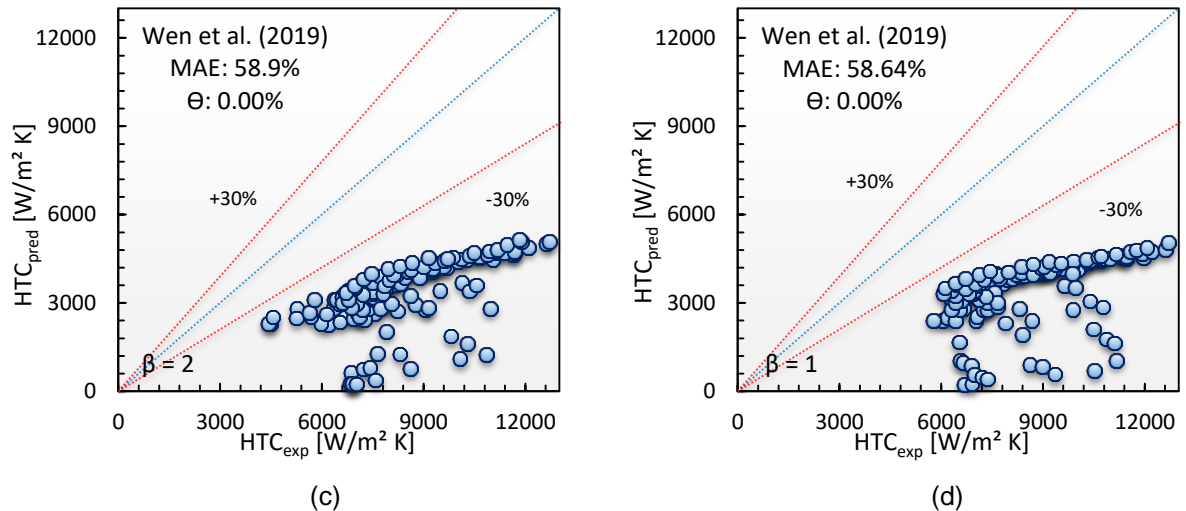


Figure 6.43 Comparison of the two-phase heat transfer data with the correlation by Wen et al. (2019) for: (a) TS.1 (b) TS.2 (c) TS.3 (d) TS.4.

In the present study, twelve existing two-phase heat transfer correlations proposed for conventional and mini/microchannels were compared with 703 experimental data. This comparison is summarized in Table 6.2 and shows that some of these correlations show large disagreement with the present data with a mean absolute error more than 50%. However, the conventional correlations, such as Shah (1982), Kandlikar (1990) and Liu and Winterton (1991), predict the results of all test sections well with a MAE ranging from 20–26%. Although the correlation by Mahmoud and Karayiannis (2013) is proposed for vertical tubes, a reasonable agreement is found with a MAE of 21–31%. The correlation by Li and Jia (2015) for horizontal rectangular multi-microchannels predicts the results well with a MAE of 14–27%. The present data are predicted very well by the modified correlation by Shah (2017). The mean absolute error of this correlation ranges from 15% to 22%. The parameters that represent a contribution from nucleate boiling may lead to increase the accuracy of the existing correlations. This is due to the present data depend strongly on the wall heat flux rather than mass flux and vapour quality. In other words, surface tension force dominates during the present study due to the low mass fluxes that were tested.

Discrepancies in experimental results were presented by Karayiannis et al. (2012) explaining that the heated length and inner surface characteristics can be important parameters. Pike-Wilson and Karayiannis (2014) presented research on the effect of

material on the heat transfer characteristics of flow boiling of R245fa. In a recent publication, Mahmoud and Karayiannis (2018) extended this work and explained in detail the dependency of the nucleation and bubble dynamics in microchannels, boiling flow patterns, heat transfer rates and pressure drop on the choice of fluid and the geometry and surface characteristics of the channels. This dependency is the result of different fluid properties, such as surface tension, latent heat and thermal conductivity, and the range of hydraulic diameter, channel aspect ratio, channel length and material and surface roughness of the channels. The effect of channel aspect ratio and geometry was discussed by Markal et al. (2017a) and Sempértegui-tapia and Ribatski (2015). Channel inclination could result in different heat transfer characteristics due to the different bubble or slug velocity, buoyancy force effect, as found by Wang et al. (2012). Flow reversal and system instability can affect the overall performance of the microchannels, see Yang et al. (2011) and Consolini and Thome (2009). Mahmoud and Karayiannis (2016b) stated that the volume of the inlet/outlet plenum had a significant effect on the flow instability, *i.e.* large volume resulted in a reduction in the amplitude of the pressure drop and the inlet/outlet pressure signals. Differences in the above as well as different experimental conditions can result in different experimental data and subsequent correlations. Accordingly, there is further work to be done in this area.

Table 6.2 Statistical comparison between the experimental data and existing two-phase heat transfer correlations.

Author(s)	β [-]	0.5 (TS.1)	1 (TS.2)	2 (TS.3)	1 (TS.4)
	Data points	181	185	175	162
Shah (1982)	MAE (%)	25.92	25.43	24.64	20.16
	Θ (%)	61.88	60.54	65.71	78.4
Kandlikar (1990)	MAE (%)	25.83	25.25	26.09	23.63
	Θ (%)	61.88	61.08	62.29	67.28
Liu and Winterton (1991)	MAE (%)	25.3	21.1	20.57	26.14
	Θ (%)	62.98	72.97	76.57	62.35
Warrier et al. (2002)	MAE (%)	41.79	42.26	48.32	40.31
	Θ (%)	44.75	34.05	38.29	35.8
Lee and Mudawar (2005)	MAE (%)	67.97	55.86	60.06	53.91
	Θ (%)	18.78	27.03	21.14	37.04

Mahmoud and Karayiannis (2013)	MAE (%)	22.57	22.63	21.04	30.78
	Θ (%)	68.51	70.27	72.57	47.53
Li and Jia (2015)	MAE (%)	27.36	21.95	13.84	14.65
	Θ (%)	49.72	68.65	96.00	96.3
Lim et al. (2015)	MAE (%)	53.74	58.03	61.42	63.56
	Θ (%)	17.13	9.73	8.00	3.7
Thiangtham et al. (2016)	MAE (%)	78.72	78.74	81.96	80.5
	Θ (%)	0.00	0.00	0.00	0.00
Markal et al. (2017a)	MAE (%)	216.96	279.57	397.59	199.85
	Θ (%)	24.86	35.68	18.86	29.01
Shah (2017)	MAE (%)	21.99	20.81	18.74	15.29
	Θ (%)	67.4	76.76	81.14	91.36
Wen et al. (2019)	MAE (%)	51.68	53.85	58.9	58.64
	Θ (%)	0.00	0.00	0.00	0.00

6.7 Summary

The following key findings are summarized based on the presented flow boiling heat transfer results:

- Boiling incipience occurred at low wall heat fluxes for all the test sections, *i.e.* around 20 kW/m². After that, the wall heat flux increased with wall superheat. Moreover, insignificant effect of mass flux on the boiling curve was found.
- For a given wall superheat, a noticeable increase in the wall heat flux was found with increasing channel aspect ratio.
- Maximum heat rates that can be achieved from the chipset increased with decreasing channel aspect ratio due to the large surface enhancement. This can outweigh the benefits from the boiling heat transfer enhancement at larger channel aspect ratio. For given base heat flux, the wall superheat was lower for the smaller channel aspect ratio.
- Insignificant material effect was identified on the boiling curve at low heat fluxes. However, at moderate and high heat fluxes, aluminium showed higher wall heat flux compared to copper. For given heat flux, aluminum surface provided lower wall superheat than copper.

- Hysteresis effect became significant at low wall heat fluxes. This was attributed to the fact that active nucleation sites remained active at low wall heat fluxes with decreasing heat flux.
- Flow reversal occurred at all mass fluxes and for all test sections. High oscillations in the pressure drop signal were measured with increasing wall heat flux.
- Flow boiling instability increased with decreasing channel aspect ratio. Moreover, the copper surface showed higher system instability than aluminium. High frequency and amplitude of pressure drop could mean high instability.
- The present flow boiling heat transfer data for the entire heat sink was not affected significantly by flow reversal. The maximum percentage of fluctuation of the measured parameters was found to be 2.37%.
- Local and average flow boiling heat transfer coefficient was found to increase with increasing wall heat flux. This was attributed to more active nucleation sites and the increase in the liquid film evaporation rate when the heat flux was low. At moderate to high heat fluxes, the contribution of both liquid film evaporation and nucleation in the liquid film of slug or annular flow could be the reason for this enhancement.
- Local flow boiling heat transfer coefficient reached peak value at boiling incipience and then decreased with increasing local vapour quality. This could be due to the reduction in local pressure along the channel at low and moderate heat fluxes. At high heat fluxes, this reduction could be due to the combined effect of the reduction in local pressure and increase in wall temperature along the channels.
- Insignificant effect of mass flux on the local and average flow boiling heat transfer coefficient was found.
- For a given wall heat flux, there was a noticeable increase in the heat transfer coefficient with increasing channel aspect ratio, *i.e.* by 14.3% from smaller to larger aspect ratio. Wide channel width could provide higher nucleation site density and thinner liquid film thickness.
- At low wall heat fluxes, the material effect on the heat transfer coefficient was insignificant. However, at moderate and high heat fluxes, aluminium

surface showed higher heat transfer coefficient than copper, *i.e.* by 12%. Aluminium surface could provide more nucleation site density and thinner liquid film thickness. This could be due to the surface microstructures.

- Twelve existing two-phase heat transfer correlations were compared with the present experimental results. Large mean absolute error, *i.e.* more than 50%, was found by some correlations. For conventional channels, the correlations by Shah (1982), Kandlikar (1990) and Liu and Winterton (1991) predicted the results well with maximum MAE of 26%. For mini/microchannels, the correlations by Mahmoud and Karayiannis (2013) and Li and Jia (2015) showed a reasonable prediction with a MAE ranging from 14% to 31%. The experimental data of all test sections were predicted fairly well by the correlation of Shah (2017) with a mean absolute error ranging from 15% to 22%.
- Surface microstructures, *i.e.* number, shape and volume of peaks and valleys, could affect the thermal performance and should be considered. These parameters may differ from surface material to other. Surface peaks may disturb the liquid film leading to thinner thickness. Surface valleys may become active cavities (nucleation sites) that generate more nucleating bubbles.
- By using the correlation by Hsu (1962), the active cavity size (cavity mouth radius) for HFE-7100 at saturation pressure of 1 bar was 0.06–58 μm . Only large cavities were active at low wall superheat, while small cavities activated with increasing wall superheat.
- Surface tension force dominated during most of the present data since low mass fluxes were tested. Wall heat flux had a significant influence on the heat transfer results, while no mass flux effect was found. The inclusion of a contribution of nucleate boiling in some existing correlations may increase the accuracy of these correlations when they were compared with the present data.

Chapter 7

Condensation Flow Patterns: Results and Discussion

7.1 Introduction

In addition to the flow boiling experiments, flow condensation experiments were also conducted in order to examine the thermal performance of a small-scale cooling system. In this chapter, the experimental flow visualization patterns and flow pattern maps are presented in Section 7.2 and 7.3, respectively. The effects of the important parameters are then described in Section 7.4 and 7.5. Section 7.6 shows a comparison between the experimental flow patterns and existing flow pattern maps. A final summary is concluded in Section 7.7.

7.2 Experimental Flow Visualization Patterns

Flow visualization was carried out at the centre of the condenser and at three locations; near channel inlet, near middle and near outlet. However, more locations along the channel were also visualized to capture any new possible features in the flow patterns. Three major flow patterns were captured along the channel; annular, slug and bubbly flow, as shown in Fig. 7.1. It can be seen that the fluid entered the channel at high vapour quality where the flow pattern was annular flow as shown in Fig. 7.1(a). This regime is characterized by a vapour core surrounded by a thin liquid film. The annular flow became distorted at the neck region due to the condensation

process along the channel, more details about this region is described in the next section. When the liquid edges in the neck region joined up, a vapour slug separated from this vapour core. Slug flow is characterized by a cylindrical vapour slug, its size equaled to the channel width, followed by trailing bubbles, see Fig. 7.1(b). This slug began to shrink and decrease in size along the axial direction due to the heat transfer from the vapour slug to the liquid. After that, bubbly flow formed at the last part of channel, which is characterized by numerous bubbles flowing in the liquid phase, as presented in Fig. 7.1(c). Some of these bubbles reached the channel width, while others were smaller. These bubbles then shrank along the channel and submerged in the condensate.

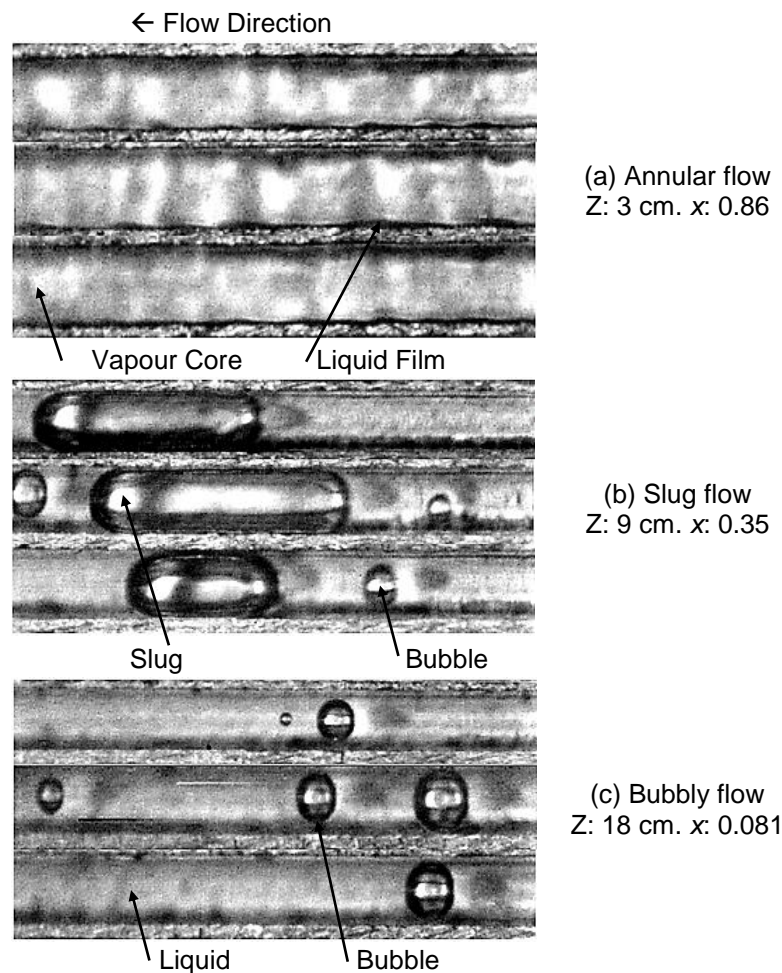


Figure 7.1 Experimental flow visualization patterns along the condenser at mass flux of $108 \text{ kg/m}^2\text{s}$, coolant flow rate of 0.8 L/min and inlet coolant temperature of $25 \text{ }^\circ\text{C}$ with corresponding local vapour quality.

Fig. 7.2 illustrates the sequence of pictures that show the neck region at which the vapour slug formed. This figure is presented at the same previous operating conditions. It is obvious that, after 2 ms, the liquid edges were found to join up, see the red circle in Fig. 7.2(a). At time of 3 ms, a vapour slug separated and its length was visualized to decrease suddenly. However, after 10 ms, this reduction occurred gradually. This reduction in the vapour slug length could be due to the condensation process and surface tension force as illustrated in Fig. 7.2(b).

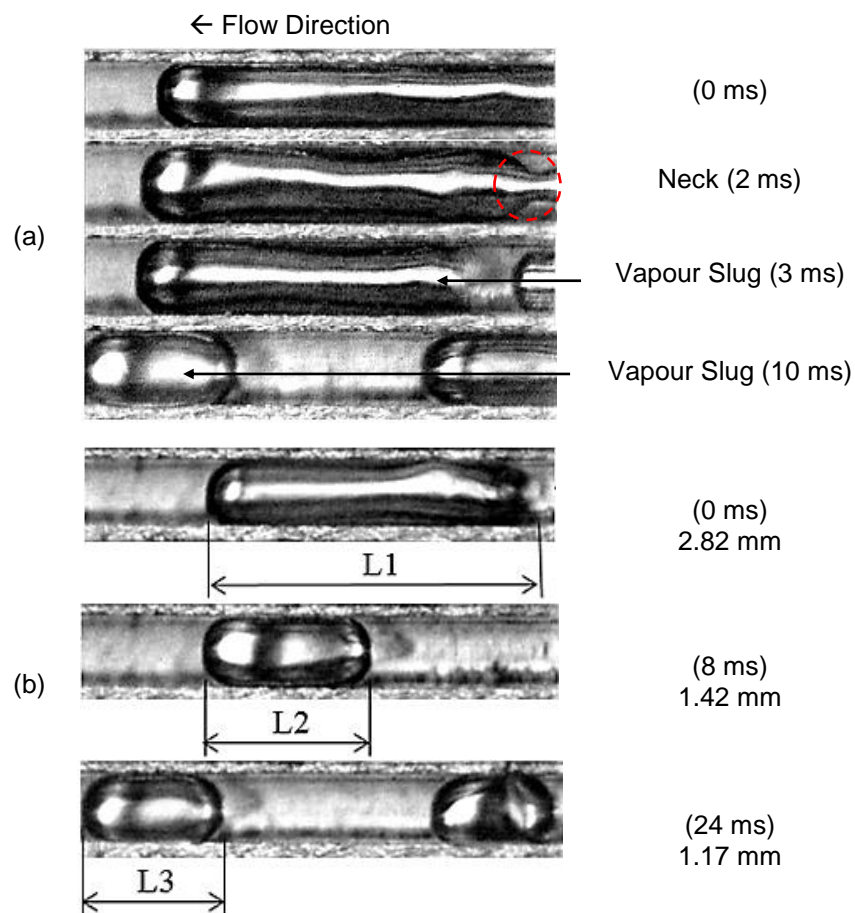


Figure 7.2 Sequence of pictures of the neck region at local vapour quality of 0.35 and Z: 9 cm: (a) Slug formation (b) Slug length.

Fig. 7.2(b) depicts the variation in the slug length with time during the necking process for 4 mm distance. At time of 0 ms (slug formation or separation), the slug length was measured to be 2.82 mm. After 8 ms, this length decreased to 1.42 mm, while it decreased further to 1.17 mm after 24 ms. Accordingly, after slug separation, *i.e.* after 8 ms, the slug length decreased by 49.6%, while it decreased by 17.6% after

16 ms. In other words, the slug length decreased rapidly in the early stage of slug formation and then decreased slowly. This could be explained as follows: when the vapour slug separates from the vapour core, the forces that affect the bubble change abruptly and become imbalanced. Surface tension force tries to pull the bubble into the spherical shape. This leads to a rapid change in the slug size. It is obvious that this rapid reduction (49.6%) could be due to the effect of both condensation process and surface tension, while the low reduction (17.6%) may be due to the condensation only as explained schematically in Fig. 7.3. It is worth mentioning that the above phenomenon was not reported by other studies.

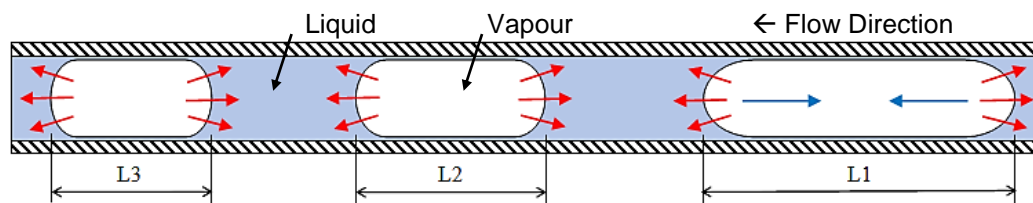


Figure 7.3 Schematic diagram of a vapour slug after the neck region (Top view), blue arrows indicate surface tension effect and red condensation of vapour.

The flow structure during the condensation experiments observed in the present study is shown schematically in Fig. 7.4. The neck region is considered as a transition regime from annular to slug flow.

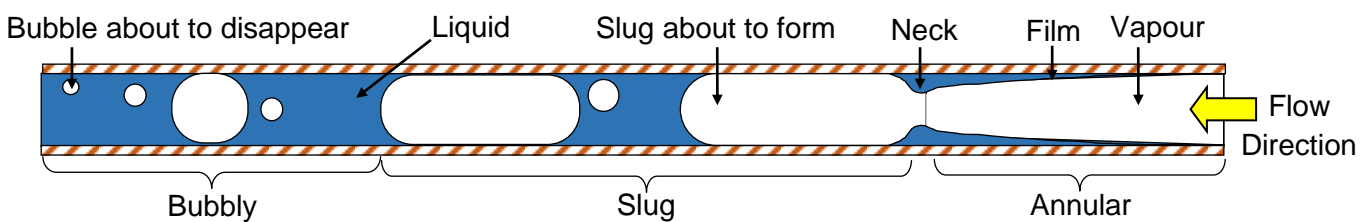


Figure 7.4 Condensation flow structure during the present study.

7.3 Experimental Flow Pattern Maps

The previous flow regimes were presented as a flow patterns map using two coordinates, namely mass flux and vapour quality as shown in Fig. 7.5. In Fig. 7.5(a), the inlet coolant temperature was 40 °C, while the data in Fig. 7.5(b) were for the inlet coolant temperature 20 °C. It is obvious that annular flow was the dominant

regime during the experiments. However, slug and bubbly flow became clearer, when the refrigerant mass flux or inlet coolant temperature decreased. More details about the effect of these parameters, *i.e.* refrigerant mass flux and coolant side conditions, are given in the next section. It is worth mentioning that the current condensation experiments covered the following dimensionless numbers:

Reduced pressure: 0.047

Bond number: 0.32

Prandtl number: 11

Superficial liquid Reynolds number: 0.36–101.4

Superficial vapour Reynolds number: 873.1–7571

Vapour only Suratman number: 886689.8

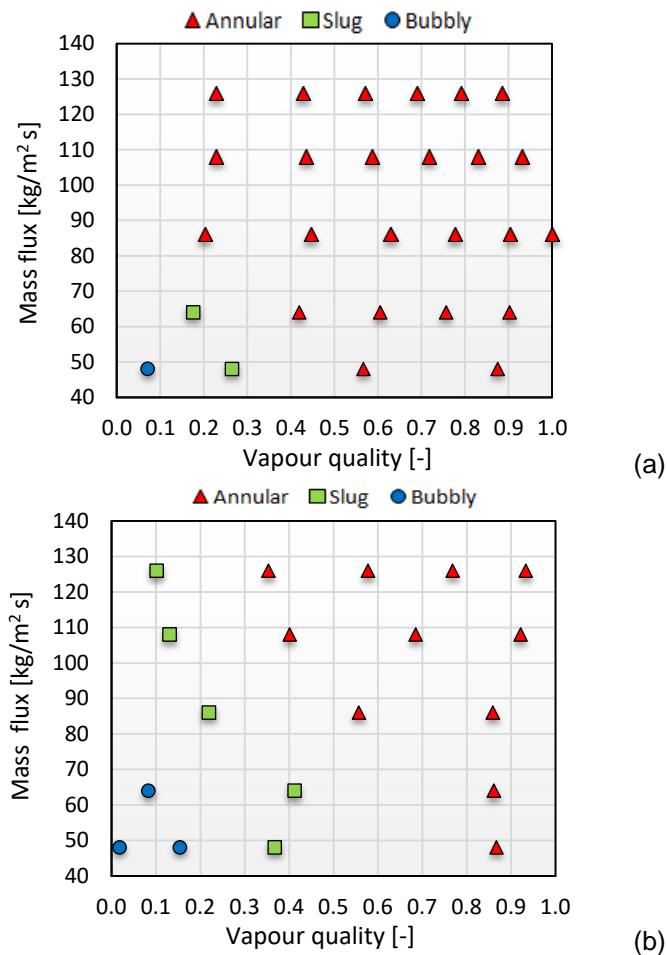


Figure 7.5 Experimental flow patterns map at five mass fluxes ranging from 48 to 126 kg/m²s, coolant flow rate of 0.5 L/min and two different inlet coolant temperatures: (a) 40 °C (b) 20 °C.

7.4 Effect of Refrigerant Mass Flux

The effect of refrigerant mass flux on the experimental flow patterns at three axial locations, coolant flow rate of 0.5 L/min and inlet coolant temperature of 40 °C is depicted in Fig. 7.6. As discussed above, annular flow was the dominant flow pattern at high mass fluxes. This becomes clear at mass flux ranging from 86 to 126 kg/m²s. However, at low mass fluxes, *i.e.* 64 and 48 kg/m²s, other flow patterns were also observed such as slug and bubbly flow. It is known that, at high refrigerant mass flux, the condensation rate along the channel becomes low, *i.e.* there is no enough time for heat transfer from the refrigerant side to the water side. This results in high wall temperature and thus annular flow shifts along the channel.

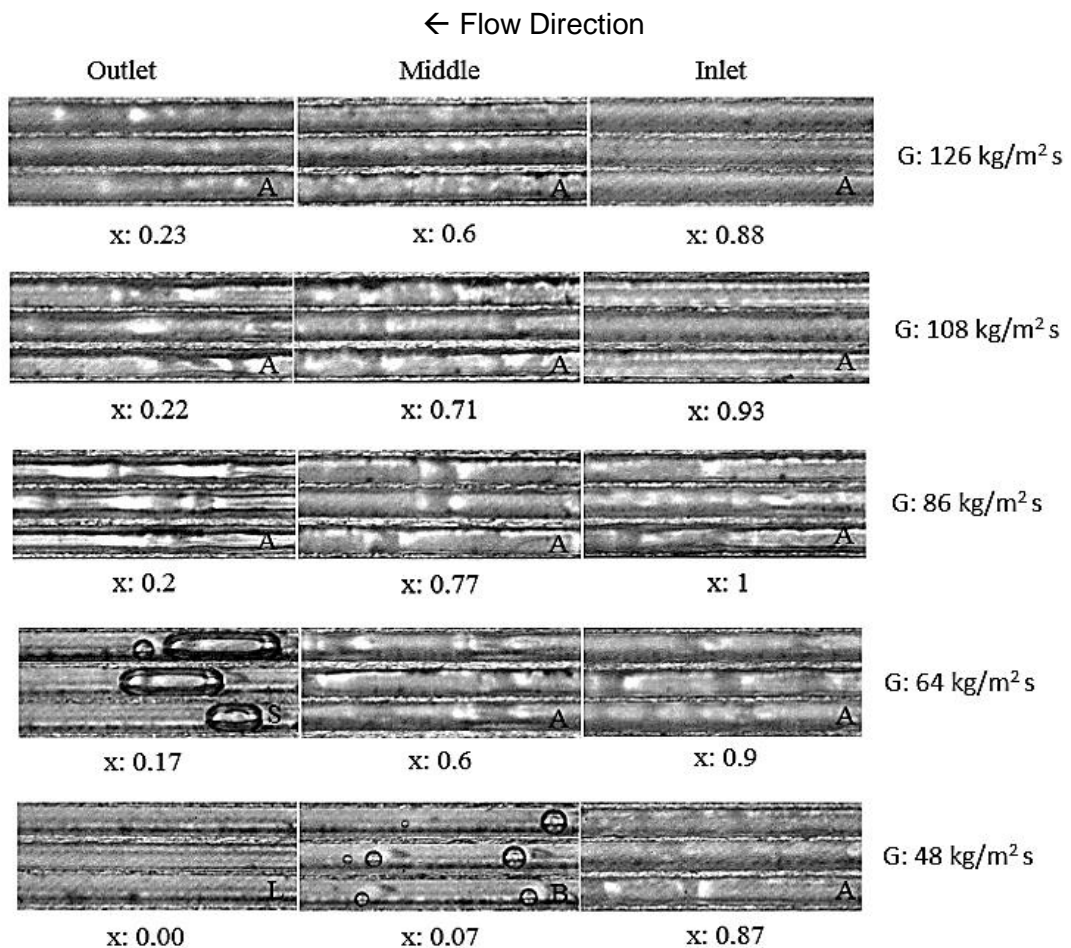


Figure 7.6 Effect of refrigerant mass flux on the experimental flow patterns at coolant flow rate of 0.5 L/min and inlet coolant temperature of 40 °C with corresponding local quality: (A) Annular (S) Slug (B) Bubbly (L) Liquid.

7.5 Effect of Coolant Conditions

The effect of coolant side conditions, *i.e.* the inlet coolant temperature and coolant flow rate, on the experimental condensation flow patterns was studied. The effect of inlet coolant temperature using larger and smaller ranges is presented in Fig. 7.5. It is obvious that annular, slug and bubbly flow regimes shifted to the right, *i.e.* higher vapour quality, when the inlet coolant temperature decreased. This could be due to an increase in the heat transfer rate, when the inlet coolant temperature decreases. An increase in the heat transfer rates leads to increase the condensation process along the channel and hence the appearance of slug and bubbly flow.

Fig. 7.7 depicts the effect of coolant flow rate on the vapour bubble diameter. This figure was drawn at mass flux of $108 \text{ kg/m}^2\text{s}$, inlet coolant temperature of $20 \text{ }^\circ\text{C}$ and two different coolant flow rates of 0.5 and 1.1 L/min. The bubble reduction size along the channel can be measured using PCC software based on the sequence of pictures for the condensing bubble as shown in Fig. 7.8. It is obvious that the vapour bubble size decreased with time due to the heat transfer from the bubble to the surrounding liquid. For example, at coolant flow rate of 0.5 L/min, the vapour bubble size decreased from 0.305 mm to 0.274 mm after 50 ms.

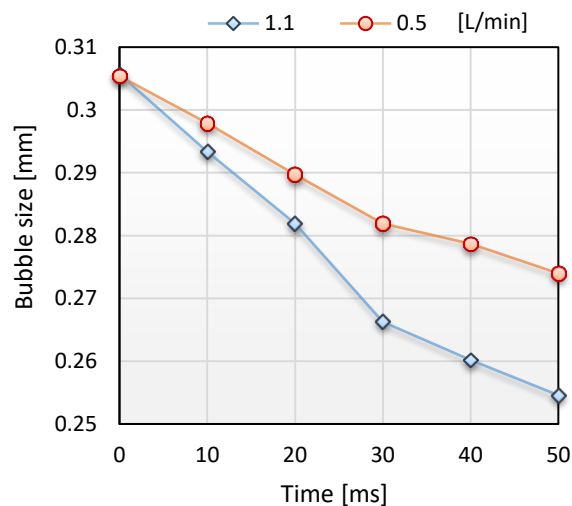


Figure 7.7 Effect of coolant flow rate on the bubble size at mass flux of $108 \text{ kg/m}^2\text{s}$, inlet coolant temperature of $20 \text{ }^\circ\text{C}$ and coolant flow rate of 0.5 and 1.1 L/min.

This figure also indicates that the size reduction rate was higher at the higher coolant flow rate compared to the lower flow rate. For instance, at time of 40 ms, the vapour bubble size reduced to 0.26 mm for the coolant flow rate of 1.1 L/min. This size became 0.278 mm when the coolant flow rate was 0.5 L/min. This confirms that the bubble reduction size decreases with increasing coolant flow rate due to the high heat transfer rate.

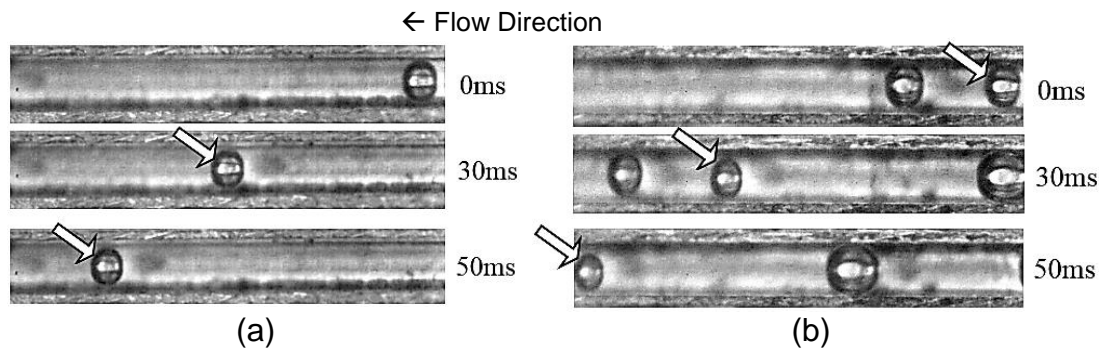


Figure 7.8 Sequence of pictures of the condensing bubble at mass flux of $108 \text{ kg/m}^2\text{s}$, inlet coolant temperature of $20 \text{ }^\circ\text{C}$ and coolant flow rate: (a) 0.5 (b) 1.1 L/min.

7.6 Comparison with Existing Flow Pattern Maps

The present experimental results were compared with existing flow pattern maps reported in the literature. These maps are widely used for comparing. The flow pattern maps proposed by Cavallini et al. (2002) and Zhuang et al. (2017) are for conventional channels, while the map by Kim and Mudawar (2012) and Nema et al. (2014) is for mini and microchannels. The details of each map are discussed in Chapter 2.

7.6.1 Flow patterns map by Cavallini et al. (2002)

This map was proposed for conventional channels with inner diameter tube ranging from 3.1 to 8.8 mm. Both of the Martinelli parameter and the dimensionless gas velocity were used to present their map. They proposed transition criteria between different flow regimes as discussed in Chapter 2, Section 2.5.2.

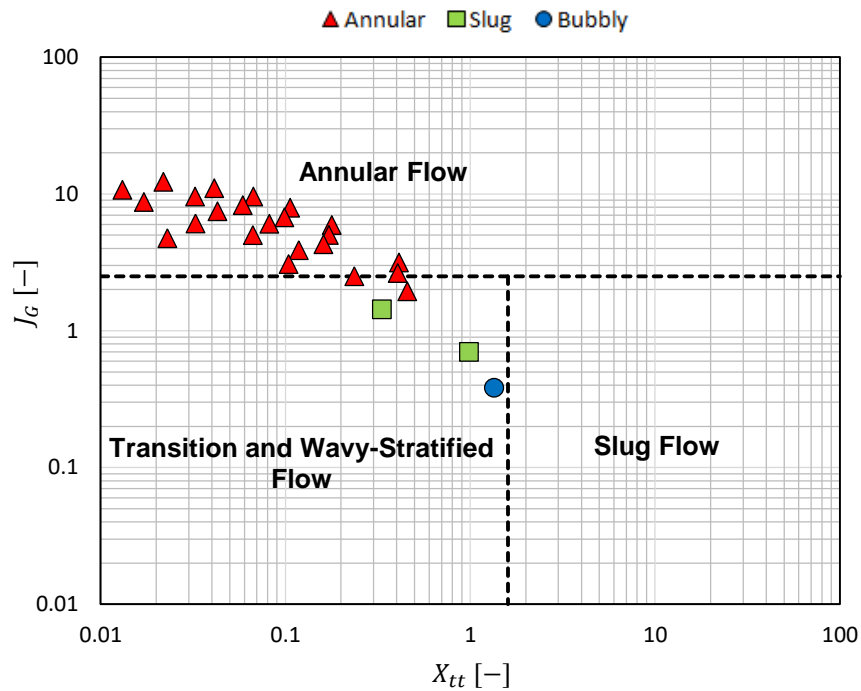


Figure 7.9 Comparison of the present results with the proposed map of Cavallini et al. (2002) at coolant flow rate of 0.5 L/min and inlet coolant temperature of 40 °C.

Fig. 7.9 depicts the comparison between the experimental results and this map. It is obvious that this map was only able to predict the annular regime. Both of bubbly and slug regimes were located within the stratified flow. This low prediction of all regimes could be due to the fact that this map was proposed for large channels (≥ 3 mm). Different flow regimes were reported in the literature at different channel diameters as discussed in detail in Chapter 2.

7.6.2 Flow patterns map by Kim and Mudawar (2012)

A flow patterns map was proposed by Kim and Mudawar (2012) including the turbulent-turbulent Martinelli parameter and the modified Weber number. They presented their condensation heat transfer data of FC-72 in horizontal square microchannels with 1 mm hydraulic diameter and 639 collected data points from eight sources. The modified Weber number was defined using Eq. (2.31) and (2.32). The present flow patterns data was compared with their map as shown in Fig. 7.10. Few data points of annular flow were within the wavy-annular region. In contrast, most points of this flow were located in the transition and slug regions. The data

points of slug and bubbly flow were found in the slug region. This discrepancy could be due to the large channel hydraulic diameter that was examined in their study. Moreover, this map does not include a transition line to bubbly flow.

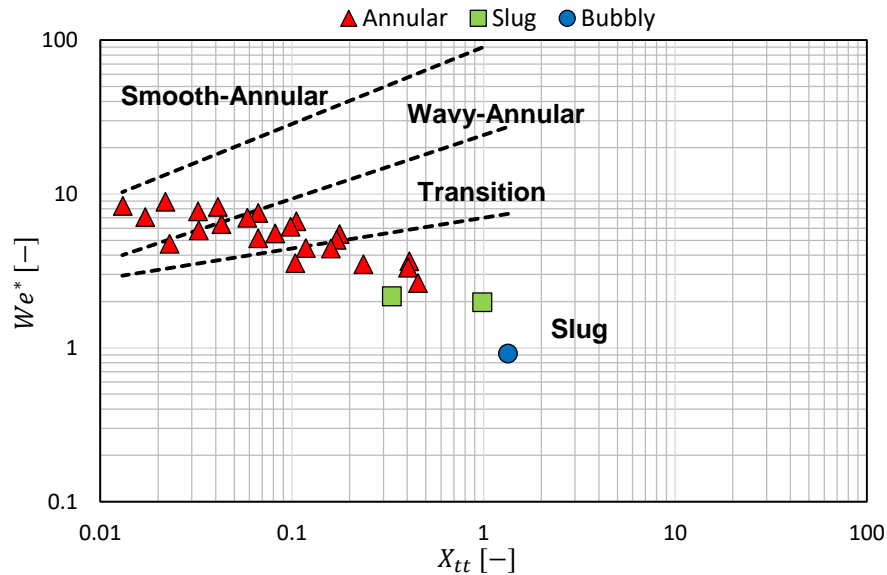


Figure 7.10 Comparison of the present results with the proposed map of Kim and Mudawar (2012) at coolant flow rate of 0.5 L/min and inlet coolant temperature of 40 °C.

7.6.3 Flow patterns map by Nema et al. (2014)

A new flow pattern map of R134a was modified by Nema et al. (2014) for horizontal mini and microchannels based on the experimental database. This database included different channel geometries and hydraulic diameter ranging from 1 to 4.91 mm. Four categories, *i.e.* dispersed, intermittent, wavy and annular flow, were classified in their map. Their transition boundaries were proposed for small tubes ($Bo \leq Bo_{cr}$) and large tubes ($Bo > Bo_{cr}$), see Chapter 2, Section 2.5.2. Fig. 7.11 shows their map compared with the present flow patterns using vapour Weber number versus turbulent-turbulent Martinelli parameter. Mist and dispersed flow were not observed during the current experiments and hence these regimes were not presented in this map. Annular flow was well predicted by this map, while their map was not able to predict the slug and bubbly flow. This could be due to the large channel hydraulic diameters (1–4.91 mm) and mass fluxes of 150–750 kg/m²s that were tested during their study.

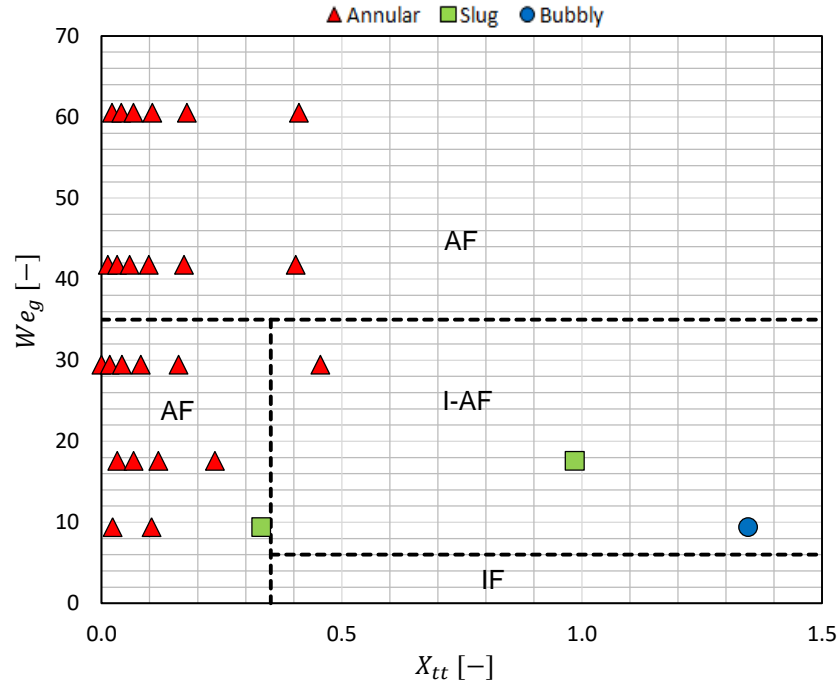


Figure 7.11 Comparison of the present results with the map of Nema et al. (2014) at coolant flow rate of 0.5 L/min and inlet coolant temperature of 40 °C:
 AF: Annular flow, I-AF: Intermittent-annular flow, IF: Intermittent flow.

7.6.4 Flow patterns map by Zhuang et al. (2017)

Zhuang et al. (2017) carried out adiabatic and condensation experiments using R50 in horizontal tubes with inner diameter of 4 mm. They conducted their experiments at a mass flux of 99–255 kg/m²s and temperature difference of 4.8–20.2 K. Flow visualization was conducted using a high-speed camera and a sight glass. They captured plug, slug, transition, wavy-annular and smooth-annular flow during the condensation experiments. A flow patterns map was proposed by the authors using the modified Webber number and the Martinelli parameter. They divided their regimes into two groups; annular and non-annular flow. The transition criterion between these regimes was defined using Eq. (2.36). Fig. 7.12 illustrates the comparison with their map and shows that slug and bubbly flow was within the non-annular regime. However, this regime included most data of annular flow. A few data points of annular flow were predicted by their map. Large tubes with 4 mm diameter could lead to this discrepancy.

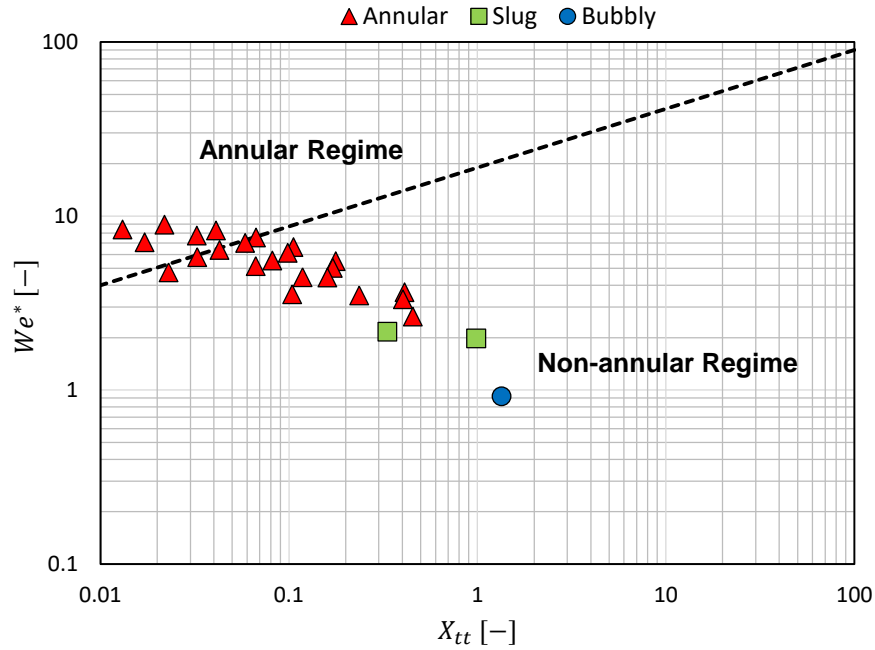


Figure 7.12 Comparison of the present results with the proposed map of Zhuang et al. (2017) at coolant flow rate of 0.5 L/min and inlet coolant temperature of 40 °C.

Four flow pattern maps were compared with the present experimental data. This comparison shows that there is no existing map can predict the present data well. This could be due to the annular flow is the prevailing regime in these proposed map. However, slug and bubbly flow are also seen during the present study. Large channel diameters may lead to appear different flow patterns compared to those in microchannels.

7.7 Summary

The following key findings can be drawn based on the experimental flow visualization investigation in the present study:

- Three condensation flow patterns were visualized in this study, namely annular, slug and bubbly flow. These regimes occurred at different locations due to the condensation process. The neck region was considered as a transition regime from annular to slug flow.
- Annular flow was found to be the dominant regime during the experiments. Slug and bubbly flow occurred with decreasing refrigerant mass flux or inlet

coolant temperature. Annular flow shifted along the channel with increasing mass flux due to the low condensation rate.

- A sudden reduction in slug length was captured after the neck region, while this rate of reduction was less slowly after a period. This was attributed to the effect of surface tension and the condensation rate.
- The bubble size decreased with increasing heat transfer rate.
- The existing flow pattern maps by Cavallini et al. (2002) and Nema et al. (2014) were able to predict the annular region. However, these maps were not able to predict all the experimental flow regimes. The flow patterns map by Kim and Mudawar (2012) predicted few points of annular flow, while the data points of slug and bubbly flow were within the slug region. The proposed map by Zhuang et al. (2017) could predict few data points of annular flow.
- There was no map that can predict all the data of the present study. A flow patterns map at low mass fluxes and micro scale passages is still required.

Chapter 8

Flow Condensation Heat Transfer: Results and Discussion

8.1 Introduction

This chapter presents the experimental condensation heat transfer results. The effect of refrigerant mass flux and coolant (water) side conditions are discussed in Section 8.2 and 8.3, respectively. The experimental results then compared with existing heat transfer correlations and shown in Section 8.4. The final key findings are summarized in Section 8.5.

8.2 Effect of Refrigerant Mass Flux

Five refrigerant mass fluxes ranging from 48 to 126 kg/m²s were examined in the present study. The experimental results at water flow rate of 0.5 L/min and inlet water temperature of 40 °C are shown in Fig. 8.1 in order to study the effect of refrigerant mass flux on the condensation heat transfer coefficient. It can be seen that the local heat transfer coefficient increased with increasing refrigerant mass flux as depicted in Fig. 8.1(a). Similar effect was also found when the average heat transfer coefficient, was calculated by integrating local heat transfer coefficient with distance, is plotted in Fig. 8.1(b).

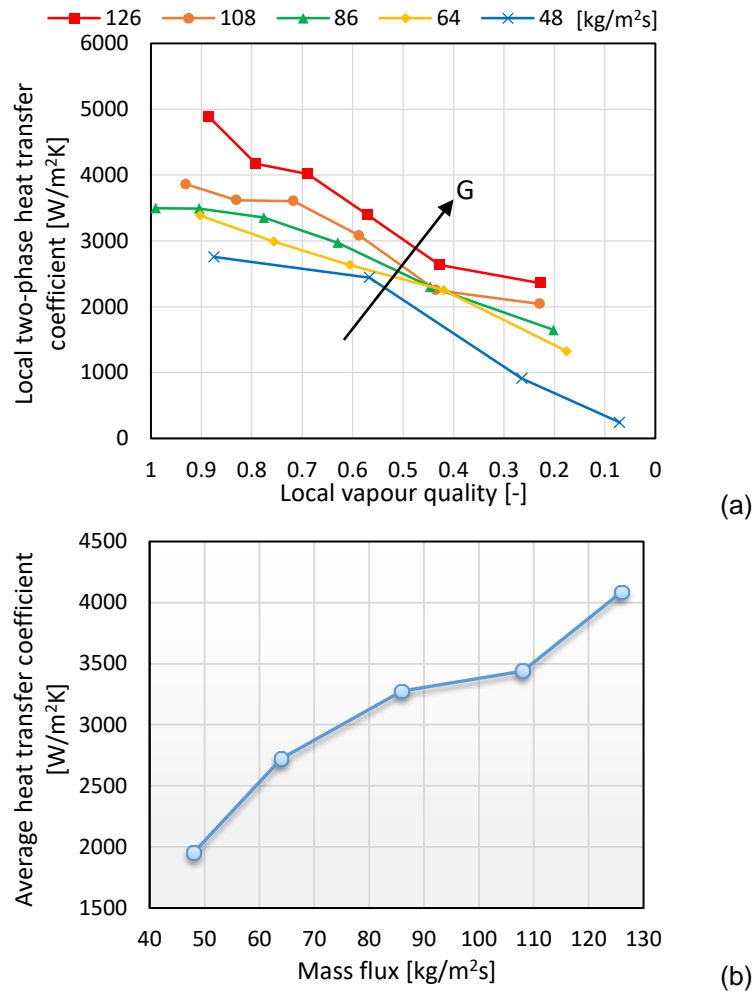


Figure 8.1 Effect of refrigerant mass flux on the condensation heat transfer coefficient at water flow rate of 0.5 L/min and inlet water temperature of 40 °C.

This mass flux effect was also reported by Cavallini et al. (2005), Agarwal et al. (2010), Al-Hajri et al. (2013) and Kim and Mudawar (2012). The enhancement in heat transfer coefficient with mass flux was attributed by the previous authors to an increase in the interfacial shear stress between the liquid and vapour phase leading to decrease the liquid film thickness and thermal resistance of fluid. Therefore, the heat transfer coefficient increases with increasing mass flux. It can be concluded that the interfacial shear stress could be the dominating regime.

In order to show the trend of the local heat transfer coefficient along the channel corresponding to the flow patterns, the heat transfer result at mass flux of 108 kg/m²s, water flow rate of 1.1 L/min and inlet water temperature of 20 °C is presented in Fig. 8.2.

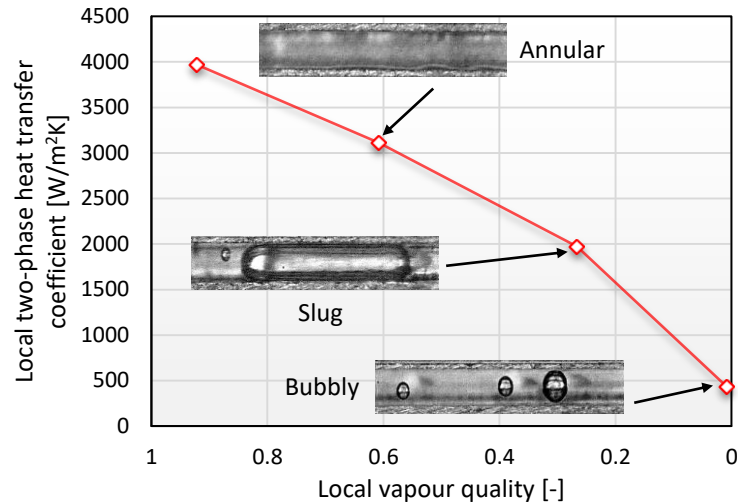


Figure 8.2 Local heat transfer coefficient versus local vapour quality corresponding to the flow patterns at mass flux of $108 \text{ kg/m}^2\text{s}$, water flow rate of 1.1 L/min , and inlet water temperature of $20 \text{ }^\circ\text{C}$.

This figure demonstrates that when the fluid entered the condenser, the flow pattern was annular flow and the local heat transfer coefficient reached the peak value. For example, the local heat transfer coefficient was found near $4000 \text{ W/m}^2\text{K}$ at local vapour quality of 0.93 . This value decreased with decreasing local vapour quality, when the flow patterns changed to slug and bubbly flow. This reduction in the local heat transfer coefficient with local quality could be due to the condensation process along the channel, *i.e.* the thickening of the liquid film leading to higher fluid thermal resistance and lower heat transfer coefficient.

8.3 Effect of Coolant Conditions

It is known that when the coolant (water) side conditions were varied during the experiments, the saturation-to-wall temperature difference also changed. Therefore, five different inlet water temperatures ranging from 20 to $40 \text{ }^\circ\text{C}$ were examined as shown in Fig. 8.3. This figure shows the local condensation heat transfer coefficient versus local vapour quality at mass flux of $86 \text{ kg/m}^2\text{s}$ and water flow rate of 0.5 L/min . It is obvious that there was no clear effect of the inlet water temperature on the local heat transfer coefficient.

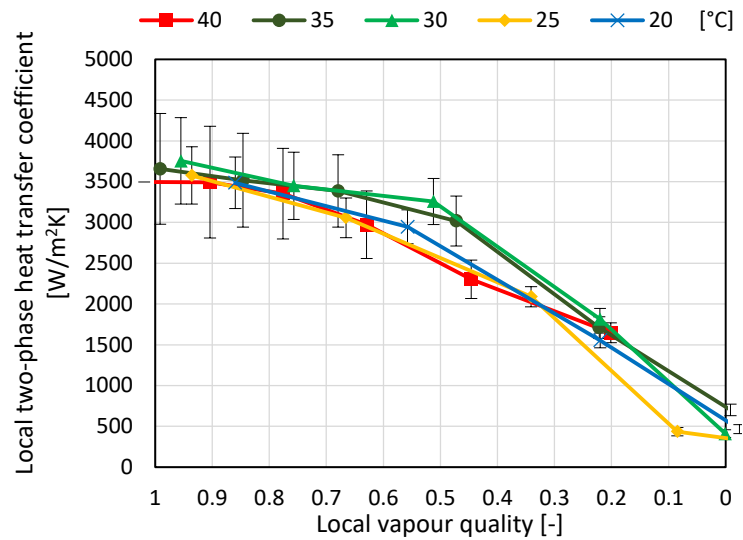


Figure 8.3 Effect of inlet water temperature on the local condensation heat transfer coefficient at mass flux of $86 \text{ kg/m}^2\text{s}$ and water flow rate of 0.5 L/min .

Fig. 8.4 depicts the effect of water flow rate on the local condensation heat transfer coefficient at mass flux of $126 \text{ kg/m}^2\text{s}$ and inlet water temperature of $30 \text{ }^\circ\text{C}$. Three different water flow rates of 0.5 , 0.8 and 1.1 L/min were examined.

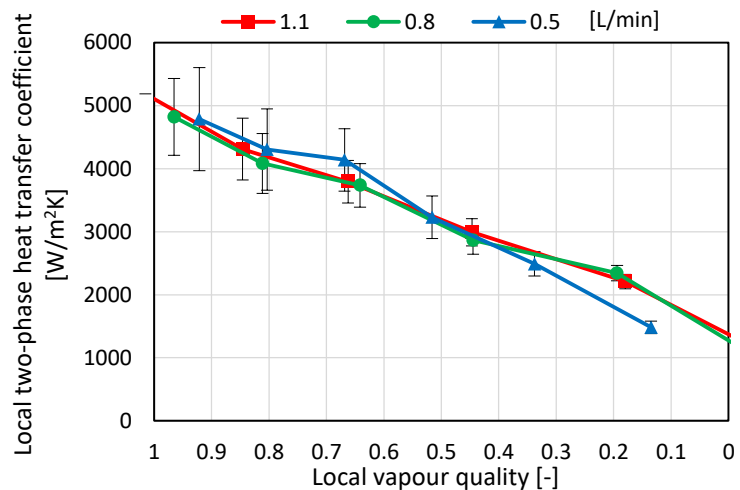


Figure 8.4 Effect of water flow rate on the local condensation heat transfer coefficient at mass flux of $126 \text{ kg/m}^2\text{s}$ and inlet water temperature of $30 \text{ }^\circ\text{C}$.

This figure shows that there was a negligible effect of water flow rate on the local heat transfer coefficient in the range studied. A variation of the coolant side conditions, *i.e.* inlet water temperature or water flow rate, with constant refrigerant

side conditions resulted in a variation of the wall temperature and thus in the saturation-to-wall temperature difference. However, the temperature difference seems to have a negligible effect on the local condensation heat transfer coefficient in the range studied. Similar conclusion was found by other studies, such as Matkovic et al. (2009b), Matkovic et al. (2009a) and Del Col et al. (2011).

8.4 Comparison with Existing Correlations

The experimental total data points of 217 were compared with a number of existing correlations. This data included refrigerant mass flux ranging from 48 to 126 kg/m²s, system pressure of 1 bar, inlet vapour quality near one, inlet water temperature of 20–40 °C and water flow rate of 0.5–1.1 L/min. These correlations were divided into conventional and mini/microchannels according to the classification by Kandlikar and Grande (2003), see Chapter 2 for more details. The mean absolute error (*MAE*) and the percentage of data points predicted within ±30% error bands (Θ) were used to evaluate the accuracy of each correlation as follows:

$$MAE = \frac{1}{N} \sum \left| \frac{h_{pred} - h_{exp}}{h_{exp}} \right| 100\% \quad (8.1)$$

$$\Theta = \frac{N_{pred}}{N_{exp}} 100\% \quad (8.2)$$

Appendix C presents a summary of the existing correlations for the prediction of condensation heat transfer coefficient. These correlations were proposed for circular tubes or rectangular channels with four-sides cooling. Therefore, a correction factor should be used to calculate the heat transfer coefficient with three-sides cooling as follows:

$$HTC = \left(\frac{Nu_3}{Nu_4} \right) h_{tp} \quad (8.3)$$

where h_{tp} , Nu_3 and Nu_4 are the two-phase heat transfer coefficient obtained from Appendix C, Nusselt number for thermally developed laminar flow with three-sides and four-sides heat transfer, respectively. The above technique was adopted by Kim and Mudawar (2012) and Kim and Mudawar (2013c). The following equations are used to find Nu_3 and Nu_4 , as proposed by Shah and London (1978).

$$Nu_3 = 8.235(1 - 1.833\beta + 3.767\beta^2 - 5.814\beta^3 + 5.361\beta^4 - 2\beta^5) \quad (8.4)$$

$$Nu_4 = 8.235(1 - 2.042\beta + 3.085\beta^2 - 2.477\beta^3 + 1.058\beta^4 - 0.186\beta^5) \quad (8.5)$$

where β is the channel aspect ratio ($\frac{W_{ch}}{H_{ch}}$). All the correlations in Appendix C are for annular flow, except one of the two correlations of Kim and Mudawar (2013c) which is for slug and bubbly flow. Therefore, the experimental data points were separated then compared as follows: 158 data points for annular flow and 59 data points for slug and bubbly flow.

8.4.1 Conventional scale flow condensation heat transfer correlations

The experimental data was compared with existing correlations proposed for conventional channels, such as Shah (1979), Dobson and Chato (1998) and Cavallini et al. (2006a). These correlations are widely used in condensation studies.

8.4.1.1 The correlation of Shah (1979)

A correlation for condensation heat transfer in vertical, horizontal and inclined tubes with inner diameter of 7–40 mm was developed by the author. The Dittus-Boelter single-phase equation multiplied by vapour quality and reduced pressure was used in this correlation. When his correlation was compared with the present results, 74.68% of the data was predicted with a MAE of 24.58% as shown in Fig. 8.5. This good agreement could be due to the range of parameters that were covered in their study. For example, the present study covers the reduced pressure of 0.047 which is within their range (0.002–0.44). They also covered saturation temperature range of 21–310 °C and the present saturation temperature is 60 °C. Low and high mass fluxes were examined in their study, *i.e.* ranging from 10.8 to 210.5 kg/m²s. This range covers the present mass fluxes (48–126 kg/m²s). Moreover, the liquid Prandtl number in their study is 1–13 and 11 in the current study. Different experimental parameters result in different heat transfer data and dominated forces and thus the applicability of any existing correlation may change, further details are discussed later.

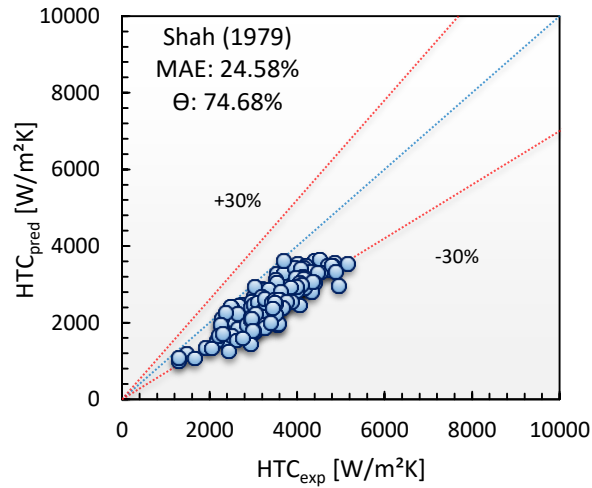


Figure 8.5 Comparison between the experimental condensation heat transfer coefficient and the correlation by Shah (1979).

8.4.1.2 The correlation of Dobson and Chato (1998)

Dobson and Chato (1998) carried out an experimental study using different fluids in horizontal tubes with diameter of 3.14 and 7.04 mm. They proposed a correlation for the annular regime which included Prandtl number, superficial liquid Reynolds number and the turbulent liquid-turbulent vapour Martinelli parameter. Fig. 8.6 depicts the comparison between the experimental data with their correlation. It is shown that this correlation can predict 90.5% of the data points with a MAE of 13.71%. This very good agreement with the present data could be due to this correlation was recommended for high mass fluxes ($G \geq 500 \text{ kg/m}^2\text{s}$) as well as low mass fluxes ($G < 500 \text{ kg/m}^2\text{s}$), *i.e.* suitable for the present mass flux range.

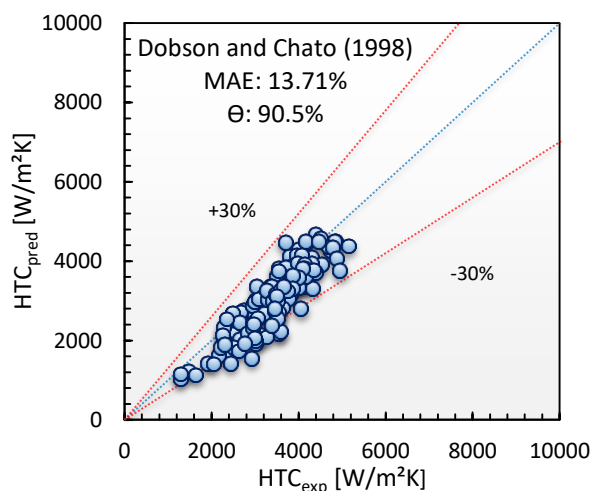


Figure 8.6 Comparison between the experimental condensation heat transfer coefficient and the correlation by Dobson and Chato (1998).

8.4.1.3 The correlation of Cavallini et al. (2006a)

425 data points including different fluids and horizontal tubes with inner diameter more than 3 mm were used to develop a heat transfer model by the authors. The independent or dependent of the heat transfer coefficient with the temperature difference was taken into account in their correlation. They proposed three correlations for annular, stratified-wavy or smooth flow and slug flow based on the value of J_G and J_G^T . Very good agreement was found when comparing their model with the present experimental data. It predicted 94.94% of the present data with a mean absolute error of 11.14% as presented in Fig. 8.7. Although their model was proposed for conventional channels, *i.e.* > 3 mm, it showed a reasonable agreement with the present data for 0.57 mm. This very good agreement was also reported by Matkovic et al. (2009b). They conducted experimental flow condensation study in a circular channel with inner diameter of 0.96 mm. This reasonable agreement between their model and the present experimental data could be due to the fact that their model was developed and validated using a large experimental data bank with different fluids. For example, it covered saturation temperature of -15 – 302 °C and mass flux ranging from 18 to 2240 kg/m²s, *i.e.* the present data are within their validation ranges.

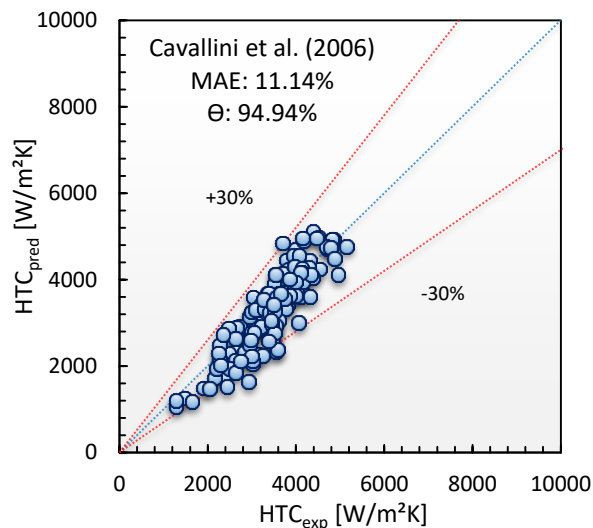


Figure 8.7 Comparison between the experimental condensation heat transfer coefficient and the correlation by Cavallini et al. (2006a).

8.4.2 Mini/Micro-scale flow condensation heat transfer correlations

Seven existing heat transfer correlations were compared with the present data. These correlations were proposed for mini and microchannels. Chapter 2 presents the full detail for each correlation. In this section, a comparison with these correlations, such as Wang et al. (2002), Koyama et al. (2003b), Bohdal et al. (2011), Park et al. (2011), Kim and Mudawar (2013c), Shah (2016) and Rahman et al. (2018), is discussed.

8.4.2.1 The correlation of Wang et al. (2002)

Flow condensation experiments of R134a were conducted by the authors using horizontal rectangular multi-channels with a hydraulic diameter of 1.46 mm. A correlation for calculating condensation annular heat transfer coefficient was proposed including Prandtl number, Reynolds number, vapour quality and the Martinelli parameter. In the present comparison, high over prediction by their correlation was found as shown in Fig. 8.8. Just 10.76% of the present experimental data was predicted with a MAE of 120.19%. This over prediction could be due to the high inlet pressure was tested during their experiments, *i.e.* 18–19.3 bar, while the present experiments were carried out at atmospheric pressure. Further details about the effect of inlet pressure are discussed later.

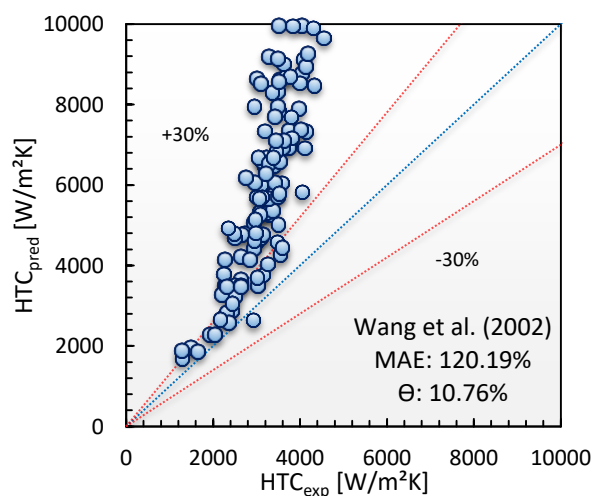


Figure 8.8 Comparison between the experimental condensation heat transfer coefficient and the correlation by Wang et al. (2002).

8.4.2.2 The correlation of Koyama et al. (2003b)

An experimental study on the condensation flow of R134a in multiport extruded tubes with hydraulic diameter of 0.807 and 1.114 mm was carried out by the authors. They proposed a correlation by taking into account the two-phase multiplier factor by Mishima and Hibiki (1995). This was based on the fact that the correlation by Mishima and Hibiki (1995) was in good agreement with their data. Fig. 8.9 depicts the comparison between this correlation and the present data. Their correlation was able to predict 34.81% of the total points with a MAE of 36.87%. This could be due to the high mass fluxes ($G \geq 100 \text{ kg/m}^2\text{s}$) that were examined by them. Moreover, they carried out their experiments at inlet pressure of 17 bar, which is much higher than the present study.

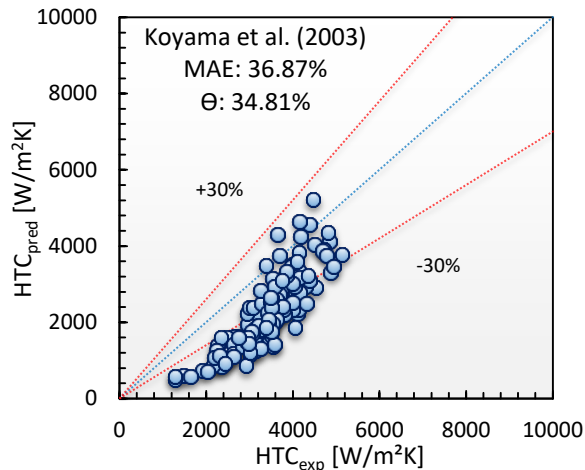


Figure 8.9 Comparison between the experimental condensation heat transfer coefficient and the correlation by Koyama et al. (2003b).

8.4.2.3 The correlation of Bohdal et al. (2011)

They performed an experimental study of R134a and R404A in tubes with inner diameter of 0.31–3.3 mm. They mentioned that the correlations by Akers et al. (1958) and Shah (1979) predicted their results but within a limited range of mass flux and inner diameter. Therefore, they proposed a correlation based on their experimental data. Their correlation was compared with the present experimental data as depicted in Fig. 8.10. This correlation highly under predicted the experimental data with a MAE of 65.78%.

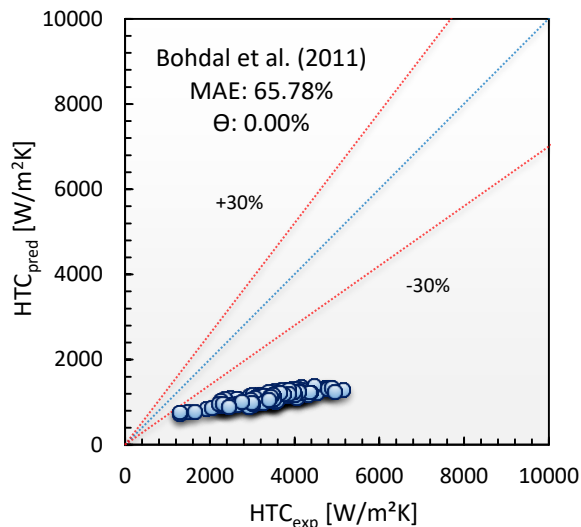


Figure 8.10 Comparison between the experimental condensation heat transfer coefficient and the correlation by Bohdal et al. (2011).

This low prediction could be due to the high mass fluxes ($G = 100\text{--}1300 \text{ kg/m}^2\text{s}$) that were tested by them. The saturation temperature during their experiments changed from 20 to 40 °C, while it was set at 60 °C in the present study.

8.4.2.4 The correlation of Park et al. (2011)

The authors conducted an experimental study of R1234ze(E), R134a and R236fa using vertical multiport tubes with hydraulic diameter of 1.45 mm. They proposed a correlation by modifying the correlation of Koyama et al. (2003a) according to their data Fig. 8.11 shows a comparison between their correlation and the present experimental results. The correlation by Park et al. (2011) predicted 71.52% of the total 113 data points, with a MAE of 23.97%. This good agreement could be due to the examined ranges of mass flux and saturation temperature. In their study, the mass flux range was 50–260 $\text{kg/m}^2\text{s}$, which covered the present ranges. The saturation temperature was set at 25–70 °C during their experiments and 60 °C during the present study, *i.e.* within their ranges.

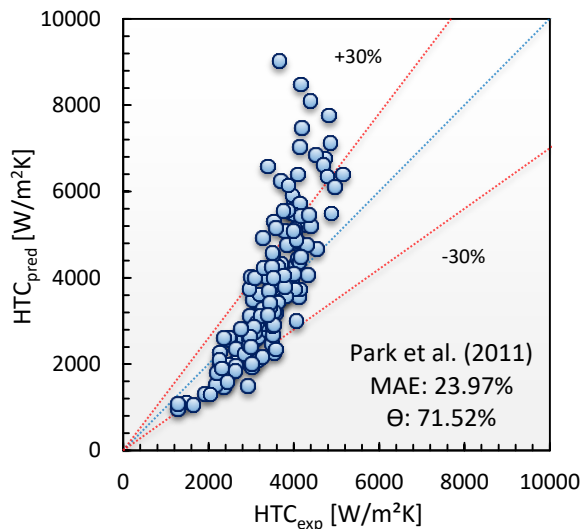


Figure 8.11 Comparison between the experimental condensation heat transfer coefficient and the correlation by Park et al. (2011).

8.4.2.5 The correlation of Kim and Mudawar (2013c)

A new universal approach for calculating the condensation heat transfer coefficient was proposed by Kim and Mudawar (2013c). They collected data from 28 sources including single and multi-channels, circular and rectangular configurations, different fluids and hydraulic diameter ranging from 0.424–6.22 mm. Two correlations, *i.e.* for annular and slug and bubbly flow, were proposed by the authors. By comparing the experimental annular data points, their correlation was able to predict 90.51% of the data, *i.e.* 143 points, with a MAE of 14.95% as shown in Fig. 8.12(a). This reasonable agreement between their correlation and the present experimental data could be due to the fact that the present experimental ranges are within their database. Their data included single and multi-channels with hydraulic diameter of 0.424–6.22 mm and mass flux of 53–1403 $\text{kg/m}^2\text{s}$. Moreover, this database covered reduced pressure of 0.04–0.91, superficial liquid Reynolds number of 0–79202 and superficial vapour Reynolds number from 0 to 247740. The present data included reduced pressure of 0.047, superficial liquid Reynolds number of 0.36–101.4 and superficial vapour Reynolds number of 873.1–7571. Fig. 8.12(b) shows their correlation for slug and bubbly flow compared to 59 data points for these regimes. It can be seen that a significant scatter was found with a MAE of 93.46%.

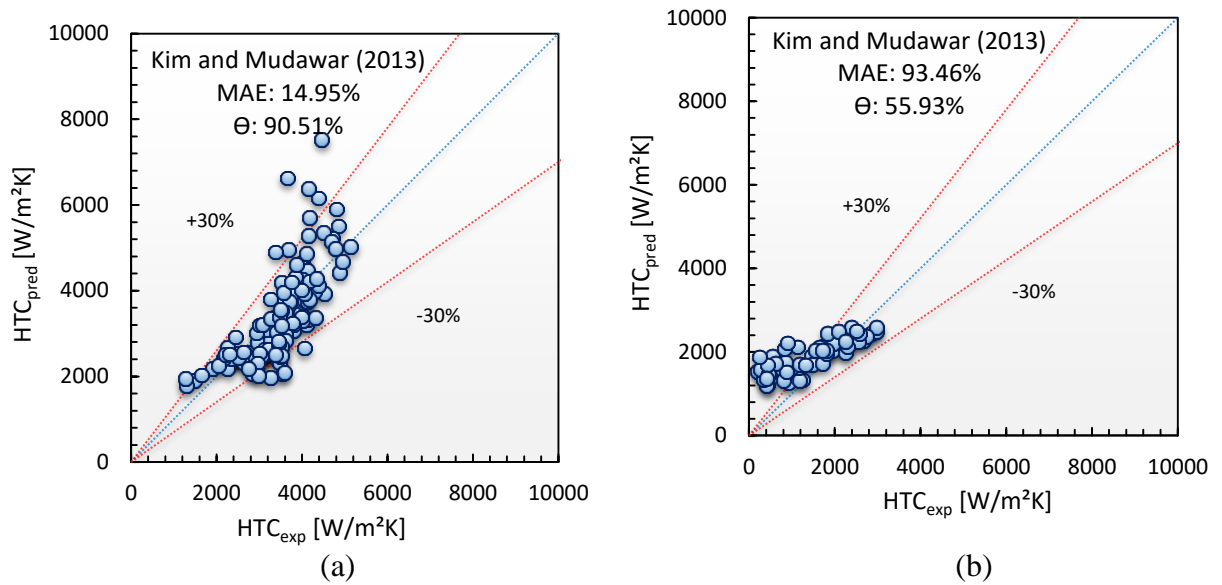


Figure 8.12 Comparison between the experimental condensation heat transfer coefficient and the correlations by Kim and Mudawar (2013c):

(a) Annular data (b) Slug and bubbly data.

8.4.2.6 The correlation of Shah (2016)

A correlation for calculating condensation heat transfer coefficient in horizontal mini and microchannels for hydraulic diameter ≤ 3 mm was proposed by the author. He verified his correlation using 67 data sets from 31 sources including different fluids, single and multi-channels and different channel shapes. His correlation included three regions, *i.e.* I, II, and III, based on the dimensionless vapour velocity. Fig. 8.13 depicts the present comparison with this correlation and a very good agreement was found. His correlation predicted 91.77% of the experimental database with a mean absolute error of 16.4%. This could be attributed to the large database that was used to validate his correlation. This data included single and multi-channels with hydraulic diameter ranging from 0.1 to 2.8 mm and aspect ratio of 0.14–13.9. The present channel hydraulic diameter and aspect ratio are 0.57 mm and 0.4, respectively, which are covered by this data. Low and high mass fluxes ($G = 20$ – 1400 kg/m^2s) were covered in their database. It also included reduced pressure ranging from 0.0055 to 0.94 and Bond number of 0.033–29.4. The range of these parameters in the present study is also within their ranges, *i.e.* reduced pressure of 0.047 and Bond number of 0.32.

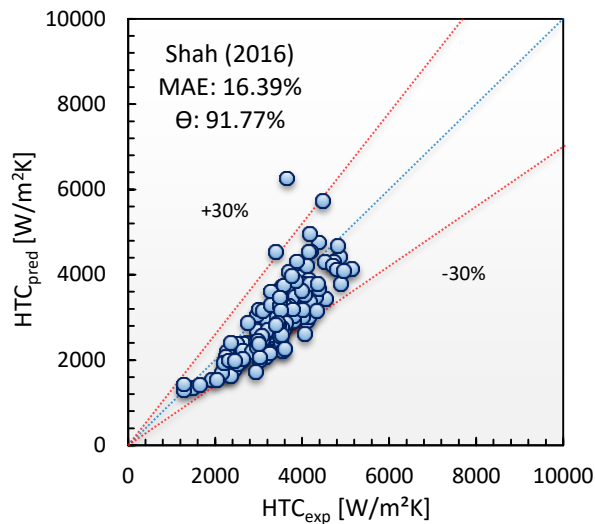


Figure 8.13 Comparison between the experimental condensation heat transfer coefficient and the correlation by Shah (2016).

8.4.2.7 The correlation of Rahman et al. (2018)

The authors carried out condensation experiments using R134a in horizontal rectangular multi-channels with and without fins at a hydraulic diameter of 0.64 and 0.81 mm. They conducted their experiments at saturation temperature of 30–35 °C and mass flux of 50–200 kg/m²s. They reported that the condensation heat transfer coefficient depended on the mass flux, vapour quality, saturation temperature and channel geometry. Their experimental data was compared with some existing correlations and overall reasonable prediction was not found. Therefore, an empirical correlation for annular flow was proposed using the same form as Kim and Mudawar (2013c). The reduced pressure and vapour quality were also proposed in their correlation. Fig. 8.14 shows their correlation compared with the present data for the test section (5). It demonstrates that the present experimental data was under predicted by this correlation. Just 15.82% of the data was predicted with a MAE of 45.11%. This under prediction could be due to the range of saturation temperature. They examined a saturation temperature ranging from 30 to 35 °C, while it was set at 60 °C during the present experiments. Different saturation temperature may result in different heat transfer results that affect the applicability of existing correlation as discussed in the next section.

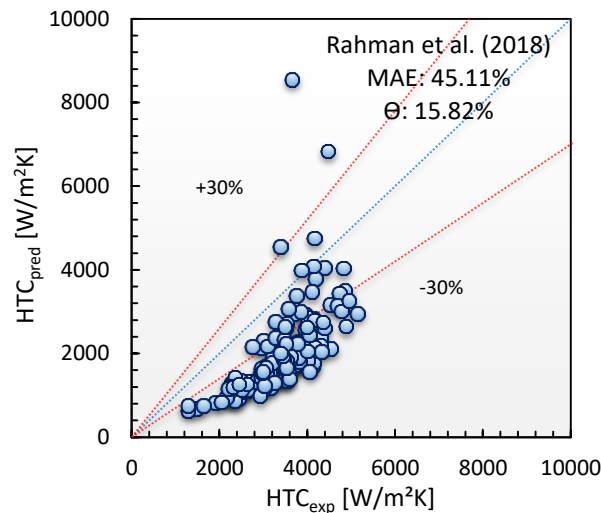


Figure 8.14 Comparison between the experimental condensation heat transfer coefficient and the correlation by Rahman et al. (2018).

Ten existing correlations proposed for conventional and mini/microchannels were compared with the present condensation data as summarized in Table 8.1. This table shows that some correlations predict the results with a MAE more than 50%. In contrast, the conventional correlations by Dobson and Chato (1998) and Cavallini et al. (2006a) provide very good prediction with a MAE less than 15%. The mini/microchannel correlations by Kim and Mudawar (2013c) and Shah (2016) are also able to predict the results well with a MAE of 15% and 16%, respectively. This large discrepancy among correlations could be due to the fact that most of these correlations were proposed based on limited experimental data. Therefore, these correlations can be used only within their ranges. Other correlations were developed and validated using wide range of collected data and thus a reasonable agreement can be found. Different operating conditions, fluids and channel geometries can result in different heat transfer data and controlling forces. For example, Matkovic et al. (2009a) reported that the heat transfer coefficient in a square channel is higher than that in a circular channel at low mass fluxes due to the fact that the surface tension tries to pull the liquid towards the channel corners leading to thinner liquid film at the channel flat sides. Del Col et al. (2016) mentioned that, in conventional channels, both gravity and shear forces are dominant, while surface tension force also becomes important in mini/microchannels. Different mass fluxes may also lead to different dominant forces. For instance, Kim and Mudawar (2012) stated that the interfacial shear stress increases with increasing mass flux. This leads to increasing the heat

transfer coefficient with mass flux. Cavallini et al. (2006a) reported that, in horizontal tubes, the dependence on temperature difference occurs when the gravity is the dominant force. Different saturation temperature or inlet pressure results in different experimental data. Rahman et al. (2018) found that the heat transfer coefficient increases with decreasing saturation temperature due to the change in the fluid properties. When the saturation temperature decreases, the density ratio and viscosity ratio increase leading to high shear stress.

Table 8.1 Statistical comparison between the experimental condensation heat transfer data and existing correlations.

Author(s)	MAE (%)	Θ (%)
Shah (1979)	24.58	74.68
Dobson and Chato (1998)	13.71	90.5
Cavallini et al. (2006a)	11.14	94.94
Wang et al. (2002)	120.19	10.76
Koyama et al. (2003b)	36.87	34.81
Bohdal et al. (2011)	65.78	0.00
Park et al. (2011)	23.97	71.52
Kim and Mudawar (2013c)	14.95	90.51
Shah (2016)	16.4	91.77
Rahman et al. (2018)	45.11	15.82

8.5 Summary

The following points can be summarized based on the present experimental flow condensation heat transfer results:

- Condensation heat transfer coefficient increased with increasing refrigerant mass flux and decreased with decreasing local vapour quality. This was attributed to the liquid film thickness and thermal resistance.
- Saturation-to-wall temperature difference, *i.e.* coolant side conditions, had a negligible effect on the local condensation heat transfer coefficient.

- The interfacial shear stress could dominate during the condensation experiments at this scale and with this particular fluid due to an increase in heat transfer coefficient with mass flux.
- The conventional correlations by Dobson and Chato (1998) and Cavallini et al. (2006a) predicted the present experimental results with a reasonable accuracy, *i.e.* with a MAE between 11% and 14%.
- The mini/microchannel correlations by Kim and Mudawar (2013c) and Shah (2016) were able to predict the present results within acceptable limits, *i.e.* with a mean absolute error of 15% and 16%, respectively.
- Different fluids, channel geometries and operating conditions lead to different dominant forces and heat transfer data. Therefore, the accuracy of existing correlations may differ.

Chapter 9

Small-scale Thermal Management System

9.1 Introduction

The main objective of the present study is to design and examine the thermal performance of both multi-microchannel evaporator and condenser. These parts could be used in a small-scale pumped loop thermal management system for cooling electronic components. 3M Novec Engineering fluid HFE-7100 was chosen since it is a dielectric and eco-friendly refrigerant and suitable choice for cooling applications that require working surface temperature equal or more than 80 °C. The present operating conditions were set at a system pressure near atmospheric (saturation temperature of 60 °C), low inlet sub-cooling and low mass fluxes in order to reduce the overall weight, size and pumping power. In this chapter, the effect of cooling load, mass flux, channel aspect ratio and surface material on the pumping power is discussed in Section 9.2, while a comparison between the present thermal management system and other cooling techniques are presented in Section 9.3. The upper cooling performance of the present test sections are given in Section 9.4. Finally, main key findings are summarized in Section 9.5.

9.2 Pumping Power

From a design point of view, the required pumping power for a given cooling load is important for the design of cooling systems. The effect of cooling load, mass flux, channel aspect ratio and surface material on the pumping power is presented in this

section. Therefore, the required pumping power was calculated using Eq. (9.1) assuming that the efficiency of the pump is 100%.

$$W_p = \dot{m}\Delta P_{meas}/\rho_l \quad (9.1)$$

where \dot{m} , ΔP_{meas} and ρ_l are the mass flow rate, the total measured pressure drop at the test section and the liquid density, respectively. The cooling load at the evaporator was calculated by multiplying the base heat flux q''_b by the base area A_b as follows:

$$Q_{evap} = q''_b A_b \quad (9.2)$$

Since the smaller channel aspect ratio shows higher base heat flux, this heat sink is used to present these two parameters as shown in Fig. 9.1. It can be seen that, for given mass flux, the pumping power increased with increasing cooling load due to an increase in the total measured pressure drop at the test section. This figure also shows that, at a fixed cooling load, the pumping power increased with increasing mass flux. This is due to an increase in the pressure drop and mass flow rate. For example, at cooling load of 110 W, the required pumping power increased from 0.82 to 3.2 mW with increasing mass flux from 100 to 250 kg/m²s. Fig. 9.1 indicates that maximum cooling load was reached at 265.6 W at a pumping power of 9.7 mW.

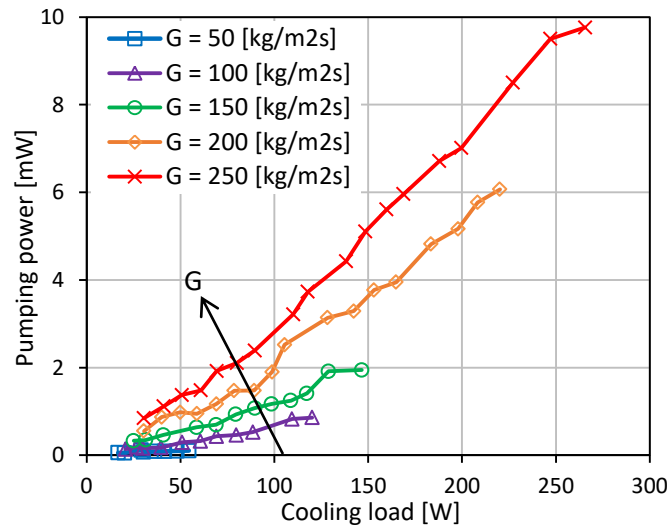


Figure 9.1 Pumping power versus cooling load for TS.1.

Fig. 9.2 illustrates the effect of channel aspect ratio on the pumping power at mass flux of 250 kg/m²s. This figure shows that, for a given wall heat flux, the required pumping power increased with decreasing channel aspect ratio. This is attributed to an increase in the total measured pressure drop and mass flow rate.

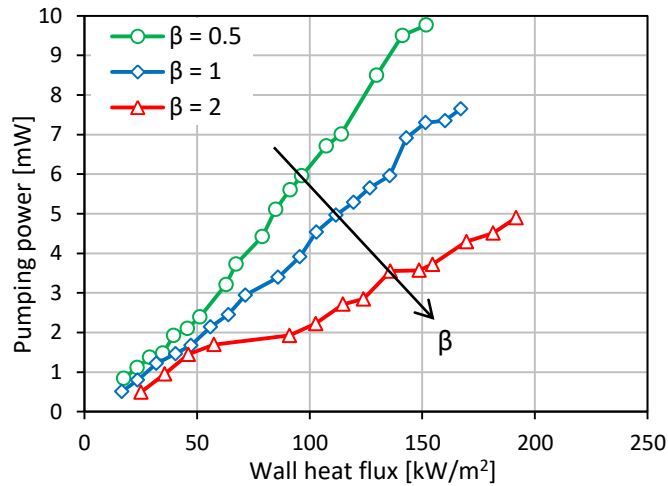


Figure 9.2 Effect of channel aspect ratio on pumping power at mass flux of 250 kg/m²s.

At a given wall heat flux, the two-phase pressure drop increases with decreasing aspect ratio as discussed in Chapter 5. Moreover, the total mass flow rate increases with decreasing aspect ratio for a given mass flux due to the large number of channels. Therefore, the pumping power increases with decreasing aspect ratio.

The effect of surface material on the pumping power is shown in Fig. 9.3. This figure is plotted at a mass flux of 200 kg/m²s for TS.2 and TS.4. It can be seen that aluminium surface showed higher pumping power compared to copper. This is due to the high pressure drop, see Chapter 5 for more details. For instance, at wall heat flux of 142 kW/m², copper surface required 5.4 mW pumping power. This increased to 6.3 mW for the aluminium surface.

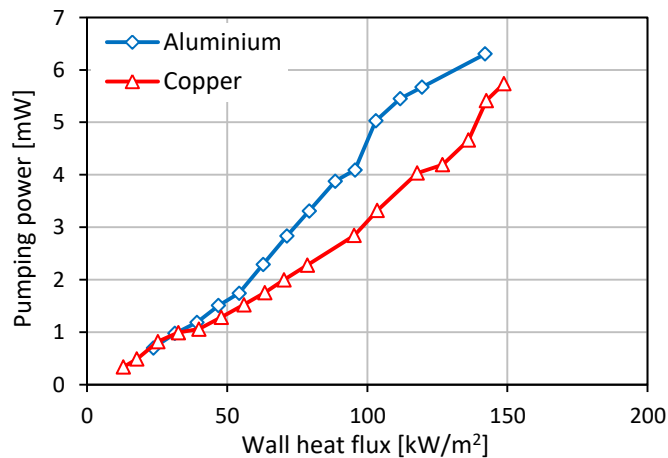


Figure 9.3 Effect of surface material on pumping power at mass flux of 200 kg/m²s.

The above discussion showed that the required pumping power is found to increase with mass flux and cooling load. Moreover, at a fixed wall heat flux, the pumping power becomes high at smaller channel aspect ratio and aluminum surface. Maximum cooling load that can be dissipated is found to be 265.5 W using deeper channels, *i.e.* aspect ratio of 0.5. This requires pumping power of 9.7 mW.

9.3 Comparison with other Cooling Techniques

Both microchannel evaporator and condenser were assumed at the same loop, *i.e.* as a small-scale pumped loop thermal management system, as shown in Fig. 9.4. This figure was drawn in scale to assess the overall system size. It is obvious that the current microchannel condenser is approximately six times larger than the evaporator. This is considered a large variation ratio of size and reducing the condenser size remains a challenge for electronic applications.

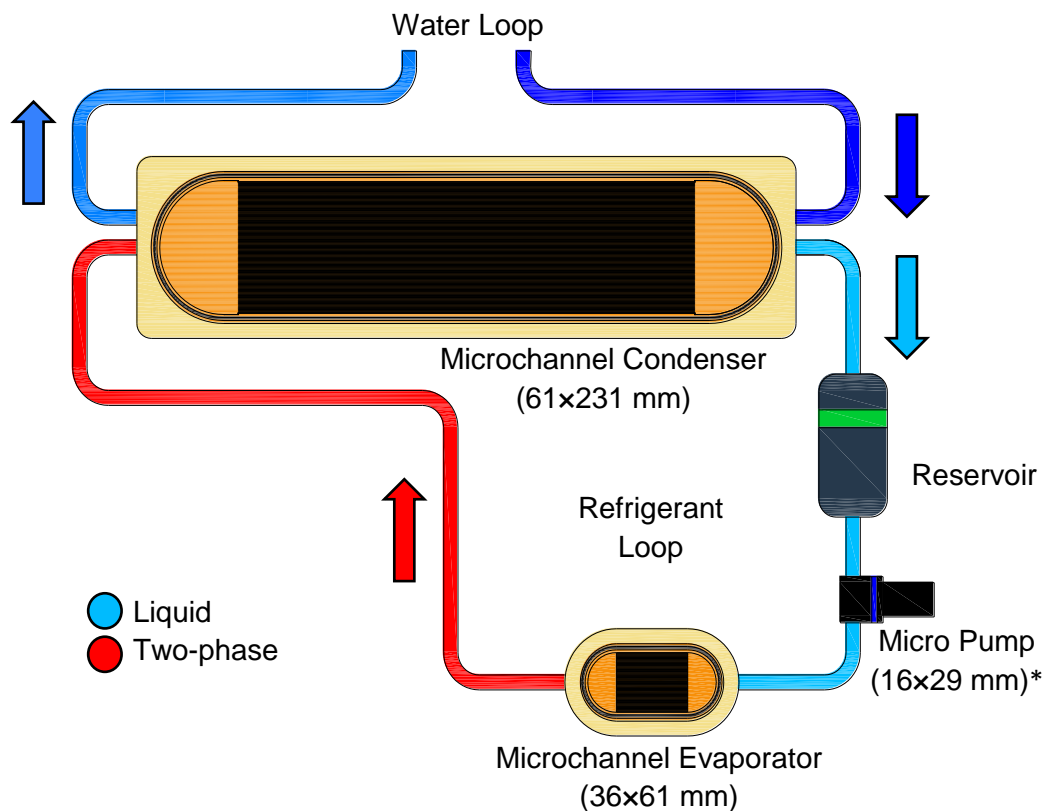


Figure 9.4 Small-scale pumped loop thermal management system (in scale);

* Pump dimensions are mentioned in (www.micropumps.co.uk).

Since the heat sink with smaller channel aspect ratio showed the maximum cooling load (265 W) at mass flux of $250 \text{ kg/m}^2\text{s}$, *i.e.* mass flow rate of 8.8 kg/hr, this heat sink was chosen to assess the thermal performance of this system. The power consumption by the micro pump of this system was calculated using Eq. (3.38). The experimental total measured pressure drop at the evaporator was found to be 5.65 kPa, while it was 0.8 kPa at the condenser. This total pressure drop at the condenser was measured at cooling load near 270 W, inlet coolant temperature of $40 \text{ }^\circ\text{C}$ and coolant flow rate of 0.5 L/min. The outlet sub-cooling at the condenser was found at 10.74 K. By assuming the refrigerant temperature increased by 5 K in the system loop, *i.e.* in the liquid reservoir, pipes and micro pump, the inlet refrigerant temperature at the evaporator will be near $55 \text{ }^\circ\text{C}$, which corresponds to the inlet sub-cooling of 5 K. Accordingly, the calculated pumping power of this small-scale system is 12 mW, which is a very small value. It is worth mentioning that this small pumping power was also reported by Harirchian and Garimella (2008), who tested flow boiling of dielectric fluid (FC-77) in horizontal multi-microchannels. Their results showed that the pumping power ranged from 0.7 to 20 mW at a mass flux of $700 \text{ kg/m}^2\text{s}$.

The current proposed thermal management system was compared with other cooling techniques that were proposed for electronics cooling as shown in Fig. 9.5. Most of these techniques are available for commercial applications, such as (i) active air cooler and finned heat sink, (ii) thermoelectric cooler, heat pipes and air fan, (iii) heat pipes-air fan and (iv) single-phase liquid cooler. A miniature vapour compression refrigeration (VCR) was also compared. This system was proposed and tested by Poachaiyapoom et al. (2019) using R134a in microchannel heat sink. This figure demonstrates that a higher cooling load can be dissipated by the system proposed in this thesis. This system also consumed lower pumping power compared to others. For example, the power consumption by the present system was found to be 0.012 W, while it increased to 8 W for the single-phase liquid cooling loop. This value increased up to 22 W, when the miniature compressor was used. Liang et al. (2019) conducted a comparison between heat pipe, thermoelectric and vapour compression refrigeration systems. They found that the last system provided better thermal performance. When their results in Fig. 9 were compared with the present

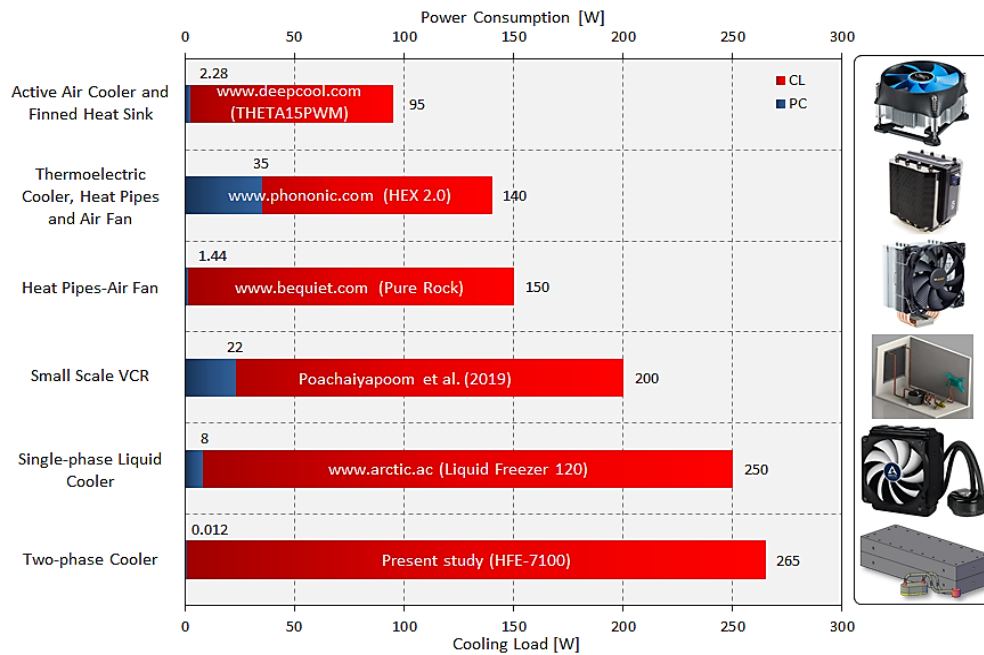


Figure 9.5 Comparison between the present thermal management system and other cooling techniques. CL: cooling load at evaporator, PC: power consumption.

study, their vapour compression refrigeration system consumed higher power than that in the present system for given cooling load. For example, at cooling load near 265 W, the vapour compression refrigeration system showed a COP of 2.5. This means that the power consumption by this system was 106 W, which is much higher than the present pumped loop system (0.012 W). In other words, flow boiling in a small-scale pumped loop cooling system requires low fluid flow rate and thus low power consumption.

Several previous studies in flow boiling of HFE-7100 or HFE-7000 were also compared with the present study as shown in Fig. 9.6. These studies were proposed for electronics cooling using a pumped loop system and different channel geometries, see Chapter 2, Section 2.3 for more details. Since the base area differed in these studies, the cooling load, instead of base heat flux, was calculated and presented in this comparison. This figure demonstrates that although high cooling load was dissipated by some studies (from 300 to 2254 W), high mass fluxes (more than $300 \text{ kg/m}^2\text{s}$) and/or very low inlet refrigerant temperatures were used. This result in high pressure drop and thus high pumping power could be required in these systems. Moreover, an extra cooling loop should be installed to achieve high inlet sub-cooling.

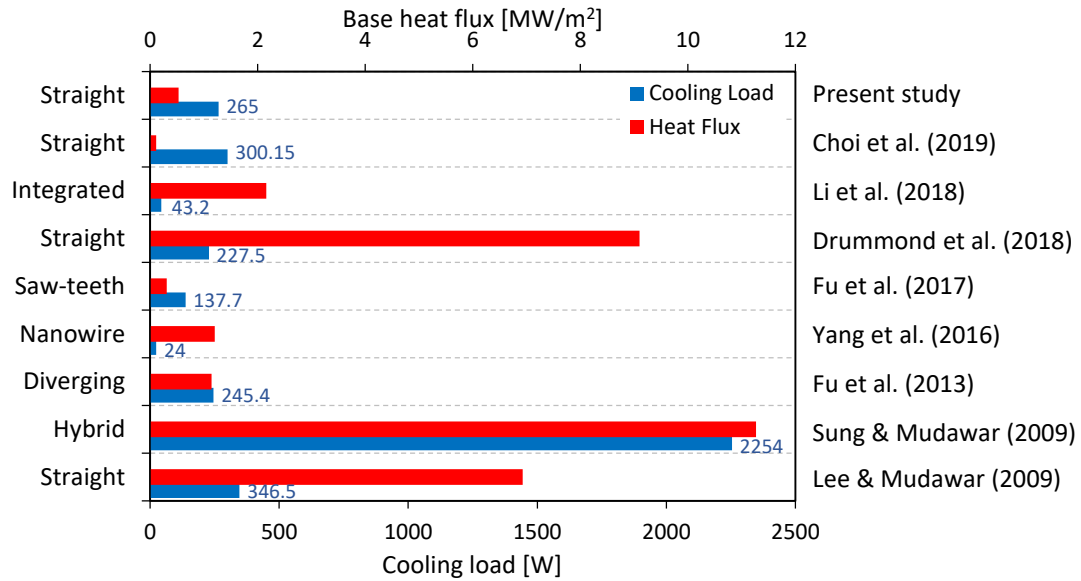


Figure 9.6 Comparison between the present system and other pumped loop systems for electronics cooling using HFE-refrigerants in different channel geometries.

For example, higher cooling load of 2254 W (11.27 MW/m^2) was reached by Sung and Mudawar (2009a) using HFE-7100 in hybrid cooling module, *i.e.* microchannels and circular micro jets. This value was dissipated at low inlet fluid temperature of $-20 \text{ }^\circ\text{C}$ and high pressure drop around 170 kPa. This figure also illustrates that the present system showed higher possible cooling load compared to the rest of the studies. Furthermore, lower pumping power was found compared to the study by Yang et al. (2016). They examined flow boiling of HFE-7000 in rectangular non-modified and modified channels (nanowire coated). The nanostructured results indicated that the cooling load was as high as 24 W, *i.e.* heat flux of 1.2 MW/m^2 at a base area of 20 mm^2 , when the mass flux was set at $2206 \text{ kg/m}^2\text{s}$, which required pumping power near 20 mW. This pumping power is much higher than that in the present system, which is 12 mW at 265 W cooling load.

Fig. 9.7 shows another comparison between the present results and the study by Olivier and Thome (2010). A simulation case study was performed by them on two-phase flow of different refrigerants and single-phase flow of water using multi-microchannels. These channels had 1.7 mm height and 0.17 mm width, *i.e.* channel hydraulic diameter of 0.31 mm. An Intel Xeon microprocessor with a chip footprint of $19.3 \text{ mm} \times 13.2 \text{ mm}$ was adopted in this simulation. They presented pumping

power versus base heat flux for a mass flux of $400 \text{ kg/m}^2\text{s}$. Therefore, the cooling load was calculated based on their base heat flux and chip footprint as shown in Fig. 9.7. This figure shows that, for a given cooling load of 265 W, two-phase flow of most refrigerants showed lower pumping power than that in single-phase flow due to the latent heat and low flow rates. Moreover, the pumping power of HFE-7100, in the present study, had lowest value compared to all fluids (single and two-phase flow). For instance, single-phase flow using 50% water-ethylene glycol mixture (EG) required a pumping power of around 18.9 mW, while this value reduced to 12 mW using two-phase flow of HFE-7100. The pumping power of the other refrigerants in two-phase flow varied from 16.3 to 21.4 mW for given cooling load and mass flux, which is higher than the refrigerant HFE-7100 in the present study. These differences could be due to the higher mass flux that was used in their simulation. For a given cooling load, *i.e.* 265 W, the pumping power ranges were found at a mass flux of $400 \text{ kg/m}^2\text{s}$ in their simulation, while this cooling load was dissipated at $250 \text{ kg/m}^2\text{s}$ during the present study.

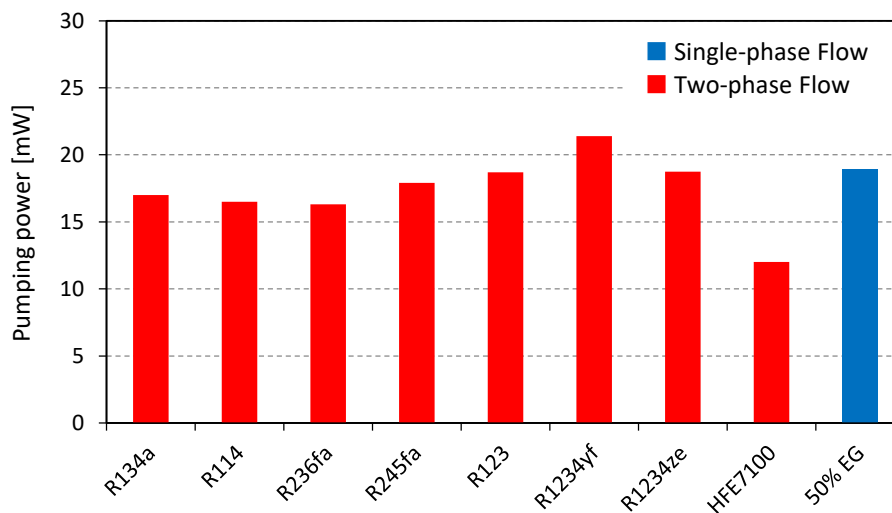


Figure 9.7 Pumping power for various fluids at a mass flux of $400 \text{ kg/m}^2\text{s}$, obtained from Olivier and Thome (2010). HFE-7100 result at mass flux of $250 \text{ kg/m}^2\text{s}$ from the present study. This figure was plotted at cooling load of 265 W.

It is worth mentioning that the present condenser can dissipate cooling capacity of 520.2 W, more details about the operating conditions are discussed in Section 9.4. Therefore, this condenser may also be used with multiple cooling points. In this system two microchannel evaporators are connected in parallel to a condenser and one micro pump as shown in Fig. 9.8. This cooling capacity requires total mass flow

rate of 0.0045 kg/s. The total measured pressure drop at the condenser is found to be 3 kPa. When two evaporators (TS.1) are assumed in this system, the total measured pressure drop is found to be 5.2 kPa at 247 W cooling load for each heat sink. By conducting the same approach described previously, the pumping power of this system is 48 mW at total dissipated cooling load of 494 W (for both evaporators).

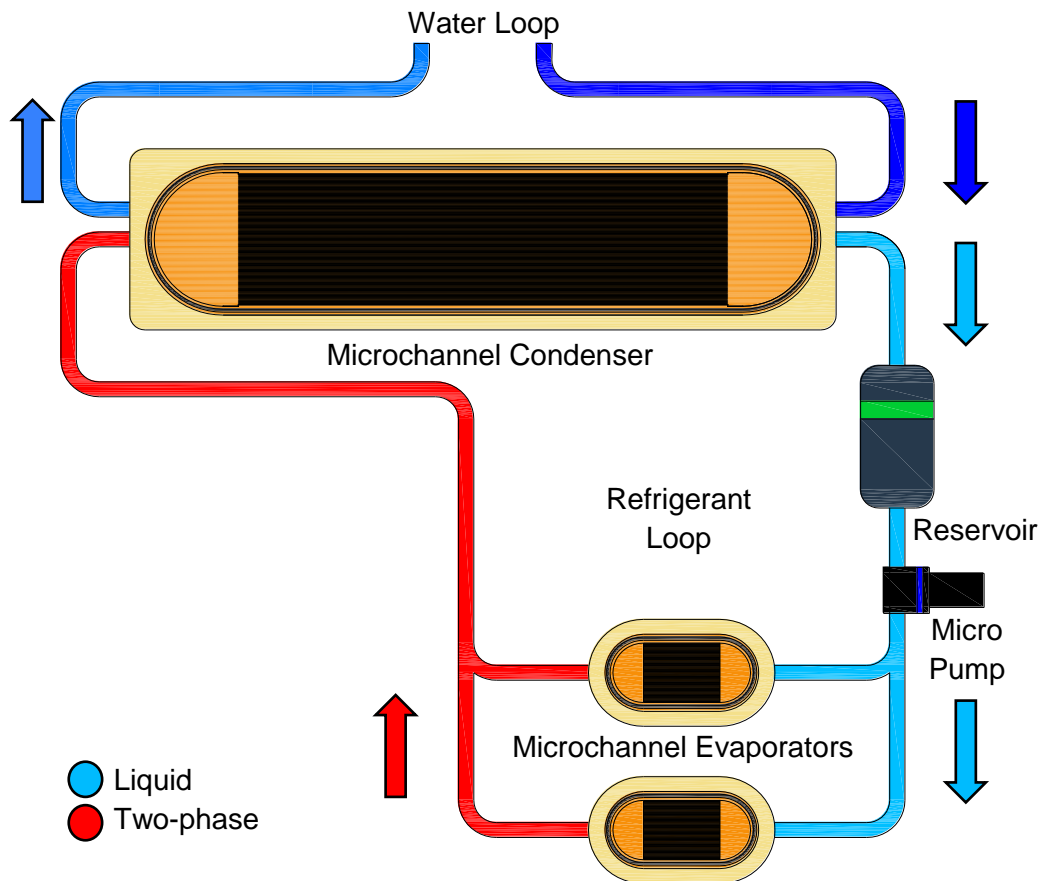


Figure 9.8 Small-scale pumped loop thermal management system with multiple cooling points.

The abovementioned discussion showed that two-phase flow of HFE-7100 in a small scale pumped loop system at atmospheric pressure, low sub-cooling and mass fluxes provides high cooling load and low pumping power. This cooling technique shows better thermal performance compared to other cooling techniques. Both microchannel evaporator and condenser in a real small-scale system should be further studied.

9.4 Upper Cooling Performance

From a design point of view, the maximum design limits of each evaporator and condenser should be specified. In the present study, the microchannel evaporator with aspect ratio of 0.5 (TS.1) could achieve maximum base heat flux up to 530 kW/m², corresponding to the hot chip area of 500 mm², *i.e.* cooling load of 265 W. The chipset temperature can be controlled up to 80 °C. Maximum flow boiling heat transfer coefficient reached by this heat sink was up to 11.25 kW/m²K at mass flux of 250 kg/m²s. The total pressure drop from the inlet to outlet plena was measured at 5.65 kPa.

The present microchannel condenser dissipated cooling capacity of 520.2 W at maximum mass flux of 126 kg/m²s, outlet sub-cooling of 3.5 K and total measured pressure drop of 3 kPa. The coolant side conditions were found at lower coolant flow rate of 0.5 L/min and standard inlet coolant temperature of 30 °C. This capacity at the condenser corresponds to a heat flux of 1 MW/m² for a chip die size of 20 mm × 25 mm (500 mm²), *i.e.* possible cooling capacity at the evaporator of an integrated thermal management system.

9.5 Summary

The performance of microchannel evaporator and condenser was experimentally investigated. The required pumping power was found to increase with increasing mass flux, cooling load and decreasing channel aspect ratio. The aluminum surface resulted in higher pumping power compared to copper. By assuming both evaporator and condenser as a part of small-scale thermal management system, this system showed more efficient than other cooling systems. Two-phase flow in microchannel configurations required low fluid flow rate and thus low pumping power. The present study demonstrated that it is possible to cool electronic components using two-phase flow in micro passages at system pressure near atmospheric and relatively low flow rates and pumping power. However, reducing condenser size is still required and remains a challenge for electronics cooling.

Chapter 10

Conclusions and Recommendations

10.1 Conclusions

In the present investigation, both flow boiling and condensation of HFE-7100 in multi-microchannels were studied. The effect of channel aspect ratio on the flow boiling heat transfer was examined. Three test sections made of copper having the same channel hydraulic diameter (0.46 mm), base area (500 mm²) and surface roughness (approximately near 0.3 μm) but different aspect ratios (0.5, 1 and 2) were manufactured. In addition to this, the material effect on the flow boiling heat transfer using two test sections was also conducted. Therefore, an aluminium heat sink with the same channel hydraulic diameter and aspect ratio of 1 was fabricated and tested. Effect of several parameters on the flow condensation was studied using counter-current flow condenser cooled by water. This microchannel condenser had channel hydraulic diameter of 0.57 mm, aspect ratio of 0.4 and surface roughness of 0.23 μm. Before conducting two-phase flow experiments, single-phase experiments were carried out to validate the experimental facility. Both calibration and degassing processes were carefully carried out to ensure high accuracy results. Local heat transfer calculations corresponding to the flow visualization was conducted. The experimental results were compared with some existing flow pattern maps, pressure drop and heat transfer correlations. These maps and correlations are available in the literature and proposed for conventional and microchannels. According to the present experimental results, several key findings can be presented as follows:

10.1.1 Flow boiling pattern characteristics

Flow visualization along the mid plane of the test section at three different locations, *i.e.* near the channel inlet, middle and outlet was carried out. This was conducted at a system pressure of 1 bar, mass flux of 50–250 kg/m²s, inlet sub-cooling of 5 K and exit vapour quality up to one. Main findings can be concluded from the flow visualization results:

1. Four flow patterns were observed during the experiments; bubbly, slug, churn and annular flow. Confined bubble was also identified during the present study, and it occurred for a short period of time.
2. When the heat flux increased gradually, the flow pattern changed from bubbly to slug flow, slug to churn flow and churn to annular flow. An increase in the heat flux led to increase the coalescence rate and vapour superficial velocity and thus different flow patterns occurred at specified location.
3. More nucleation sites were captured with increasing heat flux. Moreover, the size of these bubbles became larger when the heat flux increased. This could be due to the high bubble generation and more coalescence bubbles.
4. Few nucleating bubbles were found in the liquid film of slug and annular flow. These bubbles occurred at high heat fluxes when the wall superheat became high that led to activate these nucleation sites.
5. For a given heat flux, the flow pattern changed to the lower regime (inverse transition) with increasing mass flux. This could be due to the reduction in the evaporation rate with increasing fluid velocity.
6. When the channel aspect ratio decreased, larger bubbles were visualized. This could be due to the confinement effect and flow reversal. Slug ends were found to be more curved with bullet shape with decreasing aspect ratio. There were no clear differences in the annular flow for three different aspect ratios.
7. Insignificant effect of channel surface material on the experimental flow patterns was found.
8. At low wall heat fluxes, hysteresis effect became significant resulting in different flow patterns. This was attributed to the nucleation sites were still active with decreasing wall heat flux.
9. Flow reversal occurred for all test sections at all mass fluxes. This was attributed to the rapid bubble generation near the channel inlet and slug formation. The

cycle of flow reversal was found to be forward, stagnation period and backward motion, while the flow patterns were fluctuating between bubbly, confined bubble and slug flow.

10. The present data were compared with some existing flow pattern maps. The maps by Akbar et al. (2003), Revellin and Thome (2007a) and Choi et al. (2017) well predicted most data points of bubbly flow. Most data points of slug flow were predicted well by some maps. Moreover, some points of churn flow were predicted well by the existing maps. Most data points of annular flow were within the prediction region for these maps.
11. Generally, there was no existing flow patterns map that predicted all the experimental transition boundaries. This could be due to the different definition of flow patterns, different channel dimensions, number of channels (single or multi-channels), heated length, surface characteristics, thermophysical properties, operating conditions, flow reversal, instability and visualization location.
12. A universal flow patterns map using large database is still required. Local flow visualization along the entire heated length should be considered.

10.1.2 Flow boiling pressure drop characteristics

The flow boiling pressure drop data was obtained for four heat sinks at system pressure of 1 bar, mass flux ranging from 50 to 250 kg/m²s, inlet sub-cooling of 5 K and exit vapour quality up to one. The following key findings can be presented:

1. For a given mass flux, the flow boiling pressure drop increased with increasing heat flux due to the high coalescence rate and flow resistance.
2. The flow boiling pressure drop was found to increase with increasing mass flux for a given exit vapour quality. This was attributed to the high shear stress with increasing mass flux.
3. The flow boiling pressure drop increased with decreasing channel aspect ratio, *i.e.* by 48.6% from larger to smaller aspect ratio. Different exit vapour quality due to the different heat transfer area and different distribution of liquid film could lead to this difference in the pressure drop.

4. High flow boiling pressure drop was reached for aluminium surface compared to copper, *i.e.* by 28%. This could be due to the different surface microstructures that led to increase the frictional pressure drop component.
5. The present flow boiling pressure drop data was compared with eight existing correlations. This comparison showed that all the present data points were not predicted very well by most correlations. However, the correlations by Keepaiboon et al. (2016) and Gao et al. (2019) predicted the experimental data of all test sections with a reasonable accuracy, *i.e.* $MAE \leq 26\%$.
6. Large discrepancy among the existing pressure drop correlations could be due to the different fluids, operating conditions, channel dimensions and surface characteristics were examined. This affects the Chisholm constant in two-phase frictional multiplier (frictional pressure drop component) and the capability of the proposed correlation.

10.1.3 Flow boiling heat transfer characteristics

Four microchannel heat sinks were examined at the same experimental operating conditions. The following findings can be concluded:

1. Boiling incipience occurred at low heat fluxes (around 20 kW/m^2) for all test sections. Wall heat flux was found to increase with wall superheat. For all test sections, the effect of mass flux on the boiling curve was insignificant.
2. When the channel aspect ratio increased, a noticeable increase in the wall heat flux was identified for a given wall superheat.
3. Maximum base heat flux was found to increase with decreasing channel aspect ratio. This was attributed to the large surface enhancement. This can outweigh the benefits from the boiling heat transfer enhancement at larger channel aspect ratio. For given base heat flux, the smaller channel aspect ratio provided lower wall superheat.
4. At low wall heat fluxes, the material effect on the boiling curve was insignificant. In contrast, at moderate and high heat fluxes, aluminium surface had higher wall heat flux compared to copper surface. For given wall heat flux, lower wall superheat was found by aluminum compared to copper.
5. At low wall heat fluxes, hysteresis effect was significant. When the heat flux decreased, nucleation sites still activated at low wall heat fluxes.

6. For all test sections, flow reversal was found at all mass fluxes. The frequency and amplitude of the pressure drop signal increased with increasing wall heat flux, decreasing channel aspect ratio and with copper surface, which means more flow instability.
7. Maximum percentage of fluctuation of the measured parameters was 2.37%. This means that the experimental heat transfer results for the entire heat sink was not affected significantly by flow reversal.
8. Flow boiling heat transfer coefficient increased with increasing wall heat flux. At low heat fluxes, more active nucleation sites (at low qualities) and the increase in the liquid film evaporation rate (at moderate and high qualities) could be the reason for this increase. At moderate and high heat fluxes, this could be due to the contribution of liquid film evaporation and nucleation in the liquid film when the flow patterns were slug or annular.
9. High local heat transfer coefficient was found at boiling incipience and then decreased with increasing local vapour quality. At low and moderate heat fluxes, this was attributed to the reduction in local pressure along the channels. At high heat fluxes, the combined effect of the reduction in local pressure and increase in wall temperature along the channels could cause this reduction.
10. For given wall heat flux, the flow boiling heat transfer coefficient was not affected by mass flux.
11. For given wall heat flux, there was a noticeable increase in the heat transfer coefficient when the channel aspect ratio increased. This increase was found to be 14.3% from smaller to larger aspect ratio. This was attributed to the wide channel width could provide high nucleation site density and thinner liquid film thickness.
12. At low wall heat fluxes, there was insignificant effect of surface material on the heat transfer coefficient. In contrast, at moderate and high heat fluxes, the heat transfer coefficient increased by 12% when the surface was aluminium compared to copper. More nucleation site density and thinner liquid film thickness could lead to this enhancement due to the different surface microstructures.
13. The present heat transfer data was compared with twelve existing two-phase heat transfer correlations proposed for conventional and mini/microchannels. This comparison showed that some correlations showed large disagreement with the

present results with a MAE > 50%. The correlations for conventional channels such as Shah (1982), Kandlikar (1990) and Liu and Winterton (1991) showed good agreement with maximum MAE of 26%. The correlations for mini/microchannels, such as Mahmoud and Karayiannis (2013) and Li and Jia (2015), predicted the present data with a MAE ranging from 14% to 31%. For all test sections, the correlation by Shah (2017) predicted fairly the experimental data with a mean absolute error of 15–22%.

14. Different channel surface materials could result in different surface microstructures, *i.e.* number, shape and volume of peaks and valleys. Liquid film may be disturbed by surface peaks and became thinner due to the contact surface between peaks and fluid interface. Surface valleys may act as active cavities that generate more nucleating bubbles. Therefore, the number, shape and volume of these microstructures should be considered during two-phase flow.
15. For HFE-7100 at saturation pressure of 1 bar, the range of active cavity mouth radius was calculated using the correlation by Hsu (1962) and found to be 0.06–58 μm . At low wall superheat, only large cavities were active, while at high wall superheat, small cavities activated.
16. Since low mass fluxes were examined, surface tension became the prevalent force during the present data. Heat transfer results showed a significant dependence on the wall heat flux, while there was no mass flux effect. The inclusion of a contribution of nucleate boiling in some existing heat transfer correlations may lead to a reasonable agreement between the present data and these correlations.

10.1.4 Condensation flow pattern characteristics

Flow visualization along the channels was conducted using high-speed camera at a saturation temperature of 60 °C, refrigerant mass flux ranging from 48 to 126 $\text{kg/m}^2\text{s}$, coolant flow rate of 0.5–1.1 L/min and inlet coolant temperature of 20–40 °C. Main findings are summarized as follows:

1. Annular, slug and bubbly flow were visualized along the channels. These patterns occurred at different locations due to the condensation process. Neck region was found as a transition from annular to slug flow.

2. A sudden reduction in vapour slug length was visualized after the neck region. This could be due to the surface tension effect and condensation process. After that, this length decreased gradually due to the condensation process.
3. At high mass fluxes, annular flow was the prevalent regime, while at low mass fluxes, slug and bubbly flow were also found. At high mass fluxes, annular flow shifted along the channels due to the low condensation rate.
4. With decreasing inlet coolant temperature, the annular flow decreased along the channels and hence the appearance of slug and bubbly flow. This was attributed to an increase in the heat transfer rates.
5. The bubble size was found to decrease with increasing coolant flow rate due to high heat transfer rate.
6. The data points of annular flow were predicted well by the flow pattern maps of Cavallini et al. (2002) and Nema et al. (2014). In contrast, these maps were not able to predict all the data of slug and bubbly flow. Some points of annular flow were predicted by the map of Kim and Mudawar (2012). This map showed that the present data of slug and bubbly flow was within the slug region. The map by Zhuang et al. (2017) could predict some data points of annular flow.
7. There is no existing flow patterns map can predict all the experimental data points. Accordingly, a flow patterns map at low mass fluxes is still required.

10.1.5 Flow condensation heat transfer characteristics

Flow condensation heat transfer experiments were conducted at different operating conditions, as discussed in the previous section, using horizontal copper multi-microchannel condenser. The following findings can be concluded:

1. The heat transfer coefficient increased with increasing refrigerant mass flux. This was attributed to the reduction in the liquid film thickness and thermal resistance of fluid with increasing mass flux.
2. The heat transfer coefficient was found to decrease with decreasing local vapour quality due to the thicker liquid film thickness and higher fluid thermal resistance.
3. A negligible effect of the saturation-to-wall temperature difference, *i.e.* coolant side conditions, on the heat transfer coefficient was found.

4. The interfacial shear stress could be the dominant regime at this scale and with this particular fluid.
5. The conventional condensation heat transfer correlations by Dobson and Chato (1998) and Cavallini et al. (2006a) predicted the experimental results very well, *i.e.* with a MAE less than 20%.
6. The mini/micro scale heat transfer correlations by Kim and Mudawar (2013c) and Shah (2016) showed a reasonable agreement with the present data (MAE <20%).
7. The accuracy of the existing heat transfer correlations may differ due to the different fluids, operating conditions and channel geometries were examined.

10.1.6 Small-scale thermal management system

The thermal performance of both microchannel evaporator and condenser was experimentally investigated in this study. This is considered an important step to provide recommendations for industrial small-scale systems for cooling electronic components. In the present study, the operating conditions were kept at system pressure near atmospheric, low flow rates and low inlet sub-cooling to reduce the pumping power and the overall weight and size. According to Chapter 9 and all present experimental results, the major key findings can be concluded as follows:

1. Maximum heat rate that can be dissipated from the chipset was found to increase with decreasing channel aspect ratio due to the large surface enhancement. Reduction in the channel aspect ratio showed lower wall superheat at given base heat flux and higher pressure drop. Hence there is a compromise between higher possible base heat flux and increased two-phase pressure drop.
2. For a given heat flux, lower wall superheat was found for aluminium surface. The flow boiling pressure drop for aluminium heat sink was higher than copper, *i.e.* by 28%.
3. Maximum cooling load at the evaporator was reached up to 265 W, corresponds to a base heat flux of 530 kW/m^2 , at mass flux of $250 \text{ kg/m}^2\text{s}$ and working surface temperature near $80 \text{ }^\circ\text{C}$. This performance was found for the test section (1), *i.e.* channel aspect ratio of 0.5 using copper metal.
4. Maximum cooling load at the condenser was reached up to 520.2 W at mass flux of $126 \text{ kg/m}^2\text{s}$ and outlet sub-cooling of 3.5 K. The coolant side conditions were

set at lower coolant flow rate (0.5 L/min) and standard inlet coolant temperature (30 °C). This cooling load corresponds to the heat flux of 1 MW/m² at the evaporator for the base area of 500 mm².

5. The required pumping power increased with increasing mass flux, cooling load and decreasing channel aspect ratio. Aluminum surface showed higher pumping power compared to copper.
6. A comparison with other cooling techniques demonstrated that the present small-scale pumped loop cooling system was more efficient than these techniques. Lower pumping power by this system was found compared to others. Reducing condenser size is still challenge for cooling electronic components.
7. According to the overall experimental comparisons, the flow boiling heat transfer correlation by Shah (2017), the two-phase pressure drop correlation by Keepaiboon et al. (2016) and the condensation heat transfer correlation by Kim and Mudawar (2013c) or Shah (2016) showed a reasonable agreement with the experimental results. These correlations could be used to design such as this system at this micro scale and with this particular fluid. However, further investigations using higher mass fluxes are needed to evaluate these correlations.
8. According to the abovementioned findings, a heat sink with large surface enhancement (deeper channels and large number of channels) made of aluminium is recommended for electronics cooling that require high base heat fluxes.

10.2 Summary of Novel Contributions

The present experimental study provided several novel contributions to the research community. These contributions can be summarized as follows:

1. Effect of channel aspect ratio on the flow boiling heat transfer was studied. This was carried out using three test sections at the same channel hydraulic diameter and base area and nearly the same surface roughness. In some previous studies, the effect of channel aspect ratio was examined at different channel hydraulic diameters. Moreover, the surface roughness of these test sections was different in some previous studies and or not mentioned at all in others.
2. Effect of channel surface material on the flow boiling heat transfer was investigated using copper and aluminium. HFE-7100 in a horizontal aluminium multi-microchannel heat sink was not studied in the literature.
3. New experimental data of flow condensation heat transfer of HFE-7100 in multi-microchannels was examined. To the best of the author's knowledge, there are no data available in the literature for this fluid in single or multi-microchannels at low operating conditions.
4. The thermal performance of a small-scale pumped loop thermal management system was studied and compared with other cooling techniques. This system was recommended for electronics cooling using dielectric and eco-friendly refrigerant at system pressure near atmospheric, low flow rates and low inlet sub-cooling.
5. Several design recommendations were provided for industrial small-scale thermal management systems that could be used for electronics cooling, see Section 10.1.6 for more details.

10.3 Recommendations

According to the experimental work conducted in the present study, further work is still required. Main points can be recommended as follows:

1. Study the effect of channel aspect ratio on the flow boiling heat transfer using different aspect ratio ranges and working fluids at high mass fluxes, *i.e.* more than $250 \text{ kg/m}^2\text{s}$. The material effect should also be studied using other materials. High mass fluxes are also important to assess the dominant forces.
2. Design and examine the thermal performance of air-cooled microchannel condenser for high cooling capacity, *i.e.* more than 500 W.
3. Conduct flow condensation investigations using different channel dimensions, fluids and operating conditions. This is recommended to increase the cooling capacity and check the capability of two existing condensation heat transfer correlations, e.g. Dobson and Chato (1998) and Cavallini et al. (2006a), that were proposed for conventional channels. These two correlations predicted the present data with a reasonable agreement, and could be used for microchannels.
4. Study the aging effects, *i.e.* oxide layer, on the thermal performance by conducting several experiments for long period of time, *i.e.* after 1, 5 and 10 months.
5. Flow visualization should be carried out for the entire channel heated length. This helps to track the vapour bubble from the channel inlet until the exit, and thus more flow features could be captured and studied.
6. An infrared high-speed camera should be used to compute the nucleation sites density, *i.e.* the total number of nucleation sites divided by the heated surface area. Moreover, the liquid film thickness should be measured although this is difficult in metallic multi-channels.
7. A vacuum pump should be connected to the fluid reservoir to reduce the required time for degassing process and ensure a pure fluid without any trapped gases.
8. Design, build and examine the thermal performance of a small-scale pumped loop thermal management system for high heat fluxes, *i.e.* more than 1 MW/m^2 . Reducing condenser size should be considered in this design.
9. Surface microstructures, *i.e.* number and volume of peaks and valleys, should be considered and measured during two-phase flow experiments.

References

- 3M (2002) *3M NovecTM Engineered Fluid HFE-7100 for Heat Transfer*. Available at: www.3m.com/electronicmaterials.
- Abdou, M. A., Ying, A., Morley, N., Gulec, K., Smolentsev, S., Kotschenreuther, M., Malang, S., Zinkle, S., Rognlien, T., Fogarty, P., Nelson, B., Nygren, R., McCarthy, K., Youssef, M. Z., Ghoniem, N., Sze, D., Wong, C., Sawan, M., Khater, H., Woolley, R., Mattas, R., Moir, R., Sharafat, S., Brooks, J., Hassanein, A., Petti, D., Tillack, M., Ulrickson, M. and Uchimoto, T. (2001) 'On the exploration of innovative concepts for fusion chamber technology', *Fusion Engineering and Design*, 54(2), pp. 181–247.
- EL Achkar, G., Miscevic, M. and Lavieille, P. (2014) 'Experimental Study of Slug Flow for Condensation in a Square Cross-Section Micro-Channel at Low Mass Velocities', in *4th Micro and Nano Flows Conference (MNF2014)*. Brunel University London, pp. 7–10.
- Agarwal, A., Bandhauer, T. M. and Garimella, S. (2010) 'Measurement and modeling of condensation heat transfer in non-circular microchannels', *International Journal of Refrigeration*, 33(6), pp. 1169–1179.
- Agostini, B. and Bontemps, A. (2005) 'Vertical flow boiling of refrigerant R134a in small channels', *International Journal of Heat and Fluid Flow*, 26(2), pp. 296–306.
- Agostini, B., Watel, B., Bontemps, A. and Thonon, B. (2002) 'Friction factor and heat transfer coefficient of R134a liquid flow in mini-channels', *Applied Thermal Engineering*, 22, pp. 1821–1834.
- Akbar, M. K., Plummer, D. A. and Ghiaasiaan, S. M. (2003) 'On gas-liquid two-phase flow regimes in microchannels', *International Journal of Multiphase Flow*, 29, pp. 855–865.
- Akers, W. W., Deans, H. A. and Crosser, O. K. (1958) 'Condensing heat transfer within horizontal tubes', *Chem. Eng. Prog.*, 54, pp. 89–90.
- Al-Gaheeshi, A. M. (2018) *Flow Boiling in Vertical Small to Micro Scale Tubes*. Brunel University London (PhD thesis), London, UK.
- Al-Gaheeshi, A. M., Mahmoud, M. M. and Karayiannis, T. G. (2016) 'Flow boiling heat transfer in a vertical small-diameter tube: Effect of different fluids and surface characteristics', in *Proceedings of the 4th International Forum on Heat Transfer*. Sendai, Japan, pp. 1–9.
- Al-Hajri, E., Shooshtari, A. H., Dessiatoun, S. and Ohadi, M. M. (2013) 'Performance characterization of R134a and R245fa in a high aspect ratio microchannel condenser', *International Journal of Refrigeration*, 36(2), pp. 588–600.
- Alam, T., Lee, P. S. and Yap, C. R. (2013) 'Effects of surface roughness on flow boiling in silicon microgap heat sinks', *International Journal of Heat and Mass Transfer*, 64, pp. 28–41.

- Alam, T., Li, W., Yang, F., Chang, W., Li, J., Wang, Z., Khan, J. and Li, C. (2016) 'Force analysis and bubble dynamics during flow boiling in silicon nanowire microchannels', *International Journal of Heat and Mass Transfer*, 101, pp. 915–926.
- Ali, R., Palm, B. and Maqbool, M. H. (2012) 'Flow boiling heat transfer of refrigerants R134a and R245fa in a horizontal micro-channel', *Experimental Heat Transfer*, 25(3), pp. 181–196.
- ARCTIC (2016) *Liquid Freezer 360 | All-in-One CPU Cooler with Ultimate Performance*. Available at: https://www.arctic.ac/uk_en/liquid-freezer-360.html (Accessed: 4 February 2019).
- Balasubramanian, K., Jagirdar, M., Lee, P. S., Teo, C. J. and Chou, S. K. (2013) 'Experimental investigation of flow boiling heat transfer and instabilities in straight microchannels', *International Journal of Heat and Mass Transfer*, 66, pp. 655–671.
- Balasubramanian, K., Lee, P. S., Jin, L. W., Chou, S. K., Teo, C. J. and Gao, S. (2011) 'Experimental investigations of flow boiling heat transfer and pressure drop in straight and expanding microchannels – A comparative study', *International Journal of Thermal Sciences*, 50(12), pp. 2413–2421.
- Bao, Z. Y., Fletcher, D. F. and Haynes, B. S. (2000) 'Flow boiling heat transfer of Freon R11 and HCFC123 in narrow passages', *International Journal of Heat and Mass Transfer*, 43, pp. 3347–3358.
- Bell, S. (1999) *A Beginner's Guide to Uncertainty of Measurement, Measurement Good Practice Guide No. 11, NPL*.
- Benjamin, R. J. and Balakrishnan, A. R. (1997) 'Nucleation Site Density in Pool Boiling of Saturated Pure Liquids: Effect of Surface Microroughness and Surface and Liquid Physical Properties', *Experimental Thermal and Fluid Science*, 15(1), pp. 32–42.
- Benkheira, L., Souhar, M. and Baudouy, B. (2006) 'Heat and mass transfer in nucleate boiling regime of He I in a natural circulation loop', in *AIP Conference Proceedings*, pp. 871–878.
- Bertsch, S. S., Groll, E. A. and Garimella, S. V. (2008) 'Refrigerant flow boiling heat transfer in parallel microchannels as a function of local vapor quality', *International Journal of Heat and Mass Transfer*, 51, pp. 4775–4787.
- Bohdal, T., Charun, H. and Sikora, M. (2011) 'Comparative investigations of the condensation of R134a and R404A refrigerants in pipe minichannels', *International Journal of Heat and Mass Transfer*, 54, pp. 1963–1974.
- Borhani, N. and Thome, J. R. (2014) 'Intermittent dewetting and dryout of annular flows', *International Journal of Multiphase Flow*, 67, pp. 144–152.
- Bortolin, S., Da Riva, E. and Del Col, D. (2014) 'Condensation in a Square Minichannel: Application of the VOF Method', *Heat Transfer Engineering*, 35(2), pp. 193–203.
- Brauner, N. and Maron, D. M. (1992) 'Identification of the range of "small diameters" conduits, regarding two-phase flow pattern transitions', *International*

Communications in Heat and Mass Transfer, 19(1), pp. 29–39.

Candan, A., Markal, B., Aydin, O. and Avci, M. (2018) ‘Saturated flow boiling characteristics in single rectangular minichannels: effect of aspect ratio’, *Experimental Heat Transfer*, 31(6), pp. 531–551.

Cavallini, A., Censi, G., Del Col, D., Doretti, L., Longo, G. A. and Rossetto, L. (2002) ‘Condensation of halogenated refrigerants inside smooth tubes’, *HVAC and R Research*, 8(4), pp. 429–451.

Cavallini, A., Col, D. D., Doretti, L., Matkovic, M., Rossetto, L., Zilio, C. and Censi, G. (2006a) ‘Condensation in horizontal smooth tubes: A new heat transfer model for heat exchanger design’, *Heat Transfer Engineering*, 27(8), pp. 31–38.

Cavallini, A., Del Col, D., Doretti, L., Matkovic, M., Rossetto, L. and Zilio, C. (2005) ‘Condensation Heat Transfer and Pressure Gradient Inside Multiport Minichannels’, *Heat Transfer Engineering*, 26(3), pp. 45–55.

Cavallini, A., Doretti, L., Matkovic, M. and Rossetto, L. (2006b) ‘Update on condensation heat transfer and pressure drop inside minichannels’, *Heat Transfer Engineering*, 27(4), pp. 74–87.

Cavallini, A. and Zecchin, R. (1974) ‘Dimensionless correlation for heat transfer in forced convection condensation’, *Proc. Fifth Int. Heat Transfer*. Tokyo, Japan, 3, pp. 309–313.

Chen, J. C. (1966) ‘A correlation for boiling heat transfer to saturated fluids in convective flow’, *Ind. Eng. Chem.*, 5, pp. 322–329.

Chen, L. (2006) *Flow Patterns in Upward Two-Phase Flow in Small Diameter Tubes*.

Chen, L., Tian, Y. S. and Karayiannis, T. G. (2006) ‘The effect of tube diameter on vertical two-phase flow regimes in small tubes’, *International Journal of Heat and Mass Transfer*, 49(21–22), pp. 4220–4230.

Chen, S., Yang, Z., Duan, Y., Chen, Y. and Wu, D. (2014) ‘Simulation of condensation flow in a rectangular microchannel’, *Chemical Engineering and Processing: Process Intensification*, 76, pp. 60–69.

Chen, T. and Garimella, S. V. (2006a) ‘Effects of Dissolved Air on Subcooled Flow Boiling of a Dielectric Coolant in a Microchannel Heat Sink’, *Journal of Electronic Packaging*, 128(4), pp. 398–404.

Chen, T. and Garimella, S. V. (2006b) ‘Measurements and high-speed visualizations of flow boiling of a dielectric fluid in a silicon microchannel heat sink’, *International Journal of Multiphase Flow*, 32(8), pp. 957–971.

Chen, Y., Wu, J., Wu, R., Shi, M. and Peterson, G. P. (2009) ‘Visualization study of steam condensation in triangular microchannels’, *International Journal of Thermal Sciences*, 52(21), pp. 5122–5129.

Chisholm, D. (1967) ‘A theoretical basis for the Lockhart–Martinelli correlation for two-phase flow’, *International Journal of Heat Mass Transfer*, 10, pp. 1767–1778.

- Choi, C. W., Yu, D. I. and Kim, M. H. (2010) ‘Adiabatic two-phase flow in rectangular microchannels with different aspect ratios: Part II - Bubble behaviors and pressure drop in single bubble’, *International Journal of Heat and Mass Transfer*, 53(23–24), pp. 5242–5249.
- Choi, C. W., Yu, D. I. and Kim, M. H. (2011) ‘Adiabatic two-phase flow in rectangular microchannels with different aspect ratios: Part I - Flow pattern, pressure drop and void fraction’, *International Journal of Heat and Mass Transfer*, 54(1–3), pp. 616–624.
- Choi, E. J., Park, J. Y. and Kim, M. S. (2018) ‘A comparison of temperature distribution in PEMFC with single-phase water cooling and two-phase HFE-7100 cooling methods by numerical study’, *International Journal of Hydrogen Energy*, 43, pp. 13406–13419.
- Choi, E. J., Park, J. Y. and Kim, M. S. (2019) ‘Two-phase cooling using HFE-7100 for polymer electrolyte membrane fuel cell application’, *Applied Thermal Engineering*, 148, pp. 868–877.
- Choi, Y.-S., Lim, T.-W., You, S.-S. and Kim, H.-S. (2017) ‘Two-phase flow boiling heat transfer of FC-72 in parallel micro-channels’, *Experimental Heat Transfer*, 30(4), pp. 284–301.
- Del Col, D., Bortolato, M., Azzolin, M. and Bortolin, S. (2014) ‘Effect of inclination during condensation inside a square cross section minichannel’, *International Journal of Heat and Mass Transfer*. Elsevier Ltd, 78, pp. 760–777.
- Del Col, D., Bortolato, M., Azzolin, M. and Bortolin, S. (2015) ‘Condensation heat transfer and two-phase frictional pressure drop in a single minichannel with R1234ze(E) and other refrigerants’, *International Journal of Refrigeration*, 50(842), pp. 87–103.
- Del Col, D., Bortolin, S., Cavallini, A. and Matkovic, M. (2011) ‘Effect of cross sectional shape during condensation in a single square minichannel’, *International Journal of Heat and Mass Transfer*, 54(17–18), pp. 3909–3920.
- Del Col, D., Bortolin, S. and Da Riva, E. (2016) ‘Encyclopedia of two-phase heat transfer and flow: Special topics and applications_Prediction Methods and Numerical Modeling of Condensation Heat Transfer in Minichannels’, in. Singapore: World Scientific Publishing Co.
- Coleman, H. W. and Steele, W. G. (2009) *Experimentation and uncertainty analysis for engineers*. 3rd edn. New York: Wiley, Chichester.
- Coleman, J. W. and Garimella, S. (2003) ‘Two-phase flow regimes in round, square and rectangular tubes during condensation of refrigerant R 134a’, *International Journal of Refrigeration*, 26(1), pp. 117–128.
- Collier, J. G. and Thome, J. R. (1994) *Convective Boiling and Condensation*. third edit. Oxford, UK: Oxford University Press.
- Consolini, L. and Thome, J. R. (2009) ‘Micro-channel flow boiling heat transfer of R-134a, R-236fa, and R-245fa’, *Microfluidics and Nanofluidics*, 6(6), pp. 731–746.

- Cooper, M. G. (1984) 'Heat Flow Rates in Saturated Nucleate Pool Boiling-A Wide-Ranging Examination Using Reduced Properties', *Advances in Heat Transfer*, 16, pp. 157–239.
- Costa-Patry, E. and Thome, J. R. (2013) 'Flow pattern-based flow boiling heat transfer model for microchannels', *International Journal of Refrigeration*, 36(2), pp. 414–420.
- Deng, D., Wan, W., Shao, H., Tang, Y., Feng, J. and Zeng, J. (2015) 'Effects of operation parameters on flow boiling characteristics of heat sink cooling systems with reentrant porous microchannels', *Energy Conversion and Management*, 96, pp. 340–351.
- Díaz, M. C., Boye, H., Hapke, I., Schmidt, J., Staate, Y. and Zhekov, Z. (2006) 'Investigation of flow boiling in narrow channels by thermographic measurement of local wall temperatures', *Microfluidics and Nanofluidics*, 2(1), pp. 1–11.
- Dobson, M. K. and Chato, J. C. (1998) 'Condensation in smooth horizontal tubes', *Journal of Heat Transfer*, 120(1), pp. 193–213.
- Drummond, K. P., Back, D., Sinanis, M. D., Janes, D. B., Peroulis, D., Weibel, J. A. and Garimella, S. V. (2018) 'A hierarchical manifold microchannel heat sink array for high-heat-flux two-phase cooling of electronics', *International Journal of Heat and Mass Transfer*, 117, pp. 319–330.
- Eraghubi, M., Di Marco, P. and Robinson, A. J. (2019) 'Low Mass Flux Upward Vertical Forced Flow Boiling of HFE7000', *Experimental Thermal and Fluid Science*, 102, pp. 291–301.
- Fayyadh, E. M., Mahmoud, M. M., Sefiane, K. and Karayiannis, T. G. (2017) 'Flow boiling heat transfer of R134a in multi microchannels', *International Journal of Heat and Mass Transfer*, 110, pp. 422–436.
- Fly, A. (2015) *Thermal and water management of evaporatively cooled fuel cell vehicles*. Loughborough University (PhD thesis).
- Fronk, B. M. and Garimella, S. (2012) 'Heat transfer and pressure drop during condensation of ammonia in microchannels', in *ASME 3rd Micro/Nanoscale Heat and Mass Transfer International Conference*. Atlanta, GA.
- Fu, B.-R., Lee, C.-Y. and Pan, C. (2013) 'The effect of aspect ratio on flow boiling heat transfer of HFE-7100 in a microchannel heat sink', *International Journal of Heat and Mass Transfer*, 58(1–2), pp. 53–61.
- Fu, B. R., Chung, S. Y., Lin, W. J., Wang, L. and Pan, C. (2017) 'Critical heat flux enhancement of HFE-7100 flow boiling in a minichannel heat sink with saw-tooth structures', *Advances in Mechanical Engineering*, 9(2), pp. 1–10.
- Gao, Y., Feng, Y., Shao, S. and Tian, C. (2019) 'Two-phase pressure drop of ammonia in horizontal small diameter tubes: Experiments and correlation', *International Journal of Refrigeration*, 98, pp. 283–293.
- Goss, G., Oliveira, J. L. G. and Passos, J. C. (2015) 'Pressure drop during condensation of R 134a inside parallel microchannels', *International Journal of*

Refrigeration, 56, pp. 114–125.

Gottschalk, K. (2018) ‘IBM HPC Technology & Strategy’, in *Hyperion HPC User Forum Stuttgart*.

Haraguchi, H., Koyama, S. and Fujii, T. (1994) ‘Condensation of refrigerants HCFC22, HFC134a and HCFC123 in a horizontal smooth tube (2nd report, proposal of empirical expressions for the local heat transfer coefficient)’, *Trans JSME (B)*, 60(574), pp. 245–252.

Harirchian, T. and Garimella, S. V. (2008) ‘Microchannel size effects on local flow boiling heat transfer to a dielectric fluid’, *International Journal of Heat and Mass Transfer*, 51(15–16), pp. 3724–3735.

Harirchian, T. and Garimella, S. V. (2009a) ‘Effects of channel dimension, heat flux, and mass flux on flow boiling regimes in microchannels’, *International Journal of Multiphase Flow*, 35(4), pp. 349–362.

Harirchian, T. and Garimella, S. V. (2009b) ‘The critical role of channel cross-sectional area in microchannel flow boiling heat transfer’, *International Journal of Multiphase Flow*, 35(10), pp. 904–913.

Harirchian, T. and Garimella, S. V. (2010) ‘A comprehensive flow regime map for microchannel flow boiling with quantitative transition criteria’, *International Journal of Heat and Mass Transfer*, 53(13), pp. 2694–2702.

Harms, T. M., Kazmierczak, M. J. and Gerner, F. M. (1999) ‘Developing convective heat transfer in deep rectangular microchannels’, *International Journal of Heat and Fluid Flow*, 20(2), pp. 149–157.

Heo, J., Park, H. and Yun, R. (2013) ‘Condensation heat transfer and pressure drop characteristics of CO₂ in a microchannel’, *International Journal of Refrigeration-Revue Internationale Du Froid*, 32(6), pp. 1657–1668.

Hewitt, G. F. and Hall-Taylor, N. S. (1970) *Annular two-phase flow*. Pergamon Press, Oxford, UK.

Holcomb, B. T., Harirchian, T. and Garimella, S. V. (2009) ‘An Experimental Investigation of Microchannel Size Effects on Flow Boiling With De-Ionized Water’, in *Proceedings of the ASME 2009 Heat Transfer Summer Conference*. San Francisco, California USA, pp. 1–9.

Hosseini, R., Gholaminejad, A. and Nabil, M. (2011) ‘Concerning The Effect of Surface Material on Nucleate Boiling Heat Transfer of R-113’, *Journal of Electronics Cooling and Thermal Control*, 1(2), pp. 22–27.

Hsu, L. C., Cion, S. W., Lin, K. W. and Wang, C. C. (2015) ‘An experimental study of inclination on the boiling heat transfer characteristics of a micro-channel heat sink using HFE-7100’, *International Communications in Heat and Mass Transfer*, 62, pp. 13–17.

Hsu, Y. Y. (1962) ‘On the size range of active nucleation cavities on a heating surface’, *Journal of Heat Transfer*, 84, pp. 207–215.

Huang, H., Borhani, N. and Thome, J. R. (2016) 'Experimental investigation on flow boiling pressure drop and heat transfer of R1233zd(E) in a multi-microchannel evaporator', *International Journal of Heat and Mass Transfer*, 98, pp. 596–610.

Huang, H. and Thome, J. R. (2016) 'Local measurements and a new flow pattern based model for subcooled and saturated flow boiling heat transfer in multi-microchannel evaporators', *International Journal of Heat and Mass Transfer*. Elsevier Ltd, 103, pp. 701–714.

Huang, H. and Thome, J. R. (2017) 'An experimental study on flow boiling pressure drop in multi-microchannel evaporators with different refrigerants', *Experimental Thermal and Fluid Science*, 80, pp. 391–407.

Huh, C. and Kim, M. H. (2006) 'An experimental investigation of flow boiling in an asymmetrically heated rectangular microchannel', *Experimental Thermal and Fluid Science*, 30(8), pp. 775–784.

Huh, C. and Kim, M. H. (2007) 'Pressure Drop, Boiling Heat Transfer and Flow Patterns during Flow Boiling in a Single Microchannel', *Heat Transfer Engineering*, 28(8–9), pp. 730–737.

Illán-Gómez, F., López-Belchí, A., García-Cascales, J. R. and Vera-García, F. (2015) 'Experimental two-phase heat transfer coefficient and frictional pressure drop inside mini channels during condensation with R1234yf and R134a', *International Journal of Refrigeration-Revue Internationale Du Froid*, 51, pp. 12–23.

In, S. and Jeong, S. (2009) 'Flow boiling heat transfer characteristics of R123 and R134a in a micro-channel', *International Journal of Multiphase Flow*, 35(11), pp. 987–1000.

ITRS (2011) *International Technology Roadmap for Semiconductors (ITRS): System Drivers*, Semiconductor Industry Association. Available at: <https://www.semiconductors.org/resources/2011-international-technology-roadmap-for-semiconductors-itrs/>.

Jabardo, J. M. S., Ribatski, G. and Stelute, E. (2009) 'Roughness and surface material effects on nucleate boiling heat transfer from cylindrical surfaces to refrigerants R-134a and R-123', *Experimental Thermal and Fluid Science*, 33(4), pp. 579–590.

Jacobi, A. M. and Thome, J. R. (2002) 'Heat Transfer Model for Evaporation of Elongated Bubble Flows in Microchannels', *Journal of Heat Transfer*, 124(6), pp. 1131–1136.

Jafari, R., Okutucu-Özyurt, T., Ünver, H. Ö. and Bayer, Ö. (2016) 'Experimental investigation of surface roughness effects on the flow boiling of R134a in microchannels', *Experimental Thermal and Fluid Science*, 79, pp. 222–230.

Jiang, P. X., Fan, M. H., Si, G. S. and Ren, Z. P. (2001) 'Thermal Hydraulic Performance of Small Scale Micro-Channel and Porous-Media Heat Exchangers', *International Journal of Heat and Mass Transfer*, 44, pp. 1039–1051.

Jiang, R., Lan, Z., Hao, T., Zheng, Y., Wang, K., Yang, Y. and Ma, X. (2017) 'Two-phase flow patterns for condensation of ethanol-water mixtures in triangular

microchannels', *Applied Thermal Engineering*, 121, pp. 361–367.

Jiang, R., Ma, X., Lan, Z., Bai, Y. and Bai, T. (2015) 'Visualization study of condensation of ethanol–water mixtures in trapezoidal microchannels', *International Journal of Heat and Mass Transfer*. Elsevier Ltd, 90, pp. 339–349.

Jige, D., Inoue, N. and Koyama, S. (2016) 'Condensation of refrigerants in a multiport tube with rectangular minichannels', *International Journal of Refrigeration*, 67, pp. 202–213.

Jones, B. J. and Garimella, S. V. (2009) 'Surface Roughness Effects on Flow Boiling in Microchannels', *Journal of Thermal Science and Engineering Applications*, 1(4).

Jörg, J., Taraborrelli, S., Sarriegui, G., De Doncker, R. W., Kneer, R. and Rohlf, W. (2018) 'Direct single impinging jet cooling of a mosfet power electronic module', *IEEE Transactions on Power Electronics*, 33(5), pp. 4224–4237.

Junghans, J. (2011) *Development of Spray Cooling for High Heat Flux Electronics*. University of Arkansas (Master thesis).

Kadam, S. T. and Kumar, R. (2014) 'Twenty first century cooling solution: Microchannel heat sinks', *International Journal of Thermal Sciences*, 85, pp. 73–92.

Kaita, R. (2018) 'The Spherical Tokamak as a Compact Fusion Reactor Concept', in *ENN Symposium on Compact Fusion Technologies*. Langfang, China, pp. 1–37.

Kandlikar, S. G. (1990) 'A General Correlation for Saturated Two-Phase Flow Boiling Heat Transfer Inside Horizontal and Vertical Tubes', *Journal of Heat Transfer*, 112, p. 219.

Kandlikar, S. G. (2006) 'Nucleation characteristics and stability considerations during flow boiling in microchannels', *Experimental Thermal and Fluid Science*, 30(5), pp. 441–447.

Kandlikar, S. G. (2010) 'Scale effects on flow boiling heat transfer in microchannels: A fundamental perspective', *International Journal of Thermal Sciences*, 49(7), pp. 1073–1085. doi: 10.1016/j.ijthermalsci.2009.12.016.

Kandlikar, S. G. and Balasubramanian, P. (2005) 'An Experimental Study on the Effect of Gravitational Orientation on Flow Boiling of Water in 1054×197 μm Parallel Minichannels', *Journal of Heat Transfer*, 127(8), pp. 820–829.

Kandlikar, S. G. and Grande, W. J. (2003) 'Evolution of microchannel flow passages—thermo hydraulic performance and fabrication technology', *Heat Transfer Engineering*, 25(1), pp. 3–17.

Kandlikar, S. G. and Spiesman, P. H. (1997) 'Effect of surface characteristics on flow boiling heat transfer', in *Convective Flow and Pool Boiling Conference*. Isree, Germany.

Kandlikar, S. G. and Spiesman, P. H. (1998) 'Effect of Surface Finish on Flow Boiling Heat Transfer', *ASME Heat Transfer Div Publ HTD*, 361(1), pp. 157–163.

Karayiannis, T. G. and Mahmoud, M. M. (2017) 'Flow boiling in microchannels:

- Fundamentals and applications’, *Applied Thermal Engineering*, 115, pp. 1372–1397.
- Karayiannis, T. G., Mahmoud, M. M. and Kenning, D. B. R. (2012) ‘A study of discrepancies in flow boiling results in small to microdiameter metallic tubes’, *Experimental Thermal and Fluid Science*, 36, pp. 126–142.
- Karayiannis, T. G., Pike-Wilson, E. A., Chen, L., Mahmoud, M. and Tian., Y. (2014) ‘Flow Patterns and Comparison with Correlations for Vertical Flow Boiling of R245fa in Small to Micro Tubes’, *4th Micro and Nano Flows Conference UCL, London, UK*, (September), pp. 7–10.
- Karayiannis, T. G., Shiferaw, D. and Kenning, D. B. . (2008) ‘Saturated flow boiling in small- to micro- diameter metallic tubes: Experimental results and modeling’, in *Engineering Conferences International*.
- Kawaji, M. and Chung, P. M. Y. (2004) ‘Adiabatic gas-liquid flow in microchannels’, *Microscale Thermophysical Engineering*, 8(3), pp. 239–257.
- Keepaiboon, C., Thiangtham, P., Mahian, O., Dalkılıç, A. S. and Wongwises, S. (2016) ‘Pressure drop characteristics of R134a during flow boiling in a single rectangular micro-channel’, *International Communications in Heat and Mass Transfer*, 71, pp. 245–253.
- Kew, P. A. and Cornwell, K. (1997) ‘Correlations for the prediction of boiling heat transfer in small diameter channels’, *Applied Thermal Engineering*, 17, pp. 705–715.
- Kim, N., Sim, Y. and Min, C. (2004) ‘CONVECTIVE BOILING OF R-22 IN A FLAT EXTRUDED ALUMINUM MULTI-PORT TUBE’, in *Proceedings of ICM2004, The 2nd International Conference on Microchannels and Minichannels*. Rochester, New York, USA, pp. 1–7.
- Kim, S.-M. and Mudawar, I. (2013a) ‘Universal approach to predicting saturated flow boiling heat transfer in mini/micro-channels – Part II. Two-phase heat transfer coefficient’, *International Journal of Heat and Mass Transfer*, 64, pp. 1239–1256.
- Kim, S., Kim, J. and Mudawar, I. (2012) ‘Flow condensation in parallel micro-channels - Part 1: Experimental results and assessment of pressure drop correlations’, *International Journal of Heat and Mass Transfer*, 55(4), pp. 971–983.
- Kim, S. M. and Mudawar, I. (2013b) ‘Universal approach to predicting two-phase frictional pressure drop for mini/micro-channel saturated flow boiling’, *International Journal of Heat and Mass Transfer*, 58(1–2), pp. 718–734.
- Kim, S. M. and Mudawar, I. (2014) ‘Review of databases and predictive methods for heat transfer in condensing and boiling mini/micro-channel flows’, *International Journal of Heat and Mass Transfer*, 77, pp. 627–652.
- Kim, S. M. and Mudawar, I. (2017) ‘Thermal design and operational limits of two-phase micro-channel heat sinks’, *International Journal of Heat and Mass Transfer*, 106, pp. 861–876.
- Kim, S. and Mudawar, I. (2012) ‘Flow condensation in parallel micro-channels - Part 2: Heat transfer results and correlation technique’, *International Journal of Heat and Mass Transfer*, 55(4), pp. 984–994.

- Kim, S. and Mudawar, I. (2013c) 'Universal approach to predicting heat transfer coefficient for condensing mini/micro-channel flow', 56(2), pp. 238–250.
- Koşar, A., Kuo, C. and Peles, Y. (2006) 'Suppression of boiling flow oscillations in parallel microchannels by inlet restrictors', *Journal of Heat Transfer*, 128(3), p. 251.
- Koyama, S., Kuwahara, K. and Nakashita., K. (2003a) 'Condensation of refrigerant in a multi-port channel, International Conference on Microchannels and Minichannels', pp. 193–205.
- Koyama, S., Kuwahara, K., Nakashita, K. and Yamamoto, K. (2003b) 'An experimental study on condensation of refrigerant R134a in multi-port extruded tube', *International Journal of Refrigeration*, 26(4), pp. 425–432.
- Kureta, M., Kobayashi, T., Mishima, K. and Nishihara, H. (1998) 'Pressure Drop and Heat Transfer for Flow-Boiling of Water in Small-Diameter Tubes', *JSME International Journal*, 41(4), pp. 871–879.
- Lazarek, G. M. and Black, S. H. (1982) 'Evaporative heat transfer, pressure drop and critical heat flux in a small vertical tube with R-113', *International Journal of Heat and Mass Transfer*, 25(7), pp. 945–960.
- Lee, H. J. and Lee, S. Y. (2001) 'Heat transfer correlation for boiling flows in small rectangular horizontal channels with low aspect ratios', *International Journal of Multiphase Flow*, 27(12), pp. 2043–2062.
- Lee, J. and Mudawar, I. (2005) 'Two-phase flow in high-heat-flux micro-channel heat sink for refrigeration cooling applications: Part II - Heat transfer characteristics', *International Journal of Heat and Mass Transfer*, 48(5), pp. 941–955.
- Lee, J. and Mudawar, I. (2008a) 'Fluid flow and heat transfer characteristics of low temperature two-phase micro-channel heat sinks - Part 1: Experimental methods and flow visualization results', *International Journal of Heat and Mass Transfer*, 51(17–18), pp. 4315–4326.
- Lee, J. and Mudawar, I. (2008b) 'Fluid flow and heat transfer characteristics of low temperature two-phase micro-channel heat sinks - Part 2. Subcooled boiling pressure drop and heat transfer', *International Journal of Heat and Mass Transfer*, 51(17–18), pp. 4327–4341.
- Lee, J. and Mudawar, I. (2009) 'Critical heat flux for subcooled flow boiling in micro-channel heat sinks', *International Journal of Heat and Mass Transfer*, 52(13–14), pp. 3341–3352.
- Lee, P. and Garimella, S. V. (2008) 'Saturated flow boiling heat transfer and pressure drop in silicon microchannel arrays', *International Journal of Heat and Mass Transfer*, 51(3), pp. 789–806.
- Lee, P. S. and Garimella, S. V. (2006) 'Thermally developing flow and heat transfer in rectangular microchannels of different aspect ratios', *International Journal of Heat and Mass Transfer*, 49(17–18), pp. 3060–3067.
- Li, H. and Hrnjak, P. (2019) 'Flow visualization of R32 in parallel-port microchannel tube', *International Journal of Heat and Mass Transfer*, 128, pp. 1–11.

- Li, J. and Cheng, P. (2004) 'Bubble cavitation in a microchannel', *International Journal of Heat and Mass Transfer*, 47(12), pp. 2689–2698.
- Li, W., Ma, J., Alam, T., Yang, F., Khan, J. and Li, C. (2018) 'Flow boiling of HFE-7100 in silicon microchannels integrated with multiple micro-nozzles and reentry micro-cavities', *International Journal of Heat and Mass Transfer*, 123, pp. 354–366.
- Li, W. and Wu, Z. (2010a) 'A general correlation for adiabatic two-phase pressure drop in micro/mini-channels', *International Journal of Heat and Mass Transfer*, 53(13), pp. 2732–2739.
- Li, W. and Wu, Z. (2010b) 'A general correlation for evaporative heat transfer in micro/mini-channels', *International Journal of Heat and Mass Transfer*, 53(9), pp. 1778–1787.
- Li, X. and Hibiki, T. (2017) 'Frictional pressure drop correlation for two-phase flows in mini and micro multi-channels', *Applied Thermal Engineering*, 116, pp. 316–328.
- Li, X. and Jia, L. (2015) 'The investigation on flow boiling heat transfer of R134a in micro-channels', *Journal of Thermal Science*, 24(5), pp. 452–462.
- Liang, K., Li, Z., Chen, M. and Jiang, H. (2019) 'Comparisons between heat pipe, thermoelectric system, and vapour compression refrigeration system for electronics cooling', *Applied Thermal Engineering*, 146, pp. 260–267.
- Lim, T.-W., You, S.-S., Choi, J.-H. and Kim, H.-S. (2015) 'Experimental Investigation of Heat Transfer in Two-phase Flow Boiling', *Experimental Heat Transfer*, 28, pp. 23–36.
- Lin, S., Kew, P. A. and Cornwell, K. (2001) 'Flow boiling of refrigerant R141B in small tubes', *Chemical Engineering Research and Design*, 79(4), pp. 417–424.
- Liu, D., Lee, P. S. and Garimella, S. V. (2005) 'Prediction of the onset of nucleate boiling in microchannel flow', *International Journal of Heat and Mass Transfer*, 48(25), pp. 5134–5149.
- Liu, D. and Yu, L. (2011) 'Single-Phase Thermal Transport of Nanofluids in a Minichannel', *Journal of Heat Transfer*, 133(3), p. 31009.
- Liu, N., Li, J. M., Sun, J. and Wang, H. S. (2013) 'Heat transfer and pressure drop during condensation of R152a in circular and square microchannels', *Experimental Thermal and Fluid Science*, 47, pp. 60–67.
- Liu, Z. and Winterton, R. H. S. (1991) 'A general correlation for saturated and subcooled flow boiling in tubes and annuli, based on a nucleate pool boiling equation', *International Journal of Heat Mass Transfer*, 34, pp. 2759–2766.
- Lockhart, R. W. and Martinelli, R. C. (1949) 'Proposed Correlation of Data for Isothermal Two-Phase, Two-Component Flow in Pipes', *Chemical Engineering Progress*, pp. 39–48.
- Lu, C. T. and Pan, C. (2008) 'Stabilization of flow boiling in microchannel heat sinks with a diverging cross-section design', *Journal of Micromechanics and Microengineering*, 18(7), p. 075035.

- Ma, X., Fan, X., Lan, Z. and Hao, T. (2011) 'Flow patterns and transition characteristics for steam condensation in silicon microchannels', *Journal of Micromechanics and Microengineering*, 21(7), p. 075009.
- Madhour, Y., Olivier, J., Costa-Patry, E., Paredes, S., Michel, B. and Thome, J. R. (2011) 'Flow boiling of R134a in a multi-microchannel heat sink with hotspot heaters for energy-efficient microelectronic CPU cooling applications', *IEEE Transactions on Components, Packaging and Manufacturing Technology*, 1(6), pp. 873–883.
- Mahmoud, M. (2011) *Flow boiling of R134a in vertical mini-diameter tubes*. Brunel University London (PhD thesis), London, UK.
- Mahmoud, M. M. and Karayiannis, T. G. (2013) 'Heat transfer correlation for flow boiling in small to micro tubes', *International Journal of Heat and Mass Transfer*, 66, pp. 553–574.
- Mahmoud, M. M. and Karayiannis, T. G. (2016a) 'Flow pattern transition models and correlations for flow boiling in mini-tubes', *Experimental Thermal and Fluid Science*, 70, pp. 270–282.
- Mahmoud, M. M. and Karayiannis, T. G. (2016b) 'Performance of a Micro Scale Integrated Thermal Management System', in *5th Micro and Nano Flows Conference*. Milan, Italy, pp. 1–2.
- Mahmoud, M. M. and Karayiannis, T. G. (2018) 'Flow Boiling in Mini to Micro Diameter Channels', in John R. Thome (ed.) *Encyclopaedia of Two-Phase Heat Transfer and Flow III*. World Scientific Publishers.
- Mahmoud, M. M., Karayiannis, T. G. and Kenning, D. B. R. (2014) 'Flow boiling pressure drop of R134a in microdiameter tubes: Experimental results and assessment of correlations', *Heat Transfer Engineering*, 35(2), pp. 178–192.
- Mahmoudi, S. R., Adamiak, K. and Castle, G. S. P. (2014) 'Flattening of boiling curves at post-CHF regime in the presence of localized electrostatic fields', *International Journal of Heat and Mass Transfer*, 68, pp. 203–210.
- Maqbool, M. H., Palm, B. and Khodabandeh, R. (2012) 'Boiling heat transfer of ammonia in vertical smooth mini channels: Experimental results and predictions', *International Journal of Thermal Sciences*, 54, pp. 13–21.
- Markal, B., Aydin, O. and Avci, M. (2016a) 'An experimental investigation of saturated flow boiling heat transfer and pressure drop in square microchannels', *International Journal of Refrigeration*, 65, pp. 1–11.
- Markal, B., Aydin, O. and Avci, M. (2016b) 'Effect of aspect ratio on saturated flow boiling in microchannels', *International Journal of Heat and Mass Transfer*, 93, pp. 130–143.
- Markal, B., Aydin, O. and Avci, M. (2017a) 'Prediction of Heat Transfer Coefficient in Saturated Flow Boiling Heat Transfer in Parallel Rectangular Microchannel Heat Sinks: An Experimental Study', *Heat Transfer Engineering*. Taylor & Francis, 38(16), pp. 1415–1428.

- Markal, B., Aydin, O. and Avci, M. (2017b) 'Prediction of Pressure Drop for Flow Boiling in Rectangular Multi-Microchannel Heat Sinks', *Heat Transfer Engineering*, 0(0), pp. 1–13.
- Martin-Callizo, C., Ali, R. and Palm, B. (2007) 'New experimental results on flow boiling of R-134a in a vertical microchannel', in *UK. Heat Transfer Conference Proceedings*. Edinburgh.
- Mastrullo, R., Mauro, A. W., Thome, J. R., Vanoli, G. P. and Viscito, L. (2016) 'Critical heat flux: Performance of R1234yf, R1234ze and R134a in an aluminum multi-minichannel heat sink at high saturation temperatures', *International Journal of Thermal Sciences*, 106, pp. 1–17.
- Mastrullo, R., Mauro, A. W. and Viscito, L. (2017) 'Experimental CHF for low-GWP fluids and R134a. Effect of the Lh/D ratio at low and high mass velocities', *International Journal of Heat and Mass Transfer*, 109, pp. 1200–1216.
- Matkovic, M., Bortolin, S., Cavallini, A. and Del Col, D. (2009a) 'Experimental study of condensation inside a horizontal single square minichannel', in *ASME 2nd Micro/Nanoscale Heat and Mass Transfer International Conference*. China.
- Matkovic, M., Cavallini, A., Col, D. Del and Rossetto, L. (2009b) 'Experimental study on condensation heat transfer inside a single circular minichannel', *International Journal of Heat and Mass Transfer*, 52(9), pp. 2311–2323.
- Mehendale, S. S., Jacobi, A. M. and Shah, R. K. (2000) 'Fluid flow and heat transfer at micro and meso scale with application to heat exchanger design', *Applied Mechanics Reviews*, 53(7), pp. 175–193.
- Miner, M. J., Odom, B. A., Phelan, P. E. and Ortiz, C. A. (2014) 'An experimental investigation of pressure drop in expanding microchannel arrays', *Journal of Heat Transfer*, 136(3), p. 031502.
- Mirmanto, M. (2013) *Single-phase flow and flow boiling of water in horizontal rectangular microchannels*. Brunel University London (PhD thesis), London, UK.
- Mirmanto, M. (2016) 'Local pressure measurements and heat transfer coefficients of flow boiling in a rectangular microchannel', *Heat and Mass Transfer*, 52, pp. 73–83.
- Mishima, K. and Hibiki, T. (1995) 'Effect of inner diameter on some characteristics of air-water two-phase flows in capillary tubes', *Trans JSME (B)*, 61(589), pp. 99–106.
- Mishima, K. and Hibiki, T. (1996) 'Some characteristics of air-water two-phase flow in small diameter vertical tubes', *International Journal of Multiphase Flow*, 22(4), pp. 703–712.
- Mohanty, R. L. and Das, M. K. (2017) 'A critical review on bubble dynamics parameters influencing boiling heat transfer', *Renewable and Sustainable Energy Reviews*, 78, pp. 466–494.
- Moser, K. W., Webb, R. L. and B. Na (1998) 'A new equivalent Reynolds number model for condensation in smooth tubes', *ASME J. Heat Transfer*, 120, pp. 410–7.

- Mr3D (2011) *Project Tatami (mATX computer case from scratch)*, *bit-tech.net*. Available at: <https://forums.bit-tech.net/index.php?threads/mr3d-project-tatami-matx-computercase-from-scratch.282503/page-10> (Accessed: 29 January 2019).
- Muller-Steinhagen, H. and Heck, K. (1986) ‘A Simple Friction Pressure Drop Correlation for Two-Phase Flow in Pipes’, *Chem. Eng. Process.*, 20, pp. 297–308.
- Muszynski, T. and Mikielwicz, D. (2016) ‘Comparison of heat transfer characteristics in surface cooling with boiling microjets of water, ethanol and HFE7100’, *Applied Thermal Engineering*, 93, pp. 1403–1409.
- Nema, G., Garimella, S. and Fronk, B. M. (2014) ‘Flow regime transitions during condensation in microchannels’, *International Journal of Refrigeration*, 40, pp. 227–240.
- Nilsson, V. (2017) *Development of a Mathematical Model for the Cooling of an Electric Car Battery*. Chalmers University of Technology (M.Sc. thesis).
- Oh, H.-K. and Son, C.-H. (2011) ‘Flow boiling heat transfer and pressure drop characteristics of CO₂ in horizontal tube of 4.57-mm inner diameter’, *Applied Thermal Engineering*, 31, pp. 163–172.
- Ohadi, M. and Qi, J. (2005) ‘Thermal management of harsh-environment electronics’, *Microscale Heat Transfer Fundamentals and Applications*. Springer, pp. 479–498.
- Olivier, J. A. and Thome, J. R. (2010) ‘Two-Phase Cooling of Electronics with Multi-Microchannel Evaporators’, in *NATO: AVT-178 specialists’ meeting on system level thermal management for enhanced platform efficiency*. Bucarest, Romania.
- Ong, C. L. and Thome, J. R. (2011a) ‘Macro-to-microchannel transition in two-phase flow: Part 1 - Two-phase flow patterns and film thickness measurements’, *Experimental Thermal and Fluid Science*, 35(1), pp. 37–47.
- Ong, C. L. and Thome, J. R. (2011b) ‘Macro-to-microchannel transition in two-phase flow: Part 2 - Flow boiling heat transfer and critical heat flux’, *Experimental Thermal and Fluid Science*, 35(6), pp. 873–886.
- Özdemir, M. R. (2016) *Single – Phase Flow and Flow Boiling of Water in Rectangular Metallic Microchannels*. Brunel University London (PhD thesis), London, UK.
- Özdemir, M. R., Mahmoud, M. M. and Karayiannis, T. G. (2019) ‘Flow Boiling of Water in a Rectangular Metallic Microchannel’, *submitted to Heat Transfer Engineering*, pp. 1–26.
- Park, J. E., Vakili-Farahani, F., Consolini, L. and Thome, J. R. (2011) ‘Experimental study on condensation heat transfer in vertical minichannels for new refrigerant R1234ze(E) versus R134a and R236fa’, *Experimental Thermal and Fluid Science*, 35(3), pp. 442–454.
- Peng, X. F., Hu, H. Y. and Wang, B. X. (1998) ‘Flow boiling through v-shape microchannels’, *Experimental Heat Transfer*, 11(1), pp. 87–100.

- Peng, X. F. and Peterson, G. P. (1996) 'Convective heat transfer and flow friction for water flow in microchannel structures', *International Journal of Heat and Mass Transfer*, 39(12), pp. 2599–2608.
- Pettersen, J. (2004) 'Flow vaporization of CO₂ in microchannel tubes', *Experimental Thermal and Fluid Science*, 28(2–3), pp. 111–121.
- Phillips, R. J. (1988) *Forced Convection, Liquid Cooled, Microchannel Heat Sinks*. Cambridge.
- Pike-Wilson, E. A. (2014) *Flow boiling of R245fa in vertical small metallic tubes*. Brunel University London (PhD thesis), London, UK.
- Pike-Wilson, E. A. and Karayiannis, T. G. (2014) 'Flow boiling of R245fa in 1.1mm diameter stainless steel, brass and copper tubes', *Experimental Thermal and Fluid Science*. Elsevier Inc., 59, pp. 166–183.
- Pizzarelli, M. (2017) *Regenerative cooling of liquid rocket engine thrust chambers*. Available at: https://www.researchgate.net/publication/321314974_Regenerative_cooling_of_liquid_rocket_engine_thrust_chambers.
- Poachaiyapoom, A., Leardkun, R. and Mounkong, J. (2019) 'Miniature vapor compression refrigeration system for electronics cooling', *Case Studies in Thermal Engineering*, 13, p. 100365.
- Qian, C., Gheitaghy, A. M., Fan, J., Tang, H., Sun, B., Ye, H. and Zhang, G. (2018) 'Thermal Management on IGBT Power Electronic Devices and Modules', *IEEE Access*, 6, pp. 12868–12884.
- Qu W. (2013) 'Two-phase cross-connected micro-channel heat sink'. United States Patent US 2013/8479806B2.
- Qu, W. and Mudawar, I. (2002) 'Prediction and measurement of incipient boiling heat flux in micro-channel heat sinks', *International Journal of Heat and Mass Transfer*, 45(19), pp. 3933–3945.
- Qu, W. and Mudawar, I. (2003a) 'Flow boiling heat transfer in two-phase micro-channel heat sinks-I. Experimental investigation and assessment of correlation methods', *International Journal of Heat and Mass Transfer*, 46(15), pp. 2755–2771.
- Qu, W. and Mudawar, I. (2003b) 'Measurement and prediction of pressure drop in two-phase micro-channel heat sinks', *International Journal of Heat and Mass Transfer*, 46(15), pp. 2737–2753.
- Qu, W. and Mudawar, I. (2004) 'Transport Phenomena in Two-Phase Micro-Channel Heat Sinks', *Journal of Electronic Packaging*, 126, pp. 213–224.
- Qu, W. and Mudawar, I. (2005) 'A systematic methodology for optimal design of two-phase micro channel heat sinks', *Journal of Electronic Packaging*, 127(4), p. 381.
- Rahman, M. M., Kariya, K. and Miyara, A. (2018) 'An experimental study and development of new correlation for condensation heat transfer coefficient of

refrigerant inside a multiport minichannel with and without fins’, *International Journal of Heat and Mass Transfer*, 116, pp. 50–60.

Remsburg, R. (2001) *Thermal design of electronic equipment*, Boca Raton, Fla.: CRC Press.

Revellin, R. and Thome, J. R. (2007a) ‘A new type of diabatic flow pattern map for boiling heat transfer in microchannels’, *Journal of Micromechanics and Microengineering*, 17(4), pp. 788–796.

Revellin, R. and Thome, J. R. (2007b) ‘Experimental investigation of R-134a and R-245fa two-phase flow in microchannels for different flow conditions’, *International Journal of Heat and Fluid Flow*, 28, pp. 63–71.

Da Riva, E. and Del Col, D. (2012) ‘Numerical simulation of laminar liquid film condensation in a horizontal circular minichannel’, *Journal of Heat Transfer*, 134(5), p. 051019.

Da Riva, E., Del Col, D., Garimella, S. V. and Cavallini, A. (2012) ‘The importance of turbulence during condensation in a horizontal circular minichannel’, *International Journal of Heat and Mass Transfer*, 55(13), pp. 3470–3481.

Rodriguez, V., Sukumaran, J., Ando, M. and De Baets, P. (2011) ‘Roughness Measurement Problems in Tribological Testing’, in *Sustainable Construction and Design (SCAD)*. Ghent University, Laboratory Soete, pp. 115–121.

Safran (2011) *Space propulsion Vulcain 2*. Available at: www.snecma.com.

Sakamatapan, K. and Wongwises, S. (2014) ‘Pressure drop during condensation of R134a flowing inside a multiport minichannel’, *International Journal of Heat and Mass Transfer*, 75, pp. 31–39.

Sempértegui-Tapia, D. F. and Ribatski, G. (2017) ‘Flow boiling heat transfer of R134a and low GWP refrigerants in a horizontal micro-scale channel’, *International Journal of Heat and Mass Transfer*, 108, pp. 2417–2432.

Sempértegui-tapia, D. and Ribatski, G. (2015) ‘The effect of the cross-sectional geometry on saturated flow boiling heat transfer in horizontal micro-scale channels’, in *IV Journeys in Multiphase Flows (JEM 2015)*. Brazil.

Shah, M. M. (1979) ‘A general correlation for heat transfer during film condensation inside pipes’, *International Journal of Heat and Mass Transfer*, 22(4), pp. 547–556.

Shah, M. M. (1982) ‘Chart correlation for saturated boiling heat transfer: equations and further study’, *ASHRAE Transactions*, 88(1), pp. 185–196.

Shah, M. M. (2013) ‘General correlation for heat transfer during condensation in plain tubes: further development and verification’, *ASHRAE Trans*, 119(2), pp. 3–11.

Shah, M. M. (2016) ‘A correlation for heat transfer during condensation in horizontal mini/micro channels’, *International Journal of Refrigeration*, 64, pp. 187–202.

Shah, M. M. (2017) ‘Unified correlation for heat transfer during boiling in plain mini/micro and conventional channels’, *International Journal of Refrigeration*, 74,

pp. 606–626.

Shah, R. K. and London, A. L. (1978) *Laminar flow forced convection in ducts, Supplement 1 to Advances in Heat Transfer*. Academic Press New York.

Shah, R. K. and Sekulić, D. P. (2003) ‘Fundamentals of Heat Exchanger Design’, *John Wiley & Sons Inc.*

Shiferaw, D., Karayiannis, T. G. and Kenning, D. B. R. (2009) ‘Flow boiling in a 1.1 mm tube with R134a: Experimental results and comparison with model’, *International Journal of Thermal Sciences*, 48(2), pp. 331–341.

Singh, S. G., Bhide, R. R., Duttagupta, S. P., Puranik, B. P. and Agrawal, A. (2009) ‘Two-phase flow pressure drop characteristics in trapezoidal silicon microchannels’, *IEEE Transactions on Components and Packaging Technologies*, 32(4), pp. 887–900.

Singh, S. G., Kulkarni, A., Duttagupta, S. P., Puranik, B. P. and Agrawal, A. (2008) ‘Impact of aspect ratio on flow boiling of water in rectangular microchannels’, *Experimental Thermal and Fluid Science*, 33(1), pp. 153–160.

Sobierska, E., Kulenovic, R., Mertz, R. and Groll, M. (2006) ‘Experimental results of flow boiling of water in a vertical microchannel’, *Experimental Thermal and Fluid Science*, 31, pp. 111–119.

Soupremanien, U., Person, S. Le, Favre-Marinet, M. and Bultel, Y. (2011) ‘Influence of the aspect ratio on boiling flows in rectangular mini-channels’, *Experimental Thermal and Fluid Science*, 35, pp. 797–809.

Souza, R. R., Passos, J. C. and Cardoso, E. M. (2014) ‘Influence of nanoparticle size and gap size on nucleate boiling using HFE7100’, *Experimental Thermal and Fluid Science*, 59, pp. 195–201.

Stephan, K. and Preuber, P. (1979) ‘Warmeübergang und Maximale Warmestromdichte Beim Behaltersieden Binarer und Ternärer Flüssigkeitsgemische’, *Chem. Ing. Tech.*, 51, p. 37.

Sumith, B., Kaminaga, F. and Matsumura, K. (2003) ‘Saturated flow boiling of water in a vertical small diameter tube’, *Experimental Thermal and Fluid Science*, 27(7), pp. 789–801.

Sun, L. and Mishima, K. (2009) ‘An evaluation of prediction methods for saturated flow boiling heat transfer in mini-channels’, *International Journal of Heat and Mass Transfer*, 52, pp. 5323–5329.

Sung, M. K. and Mudawar, I. (2008) ‘Single-phase and two-phase cooling using hybrid micro-channel/slot-jet module’, *International Journal of Heat and Mass Transfer*, 51(15–16), pp. 3825–3839.

Sung, M. K. and Mudawar, I. (2009a) ‘CHF determination for high-heat flux phase change cooling system incorporating both micro-channel flow and jet impingement’, *International Journal of Heat and Mass Transfer*, 52(3–4), pp. 610–619.

Sung, M. K. and Mudawar, I. (2009b) ‘Single-Phase and Two-Phase Hybrid Cooling

- Schemes for High-Heat-Flux Thermal Management of Defense Electronics’, *Journal of Electronic Packaging*, (2), pp. 121–131.
- Suriyawong, A. and Wongwises, S. (2010) ‘Nucleate pool boiling heat transfer characteristics of TiO₂-water nanofluids at very low concentrations’, *Experimental Thermal and Fluid Science*, 34(8), pp. 992–999.
- Tamanna, A. and Lee, P. S. (2015) ‘Flow boiling instability characteristics in expanding silicon microgap heat sink’, *International Journal of Heat and Mass Transfer*, 89, pp. 390–405.
- Tesla (2017) *EVTX Monitor/Controller For Tesla Model S Battery Modules*. Version 1.
- Thiangtham, P., Keepaiboon, C., Kiatpachai, P., Asirvatham, L. G., Mahian, O., Dalkilic, A. S. and Wongwises, S. (2016) ‘An experimental study on two-phase flow patterns and heat transfer characteristics during boiling of R134a flowing through a multi-microchannel heat sink’, *International Journal of Heat and Mass Transfer*. Elsevier Ltd, 98, pp. 390–400.
- Thome, J. R. and Cioncolini, A. (2016) ‘Unified Modeling Suite for Two-Phase Flow, Convective Boiling, and Condensation in Macro-and Microchannels’, *Heat Transfer Engineering*, 37(13–14), pp. 1148–1157.
- Thome, J. R. and Cioncolini, A. (2017) *Flow Boiling in Microchannels*, *Advances in Heat Transfer*. Elsevier Inc.
- Tibiriçá, C. B. and Ribatski, G. (2011) ‘Two-phase frictional pressure drop and flow boiling heat transfer for R245fa in a 2.32-mm tube’, *Heat Transfer Engineering*, 32(13–14), pp. 1139–1149.
- Tibiriçá, C. B. and Ribatski, G. (2015) ‘Flow Boiling Phenomenological Differences Between Micro- and Macroscale Channels’, *Heat Transfer Engineering*, 36(11), pp. 937–942.
- Tong, W., Bergles, A. E. and Jensen, M. K. (1997) ‘Pressure drop with highly subcooled flow boiling in small-diameter tubes’, *Experimental Thermal and Fluid Science*, 15(3), pp. 202–212.
- TOP500 (2018) *TOP500 Supercomputer Sites*. Available at: <https://www.top500.org/lists/2018/11/> (Accessed: 12 February 2019).
- Toyota UK (2018) *Mirai goes the extra mile*. Available at: <https://www.toyota.co.uk/world-of-toyota/stories-news-events/mirai-goes-the-extra-mile> (Accessed: 30 January 2019).
- Triplett, K. A., Ghiaasiaan, S. M., Abdel-Khalik, S. I. and Sadowski, D. L. (1999) ‘Gas–liquid two-phase flow in microchannels Part I: two-phase flow patterns’, *International Journal of Multiphase Flow*, 25(3), pp. 377–394.
- Tuo, H. and Hrnjak, P. (2013) ‘Periodical reverse flow and boiling fluctuations in a microchannel evaporator of an air-conditioning system’, *International Journal of Refrigeration*, 36, pp. 1263–1275.

- Ullmann, A. and Brauner, N. (2007) 'the Prediction of Flow Pattern Maps in Minichannels', *Multiphase Science and Technology*, 19(1), pp. 49–73.
- Vetter, S., Nohria, R. and Santos, G. (2019) *IBM Power System AC922: Technical Overview and Introduction*. 1st edn. IBM Redbooks.
- Wang, C. C., Chang, W. J., Dai, C. H., Lin, Y. T. and Yang, K. S. (2012) 'Effect of inclination on the convective boiling performance of a microchannel heat sink using HFE-7100', *Experimental Thermal and Fluid Science*. Elsevier Inc., 36, pp. 143–148.
- Wang, H. S. and Rose, J. W. (2011) 'Theory of heat transfer during condensation in microchannels', *International Journal of Heat and Mass Transfer*, 54(11), pp. 2525–2534.
- Wang, S., Bi, X. and Wang, S. (2016) 'Boiling heat transfer in small rectangular channels at low Reynolds number and mass flux', *Experimental Thermal and Fluid Science*, 77, pp. 234–245.
- Wang, W. W., Radcliff, T. D. and Christensen, R. N. (2002) 'A condensation heat transfer correlation for millimeter-scale tubing with flow regime transition', *Experimental Thermal and Fluid Science*, 26(5), pp. 473–485.
- Wang, Y. and Sefiane, K. (2012) 'Effects of heat flux, vapour quality, channel hydraulic diameter on flow boiling heat transfer in variable aspect ratio microchannels using transparent heating', *International Journal of Heat and Mass Transfer*, 55, pp. 2235–2243.
- Warrier, G. R., Dhir, V. K. and Momoda, L. A. (2002) 'Heat transfer and pressure drop in narrow rectangular channels', *Experimental Thermal and Fluid Science*, 26(1), pp. 53–64.
- Wen, T., Zhan, H., Lu, L. and Zhang, D. (2018) 'Experimental investigation and development of new correlation for flow boiling heat transfer in mini-channel', *International Journal of Thermal Sciences*, 129, pp. 209–217.
- Wen, T., Zhan, H. and Zhang, D. (2019) 'Flow boiling heat transfer in mini channel with serrated fins: Experimental investigation and development of new correlation', *International Journal of Heat and Mass Transfer*, 128, pp. 1081–1094.
- Wong, P. K., Kwok, C. T., Man, H. C. and Cheng, F. T. (2012) 'Laser surface alloying (LSA) of copper for electrical erosion resistance', in *Laser Surface Modification of Alloys for Corrosion and Erosion Resistance*. Woodhead Publishing, pp. 288–319.
- Xu, Y., Fang, X., Li, D., Li, G., Yuan, Y. and Xu, A. (2016) 'An experimental study of flow boiling frictional pressure drop of R134a and evaluation of existing correlations', *International Journal of Heat and Mass Transfer*, 98, pp. 150–163.
- Yang, F., Li, W., Dai, X. and Li, C. (2016) 'Flow boiling heat transfer of HFE-7000 in nanowire-coated microchannels', *Applied Thermal Engineering*, 93, pp. 260–268. Available at: <http://dx.doi.org/10.1016/j.applthermaleng.2015.09.097>.
- Yang, K.-S., Jeng, Y.-R., Huang, C.-M. and Wang, C.-C. (2011) 'Heat Transfer and

Flow Pattern Characteristics for HFE-7100 Within Microchannel Heat Sinks', *Heat Transfer Engineering*, 32(7–8), pp. 697–704.

Yin, L., Jia, L., Guan, P. and Liu, D. (2014) 'Experimental investigation on bubble confinement and elongation in microchannel flow boiling', *Experimental Thermal and Fluid Science*, 54, pp. 290–296.

Yin, L., Xu, R., Jiang, P., Cai, H. and Jia, L. (2017) 'Subcooled flow boiling of water in a large aspect ratio microchannel', *International Journal of Heat and Mass Transfer*, 112, pp. 1081–1089.

Zhang, J. and Li, W. (2016) 'Numerical study on heat transfer and pressure drop characteristics of R410A condensation in horizontal circular mini/micro-tubes', *Canadian Journal of Chemical Engineering*, 94(9), pp. 1809–1819.

Zhang, Y., Tan, H., Li, Y., Shan, S. and Liu, Y. (2019) 'A modified heat transfer correlation for flow boiling in small channels based on the boundary layer theory', *International Journal of Heat and Mass Transfer*, 132, pp. 107–117.

Zhuang, X. R., Chen, G. F., Zou, X., Song, Q. L. and Gong, M. Q. (2017) 'Experimental investigation on flow condensation of methane in a horizontal smooth tube', *International Journal of Refrigeration*, 78, pp. 193–214.

Zivi, S. M. (1964) 'Estimation of steady-state steamvoid-fraction by means of the principle of minimum entropy production', *Journal of Heat Transfer*, 86, pp. 247–252.

Zou, L. and Jones, B. G. (2013) 'Heating surface material's effect on subcooled flow boiling heat transfer of R134a', *International Journal of Heat and Mass Transfer*, 58(1–2), pp. 168–174.

Appendix A

Two-Phase Pressure Drop Correlations

Author(s)	Correlation	Remarks
Recommended for conventional channels		
Lockhart and Martinelli (1949)	$\Delta P_{acc} = G^2 v_l \left[\frac{x_o^2}{\alpha_o} \left(\frac{v_g}{v_l} \right) + \frac{(1-x_o)^2}{1-\alpha_o} - 1 \right]$ $\alpha_o = 1 - \frac{1}{\sqrt{1 + \frac{C}{X_o} + \frac{1}{X_o^2}}}$ $\Delta P_{fr} = \frac{L_{tp}}{x_o} \int_0^{x_o} \frac{2f_l G^2 v_l (1-x)^2}{D_h} \phi_l^2 dx$ $\phi_l^2 = 1 + \frac{C}{X} + \frac{1}{X^2}$ $X = \sqrt{\frac{(dP/dz)_l}{(dP/dz)_g}}$ <p style="text-align: center;"> C=5 (for laminar liquid-laminar vapour) C=12 (for laminar liquid-turbulent vapour) C=10 (for turbulent liquid- laminar vapour) C=20 (for turbulent liquid-turbulent vapour) </p>	D = 1.5–25.8 mm Fluids (air/water, air/benzene, air/kerosene and air/oils) Circular horizontal channels
Homogenous flow model, Collier and Thome (1994)	$\Delta P_{acc} = G^2 v_{lg} x_o$ $\Delta P_{fr} = \frac{2f_{tp} G^2 v_l L_{tp}}{D_h} \left[1 + \frac{x_o}{2} \left(\frac{v_{lg}}{v_l} \right) \right]$ $v_{lg} = v_g - v_l$ <p style="text-align: center;">$f_{tp} = 0.003$ as recommended by Qu and Mudawar (2003b)</p>	
Recommended for mini/microchannels		
Qu and Mudawar (2003b)	$\Delta P_{acc} = G^2 v_l \left[\frac{x_o^2}{\alpha_o} \left(\frac{v_g}{v_l} \right) + \frac{(1-x_o)^2}{1-\alpha_o} - 1 \right]$ $\alpha_o = \left[1 + \frac{1-x_o}{x_o} \left(\frac{\rho_g}{\rho_l} \right)^{0.67} \right]^{-1} \quad \text{[proposed by Zivi (1964)]}$ $\Delta P_{fr} = \frac{L_{tp}}{x_o} \int_0^{x_o} \frac{2f_l G^2 v_l (1-x)^2}{D_h} \phi_l^2 dx$ $\phi_l^2 = 1 + \frac{C}{X} + \frac{1}{X^2}$ $C = 21(1 - e^{-319D_h})(0.00418G + 0.0613)$	$D_h = 0.35$ mm Fluid (Water) Horizontal, rectangular multi-channels
Lee and Garimella (2008)	$\Delta P_{acc} = G^2 v_l \left[\frac{x_o^2}{\alpha_o} \left(\frac{v_g}{v_l} \right) + \frac{(1-x_o)^2}{1-\alpha_o} - 1 \right]$ $\alpha_o = \left[1 + \frac{1-x_o}{x_o} \left(\frac{\rho_g}{\rho_l} \right)^{0.67} \right]^{-1}$ $\Delta P_{fr} = \frac{L_{tp}}{x_o} \int_0^{x_o} \frac{2f_l G^2 v_l (1-x)^2}{D_h} \phi_l^2 dx$ $\phi_l^2 = 1 + \frac{C}{X} + \frac{1}{X^2}$ $C = 2566G^{0.5466} D_h^{0.8819} (1 - e^{-319D_h})$	$D_h = 0.162$ – 0.571 mm Fluid (Water) Horizontal rectangular multi-channels

<p>Keepaiboon et al. (2016)</p>	$\Delta P_{acc} = G^2 v_l \left[\frac{x_o^2}{\alpha_o} \left(\frac{v_g}{v_l} \right) + \frac{(1-x_o)^2}{1-\alpha_o} - 1 \right]$ $\alpha_o = \left[1 + \frac{1-x_o}{x_o} \left(\frac{\rho_g}{\rho_l} \right)^{0.67} \right]^{-1}$ $\Delta P_{fr} = \frac{L_{tp}}{x_o} \int_0^{x_o} \frac{2f_l G^2 v_l (1-x)^2}{D_h} \phi_l^2 dx$ $\phi_l^2 = 1 + \frac{C}{X} + \frac{1}{X^2}$ $C = 1.9310^5 Re^{-1.18} Co^{-27.99} X^{0.93}$	<p>$D_h = 0.68$ mm Fluid (R134a) Horizontal single rectangular channel</p>
<p>Huang and Thome (2017)</p>	$\Delta P_{acc} = G^2 v_l \left[\frac{x_o^2}{\alpha_o} \left(\frac{v_g}{v_l} \right) + \frac{(1-x_o)^2}{1-\alpha_o} - 1 \right]$ $\alpha_o = \left[1 + \frac{1-x_o}{x_o} \left(\frac{\rho_g}{\rho_l} \right)^{0.67} \right]^{-1}$ $\Delta P_{fr} = \frac{L_{tp}}{x_o} \int_0^{x_o} \frac{2f_l G^2 v_l (1-x)^2}{D_h} \phi_l^2 dx$ $\phi_l^2 = 1 + \frac{C}{X} + \frac{1}{X^2}$ <p>For $Re_{ls} \leq 2000$ and R1233zd(E): $f_l = \frac{8.058}{Re_{ls}}$</p> <p>For $Re_{ls} \leq 2000$ and others: f_l: is obtained from Shah and London (1978)</p> <p>For $Re_{ls} > 2000$: $f_l = \frac{0.079}{Re_{ls}^{-0.25}}$</p> <p>For $Re_{ls} \leq 2000$ and $Re_{gs} \leq 2000$: $C = 0.0037 Re_{gs}^{1.7} Re^{-0.83}$</p> <p>For $Re_{ls} \leq 2000$ and $Re_{gs} > 2000$: $C = 0.9 Re_{gs}^{0.034} Re^{0.2}$</p>	<p>$D_h = 0.1$ mm Fluid (R1233zd(E), R245fa and R236fa) Horizontal square multi-channels</p>
<p>Markal et al. (2017b)</p>	$\Delta P_{acc} = G^2 v_l \left[\frac{x_o^2}{\alpha_o} \left(\frac{v_g}{v_l} \right) + \frac{(1-x_o)^2}{1-\alpha_o} - 1 \right]$ $\alpha_o = \left[1 + \frac{1-x_o}{x_o} \left(\frac{\rho_g}{\rho_l} \right)^{0.67} \right]^{-1}$ $\Delta P_{fr} = \frac{L_{tp}}{x_o} \int_0^{x_o} \frac{2f_l G^2 v_l (1-x)^2}{D_h} \phi_l^2 dx$ $\phi_l^2 = 1 + \frac{C}{X} + \frac{1}{X^2}$ $C = -7.1 + \left(\frac{(1-x_o)^{1.766}}{Re^{0.12} \beta^{0.031} Bo^{0.165} We^{0.074} \left(\frac{v_l}{v_g} \right)^{0.233} \left(\frac{L_{tp}}{D_h} \right)^{0.247}} \right)$	<p>$D_h = 0.1-0.25$ mm Fluid (Deionized water) Horizontal rectangular multi-channels</p>

<p>Gao et al. (2019)</p>	$\Delta P_{acc} = G^2 v_l \left[\frac{x_o^2}{\alpha_o} \left(\frac{v_g}{v_l} \right) + \frac{(1-x_o)^2}{1-\alpha_o} - 1 \right]$ $\alpha_o = 1 / \left[1 + 0.28 \left(\frac{1-x_o}{x_o} \right)^{0.64} \left(\frac{\rho_g}{\rho_l} \right)^{0.36} \left(\frac{\mu_l}{\mu_g} \right)^{0.07} \right]$ $\Delta P_{fr} = \frac{L_{tp}}{x_o} \int_0^{x_o} F(1-x)^{1/3} + Bx^3 dx$ $F = A + (1 + 0.07695Bd^{-0.03573} Re_l^{0.394})(B-A)x$ $A = \frac{2f_l G^2}{D_h \rho_l}$ $B = \frac{2f_g G^2}{D_h \rho_g}$ $f_k = \frac{24}{Re_k} (1 - 1.355\beta + 1.946\beta^2 - 1.7012\beta^3 + 0.9564\beta^4 - 0.2537\beta^5) \quad (\text{for } Re_k < 2000 \text{ "rectangular channel, Shah and London (1978)"})$ $f_k = \frac{0.079}{Re_k^{0.25}} \quad (\text{for } 2000 \leq Re_k < 20,000)$ $f_k = \frac{0.046}{Re_k^{0.2}} \quad (\text{for } Re_k \geq 20,000)$ $Re_k = G * D_h / \mu_k$ <p>(k) refers to l or g</p>	<p>$D_h = 4$ & 8 mm Fluid (Ammonia) Horizontal tubes This correlation was evaluated based on 11 sources including: $D_h = 0.81$–14 mm Fluid (R22, R134a, Ammonia, CO₂) Horizontal and vertical tubes</p>
------------------------------	---	---

Appendix B

Flow Boiling Heat Transfer Correlations

Author(s)	Correlation	Remarks
Recommended for conventional channels		
Shah (1982)	$h_{tp} = \text{Max}(E, S)h_{sp}$ $S = 1.8/N^{0.8}$ <p>For $1 < N$:</p> $E = 230Bo^{0.5} \quad (\text{for } Bo > 3 \times 10^{-5})$ $E = 1 + 46Bo^{0.5} \quad (\text{for } Bo < 3 \times 10^{-5})$ <p>For $0.1 < N \leq 1$:</p> $E = FBo^{0.5} \exp(2.74N^{-0.1})$ <p>For $N \leq 1$:</p> $E = FBo^{0.5} \exp(2.47N^{-0.15})$ $F = 14.7 \quad (\text{for } Bo \geq 11 \times 10^{-4})$ $F = 15.43 \quad (\text{for } Bo < 11 \times 10^{-4})$ $N = N_{co} \quad (\text{for } Fr \geq 0.04)$ $N = 0.38Fr^{-0.3}N_{co} \quad (\text{for } Fr < 0.04)$	<p>D = 6–25.4 mm Fluids (water, R11, R12, R22, R113, cyclohexane) For saturated boiling in vertical and horizontal channels</p>
Kandlikar (1990)	$h_{tp} = \text{Max}(E, S)h_{sp}$ $E = 0.6683N_{co}^{-0.2}f(Fr) + 1058Bo^{0.7}F_{fl}$ $S = 1.136N_{co}^{-0.9}f(Fr) + 667.2Bo^{0.7}F_{fl}$ $f(Fr) = 1 \quad (\text{for } Fr \geq 0.04)$ $f(Fr) = (25Fr)^{0.3} \quad (\text{for } Fr < 0.04)$ <p>Where F_{fl} is:</p> <p>Water: 1 R11: 1.3 R12: 1.5 R22: 2.2 R113: 1.3 R134a: 1.63 R152a: 1.1</p>	<p>D = 4–32 mm Fluids (water, R11, R12, R22, R113, R134a, R152a) G = 13–8179 kg/m²s q" = 0.3–228 kW/m² For saturated boiling in vertical and horizontal tubes</p>
Liu and Winterton (1991)	$h_{tp} = \sqrt{(Eh_{sp})^2 + (Sh_{coop})^2}$ $E = \left(1 + xPr \left(\frac{v_g}{v_l} - 1\right)\right)^{0.35}$ $h_{coop} = 55P_R^{0.12-0.21\log_{10}Rp} (-\log_{10}(P_R))^{-0.55} M^{-0.5} q_w''^{0.67}$ $S = (1 + 0.055E^{0.1}Re^{0.16})^{-1}$	<p>D = 2.95–32 mm Fluids (water, R11, R12, R113, R114, R22, ethylene glycol) G = 12.4–8179.3 kg/m²s q" = 0.35–2620 kW/m² For vertical and horizontal channels</p>

Recommended for mini/microchannels		
Warrier et al. (2002)	$h_{tp} = [1 + 6Bo^{\frac{1}{16}} - 5.3(1 - 855Bo)x^{0.65}]h_{sp}$	$D_h = 0.75$ mm Fluid (FC-84) $G = 557\text{--}1600$ kg/m ² s $q'' = \text{up to } 59.9$ kW/m ² For saturated boiling in horizontal rectangular multi-channels
Lee and Mudawar (2005)	$h_{tp} = 3.856X^{0.267}h_{sp} \quad (\text{for } 0 < x < 0.05)$ $h_{tp} = 436.48Bo^{0.522}We^{0.351}X^{0.665}h_{sp} \quad (\text{for } 0.05 < x < 0.55)$ $h_{tp} = \text{Max}\{(108.6X^{1.665}h_{sp,g}), h_{sp,g}\} \quad (\text{for } 0.55 < x < 1)$ $h_{sp,g} = \frac{Nu_3 k_g}{D_h} \quad (\text{for laminar vapour flow})$ $h_{sp,g} = 0.023Re_{gs}^{0.8}Pr_g^{0.4} \frac{k_g}{D_h} \quad (\text{for turbulent vapour flow})$	$D_h = 0.348$ mm Fluids (water, R134a) $G = 127\text{--}654$ kg/m ² s $q'' = 159\text{--}938$ kW/m ² For saturated boiling in horizontal rectangular multi-channels
Mahmoud and Karayiannis (2013)	$h_{tp} = Sh_{coop} + Fh_{sp}$ $S = \frac{1}{1 + 2.56 \times 10^{-6}(Re_{ls}F^{1.25})^{1.17}}$ $F = \left(1 + \frac{A}{X}\right)^{0.64}$ $A = 2.812C_o^{-0.408}$	$D = 0.52\text{--}4.26$ mm Fluid (R134a) $G = 100\text{--}700$ kg/m ² s $q'' = 1.7\text{--}158$ kW/m ² For saturated boiling in vertical single tubes
Li and Jia (2015)	For nucleate boiling regime: $h_{tp} = 189Bo^{0.178}Bd^{0.4}Re_{ls}^{0.12} \frac{k_l}{D_h}$ For convective boiling regime: $h_{tp} = 277.3Bo^{0.978}Re_{ls}^{0.94}(1-x)^{0.47} \frac{k_l}{D_h}$	$D_h = 0.5$ mm Fluid (R134a) $G = 373.33\text{--}1244.44$ kg/m ² s $q'' = \text{up to } 802.12$ kW/m ² For saturated boiling in horizontal rectangular multi-channels
Lim et al. (2015)	$h_{tp} = \frac{Re^{0.196}k_l}{Bo^{0.117}C_{FR}^{0.42}D_h}$ $C_{FR} = 0.4905 + Fr(1 - x^{3.134})$	$D_h = 0.5$ mm Fluid (water) $G = 200\text{--}600$ kg/m ² s $q'' = 100\text{--}400$ kW/m ² For saturated boiling in horizontal square single channel
Thiangtham et al. (2016)	$h_{tp} = \frac{10^{16.7}Bo^{0.3}We^{2.7}k_l}{Re^{4.95}(\rho_l/\rho_g)^{0.9}D_h}$	$D_h = 0.421$ mm Fluid (R134a) $G = 150\text{--}600$ kg/m ² s $q'' = 3\text{--}127$ kW/m ² $T_{sat} = 13, 18, 23$ °C For saturated boiling in horizontal rectangular multi-channels

<p>Markal et al. (2017a)</p>	$h_{tp} = \frac{0.054 Re_{ls}^{0.214} Bo^{0.913} \beta^{0.552} \left(\frac{1-x}{x}\right)^{0.7} \left(\frac{k_l}{D_h}\right)^{1.959}}{We^{0.094} Pr^{0.333}}$	<p>Fluid (de-ionized water) Different aspect ratios: 0.37–5 at constant $D_h = 0.1$ mm Different hydraulic diameters: 0.1–0.25 mm at constant aspect ratio: 1 $G = 51\text{--}728.7$ kg/m² s $q'' = 36\text{--}221.7$ kW/m² $x = 0.01\text{--}0.69$ $7.72 \leq Re_{ls} \leq 190$ For saturated boiling in horizontal rectangular multi-channels</p>
<p>Shah (2017)</p>	$h_{tp} = F h_{Shah(1982)}$ $F = 2.1 - 0.008 We_g - 110 Bo$ <p>If $F < 1$, use $F = 1$. If the channel is fully heated, use $D_h = D_{HP}$ If the channel is partially heated, use D_h in We_g and Fr. Also, use D_{HP} in other expressions.</p> $D_{HP} = \frac{4 \text{Flow Area}}{\text{Perimeter with heat transfer}}$	<p>$D = 0.38\text{--}27.1$ mm Fluids (Water, CO₂, R11, R12, R22, R32, R113, R123, R114, R123, R134a, R152a, R1234yf, R236fa, R245fa, ammonia, propane, isobutane, carbon tetrachloride, isopropyl alcohol, ethanol, methanol, n-butanol, cyclohexane, benzene, heptane, pentane, argon, hydrogen, nitrogen, helium) $G = 15\text{--}2437$ kg/m² s For saturated boiling in vertical and horizontal (single and multi) channels</p>
<p>Wen et al. (2019)</p>	$h_{tp} = h_{sp} + \frac{1}{1 + e^{\frac{x-F}{12}}} h_{nb}$ $h_{sp} = x h_{sp,g} + (1-x) h_{sp,l}$ $h_{nb} = 2155.4 P_R^{0.12} (-0.4343 \log P_R)^{-0.55} M^{-0.5} q_w''^{0.27} \left(\frac{Fr}{We}\right)^{0.18}$ $F = (Bo We)^{0.07}$ $h_{sp,k} = 0.023 Re_k^{0.8} Pr_k^{0.4} \frac{k_k}{D_h}$ <p>(k) refers to l or g</p>	<p>$D_h = 1.28$ & 1.59 mm Fluid (R134a) $G = 60\text{--}308$ kg/m² s $q'' = 6\text{--}48$ kW/m² $P_{sat} = 2.7\text{--}4.5$ bar For flow boiling in horizontal rectangular multi-channels with serrated fins</p>

$$Re_{ls} = G(1-x)D_h/\mu_l$$

$$Re_{gs} = GxD_h/\mu_g$$

$$h_{sp} = \frac{Nu_3 k_l}{D_h} \quad (\text{for } Re_{ls} < 2000)$$

$$h_{sp} = 0.023 Re_{ls}^{0.8} Pr^{0.4} \frac{k_l}{D_h} \quad (\text{for } Re_{ls} > 3000)$$

$$Nu_3 = 8.235(1 - 1.833\beta + 3.767\beta^2 - 5.814\beta^3 + 5.361\beta^4 - 2\beta^5) \quad (\text{for three walls heat transfer, Shah and London (1978)})$$

For $Re_{ls} < 2000$ and $Re_{gs} < 2000$:

$$X_{ll} = \left(\frac{\mu_l}{\mu_g}\right)^{0.5} \left(\frac{1-x}{x}\right)^{0.5} \left(\frac{\rho_g}{\rho_l}\right)^{0.5}$$

For $Re_{ls} < 2000$ and $Re_{gs} \geq 2000$:

$$X_{lt} = \left(\frac{f_l}{f_g}\right)^{0.5} \left(\frac{1-x}{x}\right)^{1.0} \left(\frac{\rho_g}{\rho_l}\right)^{0.5}$$

For $Re_{ls} \geq 2000$ and $Re_{gs} < 2000$:

$$X_{tl} = \left(\frac{f_l}{f_g}\right)^{0.5} \left(\frac{1-x}{x}\right)^{1.0} \left(\frac{\rho_g}{\rho_l}\right)^{0.5}$$

For $Re_{ls} \geq 2000$ and $Re_{gs} \geq 2000$:

$$X_{tt} = \left(\frac{\mu_l}{\mu_g}\right)^{0.1} \left(\frac{1-x}{x}\right)^{0.9} \left(\frac{\rho_g}{\rho_l}\right)^{0.5}$$

Fanning friction factor:

$$f_k = \frac{24}{Re_{ks}} (1 - 1.355\beta + 1.946\beta^2 - 1.7012\beta^3 + 0.9564\beta^4 - 0.2537\beta^5) \quad (\text{for } Re_{ks} < 2000 \text{ "rectangular channel, Shah and London (1978)"})$$

$$f_k = \frac{0.079}{Re_{ks}^{0.25}} \quad (\text{for } 2000 \leq Re_{ks} < 20,000)$$

$$f_k = \frac{0.046}{Re_{ks}^{0.2}} \quad (\text{for } Re_{ks} \geq 20,000)$$

(k) refers to l or g

Appendix C

Flow Condensation Heat Transfer Correlations

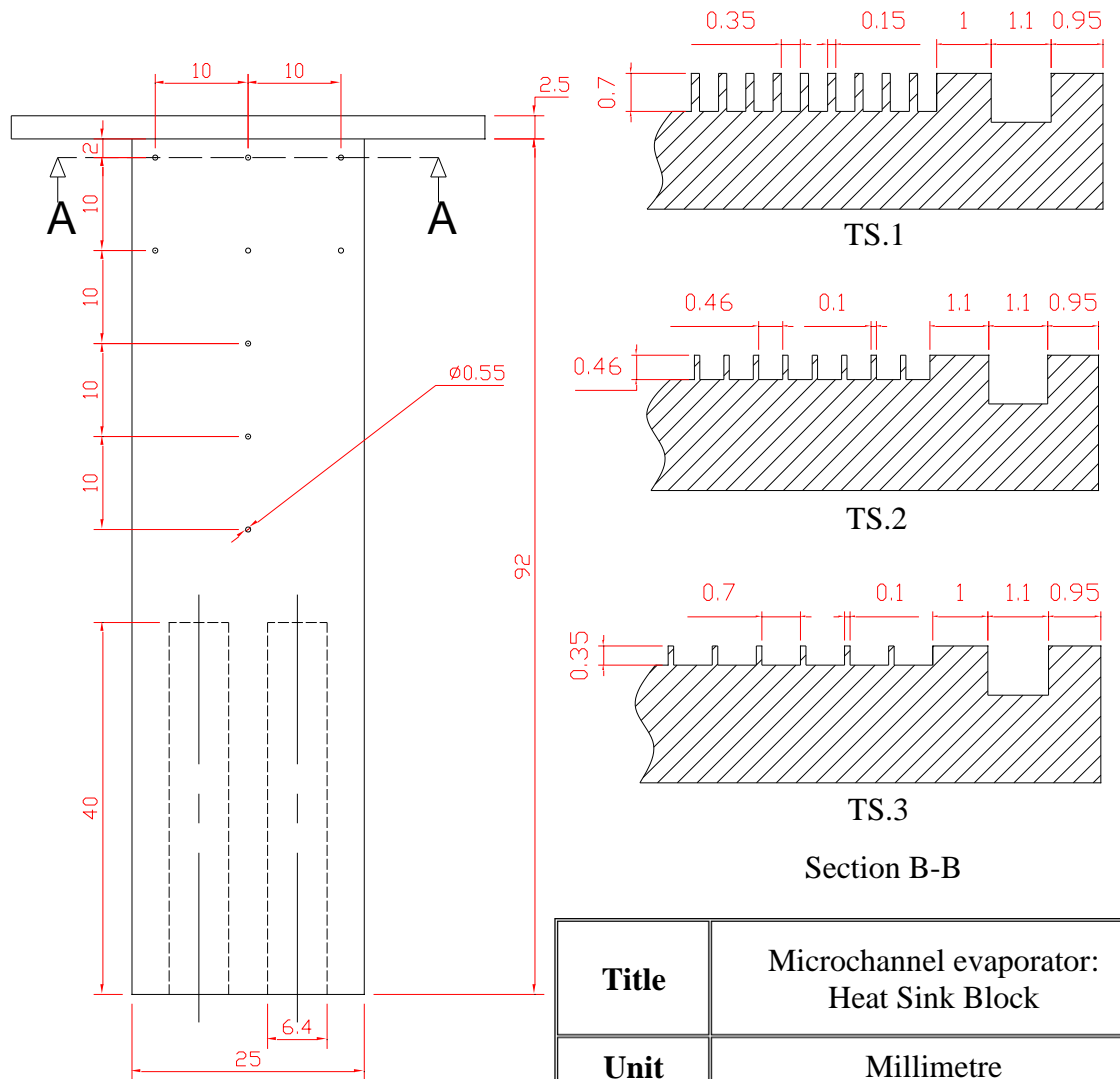
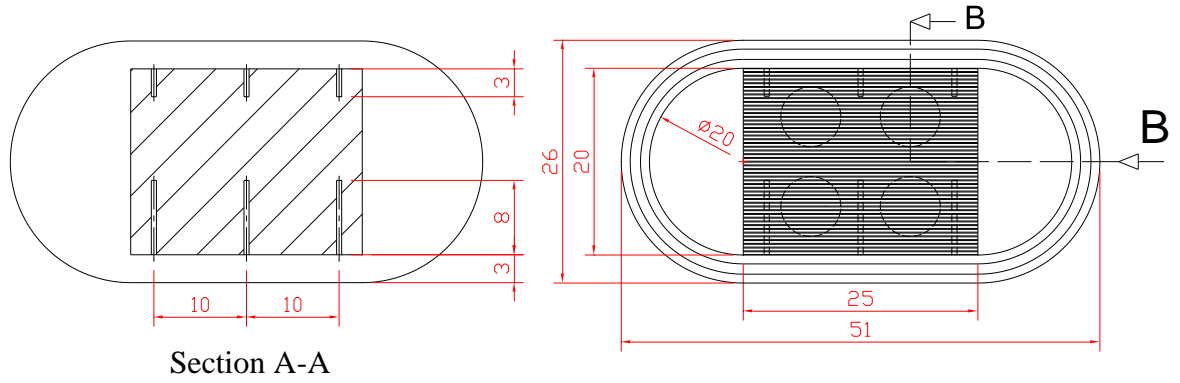
Author(s)	Correlation	Remarks
Recommended for conventional channels		
Shah (1979)	$h_{tp} = 0.023Re^{0.8}Pr_l^{0.4} \left[(1-x)^{0.8} + \frac{3.8x^{0.76}(1-x)^{0.04}}{P_R^{0.38}} \right] k_l/D_h$	Fluids (benzene, ethanol, toluene, water, methanol, trichloroethylene, R11, R12, R22, R113) $D = 7\text{--}40$ mm
Dobson and Chato (1998)	$h_{tp} = 0.023Re_{ls}^{0.8}Pr_l^{0.4} \left[1 + \frac{2.22}{X_{tt}^{0.89}} \right] k_l/D_h$	Fluids (R134a, R12, R22, R32/R125) $D = 3.14\text{--}7.04$ mm
Cavallini et al. (2006a)	<p>For annular flow, ΔT-independent flow regime ($J_G > J_G^T$):</p> $h_{tp,1} = h_{sp} \left[1 + 1.128x^{0.817} \left(\frac{\rho_l}{\rho_g} \right)^{0.3685} \left(\frac{\mu_l}{\mu_g} \right)^{0.2363} (1 - \mu_g/\mu_l)^{2.144} Pr_l^{-0.1} \right]$ <p>For stratified-wavy or smooth flow, ΔT-dependent flow regime ($J_G \leq J_G^T$):</p> $h_{tp,2} = \left[h_{tp,1} \left(\frac{J_G^T}{J_G} \right)^{0.8} - h_{tp,3} \right] \left(\frac{J_G}{J_G^T} \right) + h_{tp,3}$ <p>For slug flow, both $h_{tp,1}$ and $h_{tp,2}$</p> $h_{tp,3} = 0.725 \left(1 + 0.741 \left[\frac{(1-x)}{x} \right]^{0.3321} \right)^{-1} \left[\frac{k_f^3 \rho_l \Delta \rho g i_{lg}}{\mu_l D \Delta T} \right]^{0.25} + (1 - x^{0.087}) h_{sp}$ $h_{sp} = 0.023Re^{0.8}Pr_l^{0.4} k_f/D_h$ $J_G^T = \left([7.5/(4.3X_{tt}^{1.111} + 1)]^{-3} + C_T^{-3} \right)^{-0.333}$ $C_T = 1.6 \quad (\text{for hydrocarbons})$ $C_T = 2.6 \quad (\text{for other refrigerants})$ $\Delta T = T_{sat} - T_{wi}$	Fluid (R134a, R125, R236ea, R32, R410A) $D > 3$ mm
Recommended for Mini/microchannels		
Wang et al. (2002)	$h_{tp} = 0.0274Re_{ls}^{0.6792}Pr_l x^{0.2208} \left[\frac{\phi_g}{X_{tt}} \right] k_l/D_h$ $\phi_g = [1.376 + 8X_{tt}^{1.665}]^{0.5}$	Fluid (R134a) $D_h = 1.46$ mm Multi-channels
Koyama et al. (2003b)	$h_{tp} = 0.0152Re_{ls}^{0.77} (1 + 0.6Pr_l^{0.8}) \left[\frac{\phi_g}{X_{tt}} \right] k_l/D_h$ $\phi_g = [1 + 21 (1 - \exp(-0.319D_h)) X_{tt} + X_{tt}^2]^{0.5}$	Fluid (R134a) $D_h = 0.8$ & 1.11 mm Multi-channels

Bohdal et al. (2011)	$h_{tp} = 25.084 Re_{ls}^{0.258} Pr_l^{-0.495} P_R^{-0.288} \left[\frac{x}{1-x} \right]^{0.266} k_l / D_h$	Fluids (R134a, R404A) $D = 0.31\text{--}3.3$ mm
Park et al. (2011)	$h_{tp} = 0.0055 Re_{ls}^{0.7} Pr_l^{1.37} \left[\frac{\phi_g}{X_{tt}} \right] k_l / D_h$ $\phi_g = \left[1 + 13.17 \left(\frac{\rho_g}{\rho_l} \right)^{0.17} \left(1 - \exp(-0.6 \sqrt{\frac{g \Delta \rho D_h^2}{\sigma}}) \right) X_{tt} + X_{tt}^2 \right]^{0.5}$	Fluids (R134a, R1234ze(E), R236fa) $D_h = 1.45$ mm Multi-channels
Kim and Mudawar (2013c)	<p>For annular flow where $We^* > 7X_{tt}^{0.2}$</p> $h_{tp} = 0.048 Re_{ls}^{0.69} Pr_l^{0.34} \left[\frac{\phi_g}{X_{tt}} \right] k_f / D_h$ <p>For slug and bubbly flow where $We^* < 7X_{tt}^{0.2}$</p> $h_{tp} = \left[\left(0.048 Re_{ls}^{0.69} Pr_l^{0.34} \left[\frac{\phi_g}{X_{tt}} \right] \right)^2 + (3.2 \times 10^{-7} Re_{ls}^{-0.38} Su_{go}^{1.39})^2 \right]^{0.5} k_f / D_h$ $\phi_g^2 = 1 + CX + X^2$ $X = \sqrt{\frac{(dP/dz)_l}{(dP/dz)_g}}$ $\left(\frac{dP}{dz} \right)_l = \frac{2f_l v_l G^2 (1-x)^2}{D_h}$ $\left(\frac{dP}{dz} \right)_g = \frac{2f_g v_g G^2 x^2}{D_h}$ <p>For turbulent-turbulent ($Re_{ls} \geq 2000, Re_{gs} \geq 2000$): $C = 0.39 Re^{0.03} Su_{go}^{0.1} \left(\frac{\rho_l}{\rho_g} \right)^{0.35}$</p> <p>For turbulent-laminar ($Re_{ls} \geq 2000, Re_{gs} < 2000$): $C = 8.7 \times 10^{-4} Re^{0.17} Su_{go}^{0.5} \left(\frac{\rho_l}{\rho_g} \right)^{0.14}$</p> <p>For laminar-turbulent ($Re_{ls} < 2000, Re_{gs} \geq 2000$): $C = 0.001 Re^{0.59} Su_{go}^{0.19} \left(\frac{\rho_l}{\rho_g} \right)^{0.36}$</p> <p>For laminar-laminar ($Re_{ls} < 2000, Re_{gs} < 2000$): $C = 3.5 \times 10^{-5} Re^{0.44} Su_{go}^{0.5} \left(\frac{\rho_l}{\rho_g} \right)^{0.48}$</p> $We^* = 2.45 \frac{Re_{gs}^{0.64}}{Su_{go}^{0.3} (1 + 1.09 X_{tt}^{0.039})^{0.4}} \quad \text{For } Re_{ls} \leq 1250$ $We^* = 0.85 \frac{Re_{gs}^{0.79} X_{tt}^{0.157}}{Su_{go}^{0.3} (1 + 1.09 X_{tt}^{0.039})^{0.4}} \left[\left(\frac{\mu_g}{\mu_l} \right)^2 \left(\frac{v_g}{v_l} \right) \right]^{0.084} \quad \text{For } Re_{ls} > 1250$ $f_k Re_{ks} = 24(1 - 1.355\beta + 1.946\beta^2 - 1.7012\beta^3 + 0.9564\beta^4 - 0.2537\beta^5)$ <p>($k = l$ or g) for laminar flow in a rectangular channel ($\beta < 1$)</p>	17 different fluids $D_h = 0.42$ to 6.2 mm Single/multi-channels

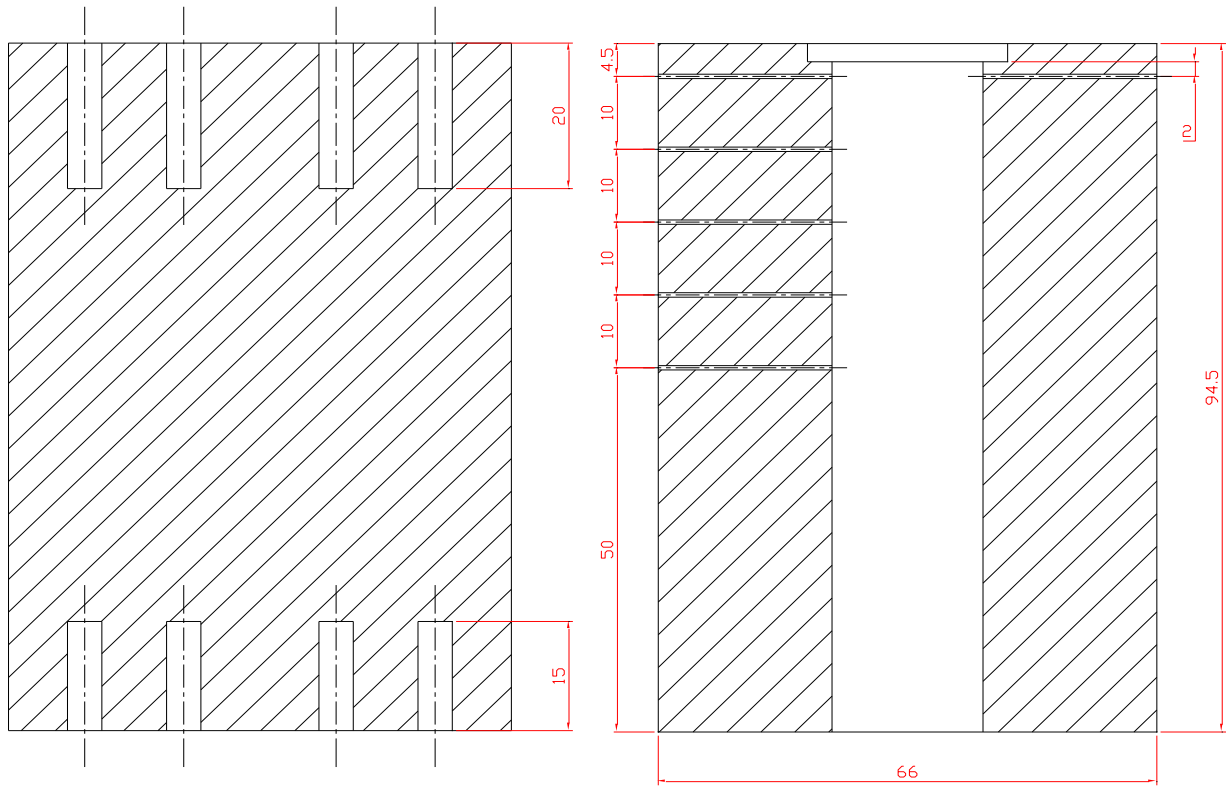
<p>Shah (2016)</p>	$h_{tp} = h_l \quad \text{For region I}$ $h_{tp} = h_l + h_{NU} \quad \text{For region II}$ $h_{tp} = h_{NU} \quad \text{For region III}$ $h_l = h_{LT} \left[1 + 1.128x^{0.817} \left(\frac{\rho_l}{\rho_g} \right)^{0.3685} \left(\frac{\mu_l}{\mu_g} \right)^{0.2363} \left(1 - \frac{\mu_g}{\mu_l} \right)^{2.144} Pr_l^{-0.1} \right]$ $h_{NU} = 1.32 Re_{ls}^{-1/3} \left[\frac{\rho_l(\rho_l - \rho_g)gk_l^3}{\mu_l^2} \right]^{1/3}$ $h_{LT} = 0.023 Re^{0.8} Pr_l^{0.4} k_l / D_h$ <p>For region I: $J_G \geq 0.98(Z + 0.263)^{-0.62}$ and $We_g \geq 100$ For region III: $J_G \leq 0.95(1.254 + 2.27Z^{1.249})^{-1}$ For region II: if the above criteria do not match $Z = (1/x - 1)^{0.8} Pr^{0.4}$ $D_h = \frac{4A_{sec}}{Per}$ 'For Weber number' $D_h = \frac{4A_{sec}}{perimeter \text{ with heat transfer}}$ 'For all equations'</p>	<p>13 different fluids D_h = 0.1 to 2.8 mm Various shapes Single/multi-channels</p>
<p>Rahman et al. (2018)</p>	$h_{tp} = Re_{ls}^{0.11} Pr_l^{0.45} \left(\frac{P}{P_{cr}} \right)^{0.1} \left(\frac{x}{1-x} \right)^{0.09} \left[\frac{\phi_g}{X} \right] k_f / D_h$ $\phi_g^2 = 1 + CX + X^2$ $C = \lambda x^{0.35} (1-x)^{0.25} \left(\frac{P}{P_{cr}} \right)^{0.31} Re_{tp}^{0.09} We_{tp}^{0.09}$ $\lambda = 24(1 - 1.355\beta + 1.947\beta^2 - 1.701\beta^3 + 0.956\beta^4 - 0.254\beta^5)$ $We_{tp} = \frac{G^2 D_h}{\rho_{tp} \sigma}$ $Re_{tp} = \frac{GD_h}{\mu_{tp}}$ $\frac{1}{\rho_{tp}} = \frac{x}{\rho_g} + \frac{1-x}{\rho_l}$ $\frac{1}{\mu_{tp}} = \frac{x}{\mu_g} + \frac{1-x}{\mu_l}$	<p>Fluid (R134a) D_h = 0.64 & 0.81 mm Multi-channels</p>

Appendix D

Engineering Drawings

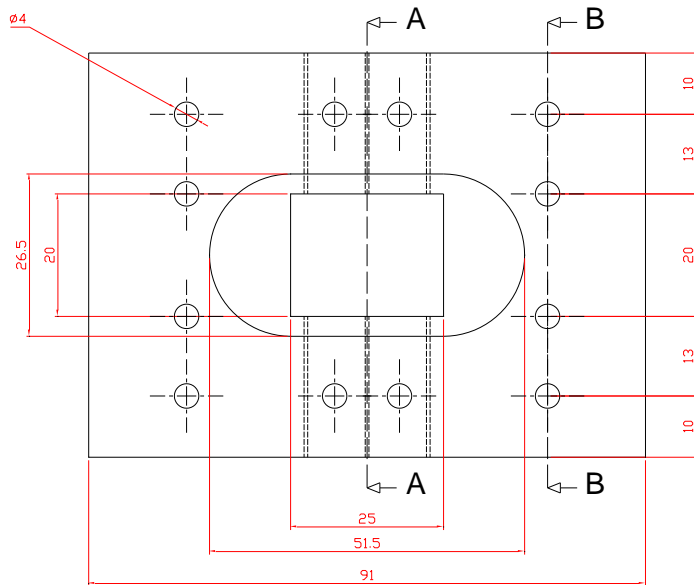


Title	Microchannel evaporator: Heat Sink Block
Unit	Millimetre
Material	Oxygen-free Copper

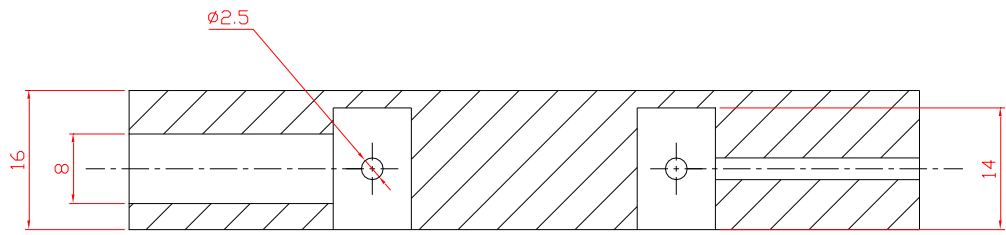


Section B-B

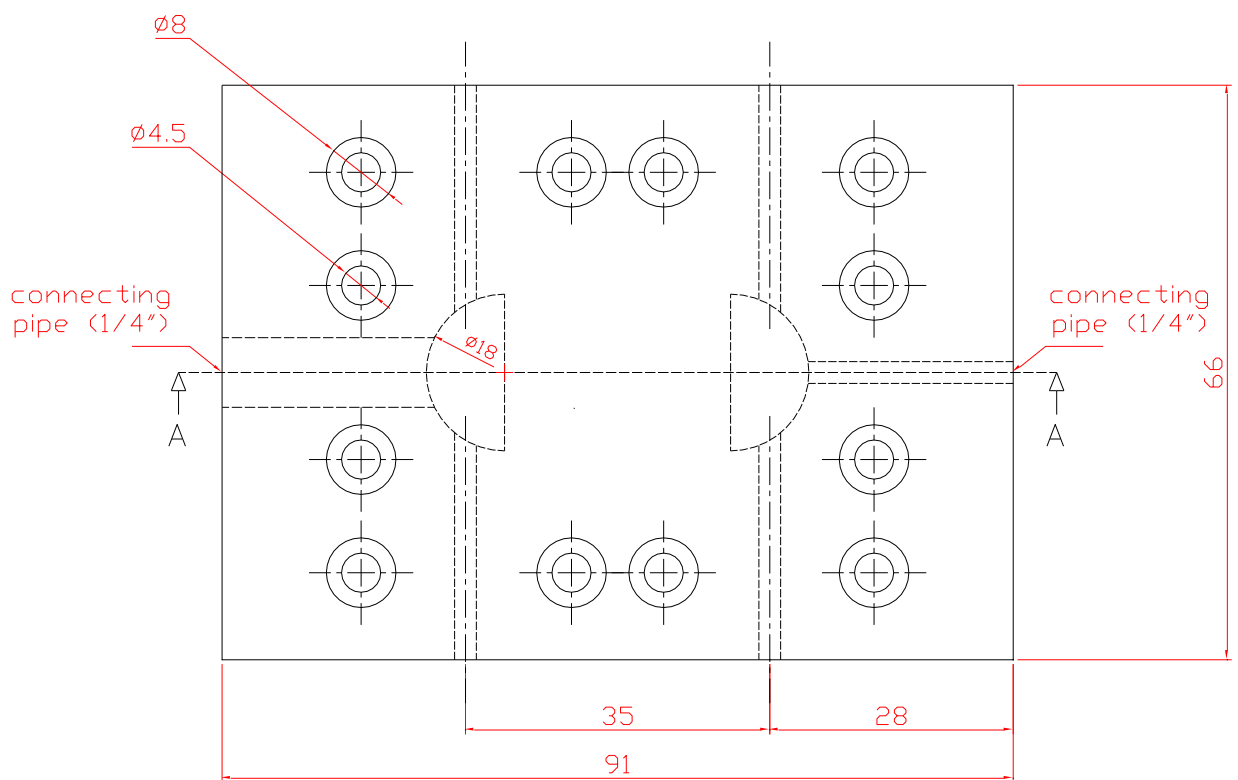
Section A-A



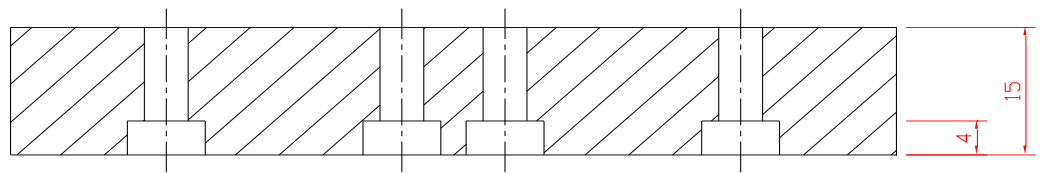
Title	Microchannel evaporator: Housing
Unit	Millimetre
Material	PTFE



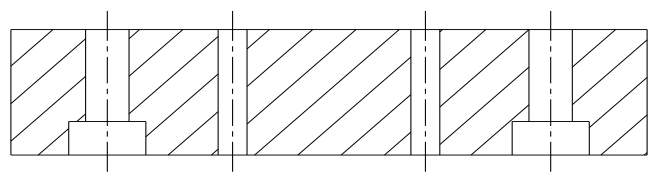
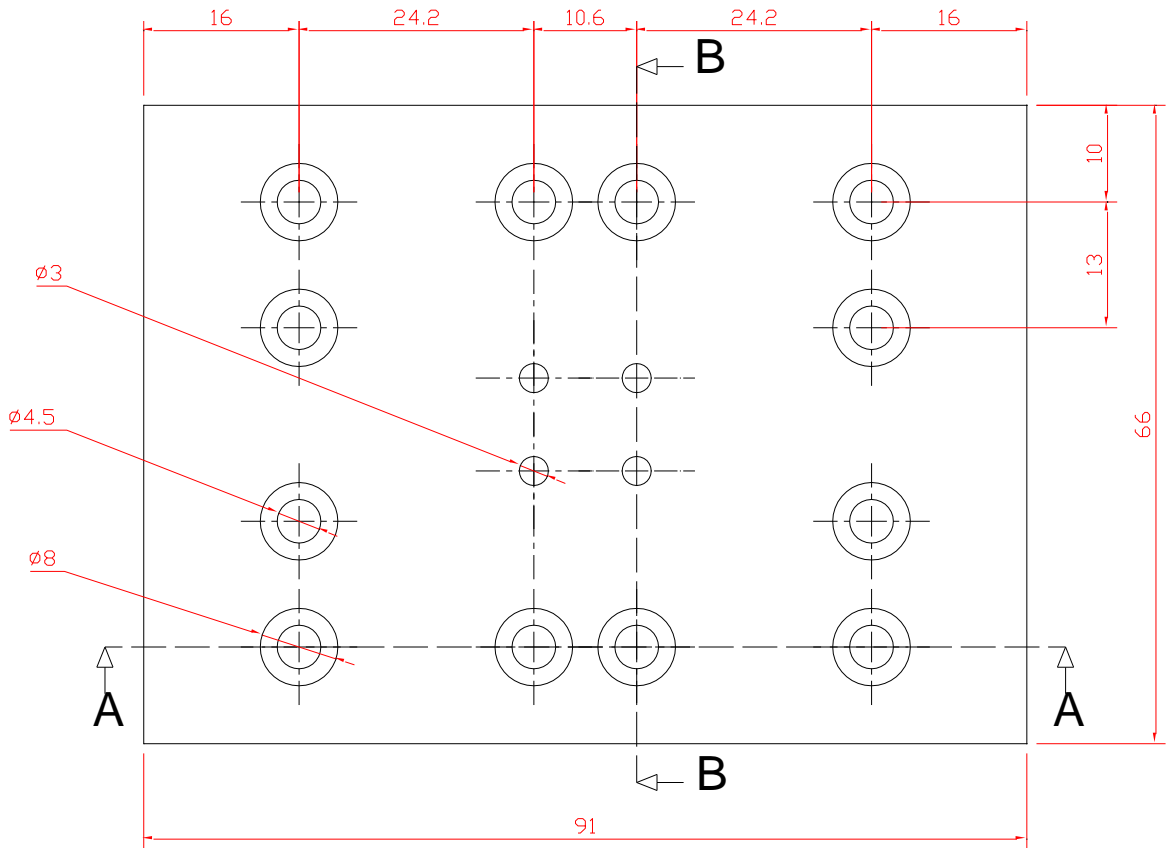
Section A-A



Title	Microchannel evaporator: Cover Plate
Unit	Millimetre
Material	Polycarbonate

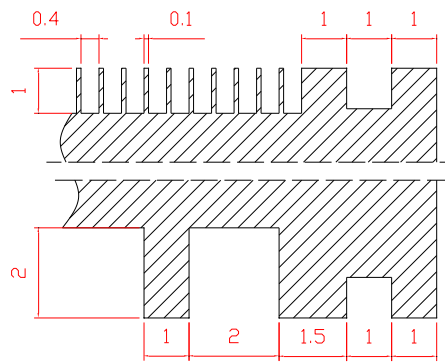
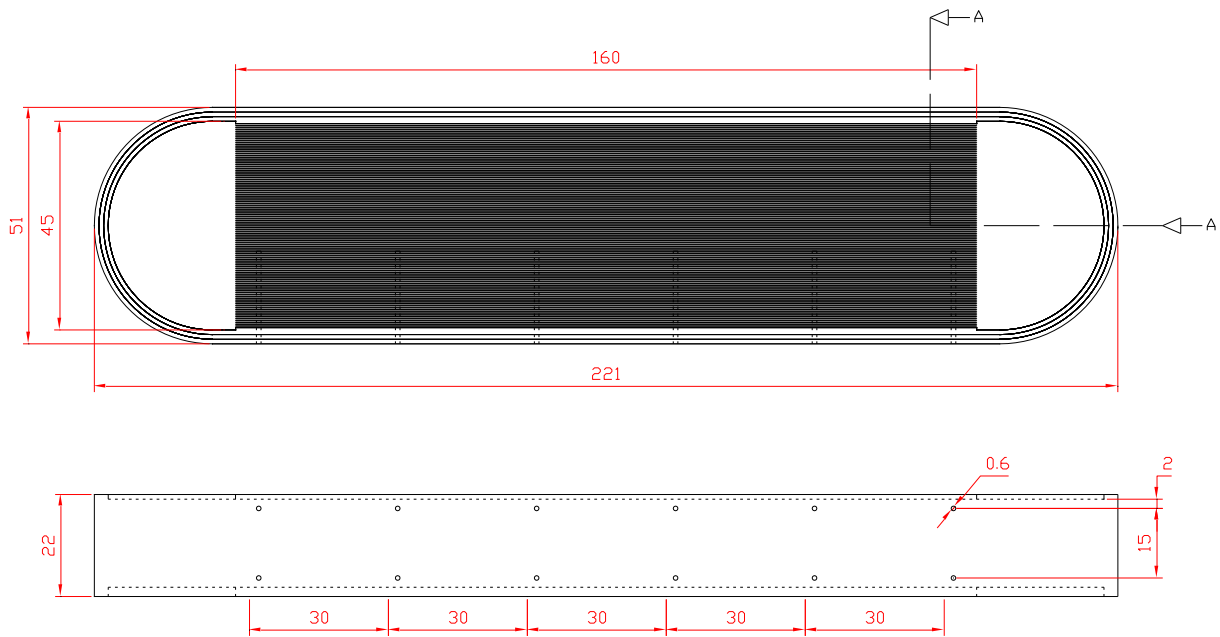


Section A-A



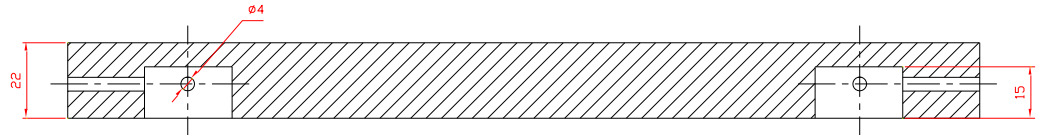
Section B-B

Title	Microchannel evaporator: Bottom Plate
Unit	Millimetre
Material	PTFE

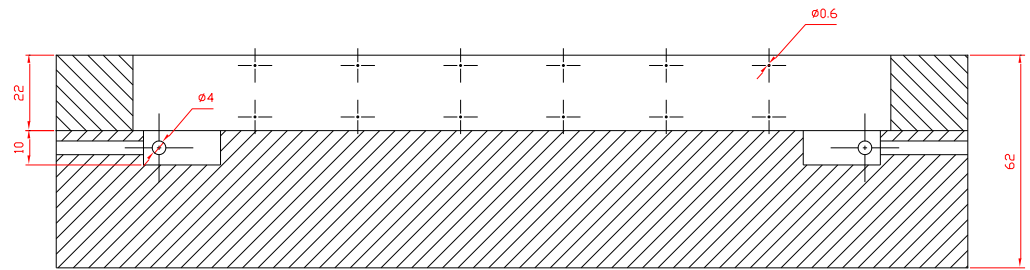
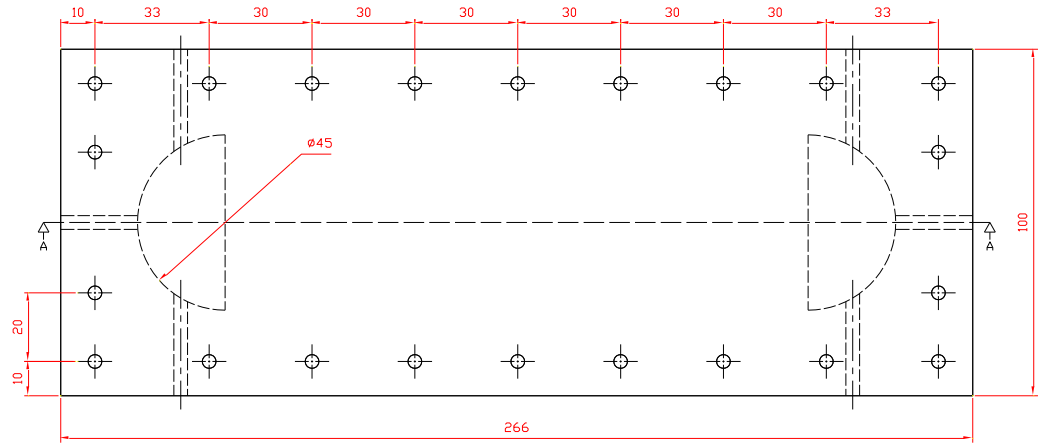


Section A-A

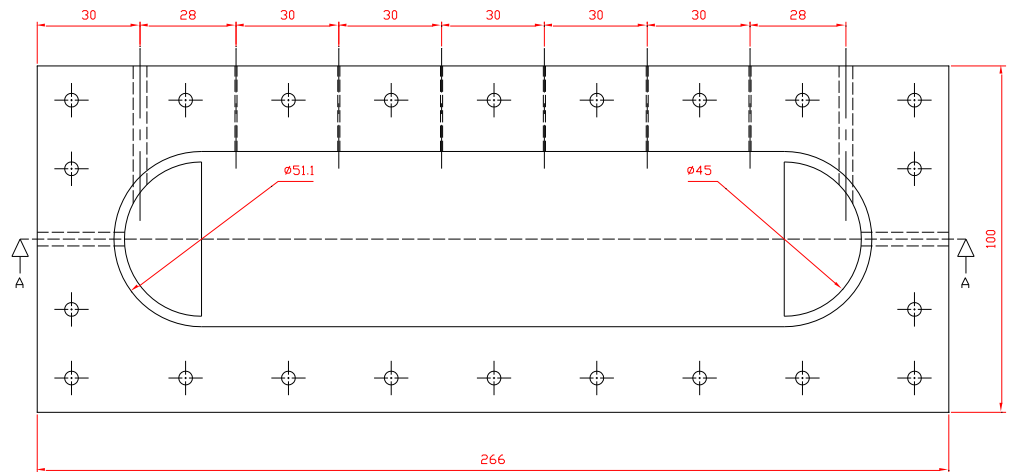
Title	Microchannel Condenser: Condenser Block
Unit	Millimetre
Material	Oxygen-free Copper



Section A-A

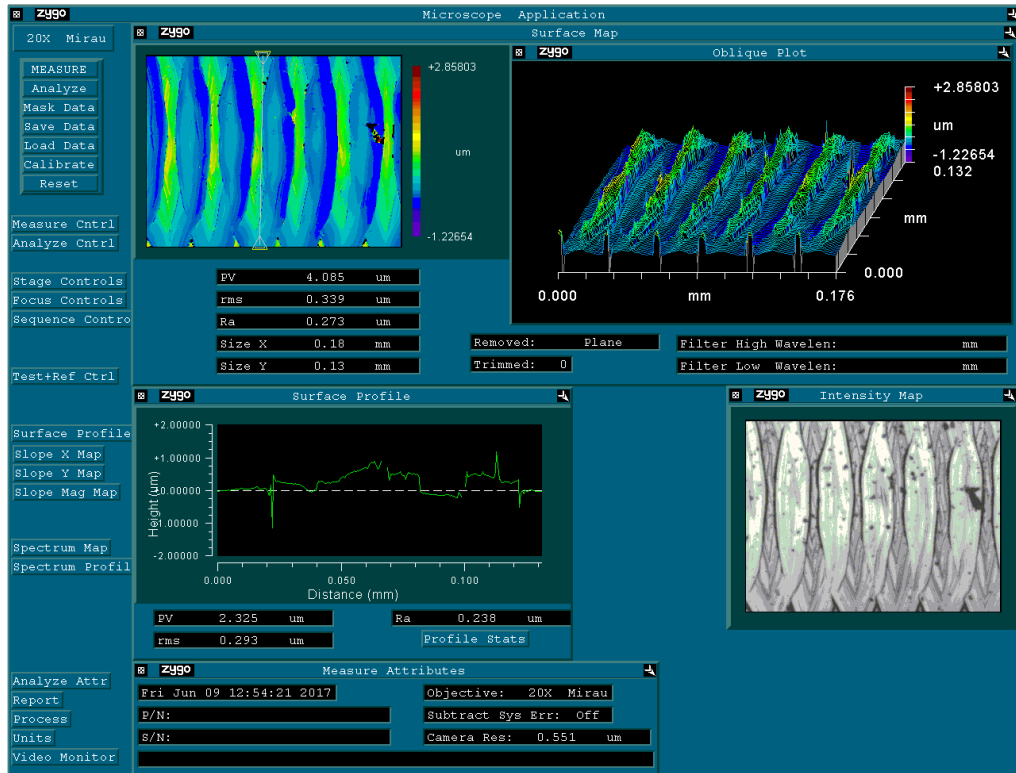


Section A-A

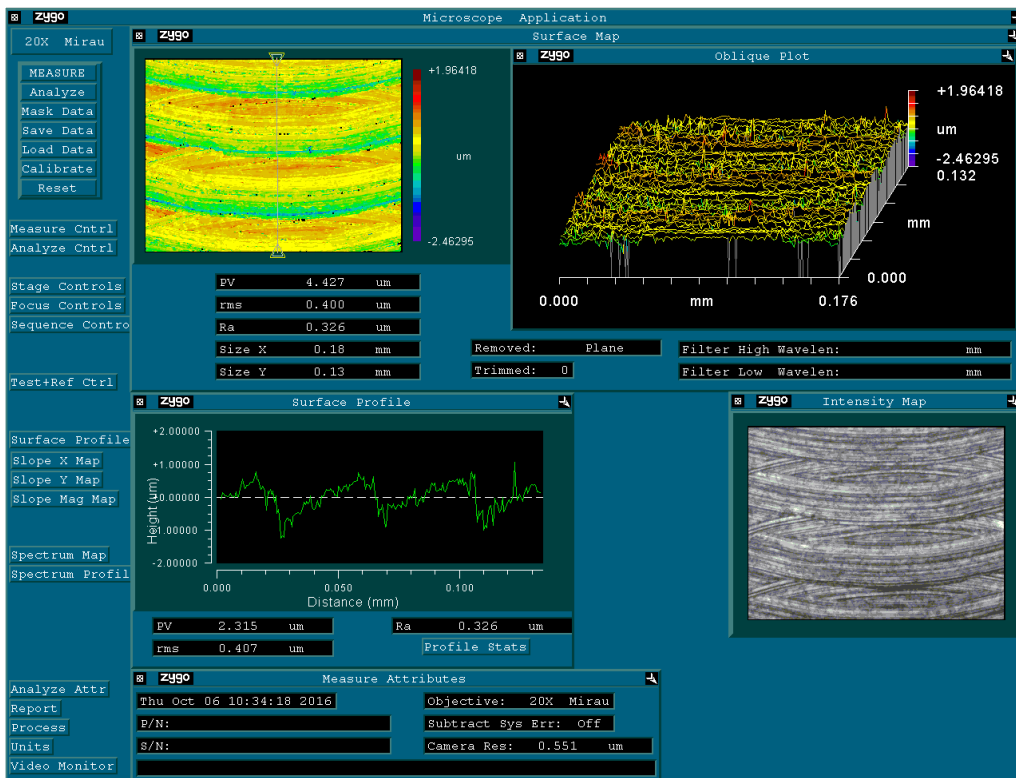


Title	Microchannel Condenser: Cover Plate and Housing
Unit	Millimetre
Material	Polycarbonate

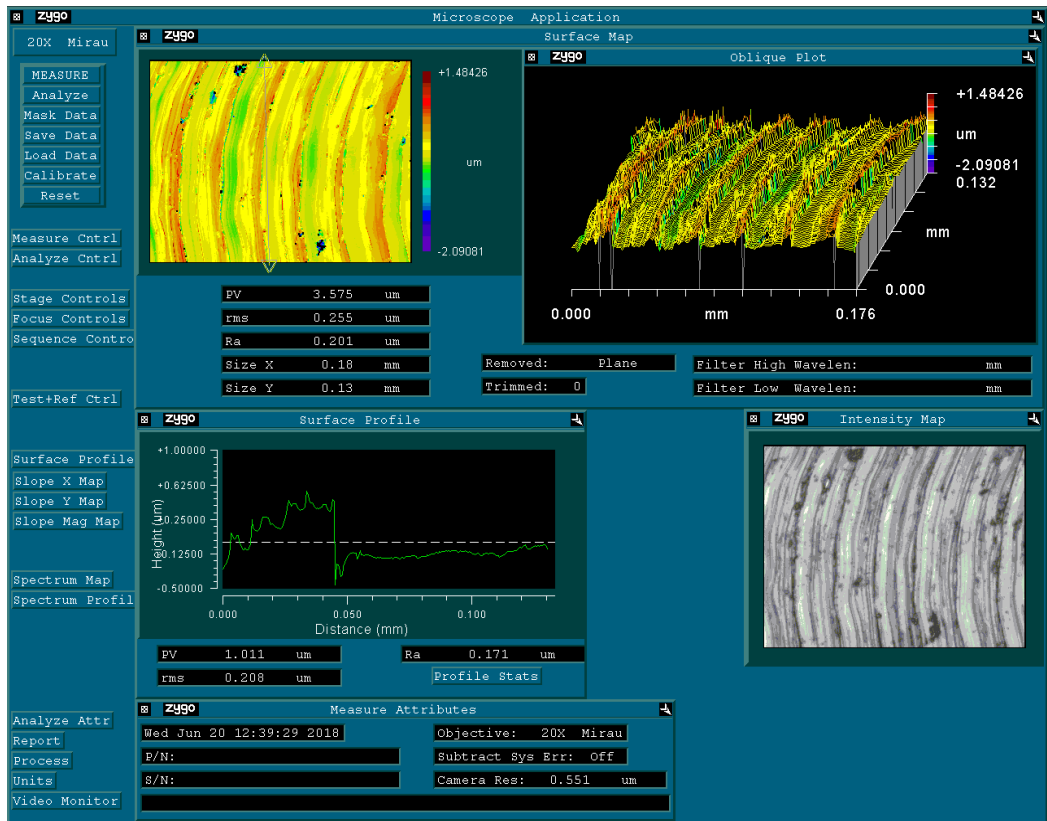
Appendix E Surface Characteristics by Zygo



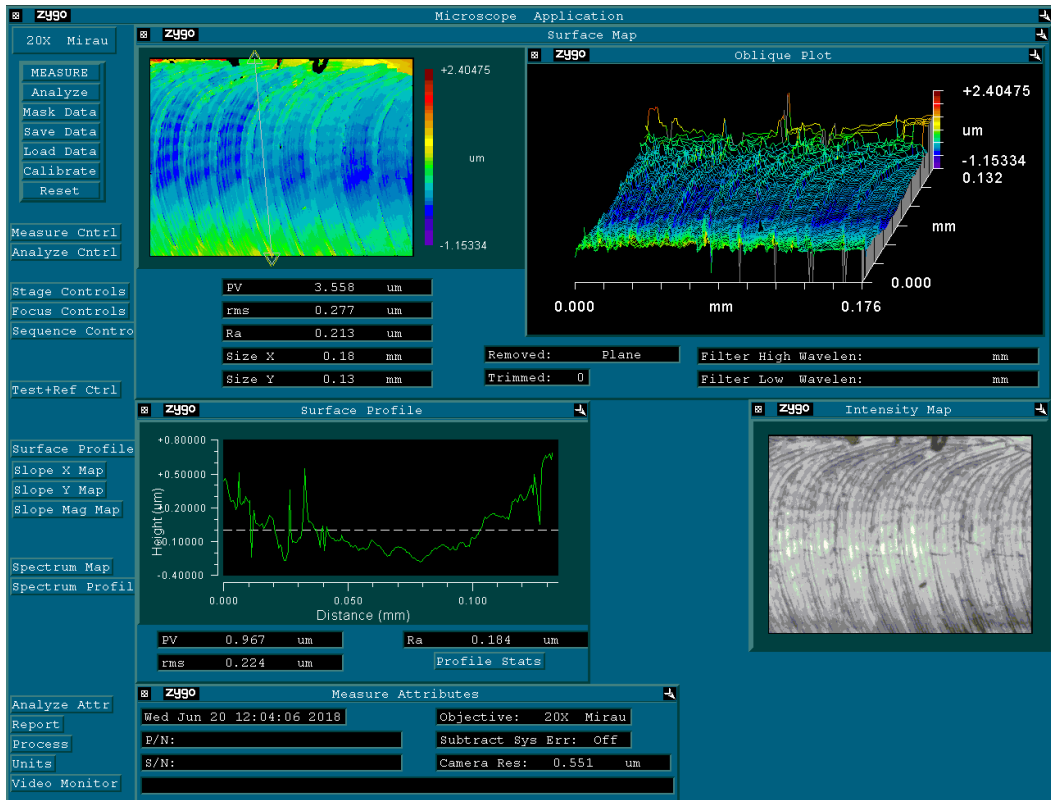
(a)



(b)



(c)



(d)

Figure C.1 Surface characteristics of: (a) TS.2 (b) TS.3 (c) TS.4 (d) TS.5.

Publications

A. Conference

1. Al-Zaidi, A.H., Karayiannis, T.G. and Mahmoud, M.M. (2017) 'Condensation heat transfer in microchannels', *15th UK Heat Transfer Conference*, London, UK, 4-5 September.
2. Al-Zaidi, A.H., Mahmoud, M.M. and Karayiannis, T.G. (2018) 'Flow boiling in microchannels with HFE-7100: Experimental results and comparison with correlations', *16th Int. Heat Transfer Conf. IHTC16*, China National Convention Center, Beijing, China, 10-15 August.
3. Al-Zaidi, A.H., Mahmoud, M.M. and Karayiannis, T.G. (2018) 'Flow boiling of HFE-7100 in multi-microchannels: aspect ratio effect', *6th Micro and Nano flows Conf.*, Atlanta, USA, 9-12 September.
4. Lee, V.Y.S., Al-Zaidi, A.H., Henderson, G., Karayiannis, T.G. (2019) 'Flow Boiling Results of HFE-7200 in a Multi-Microchannel Evaporator and Comparison with HFE-7100', *4th World Congress on Momentum, Heat and Mass Transfer (MHMT19)*, Rome, Italy, 10-12 April.

B. Journal

1. Al-Zaidi, A.H., Mahmoud, M.M., Karayiannis, T.G. (2018) 'Condensation flow patterns and heat transfer in horizontal microchannels', *Experimental Thermal and Fluid Science*, 90:153-173.
2. Al-Zaidi, A.H., Mahmoud, M.M., Karayiannis, T.G. (2019) 'Flow boiling of HFE-7100 in microchannels: experimental study and comparison with correlations', *International Journal of Heat and Mass Transfer*, 140:100-128.